# INORGANIC CHEMISTRY EDITOR'S PICK 2021

**EDITED BY: Luís D. Carlos**

**frontiers** Research Topics

## About Frontiers

Frontiers is more than just an open-access publisher of scholarly articles: it is a pioneering approach to the world of academia, radically improving the way scholarly research is managed. The grand vision of Frontiers is a world where all people have an equal opportunity to seek, share and generate knowledge. Frontiers provides immediate and permanent online open access to all its publications, but this alone is not enough to realize our grand goals.

## Frontiers Journal Series

The Frontiers Journal Series is a multi-tier and interdisciplinary set of open-access, online journals, promising a paradigm shift from the current review, selection and dissemination processes in academic publishing. All Frontiers journals are driven by researchers for researchers; therefore, they constitute a service to the scholarly community. At the same time, the Frontiers Journal Series operates on a revolutionary invention, the tiered publishing system, initially addressing specific communities of scholars, and gradually climbing up to broader public understanding, thus serving the interests of the lay society, too.

## Dedication to Quality

Each Frontiers article is a landmark of the highest quality, thanks to genuinely collaborative interactions between authors and review editors, who include some of the world's best academicians. Research must be certified by peers before entering a stream of knowledge that may eventually reach the public - and shape society; therefore, Frontiers only applies the most rigorous and unbiased reviews.
Frontiers revolutionizes research publishing by freely delivering the most outstanding research, evaluated with no bias from both the academic and social point of view. By applying the most advanced information technologies, Frontiers is catapulting scholarly publishing into a new generation.

## What are Frontiers Research Topics?

Frontiers Research Topics are very popular trademarks of the Frontiers Journals Series: they are collections of at least ten articles, all centered on a particular subject. With their unique mix of varied contributions from Original Research to Review Articles, Frontiers Research Topics unify the most influential researchers, the latest key findings and historical advances in a hot research area! Find out more on how to host your own Frontiers Research Topic or contribute to one as an author by contacting the Frontiers Editorial Office: frontiersin.org/about/contact

# INORGANIC CHEMISTRY EDITOR'S PICK 2021

Topic Editor:
**Luís D. Carlos,** University of Aveiro, Portugal

# Table of Contents

# Editorial: Inorganic Chemistry Editor's Pick 2021

*Luís D. Carlos[1]\**

[1]*Phantom-g, CICECO – Aveiro Institute of Materials, Department of Physics, University of Aveiro, Aveiro, Portugal*

**Editorial on the Research Topic**

**Inorganic Chemistry Editor's Pick 2021**

We are pleased to introduce the collection Inorganic Chemistry Editor's Pick 2021.

This collection showcases 19 manuscripts (including four review papers) from the past couple of years authored by scientists of distinct countries such as Australia, Chile, China, France, Germany, India, Iran, Italy, Pakistan, Poland, Portugal, Saudi Arabia, Switzerland, and United Kingdom. The collection aims to further support Frontiers' strong community by recognizing highly deserving authors. The selected manuscripts highlight the broad diversity of research performed across the section, including the synthesis and general characterization (e.g., structural, magnetic, optical) of coordination polymers and metal-organic frameworks (MOFs) and its application for sensing, nanoplates for supercapacitors, nanophosphors for upconversion and the dielectric properties of carbon nanotubes, for instance. The review manuscripts encompass the biomolecular modification of MOFs, bulk and nano metal oxysulfides, rhenium complexes as probes for prokaryotic and fungal cells, and atomistic simulations of rare-earth orthophosphates.

All research presented here illustrates strong advances in experiments, theory, and *in silico* with applications to compelling problems aiming to put a spotlight on the main areas of interest for the section.

## AUTHOR CONTRIBUTIONS

The author confirms being the sole contributor of this work and has approved it for publication.

**Conflict of Interest:** The author declares that the research was conducted in the absence of any commercial or financial relationships that could be construed as a potential conflict of interest.

# The Quantification of Radiation Damage in Orthophosphates Using Confocal μ-Luminescence Spectroscopy of Nd³⁺

*Christoph Lenz[1,2]\*, Gordon Thorogood[1], Robert Aughterson[1], Mihail Ionescu[1], Daniel J. Gregg[1], Joel Davis[1] and Gregory R. Lumpkin[1]*

[1] *Australian Nuclear Science and Technology Organisation, Sydney, NSW, Australia,* [2] *Institut für Mineralogie und Kristallographie, Universität Wien, Vienna, Austria*

In this study, we present a new concept based on the steady-state, laser-induced photoluminescence of $Nd^{3+}$, which aims at a direct determination of the amorphous fraction $f_a$ in monazite- and xenotime-type orthophosphates on a micrometer scale. Polycrystalline, cold-pressed, sintered $LaPO_4$, and $YPO_4$ ceramics were exposed to quadruple Au-ion irradiation with ion energies 35 MeV (50% of the respective total fluence), 22 MeV (21%), 14 MeV (16%), and 7 MeV (13%). Total irradiation fluences were varied in the range $1.6 \times 10^{13}$–$6.5 \times 10^{13}$ ions/cm². Ion-irradiation resulted in amorphization and damage accumulation unto a depth of $\sim 5\,\mu m$ below the irradiated surfaces. The amorphous fraction created was quantified by means of surface-sensitive grazing-incidence X-ray diffraction and photoluminescence spectroscopy using state-of-the-art confocal spectrometers with spatial resolution in the μm range. Monazite-type $LaPO_4$ was found to be more susceptible to ion-irradiation induced damage accumulation than xenotime-type $YPO_4$. Transmission electron microscopy of lamella cut from irradiated surfaces with the focused-ion beam technique confirmed damage depth-profiles with those obtained from PL hyperspectral mapping. Potential analytical advantages that arise from an improved characterization and quantification of radiation damage (i.e., $f_a$) on the μm-scale are discussed.

Keywords: xenotime $YPO_4$, monazite $LaPO_4$, nuclear waste forms, rare-earth elements REE, luminescence spectroscopy, grazing-incidence X-ray diffraction, amorphous fraction, structural disorder

## INTRODUCTION

Orthophosphates of the $REE^{3+}[PO_4]^{-3}$ group (with REE = Rare-earth elements Sc,Y + Ln; Ln = lanthanides La to Lu) have gained much attention in the past few decades from the nuclear materials science community. Their potential use as inert matrix fuel or waste-form material to immobilize hazardous actinides (e.g., U, Th, Pu, Np, Cm, Am) and fission products from high-level radioactive (HLW) wastes have been proposed in various studies (e.g., Boatner et al., 1980; Ewing and Wang, 2002; Lumpkin, 2006; Omel'yanenko et al., 2007; Weber et al., 2009; Burakov et al., 2011; Neumeier et al., 2017; Schlenz et al., 2018). The high structural flexibility of these compounds is one of their major advantages with respect to the latter purpose (Dacheux et al., 2013). At ambient conditions and depending on the

radius of the REE cation, endmembers of this phosphate group either crystallize in the monoclinic monazite-structure type (La to Gd; space-group P2$_1$/n) with 9-fold, or the tetragonal zircon-type structure (Gd to Lu, including Sc and Y; space-group I4$_1$/amd) with 8-fold cationic coordination, whereas Gd-, Tb-, Dy-, and Ho-endmembers have been synthesized with both structure types (Ni et al., 1995; Kolitsch and Holtstam, 2004; Clavier et al., 2011). Orthophosphates of both structure types, however, have been reported to show a wide miscibility among their endmembers and the monazite structure has the ability to accommodate large amounts of the trivalent actinides Pu, Am, and Cm (Clavier et al., 2011 and references therein). The trivalent neutron absorber Gd can be accommodated easily in the crystal structure to control the criticality of radioactive chain-reactions at high actinide loadings. Heterovalent substitutions by mono-, di-, and tetravalent elements on cation sites are possible via vacancy, double or coupled charge-balanced substitutions. The latter substitution mechanisms are of major importance to accommodate Th$^{4+}$, U$^{4+}$, and other minor tetravalent actinides in the crystal structure of the orthophosphates (Clavier et al., 2011; Schlenz et al., 2018). Leaching experiments in static as well as dynamic experiment setups, performed to assess the ability of potential nuclear waste-form materials to retain structurally incorporated actinides upon leaching, reveal that orthophosphates have comparably low dissolution rates in hydrous and acidic media (Boatner and Sales, 1988; Tropper et al., 2011; Arinicheva et al., 2018; Gausse et al., 2018). A crucial factor that is generally considered to determine the long-term integrity of waste-form materials is their resistance against damage as caused by (self-)irradiation. The accumulation of radiation-induced damage in crystalline material is usually accompanied with reduced chemical durability and physical integrity, swelling and crack formation (Ojovan et al., 2018 and references therein). The interest in monazite-type compounds to be used as radiation-resistant fuel or waste-form material was substantially supported from findings of their natural analogs. The mineral monazite-(Ce) typically shows only moderate radiation damage accumulation, but to the best of our knowledge never has been found in an amorphous structural state. This is despite containing significant Th and U concentrations, which should have caused substantial accumulation of α-decay-induced radiation damage over geological periods of time (e.g., Boatner and Sales, 1988; Seydoux-Guillaume et al., 2004; Ruschel et al., 2012; Nasdala et al., 2018). The enhanced "radiation tolerance" in comparison to other accessory minerals like zircon (ZrSiO$_4$), which is frequently found to be strongly damaged or metamict, have been attributed to self-annealing at comparably low temperatures. An effective accumulation of radiation damage is largely controlled by temperature-dependent kinetic effects (e.g., point-defect annealing, epitaxial recrystallization at crystalline-amorphous interfaces, recrystallization by nucleation) that may lead to simultaneous or post-damage recovery of the orthophosphates crystallinity (e.g., Nasdala et al., 2013). In comparison to zircon, exceptionally low critical amorphization temperatures T$_c$ of REEPO$_4$ orthophosphates have been identified by *in-situ* TEM (transition electron microscopy) ion-irradiation experiments (Meldrum et al., 1997a, 1998).

Monazite-type phosphates have been found to have lower T$_c$ (i.e., are more efficiently annealed) than phosphates with xenotime structure. Within the respective orthophosphate groups, T$_c$ decreases systematically with increasing cationic radius (i.e., decreasing atomic mass) to be as low as 60°C for monazite-(La) (Meldrum et al., 1997a). Notably, Helean et al. (2004) found a linear positive correlation of T$_c$ with the formation enthalpies ΔH$_{f-ox}$ of the orthophosphate members, respectively. Thus, within the orthophosphate group, monazite-type LaPO$_4$ is most thermodynamically stable with respect to its oxides (ΔH$_{f-ox}$ ∼-350 kJ/mol) and most efficient to anneal (T$_c$ = 60°C), whereas xenotime-type LuPO$_4$ is the least stable member (ΔH$_{f-ox}$ ∼-260 kJ/mol) and is annealed most inefficiently (T$_c$ = 300°C). The annealing behavior of zircon fits well into the latter correlation. A comparably high T$_c$ (1065°C; Meldrum et al., 1998) and a much lower thermodynamic stability (ΔH$_{f-ox}$ = −28 kJ/mol; Ellison and Navrotsky, 1992) have been reported for zircon. The thermodynamic driving force to anneal radiation damage in zircon, hence, is much lower in comparison to the orthophosphates and may explain that annealing effects are more effective in the orthophosphates at lower temperatures. In addition to annealing effects as caused by elevated temperatures, α-particle induced annealing has been discussed recently to explain the absence of severe radiation damage of actinide-bearing orthophosphates stored at ambient (geo-)thermal conditions (Deschanels et al., 2014; Seydoux-Guillaume et al., 2018). For instance, single-phase $^{238}$Pu-doped La-monazite (Burakov et al., 2004; Deschanels et al., 2014; Shiryaev et al., 2016; Zubekhina and Burakov, 2016) or $^{244}$Cm-doped Lu-xenotime (Luo and Liu, 2001) stored under ambient conditions remained crystalline even at very high self-irradiation doses. On the other hand, however, monazite-type $^{241}$AmPO$_4$ (Deschanels et al., 2014) and $^{238}$PuPO$_4$ (Burakov et al., 2004) underwent metamictization at lower or comparable doses.

Studies that aim at an improved understanding of complex radiation-damage accumulation processes substantially benefit from an accurate quantification of the radiation damage present in the material of interest (e.g., Weber, 2000; Lang et al., 2009; Thomé et al., 2012; Liu et al., 2016). However, a quantitative determination of the amorphous fraction, i.e., the fraction of the material that underwent severe structural degradation, and the analytical access to effects caused by damage accumulation is very limited on the micrometer scale. The interpretation of diffuse scattering (as caused by the presence of amorphous material) in TEM investigations typically remains of qualitative nature and reliable estimates of the amount of damage present based on XRD techniques are restricted to monophase, bulk materials (e.g., Ríos et al., 2000; Lang et al., 2009). Rutherford backscattering and channeling (RBS/C) experiments give detailed information on the amount of displaced atoms, but are restricted to the characterization of radiation-damage accumulation in ion-irradiation experiments as non-damaged, crystalline starting material is needed for a quantitative interpretation (e.g., Thomé et al., 2012). In recent years, confocal spectroscopic techniques that operate on the micrometer scale, including Raman (e.g., Nasdala et al., 1995, 2010; Geisler et al., 2001; Picot et al., 2008; Shimizu and Ogasawara, 2014; Wang et al.,

2014; Marillo-Sialer et al., 2016; Švecová et al., 2016; Baughman et al., 2017; Váczi and Nasdala, 2017; Zietlow et al., 2017) and luminescence spectroscopy (Panczer et al., 2012; Nasdala et al., 2013, 2018; Lenz and Nasdala, 2015) are applied frequently to characterize and estimate the degree of irradiation damage in orthophosphates and other accessory minerals. The latter techniques are based upon a correlation of spectral changes with structural modifications (i.e., band width broadening of narrow peaks) associated with radiation damage accumulation. Their applicability for a quantitative manner, however, is limited and hampered by a lack of reference samples of known amorphous fraction $f_a$ or $\alpha$-dose. For reasons discussed above, natural orthophosphate minerals do not serve as reliable references because of the insufficient knowledge of the samples annealing history. The damage characterized at present state, hence, cannot be correlated with its theoretically calculated $\alpha$-dose, which gives the number of $\alpha$-decays of a certain concentration of Th and U within the geological time span since its formation. For zircon, this problem has been addressed and discussed extensively (Geisler et al., 2001; Nasdala et al., 2001, 2010; Palenik et al., 2003; Lenz and Nasdala, 2015).

In the present study, we address the question of whether the analytical advantages of confocal spectroscopy can be combined with the possibility to quantitatively determine the amorphous fraction of radiation-damaged orthophosphates directly from single confocal luminescence spectroscopic measurements. To test this, we systematically accumulated radiation damage in polycrystalline, monophase $LaPO_4$ and $YPO_4$ ceramics using heavy ion-irradiation (Au) with various energies and fluences. The amount of structural breakdown, i.e., the amorphous fraction $f_a$ created in the surface region of the irradiated ceramics, was then quantified using grazing-incidence X-ray diffraction (GI-XRD) and compared with results from confocal laser-induced photoluminescence spectroscopy of $Nd^{3+}$. The orthophosphates are well-known for its excellent luminescence properties and have been proposed variously as effective phosphor pigments (e.g., Ropp, 1968; Gavrilović et al., 2018) or laser material (e.g., Guillot-Noël et al., 2000). In this study, however, we took advantage of the REEs unique spectroscopic properties to serve as structural probes of their local crystallographic environment (e.g., Bünzli and Piguet, 2005; Mendoza et al., 2011; Lenz et al., 2013). Emissions of $Nd^{3+}$ have been favored among other potential REE probes here because its $^4F_{3/2} \rightarrow {}^4I_{9/2}$ electronic transition in the near-infrared (NIR) spectral range between 10,600 and 11,800 $cm^{-1}$ (830–940 nm) is effectively excited in orthophosphates by standard steady-state lasers (e.g., $Ar^+$ −488 nm, 514 nm; $YAG:Nd^{3+}$ −532 nm; or diode pumped solid-state IR −785 nm) even at very low Nd concentrations in the ppm range. Moreover, the $Nd^{3+}$ ($^4F_{3/2} \rightarrow {}^4I_{9/2}$) emission is typically characterized by a small number of individual sublevels that simplifies data reduction (i.e., fitting/deconvolution). Other competitive luminescence emissions of $REE^{3+}$ in the respective spectral range are rare and hence do not interfere with interpretation of the $Nd^{3+}$ spectral signal (Lenz et al., 2013; Chen and Stimets, 2014). Moreover, Nd is commonly applied as non-hazardous surrogate in studies of actinide crystal chemistry of waste-form materials. Because of the

high radioactivity and toxicity of e.g., Am, Cm, that are difficult to handle in standard laboratories, surrogates of similar chemical properties and behavior are applied frequently (e.g., Loiseau et al., 2004; Neumeier et al., 2017).

## MATERIALS AND METHODS

Monophase phosphate powders of $LaPO_4$ and $YPO_4$ were produced using a wet-chemistry route. Oxide precursors ($La_2O_3$ and $Y_2O_3$; Sigma-Aldrich 99.95%) were dissolved in hot nitric acid and La- and Y-phosphate precipitates form, respectively, while dropwise adding an aqueous solution of $(NH_4)_2HPO_4$. The pH was carefully adjusted to 9–10 using $NH_3$ (aq.) to complete phosphate precipitation. To produce 100 g $YPO_4$ monophosphate powder, 61.4 g $Y_2O_3$ was dissolved in ~220 ml $HNO_3$ (3M) and 71.8 g $(NH_4)_2HPO_4$ dissolved in 150 ml de-ionized water was added. For preparation of $LaPO_4$ phosphate, 69.6 g $La_2O_3$ was dissolved in ~170 ml $HNO_3$ (3M) and 56.5 g $(NH_4)_2HPO_4$ dissolved in 150 ml de-ionized water was added to produce approximately 100 g of $LaPO_4$ precipitate. Note, that an excess of approx. 20% $HNO_3$ was needed to completely dissolve the respective precursor $REE_2O_3$ oxide. Dried precipitates were crushed with agate mortars, calcined at 800°C for 3 h, and ground in a zirconia-bead ball mill repeatedly to remove phosphate hydrates (Bregiroux et al., 2006; Sujith et al., 2014). Phosphate powders were then uniaxial cold-pressed to pellets of 10 mm diameter (steal die with a load of ~200 MPa) and sintered in the furnace at 1,300°C for 3 days. Sintered $YPO_4$ pellets were found to have a specific gravity of ~4.08 g/cm³ as obtained from weight measurements with a hydrostatic balance and applying Archimedes principle. The density obtained is about 95.3% of the theoretical density



**FIGURE 1 |** Simplified sketch (not to scale) that summarizes preparation and techniques as applied to orthophosphate ceramics in this study: (1) Polished ceramic pellets were irradiated with Au-ions sequentially with four different energies (see details in **Figure 2** and discussion in the text); (2) grazing-incidence X-ray diffraction (GI-XRD) was applied to characterize ion-irradiation induced damage in the uppermost surface layer. (3) Pellets were embedded in epoxy and prepared to cross-sectional mounts; (4) confocal laser-induced Photoluminescence (PL) spectroscopy and hyperspectral mapping; and (5) focused ion-beam preparation of TEM foils.

4.28 g/cm$^3$ given by Milligan et al. (1982). Accordingly, LaPO$_4$ pellets were determined to have a density of 4.56 g/cm$^3$, which is 89.8% of the calculated density of 5.08 g/cm$^3$ (Ni et al., 1995). The surfaces of ceramic pellets were polished using a Struers Tegramin preparation system with diamond suspension of various particle sizes (5–3 μm for coarse and 0.25 μm for fine polishing). A final chemical-abrasion procedure with colloidal silica (typical abrasive size is ∼0.05 μm) was applied to remove mechanically induced stress at the surface during mechanical polishing.

A graphical summary of analytical techniques and further preparation steps applied to LaPO$_4$ and YPO$_4$ ceramic pellets is given in **Figure 1**. Radiation damage was accumulated in the ceramics surface region utilizing irradiation of high energetic gold (Au) ions. Irradiation experiments were conducted using the 10 MV Tandem Van de Graaf, Australian National Tandem Research Accelerator (ANTARES) at ANSTO facility. Four different energies have been sequentially applied in the order highest to lowest energy (35, 22, 14, and 7 MeV). Picot et al. (2008), Nasdala et al. (2010), and Nasdala et al. (2018) have applied sequential triple ion-irradiations with the aim to create an extended, more homogeneous damage-depth profile in monazite-(Ce). We used the Monte Carlo simulation code SRIM-2013 (Stopping range of ions in matter; Ziegler et al., 2010) to calculate ion stopping-ranges and to pre-estimate damage accumulation as caused by the creation of displacements (full cascade mode). The rather high Au-ion energy of 35 MeV was chosen to produce a sufficiently large damage layer unto a depth of ∼5 μm below the ceramic surface that is accessible to a broad range of analytical techniques. The four sequential Au-ion energies and their respective fluences were adjusted to generate a homogeneous damage profile over the irradiation depth as expected from cumulative displacements predicted by SRIM. Based on these calculations, each quadruple irradiation comprises 50% of the total fluence being from 35 MeV Au-ions, 21% from 22 MeV, 16% from 14 MeV and 13% from 7 MeV Au-ions (cp. **Figure 2A**). We exposed five LaPO$_4$ and YPO$_4$ ceramic pellets, each to five different total fluences (1.6 × 10$^{13}$, 2.3 × 10$^{13}$, 3.5 × 10$^{13}$, 4.85 × 10$^{13}$ and 6.5 × 10$^{13}$ ions/cm$^2$). Detailed fluences of each energy applied may be found in **Table 1**. Note that the ceramic pellets were irradiated at room temperature, i.e., cooling of samples during irradiation has not been applied. Samples were mounted on an aluminum plate with conductive tape, and the sample temperature was measured using K-type thermocouple. Monitored maximum temperatures did not exceed a maximum temperature of 45°C.

Irradiated ceramics and un-irradiated references were examined by GI-XRD performed on a Bruker D8 A25 fitted with a Cu source. The diffractometer was configured for parallel beam geometry using a Goebel mirror (deflection 0.812°) and a parallel plate collimator with an equatorial divergence of 0.2°. The lynxeye detector was configured to run in 0D mode to act as a point detector measuring in the 2θ range from 25 to 80°. Multiple runs with variable incident angles were performed to access and probe various depths below the surface. Details on incident angles and geometry specific X-ray attenuation lengths after Henke et al. (1993) are given in **Table 2** and discussed in
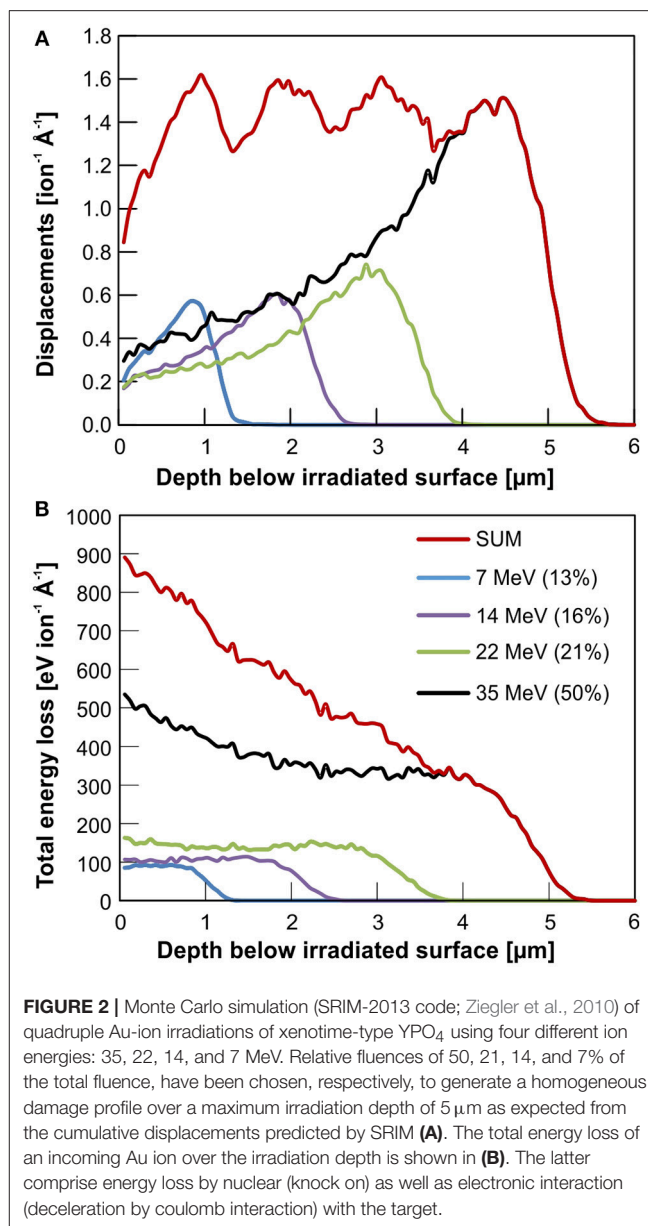


**FIGURE 2 |** Monte Carlo simulation (SRIM-2013 code; Ziegler et al., 2010) of quadruple Au-ion irradiations of xenotime-type YPO$_4$ using four different ion energies: 35, 22, 14, and 7 MeV. Relative fluences of 50, 21, 14, and 7% of the total fluence, have been chosen, respectively, to generate a homogeneous damage profile over a maximum irradiation depth of 5 μm as expected from the cumulative displacements predicted by SRIM **(A)**. The total energy loss of an incoming Au ion over the irradiation depth is shown in **(B)**. The latter comprise energy loss by nuclear (knock on) as well as electronic interaction (deceleration by coulomb interaction) with the target.

more detail below. Rietveld refinements were performed using Bruker AXS software package Topas Vers. 5.

After XRD investigation, ceramic pellets were cut in half, and one of each half was embedded in epoxy and prepared to cross-sectional mounts and again carefully polished (see polishing procedure above). Steady-state, laser-induced photoluminescence spectroscopic measurements were performed using a Horiba LabRam Evolution HR800 spectrometer coupled to an Olympus BX80 optical microscope. A confocal hole in the analyzing beam path reduces the spatial resolution to 1 μm lateral and ∼2–3 μm in depth using a 100× objective. Here, we used a 532 nm frequency-double YAG:Nd$^{3+}$ solid-sate laser with the beam path aligned through the microscope objective (quasi-backscattering configuration) to

**TABLE 1 |** Detailed Au-irradiation plan as applied to $YPO_4$ and $LaPO_4$ ceramics.

| Samples | | Individual fluences of ion energies applied [ions/cm$^2$] | | | | Total fluence [ions/cm$^2$] |
|---|---|---|---|---|---|---|
| YPO$_4$ | LaPO$_4$ | 35 MeV (50%) | 22 MeV (21%) | 14 MeV (26%) | 7 MeV (13%) | Sum (100%) |
| d0 | e0 | 0 | 0 | 0 | 0 | 0 |
| d1 | e1 | $8.00 \times 10^{12}$ | $3.36 \times 10^{12}$ | $2.56 \times 10^{12}$ | $2.08 \times 10^{12}$ | $1.6 \times 10^{13}$ |
| d2 | e2 | $1.15 \times 10^{13}$ | $4.83 \times 10^{12}$ | $3.68 \times 10^{12}$ | $2.99 \times 10^{12}$ | $2.3 \times 10^{13}$ |
| d3 | e3 | $1.75 \times 10^{13}$ | $7.35 \times 10^{12}$ | $5.60 \times 10^{12}$ | $4.55 \times 10^{12}$ | $3.50 \times 10^{13}$ |
| d4 | e4 | $2.43 \times 10^{13}$ | $1.02 \times 10^{13}$ | $7.76 \times 10^{12}$ | $6.31 \times 10^{12}$ | $4.85 \times 10^{13}$ |
| d5 | e5 | $3.25 \times 10^{13}$ | $1.37 \times 10^{13}$ | $1.04 \times 10^{13}$ | $8.45 \times 10^{12}$ | $6.50 \times 10^{13}$ |

*Ceramic pellets were irradiated with Au-ions of four different energies in the order 35, 22, 17, and 7 MeV at fixed proportions, but with variable total fluences. A quadruple Au-irradiation was chosen to produce a homogeneous damage profile over a maximum irradiation depth of 5 μm as expected from the cumulative displacements predicted by SRIM (cp.* **Figure 2**).

**TABLE 2 |** Detailed data of accumulated radiation damage in xenotime-type $YPO_4$ ceramics of various depths below the irradiated surface as obtained from the two independent methods grazing-incidence X-Ray diffraction and laser-induced photoluminescence (Nd$^{3+}$).

| YPO$_4$ sample | Fluence [ions/cm$^2$] | Amorphous fraction $f_a$ from GI-XRD data | | | | Amorphous fraction $f_a$ from PL data* | | | |
|---|---|---|---|---|---|---|---|---|---|
| | | Incident angle [°] | 0.5 | 1.1 | 2.1 | 3.2 | | | |
| | | Attenuation length$^§$ [μm] | 0.25 | 0.50 | 1.00 | 1.50 | Depth [μm] | 1.5 | 2.5 | 5.0 |
| d0 | 0.00 | | 0% | 0% | 0% | 0% | | 0% | 0% | 0% |
| d1 | $1.60 \times 10^{13}$ | | 83% | 78% | 75% | 69% | | 72% | 66% | 47% |
| d2 | $2.30 \times 10^{13}$ | | 92% | 89% | 87% | 89% | | 88% | 85% | 68% |
| d3 | $3.50 \times 10^{13}$ | | 86% | 81% | 78% | 72% | | 69% | 60% | 38% |
| d4 | $4.85 \times 10^{13}$ | | 93% | 87% | 85% | 80% | | 78% | 73% | 54% |
| d5 | $6.50 \times 10^{13}$ | | 97% | 95% | 94% | 90% | | 85% | 80% | 63% |

$^§$*Approximate probing depths of X-rays at given incident angles and their attenuation lengths were calculated after* Henke et al. (1993).

**The amorphous fraction $f_a$ is obtained from PL hyperspectral profiles across the irradiation-damaged surface. Multiple data points were (i) averaged unto distinct depths specified, and (ii) averaged among different profiles of various grains. See detailed discussion in the text. An error of ±5% is accepted to represent statistical variation.*

non-resonantly excite Nd$^{3+}$ emissions that are most prominent in the orthophosphates (Lenz et al., 2013). Photoluminescence spectra in the NIR range were recorded using a grating with 600 lines/mm with a spectral resolution determined to be ∼2 cm$^{-1}$. Hyperspectral maps and transection profiles were obtained using a mechanic, software-controlled x-y table. Note, however, that although the lateral spatial resolution is limited to 1 μm, an over-stepping with step-widths of 0.2–0.5 μm was applied to maps and profiles to improve data and image quality.

Scanning electron microscopy (SEM) was performed using a Zeiss Ultra Plus Gemini equipped with an X-Max silicon drift detector Energy Dispersive X-Ray spectrometer (EDX). Specimen preparation for TEM was carried out using a Zeiss Auriga 60—focused ion beam (FIB) with Ga source. A 20 × 2 μm rectangular layer of protective platinum was deposited on the sample to protect the surface from the ion beam. Coarse milling of a trapezoidal shaped trench was performed on both sides of this platinum layer at 30 kV and 16 nA and then a rectangular shaped cut is done 1.5° off axis using a Ga beam with 30 kV and 2 nA to reduce the thickness of the lamella before lift-out. A "u" cut is then performed at shallow tilt angle in order to free the bottom and sides of the lamella. The lamella is lifted out *in situ* using an OmniProbe 200 nanomanipulator system and welded onto a TEM copper grid for further thinning and polishing inside the

FIB. The polishing process involves positioning the lamella 0.5° off the axis of the ion beam on each side starting with a 30 kV and 1 nA, followed by a 30 kV and 120 pA ion probe thinning. Further fine thinning of the foils is done with 15 kV and 80 pA ion probe at 3° off axis to remove the damage created by the 30 kV gallium ions. Final polishing is done with a 5 kV 20 pA ion probe at 3° off axis and a long polish in deposition mode at 2 kV and 20 pA at 6° off axis milling to remove any further damage created by the higher energy gallium ions in previous steps. Thin TEM foils (with a final thickness <200 nm) of selected ceramics were prepared perpendicular to the irradiated surface of cross-sectioned ceramic samples. This was done to guarantee that complete irradiation-induced damage profiles of ∼5 μm length are accessible to TEM within a single foil (cp. **Figures 1**, **6A**).

Transmission electron microscopy was carried out using a JEOL 2200FS operated at 200 kV. Specimen analysis of the cross-sectional damage depth profile was performed using bright-field and dark-field images. Lower magnification images were collected using a Gatan Orius SC200 D camera, whilst higher resolution images were collected on a Gatan UltraScan 1000. Selected area electron diffraction patterns (SADP) were collected using an aperture of approximately 600 nm diameter. Multiple SADPs were collected along the samples damage profile from the irradiated surface to the crystalline sub-surface in 0.5 μm steps.

The Gatan Microscopy software-package DigitalMicrograph was used for image and diffraction pattern analysis.

## RESULTS AND DISCUSSION

As revealed by optical microscopy (OM) and SEM investigation, sintering of LaPO$_4$ and YPO$_4$ cold-pressed pellets at 1,300°C for 3 days caused effective compaction and considerable grain growth with grain dimension of 1–10 μm and even larger grains up to 20 μm in case of YPO$_4$ (cp. OM images in **Figure 7**). The phase structure was confirmed using GI-XRD. Rietveld refinement of XRD patterns revealed lattice constants in accordance to values reported in literature (YPO4: a = 6.88 Å, c = 6.01Å, cp. Milligan et al., 1982; LaPO4: a = 6.83 Å, b = 7.07, c = 6.50, β = 103.2°, cp. Ni et al., 1995). Pores appear occasionally in between grain boundaries that cause ceramics to have a lower density in comparison to theoretical values (theoretical calculated porosity of 4.7% in YPO$_4$ and 10.2% in LaPO$_4$ ceramics; see materials description in section Methods and Materials). A secondary, very minor phase was observed in YPO$_4$ ceramics filling pendentives of large-grains. This phase, however, was found to be rich in Zr, contains no P (EDX) and show brighter contrast in SEM and reflectance in OM. We interpret this phase to be zirconia as introduced by milling with zirconia beads during preparation process. A minor XRD reflection at 2θ ∼30° in XRD patterns of YPO$_4$ ceramics (**Figure 2A**) may arise from this phase which was potentially formed during sintering by reaction of ZrO$_2$ with omnipresent Y to tetragonal Y-stabilized zirconia (Y-TZP; Strasberg et al., 2014).
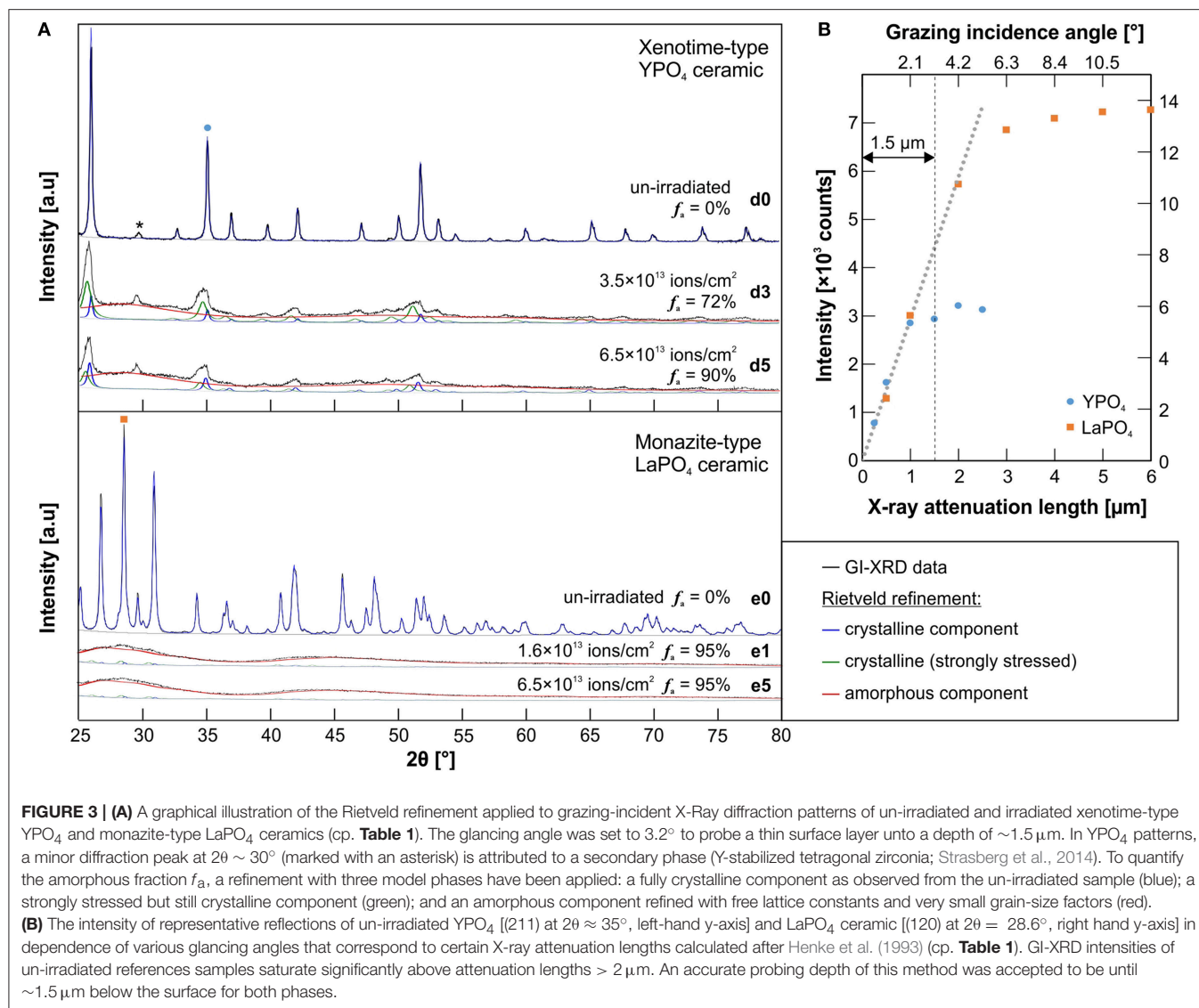
To establish the limits of the GI-XRD probing depth, un-irradiated reference samples of both, LaPO$_4$ and YPO$_4$ ceramics were examined in detail. Diffraction patterns obtained by using various grazing angles, which correspond to certain calculated X-ray attenuation lengths (Henke et al., 1993), were compared. In **Figure 3B**, the intensity of major reflection peaks of both ceramic references are plotted against the X-ray attenuation lengths as calculated from the respective incident angles. The higher the incident angle of the X-ray beam is set, the deeper it may penetrate into the material. In practice, the probing depth is limited effectively by the materials specific X-ray absorption, geometrical constraints, and measurement specific analytical conditions (e.g., type of X-ray source and respective energy). The incident angle above which the intensity of diffraction peaks does not increase any further is interpreted to reflect the maximum probing depth. Intensities of un-irradiated references saturate significantly at attenuation lengths >2 μm (**Figure 3B**). Hence, a probing volume that reaches a depth unto ∼1.5 μm was accepted to most reliably be characterized with GI-XRD. This corresponds to an instrument set-up with the X-ray beam set to an incident angle of max. 3.2° for both phases.

The effect of quadruple ion-irradiation on the structural state of irradiated xenotime-type YPO$_4$ and LaPO$_4$ ceramics and its GI-XRD patterns is demonstrated in **Figure 3A**. Irradiations of Au onto YPO$_4$ with total fluences of 3.5 × 10$^{13}$ (d3) and 6.5 × 10$^{13}$ ions/cm$^2$ (d5) caused diffraction peaks to significantly decrease and broaden, together with broad humps that appear across the entire diffraction pattern in the background. The latter contribution to the diffraction pattern is considered to arise from diffuse scattering of X-rays from the surface layer that is altered by ion-irradiation, lost long-range order, and hence, represents the amorphous component in the analyzed volume fraction. Note, however, that remnant YPO$_4$ diffraction peaks broadened asymmetrically with a shift to lower 2θ, and hence, indicate increasing lattice planes *d* and swelling of the unit cell. This is a common effect accompanied with radiation damage accumulation in ceramic materials (e.g., Trachenko et al., 2002; Deschanels et al., 2014). In contrast to YPO$_4$, GI-XRD patterns of all irradiated LaPO$_4$ ceramics are characterized by the presence of broad humps only. Almost complete amorphization of the irradiated surface was detected even at the lowest irradiation fluence applied (1.6 × 10$^{13}$ ions/cm$^2$; see LaPO$_4$ sample e1 in **Figure 3A**).

To properly quantify the degree of amorphization in the irradiated surface layer, we applied a Rietveld refinement using three chemically identical, but structurally different model phases that are deduced from the reference structure model and considered to persist simultaneously in the ion-irradiated ceramics: (i) fully crystalline remnants that are identical to the un-irradiated references, (ii) a strongly stressed and disrupted, but still crystalline component that is modeled with carefully adjusted lattice constants and grain size factors to account for substantial peak broadening and shifting, and (iii) the amorphous component modeled with unrealistic, freely refined lattice constants and very low grain size factors to represent the broad humps that underlay remnant diffraction peaks. Note, however, that a general background correction applied to GI-XRD patterns of irradiated ceramics was adopted from the un-irradiated reference and assumed to be comparable due to the very same analytical measurement conditions. Graphical representations of refinement results are given in **Figure 3A**. The amorphous fraction $f_a$ of the irradiated YPO$_4$ ceramics as quantified from GI-XRD Rietveld refinement is denoted and further summarized in **Table 2** for various incident angles (i.e., probing depths). All five irradiated monazite-type LaPO$_4$ pellets are characterized by strong accumulation of radiation damage in the surface layer. All of the irradiated LaPO$_4$ ceramics gave similar patterns with broad humps and almost no remnant diffraction peaks. An equivalent Rietveld refinement as applied to YPO$_4$, yielded a very high amorphous fraction of 95 ± 5% (see again **Figure 3A**).

Laser-induced photoluminescence of Nd$^{3+}$ ($^4F_{3/2} \rightarrow {}^4I_{9/2}$) in monazite and xenotime-type orthophosphate ceramics was effectively excited with a 532 nm laser. Sufficient signal intensity in the spectral range 11,800–10,600 cm$^{-1}$ (∼ 830–940 nm) was obtained in high-confocal measurement mode that permits the probing volume to be reduced to a few μm$^3$. Note that the orthophosphates were not doped with additional Nd during their preparation process. Trace impurities of Nd in the precursor Y and La-oxides were sufficient to obtain its very sensitive PL. The impact of heavy-ion irradiation-induced structural disorder on the emission of Nd$^{3+}$ is exemplified in **Figures 4**, **5**. They show hyperspectral images of the cross-sectional damage profile of LaPO$_4$ pellet e1 (irradiated with 1.5 × 10$^{13}$ ions/cm$^2$), and YPO$_4$ pellet d5 (irradiated with a total fluence of 6.5 × 10$^{13}$ ions/cm$^2$), respectively, in addition to representative single spectra from various depths across the damage profile. Note that

**FIGURE 3 | (A)** A graphical illustration of the Rietveld refinement applied to grazing-incident X-Ray diffraction patterns of un-irradiated and irradiated xenotime-type $YPO_4$ and monazite-type $LaPO_4$ ceramics (cp. **Table 1**). The glancing angle was set to 3.2° to probe a thin surface layer unto a depth of ~1.5 μm. In $YPO_4$ patterns, a minor diffraction peak at 2θ ~ 30° (marked with an asterisk) is attributed to a secondary phase (Y-stabilized tetragonal zirconia; Strasberg et al., 2014). To quantify the amorphous fraction $f_a$, a refinement with three model phases have been applied: a fully crystalline component as observed from the un-irradiated sample (blue); a strongly stressed but still crystalline component (green); and an amorphous component refined with free lattice constants and very small grain-size factors (red).
**(B)** The intensity of representative reflections of un-irradiated $YPO_4$ [(211) at 2θ ≈ 35°, left-hand y-axis] and $LaPO_4$ ceramic [(120) at 2θ = 28.6°, right hand y-axis] in dependence of various glancing angles that correspond to certain X-ray attenuation lengths calculated after Henke et al. (1993) (cp. **Table 1**). GI-XRD intensities of un-irradiated references samples saturate significantly above attenuation lengths > 2 μm. An accurate probing depth of this method was accepted to be until ~1.5 μm below the surface for both phases.

crystal-field split sub-level bands are easily identified in spectra of the unaffected crystalline area of both materials. Those narrow bands are characteristic luminescence features that arise from REEs shielded electronic intra $f$–$f$ transitions. Their number and positions are strongly dependent on the local cationic structural environment the Nd ions are incorporated in, and hence, are specific for indivuidual phases (cp. Nd emission from 9-fold cation-site in monazite vs. 8-fold site in xenotime-type ceramic in **Figures 4**, **5**). Structural disorder is typically interpreted to result in inhomogeneous broadening of these PL bands that arise from statistical variation of the local cationic crystal field as induced by stress/strain and/or structural defects (Skinner and Moerner, 1996; Liu et al., 2000; Lenz et al., 2013). In addition to band-broadening, however, we observed that a seperate broad-band component emerges in $Nd^{3+}$ emission spectra of irradiated orthosphosphates in dependence of the amount of radiation-damage accumulation which is most dominant close to the

irradiated surface. This component is marked as red-hatched curve in spectra of **Figures 4**, **5** and represents a spectrum of the very same $Nd^{3+}$ emission of completely amorphized reference samples, i.e., narrow bands from spectroscopic sub-levels are not observable and degenerated completely. That component in spectra of radiation-damaged xenotime- and monazite-type ceramics may be interpreted as emissions arising from $Nd^{3+}$ ions in a completely "amorphized" cationic environment. The detected PL signal of individual spot measurements (of μm³-volume) are, hence, considered to be a superposition of emissions from a multitude of individual Nd ions in sites with different degree of structural integrity. We used the integrated intensity of the deconvoluted amorphous component in relation to the overall integrated intensity of the $Nd^{3+}$ emission as a reasonable estimate of the amorphous fraction $f_a$ present. The latter estimate is valid given the assumption that trace Nd ions are distributed statistically within the analyzed volume and all
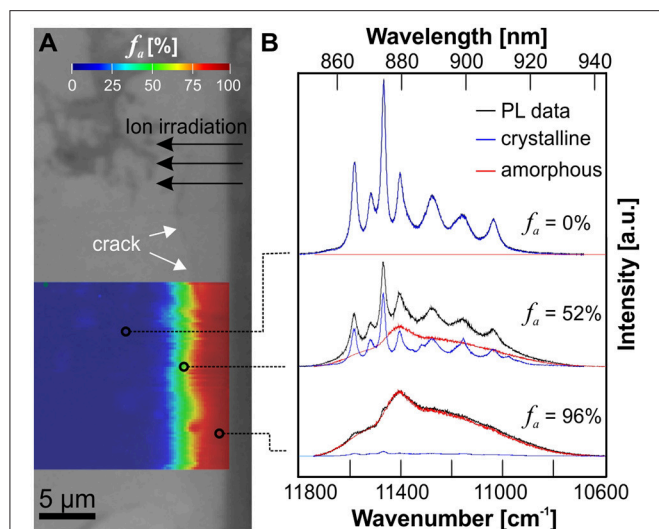
FIGURE 4 | (A) Optical micrograph image of a cross-sectioned LaPO$_4$ ceramic (e1, irradiated with $1.5 \times 10^{13}$ ions/cm$^2$) superimposed by a PL hyperspectral map with the amorphous fraction $f_a$ given color-coded. (B) Representative PL spectra of the Nd$^{3+}$ emission ($^4F_{3/2} \rightarrow$ $^4I_{9/2}$) obtained from various depths below the irradiated surface illustrating the deconvolution procedure used to determine $f_a$ from PL data. The red component represents a spectrum of the very same Nd$^{3+}$ emission from a completely amorphized reference sample. Note, that the lowest irradiation fluence applied in this study was sufficient to produce an almost completely amorphized surface layer in LaPO$_4$.
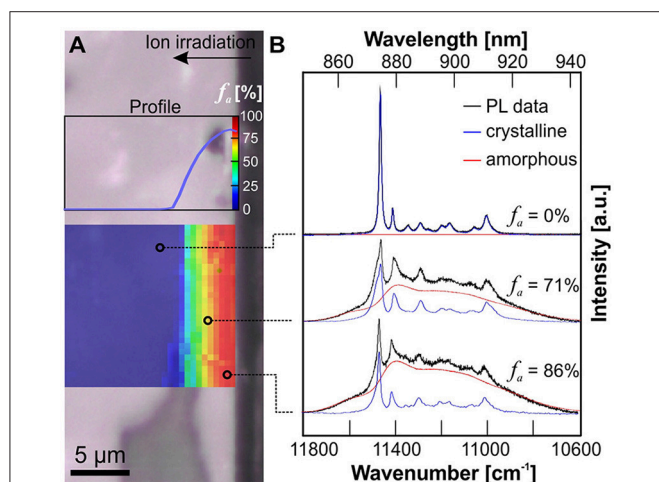


FIGURE 5 | (A) Optical micrograph image of a cross-sectioned YPO$_4$ ceramic (d5, irradiated with $6.5 \times 10^{13}$ ions/cm$^2$) superimposed by a PL hyperspectral map with the amorphous fraction $f_a$ given color-coded. (B) Representative PL spectra of the Nd$^{3+}$ emission obtained from various depths below the irradiated surface illustrating the deconvolution procedure used to determine $f_a$ from PL data. The red component represents a PL spectrum of the very same Nd$^{3+}$ emission from a completely amorphized reference sample. The accumulated radiation-damage shows a non-uniform profile with $f_a$ decreasing from surface to a depth of ca. 5 μm.



FIGURE 6 | (A) SEM image illustrating the focused-ion beam (FIB) preparation of a TEM-foil obtained from the cross-sectioned irradiated surface of YPO$_4$ ceramic sample d5 (the direction of the ion-irradiation indicated by arrows). (B) TEM bright-field image of the FIB-prepared foil with selected-area electron-diffraction (SAED) patterns from various depths below the irradiated surface (dbs). Diffuse scattering in SAED patterns decrease with depth, indicating a decreasing fraction of amorphous YPO$_4$ from the surface to a depth of ~5 μm.

of them contribute similarly to the detected PL signal (i.e., the quantum conversion is the same and independent among different sites). Note, however, that the relation of these two components is in principle independent of the absolute intensity of the luminescence signal, which may strongly depend on (1) the luminescence scattering profile of the analyzed sample surface determined e.g., by the surface roughness, (2) the concentration of Nd ions present in the sample and its distribution, and on (3) further potential luminescence quenching effects (e.g., quenching by irradiation-induced defect centers that have been reported to cause a substantial decrease in luminescence intensity in zircon: for photo- and cathodoluminescence see Lenz and Nasdala, 2015; for ionoluminescence cp. Finch et al., 2004). We applied an automated deconvolution (i.e., a least-squares component fitting) to all individual spectra (i.e., pixels) of the hyperspectral maps obtained from the cross-sectional damage profiles with results given color-coded in **Figures 4**, **5**. The irradiated surface area of LaPO$_4$ ceramics is heavily damaged by Au-irradiation with an $f_a$ estimated to be around 96% (**Figure 4**) that is consistent with f$_a$ observed with GI-XRD. While the probing depth of GI-XRD is limited to max. 2 μm, confocal PL mapping of the cross-sectioned surface of LaPO$_4$ ceramics

**FIGURE 7** | Optical micrograph images (reflection) of cross-sectioned orthophosphates ceramics superimposed by PL hyperspectral maps with the amorphous fraction $f_a$ given color-coded (determined as illustrated in **Figures 4**, **5**). **(A)** $YPO_4$ ceramic d4 irradiated with a total fluence of 4.85 × $10^{13}$ ions/cm². Note, that the dimension of the irradiated surface layer is not homogeneous across various grains. The irradiation depths vary notably with crystal orientation relative to surface-directed ion-irradiation (indicated by arrows). **(B)** $LaPO_4$ ceramic e1 irradiated with a total fluence of 1.5 × $10^{13}$ ions/cm². The entire irradiated 5 µm thick surface layer was found to be almost completely amorphized at the lowest irradiation fluence applied.

revealed a damage profile that is characterized by a very high structural damage unto depths 4–4.5 µm, followed by a strong continous reduction of $f_a$ unto the maximum irradiation depth at ~5 µm (cp. **Figure 7B**). Somewhat different trends of damage accumulation are found for irradiated $YPO_4$ ceramics. Here, the maximum damage levels are limited to the surface region, are much lower than for $LaPO_4$, and subsequently decrease appreciably unto a depth of 5 µm (see $f_a$ profile in **Figures 5A**, **7A**). Note that, similar to diffraction peaks in GI-XRD patterns, spectroscopic bands of the remnant crystalline fraction in $YPO_4$ broadened assymetrically (see shoulder next to the main peak at 11,470 cm⁻¹) which confirms the presence of a strongly altered and stressed, but still crystalline fraction. The latter inhomogeneous trend of damage accumulation in $YPO_4$ was qualitatively confirmed using TEM with results summarized exemplarily in **Figure 6** (sample d5; ion-irradiated with a total fluence of 6.5 × $10^{13}$ ions/cm²). Thin TEM foils were prepared from the irradiated surface area by FIB preparation so that the entire ion-irradiation induced damage profile is accessible to TEM (**Figure 6A**; cp. **Fi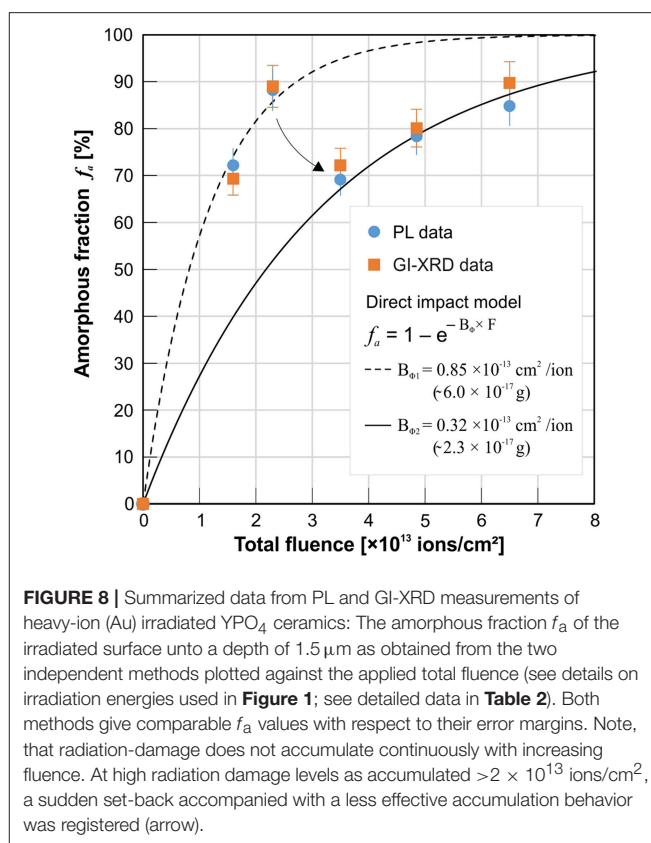gure 1**). Diffuse scattering in selected-area electron-diffraction (SAED) patterns as obtained from various depths below the irradiated surface indicate a decreasing

presence of amorphous material from surface to a depth of 5 µm. Contrasts in TEM bright-field (BF) images are homogeneous and SAED patterns are characterized by bright diffuse rings unto a depth of 1.5 µm. Contrast features in BF are increasingly apparent with increasing depth below the surface (dbs) and finally lattice fringes are clearly visible at the end of the damage profile, together with a loss of diffuse scattering in SAED patterns. Diffraction spots from crystalline components between 0.5 and 4 µm smear out notably in discrete crystallographic directions in reciprocal space. Continuous shifts of diffraction spots in SAED patterns are considered as TEM analog to effects observed with peaks in GI-XRD patterns that shift to lower 2θ (i.e., increasing lattice planes distances $d$), and again, interpreted to be a result from strongly stressed crystalline remnants in irradiated $YPO_4$.

The accumulation of radiation damage in the $YPO_4$ orthophosphate irradiated surface layer is high close to the surface and decreases with irradiation depth. This is confirmed by three independent methods as applied in this study (cp. $f_a$ as obtained by GI-XRD in shallow dbs in **Table 2**; quantitative PL damage profiles in **Figure 5**; and qualitative TEM results discussed above, **Figure 6**). Obtained damage profiles clearly do not resemble expected theoretical, though qualitative, results of SRIM Monte-Carlo simulations that predict a rather homogeneous accumulation of displacements over an ion penetration depth of 5 µm (cp. **Figure 2A**). We consider two potential reasons that may explain deviations from the theoretical damage profile as observed in our irradiation experiments. Firstly, epitaxial, concurrent or post-irradiation annealing may emanate from the unaffected crystalline back into the stopping range of Au ions at the end of their trajectory. As briefly reviewed in the introduction, orthophosphates are known for their sensitivity to spontaneous annealing as induced by the subtle increase of temperature (Meldrum et al., 1997a), and dissemination of energy due to electronic excitation as observed from electron-beam induced nucleation and growth (Meldrum et al., 1997b) or electronic stopping as discussed for α-particle annealing (Deschanels et al., 2014; Seydoux-Guillaume et al., 2018). Progressive epitaxial recovery of crystallinity at the crystalline/amorphous interfaces has been reported e.g., from in situ TEM annealing experiments of ion-irradiated pyrochlores (Aughterson et al., 2018). Secondly, damage profiles on the basis of displacements predicted by SRIM may be insufficient to describe damage accumulation as caused by heavy ions in the MeV range as applied in our study. The amount of displacements calculated in SRIM simulations is deduced from the deposition of nuclear-stopping energy only. Amorphization that arises from electronic interaction of high-energy heavy ions with the bombarded material is not accounted for in SRIM calculations. Various experiments with heavy-ions in the MeV and GeV energy range that show a large electronic stopping regime (i.e., swift heavy ions) have demonstrated that the dissemination of electronic stopping energy through the interaction of high-energetic, charged ions with the coulomb-field of bombarded materials resulted in formation of amorphous ion tracks (e.g., Sales et al., 1992; Toulemonde et al., 2001; Lang et al., 2009; Liu et al., 2016).

A comprehensive overview of models that explain ion-beam damage in the electronic stopping regime is given by Agulló-López et al. (2016). The impact of electronic energy loss of irradiated MeV ions on the accumulation of radiation damage as an explanation of damage profiles observed in our experiments is supported by SRIM calculations of ion energy-loss that includes both contributions, nuclear as well as electronic stopping (**Figure 2B**). The cumulative profile of energy loss, however, reproduce damage profiles obtained in this study more concisely.

Despite apparent discrepancies between damage profiles calculated by SRIM and those observed in our experiments, predictions on the ion-penetration trajectory-lengths were found to be reasonably accurate to a first approximation. Hyperspectral PL maps indicate damage accumulation to extend to a depth of ~5 μm in both, LaPO4 and YPO$_4$ ceramics, as predicted from the stopping range of the maximum applied Au-ion irradiation with 35 MeV (cp. **Figure 2**). This is most apparent from LaPO$_4$ ceramics that were entirely amorphized throughout the irradiated surface layer (**Figure 7B**). In YPO$_4$ ceramics, however, we found small deviations in irradiation depths in dependence of the crystal orientation relative to the surface directed ion-beam (**Figure 7A**). Depths of damage accumulation as revealed by detailed PL hyperspectral images across multiple grains were found to deviate slightly between adjacent crystal grains. Also, grain boundaries and pores that phase out at the polished surface were found to promote damage accumulation in those areas. Variable radiation-damage depth-profiles across different grains complicate the comparability of quantitative estimates of the amorphous fraction $f_a$ as obtained from the surface-sensitive, but bulk method GI-XRD and point analyses of confocal PL spectroscopy in the μm-range. To quantitatively compare results from PL depth profiles of $f_a$ with those from GI-XRD, we (i) averaged $f_a$ values obtained from PL depth profiles unto the maximum effective probing depth of GI-XRD at 1.5 μm, and further (ii) took the mean from multiple depth profiles of the same and/or different grains to account for statistical variation as introduced by effects discussed above. Latter results are summarized in **Table 2** and plotted in **Figure 8** together with $f_a$ data obtained from GI-XRD. With their strongly deviating probing volumes taken into account, both techniques give very consistent estimates of the amorphous fraction $f_a$ within their error margins of ±5%. Note, however, that both applied techniques reveal an extraordinary discontinuous damage-accumulation behavior of YPO$_4$ with increasing Au-ion fluence (see **Figure 8** again). The amount of radiation damage increases with the first two applied irradiation fluences (d1 = 1.6 × 10$^{13}$ ions/cm$^2$; d2 = 2.3 × 10$^{13}$ ions/cm$^2$) that result in a high $f_a$ ~ 90% present in the uppermost irradiated layer. The accumulation of the amorphous fraction $f_a$ follows the direct impact model as given in **Figure 8** (with variables B$_\Phi$ = cross-section of amorphous ion tracks, and F = Au-ion fluence applied). A decrease of $f_a$ was then recorded for xenotime-type YPO$_4$ sample d3 irradiated with a slightly elevated fluence at 3.5 × 10$^{13}$ ions/cm$^2$ (see arrow in **Figure 8**). Fluences >3.5 × 10$^{13}$ ions/cm$^2$ cause the radiation damage to accumulate again, but with less efficiency as demonstrated



**FIGURE 8 |** Summarized data from PL and GI-XRD measurements of heavy-ion (Au) irradiated YPO$_4$ ceramics: The amorphous fraction $f_a$ of the irradiated surface unto a depth of 1.5 μm as obtained from the two independent methods plotted against the applied total fluence (see details on irradiation energies used in **Figure 1**; see detailed data in **Table 2**). Both methods give comparable $f_a$ values with respect to their error margins. Note, that radiation-damage does not accumulate continuously with increasing fluence. At high radiation damage levels as accumulated >2 × 10$^{13}$ ions/cm$^2$, a sudden set-back accompanied with a less effective accumulation behavior was registered (arrow).

by the regression model with a much lower ion-track cross-section B$_{\Phi 2}$. The latter erratic damage-accumulation behavior accounts for a competitive process that prevents and counteracts further damage accumulation by MeV Au ion-irradiation at high $f_a$. Potential epitaxial annealing effects as caused by the input of energy due to high electronic loss of MeV swift ions have been reported for orthophosphates (Rafiuddin and Grosvenor, 2015), and repeatedly for SiC (Benyagoub et al., 2006; Debelle et al., 2012; Backman et al., 2013). In this study, however, we cannot clarify conclusively if the impact of electronic energy loss is the most probable explanation for competitive annealing observed at elevated total ion-fluences in YPO$_4$, because temperature-assisted annealing may occur as a result of sample heating at higher fluences (an increase of sample temperature to a maximum of 45°C have been recorded during irradiation experiments). To differentiate between annealing effects as caused by the impact of electronic energy loss of MeV heavy-ions and potential sample heating, we strongly suggest to apply effective sample cooling (e.g., liquid nitrogen) during ion-irradiation of the very temperature-sensitive orthophosphates.

## CONCLUSIONS AND IMPLICATIONS

The luminescence of Nd$^{3+}$ ($^4$F$_{3/2}$ → $^4$I$_{9/2}$) in monazite-type and xenotime-type orthophosphates was identified as a promising structural probe that bears quantitative information on the degree of amorphization as induced by ion-irradiation. Careful

investigation of PL spectra from heavy-ion irradiated ceramic surfaces revealed that the detected luminescence signal may be interpreted as a superposition of emissions from Nd ions situated in structurally different components in the damaged crystal structure. The latter comprise completely amorphous domains (with a structurally degenerated Nd-cation environment) that are created upon damage accumulation and persist next to unaffected or slightly affected, stressed crystalline remnants on a submicroscopic scale. We found, that the integrated area of the deconvoluted amorphous component in relation to the fully integrated luminescence signal gives a reliable estimate of the amorphous fraction $f_a$ present in the probed sample volume. This approach was substantiated and confirmed by quantitative Rietveld refinements of GI-XRD patterns obtained from ion-irradiation damaged $LaPO_4$ and $YPO_4$ ceramics.

Laser-induced PL spectroscopy has a number of analytical advantages, that includes (1) the option to perform analyses non-destructively and without the need for special sample preparation, (2) the application as a remote technique e.g., through optical transparent windows if protection against hazardous samples is needed, and (3) the possibility to perform spot analyses using highly confocal spectrometers coupled to optical probe-heads or microscopes with the latter operating on the micrometer length-scale. The analytical flexibility to detect the $Nd^{3+}$ ($REE^{3+}$) luminescence in the orthophosphates opens up the opportunity to investigate their complex damage-accumulation behavior in more detail and give rise to an improved comparability to results obtained from very different samples or experiment setups, e.g., studies that require quantification of the amorphous fraction in natural mineral-analogs, self-irradiation damaged synthetic samples doped with fast decaying actinides such as $^{238}Pu$, $^{241}Am$, or $^{244}Cm$, in ion-irradiation experiments, or studies that involves minute *in-situ* monitoring of $f_a$ in e.g., radiation-damage annealing studies under controlled conditions. Further, quantitative information of structural damage may be deduced from REE luminescence in advanced orthophosphate nuclear waste-forms that is not stimulated externally (e.g., PL: with optical lasers or UV lamps), but by inherent β- or γ-radiation from the radioactive decay

of substituted actinides (radioluminescence). "Self-glowing" phosphate crystals that contain highly-active actinides and adjusted concentrations of luminescing REEs have been prepared successfully (Burakov et al., 2011). We, however, consider that the presented interpretation of luminescence $Nd^{3+}$ spectra for a quantitative estimation $f_a$ in orthophosphates is, in principle, applicable to other $REE^{3+}$ probes, that may be substituted in alternative nuclear waste-form materials and their mineral analogs, e.g., apatite $Ca_5(PO_4)_3(F,Cl,OH)$, zircon $ZrSiO_4$, titanite $CaTiSiO_5$, zirconolite $CaZrTi_2O_7$.

## AUTHOR CONTRIBUTIONS

All authors listed have made a substantial, direct, and intellectual contribution to the work. CL and GL initiated and led the study. Sample synthesis was done by DG and CL. Ion irradiations were performed by MI. Electron microscopy (including SEM and TEM analysis) and FIB preparation are conducted by RA and JD. X-Ray diffraction analysis were performed by GT. The manuscript was compiled and prepared by CL.

## FUNDING

## ACKNOWLEDGMENTS

## REFERENCES

Agulló-López, F., Climent-Font, A., Muñoz-Martín, Á., Olivares, J., and Zucchiatti, A. (2016). Ion beam modification of dielectric materials in the electronic excitation regime: cumulative and exciton models. *Prog. Mater. Sci.* 76, 1–58. doi: 10.1016/j.pmatsci.2015.06.002

Arinicheva, Y., Gausse, C., Neumeier, S., Brandt, F., Rozov, K., Szenknect, S., et al. (2018). Influence of temperature on the dissolution kinetics of synthetic $LaPO_4$-monazite in acidic media between 50 and 130°C. *J. Nucl. Mater.* 509, 488–495. doi: 10.1016/j.jnucmat.2018.07.009

Aughterson, R. D., Lumpkin, G. R., Smith, K. L., de los Reyes, M., Davis, J., Avdeev, M., et al. (2018). The ion-irradiation tolerance of the pyrochlore to fluorite Ho (x) Yb (2-x) TiO5 and Er2TiO5 compounds: a TEM comparative study using both *in-situ* and bulk *ex-situ* irradiation approaches. *J. Nucl. Mater.* 507, 316–326. doi: 10.1016/j.jnucmat.2018.05.026

Backman, M., Toulemonde, M., Pakarinen, O. H., Juslin, N., Djurabekova, F., Nordlund, K., et al. (2013). Molecular dynamics simulations of swift

heavy ion induced defect recovery in SiC. *Comput. Mater. Sci.* 67, 261–265. doi: 10.1016/j.commatsci.2012.09.010

Baughman, J. S., Flowers, R. M., Metcalf, J. R., and Dhansay, T. (2017). Influence of radiation damage on titanite He diffusion kinetics. *Geochim. Cosmochim. Acta* 205, 50–64. doi: 10.1016/j.gca.2017.01.049

Benyagoub, A., Audren, A., Thomé, L., and Garrido, F. (2006). Athermal crystallization induced by electronic excitations in ion-irradiated silicon carbide. *Appl. Phys. Lett.* 89:241914. doi: 10.1063/1.2405410

Boatner, L. A., Beall, G. W., Abraham, M. M., Finch, C. B., Huray, P. G., and Rappaz, M. (1980). "Monazite and other lanthanide orthophosphates as alternate actinide waste forms," in *Scientific Basis for Nuclear Waste Management*, ed C. J. M. Northrup Jr (Boston, MA: Springer), 289–296.

Boatner, L. A., and Sales, B. C. (1988). "Monazite," in *Radioactive Waste Forms for the Future*, eds W. Lutze and R. C. Ewing (Amsterdam; New York, NY: Elsevier Science Publishers), 712.

Bregiroux, D., Lucas, S., Champion, E., Audubert, F., and Bernache-Assollant, D. (2006). Sintering and microstructure of rare earth phosphate ceramics

REPO₄ with RE= La, Ce or Y. *J. Eur. Ceram. Soc.* 26, 279–287. doi: 10.1016/j.jeurceramsoc.2004.11.004

Bünzli, J. C. G., and Piguet, C. (2005). Taking advantage of luminescent lanthanide ions. *Chem. Soc. Rev.* 34, 1048–1077. doi: 10.1039/b406082m

Burakov, B. E., Ojovan, M. I., and Lee, W. E. (2011). *Crystalline Materials for Actinide Immobilisation. Materials for Engineering.* Vol. 1. London: Imperial College Press, World Scientific Publishing Co. Pte. Ltd.

Burakov, B. E., Yagovkina, M. A., Garbuzov, V. M., Kitsay, A. A., and Zirlin, V. A. (2004). Self-Irradiation of monazite ceramics: contrasting behavior of PuPO₄ and (La, Pu)PO₄ doped with Pu-238. *MRS Online Proc. Lib. Arch.* 824, CC4.1.1–CC4.1.5. doi: 10.1557/PROC-824-CC4.1

Chen, H., and Stimets, R. W. (2014). Fluorescence of trivalent neodymium in various materials excited by a 785 nm laser. *Am. Mineral.* 99, 332–342. doi: 10.2138/am.2014.4311

Clavier, N., Podor, R., and Dacheux, N. (2011). Crystal chemistry of the monazite structure. *J. Eur. Ceram. Soc.* 31, 941–976. doi: 10.1016/j.jeurceramsoc.2010.12.019

Dacheux, N., Clavier, N., and Podor, R. (2013). Monazite as a promising long-term radioactive waste matrix: benefits of high-structural flexibility and chemical durability. *Am. Mineral.* 98, 833–847. doi: 10.2138/am.2013.4307

Debelle, A., Backman, M., Thome, L., Weber, W. J., Toulemonde, M., Mylonas, S., et al. (2012). Combined experimental and computational study of the recrystallization process induced by electronic interactions of swift heavy ions with silicon carbide crystals. *Phys. Rev. B* 86:100102. doi: 10.1103/PhysRevB.86.100102

Deschanels, X., Seydoux-Guillaume, A. M., Magnin, V., Mesbah, A., Tribet, M., Moloney, M. P., et al. (2014). Swelling induced by alpha decay in monazite and zirconolite ceramics: a XRD and TEM comparative study. *J. Nucl. Mater.* 448, 184–194. doi: 10.1016/j.jnucmat.2014.02.003

Ellison, A. J., and Navrotsky, A. (1992). Enthalpy of formation of zircon. *J. Am. Ceram. Soc.* 75, 1430–1433. doi: 10.1111/j.1151-2916.1992.tb04205.x

Ewing, R. C., and Wang, L. (2002). Phosphates as nuclear waste forms. *Rev. Mineral. Geochem.* 48, 673–699. doi: 10.2138/rmg.2002.48.18

Finch, A. A., Garcia-Guinea, J., Hole, D. E., Townsend, P. D., and Hanchar, J. M. (2004). Ionoluminescence of zircon: rare earth emissions and radiation damage. *J. Phys. D Appl. Phys.* 37:2795. doi: 10.1088/0022-3727/37/20/004

Gausse, C., Szenknect, S., Mesbah, A., Clavier, N., Neumeier, S., and Dacheux, N. (2018). Dissolution kinetics of monazite LnPO4 (Ln= La to Gd): a multiparametric study. *Appl. Geochem.* 93, 81–93. doi: 10.1016/j.apgeochem.2018.04.005

Gavrilović, T., Periša, J., Papan, J., Vuković, K., Smits, K., Jovanović, D. J., et al. (2018). Particle size effects on the structure and emission of Eu³⁺: LaPO₄ and EuPO₄ phosphors. *J. Lumin.* 195, 420–429. doi: 10.1016/j.jlumin.2017.12.042

Geisler, T., Pidgeon, R. T., van Bronswijk, W., and Pleysier, R. (2001). Kinetics of thermal recovery and recrystallization of partially metamict zircon: a Raman spectroscopic study. *Eur. J. Mineral.* 13, 1163–1176. doi: 10.1127/0935-1221/2001/0013-1163

Guillot-Noël, O., Viana, B., Bellamy, B., Gourier, D., Zogo-Mboulou, G. B., and Jandl, S. (2000). Spectroscopic evidence of inhomogeneous distribution of Nd³⁺ in YVO₄, YPO₄ and YAsO₄ crystals. *Opt. Mater.* 13, 427–437. doi: 10.1016/S0925-3467(99)00097-X

Helean, K. B., Navrotsky, A., Lian, J., and Ewing, R. C. (2004). Correlation of formation enthalpies with critical amorphization temperature for pyrochlore and monazite. *MRS Online Proc. Library Arch.* 824. doi: 10.1557/PROC-824-CC4.7

Henke, B. L., Gullikson, E. M., and Davis, J. C. (1993). X-ray interactions: photoabsorption, scattering, transmission, and reflection at E=50-30000 eV, Z=1-92. *Atom. Data Nucl. Data Tab.* 54, 181–342. doi: 10.1006/adnd.1993.1013

Kolitsch, U., and Holtstam, D. (2004). Crystal chemistry of REE X O4 compounds (X= P, As, V). II. Review of REE X O4 compounds and their stability fields. *Eur. J. Mineral.* 16, 117–126. doi: 10.1127/0935-1221/2004/0016-0117

Lang, M., Zhang, F. X., Ewing, R. C., Lian, J., Trautmann, C., and Wang, Z. (2009). Structural modifications of Gd₂Zr₂₋ₓTiₓO₇ pyrochlore induced by swift heavy ions: disordering and amorphization. *J. Mater. Res.* 24, 1322–1334. doi: 10.1557/jmr.2009.0151

Lenz, C., and Nasdala, L. (2015). A photoluminescence study of REE³⁺ emissions in radiation-damaged zircon. *Am. Mineral.* 100, 1123–1133. doi: 10.2138/am-2015-4894CCBYNCND

Lenz, C., Talla, D., Ruschel, K., Škoda, R., Götze, J., and Nasdala, L. (2013). Factors affecting the Nd³⁺(REE³⁺) luminescence of minerals. *Mineral. Petrol.* 107, 415–428. doi: 10.1007/s00710-013-0286-2

Liu, G. K., Zhorin, V. V., Li, S. T., and Beitz, J. V. (2000). Crystal field analysis and Monte Carlo simulation of lattice disordering for Cm³⁺ in YPO₄ and LuPO₄. *J. Chem. Phys.* 112, 373–382. doi: 10.1063/1.480587

Liu, P., Zhang, Y., Xue, H., Jin, K., Crespillo, M. L., Wang, X., et al. (2016). A coupled effect of nuclear and electronic energy loss on ion irradiation damage in lithium niobate. *Acta Mater.* 105, 429–437. doi: 10.1016/j.actamat.2015.12.048

Loiseau, P., Caurant, D., Baffier, N., Mazerolles, L., and Fillet, C. (2004). Glass–ceramic nuclear waste forms obtained from SiO₂-Al₂O₃-CaO–ZrO₂-TiO₂ glasses containing lanthanides (Ce, Nd, Eu, Gd, Yb) and actinides (Th): study of internal crystallization. *J. Nucl. Mater.* 335, 14–32. doi: 10.1016/j.jnucmat.2004.05.020

Lumpkin, G. R. (2006). Ceramic waste forms for actinides. *Elements* 2, 365–372. doi: 10.2113/gselements.2.6.365

Luo, J. S., and Liu, G. K. (2001). Microscopic effects of self-radiation damage in ²⁴⁴Cm-doped LuPO₄ crystals. *J. Mater. Res.* 16, 366–372. doi: 10.1557/JMR.2001.0056

Marillo-Sialer, E., Woodhead, J., Hanchar, J. M., Reddy, S. M., Greig, A., Hergt, J., et al. (2016). An investigation of the laser-induced zircon 'matrix effect'. *Chem. Geol.* 438, 11–24. doi: 10.1016/j.chemgeo.2016.05.014

Meldrum, A., Boatner, L. A., and Ewing, R. C. (1997a). Displacive radiation effects in the monazite-and zircon-structure orthophosphates. *Phys. Rev. B* 56:13805. doi: 10.1103/PhysRevB.56.13805

Meldrum, A., Boatner, L. A., and Ewing, R. C. (1997b). Electron-irradiation-induced nucleation and growth in amorphous LaPO₄, ScPO₄, and zircon. *J. Mater. Res.* 12, 1816–1827. doi: 10.1557/JMR.1997.0250

Meldrum, A., Boatner, L. A., Weber, W. J., and Ewing, R. C. (1998). Radiation damage in zircon and monazite. *Geochim. Cosmochim. Acta* 62, 2509–2520. doi: 10.1016/S0016-7037(98)00174-4

Mendoza, C., de Ligny, D., Panczer, G., Peuget, S., Bardez-Giboire, I., and Schuller, S. (2011). Behaviour of the Eu³⁺ ⁵D₀→ ⁷F₀ transition in CaMoO₄ powellite type ceramics under Ar and Pb ions implantation. *Opt. Mater.* 34, 386–390. doi: 10.1016/j.optmat.2011.05.004

Milligan, W. O., Mullica, D. F., Beall, G. W., and Boatner, L. A. (1982). Structural investigations of YPO₄, ScPO₄, and LuPO₄. *Inorg. Chim. Acta* 60, 39–43. doi: 10.1016/S0020-1693(00)91148-4

Nasdala, L., Akhmadaliev, S., Artac, A., Habler, G., and Lenz, C. (2018). Irradiation effects in monazite–(Ce) and zircon: Raman and photoluminescence study of Au-irradiated FIB foils. *Phys. Chem. Minerals* 45, 855–871. doi: 10.1007/s00269-018-0975-9

Nasdala, L., Grambole, D., and Ruschel, K. (2013). Review of effects of radiation damage on the luminescence emission of minerals, and the example of He-irradiated CePO₄. *Mineral. Petrol.* 107, 441–454. doi: 10.1007/s00710-013-0274-6

Nasdala, L., Grötzschel, R., Probst, S., and Bleisteiner, B. (2010). Irradiation damage in monazite-(Ce): an example to establish the limits of Raman confocality and depth resolution. *Can. Mineral.* 48, 351–359. doi: 10.3749/canmin.48.2.351

Nasdala, L., Irmer, G., and Wolf, D. (1995). The degree of metamictization in zircons: a Raman spectroscopic study. *Eur. J. Mineral.* 7, 471–478. doi: 10.1127/ejm/7/3/0471

Nasdala, L., Wenzel, M., Vavra, G., Irmer, G., Wenzel, T., and Kober, B. (2001). Metamictisation of natural zircon: accumulation versus thermal annealing of radioactivity-induced damage. *Contrib. Mineral. Petrol.* 141, 125–144. doi: 10.1007/s004100000235

Neumeier, S., Arinicheva, Y., Ji, Y., Heuser, J. M., Kowalski, P. M., Kegler, P., et al. (2017). New insights into phosphate based materials for the immobilisation of actinides. *Radiochim. Acta* 105, 961–984. doi: 10.1515/ract-2017-2819

Ni, Y., Hughes, J. M., and Mariano, A. N. (1995). Crystal chemistry of the monazite and xenotime structures. *Am. Mineral.* 80, 21–26. doi: 10.2138/am-1995-1-203

Ojovan, M. I., Burakov, B. E., and Lee, W. E. (2018). Radiation-induced microcrystal shape change as a mechanism of wasteform degradation. *J. Nucl. Mater.* 501, 162–171. doi: 10.1016/j.jnucmat.2018.01.030

Omel'yanenko, B. I., Livshits, T. S., Yudintsev, S. V., and Nikonov, B. S. (2007). Natural and artificial minerals as matrices for immobilization of actinides. *Geol. Ore Depos.* 49, 173–193. doi: 10.1134/S1075701507030014

Palenik, C. S., Nasdala, L., and Ewing, R. C. (2003). Radiation damage in zircon. *Am. Mineral.* 88, 770–781. doi: 10.2138/am-2003-5-606

Panczer, G., De Ligny, D., Mendoza, C., Gaft, M., Seydoux-Guillaume, A.-M., and Wang, X. (2012). "Raman spectroscopy applied to Earth sciences and cultural heritage," in *Raman and Fluorescence,* eds J. Dubessy, M-C. Caumon, and F. Rull (London: European Mineralogical Union, Notes in Mineralogy), 61–82.

Picot, V., Deschanels, X., Peuget, S., Glorieux, B., Seydoux-Guillaume, A. M., and Wirth, R. (2008). Ion beam radiation effects in monazite. *J. Nucl. Mater.* 381, 290–296. doi: 10.1016/j.jnucmat.2008.09.001

Rafiuddin, M. R., and Grosvenor, A. P. (2015). Probing the effect of radiation damage on the structure of rare-earth phosphates. *J. Alloys Comp.* 653, 279–289. doi: 10.1016/j.jallcom.2015.08.276

Ríos, S., Salje, E. K., Zhang, M., and Ewing, R. C. (2000). Amorphization in zircon: evidence for direct impact damage. *J. Phys. Condens. Matter* 12, 2401–2412. doi: 10.1088/0953-8984/12/11/306

Ropp, R. C. (1968). Phosphors based on rare earth phosphates I. Spectral properties of some rare earth phosphates. *J. Electrochem. Soc.* 115, 841–845.

Ruschel, K., Nasdala, L., Kronz, A., Hanchar, J. M., Többens, D. M., Škoda, R., et al. (2012). A Raman spectroscopic study on the structural disorder of monazite–(Ce). *Mineral. Petrol.* 105, 41–55. doi: 10.1007/s00710-012-0197-7

Sales, B. C., Zuhr, R. A., McCallum, J. C., and Boatner, L. A. (1992). Electronic damage in the ion-beam amorphization of $Pb_2P_2O_7$. *Phys. Rev. B* 46, 3215–3218. doi: 10.1103/PhysRevB.46.3215

Schlenz, H., Neumeier, S., Hirsch, A., Peters, L., and Roth, G. (2018). "Phosphates as safe containers for radionuclides," in *Highlights in Applied Mineralogy*, eds S. Heuss-Aßbichler, G. Amthauer, and M. John (Berlin: De Gruyter), 344.

Seydoux-Guillaume, A. M., Deschanels, X., Baumier, C., Neumeier, S., Weber, W. J., and Peuget, S. (2018). Why natural monazite never becomes amorphous: experimental evidence for alpha self-healing. *Am. Mineral.* 103, 824–827. doi: 10.2138/am-2018-6447

Seydoux-Guillaume, A. M., Wirth, R., Deutsch, A., and Schärer, U. (2004). Microstructure of 24-1928 Ma concordant monazites; implications for geochronology and nuclear waste deposits. *Geochim. Cosmochim. Acta* 68, 2517–2527. doi: 10.1016/j.gca.2003.10.042

Shimizu, R., and Ogasawara, Y. (2014). Radiation damage to Kokchetav UHPM diamonds in zircon: variations in Raman, photoluminescence, and cathodoluminescence spectra. *Lithos* 206, 201–213. doi: 10.1016/j.lithos.2014.07.002

Shiryaev, A. A., Nickolsky, M. S., Averin, A. A., Grigoriev, M. S., Zubavichus, Y. V., Vlasova, I. E., et al. (2016). Structural peculiarities of aged [238]Pu-doped monazite. *MRS Adv.* 1, 4275–4281. doi: 10.1557/adv.2017.220

Skinner, J. L., and Moerner, W. E. (1996). Structure and dynamics in solids as probed by optical spectroscopy. *J. Phys. Chem.* 100, 13251–13262. doi: 10.1021/jp9601328

Strasberg, M., Barrett, A. A., Anusavice, K. J., Mecholsky, J. J., and Nino, J. C. (2014). Influence of roughness on the efficacy of grazing incidence X-ray diffraction to characterize grinding-induced phase changes in yttria-tetragonal zirconia polycrystals (Y-TZP). *J. Mater. Sci.* 49, 1630–1638. doi: 10.1007/s10853-013-7846-z

Sujith, S. S., Kumar, S. A., Mangalaraja, R. V., Mohamed, A. P., and Ananthakumar, S. (2014). Porous to dense $LaPO_4$ sintered ceramics for advanced refractories. *Ceram. Int.* 40, 15121–15129. doi: 10.1016/j.ceramint.2014.06.125

Švecová, E., Copjaková, R., Losos, Z., Škoda, R., Nasdala, L., and Cícha, J. (2016). Multi-stage evolution of xenotime–(Y) from Písek pegmatites, Czech Republic: an electron probe micro-analysis and Raman spectroscopy study. *Mineral. Petrol.* 110, 747–765. doi: 10.1007/s00710-016-0442-6

Thomé, L., Moll, S., Debelle, A., Garrido, F., Sattonnay, G., and Jagielski, J. (2012). Radiation effects in nuclear ceramics. *Adv. Mater. Sci. Eng.* 2012:905474. doi: 10.1155/2012/905474

Toulemonde, M., Ramos, S. M. M., Bernas, H., Clerc, C., Canut, B., Chaumont, J., et al. (2001). MeV gold irradiation induced damage in α-quartz: competition between nuclear and electronic stopping. *Nucl. Instr. Methods Phys. Res. Sec. B Beam Interact. Mater. Atoms* 178, 331–336. doi: 10.1016/S0168-583X(00)00496-1

Trachenko, K., Dove, M. T., and Salje, E. K. (2002). Large swelling and percolation in irradiated zircon. *J. Phys. Condens. Matter* 15:L1. doi: 10.1088/0953-8984/15/2/101

Tropper, P., Manning, C. E., and Harlov, D. E. (2011). Solubility of $CePO_4$ monazite and $YPO_4$ xenotime in H2O and H2O–NaCl at 800 C and 1 GPa: implications for REE and Y transport during high-grade metamorphism. *Chem. Geol.* 282, 58–66. doi: 10.1016/j.chemgeo.2011.01.009

Váczi, T., and Nasdala, L. (2017). Electron-beam-induced annealing of natural zircon: a Raman spectroscopic study. *Phys. Chem. Minerals* 44, 389–401. doi: 10.1007/s00269-016-0866-x

Wang, X., Panczer, G., De Ligny, D., Motto-Ros, V., Yu, J., Dussossoy, J. L., et al. (2014). Irradiated rare-earth-doped powellite single crystal probed by confocal Raman mapping and transmission electron microscopy. *J. Raman Spectrosc.* 45, 383–391. doi: 10.1002/jrs.4472

Weber, W. J. (2000). Models and mechanisms of irradiation-induced amorphization in ceramics. *Nucl. Instr. Methods Phys. Res. Sec. B Beam Interact. Mater. Atoms* 166, 98–106. doi: 10.1016/S0168-583X(99)00643-6

Weber, W. J., Navrotsky, A., Stefanovsky, S., Vance, E. R., and Vernaz, E. (2009). Materials science of high-level nuclear waste immobilization. *Mrs Bulletin* 34, 46–53. doi: 10.1557/mrs2009.12

Ziegler, J. F., Ziegler, M. D., and Biersack, J. P. (2010). SRIM-The stopping and range of ions in matter (2010). *Nucl. Instrum. Methods Phys. Res. Sect. B* 268, 1818–1823. doi: 10.1016/j.nimb.2010.02.091

Zietlow, P., Beirau, T., Mihailova, B., Groat, L. A., Chudy, T., Shelyug, A., et al. (2017). Thermal annealing of natural, radiation-damaged pyrochlore. *Zeitschr. Kristallogr. Crystal. Mater.* 232, 25–38. doi: 10.1515/zkri-2016-1965

Zubekhina, B. Y., and Burakov, B. E. (2016). Leaching of Plutonium from "Old" samples of single phase ceramics based on $Zr_{0.79}Gd_{0.14}Pu_{0.04}O_{1.93}$ and $La_{0.9}Pu_{0.1}PO_4$ doped with [238]Pu. *MRS Adv.* 1, 4249–4253. doi: 10.1557/adv.2017.216

# Toward Low-Cost and Sustainable Supercapacitor Electrode Processing: Simultaneous Carbon Grafting and Coating of Mixed-Valence Metal Oxides by Fast Annealing

*Keyvan Malaie[1]\*, Mohammad Reza Ganjali[1,2] and Francesca Soavi[3]\**

[1] *Center of Excellence in Electrochemistry, School of Chemistry, College of Science, University of Tehran, Tehran, Iran,*
[2] *Biosensor Research Center, Endocrinology and Metabolism Molecular-Cellular Sciences Institute, Tehran University of Medical Sciences, Tehran, Iran,* [3] *Department of Chemistry "Giacomo Ciamician", Alma Mater Studiorum-Università di Bologna, Bologna, Italy*

There is a rapid market growth for supercapacitors and batteries based on new materials and production strategies that minimize their cost, end-of-life environmental impact, and waste management. Herein, mixed-valence iron oxide ($FeO_x$) and manganese oxide ($Mn_3O_4$) and $FeO_x$-carbon black ($FeO_x$-CB) electrodes with excellent pseudocapacitive behavior in 1 M $Na_2SO_4$ are produced by a one-step thermal annealing. Due to the *in situ* grafted carbon black, the $FeO_x$-CB shows a high pseudocapacitance of 408 mF cm$^{-2}$ (or 128 F g$^{-1}$), and $Mn_3O_4$ after activation shows high pseudocapacitance of 480 mF cm$^{-2}$ (192 F g$^{-1}$). The asymmetric supercapacitor based on $FeO_x$-CB and activated-$Mn_3O_4$ shows a capacitance of 260 mF cm$^{-2}$ at 100 mHz and a cycling stability of 97.4% over 800 cycles. Furthermore, due to its facile redox reactions, the supercapacitor can be voltammetrically cycled up to a high rate of 2,000 mV s$^{-1}$ without a significant distortion of the voltammograms. Overall, our data indicate the feasibility of developing high-performance supercapacitors based on mixed-valence iron and manganese oxide electrodes in a single step.

**Keywords: iron oxide, manganese oxide, carbon black, nanocomposite, thermal annealing, pseudocapacitor**

## INTRODUCTION

Supercapacitors are attracting increasing attention in today's fast-growing electronics industry. They can provide high power density and stability because they utilize fast charge/discharge processes at the electrode/electrolyte interface. These processes are of two types: ion adsorption/desorption at the interface (i.e., EDLC) and fast faradaic electrode reactions that are exploited in pseudocapacitors (Brousse et al., 2015).

There is a growing interest in pseudocapacitors due to their potential for accessing higher energy densities than those of the traditional EDLC supercapacitors. Their fast redox reactions bring about charge storage capability in the bulk of materials higher than the EDLC that stores charge by a surface electrostatic process (Lukatskaya et al., 2017). Iron oxide and manganese oxide are examples of materials with pseudocapacitive behavior (Simon et al., 2017). They are universally

abundant, environmentally benign, inexpensive, electrochemically-active in non-corrosive neutral electrolytes, and completely safe after disposal of the supercapacitor (Dyatkin et al., 2013).

In addition, iron and manganese oxides have complementary working potential windows, making them appealing for developing high-voltage aqueous asymmetric supercapacitors. Probably their only undesirable property is their low electrical conductivity that results in high IR drops at high charge/discharge rates. However, the mixed-valance iron or manganese oxides (i.e., spinel oxides) have a better conductivity. For example, $Fe_3O_4$ has a very high electric conductivity of $2 \times 10^4$ S m$^{-1}$ at $25°C$ (Malaie et al., 2018).

Recent research is focused on development of supercapacitor materials and processes that enable low cost and low end-of-life environmental impact and easy waste management on a large production scale (Dyatkin et al., 2013). Therefore, non-precious metal oxides like $FeO_x$ and MnOx-based electrodes are attracting much attention. Pseudocapacitors based on $Fe_3O_4$ as the negative electrode and $MnO_2$ as the positive electrode have been synthesized by various methods (Brousse and Bélanger, 2003; Yang et al., 2014; Gund et al., 2015). These methods include chemical vapor deposition (CVD), electrodeposition, hydrothermal, and sol-gel. However, there are several concerns that make these synthesis strategies unappealing for scaling-up applications. First, the films grown by the CVD, electrodeposition and hydrothermal methods provide a loading mass in the range of tens of $\mu$g cm$^{-2}$ to a few mg cm$^{-2}$, while commercial supercapacitors require 8–10 mg cm$^{-2}$ to give a practical areal capacitance (Balducci et al., 2017; Song et al., 2017). Second, for the preparation of hybrid materials, these methods usually utilize prolonged and multi-step processes, elevated temperatures, complex instruments, and special precursor materials (Qian et al., 2012). Third, the conductive additives (e.g., graphene, CNT, …) that are usually composited with redox materials to reduce electrical resistance and enhance utilization of redox sites are very expensive for large-scale production; but carbon black materials that are easily obtained by carbonization of organic materials are significantly cheaper. On the other hand, rapid preparation of nanomaterials especially at elevated temperatures usually results in the enlargement and aggregation of the particles because under these conditions the growth of the particles is hardly controllable. Therefore, there is a need for general electrode processing methods that afford high-areal capacitance electrodes with time and cost efficiency.

Herein, for the first time, we report a novel synthesis approach to develop green supercapacitors based on binder-free, non-precious metal oxides electrodes, that is, a fast thermal annealing (FTA) method for the preparation of pseudocapacitor electrodes based on amorphous iron oxide-carbon black ($FeO_x$-CB) and $Mn_3O_{4x}$ with high areal capacitances. Our method unifies the following three common steps of electrode preparation into a single step: (i) synthesis of the metal oxides, (ii) composite material processing with a carbon conductive additive, and (iii) coating on the current collector. We show that CB (or other conductive elements) can be *in situ* composited with the metal oxides and simultaneously coated on the nickel foam without

employing any binder, which improves the electrochemical performance of the pseudocapacitor substantially by reducing the electrical resistance and promoting charge transfer rate. FTA is carried out at moderately low temperatures that reduces the energy cost of electrode production at large scale. It also requires a minimum amount of materials (i.e., only a metal nitrate in 5–10 ml of ethylene glycol as solvent) to prepare the electrodes; therefore, the waste produced during the electrode processing is also very small. Finally, our method paves the way toward new electrode manufacturing processes that exclude the use of binders, like Teflon and PVDF. It avoids the use of binders and solvents required to cast active materials on current collectors, that represents an additional value for green and low-energy demanding processes.

## EXPERIMENTAL

Ferric nitrate nonahydrate ($Fe(NO_3)_3.9H_2O$, 99%), manganese nitrate hexahydrate ($Mn(NO_3)_2.6H_2O$, 99%), ethylene glycol (98%), and sodium sulfate nonahydrate ($Na_2SO_4.9H_2O$, 99.99%) were purchased from Sigma-Aldrich Company. Carbon black (Super-P$^®$, BET 65.5 m$^2$ g$^{-1}$) was purchased from Erachem Comilog Company. Nickel foam was purchased from Changsha Lyrun Material Company (Shangsha, China).

## Preparation of FeO$_x$-CB/Ni Foam

Nickel foam was cut into circular pieces with a diameter of 0.9 cm (area: 0.64 cm$^2$). Then they were cleaned with 10% HCl and deionized water, sequentially. The $FeO_x$-CB was synthesized directly onto the Ni foam. In a typical synthesis, 0.5 mmol $Fe(NO_3)_3.9H_2O$ and 10 mg CB were dissolved in 10 mL of ethylene glycol by vigorous stirring. The Ni foam was immersed in the solution and the solution was heated on a hot plate to $150°C$ for 20 min during which the solution is quickly dehydrated. Then it was immediately heated to $300°C$ for 5 min, resulting in the deposition of $FeO_x$-CB on the Ni foam after a brief exhaust of voluminous smoke. Finally, the $FeO_x$-CB/Ni foam was taken out and washed successively with water and ethanol. The $FeO_x$ was also prepared by the same method but without the CB.

## Preparation of Mn$_3$O$_4$/Ni Foam

The $Mn_3O_4$/Ni foam was prepared according to the method in section Preparation of $FeO_x$-CB/Ni Foam. Then, it was electrochemically activated by 200 successive voltammetric cycles in 1 M $Na_2SO_4$, and named a-$Mn_3O_4$.

## Physical Characterization

The materials were characterized by X-ray diffraction (XRD) on a Philips PW-1730 X-ray diffractometer using Cu K$\alpha$ radiation $\lambda$ = 1.5405 Å. Thermal gravimetric analysis (TGA) measurements were carried out in oxygen atmosphere. The samples were analyzed on a platinum pan under an oxygen flow rate of 60.0 mL/min with a temperature ramp of $10°C$/min up to $600°C$. Surface morphology and elemental composition of the materials were studied by the field emission scanning electron

microscopy (FE-SEM) equipped with an energy dispersive X-ray spectrometer (EDS) on a Zeiss SIGMA VP. Transmission electron microscopy (TEM) images were obtained by using a Philips CM100.

## Electrochemical Measurements

The oxidation state and the stoichiometry of the iron oxide in $FeO_x$-CB sample was determined based on a simple potentiometric redox titration of Fe(II) ions in the dissolved sample. Details can be found in section Preparation of $FeO_x$-CB/Ni Foam, **Supplementary Material**. The electrodes were studied by cyclic voltammetry (CV), galvanostatic charge-discharge (GCD), and electrochemical impedance spectroscopy (EIS) using a potentiostat/galvanostat (PGSTAT M101, Metrohm Autolab B.V) in three-electrode and two-electrode configurations. For three-electrode measurements, $Hg/Hg_2Cl_2$ (3 M KCl), platinum coil, and $FeO_x$-CB/Ni foam or a-$Mn_3O_4$/Ni foam were used as the reference electrode, counter electrode, and working electrode, respectively. EIS measurements were carried out in a frequency range from 100 kHz to 100 mHz with an AC potential of 10 mV. One molar of $Na_2SO_4$ was used as the electrolyte. The mass loading of the materials on the Ni foam was 3–4 mg $cm^{-2}$.
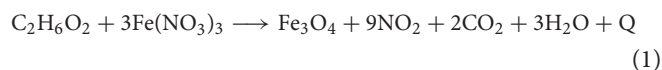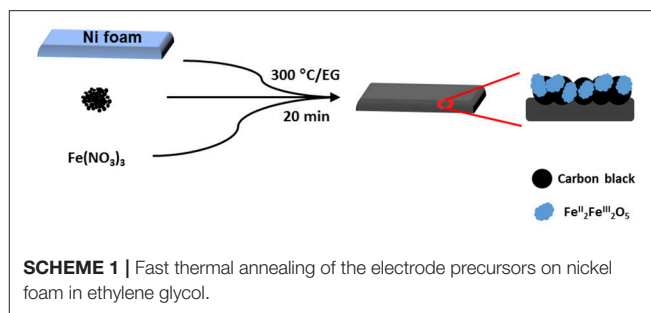
Preliminary three-electrode studies were carried out using conventional glass electrochemical cells. For the full cell studies, T-shape Teflon Swagelok-type cells (BOLA) with a 100 μm separator and 0.64 $cm^2$ electrode disks were used. The reference electrode was set in the middle of the cell to monitor each electrode potential during the supercapacitor cycling tests.

The electrode capacitance (C) was calculated from cyclic voltammetry by the slope of the linear part of the plots of the integrated current over time (upon CV discharge) vs. electrode potential. Electrode areal capacitance (F $cm^{-2}$) and electrode specific capacitance (F $g^{-1}$) were obtained by normalizing the capacitance to the electrode geometric area and to the mass of $FeO_x$-CB or a-$Mn_3O_4$, respectively (Ni foam weight is excluded).

For measuring specific capacitance based on the GCD, the discharge curves were first fitted to a straight line, and then the capacitance was calculated from the reciprocal of the slope of electrode potential (for three-electrode set up) or cell voltage (for 2-electrode set up) vs. discharge capacity. More details on the calculation of the supercapacitor parameters (Capacitance, and energy/power density) and their formulas can be found in section Preparation of $Mn_3O_4$/Ni Foam, **Supplementary Material**.

## RESULTS AND DISCUSSIONS

A schematic representation of the electrode processing for iron oxide nanocomposite is shown in **Scheme 1**. The mechanism for FTA deposition of the metal oxides is proposed as follows. During the thermal annealing, $M^{n+}$ ions are solvolysed and form metal alkoxides. Then, an exothermic flameless auto-combustion reaction between EG and $NO_3^-$ takes place, that raises the temperature further and drives the olation reaction of metal alkoxides to metal oxides. An overall reaction can be proposed as follows:



SCHEME 1 | Fast thermal annealing of the electrode precursors on nickel foam in ethylene glycol.

$$C_2H_6O_2 + 3Fe(NO_3)_3 \longrightarrow Fe_3O_4 + 9NO_2 + 2CO_2 + 3H_2O + Q \quad (1)$$

In the meantime, the ethylene glycol is also polymerized to polyglycolic acid (Takahashi et al., 2016) that can act as an internal binder in the carbon-metal oxides coated on the nickel foam.

## Structure and Morphology

**Figure 1A** shows the XRD patterns of the $FeO_x$-CB powder and $FeO_x$-CB/Ni foam. They show any a few slight peaks, signifying the rather amorphous nature of the nanocomposite. The XRD pattern of $FeO_x$-CB powder shows a peak between 20 and 30° due to the (002) plane of graphitic carbon (Liu et al., 2010) and two other peaks at 35 and 42.5° due to the (311) and (400) planes of $Fe_3O_4$. **Figure 1B** shows the XRD pattern of the manganese oxide/Ni foam obtained by the FTA method. The reflections for the planes of (101), (112), (103), (211), (004), (220), (321), (324), and (400) are indexed to the tetragonal hausmannite structure of $Mn_3O_4$ [Ref. Code 24-0734] in agreement with other reported $Mn_3O_4$ compound (Dubal et al., 2010a). **Figures 1C,D** shows the IR spectra of the $FeO_x$-CB and $Mn_3O_4$ samples. The peak at 590 $cm^{-1}$ is due to Fe-O stretch in $Fe_3O_4$ (**Figure 1C**), and the two strong peaks at 490 and 607 $cm^{-1}$ for $Mn_3O_4$ (**Figure 1D**) are due to coupling between Mn-O stretching vibrations at tetrahedral and octahedral sites (Tian et al., 2013). Both spectra share carbon-oxygen functional features including alcoholic hydroxyl stretch (3,420 $cm^{-1}$), symmetric and asymmetric stretch of carboxylate (~1,590 and 1,385 $cm^{-1}$), and C-O stretch (~1,070). Therefore, both materials are highly hydrophilic.

**Figure 1E** shows the TGA of the $FeO_x$-CB sample. It shows two distinct weight losses at about 250 and 450°C. The first weight loss is due to the decomposition of carbon-oxygen functional groups such as –COH and –COOH that have survived the thermal annealing. Similar weight losses in TGA has been also reported for the decomposition of oxygen functional groups in graphene oxide (Wojtoniszak et al., 2012; Dehghanzad et al., 2016). The second weight loss at 450°C is due to the oxidation of the added carbon black in the nanocomposite (Lim et al., 2013; Zha et al., 2015; Li et al., 2017). Based on these two weight losses, the amount of total carbon content in the sample is 30.2 wt.%. **Figure 1F** shows the TGA of the $Mn_3O_4$ sample. As expected, it shows only
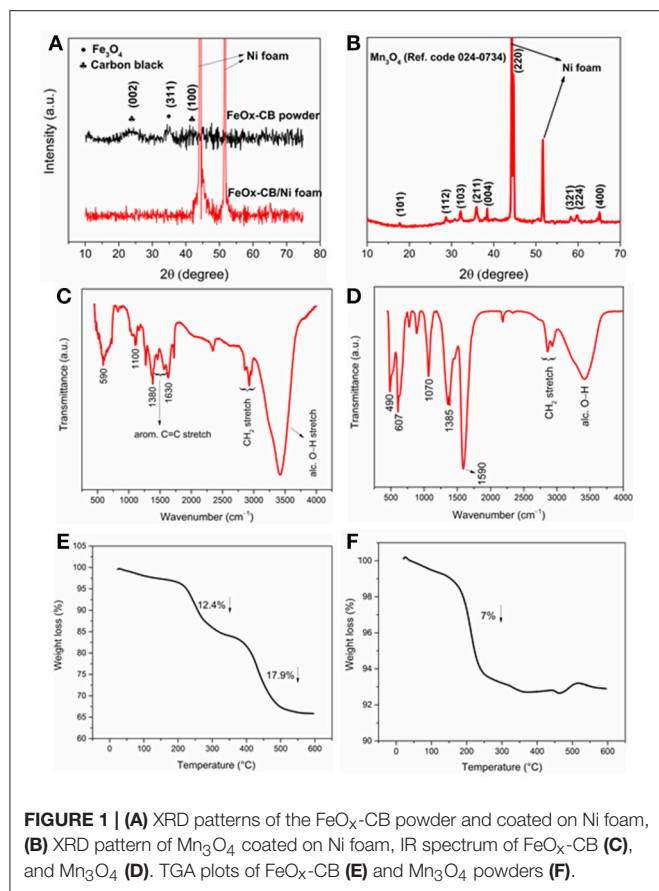
FIGURE 1 | (A) XRD patterns of the $FeO_x$-CB powder and coated on Ni foam, (B) XRD pattern of $Mn_3O_4$ coated on Ni foam, IR spectrum of $FeO_x$-CB (C), and $Mn_3O_4$ (D). TGA plots of $FeO_x$-CB (E) and $Mn_3O_4$ powders (F).

one weight loss at around 225°C due to the decomposition of carbon-oxygen groups that account for 7.0 wt.% of the sample.

**Figure 2a** shows a representative FESEM image of the $FeO_x$-CB sample. The $FeO_x$-CB particles appear as interconnected nanospheres creating a macroporous surface structure. The FESEM image of the $Mn_3O_4$ (**Figure 2b**) shares similar morphological features. **Figure 2c** shows the EDS of the $FeO_x$-CB. It confirms the presence of Fe, O, and C elements in the powder, and its elemental mapping analysis (**Figure S1**) shows that these elements are distributed quite homogeneously within the particles. According to the EDS, the carbon element accounts for 26.5 wt.% of the $FeO_x$-CB sample (**Table S1**), agreeing with the total carbon content from the TGA (30.2 wt.%.). The molar ratio of O/Fe is almost three times higher than those of the known stoichiometric iron oxides (i.e., $Fe_3O_4$ or $Fe_2O_3$) (**Table S1**), confirming the presence of abundant hydrophilic oxygen-carbon groups in the sample. The EDS of $Mn_3O_4$ (**Figure 2d**) also confirms the presence of Mn, O, and partial amount of C from the burnt ethylene glycol.

**Figure 3** shows the TEM images of $FeO_x$, $FeO_x$-CB, and pristine CB. The TEM images of $FeO_x$ (**Figures 3a,b**) show that $FeO_x$ particles are highly aggregated without a specific shape. However, the TEM image of the $FeO_x$-CB (**Figure 3c**) shows that $FeO_x$ particles have been anchored on the CB particles

leading to higher dispersity. The CB particles, in fact, have created a conducting network within the iron oxide particles. Furthermore, **Figure 3d** shows (meso) porous regions for $FeO_x$-CB, as indicated by the arrows, that are favorable for facile ion diffusion. **Figures 3e,f** show the TEM images of pristine CB. It shows CB particles with an average diameter of 50 nm without any surface porosity.

## Electrochemical Studies

Before studying the electrochemical performance of the $FeO_x$-CB/Ni foam electrode developed based on the FTA method, the oxidation state of the iron oxide and its stoichiometry were estimated by a simple method. A potentiometric redox titration of the dissolved iron oxide by permanganate revealed that the sample contains 24.3 wt.% Fe(II). A simple calculation revealed a stoichiometry of $Fe_2^{II}Fe_2^{III}O_5$ that is consistent with a mixture of FeO (wustite) and $Fe_3O_4$ (magnetite) (**Figure S2** and section Electrochemical Studies in **Supplementary Material**). **Figure 4A** shows the CVs at 50 mV s$^{-1}$ of the $FeO_x$–CB electrodes synthesized from starting solutions containing different amounts of carbon black annealed at 300°C. The $FeO_x$ without carbon black shows the lowest current densities. The samples containing carbon black show significant enhancements in their current densities along with more defined redox peaks. This effect can be explained as follows: the carbon black promotes the electrical contact among the $FeO_x$ particles and the Ni foam and promotes charge transfer (Sayahi et al., 2014), therefore, it increases the utilization of the electroactive material. The redox peaks are around −0.4 and −0.8 V vs. $Hg/Hg_2Cl_2$ (cathodic peaks) and −0.6 and −0.1 V vs. $Hg/Hg_2Cl_2$ (anodic peaks). The underlying redox reactions are not fully known, but similar redox peaks have been also reported by Brousse et al. for iron oxide-carbon composites in $Na_2SO_4$ solution (Gao et al., 2014; Rebuttini et al., 2015). **Figure 4B** shows a plot of discharge Q, calculated based on the cyclic voltammograms vs. the pre-mixing weight of the carbon black. It shows that the discharge capacity Q normalized to the amount of $FeO_x$-CB composite on the electrode reaches its highest value of 36 C g$^{-1}$ when the pre-mixing weight of carbon black is 10 mg (about 18 wt.% of the $FeO_x$-CB weight); therefore, this value was selected as the optimum amount of CB. **Figure 4C** compares the Nyquist plots of the $FeO_x$ and the optimum $FeO_x$-CB, demonstrating the beneficial effect of CB. Indeed, while for the $FeO_x$ electrodes the Nyquist plot is a Warburg line with a slope close to 45° (slope = 55.6°), that is representative of diffusion-limited processes, for $FeO_x$-CB electrode the Nyquist plot with a low frequency tale almost parallel to the imaginary axis (slope = 81.1°) describes a capacitive element. This enhancement confirms a remarkable improvement in charge (ions and electrons) diffusion for the nanocomposite. The uncompensated resistance that is evaluated at the highest frequency, $R_u$, of $FeO_x$-CB has not changed compared with that of $FeO_x$ ($R_u$ ~2.5 Ω) because this value is strictly controlled by the solution resistance and cell geometry which were the same for all the experiments.

**Figure 5** exhibits the rate performance of the $FeO_x$-CB, which is a crucial parameter in the evaluation of the supercapacitor electrodes. **Figure 5A** shows the effect of potential scan rate on
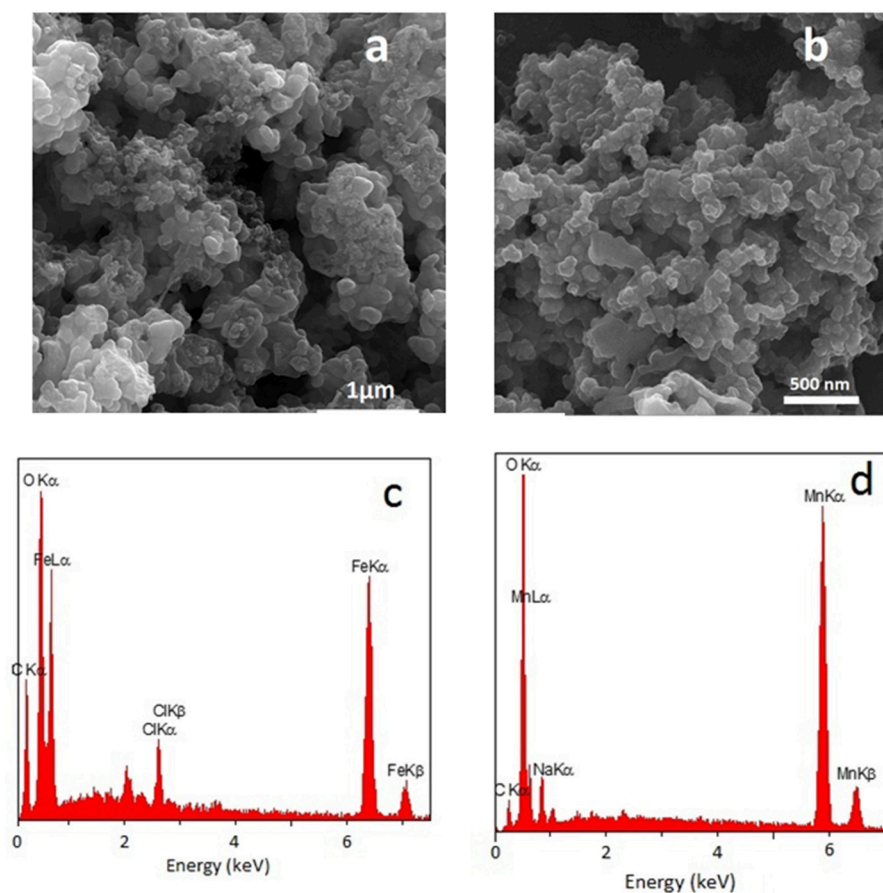
**FIGURE 2 |** FESEM image and EDS spectrum of FeO$_x$-CB containing 30 wt.% total carbon annealed at 300°C **(a,c)** and FESEM image and EDS spectrum of Mn$_3$O$_4$ **(b,d)**.

the CVs of the FeO$_x$-CB synthesized with 10 mg of CB (18 wt.% CB) at 300°C. The redox peaks are no longer seen at relatively high scan rates. However, it is reasonable to assume that the charge is stored dominantly through one or two electron transfer reactions between Fe$^{II}$ and Fe$^{III}$ (Xie et al., 2016). The CVs show a fair symmetry vs. potential axis at scan rates below 50 mV s$^{-1}$, but they lose the symmetry at higher scan rates, which is due to the increasing limitation on ion diffusion in the electrode pores and the electron transfer within the electrode.

**Figure 5B** shows the GCD cycles of an FeO$_x$-CB electrode with mass loading of 3.4 g cm$^{-2}$ from 0.2 to −0.8 V at different current densities. The charge and discharge curves are symmetric with a coulombic efficiency of 91%, and the pseudocapacitive response holds in the same potential region of 0 to −0.8 V as that in the CVs. At 1 mA cm$^{-2}$ the GCD curves do not show a noticeable ohmic drop. At 2.5 mA cm$^{-2}$ the ohmic drop is 42 mV (**Figure S3**) which is fairly small and can be attributed to the facile electron migration and ion diffusion in the nanocomposite. The areal and specific capacitance and the corresponding capacitance retention at different current densities are shown in **Figure 5C**. The areal capacitance for FeO$_x$-CB is 435 and 180 mF cm$^{-2}$ at the current density of 1 and 20 mA cm$^{-2}$, respectively, showing

a capacitance retention of 41.3%. It has to be noted that at the highest current, which corresponds to 6 A g$^{-1}$, the specific capacitance is 54 F g$^{-1}$, a still high value which demonstrates the good performance of the proposed material.

**Table 1** compares the specific capacitance of the FeO$_x$-CB with some of the best iron oxide-based electrodes prepared by various methods. A specific capacitance of 128 F g$^{-1}$ at a current density of 0.3 A g$^{-1}$ with a high loading mass of 3.4 mg cm$^{-2}$ make the FeO$_x$-CB a competitive material that has the advantage of being produced by a low-cost, and sustainable method.

Hausmannite (Mn$_3$O$_4$) was also coated *in situ* on Ni foam using a similar FTA method and investigated as the positive electrode by the CV and GCD techniques. For the Mn$_3$O$_4$/Ni foam, interestingly, the current density increases during the first 200 CV cycles (**Figure S4**). This effect has been also observed by Lokhande et al. and other groups for voltammetric cycling of Mn$_3$O$_4$ in alkali sulfate solutions, and it was attributed to the phase transformation of hausmanite (Mn$_3$O$_4$) to birnessite (MnO$_2$) (Dubal et al., 2010a,b; Komaba et al., 2012). Therefore, an XRD of the Mn$_3$O$_4$/Ni foam after 200 cycles was recorded (**Figure S5**). The XRD pattern does not show any peak for MnO$_2$; however, the Mn$_3$O$_4$

**TABLE 1 |** Comparison of the $FeO_x$-CB electrode features with iron oxide-based materials reported in the literature.

| | Synthesis method | Areal capacitance [mF cm$^{-2}$] | Specific capacitance [F g$^{-1}$] | Mass loading [mg cm$^{-2}$] | Electrolyte |
|---|---|---|---|---|---|
| $Fe_3O_4$ nanospheres (Aparna et al., 2018) | Solvothermal | – | 101@2mV s$^{-1}$ | 0.3 | 3 M KOH |
| $Fe_3O_4$/RGO (Yan et al., 2015) | Electrostatic | – | 193@0.3 A g$^{-1}$ | – | 6 M KOH |
| $FeO_x$/RGO (Gao et al., 2014) | Benzyl alcohol | – | 126@5mV s$^{-1}$ | – | 1 M Na$_2$SO$_4$ |
| $Fe_2O_3$ nanorods (Lu et al., 2014) | Hydrothermal | 277.3@10 mV s$^{-1}$ | 64.5@10mV s$^{-1}$ | 4.3 | 1 M LiCl |
| $Fe_3O_4$/n-doped graphene (Liu et al., 2016) | Solvothermal | – | 274@1 A g$^{-1}$ | 2 | 2 KOH |
| $Fe_xO_y$-f-RGO (Rebuttini et al., 2015) | Solvothermal | – | 79.7@20 mV s$^{-1}$ | **–** | 1 M Na$_2$SO$_4$ |
| $Fe_2O_3$ nanotubes (Yang et al., 2014) | Hydrothermal | 180.4@1 mA cm$^{-2}$ | 257.8@1.4 A g$^{-1}$ | 0.7 | 5 M LiCl |
| $Fe_3O_4$/RGO (Lalwani et al., 2017) | Hydrothermal | – | 63.5 @1 A g$^{-1}$ | 0.3–0.5 | H$_2$SO$_4$ |
| Iron oxide/RGO (Wang et al., 2016) | Electrodeposition | 406.5@10 mV s$^{-1}$ | – | 0.15 | 5 M LiCl |
| $FeO_x$-CB | FTA | 408@0.3 A g$^{-1}$ | 128@0.3 A g$^{-1}$ | 3.4 | 1 M Na$_2$SO$_4$ |



**FIGURE 3 |** TEM images of $FeO_x$ annealed at 300°C **(a,b)**, $FeO_x$-CB containing 18 wt.% carbon black annealed at 300°C **(c,d)** (Inset in **c** shows $FeO_x$ anchored on CB particles), and **(e,f)** pristine carbon black.
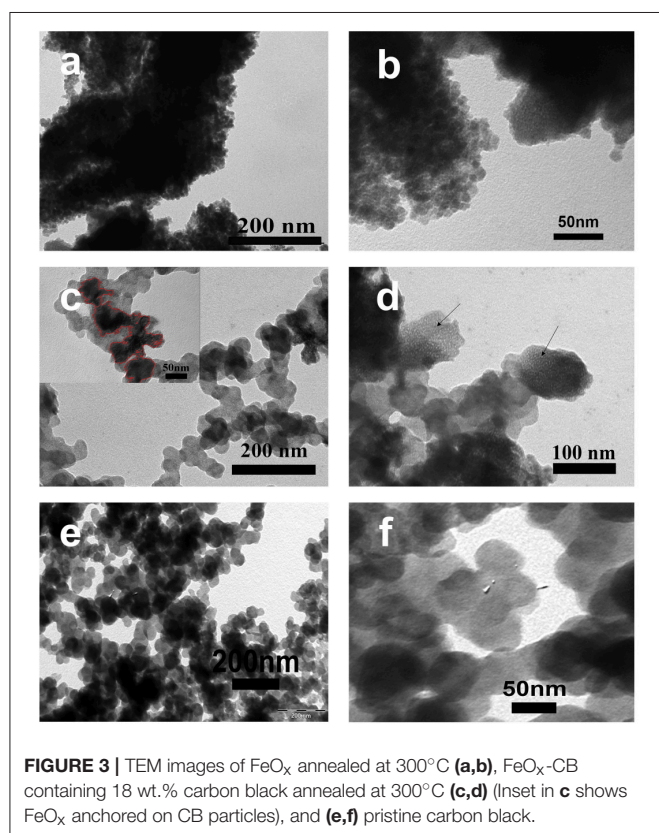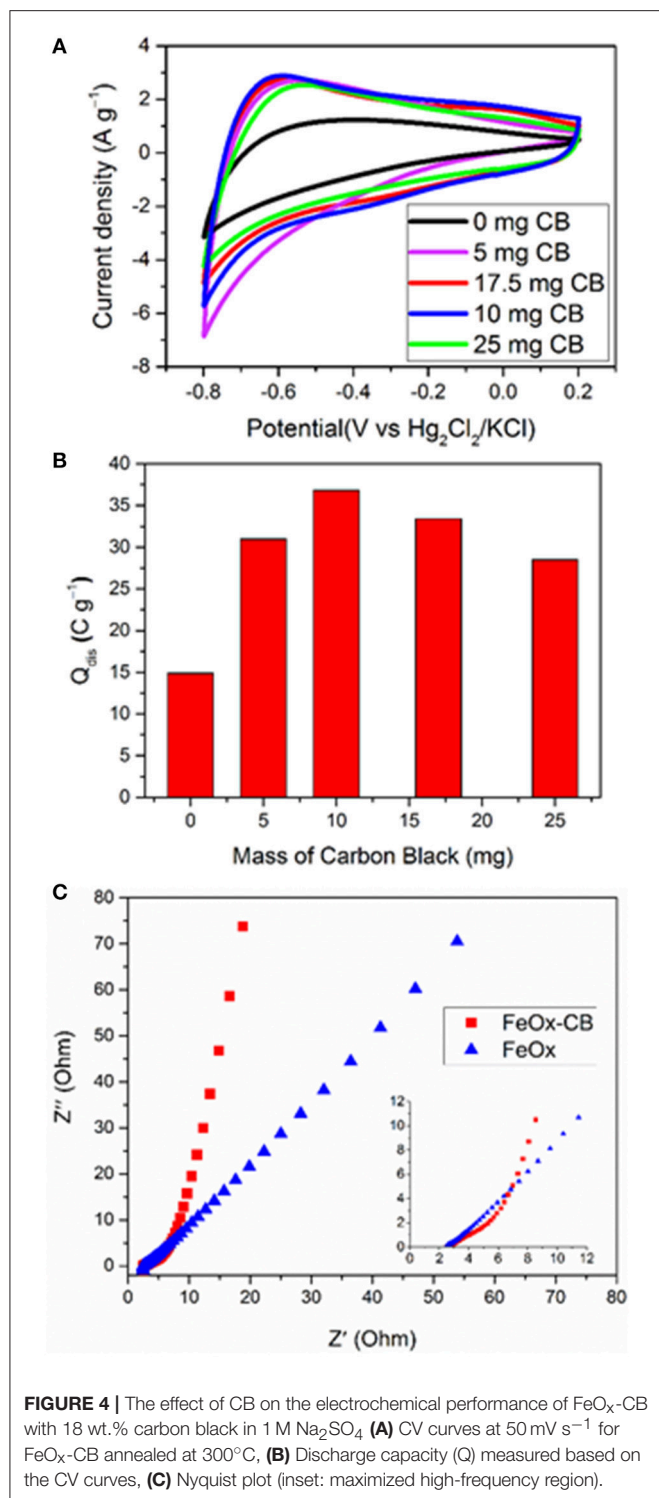
peaks are significantly less intense; therefore, the activation processes can be attributed to amorphisation during bulk sodium intercalation/deintercalation. This process is assisted by the intrinsic hydrophilicity of $Mn_3O_4$ (contact angle of 2–8°; Kulkarni et al., 2017) and the presence of carbon-oxygen groups. **Figure 6A** shows the effect of different scan rates on the electrochemical performance of a-$Mn_3O_4$ (activated by 200

cycles) from −0.2 to 0.8 V. It shows a semi-rectangular shape with a little distortion at high scan rates. **Figure 6B** shows the GCD cycles of the same electrode in the same potential window at 2.5 mA cm$^{-2}$. The charge and discharge curves show a good symmetry with a coulombic efficiency of 98.4% and an ohmic drop of 82 mV measured from the discharge curves (**Figure S6**). The a-$Mn_3O_4$/Ni foam electrode exhibits a high areal capacitance of 480 mF cm$^{-2}$. It is worth noting that the CVs and galvanostatic plots are representative of faradaic reactions involving (multi) electron transfer between $Mn^{4+}$ and $Mn^{3+}$ coupled with the deintercalation/intercalation of Na$^+$ ions that is dominantly responsible for the charge storage of the material (Guillemet et al., 2012; Brousse et al., 2015; Kong et al., 2016; Costentin et al., 2017). Such good electrochemical performance of the a-$Mn_3O_4$ electrode was achieved without the need for adding CB in the composite. Therefore, in order to reduce the impact of electrochemically-inactive components on the total mass of supercapacitor, a-$Mn_3O_4$ electrodes were used without CB.

## Two-Electrode Studies

As indicated above, both EDLC and pseudocapacitve processes operate in these electrodes. A definitive, yet simple, diagnostic test to distinguish both charging processes in these electrodes is to examine the shapes of the low-scan rate CVs (Costentin et al., 2017). **Figure 7A** shows the CVs of the two electrodes and the pristine Ni foam at 5 mV s$^{-1}$ in a typical electrochemical glass cell. The improvements observed in the CV current densities of the electrodes compared to the Ni foam are mainly due to pseudocapacitive processes as revealed by their mirror-like broad redox peaks vs. potential axis. Similar redox peaks for carbon-$Fe_3O_4$ composites in the potential range of 0 to −0.5 V vs. Hg/Hg$_2$Cl$_2$ in sodium sulfate solution have been also reported by other groups. The redox peaks are attributed to Fe$^{II}$/Fe$^{III}$ electron transfer reaction, and as observed here, they are significantly promoted by the carbon supports such as reduced graphene oxide (Rebuttini et al., 2015; Naderi et al., 2016; Li et al., 2018)

**FIGURE 4 |** The effect of CB on the electrochemical performance of $FeO_x$-CB with 18 wt.% carbon black in 1 M $Na_2SO_4$ **(A)** CV curves at 50 mV s$^{-1}$ for $FeO_x$-CB annealed at 300°C, **(B)** Discharge capacity (Q) measured based on the CV curves, **(C)** Nyquist plot (inset: maximized high-frequency region).



**FIGURE 5 |** Rate performance: effect of different scan rates **(A)** and current densities **(B)** on the $FeO_x$-CB obtained at 300°C with 18 wt.% carbon black, and the corresponding capacitance retention **(C)**.

and carbon black (Sayahi et al., 2014). For $Mn_3O_4$, the redox peaks between 0.4 and 0.6 V are attributed to the reversible redox reaction between tetrahedral $[Mn^{II}O_4]$ and octahedral $[Mn^{III}O_6]$ (Yeager et al., 2013), in contrast to $MnO_2$ which does not show any obvious redox peaks (Wang et al., 2017). Therefore, it can be concluded that the redox reactions in
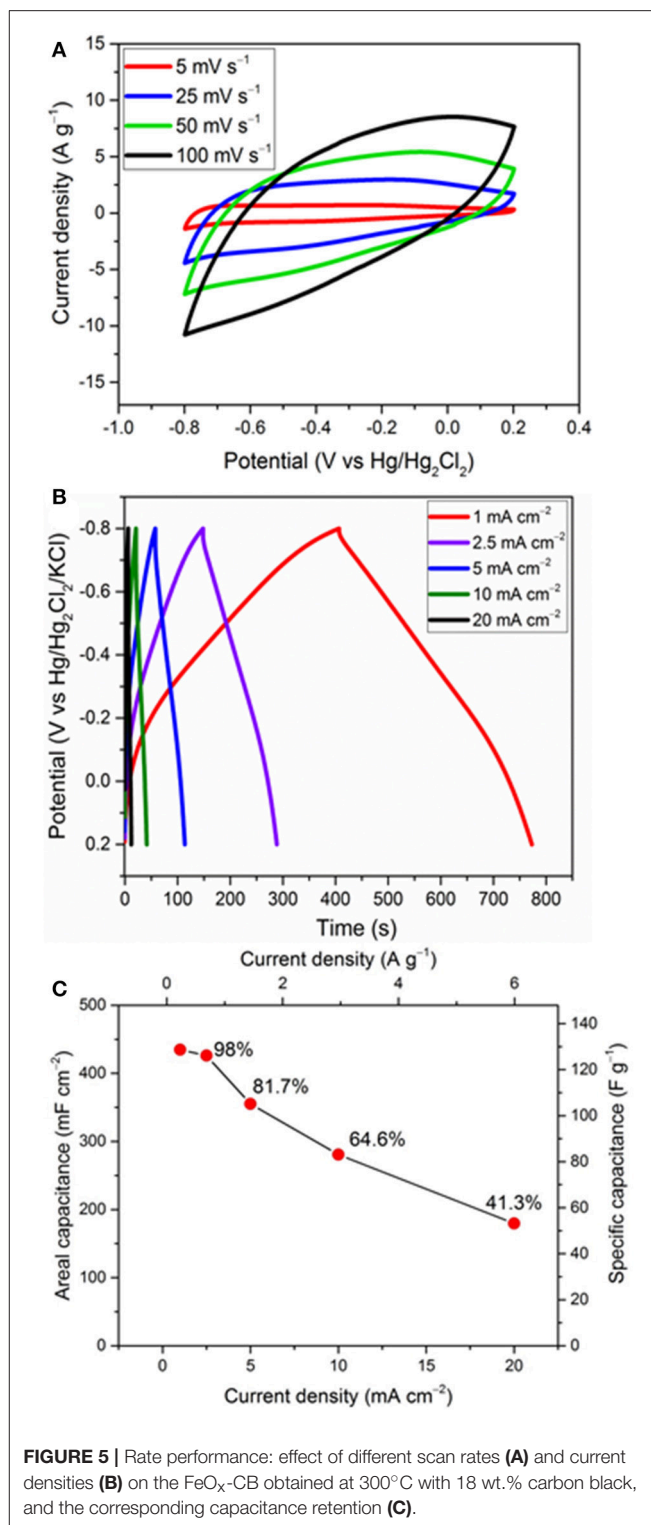
$Fe_3O_4$ and $Mn_3O_4$ are facilitated by simultaneous presence of two oxidation states of $M^{2+}$ and $M^{3+}$. The potential for the $FeO_x$-CB and a-$Mn_3O_4$ pseudocapacitive processes span in the ranges of 0/−0, 8 V and −0.2/0, 8 V vs. $Hg/Hg_2Cl_2$, respectively,
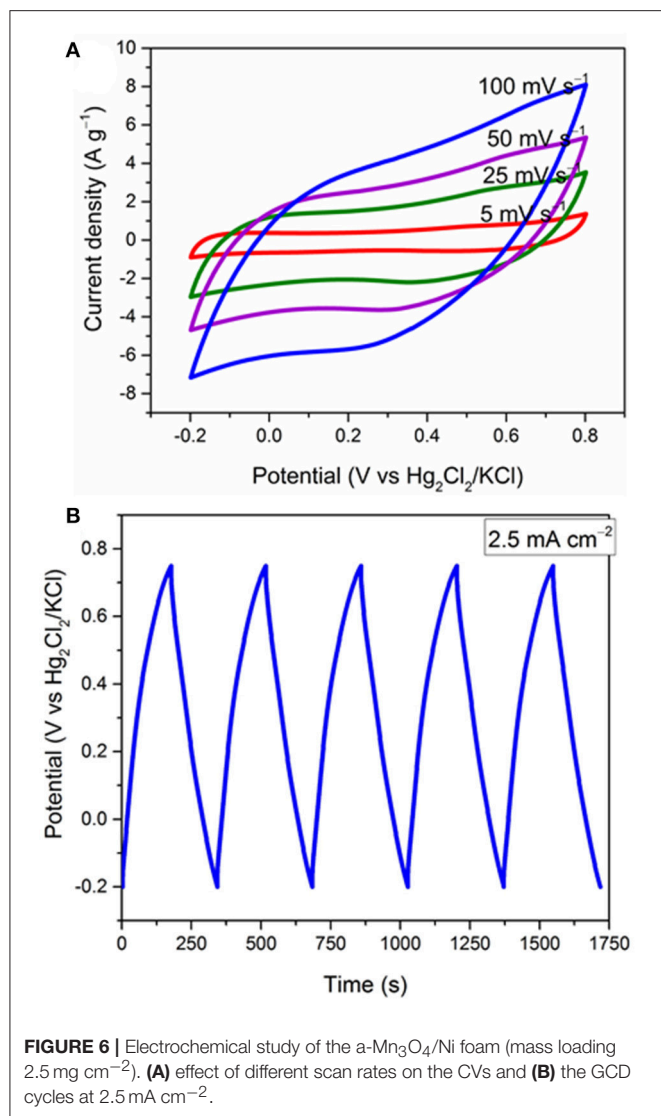
**FIGURE 6 |** Electrochemical study of the a-$Mn_3O_4$/Ni foam (mass loading 2.5 mg cm$^{-2}$). **(A)** effect of different scan rates on the CVs and **(B)** the GCD cycles at 2.5 mA cm$^{-2}$.

that allows charging the supercapacitor at a voltage of 1.6 V at maximum.

The FeO$_x$-CB and a-$Mn_3O_4$ were used as the negative and positive electrodes, respectively, to assemble an asymmetric supercapacitor (FeO$_x$-CB//a-$Mn_3O_4$). **Figure 7B** shows the voltammetric response of the supercapacitor at different scan rates over 1.5 V. Remarkably, the supercapacitor does not show a significant deviation in its mirror-like CV up to a high scan rate of 1,000 mV s$^{-1}$, suggesting a small equivalent series resistance of the supercapacitor. However, at a still higher scan rate of 2,000 mV s$^{-1}$ the CVs show a severe distortion, mainly due to ohmic contributions of the electrodes. A comparison of the CVs of the supercapacitor with that of the electrodes presented in **Figures 5A**, **6A** reveals that the charge-discharge rate performance has improved for the Swagelok supercapacitor cell. This can be explained considering that cell geometry is optimized. In the supercapacitor cell, electrodes are contacted by their rear side while for 3-electrode test they were connected by

co-axially climping the Nickel foam. Also, in the supercapacitor, the two electrodes are stacked and their distance is very small, corresponding to the separator thickness (ca. 100 μm), which in turn makes any contribution from electrolyte to the impedance of the system negligible.

**Figure 7C** shows the GCD cycles of the supercapacitor at a high current density of 10 mA cm$^{-2}$ with simultaneous monitoring of the electrode potentials. Both electrodes actively participate in the charge/discharge in their respective potential windows, and the charge-discharge cycles for the supercapacitor are fairly symmetric vs. the potential axis. A negligible ohmic drop, resulting from a small ESR, is detectable at the start of the discharge. The supercapacitor shows a remarkable areal capacitance of 196 mF cm$^{-2}$ at the current density of 10 mA cm$^{-2}$. The energy density and power density calculated at 10 mA cm$^{-2}$ are 0.06 mW h cm$^{-2}$ (0.01 Wh/kg) and 8.3 mW cm$^{-2}$ (1.4 W/kg), respectively. The coulombic efficiency is 99.1%.

EIS spectroscopy was used to disentangle the different underlying electrode processes and their effect on the performance of the supercapacitor. **Figure 7D** shows the Nyquist plots of the supercapacitor and the electrodes. The plots display three features: (i) small semicircles at the highest frequencies that are representative of the charge-transfer process, (ii) a middle frequency line with 45° slope, attributed to diffusion limited processes, and (iii) al low frequency line almost parallel to the imaginary axis that is related to the capacitive response of the system. The circuit model shown in **Scheme 2** was used to fit the experimental nyquist plots. The ESR measured from the high frequency intercept of the Nyquist plots gives the real equivalent series resistance coupled with the capacitor (Yu et al., 2013). The ESR corresponds to the sum of each half-cell high frequency resistance Rei (ionic resistance of the electrolyte and the electrode electronic resistance). The ESR of 7 Ω was obtained for the supercapacitor, that agrees with the 7.2 Ω measured from the Bode plot when the phase shift is close to zero (**Figure S7**). It also agrees well with the ESR calculated from the Rei values for the electrodes (Rei(a-$Mn_3O_4$), Rei(FeO$_x$-CB), the electrodes are equally spaced from the reference, therefore each term also includes ionic contribution from the electrolyte):

$$ESR = R_{ei,(MnOx)} + R_{ei,(FeOx-CB)} = 3.7\,\Omega + 2.5\,\Omega = 6.2\Omega$$

The ESR measured here for the supercapacitor reflects on first the solution resistance of the 1 M Na$_2$SO$_4$, and second the electrode resistance including the charge transfer resistance, Rct, which in turn depends on the interparticle electronic resistance and film-current collector contact resistance (Fic et al., 2012; Barsoukov and Macdonald, 2018). The Rct values measured for the FeO$_x$-CB, a-$Mn_3O_4$, and the supercapacitor from the high frequency semicircle diameter of the Nyquist plots are 1.25, 0.15, and 1.7 Ω, respectively, indicating a more sluggish electron-transfer kinetics of the FeO$_x$-CB compared with that of a-$Mn_3O_4$. However, comparison of the slopes of the lines in the low-frequency region reveals that the diffusional resistance of the supercapacitor is due more to the a-$Mn_3O_4$ electrode, that, therefore drives the overall response of the cell at the low
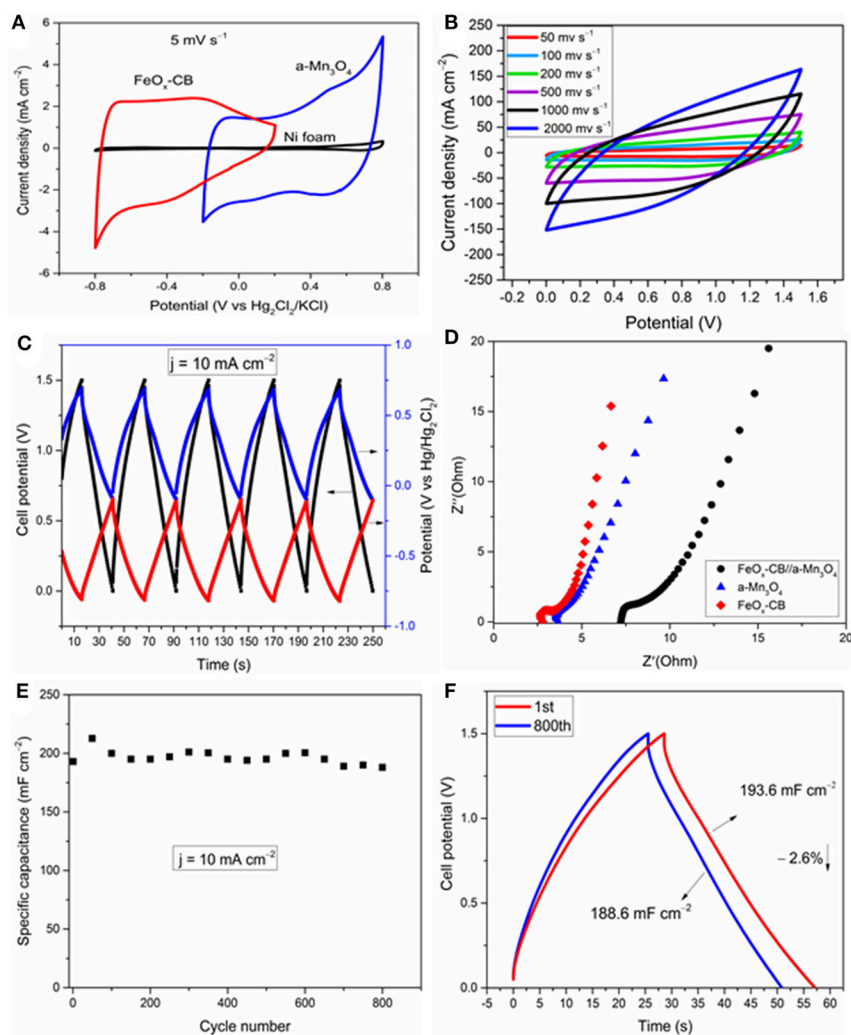
**FIGURE 7 |** Electrochemical study of the $FeO_x$-CB//a-$Mn_3O_4$ and the electrodes in the same cell. **(A)** CV cycles of the supercapacitor electrodes at 5 mV s$^{-1}$, effect of scan rate **(B)**, GCD cycles at 10 mA cm$^{-2}$: the black curve represents the cell voltage (left axis), the blue and red curves are the postive and negative electrode potentials (right axis) **(C)**, Nyquist plots **(D)**, areal capacitance vs. cycle number **(E)**, and comparison of the 1st and 800th cycle **(F)** at 10 mA cm$^{-2}$.
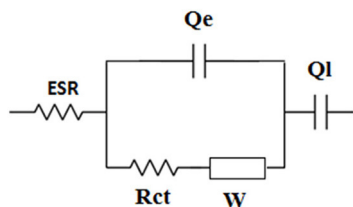


**SCHEME 2 |** Equivalent circuit model used to fit the experimental Nyquist plots. ESR includes the electrolyte ionic resistance and electrode and current collector electronic resistances. Rct and Qe are the charge transfer resistance and the double layer capacitance. W is the Warburg element that describes diffusion/limited processes and Ql is the limit capacitance. Constant phase elecments Q are used to take into account the deviation by ideal capacitive behavior. $Q = Y_0(j\,\omega)^{-n}$, where $Y_0$ is the admittance and Q is a capacitance for $n = 1$.

frequency region. Nonetheless, a phase angle of $-70°$ at 100 mHz for the supercapacitor (**Figure S7**) indicates that, though affected by diffusion, the process acting on the supercapacitor at low-frequency region approaches the limit capacitance. The areal capacitance of the supercapacitor was calculated to be 260 mF cm$^{-2}$ at 100 mHz. In addition, the Bode plot of the supercapacitor in **Figure S7** shows that at frequencies higher than 10 Hz the phaseshift angle tends to zero (i.e., between 0 and 10°); this indicates that for charge/discharge rates with a timescale lower than 0.1 s (i.e., logf = 1) the supercapacitor approaches the behavior of a resistor. This pattern agrees with that of the CVs in **Figure 7B** in which for a timescale lower than 0.8 s (i.e., 2,000 mV s$^{-1}$) the supercapacitor approaches a resistive behavior.

**Figures 7E,F** show the cycling stability of the $FeO_x$-CB//a-$Mn_3O_4$ supercapacitor over 800 GCD cycles. The specific capacitance of the supercapacitor after 800 cycles at 10 mA cm$^{-2}$

reduced only by 2.6% from an initial value of 194 to 189 mF $cm^{-2}$, showing a high cycling stability for the supercapacitor.

## CONCLUSION

If supercapacitors were to speak to the current demands in the electronics market, cost-effective and high-performance pseudocapacitor electrodes are indispensable. The use of benign materials and electrode processings that consume minimum amount of energy and materials are mandatory to meet the increasing market demand for supercapacitors and address the mounting environmental concerns. To this end, a fast annealing treatment of the Ni foam in a solution of the ethylene glycol was used to prepare high-performance pseudocapacitors without the need of any binder and energy, time, and cost demanding electrode lamination processes. Furthermore, it was shown that the *in-situ* added carbon black acts as a scaffold to disperse amorphous iron oxide particles; this resulted in the remarkable improvement of the electrochemical performance of $FeO_x$-CB due to the promoted ion and electron transport. A manganese oxide electrode was also fabricated by a similar method and used as the positive electrode. Finally, the developed psuedocapacitor electrodes were used to assemble an asymmetric supercapacitor, and their true performance were proved promising. FTA can also be used to

develop other metal-oxide electrodes for energetics and paves the way for a sustainable production of materials for energy storage.

## AUTHOR CONTRIBUTIONS

Our submission is approved by all the authors and responsible authorities. FS and KM equally contributed to the research and result analysis and discussion. MG assisted in the synthesis and analysis of the materials.

## ACKNOWLEDGMENTS

## SUPPLEMENTARY MATERIAL

The Supplementary Material for this article can be found online at: https://www.frontiersin.org/articles/10.3389/fchem.2019.00025/full#supplementary-material

## REFERENCES

Aparna, M. L., Grace, A. N., Sathyanarayanan, P., and Sahu, N. K. (2018). A comparative study on the supercapacitive behaviour of solvothermally prepared metal ferrite (MFe₂O₄, M = Fe, Co, Ni, Mn, Cu, Zn) nanoassemblies. *J. Alloys Compd.* 745, 385–395. doi: 10.1016/j.jallcom.2018.02.127

Balducci, A., Belanger, D., Brousse, T., Long, J. W., and Sugimoto, W. A. (2017). Guideline for reporting performance metrics with electrochemical capacitors: from electrode materials. *J. Electrochem. Soc.* 164, 1487–1488. doi: 10.1149/2.0851707jes

Barsoukov, E., and Macdonald, J. R. (2018). *Impedance Spectroscopy: Theory, Experiment, and Applications, 3rd Edn.* Hoboken, NJ: Wiley.

Brousse, T., Belanger, D., and Long, J. W. (2015). To be or not to be pseudocapacitive? *J. Electrochem. Soc.* 162, A5185–A5189. doi: 10.1149/2.0201505jes

Brousse, T., and Bélanger, D. A. (2003). Hybrid Fe₃O₄-MnO₂ capacitor in mild aqueous electrolyte. *Electrochem. Solid State Lett.* 6:A244. doi: 10.1149/1.1614451

Costentin, C., Porter, T. R., and Savéant, J. M. (2017). How do pseudocapacitors store energy? Theoretical analysis and experimental illustration. *ACS Appl. Mater. Interfaces* 9, 8649–8658. doi: 10.1021/acsami.6b14100

Dehghanzad, B., Razavi Aghjeh, M. K., Rafeie, O., Tavakoli, A., and Jameie Oskooie, A. (2016). Synthesis and characterization of graphene and functionalized graphene via chemical and thermal treatment methods. *RSC Adv.* 6, 3578–3585. doi: 10.1039/C5RA19954A

Dubal, D. P., Dhawale, D. S., Salunkhe, R. R., and Lokhande, C. D. (2010a). Conversion of chemically prepared interlocked cubelike Mn₃O₄ to birnessite MnO₂ using electrochemical cycling. *J. Electrochem. Soc.* 157:A812. doi: 10.1149/1.3428675

Dubal, D. P., Dhawale, D. S., Salunkhe, R. R., and Lokhande, C. D. (2010b). Conversion of interlocked cube-like Mn₃O₄ into nanoflakes of layered birnessite MnO₂ during supercapacitive studies. *J. Alloys Compd.* 496, 370–375. doi: 10.1016/j.jallcom.2010.02.014

Dyatkin, B., Presser, V., Heon, M., Lukatskaya, M. R., Beidaghi, M., and Gogotsi, Y. (2013). Development of a green supercapacitor composed entirely of environmentally friendly materials. *ChemSusChem* 6, 2269–2280. doi: 10.1002/cssc.201300852

Fic, K., Lota, G., Meller, M., and Frackowiak, E. (2012). Novel insight into neutral medium as electrolyte for high-voltage supercapacitors. *Energy Environ. Sci.* 5, 5842–5850. doi: 10.1039/C1EE02262H

Gao, P. C., Russo, P. A., Conte, D. E., Baek, S., Moser, F., Pinna, N., et al. (2014). Morphology effects on the supercapacitive electrochemical performances of iron oxide/reduced graphene oxide nanocomposites. *ChemElectroChem* 1, 747–754. doi: 10.1002/celc.201300087

Guillemet, P., Brousse, T., Crosnier, O., Dandeville, Y., Athouel, L., and Scudeller, Y. (2012). Modeling pseudo capacitance of manganese dioxide. *Electrochim. Acta* 67, 41–49. doi: 10.1016/j.electacta.2012.01.110

Gund, G. S., Dubal, D. P., Chodankar, N. R., Cho, J. Y., Gomez-Romero, P., Park, C., et al. (2015). Low-cost flexible supercapacitors with high-energy density based on nanostructured MnO₂ and Fe₂O₃ thin films directly fabricated onto stainless steel. *Sci. Rep.* 5:12454. doi: 10.1038/srep12454

Komaba, S., Tsuchikawa, T., Ogata, A., Yabuuchi, N., Nakagawa, D., and Tomita, M. (2012). Nano-structured birnessite prepared by electrochemical activation of manganese(III)-based oxides for aqueous supercapacitors. *Electrochim. Acta* 59, 455–463. doi: 10.1016/j.electacta.2011.10.098

Kong, S., Cheng, K., Gao, Y., Ouyang, T., Ye, K., Wang, G., et al. (2016). A novel three-dimensional manganese dioxide electrode for high performance supercapacitors. *J. Power Sources* 308, 141–148. doi: 10.1016/j.jpowsour.2016.01.076

Kulkarni, S., Puthusseri, D., Thakur, S., Banpurkar, A., and Patil, S. (2017). Hausmannite manganese oxide cathodes for supercapacitors: surface wettability and electrochemical properties. *Electrochim. Acta* 231, 460–467. doi: 10.1016/j.electacta.2017.01.165

Lalwani, S., Sahu, V., Marichi, R. B., Singh, G., and Sharma, R. K. (2017). *In situ* immobilized, magnetite nanoplatelets over holey graphene nanoribbons for high performance solid state supercapacitor. *Electrochim. Acta* 224, 517–526. doi: 10.1016/j.electacta.2016.12.057

Li, X., Li, X., Fan, L., Yu, Z., Yan, B., Xiong, D., et al. (2017). Rational design of Sn/SnO$_2$/porous carbon nanocomposites as anode materials for sodium-ion batteries. *Appl. Surf. Sci.* 412, 170–176. doi: 10.1016/j.apsusc.2017.03.203

Li, Y., Yu, J., Chen, S., Huang, Z., and Wang, L. (2018). Fe$_3$O$_4$/functional exfoliation graphene on carbon paper nanocomposites for supercapacitor electrode. *Ionics* 24, 2697–2704. doi: 10.1007/s11581-017-2409-y

Lim, J., Ryu, S. Y., Kim, J., and Jun, Y. (2013). A study of TiO$_2$/carbon black composition as counter electrode materials for dye-sensitized solar cells. *Nanoscale Res. Lett.* 8:227. doi: 10.1186/1556-276X-8-227

Liu, L., Lang, J., Zhang, P., Hu, B., and Yan, X. (2016). Facile synthesis of Fe$_2$O$_3$ nano-dots@nitrogen-doped graphene for supercapacitor electrode with ultralong cycle life in koh electrolyte. *ACS Appl. Mater. Interfaces* 8, 9335–9344. doi: 10.1021/acsami.6b00225

Liu, X. Y., Huang, M., Ma, H. L., Zhang, Z. Q., Gao, J. M., Zhu, Y. L., et al. (2010). Preparation of a carbon-based solid acid catalyst by sulfonating activated carbon in a chemical reduction process. *Molecules* 15, 7188–7196. doi: 10.3390/molecules15107188

Lu, X., Zeng, Y., Yu, M., Zhai, T., Liang, C., Xie, S., et al. (2014). Oxygen-deficient hematite nanorods as high-performance and novel negative electrodes for flexible asymmetric supercapacitors. *Adv. Mater.* 26, 3148–3155. doi: 10.1002/adma.201305851

Lukatskaya, M. R., Kota, S., Lin, Z., Zhao, M.-Q., Shpigel, N., Levi, M. D., et al. (2017). Ultra-high-rate pseudocapacitive energy storage in two-dimensional transition metal carbides. *Nat. Energy* 6:17105. doi: 10.1038/nenergy.2017.105

Malaie, K., Ganjali, M., Alizadeh, T., and Norouzi, P. (2018). Electrochemical investigation of magnetite-carbon nanocomposite *in situ* grown on nickel foam as a high-performance binderless pseudocapacitor. *J. Solid State Electrochem.* 22, 2597–2604. doi: 10.1007/s10008-018-3976-1

Naderi, H. R., Norouzi, P., Ganjali, M. R., and Gholipour-Ranjbar, H. (2016). Synthesis of a novel magnetite/nitrogen-doped reduced graphene oxide nanocomposite as high performance supercapacitor. *Powder Technol.* 302, 298–308. doi: 10.1016/j.powtec.2016.08.054

Qian, W., Chen, Z., Cottingham, S., Merrill, W. A., Swartz, N. A., Goforth, A. M., et al. (2012). Surfactant-free hybridization of transition metal oxide nanoparticles with conductive graphene for high-performance supercapacitor. *Green Chem.* 14, 371–377. doi: 10.1039/C1GC16134B

Rebuttini, V., Fazio, E., Santangelo, S., Neri, F., Caputo, G., Martin, C., et al. (2015). Chemical modification of graphene oxide through diazonium chemistry and its influence on the structure-property relationships of graphene oxide-iron oxide nanocomposites. *Chem. A Eur. J.* 21, 12465–12474. doi: 10.1002/chem.201500836

Sayahi, H., Kiani, M. A., and Kazemi, S. H. (2014). Ultrasonic-assisted synthesis of magnetite/carbon nanocomposite for electrochemical supercapacitor. *J. Solid State Electrochem.* 18, 535–543. doi: 10.1007/s10008-013-2289-7

Simon, P., Brousse, T., and Favier, F. (2017). *Supercapacitors Based on Carbon or Pseudocapacitive Materials.* Somerset: Wiley.

Song, Y., Liu, T., Yao, B., Li, M., Kou, T., Huang, Z. H., et al. (2017). Ostwald ripening improves rate capability of high mass loading manganese oxide for supercapacitors. *ACS Energy Lett.* 2, 1752–1759. doi: 10.1021/acsenergylett.7b00405

Takahashi, K., Yokoyama, S., Matsumoto, T., Cuya Huaman, J. L., Kaneko, H., Piquemal, J.-Y., et al. (2016). Towards a designed synthesis of metallic nanoparticles in polyols—elucidation of the redox scheme in a cobalt–ethylene glycol system. *New J. Chem.* 40, 8632–8642. doi: 10.1039/C6NJ01738J

Tian, Z. Y., Mountapmbeme Kouotou, P., Bahlawane, N., and Tchoua Ngamou, P. H. (2013). Synthesis of the catalytically active Mn$_3$O$_4$ spinel and its thermal properties. *J. Phys. Chem. C* 117, 6218–6224. doi: 10.1021/jp312444s

Wang, F., Zeng, Y., Zheng, D., Li, C., Liu, P., Lu, X., et al. (2016). Three-dimensional iron oxyhydroxide/reduced graphene oxide composites as advanced electrode for electrochemical energy storage. *Carbon* 103, 56–62. doi: 10.1016/j.carbon.2016.02.088

Wang, Y., Lai, W., Wang, N., Jiang, Z., Wang, X., Zou, P., et al. (2017). A reduced graphene oxide/mixed-valence manganese oxide composite electrode for tailorable and surface mountable supercapacitors with high capacitance and super-long life. *Energy Environ. Sci.* 10, 941–949. doi: 10.1039/C6EE03773A

Wojtoniszak, M., Zielinska, B., Kalenczuk, R. J., and Mijowska, E. (2012). Photocatalytic performance of titania nanospheres deposited on graphene in coumarin oxidation reaction. *Mater. Sci. Pol.* 30, 32–38. doi: 10.2478/s13536-012-0008-1

Xie, J., Xia, Q., Xu, M., and Xia, H. (2016). Nanostructured iron oxide/hydroxide-based electrode materials for supercapacitors. *ChemNanoMat* 13, 287–288. doi: 10.1002/cnma.201600110

Yan, F., Ding, J., Liu, Y., Wang, Z., Cai, Q., and Zhang, J. (2015). Fabrication of magnetic irregular hexagonal-Fe$_3$O$_4$ sheets/reduced graphene oxide composite for supercapacitors. *Synth. Met.* 209, 473–479. doi: 10.1016/j.synthmet.2015.08.023

Yang, P., Ding, Y., Lin, Z., Chen, Z., Li, Y., Qiang, P., et al. (2014). Low-cost high-performance solid-state asymmetric supercapacitors based on MnO$_2$ nanowires and Fe$_2$O$_3$ nanotubes. *Nano Lett.* 14, 731–736. doi: 10.1021/nl404008e

Yeager, M. P., Du, W., Wang, Q., Deskins, N. A., Sullivan, M., Bishop, B., et al. (2013). Pseudocapacitive hausmannite nanoparticles with (101) facets: synthesis, characterization, and charge-transfer mechanism. *ChemSusChem* 6, 1983–1992. doi: 10.1002/cssc.201300027

Yu, A., Chabot, V., and Zhang, J. (2013). *Electrochemical Supercapacitors for Energy Storage and Delivery Fundamentals and Applications.* Boca Raton, FL: CRC Press.

Zha, D., Xiong, P., and Wang, X. (2015). Strongly coupled manganese ferrite/carbon black/polyaniline hybrid for low-cost supercapacitors with high rate capability. *Electrochim. Acta* 185, 218–228. doi: 10.1016/j.electacta.2015.10.139

# Rare-Earth Orthophosphates From Atomistic Simulations

Yaqi Ji [1,2], Piotr M. Kowalski [1,2]*, Philip Kegler [1,2], Nina Huittinen [3], Nigel A. Marks [4], Victor L. Vinograd [1,2], Yulia Arinicheva [1,2,5], Stefan Neumeier [1,2] and Dirk Bosbach [1,2]

[1] Forschungszentrum Jülich GmbH, Institute of Energy and Climate Research - IEK-6: Nuclear Waste Management and Reactor Safety, Jülich, Germany, [2] JARA High-Performance Computing, Aachen, Germany, [3] Institute of Resource Ecology, Helmholtz-Zentrum Dresden-Rossendorf, Dresden, Germany, [4] Curtin University, Perth, WA, Australia, [5] Forschungszentrum Jülich GmbH, Institute of Energy and Climate Research - IEK-1: Materials Synthesis and Processing, Jülich, Germany

Lanthanide phosphates ($LnPO_4$) are considered as a potential nuclear waste form for immobilization of Pu and minor actinides (Np, Am, and Cm). In that respect, in the recent years we have applied advanced atomistic simulation methods to investigate various properties of these materials on the atomic scale. In particular, we computed several structural, thermochemical, thermodynamic and radiation damage related parameters. From a theoretical point of view, these materials turn out to be excellent systems for testing quantum mechanics-based computational methods for strongly correlated electronic systems. On the other hand, by conducting joint atomistic modeling and experimental research, we have been able to obtain enhanced understanding of the properties of lanthanide phosphates. Here we discuss joint initiatives directed at understanding the thermodynamically driven long-term performance of these materials, including long-term stability of solid solutions with actinides and studies of structural incorporation of $f$ elements into these materials. In particular, we discuss the maximum load of Pu into the lanthanide-phosphate monazites. We also address the importance of our results for applications of lanthanide-phosphates beyond nuclear waste applications, in particular the monazite-xenotime systems in geothermometry. For this we have derived a state-of-the-art model of monazite-xenotime solubilities. Last but not least, we discuss the advantage of usage of atomistic simulations and the modern computational facilities for understanding of behavior of nuclear waste-related materials.

Keywords: rare-earth phosphates, atomistic simulations, monazite, xenotime, nuclear waste management, ceramics, thermodynamics, solid solutions

## 1. INTRODUCTION

Lanthanide phosphates ($LnPO_4$) are ceramic materials of interest in various research fields, including geochronology (Williams et al., 2007), geothermometry (Andrehs and Heinrich, 1998; Mogilevsky, 2007), and nuclear waste management (Ewing and Wang, 2002; Neumeier et al., 2017a; Schlenz et al., 2017). Occurring in nature, these are also important ores for thorium, lanthanum, and cerium (McGill, 2000; Stoll, 2000). Most of the potential applications come from high durability and radiation damage resistance of these materials (Neumeier et al., 2017a). There exist large varieties of phosphate-based ceramics of different crystalline structures [e.g., cheralite, apatites, kosnarite, see Neumeier et al. (2017a)], but anhydrous lanthanide orthophosphates form

two structures called monazite and xenotime. Anhydrous lanthanide orthophosphates crystallize in the monazite form with the $P2_2/n$ space group for light lanthanides, from La to Gd. In this structure, $Ln$ cations are 9-fold coordinated. For heavier lanthanides, from Tb to Lu, $LnPO_4$ compounds adopt a zircon type tetragonal structure called xenotime which has $I4_1/amd$ symmetry and 8-fold coordinated $Ln$ cations. Both these materials are considered in nuclear waste management as potential immobilization matrices for minor actinides and plutonium because of enhanced radiation damage resistance and durability of these materials (Ewing and Wang, 2002; Clavier et al., 2011; Schlenz et al., 2013, 2017; Neumeier et al., 2017a; Seydoux-Guillaume et al., 2018). Their natural analogues can contain significant amounts of actinides [up to ∼ 50%wt of Th and U, see Stoll (2000); Ewing and Wang (2002); Lumpkin and Geisler-Wierwille (2012)] and still preserve their crystalline structure over geological time scales (Ewing and Wang, 2002). The aim is a potential usage of these materials as an immobilization matrix for radionuclides, such as the already mentioned Pu and minor actinides. The immobilization of Pu could reduce the proliferation risk associated with large stockpiles of weapons grade plutonium (Ewing, 1999; Macfarlane, 1999).

In the last two decades, atomistic modeling became a very popular research tool in various research fields, including nuclear materials (Chroneos et al., 2013). This is because steady advancements in supercomputing facilities and computational software, especially *ab initio* methods, allows nowadays for simulation and investigation of systems containing hundreds of atoms using first principle simulation methods (Jahn and Kowalski, 2014). Monazite became a topic of atomistic simulations effort in the last decade. Computational studies have been used to deliver information on: the structural (Rustad, 2012; Feng et al., 2013; Blanca-Romero et al., 2014; Beridze et al., 2016; Huittinen et al., 2017), the elastic (Wang et al., 2005; Feng et al., 2013; Ali et al., 2016; Kowalski and Li, 2016; Ji et al., 2017a; Kowalski et al., 2017b), the thermodynamic (Mogilevsky, 2007; Feng et al., 2013; Li et al., 2014; Kowalski et al., 2015, 2016; Ji et al., 2017b; Neumeier et al., 2017b; Eremin et al., 2019), the thermochemical (Rustad, 2012; Beridze et al., 2016), the radiation damage resistance (Kowalski et al., 2016; Li et al., 2016; Ji et al., 2017c; Jolley et al., 2017) parameters, the electronic structure (Blanca-Romero et al., 2014; Kowalski et al., 2017a) as well as high-pressure behavior (López-Solano et al., 2010; Stavrou et al., 2012; Ali et al., 2016; Shein and Shalaeva, 2016; Gomis et al., 2017). There is a steadily increasing relevant simulation effort with most of the papers published just recently.

In this contribution we provide an overview of the recent atomistic modeling activities on the lanthanide-phosphates, focusing on the information that have been delivered by atomistic modeling activities at Forschungszentrum Jülich and that allowed for better characterization of these materials, including long-term thermodynamic stability in the context of using them as a nuclear waste form. Besides this overview, we present results of computation of thermochemical parameters of $La_{1-x}Pu_xPO_4$ solid solution and the first *ab initio*-based evaluation of the relative solubilities in the monazite-xenotime

system. These studies aim at the assessment of the maximum Pu load in $LaPO_4$ and the long-term thermodynamic stability of such solid solution. The results of our studies are not limited to the field of nuclear waste management and in a general science aspect could be used to improve computational methods (Blanca-Romero et al., 2014) or the monazite-xenotime geothermometry (Mogilevsky, 2007). We especially highlight a cross-linking, interdisciplinary character of our research, from which the general science community could highly benefit.

## 2. COMPUTATIONAL APPROACH

In the *ab initio*[1] investigation of the lanthanide phosphate systems we presented here we apply a density functional theory (DFT)-based quantum chemistry approach. For that purpose we utilize Quantum-ESPRESSO simulation package (Giannozzi et al., 2009). We apply the PBESol exchange-correlation functional (Perdew et al., 2008), the plane-wave energy cutoff of 50 Ryd and ultrasoft pseudopotentials to represent the core electrons of the atoms (Vanderbilt, 1990). Following our broad experience on computation of lanthanide phosphates (Blanca-Romero et al., 2014; Beridze et al., 2016) we apply two methods: (1) with $4f$ electrons included into the pseudopotential core and (2) with $4f$ electrons computed explicitly, which we use for DFT+$U$ calculations. The DFT+$U$ calculations were performed with the Hubbard $U$ parameter values computed from first principles using the linear response method of Cococcioni and de Gironcoli (2005). These computational setups were extensively tested and proved to give very good results for monazite-xenotime systems (Blanca-Romero et al., 2014; Beridze et al., 2016).

Besides quantum chemistry methods, force-field-based molecular modeling has been also used in the investigation of lanthanide phosphates. In this approach, the interatomic interactions are described by an analytical function, for instance by the pair interaction potentials such as Buckingham type (Buckingham, 1938). The advantage of this method is that it allows for simulations of systems containing thousands and even millions of atoms, as opposite to more computationally intensive DFT-based methods, which is currently suitable for simulations of up to a few hundred atoms (Jahn and Kowalski, 2014). The force-field methods are used for the large scale simulations of processes such as radiation cascades (Ji et al., 2017c) or computationally intensive computation of statistical distributions, like different possibilities of incorporating doping elements (Huittinen et al., 2017, 2018). For that purpose, there has been some development in the force fields for lanthanide phosphates (Ji et al., 2017c; Jolley et al., 2017). Nevertheless, these methods do not guarantee to deliver information on the level of quantum-chemical methods. Interaction potentials are also not guaranteed to be transferable, even between the system of identical chemical composition like monazite and xenotime.

---

[1]In this contribution we call DFT methods an *ab initio* approach as the exchange-correlation functionals utilized in our studies were designed based on pure-theoretical considerations.

# 3. RESULTS AND DISCUSSION

## 3.1. Structural Data

The first test of a computational method is its ability to reproduce the measured lattice parameters of the computed crystalline solid. The lattice parameters of lanthanide phosphates were measured by different studies and are known for all the *Ln* cations, except Pm (Ni et al., 1995; Clavier et al., 2011). These could be also accurately estimated from the values of ionic radii of *Ln* cations (Shannon, 1976; Ni et al., 1995). The first DFT-based computational studies of structural parameters of lanthanide phosphates were performed for LaPO$_4$ monazite (Wang et al., 2005). In these studies the applied PW91 exchange-correlation functional (Perdew and Wang, 1992) resulted in slight overestimation of lattice parameters (by $\sim$ 1% on average). Rustad (2012) used the PBE exchange-correlation functional (Perdew et al., 1996) to compute structural and thermochemical parameters of all lanthanide phosphates and obtained lattice parameters that are also $\sim$ 1% too large. In similar, extensive studies of *Ln*PO$_4$ monazite compounds, Feng et al. (2013) applied local spin approximation, but obtained lattice parameters that are far smaller than the experimental values (up to 10% underestimation of volume). These studies show that the structural parameters of lanthanide-phosphates are very sensitive to the applied computational method, especially to the exchange-correlation functional. A correct treatment of strongly correlated 4*f* electrons also plays an important role here.

Blanca-Romero et al. (2014) performed extensive tests of the ability of different DFT-based approaches to reproduce the measured lattice parameters and bond-distances of monazite-type lanthanide-phosphates and the related lanthanide-oxides. In that paper, they found that the standard DFT method with explicitly computed 4*f* electrons overestimates the lattice parameters and bond-lengths by up to 3%, consistent with previous studies (Wang et al., 2005; Rustad, 2012). A very good match to the experimental values of structural parameters was obtained with the DFT+*U* method, in which the PBEsol

exchange-correlation functional was applied (Perdew et al., 2008) and the Hubbard *U* parameters that represent the strength of the on-site Coulomb repulsion between 4*f* electrons (thus electronic correlations), were derived *ab initio*. In **Figure 1** we present the *Ln*-O bond lengths computed with this method vs. the measured data for monazite and xenotime systems. The match is excellent and the key to get such a good result was to compute the Hubbard *U* parameters for each *Ln* case. As demonstrated in **Figure 1**, this parameter varies a lot for the different *Ln* cations (from $\sim$3 to $\sim$ 10 eV). Having an improved description of structures using the PBEsol exchange-correlation functional is also expected, as by recovering the exact charge density limit for slowly varying densities, it improves the description of structural parameters over the widely used PBE functional [see discussion by Perdew et al. (2008)]. Another practice in computation of 4*f* elements is to include the 4*f* electrons into the pseudopotential core and to not compute them explicitly [as done, for instance, by Rustad (2012)]. This is due to the fact that these do not participate in the chemistry (bonding). Blanca-Romero et al. (2014) and Beridze et al. (2016) illustrated this for lanthanide phosphates. They found that such a *"f in the core"* approach results in the formation enthalpies (energies) that are consistent with the ones derived with the DFT+*U* method (see discussion in section 3.2). This method, although not that accurate for the structural parameters as the aforementioned DFT+*U* approach (Beridze et al., 2016), was shown to be accurate for prediction of the thermodynamic and elastic parameters of lanthanide phosphates, which is discussed in the following sections.

## 3.2. Formation Enthalpies

The formation enthalpies of series of monazites and xenotimes have been measured by Ushakov et al. (2001). These were first computed at the DFT level by Rustad (2012). He noticed that there is a systematic offset between the computed and measured values of $\sim$ 40 kJ/mol, with the computed enthalpies being less exothermic. Blanca-Romero et al. (2014) have shown that this
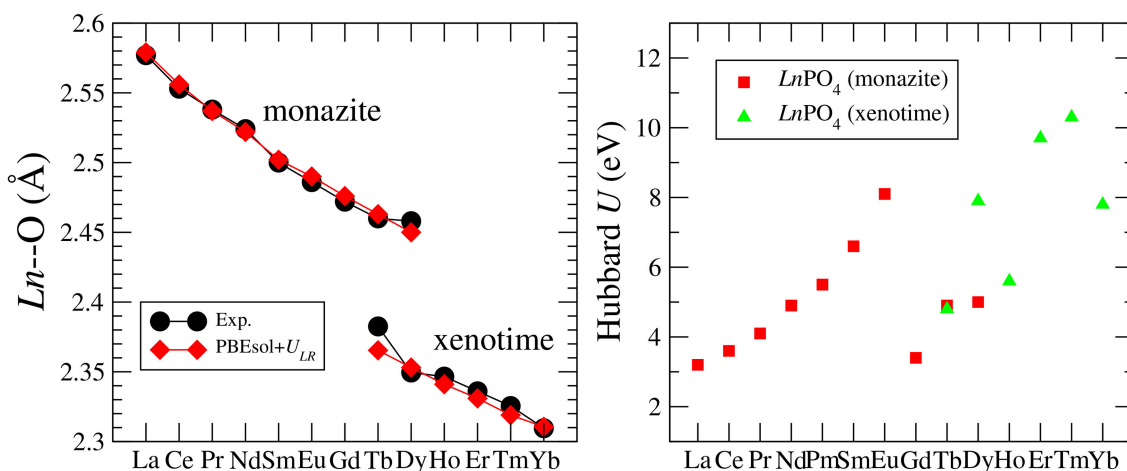


**FIGURE 1 | (Left)** The measured and computed *Ln*-O bond-length in *Ln*PO$_4$ compounds. **(Right)** The Hubbard *U* parameter computed for *Ln*PO$_4$ compounds. The data come from Blanca-Romero et al. (2014) and Beridze et al. (2016).
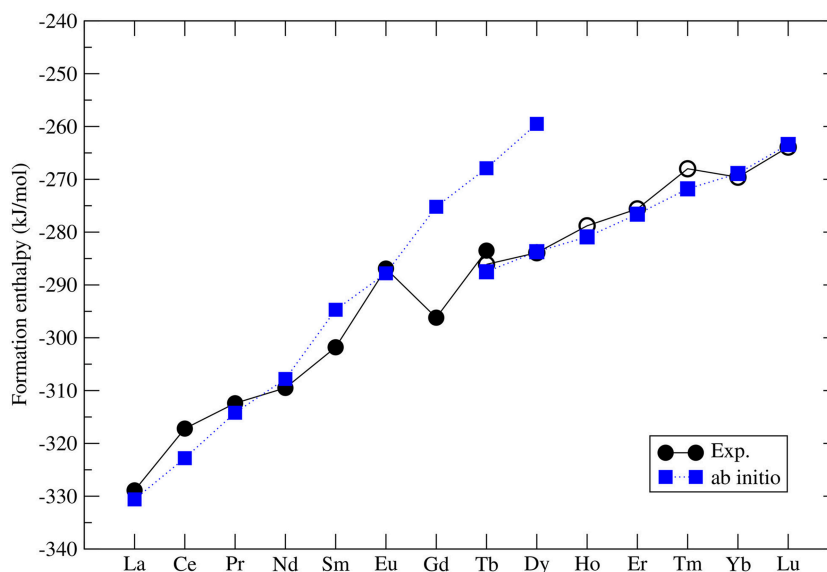
**FIGURE 2** | The computed (blue filled squares) and measured (black filled (monazite) and open (xenotime) circles) (Ushakov et al., 2001) formation enthalpy from oxides for *Ln*PO$_4$ compounds. The following *Ln*$_2$O$_3$ oxides were taken into account: *A*-type (La-Nd), *B*-type (Sm), and *C*-type (Eu-Lu). The data comes from Beridze et al. (2016).

offset is present also in the DFT+$U$ calculations and is to a large extent *Ln*-cation independent, which rules out the 4$f$ electrons correlations as the underlying reason for it. They attributed this to the overestimation of P-O bond lengths, and thus volumes, of the *Ln*PO$_4$ and P$_2$O$_5$ compounds. Beridze et al. (2016) have found an identical offset for xenotimes. When a constant shift of $\sim$ 30 kJ/mol is applied to the computed formation enthalpies the measured values are nicely reproduced. The final result for series of *Ln*PO$_4$ compounds is given in **Figure 2**. The computed formation enthalpies reproduce well the experimental trend for most of the compounds. The only significant discrepancies are observed for GdPO$_4$ and TbPO$_4$, which however is crucial for the discussion of the relative solubilities provided in section 3.7.

The correct prediction of the formation enthalpies of monazite and xenotime phases is essential to properly model the relative solubilities in the monazite-xenotime system. Mogilevsky (2007) in his estimations used an extrapolation of the experimentally measured values for TbPO$_4$ (Ushakov et al., 2001) - the only system for which formation enthalpies of both phases have been measured. Mogilevsky (2007) extrapolated these values by the following formula:

$$\Delta h_x = (R_{tr} - R_x)/(R_{tr} - R_{Tb})\Delta h_{TbPO_4}, \tag{1}$$

$$\Delta h_m = (R_m - R_{tr})/(R_{tr} - R_{Tb})\Delta h_{TbPO_4}, \tag{2}$$

where $R_{tr}$ is the ionic radius of a hypothetical ion located between Gd and Tb for which energies in the monazite and xenotime structures are identical, $R_{m,x}$ is the ionic radius of *Ln* cations, which at normal conditions form monazite (m) or xenotime (x), respectively. He assumed that $R_{tr} = 1.0516$Å and derived $\Delta h_{m,x}$ which is the enthalpy difference between the standard phase and the other phase (e.g., for LaPO$_4$ the enthalpy difference between

monazite and xenotime phase of LaPO$_4$). His result is given in **Figure 3**. In order to check these values we performed *ab initio* calculations of series of monazite and xenotimes counterparts of the existent phases. The advantage of atomistic simulations is that even non existing phases could be modeled (e.g., LaPO$_4$ xenotime). The result is given in **Figure 3**. The computed $\Delta h_{m-x}$ is significantly different from the estimation of Mogilevsky (2007), with the differences for LaPO$_4$ of $\sim$ 20 kJ/mol. We note that our *ab initio* data could be reproduced assuming $R_{tr} = 1.507$ Å. Having a good match to the experimental values of the measured compounds (see **Figure 2**) there is no reason to believe that our prediction for the non-existing phases could be that much wrong. We thus assume that the values computed here are correct.

## 3.3. Elastic Parameters

The elastic properties of lanthanide phosphates have been a topic of several experimental studies (Thomä et al., 1974; Harley and Manning, 1978; Nipko et al., 1996; Mogilevsky et al., 2006; Du et al., 2009; Thust et al., 2015). Also on the computational side these have been extensively investigated. Wang et al. (2005), Feng et al. (2013), and Kowalski and Li (2016) computed elastic constants and moduli for a series of monazites. We note that the later study gave the best match to the measured values. The key factor to obtain accurate results has been a good reproduction of structural parameters of the investigated materials. For instance, Kowalski and Li (2016) obtained volumes that are within 1% of the measured values, while in the earlier studies by Feng et al. (2013) the differences were as large as 10%. In the follow-up studies, Kowalski et al. (2017b) computed the variation of the Young's modulus along the La$_{1-x}$Eu$_x$PO$_4$ solid solution, which reproduced the experimental trend (Thust et al., 2015) and
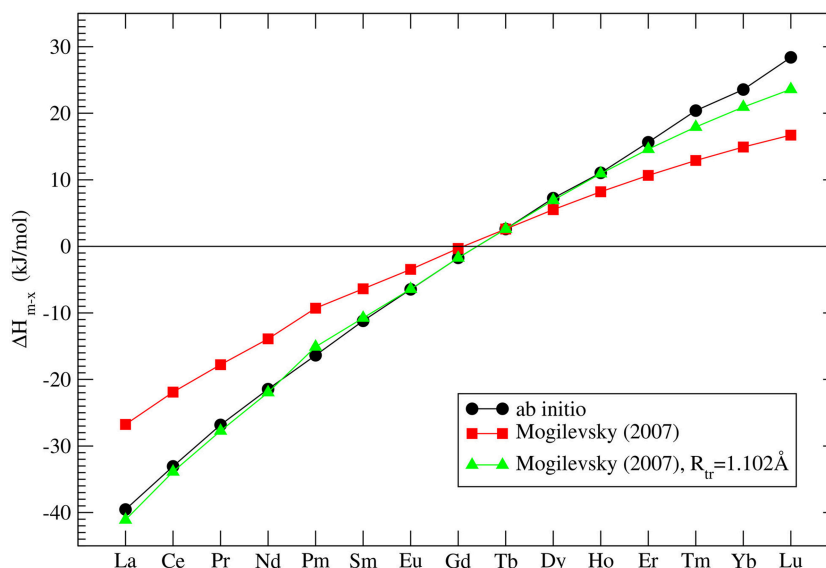
**FIGURE 3 |** The computed enthalpy difference between monazite and xenotime $Ln$PO$_4$ compounds. The three data series represent our *ab initio* calculations (black filled circles), the model of Mogilevsky (2007) (red filled squares) and the model of Mogilevsky (2007) (Equations 1, 2) assuming the ionic radius of the 9-fold coordinated transition $Ln$ cation is 1.102Å.

allowed for better interpretation of these data. Computational methods were also applied to study the pressure effect on the elastic moduli and the relevant elastic anisotropy (Ali et al., 2016; Gomis et al., 2017).

The computed elastic moduli were also used to derive some related thermodynamic parameters. Feng et al. (2013) and Ji et al. (2017b) used the Slack model (Slack, 1973), and derived thermal conductivities of monazite and xenotime compounds, respectively. According to Slack (1973) the thermal conductivity can be estimated as:

$$\kappa = A \frac{\bar{M} \delta \Theta_D^3}{\gamma^2 n^{\frac{2}{3}} T}, \tag{3}$$

where $A = 3.12 \cdot 10^{-8}$ W mol kg$^{-1}$ m$^{-2}$ K$^{-3}$ is a constant, $\bar{M}$ is the average atomic mass, $\delta^3$ is the average volume per atom in the system, $\Theta_D$ is the Debye temperature, $n$ is the number of atoms per primitive unit cell and $\gamma$ is the acoustic Grüneisen parameter. Here, using the same approach as by Ji et al. (2017b) we computed the standard thermal conductivity of LaPO$_4$. The obtained value of room temperature thermal conductivity of 4.0 W m$^{-1}$ K$^{-1}$ is consistent with the measured value of 3.6 W m$^{-1}$ K$^{-1}$ (Du et al., 2009) and the data computed by Feng et al. (2013). The data for LaPO$_4$ (m) and LuPO$_4$ (x) are reported in **Table 1**. Interestingly, both experiment and simulation show significant differences in the thermal conductivity of the monazite and xenotime phases. This comes mainly from the different number of atoms in the primitive cell of both phases, 12 for xenotime and 24 for monazite (see Equation 3).

Mogilevsky (2007) used the Young's modulus to estimate the excess energy of mixing [the Margules interaction parameter (Prieto, 2009)] in monazite-xenotime solid solution systems. By

**TABLE 1 |** The thermal conductivity in (W m$^{-1}$ K$^{-1}$) simulated and measured for LaPO$_4$ (monazite) and LuPO$_4$ (xenotime).

| Compound | Calculations | Measurements |
|---|---|---|
| LaPO$_4$ | 4.0[a], 4.5[b] | 3.6[c] |
| LuPO$_4$ | 11.7[d] | 12.0[e] |

*The references are these of:* [a]*this work,* [b]*Feng et al. (2013),* [c]*Du et al. (2009),* [d]*Ji et al. (2017b),* [e]*Hikichi et al. (1998).*

a combination of fitting to the existing data on solubilities and so computed mixing energies he proposed an accurate model to describe the maximum solubilities and miscibility gap in the monazite-xenotime system. Kowalski and Li (2016) have shown that this Young's modulus-based approximation of elastic strain energy leads to a good description of the *ab initio* Margules interaction parameters. These issues will be discussed in details in sections 3.6 and 3.7. Nevertheless, Mogilevsky (2007) used an approximation for the variation of Young's modulus along lanthanide series. According to his derivation, for monazite compounds the Young's modulus decreases along the series, while the computation of Kowalski and Li (2016) and the aforementioned measurements show an increase (from 140 GPa for La to ∼ 160 GPa for Gd). In **Figure 4** we present the collection of measured and computed Young's moduli together with the Mogilevsky (2007) approximation. These results are important in the context of estimation of excess enthalpies of mixing and solubilities in the monazite-xenotime system (sections 3.6 and 3.7).

In the next section we will discuss that a careful selection of the computational method, which results in good description of
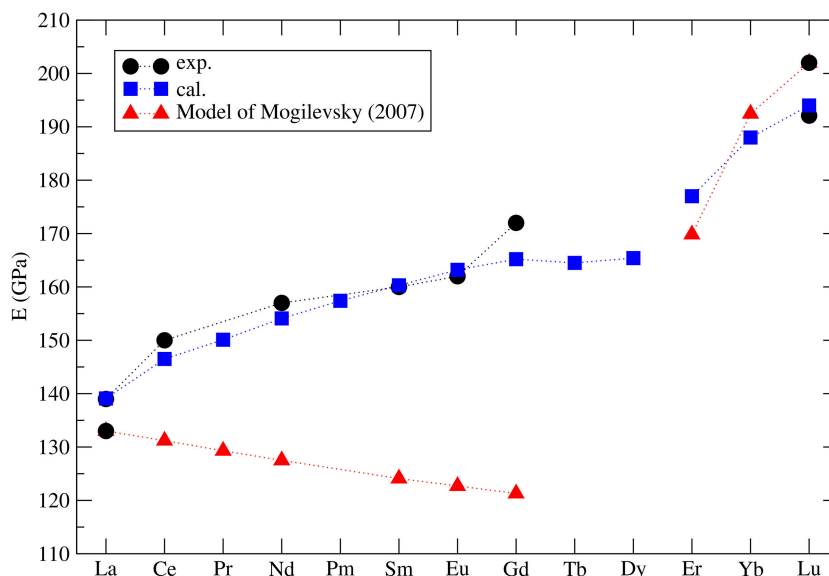
**FIGURE 4 |** The computed (blue filled squares) (Kowalski and Li, 2016; Ji et al., 2017a) and measured (black filled circles) Young's modulus for selected lanthanide phospahtes monazites and xenotimes. Red triangles represent the model used by Mogilevsky (2007).
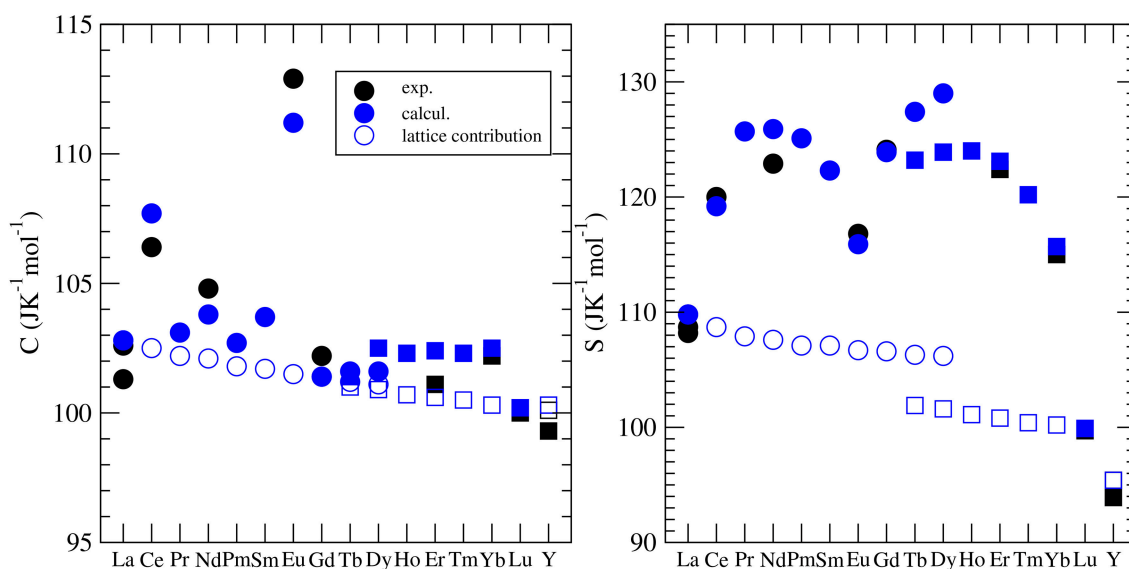


**FIGURE 5 |** The variation of the standard heat capacity and standard entropy from *Ln*PO$_4$. The different symbols represent the computed $C_V$ [filled blue cirlces (monazite) and squares (xenotime)] and measured ($C_p$) values [see Kowalski et al. (2015); Ji et al. (2017a)]. The open blue symbols represent the lattice vibration contribution to the heat capacity and entropy. The difference between the filled and open blue circles is due to the thermal excitation of 4*f* electrons (Schottky effect).

the structural and elastic parameters, is also important to obtain good predictions for thermodynamic parameters such as the heat capacity and the thermal conductivity.

## 3.4. Thermodynamic Parameters
Besides the thermal conductivity, the heat capacity is the most widely investigated thermodynamic parameter of lanthanide phosphates. There is a series of experimental papers on measurements of this parameter for different monazite compositions (Thiriet et al., 2004, 2005a; Popa and Konings,

2006; Popa et al., 2006a,b; Gavrichev et al., 2008, 2009; Bauer et al., 2016), including Pu-rich compounds (Thiriet et al., 2005b; Popa et al., 2007a; Benes et al., 2011), and xenotime (Gavrichev et al., 2006, 2010, 2012, 2013; Nikiforova et al., 2012; Gysi et al., 2016). These measurements revealed a quasi-random-like variation of the standard heat capacity and the standard entropy along the lanthanide series. This is illustrated in **Figure 5**. For instance, the standard values are largest for EuPO$_4$ and smallest for GdPO$_4$ with no visible trend. The first systematic computational studies of Feng et al. (2013) were unable to match

the experimental data and tried to explain these discrepancies by the large difference between computed constant volume ($C_v$) and measured ($C_p$) heat capacities. In order to shed the light on this variation, Kowalski et al. (2015) and Ji et al. (2017a) performed accurate *ab initio* calculations of the heat capacity of monazites and xenotimes, respectively. They accounted for two effects: (1) the lattice vibration and (2) the thermal excitation of 4*f* electrons, which had been known from experimental studies to significantly influence the heat capacity of monazites [e.g., Thiriet et al. (2005a,b)]. By doing so, Kowalski et al. (2015) were able to accurately reproduce the measured values for all the investigated cases. Using the same computational approach, Kowalski et al. (2017b) were able to explain the low temperature variation of heat capacity in the $La_{1-x}Eu_xPO_4$ monazite-type solid solution system (Thust et al., 2015). By applying a theoretically justified extrapolation, Kowalski et al. (2015) could also account for high temperature ($T > 800$ K) anharmonic effects in monazites. We note however, that such a procedure was not that successful for xenotime phases, as here the anharmonic effects become important at a much lower temperature of $\sim 400$ K (Ji et al., 2017a). Computational studies of the heat capacity of xenotime by Ji et al. (2017a) allowed also for the verification of the slightly conflicting experimental data sets published recently in the literature (Gavrichev et al., 2010, 2012, 2013; Gysi et al., 2016).

The thermodynamics of lanthanide phosphate solid solutions is discussed in section 3.6.

## 3.5. Incorporation of Radionuclides

Incorporation of actinides into lanthanide phosphates ceramic is an important topic in terms of using these materials as potential nuclear waste forms. It is well known that the trivalent actinides such as Pu, Am and Cm could form monazite phases (e.g., PuPO$_4$ Thiriet et al., 2005b; Clavier et al., 2011) and that the tetra-valent actinides such as U or Np can be introduced into the monazite lattice jointly with divalent cations [e.g., Ca, Clavier et al. (2011)]. However, an important aspect of the formation of such a solid solution is its homogeneity. In that respect, Huittinen et al. (2017) and Huittinen et al. (2018) investigated incorporation of Eu$^{3+}$ into monazite and Cm$^{3+}$ into monazite and rhabdophane phases, respectively. The latter compound is a hydrated lanthanide-phosphate which is a stable phase at lower temperatures (below $T \sim 400$ K) (de Kerdaniel et al., 2007; Clavier et al., 2011). By a combination of time-resolved laser fluorescence spectroscopy (TRLFS) and atomistic modeling, Huittinen et al. (2017) have shown that monazite-type solid solutions are homogeneous. This conclusion was reached by explanation of the increased broadening of TRLFS profiles for the $La_{1-x}Gd_xPO_4$ solid solutions by the broad distribution of the dopant-O bond lengths in the measured mixed compounds. In these studies force-field methods were used to describe the interatomic interactions and special quasi-random structures (SQS) (Zunger et al., 1990) were used to model the ideal, homogeneous solid solutions. The same approach was used by Huittinen et al. (2018) to show homogeneous incorporation of Cm$^{3+}$ into monazite. On the other hand, rhabdophane-type $La_{1-x}Gd_xPO_4$ solid solutions were found to be very selective in terms of actinides incorporation, with the

anhydrous cation site (i.e., not coordinated to H$_2$O molecules) being preferred by the Cm dopant, and the preference increasing toward larger and lighter lanthanides [greater for LaPO$_4$ · 0.67H$_2$O than GdPO$_4$ · 0.67H$_2$O, Huittinen et al. (2018)]. This selectivity was confirmed by the computation of the Cm solution (incorporation) energies.

## 3.6. Solid Solutions

Formation and thermodynamic stability of solid solutions of radionuclides-bearing lanthanide phosphates ceramic waste forms is a topic of extensive studies in the context of nuclear waste management (Popa et al., 2007a; Li et al., 2014; Kowalski and Li, 2016; Arinicheva et al., 2017; Hirsch et al., 2017; Neumeier et al., 2017b; Eremin et al., 2019). This is because the information gained allows for the assessment of long term stability of ceramic nuclear waste forms against phase separation. In that aspect there are two streams of research: (1) the investigation of homogeneity of a solid solution discussed in section 3.5 and (2) the investigation of its long-term thermodynamic stability. The second problem is a key issue for nuclear waste disposal because any desired waste form should be stable against formation of the miscibility gap. It was shown experimentally (Popa et al., 2007b) and by *ab initio* simulations (Li et al., 2014) that monazite-type solid solutions are highly regular. The excess enthalpy of mixing, $H^E$, of a $(A_{1-x}B_xPO_4)$ could be described by a simple equation (Popa et al., 2007b):

$$H^E = Wx(1 - x), \tag{4}$$

where $W$ is a Margules interaction parameter (Prieto, 2009). A solid solution is stable against formation of a miscibility gap if $W < 2RT$, where $R$ is the gas constant. It is thus of interest to nuclear waste management strategies to characterize $W$ for the considered solid solutions, especially for the mixture of actinides with the host matrix cations like Pu with La in a $La_{1-x}Pu_xPO_4$ solid solution.

The first systematic *ab initio* calculations of $W$ parameters for monazite-type solid solutions were performed by Li et al. (2014). They found that for the $La_{1-x}Ln_xPO_4$ solid solutions, $W = 0.618(\Delta V(\text{cm}^3/\text{mol}))^2$, where $\Delta V$ is the difference in the volume of solid solution endmembers. The obtained results suggest thermodynamic instability, characterized with $W > 5$ kJ/mol at ambient conditions, of various solid solutions [e.g., $(La_{1-x}Gd_xPO_4)$]. In follow-up studies, Kowalski and Li (2016) explained the quadratic dependence of $W$ parameter on the volumes difference by a strain energy-based model, in which

$$W = \frac{E}{6V}(\Delta V)^2, \tag{5}$$

where $E$ is the Young's modulus and $V$ is the volume. These studies show that $\Delta V$ is an important parameter that determines the value of the $W$ parameter.

Neumeier et al. (2017b) compared the derived *ab initio* $W$ parameters with the calorimetric measurements of $La_{1-x}Ln_xPO_4$ ($Ln = $ Eu, Gd) solid solutions. The measured values are smaller than the computed ones. The reason for this discrepancy is the difference in the value of measured and computed $\Delta V$. These are summarized in **Table 2**. When Neumeier et al. (2017b) used the

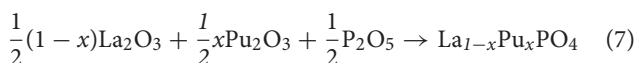| Compound | $\Delta V_{computed}$ | $\Delta V_{measured}$ | $W_{ab\,initio}$[a] | $W_{rescaled}$[b] | $W_{measured}$[c] |
|---|---|---|---|---|---|
| La$_{1-x}$Eu$_x$PO$_4$ | 7.6 | 5.2 | 13.4 | 6.2 | 2.5 ± 2.6 |
| La$_{1-x}$Gd$_x$PO$_4$ | 8.4 | 6.1 | 16.5 | 8.6 | 11.4 ± 3.1 |
| La$_{1-x}$Pu$_x$PO$_4$ | 4.3 | 2.9 | 4.0 | 1.9 | |

*The provided W parameters come from:* [a]*Li et al. (2014),* [b]*Kowalski and Li (2016),* [c]*Neumeier et al. (2017b).*

measured $\Delta V$ values and rescaled the *ab initio* computed values according to Equation 5, namely:

$$W = \left(\frac{\Delta V_{exp}}{\Delta V_{comp.}}\right)^2 W_{computed}, \qquad (6)$$

as provided in **Table 2**, they obtained a good match to the measured values.

The most important outcome of these studies is their implication for immobilization of actinides, for instance Pu. The obtained Margules interaction parameter for La$_{1-x}$Pu$_x$PO$_4$ solid solution case is $W = 1.8$ kJ/mol (**Table 2**), thus indicating thermodynamic stability of this solid solution against formation of a miscibility gap (as $W$ is $< 5$ kJ/mol). On the other hand, although synthesis of the pure PuPO$_4$ monazite has been successful (Thiriet et al., 2005b; Clavier et al., 2011), the experimental studies suggest a maximum content of Pu in La$_{1-x}$Pu$_x$PO$_4$ solid solution at $x \sim 0.15$ (Popa et al., 2007a; Arinicheva et al., 2017). In particular, recent experimental investigation by Arinicheva et al. (2017) indicates formation of Pu-oxides (PuO$_2$) for $x > 0.15$. In order to understand this contradiction, we computed the formation enthalpy of La$_{1-x}$Pu$_x$PO$_4$ solid solution from oxides. We consider the following reaction:

$$\frac{1}{2}(1-x)\text{La}_2\text{O}_3 + \frac{1}{2}x\text{Pu}_2\text{O}_3 + \frac{1}{2}\text{P}_2\text{O}_5 \rightarrow \text{La}_{1-x}\text{Pu}_x\text{PO}_4 \quad (7)$$

Because PuO$_2$ is the most stable Pu-oxide at ambient conditions, we also account for the enthalpy of oxidation of Pu$_2$O$_3$ of 285 kJ/mol (Konings et al., 2014). The result is given in **Figure 6**. Interestingly, the formation enthalpy becomes positive, and the solid solution becomes unstable against formation of PuO$_2$ for $x \sim 0.15$. We thus conclude that the experimentally observed maximum load of Pu in LaPO$_4$ results from the positive formation enthalpies, and thus thermodynamic instability of La$_{1-x}$Pu$_x$PO$_4$ compounds for $x > 0.15$ [2].

---

[2]We notice that in order to correctly quantify the thermodynamics of this process, the free energies should be considered. However, the consideration of the entropy terms (main contributor to the difference between the enthalpies and the free energies of the reaction 7) in the reaction 7 would slightly increase the threshold $x$ value but on qualitative level, the outlined picture will not change.
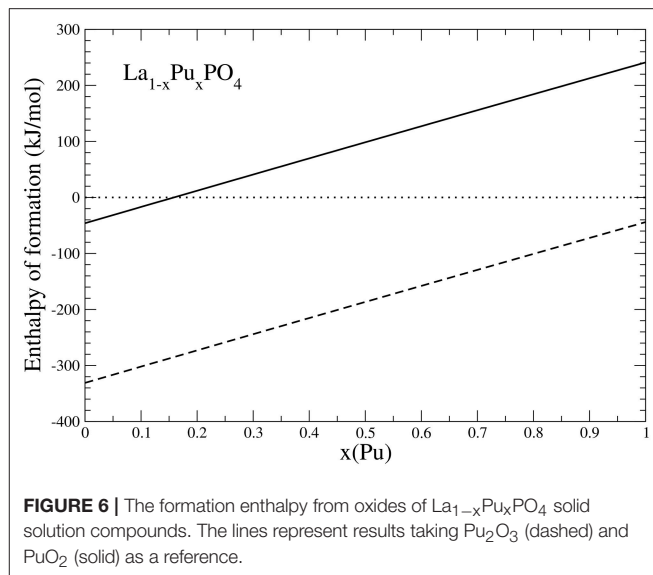


**FIGURE 6** | The formation enthalpy from oxides of La$_{1-x}$Pu$_x$PO$_4$ solid solution compounds. The lines represent results taking Pu$_2$O$_3$ (dashed) and PuO$_2$ (solid) as a reference.

## 3.7. Solubilities in Monazite-Xenotime System

The thermodynamic parameters of mixing, such as the $W$ parameter, are very important for assessment of thermodynamic stability of monazite-type nuclear waste forms. Therefore, it is of high importance to validate the model presented in section 3.6 against all the available data. Interestingly, the Margules interaction parameters are equally important for the description of the miscibility gap, and the maximum solubilities, in the naturally occurring monazite-xenotime systems. The monazite-xenotime system has been proposed as a potential geothermometer and some relevant data on solubilities have been measured (Andrehs and Heinrich, 1998; Mogilevsky, 2007). Monazite-xenotime system shows a large miscibility gap, which is associated with a large difference between the formation enthalpies of monazite and xenotime (**Figure 3**). Nevertheless, the measured maximum solubilities can be good indicators of temperature and this phenomenon have been investigated "*in situ*" experimentally (Andrehs and Heinrich, 1998), and by thermodynamic modeling (Mogilevsky, 2007). In order to model the maximum solubility of one phase in another we have to know the Margules interaction parameters $W$ and the difference in the formation enthalpies between monazite and xenotime phases. The first is discussed in section 3.6 and as we concluded there, we have a good model for it. The latter is discussed in section 3.2.

The maximum solubilities of xenotime in monazite ($x_1$) and monazite in xenotime ($x_2$) are obtained by solving self-consistently two equations (Mogilevsky, 2007):

$$\Omega_m(1-x_1)^2 + RT\ln(x_1/(1-x_2)) = \Delta h_x + \Omega_x x_2^2, \quad (8)$$
$$\Omega_x(1-x_2)^2 + RT\ln(x_2/(1-x_1)) = \Delta h_m + \Omega_m x_1^2, \quad (9)$$

where $\Omega_{x,m} = -\Delta h_{m,x} + W_{m,x}$. $\Delta h_{m,x}$ is given by Equations 1, 2 (see also section 3.2) and $W_{m,x}$ are the Margules interaction parameters for monazite (m)- and xenotime (x)-type solid solutions. The self-consistent solution of Equations 8 and 9

**FIGURE 7 |** The computed maximum solubility of Y-xenotime in monazite at $T = 1473$ K. Different sets represent our *ab initio* prediction (filled blue squares), prediction using Equation 5 [open blue squares, Kowalski and Li (2016)] and measurements [filled black circles, Andrehs and Heinrich (1998); Mogilevsky (2007)]. $\Delta r$ is the difference in ionic radius of *Ln* and Y cations.
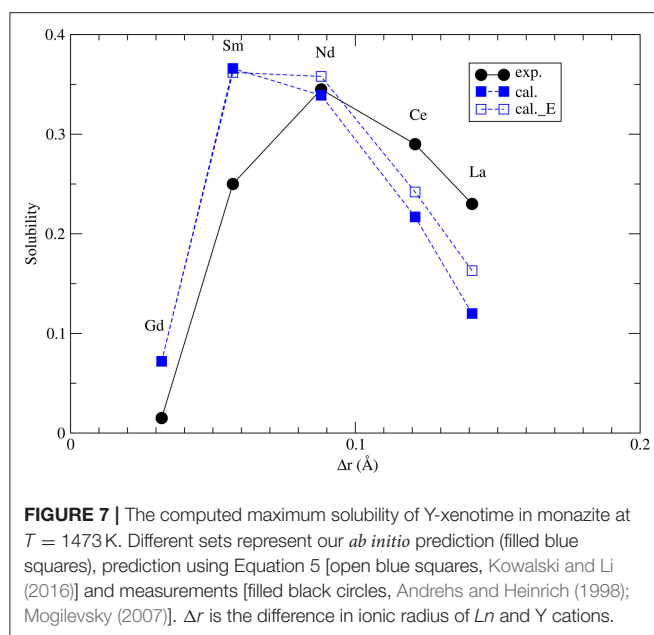
can be easily done in a numerical way. The resulted maximum solubilities for the selected solid solution compositions at $T = 1453$ K are given in **Figure 7**. The solubility of xenotime in monazite is much larger than monazite in xenotime (Mogilevsky, 2007), so here we focus on the former phenomenon. For the solubility of Y-xenotime ($YPO_4$) in monazite there is a maximum at Sm - Nd. We note that the match to *in situ* data (Andrehs and Heinrich, 1998) is not perfect and is not that good as the empirically-based thermodynamic modeling of Mogilevsky (2007), but the trend is well described on the qualitative level. The main discrepancy comes from the $\Delta H_{m-x}$, which we have reasons to think are quite accurate by the *ab initio* calculations. Therefore, more testing against larger data sets would be required to work out and validate a more accurate model for the maximum solubilities in the monazite-xenotime system. This example also shows the importance of correct thermodynamic modeling of monazite-xenotime system, which could be performed and validated by a joint atomistic modeling and experimental effort.

## 4. CONCLUSIONS

In this contribution we presented recent atomistic modeling contribution to the research on lanthanide phosphates, focusing on the studies performed at Forschungszentrum Jülich. We have shown that on many occasions joint atomistic modeling and experimental work resulted in the enhanced description of the investigated materials. Examples of such joint studies are investigations of homogeneity and thermodynamic parameters of solid solutions and incorporation of actinides into lanthanide phosphate ceramics. With the improved understanding and description of the $4f$ electrons, achieved with the parameter free DFT+$U$ approach, we were able to obtain very accurate

description of the local $Ln - O$ bonding environments and the formation enthalpies. This allowed us to obtain better estimates of the relative solubilities in the monazite-xenotime system, elastic and thermodynamic parameters for pure phases and solid solutions. The joint modeling and experimental investigation of the excess enthalpies of mixing in monazite-type solid solutions provided solid arguments for the long-term thermodynamic stability of the plutonium-lanthanum monazite-type ceramic waste form. With respect to our previously published studies, the novel contribution discussed here is the investigation of incorporation of Pu into $LaPO_4$ ceramics, which shows that the experimentally observed maximum load limit for $La_{1-x}Pu_xPO_4$ is governed by the formation enthalpy from oxides, which becomes positive at $\sim x = 0.15$. This value is consistent with the experimental observations. In addition, we reinvestigated the thermodynamics of monazite-xenotime system. We provide accurate values of the enthalpy difference between monazite and xenotime phases and estimates of maximal solubilities computed from the best available *ab initio* data. These results are of great importance for monazite/xenotime-based geothermometry. However, the obtained slight discrepancies between theoretical prediction and the available *in situ* data show a need for more in-depth experimental and theoretical studies of solubilities in the monazite-xenotime system.

The assortment of results provided here shows that atomistic modeling is a valuable research tool for the investigation of lanthanide phosphates. The best results have been obtained by a joint computational and experimental approach, or at least by extensive testing and comparison to the available experimental data. With the steady increase in the availability of computational power we expect that atomistic modeling research will be applied to tackle more complex problems, such as dissolution or corrosion kinetics, an important aspects of nuclear waste performance.

## DATA AVAILABILITY

All datasets generated for this study are included in the manuscript and/or the supplementary files.

## AUTHOR CONTRIBUTIONS

YJ and PMK contributed equally to computing the data, analysis and editing the manuscript. PK, NH, and YA contributed experimental support and expertise. VV contributed to the computation of thermodynamic parameters of solid solutions. NM contributed to the computation of thermal conductivity and force-field simulations. SN and DB contributed expertise on ceramic waste forms.

## FUNDING

# ACKNOWLEDGMENTS

# REFERENCES

Ali, K., Arya, A., Ghosh, P. S., and Dey, G. K. (2016). "A first principle study of the pressure dependent elastic properties of monazite LaPO$_4$," *AIP Conference Proceedings* 1728:020090. doi: 10.1063/1.4946141

Andrehs, G. and Heinrich, W. (1998). Experimental determination of REE distributions between monazite and xenotime: potential for temperature-calibrated geochronology. *Chem. Geol.* 149, 83–96.

Arinicheva, Y., Popa, K., Scheinost, A. C., Rossberg, A., Dieste-Blanco, O., Raison, P., et al. (2017). Structural investigations of (La,Pu)PO$_4$ monazite solid solutions: XRD and XAFS study. *J. Nucl. Mater.*, 493, 404–411. doi: 10.1016/j.jnucmat.2017.06.034

Bauer, J., Hirsch, A., Bayarjargal, L., Peters, L., Roth, G., and Winkler, B. (2016). Schottky contribution to the heat capacity of monazite type (La, Pr)PO$_4$ from low temperature calorimetry and fluorescence measurements. *Chem. Phys. Lett.* 654, 97–102. doi: 10.1016/j.cplett.2016.05.012

Benes, O., Popa, K., Reuscher, V., Zappia, A., Staicu, D., and Konings, R. J. M. (2011). High temperature heat capacity of PuPO$_4$ monazite-analogue. *J. Nucl. Mater.* 418, 182–185. doi: 10.1016/j.jnucmat.2011.06.037

Beridze, G., Birnie, A., Koniski, S., Ji, Y., and Kowalski, P. M. (2016). DFT+$U$ as a reliable method for efficient ab initio calculations of nuclear materials. *Prog. Nucl. Energ.* 92, 142–146. doi: 10.1016/j.pnucene.2016.07.012

Blanca-Romero, A., Kowalski, P. M., Beridze, G., Schlenz, H., and Bosbach, D. (2014). Performance of DFT+$U$ method for prediction of structural and thermodynamic parameters of monazite-type ceramics. *J. Comput. Chem.* 35, 1339–1346. doi: 10.1002/jcc.23618

Buckingham, R. (1938). The classical equation of state of gaseous helium, neon and argon. *Proc. Roy. Soc. A: Math. Phys. Eng. Sci.* 168, 264–283.

Chroneos, A., Rushton, M., Jiang, C., and Tsoukalas, L. (2013). Nuclear wasteform materials: atomistic simulation case studies. *J. Nucl. Mater.* 441, 29–39. doi: 10.1016/j.jnucmat.2013.05.012

Clavier, N., Podor, R., and Dacheux, N. (2011). Crystal chemistry of the monazite structure. *J. Eur. Ceram. Soc.* 31, 941–976. doi: 10.1016/j.jeurceramsoc.2010.12.019

Cococcioni, M. and de Gironcoli, S. (2005). Linear response approach to the calculation of the effective interaction parameters in the LDA+U method. *Phys. Rev. B* 71:035105. doi: 10.1103/PhysRevB.71.035105

de Kerdaniel, E. D. F., Clavier, N., Dacheux, N., Terra, O., and Podor, R. (2007). Actinide solubility-controlling phases during the dissolution of phosphate ceramics. *J. Nucl. Mater.* 362, 451–458. doi: 10.1016/j.jnucmat.2007.01.132

Du, A., Wan, C., Qu, Z., and Pan, W. (2009). Thermal conductivity of monazite-type repo4 (Re=La, Ce, Nd, Sm, Eu, Gd). *J. Am. Ceram. Soc.* 92, 2687–2692. doi: 10.1111/j.1551-2916.2009.03244.x

Eremin, N. N., Marchenko, E. I., Petrov, V. G., Mitrofanov, A. A., and Ulanova, A. S. (2019). Solid solutions of monazites and xenotimes of lanthanides and plutonium: atomistic model of crystal structures, point defects and mixing properties. *Comput. Mater. Sci.* 157, 43–50. doi: 10.1016/j.commatsci.2018.10.025

Ewing, R. (1999). Nuclear waste forms for actinides. *Proc. Natl. Acad. Sci. U.S.A.* 96, 3432–3439.

Ewing, R. and Wang, L. (2002). Phosphates as nuclear waste forms. *Rev. Mineral. and Geochem.* 48, 673–699. doi: 10.2138/rmg.2002.48.18

Feng, J., Xiao, B., Zhou, R., and Pan, W. (2013). Anisotropy in elasticity and thermal conductivity of monazite-type repo4 (re=la, ce, nd, sm, eu and gd) from first-principles calculations. *Acta Mater.* 61, 7364–7383. doi: 10.1016/j.actamat.2013.08.043

Gavrichev, K. S., Ryumin, M. A., Tyurin, A. V., Gurevich, V. M., Khoroshilov, A. V., and Komissarova, L. N. (2012). Thermodynamic functions of erbium orthophosphate ErPO$_4$ in the temperature range of 0-1600 K. *Thermochim. Acta* 535, 1–7. doi: 10.1016/j.tca.2012.02.002

Gavrichev, K. S., Ryumin, M. A., Tyurin, A. V., Gurevich, V. M., and Komissarova, L. N. (2008). Refined heat capacity of LaPO$_4$ in the temperature range 0-1600 K. *Thermochim. Acta* 474, 47–51. doi: 10.1016/j.tca.2008.05.004

Gavrichev, K. S., Ryumin, M. A., Tyurin, A. V., Gurevich, V. M., and Komissarova, L. N. (2009). The heat capacity and thermodynamic functions of EuPO$_4$ over the temperature range 0-1600 K. *Russ. J. Phys. Chem. A* 83, 901–906. doi: 10.1134/S0036024409060053

Gavrichev, K. S., Ryumin, M. A., Tyurin, A. V., Gurevich, V. M., and Komissarova, L. N. (2010). Heat capacity and thermodynamic functions of xenotime YPO$_4$(c) at 0-1600 K. *Geochem. Int.* 48, 932–939. doi: 10.1134/S0016702910090065

Gavrichev, K. S., Ryumin, M. A., Tyurin, A. V., Gurevich, V. M., Nikiforova, G. E., and Komissarova, L. N. (2013). Heat capacity and thermodynamic functions of YbPO$_4$ from 0 to 1800 K. *Inorg. Mater.* 49, 701–708. doi: 10.1134/S0020168513070042

Gavrichev, K. S., Smirnova, N. N., Gurevich, V. M., Danilov, V. R., Tyurin, A. V., Ryumin, M. A., et al. (2006). Heat capacity and thermodynamic functions of LuPO$_4$ in the range 0-320 K. *Thermochim. Acta* 448, 63–65. doi: 10.1016/j.tca.2006.05.019

Giannozzi, P., Baroni, S., Bonini, N., Calandra, M., Car, R., Cavazzoni, C., et al. (2009). Quantum espresso: a modular and open-source software project for quantum simulations of materials. *J. Phys. Condens. Matter* 21:395502. doi: 10.1088/0953-8984/21/39/395502

Gomis, O., Lavina, B., Rodríguez-Hernández, P., Muñoz, A., Errandonea, R., Errandonea, D., et al. (2017). High-pressure structural, elastic, and thermodynamic properties of zircon-type HoPO$_4$ and TmPO$_4$. *J. Phys. Condens. Matter* 29:095401. doi: 10.1088/1361-648X/aa516a

Gysi, A. P., Harlov, D., Costa Filho, D., and Williams-Jones, A. E. (2016). Experimental determination of the high temperature heat capacity of a natural xenotime-(Y) solid solution and synthetic DyPO4 and ErPO4 endmembers. *Thermochim. Acta* 627, 61–67. doi: 10.1016/j.tca.2016.01.016

Harley, R. T. and Manning, D. I. (1978). Jahn-Teller induced elastic constant changes in TmPO$_4$. *J. Phys. C Solid State Phys.*. 11:L633.

Hikichi, Y., Ota, T., Daimon, K., Hattori, T., and Mizuno, M. (1998). Thermal, mechanical, and chemical properties of sintered xenotime-type RPO4 (R = Y, Er, Yb, or Lu). *J. Am. Ceram. Soc.* 81, 2216–2218.

Hirsch, A., Kegler, P., Alencar, I., Ruiz-Fuertes, J., Shelyug, A., Peters, L., et al. (2017). Structural, vibrational, and thermochemical properties of the monazite-type solid solution La$_{1-x}$Pr$_x$PO$_4$. *J. Solid State Chem.* 245, 82–88. doi: 10.1016/j.jssc.2016.09.032

Huittinen, N., Arinicheva, Y., Kowalski, P., Vinograd, V., Neumeier, S., and Bosbach, D. (2017). Probing structural homogeneity of La$_{1-x}$Gd$_x$PO$_4$ monazite-type solid solutions by combined spectroscopic and computational studies. *J. Nucl. Mater.* 486, 148 – 157. doi: 10.1016/j.jnucmat.2017.01.024

Huittinen, N., Scheinost, A. C., Ji, Y., Kowalski, P. M., Arinicheva, Y., Wilden, A., et al. (2018). A spectroscopic and computational study of Cm$^{3+}$ incorporation in lanthanide phosphate rhabdophane (LnPO$_4$·0.67H$_2$O) and monazite (LnPO$_4$). *Inorg. Chem.* 57, 6252–6265. doi: 10.1021/acs.inorgchem.8b00095

Jahn, S. and Kowalski, P. M. (2014). Theoretical approaches to structure and spectroscopy of earth materials. *Rev. Mineral. Geochem.* 78, 691–743. doi: 10.2138/rmg.2014.78.17

Ji, Y., Beridze, G., Bosbach, D., and Kowalski, P. M. (2017a). Heat capacities of xenotime-type ceramics: An accurate ab initio prediction. *J. Nucl. Mater.* 494, 172–181. doi: 10.1016/j.jnucmat.2017.07.026

Ji, Y., Beridze, G., Li, Y., and Kowalski, P. M. (2017b). Large scale simulation of nuclear waste materials. *Energy Procedia* 127, 416–424. doi: 10.1016/j.egypro.2017.08.108

Ji, Y., Kowalski, P. M., Neumeier, S., Deissmann, G., Kulriya, P. K., and Gale, J. D. (2017c). Atomistic modeling and experimental studies of radiation damage in monazite-type LaPO$_4$ ceramics. *Nucl. Instrum. Methods Phys. Res. Sect. B* 393, 54–58. doi: 10.1016/j.nimb.2016.09.031

Jolley, K., Asuvathraman, R., and Smith, R. (2017). Inter-atomic potentials for radiation damage studies in CePO$_4$ monazite. *Nucl. Instrum. Methods Phys. Res. B* 393, 93–96. doi: 10.1016/j.nimb.2016.10.016

Konings, R. J. M., Beneš, O., Kovács, A., Manara, D., Sedmidubské, D., Gorokhov, L., et al. (2014). The thermodynamic properties of the f-elements and their compounds. Part 2: The lanthanide and actinide oxides. *J. Phys. Chem. Ref. Data* 43:013101. doi: 10.1063/1.4825256

Kowalski, P. M., Beridze, G., Ji, Y., and Li, Y. (2017a). Towards reliable modeling of challenging f electrons bearing materials: experience from modeling of nuclear materials. *MRS Advances* 2, 491–497. doi: 10.1557/adv.2017.46

Kowalski, P. M., Beridze, G., Li, Y., Ji, Y., Friedrich, C., Sasioglu, E., et al. (2016). Feasible and reliable ab initio approach to computation of materials relevant for nuclear waste management. *Ceram. Trans.* 258, 205–217. doi: 10.1002/9781119236016.ch21

Kowalski, P. M., Beridze, G., Vinograd, V. L., and Bosbach, D. (2015). Heat capacities of lanthanide and actinide monazite-type ceramics. *J. Nucl. Mater.* 464, 147–154. doi: 10.1016/j.jnucmat.2015.04.032

Kowalski, P. M., Ji, Y., Li, Y., Arinicheva, Y., Beridze, G., Neumeier, S., et al. (2017b). Simulation of ceramic materials relevant for nuclear waste management: Case of *La*$_{1-x}$*Eu*$_x$PO$_4$ solid solution. *Nucl. Instrum. Methods Phys. Res. Sect. B*, 393, 68–72. doi: 10.1016/j.nimb.2016.09.029

Kowalski, P. M. and Li, Y. (2016). Relationship between the thermodynamic excess properties of mixing and the elastic moduli in the monazite-type ceramics. *J. Eur. Ceram. Soc.* 36, 2093–2096. doi: 10.1016/j.jeurceramsoc.2016.01.051

Li, Y., Kowalski, P. M., Beridze, G., Blanca-Romero, A., Ji, Y., Vinograd, V. L., et al. (2016). Atomistic simulations of ceramic materials relevant for nuclear waste management: cases of monazite and pyrochlore. *Ceram. Trans.* 255:165. doi: 10.1002/9781119234531.ch15

Li, Y., Kowalski, P. M., Blanca-Romero, A., Vinograd, V., and Bosbach, D. (2014). Ab initio calculation of excess properties of solid solutions. *J. Solid State Chem.* 220, 137–141. doi: 10.1016/j.jssc.2014.08.005

López-Solano, J., Rodríguez-Hernández, P., Muñoz, A., Gomis, O., Santamaría-Perez, D., Errandonea, D., et al. (2010). Theoretical and experimental study of the structural stability of TbPO$_4$ at high pressures. *Phys. Rev. B* 81:144126. doi: 10.1103/PhysRevB.81.144126

Lumpkin, G. and Geisler-Wierwille, T. (2012). *Comprehensive Nuclear Materials: Minerals and Natural Analogues*, Vol 5. Oxford: Elsevier.

Macfarlane, A. (1999). Immobilization of excess weapon plutonium: a better alternative to glass. *Sci. Glob. Secur.* 7, 271–309. doi: 10.1080/08929889808426463

McGill, I. (2000). *Rare Earth Elements*. Reading: American Cancer Society.

Mogilevsky, P. (2007). On the miscibility gap in monazite–xenotime systems. *Phys. Chem. Miner.* 34, 201–214. doi: 10.1007/s00269-006-0139-1

Mogilevsky, P., Zaretsky, E. B., Parthasarathy, T. A., and Meisenkothen, F. (2006). Composition, lattice parameters, and room temperature elastic constants of natural single crystal xenotime from novo horizonte. *Phys. Chem. Miner.* 33, 691–698. doi: 10.1007/s00269-006-0118-6

Neumeier, S., Arinicheva, Y., Ji, J. M., Kowalski, P. M., Kegler, P., et al. (2017a). New insights into phosphate based materials for the immobilisation of actinides. *Radiochim. Acta* 105, 961–984. doi: 10.1515/ract-2017-2819

Neumeier, S., Kegler, P., Arinicheva, Y., Shelyug, A., Kowalski, P. M., Schreinemachers, C., et al. (2017b). Thermochemistry of La$_{1-x}$Ln$_x$PO$_4$ monazites (*ln*=gd, eu). *J. Chem. Thermodyn.* 105, 396–403. doi: 10.1016/j.jct.2016.11.003

Ni, Y., Hughes, J., and Mariano, A. (1995). Crystal-chemistry of the Monazite and Xenotime Structures. *Am. Mineral.* 80, 21–26.

Nikiforova, G. E., Ryumin, M. A., Gavrichev, K. S., and Gurevich, V. M. (2012). High-temperature thermodynamic properties of LuPO4. *Inorg. Mater.* 48, 841–844. doi: 10.1134/S0020168512080122

Nipko, J., Grimsditch, M., Loong, C.-K., Kern, S., Abraham, M. M., and Boatner, L. A. (1996). Elastic-constant anomalies in YbPO$_4$. *Phys. Rev. B* 53, 2286–2290.

Perdew, J. P., Burke, K., and Ernzerhof, M. (1996). Generalized gradient approximation made simple. *Phys. Rev. Lett.* 77:3865.

Perdew, J. P., Ruzsinszky, A., Csonka, G. I., Vydrov, O. A., Scuseria, G. E., Constantin, L. A., et al. (2008). Restoring the density-gradient expansion for exchange in solids and surfaces. *Phys. Rev. Lett.* 100:136406. doi: 10.1103/PhysRevLett.100.136406

Perdew, J. P. and Wang, Y. (1992). Accurate and simple analytic representation of the electron-gas correlation energy. *Phys. Rev. B* 45, 13244–13249.

Popa, K., Colineau, E., Wastin, F., and Konings, R. J. M. (2007a). The low-temperature heat capacity of (Pu$_{0.1}$La$_{0.9}$)PO$_4$. *Solid State Commun.* 144, 74–77. doi: 10.1016/j.ssc.2007.07.011

Popa, K., Jutier, F., Wastin, F., and Konings, R. J. M. (2006a). The heat capacity of NdPO$_4$. *J. Chem. Thermodyn.* 38, 1306–1311. doi: 10.1016/j.jct.2006.02.006

Popa, K. and Konings, R. J. M. (2006). High-temperature heat capacities of eupo4 and smpo4 synthetic monazites. *Thermochim. Acta* 445, 49–52. doi: 10.1016/j.tca.2006.03.023

Popa, K., Konings, R. J. M., and Geisler, T. (2007b). High-temperature calorimetry of (La$_{1-x}$Ln$_x$)PO$_4$ solid solutions. *J. Chem. Thermodyn.* 39, 236–239. doi: 10.1016/j.jct.2006.07.010

Popa, K., Sedmidubsky, D., Benes, O., Thiriet, C., and Konings, R. J. M. (2006b). The high-temperature heat capacity of LnPO$_4$ (Ln=La, Ce, Gd) by drop calorimetry. *J. Chem. Thermodyn.* 38, 825–829. doi: 10.1016/j.jct.2005.08.019

Prieto, M. (2009). "Thermodynamics of solid solution-aqueous solution systems," *19th Annual V M Goldschmidt Conference*, Davos.

Rustad, J. R. (2012). Density functional calculations of the enthalpies of formation of rare-earth orthophosphates. *Am. Mineral.* 97, 791–799. doi: 10.2138/am.2012.3948

Schlenz, H., Heuser, J., Neumann, A., Schmitz, S., and Bosbach, D. (2013). Monazite as a suitable actinide waste form. *Z. Kristallogr.* 228, 113–123. doi: 10.1524/zkri.2013.1597

Schlenz, H., Neumeier, S., Hirsch, A., Peters, L., and Roth, G. (2017). "Phosphates as safe containers for radionuclides," in *Highlights in Applied Mineralogy*, eds S. Heuss-Aßbichler, G. Amthauer, and M. John (Berlin ; Boston : De Gruyter) , 171–195.

Seydoux-Guillaume, A.-M., Deschanels, X., Baumier, C., Neumeier, S., Weber, W. J., and Peuget, S. (2018). Why natural monazite never becomes amorphous: experimental evidence for alpha self-healing. *Am. Mineral.* 103, 824–827. doi: 10.2138/am-2018-6447

Shannon, R. D. (1976). Revised effective ionic radii and systematic studies of interatomic distances in halides and chalcogenides. *Acta Cryst. A* 32, 751–767.

Shein, I. R., and Shalaeva, E. V. (2016). Pressure-induced zircon to monazite phase transition in Y$_{1-x}$La$_x$PO$_4$: First-principles calculations. *J. Struct. Chem.* 57, 1513–1518. doi: 10.1134/S0022476616080047

Slack, G. (1973). Nonmetallic crystals with high thermal-conductivity. *J. Phys. Chem. Solids* 34, 321–335.

Stavrou, E., Tatsi, A., Raptis, C., Efthimiopoulos, I., Syassen, K., Muñoz, A., et al. (2012). Effects of pressure on the structure and lattice dynamics of TmPO$_4$: experiments and calculations. *Phys. Rev. B* 85:024117. doi: 10.1103/PhysRevB.85.024117

Stoll, W. (2000). *Thorium and Thorium Compounds*. Hanau: American Cancer Society.

Thiriet, C., Konings, R. J. M., Javorsky, P., Magnani, N., and Wastin, F. (2005a). The low temperature heat capacity of LaPO$_4$ and GdPO$_4$, the thermodynamic functions of the monazite-type LnPO$_4$ series. *J. Chem. Thermodyn.* 37, 131–139. doi: 10.1016/j.jct.2004.07.031

Thiriet, C., Konings, R. J. M., Javorsky, P., and Wastin, F. (2004). The heat capacity of cerium orthophosphate CePO$_4$, the synthetic analogue of monazite. *Phys. Chem. Miner.* 31, 347–352. doi: 10.1007/s00269-004-0397-8

Thiriet, C., Konings, R. J. M., and Wastin, F. (2005b). Low temperature heat capacity of PuPO$_4$. *J. Nucl. Mater.* 344, 56–60. doi: 10.1016/j.jnucmat.2005.04.016

Thomä, R., Wehrle, H., and Armbruster, A. (1974). Measurement of the elastic constants of luaso4 and lupo4 by brillouin scattering and determination of the debye temperatures. *Phys. Status Solidi A* 24, K71–K73.

Thust, A., Arinicheva, Y., Haussühl, E., Ruiz-Fuertes, J., Bayarjargal, L., Vogel, S. C., et al. (2015). Physical properties of La$_{1-x}$Eu$_x$PO$_4$, $0 \leq x \leq 1$, Monazite-Type Ceramics. *J. Am. Ceram. Soc.* 98, 4016–4021. doi: 10.1111/jace.13841

Ushakov, S., Helean, K., and Navrotsky, A. (2001). Thermochemistry of rare-earth orthophosphates. *J. Mater. Res.* 16:2623–2633. doi: 10.1557/JMR.2001.0361

Vanderbilt, D. (1990). Soft self-consistent pseudopotentials in a generalized eigenvalue formalism. *Phys. Rev. B* 41:7892. doi: 10.1103/PhysRevB.41.7892

Wang, J., Zhou, Y., and Lin, Z. (2005). First-principles elastic stiffness of LaPO$_4$ monazite. *Appl. Phys. Lett.* 87:051902. doi: 10.1063/1.2005392

Williams, M. L., Jercinovic, M. J., and Hetherington, C. J. (2007). Microprobe monazite geochronology: understanding geologic processes by integrating composition and chronology. *Annu. Rev. Earth Planet. Sci.* 35, 137–175. doi: 10.1146/annurev.earth.35.031306.140228

Zunger, A., Wei, S. H., Ferreira, L. G., and Bernard, J. E. (1990). Special quasirandom structures. *Phys. Rev. Lett.* 65, 353–356.

**Conflict of Interest Statement:** The authors declare that the research was conducted in the absence of any commercial or financial relationships that could be construed as a potential conflict of interest.

# A New 3D 10-Connected Cd(II) Based MOF With Mixed Ligands: A Dual Photoluminescent Sensor for Nitroaroamatics and Ferric Ion

*Jun Wang[1]\*, Jian Wu[2], Lu Lu[1], Hongjia Xu[3], Manoj Trivedi[4], Abhinav Kumar[5]\*, Jianqiang Liu[3]\* and Mingbin Zheng[3]\**

[1] School of Chemistry and Environmental Engineering, Sichuan University of Science and Engineering, Zigong, China, [2] Guangxi Key Laboratory of Chemistry and Engineering of Forest Products, Guangxi University for Nationalities, College of Chemistry and Chemical Engineering, Nanning, China, [3] Dongguan Key Laboratory of Drug Design and Formulation Technology, Key Laboratory of Research and Development of New Medical Materials of Guangdong Medical University, School of Pharmacy, Guangdong Medical University, Dongguan, China, [4] Department of Chemistry, University of Delhi, New Delhi, India, [5] Department of Chemistry, Faculty of Science, University of Lucknow, Lucknow, India

The precise unification of functional groups and photoluminescence properties can give rise to MOFs that can offer diverse applications like selective detection of nitroaromatic compounds (NACs) which are considered to be an important ingredient of explosive as well as cation and anion sensing. Hence, a new 3D metal-organic framework (MOF) [Cd$_2$(btc)(bib)(HCOO)(H$_2$O)·H$_2$O]$_n$ (**1**) has been synthesized using mixed ligand strategy by solvothermal reaction of cadmium acetate with two ligands *viz.* 1,3,5-benzenetricarboxylic acid (H$_3$btc) and 1,4-bis(2-methyl-imidazol-1-yl)butane (bib). The MOF **1** possesses highly 10-connected network which is based on {Cd$_4$(btc)$_2$(bib)$_4$} molecular building block. The studies showed that **1** could be taken as the fluorescent sensor for sensitive recognition of NACs, in particular 2,4,6-trinitrophenol (TNP) with notable quenching ($K_{sv} = 5.42 \times 10^4$ M$^{-1}$) and LOD of 1.77 ppm. Additionally, **1** also displayed selective sensing for Fe$^{3+}$ ions with $K_{sv} = 6.05 \times 10^3$ M$^{-1}$ and LOD = 1.56 ppm. Also, this dual sensor displayed excellent reusability toward the detection of TNP and Fe$^{3+}$ ion. Theoretical calculations have been performed to propose the probable mechanism for the sensing luminescence intensity. Calculations indicated that because of the charge transfer and weak interaction that is operating between NACs and MOF, the weakening in the photoluminescence intensity resulted.

Keywords: MOF, nitroaromatics, sensor, theoretical calculation, topology

## INTRODUCTION

Currently, tremendous amount of efforts have been devoted in developing new metal-organic frameworks (MOFs) which display photoluminescent properties and hence this class of luminescence materials can be in demand for solving the pollution problems and can offer potential application as luminescent sensors (Hua et al., 2015; Li et al., 2015; Shi et al., 2015; Wang et al., 2015, 2017; Liu et al., 2016a,b, 2017; Chen et al., 2017; Lu et al., 2017; Ma et al., 2017). To prepare useful and excellent luminescent MOF based sensors, the ligand-based strategy had been proposed in which the precise incorporation of functional groups in the π-conjugated organic ligands and their

coordination with $d^{10}$-metal ions deliver MOFs which can be used as luminescent materials (Ma et al., 2013; Zheng et al., 2014; Wang et al., 2016; Guo et al., 2017; Chen et al., 2018a,b; Shen et al., 2018). Up to now, numerous luminescent MOFs have been documented which had been utilized to detect metal ions and small organic compounds (Cui et al., 2012). Sun et al. had synthesized two Cd(II)-based MOFs which demonstrated selectivity to detect acetone (Yi et al., 2012). Chen et al. proposed that the choice of metal centers play a crucial role in molecular recognition by binding interactions of metal sites of the host MOF with guest molecules (Chen et al., 2007). Bu et al. reported a highly sensitive luminescent Cd(II)-based MOF that quenched at 100 ppm of TNP and display a high quenching efficiency of 92.5% (Tian et al., 2014). Thus, luminescence quenching based detection of compounds offers an alternative that is simple, sensitive, and convenient in nature. The possible mechanism associated with the sensing properties of these materials depend on monitoring of the transmission signals generated during interactions that are taking place between sensors (guest) and substrates (host) (Gole et al., 2011; Pramanik et al., 2011; Chen et al., 2013; Balamurugan et al., 2014).

The recent investigations have proved that MOFs, constructed from mixed organic ligands comprising of dicarboxylate and N-donor linkers display interesting dynamic properties (Zhan et al., 2014). Bearing these aspects in mind and in continuation to our efforts in the area of metal-organic frameworks (MOFs) (Li et al., 2016; Liu et al., 2016c; Jin et al., 2017), which were aimed toward the syntheses of multifunctional MOFs we have chosen a flexible 1,4-bis(2-methyl-imidazol-1-yl)butane (bib) ligand (Hou et al., 2014a,b; Shi et al., 2014), and a rigid 1,3,5-benzenetricarboxylic acid ($H_3$btc) ligand as well as $d^{10}$ transition-metal center ($Cd^{2+}$) to develop new structures with potential applications as luminescence sensor. The choice of using this strategy has been based on the following considerations (Marin et al., 2006; Kent et al., 2010; Saini and Das, 2012; Son et al., 2013; Banerjee et al., 2014; Li et al., 2014; Park and Lee, 2015; Wen et al., 2015; Park et al., 2016; Das and Mandal, 2018): (1) the binding capacity between bib ligand and metal centers not only induces flexible and diverse structures but also facilitates the surface functionalities of the materials; (2) rigid ligand btc with aromatic rings could effectively favor intra-ligand interactions and induce luminescent character. Herein, we are presenting a new Cd(II) MOF having formula$[Cd_2(btc)(bib)(HCOO)(H_2O)\cdot H_2O]_n$ (1) which have been utilized as dual photoluminescent sensor for the selective detection of nitroaromatics (NACs) especially TNP and ferric ions.

## MATERIALS AND METHODS

The instrumental, X-ray crystallographic, and computational details are presented in the **Supplementary Information**.

## Synthesis of [Cd$_2$(btc)(bib)(HCOO)(H$_2$O)·H$_2$O]$_n$ (1)

A mixture of $H_3$btc (0.10 mmol, 0.021 g), bib (0.10 mmol, 0.022 g), $Cd(NO_3)_2\cdot 4H_2O$ (0.15 mmol, 0.027 g) in 20 mL

DMF/$H_2$O mixture (v/v = 3:1) was stirred for 30 min. This mixture was then transferred in a 25-mL Teflon-lined reactor, sealed and heated up to 120°C and this temperature was maintained for 72 h. The mixture was cooled down to room temperature with a cooling rate of 5°C/h. Yellow block type crystals of **1** were obtained in 74% yield on the basis of cadmium. Elemental analysis (% calc/found): C: 35.17/34.92, H:3.37/3.28, N:7.81/7.55.

## RESULTS AND DISCUSSION

### Crystal Structure Description

The single-crystal X-ray diffraction results indicate that **1** crystallizes in triclinic space group *P*-1. **1** is a 3D architecture having binuclear Cd(II) clusters as secondary building units(SBUs) which in turn is constructed by mixed ligands *viz.* btc and bib. **1** shows two types of Cd(II) centers with different coordination fashions. The SBUs of **1** are bonded by two bib, one $\mu_2$-$\eta^2$:$\eta^2$ formate anion and two bidentate chelating carboxylic anions and one bridging bidentate carboxylic anion (**Figure 1A** and **Scheme S1**). The formate anion was generated from DMF under acid condition. This conversion had already been reported previously many times (Lu et al., 2017). The Cd1 ion is hexa-coordinated where the CdO5N unit possess distorted octahedral geometry, while the Cd2 ion is seven-coordinated in which CdO6N moiety display distorted pentagonal bipyramidal geometry. The Cd1 coordinates to one carboxylate group from one btc, one O-atom of one bridged carboxylate from another btc, one $\mu_2$-O of one formate, one N from imidazole and is capped by the O of one $H_2$O.The Cd2 center of **1** is connected to one carboxylate from one btc, one O of one bridged carboxylate from the other btc, three $\mu_2$-O of two formate anions and one N from imidazole. The dimeric units in SBU are formed by completely deprotonated btc anions to generate a 2D layered arrangement (**Figure 1B** and **Figure S1**). Further these 2D layers further linked by bib ligand to generate 3D framework (**Figure 1C**). Thus, the four Cd(II)centers are divulged by two bridged formates and two carboxylates of btc. Further it spreads out with six 3-connected btc and four linear imidazole-based bib ligands and in this way, this tetra-cadmium SBU can be simplified into a 10-connected node. The full motif of **1** can be taken as a 10-connected 3D network with $(3^6.4^4.5^{10}.\ 5^{12}.6^8.6^5)$ topology (**Figure 1D**). The evacuated **1** shows theoretical porosity of 15.8% according to PLATON calculations with a probe radius of 1.65 Å (Spek, 2003). Thermogravimetric result indicates that **1** remains stable till 350°C (**Figure S2**). Also, PXRD experiment had been performed to assess whether the MOF is having phase purity in the solid state. The PXRD patterns confirm the phase purity of the bulk sample (**Figure S3**).

### Luminescence Sensing

In general, the MOFs based on $d^{10}$-based metal centers and conjugated linkers are excellent candidates for the photoluminescent properties. It has been reported that the btc and bib exhibit emissions at 375 nm ($\lambda_{ex}$ = 300 nm) and 445 nm ($\lambda_{ex}$ = 370 nm), respectively (Li et al., 2015). **1** displayed emission with the maxima at 395 nm ($\lambda_{ex}$ = 300 nm).The
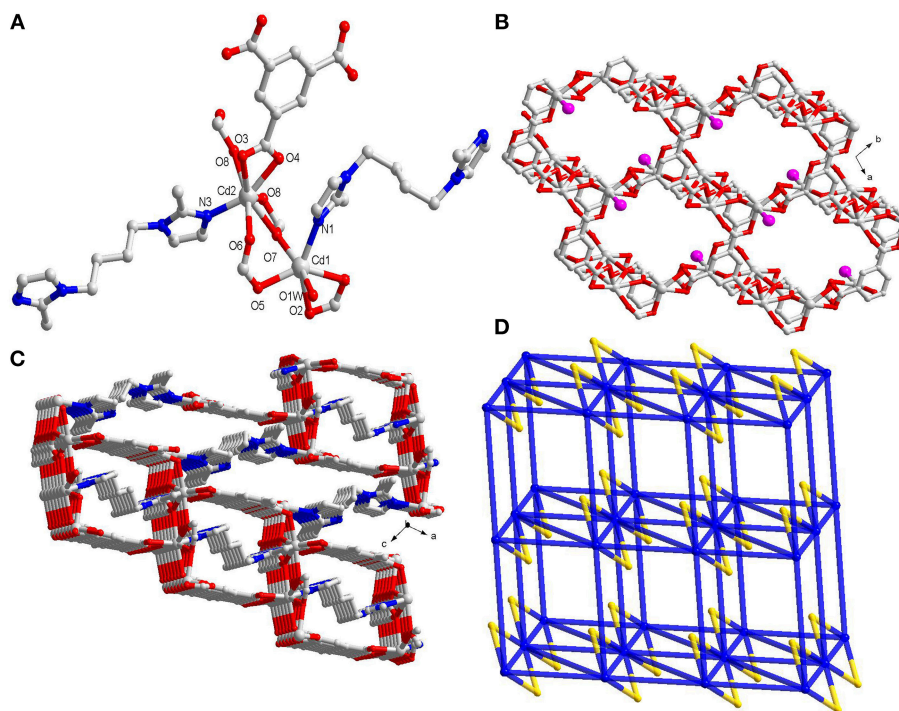
**FIGURE 1 | (A)** The coordination environment around Cd(II) centers in **1**; **(B)** Perspective view of 2D layer constructed by Cd(II) centers and btc linkers(the pink ball represents the uncoordinated carboxylate group); **(C)** The 3D framework connected by btc and bib ligands; **(D)** Schematic representation of the 3D 10-connected network(the yellow ball represents the formate linker).

red-shift in emission maximum in the case of **1** as compared to btc with concomitant enhancement in the intensity indicates that the electron transfer may be taking place between the ligands and metalcenters (Allendorf et al., 2009; Rocha et al., 2011; Heine and Buschbaum, 2013; Hu et al., 2015). The spectral feature associated with **1** provided us impetus to use this MOF as the luminescent sensor for the detection of organic compounds (**Figure S4**). Thus, the photoluminescent property of the emulsion of **1** in different solvent was investigated. It has been found that luminescent spectrum of **1** is largely dependent on nature of small solvents, especially nitrobenzene (NB) (**Figure S5**) where **1** exhibits the most significant quenching effect in intensity (**Figure 2a**). The possible mechanism of the quenching in photoluminescent intensity in presence of NB has been proposed to originate from the electron-withdrawing effect from its nitro groups (Chen et al., 2009; Zheng M. et al., 2013; Song et al., 2014). Such solvent reliant luminescence properties can be interesting for sensing of different derivatives of NB. Hence, the luminescence intensity of emulsion of **1** in presence of different nitroaromatic compounds (NACs), *viz.*2,6-dinitrotoluene (2,6-DNT), *o*-nitrophenol (ONP),2,4-dinitrophenol (2,4-DNP), 2,4,6-trinitrophenol (TNP), *p*-nitrophenol (PNP),2-nitrotoluene (2-NT), 4-nitrotoluene (4-NT), 1,3-dinitrobenzene (1,3-DNB),1,2,4-trimethylbenzene 1,3,5-trimethylbenzene (1,3,5-TMB),2,4-dinitrotoluene (2,4-DNT),were recorded. The experiments showed that the addition of same concentration of NACs to the emulsion of **1** will results



**SCHEME 1 |** The schematic illustration of the electron transfer process between **1** and NACs.
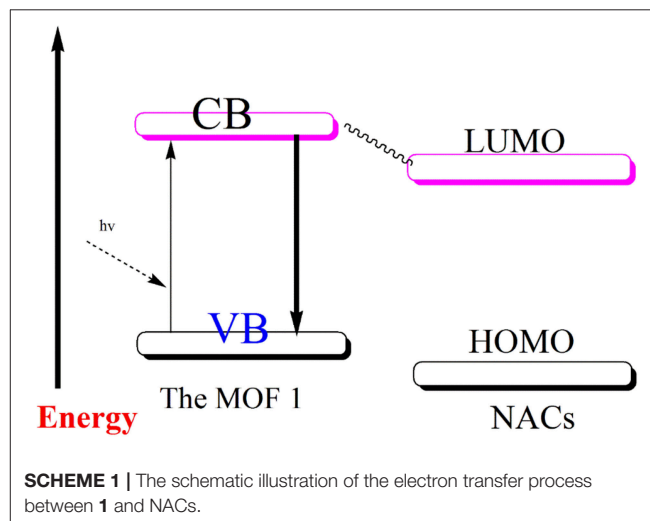
in the decline in its luminescent intensity to different levels (**Figure 2b** and **Figures S6–S26**). However, aromatic compounds not having such electron withdrawing nitro group, *viz.*1,3,5-TMB and 1,2,4-TMB have displayed intensity enhancement in **1**.

To further explore the sensing property of **1** toward TNP, the emission spectra of the suspension of **1** were recorded by gradual addition of batches of TNP solutions. The experiment

**FIGURE 2 | (a)** The plots of varied luminescent intensity of **1** when dispersed in different small organic molecules ($\lambda_{ex}$ = 320 nm); **(b)** The quenching efficiency of different nitro compounds (Emiss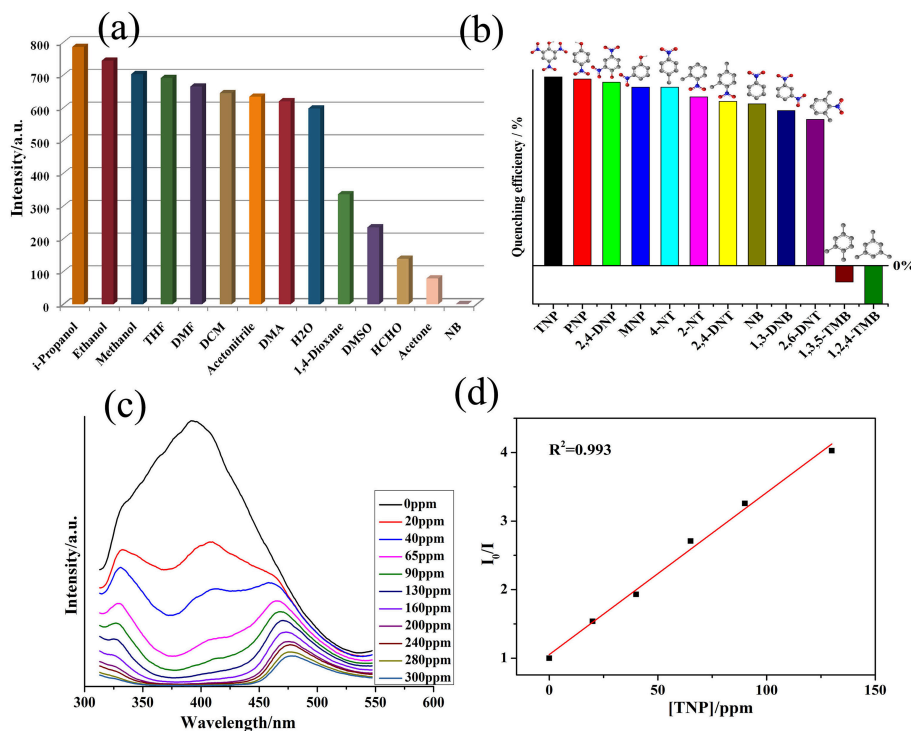ion intensities at 375 nm were selected); **(c)** The luminescence intensity of **1** recorded after addition of 1 mM TNP ($\lambda_{ex}$ = 320 nm); **(d)** SV plot in the presence of **1** at different TNP concentrations.

indicated that the luminescence intensity of **1** declined with augmenting concentration of TNP (**Figure 2c**). The quenching efficiency was evaluated to be 44.5% for 20 ppm of TNP and 85% for 240 ppm of TNP. The Stern–Volmer (SV) equation which is used quantitatively to calculate the quenching efficiency was employed (Sanchez and Trogler, 2008; Sanchez et al., 2008; Zhang et al., 2015). The SV plot of TNP was almost linear at related low concentrations (**Figure 2d**), and its quenching constant ($K_{sv}$) of **1** is 5.42 × $10^4$ $M^{-1}$ and its LOD is 1.77 ppm, which was similar to some previously reported examples (**Table S3**). Additionally the $K_{sv}$ value of **1** for TNP is 3.64 × $10^3$ $M^{-1}$ and LOD parameter is 1.35 ppm. These observations clearly indicates that the **1** under study may be a highly selective sensor for TNP in comparison to other NACs (Qin et al., 2014; Singh and Nagaraja, 2014). The PXRD pattern of the recovered sample after performing 5 cycles of sensing studies indicate high stability of **1** and hence it can be concluded that the integrity of **1** remained almost unchanged after operational sensing works (**Figure S3**). On the basis of the structural feature of **1** which indicated only 15.8% porosity (*vide supra*), the encapsulation of TNP into the channels of MOF cannot take place. Thus, the interaction of analytes with **1** are more inclined toward the surface interaction operating between the analytes and **1**.

To offer the possible explanation for the decline in the photoluminescent intensity of MOF to varying magnitudes in the presence of different aromatic compounds, the computational investigation was done at the B3LYP level of theory (**Table 1** and **Figure S27**). The weakening in photoluminescence intensity of MOFs when aromatic compounds comprising of –$NO_2$ functions are added to them may be attributed to charge transfer that is taking place from conduction band of MOF to LUMO of these compounds (**Scheme 1**). To enable such transition the conduction band of MOFs should lie at higher energy scale than the conduction band of aromatic nitro-analytes (Lan et al., 2009; Zhang et al., 2010, 2011, 2016; Kreno et al., 2012; Li et al., 2013; Lin et al., 2016; Yang et al., 2016; Zhao et al., 2016, 2017). The **Table 1** elucidatesthe conduction band energy levels of the full nitro-aromatic compounds, which are low than that of **1**.

So, these nitro-aromatic analytes are in the apt position to accept the charge from **1** which is photo-excited. Hence, this phenomenon results in deterioration in photoluminescence intensity of the MOF to varying degree different nitro-aromatic compounds are added to it. Also, the **Table 1** indicates that 1,3,5-TMB and 1,2,4-TMBare possessing higher LUMO energy level position than **1**. Therefore, these aromatic compounds deprived of –$NO_2$ functions display small effect on photoluminescence intensity of **1**. However, the experimental order of decrement in photoluminescence intensity of **1** when different nitroaromatic analytes are added to it is not in accordance with their corresponding LUMO energy values. Therefore, it assessed that

charge transfer may not be the solitary phenomenon responsible for decline in the photoluminescence. Additionally, along with the charge transfer phenomenon, weak interactions between the MOF and nitroaromatic analytes may also contribute toward the decline in the photoluminescence (Lan et al., 2009; Zhang et al., 2010, 2011; Kreno et al., 2012; Lin et al., 2016). Probably because of this reason the aromatic compounds 1,3,5-TMB and 1,2,4-TMB even though having relatively high LUMO energy values than **1** are slightly enhancing the photoluminescence intensity of **1** (Toal and Trogler, 2006; Kim et al., 2013; Wang et al., 2013; Zheng Q. et al., 2013; Hu et al., 2016).

Furthermore, to authenticate the selective sensing behavior of **1** toward TNP, the competitive experiments were executed by the adding different nitroaromatic compounds in the suspension of **1** followed by TNP (**Figure S28**). Results indicated that effective photoluminescent quenching was observed only when the TNP solution was added (**Figure S28**). These experiments validate the remarkable selectivity of **1** toward TNP. Further, to have better understanding into the selective TNP-sensing ability of **1**, the electronic properties of MOF reported herein as well as the nitroaromatic compounds were analyzed. The mechanism for photoluminescent quenching through electronic migration from conduction band of probes MOFs to LUMO of NAC shaving electron deficient nature is well-established (Toal and Trogler, 2006; Lan et al., 2009; Zhang et al., 2010, 2011; Kreno et al., 2012; Kim et al., 2013; Wang et al., 2013; Zheng M. et al., 2013; Hu et al., 2016; Lin et al., 2016). In general, the conduction band of rich electric probes MOFs is having higher energy in comparison to the energies of LUMO corresponding to nitro-aromatic compounds. With downfall in the LUMO energy values of NACs, the tendency to accept electron by these analytes and photoluminescent quenching becomes higher. The selective sensing for TNP is in agreement with its lower LUMO energy in comparison to other NACs (**Table 1**). The disagreements between quenching of photoluminescent intensity for others NACs except for TNP and their LUMO energy parametersare conducted, in which may contain the electronic migration and/or resonance energy transfer (RET).The correlative factors responsible for photoluminescent intensity quenching process (Hu et al., 2016). Also, the efficiency of energy transfer depend on the extent of overlap between the emission spectrum of MOF and the electronic absorption spectrum of the analyte (Marin et al., 2006; Kent et al., 2010; Saini and Das, 2012; Son et al., 2013; Banerjee et al., 2014; Li et al., 2014; Park and Lee, 2015; Wen et al., 2015; Park et al., 2016; Das and Mandal, 2018). In sharp contrast to other NACs the absorption spectrum for TNP displays good full coverage the emission spectrum of **1** (**Figure S29**). This clearly suggests the electronic migration and energy conversion mechanisms are associated with the luminescence quenching in **1** by TNP, but electron transfer mechanism solely exists for other nitro-aromatic compounds. The existence of the dominating energy transfer between **1** and TNP has also been substantiated by the preferential quenching of the 375 nm band over 475 nm during the titration experiments (**Figure 2c**). The emission band at ~375 nm display spectral overlap with the electronic absorption spectrum of TNP which lead to efficient quenching of this band by an energy transfer mechanism (**Figure S29**).

**TABLE 1 |** The HOMO-LUMO energies (in eV) for 1, ligand and aromatic analytes, ligand.

| Ligand/1/Analyte | HOMO | LUMO |
| --- | --- | --- |
| H$_3$btc | −7.73 | −1.97 |
| **1** | −2.21 | −1.13 |
| 2-nitrotoluene (2-NT) | −7.28 | −2.32 |
| 4-nitrotoluene (4-NT) | −7.36 | −2.32 |
| Nitrobenzene (NB) | −7.60 | −2.43 |
| 2, 6-dinitrotoluene (2,6-DNT) | −7.91 | −2.87 |
| 2, 4-dinitrotoluene (2,4-DNT) | −8.11 | −2.98 |
| 1, 3-dinitrobenzene (1,3-DNB) | −8.42 | −3.14 |
| 2,4,6-trinitrophenol (TNP) | −8.54 | −3.55 |
| 1,2,4-trimethylbenzene1,2,4-TMB | −6.03 | 0.28 |
| 1,3,5-trimethylbenzene1,3,5-TMB | −6.18 | 0.26 |
| 2,4-DNP | −7.62 | −3.33 |
| o-nitrophenol (ONP) | −6.80 | −2.72 |
| p-nitrophenol (PNP) | −7.43 | −2.39 |

Antagonistically, the emission band at ~475 nm display poor spectral overlap with the electronic absorption spectrum of TNP because of which the quenching of this emission band occurs by a "less efficient" photo-induced electron transfer (PET) mechanism (Banerjee et al., 2014). In addition, there might be electrostatic interactions between TNP and the nitrogen centers of the ligands in **1** (Marin et al., 2006; Kent et al., 2010; Saini and Das, 2012; Son et al., 2013; Banerjee et al., 2014; Li et al., 2014; Park and Lee, 2015; Wen et al., 2015; Park et al., 2016; Das and Mandal, 2018) Hence due to combination of electron-transfer, energy-transfer and electrostatic interaction between TNP **1**, the quenching efficiency for TNP gets significantly enhanced (Marin et al., 2006; Kent et al., 2010; Son et al., 2013; Li et al., 2014; Das and Mandal, 2018).

The MOF**1** was suspended in distilled water having 1 × 10$^2$ M M(NO$_3$)$_n$ to form the M$^{n+}$@**1** to perform sensing experiments for the detection of metal cations. The intensities were enhanced upon adding Na$^+$, K$^+$, and Ca$^{2+}$ ions in solutions when compared to the blank experiment (**Figure 3A**), while other metal ions exhibited different levels of quenching effects. Notably in the presence of Fe$^{3+}$ ions the significant quenching in the luminescence intensity of MOF was observed. Thus, the relationship between the concentrations of Fe$^{3+}$ ions upon the intensity of **1** was explored by varying the concentration of Fe$^{3+}$ (**Figure 3B**). When the concentration of ferric ion in the emulsion of **1** was 500 ppm, then the luminescent intensity was completely disappeared. The mechanism pertaining to the quenching effect caused by Fe$^{3+}$could be explicated on the basis of electronic migration operating from the organic ligands of the MOF which behave as donor toward the metal ions which act as acceptor (Wu et al., 2015). The crystal structure investigation indicates that in**1** the uncoordinated oxygens of the carboxylate groups of btc ligands can behave as potential electrons donors.

Based on the above results, **1** shows a highly selective to Fe$^{3+}$. The photoluminescent intensity of **1** was nearly nullified at a
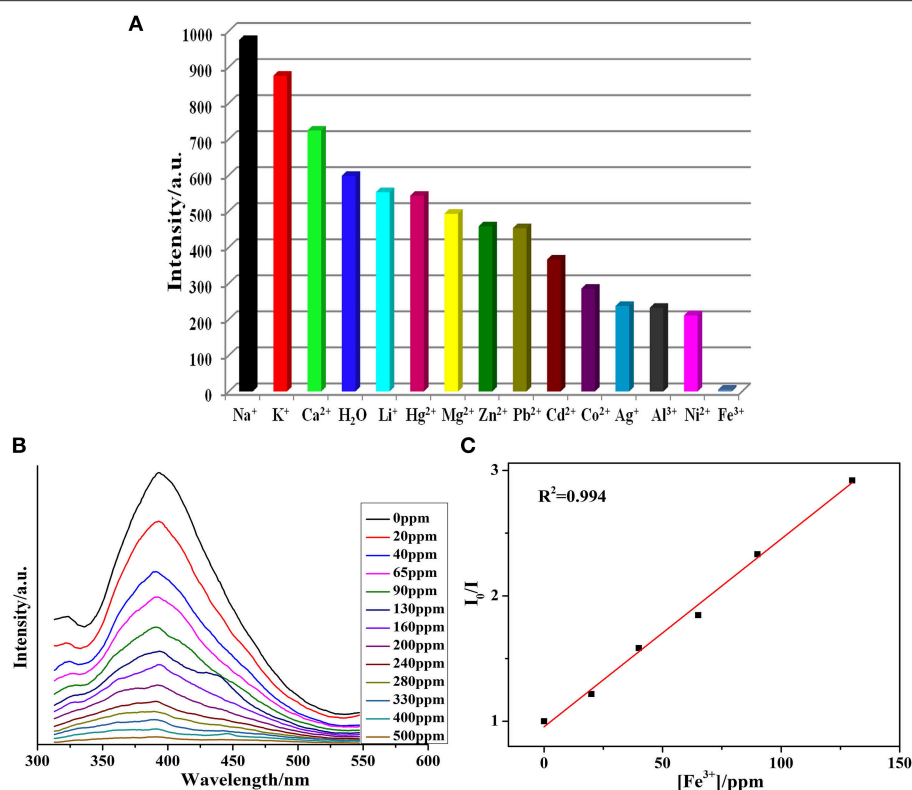
**FIGURE 3 | (A)** Photoluminescence intensity of **1** when it was dispersed in different metal ions solutions in $H_2O$ ($\lambda_{ex} = 320$ nm); **(B)** Quenching in photoluminescence intensity after adding 1 mM $Fe^{3+}$ solution; **(C)** SV plot after adding different $Fe^{3+}$ concentrations.

$Fe^{3+}$ concentration of $6.05 \times 10^3$ $M^{-1}$. Further, the LOD was calculated *ca.* 1.56 ppm, which is comparable to the reported examples (**Table S4**) (Xiang et al., 2010; Jayaramulu et al., 2012; Liu et al., 2014; Cao et al., 2015; Xu et al., 2015). Moreover, the PXRD patterns of **1** after accomplishing sensing experiments indicated that the MOF retain its structural integrity and hence can be reused as a probe to detect ferric ions (**Figure S3**). The highly selective sensing for $Fe^{3+}$ ions stimulated us to further inspect the effect of the related metal ions on $Fe^{3+}$ sensing. This had been checked by the addition of metal ions other than $Fe^{3+}$ to **1** followed by $Fe^{3+}$. The experiments revealed that the luminescence intensity of **1** will be completely quenched while the $Fe^{3+}$ ion ($10^{-2}$ M) is added to **1**. The $K_{sv}$ of $Fe^{3+}$ in the above systems is little greater that the value obtained for the pure **1** (**Figure S30**).

The possible sensing mechanism associated with the luminescence quenching of in the presence of $Fe^{3+}$ has been further examined. Till date, some pertinent reasons for quenching in the luminescence intensity are: (Xu et al., 2011; Dang et al., 2012; Tang et al., 2013; Yang et al., 2013; Hu et al., 2014; Zhou et al., 2014; Xu and Yan, 2015) (I) the breakdown of framework; (II) ion exchange operating between sensing ions and the metal centers of probes; (III) resonance energy transfer (RET); and (IV) the weak interactions that are operating between metal cations and the functional groups from the

organic ligands. The PXRD patterns (**Figure S3**) indicates that the MOF **1** even when immersed in metal ion solutions maintain its structural integrity. To substantiate the probable mechanism, the ICP has also been performed which showed that negligible Cd content is present in the filtrate obtained after suspending **1** in the $Fe^{3+}$ solution for 1 day. This rules out that the exchange of $Fe^{3+}$ with the $Cd^{2+}$ of the MOF during sensing experiment (**Table S5**). Additionally, UV-Vis absorption data have been also conducted (**Figure S31**). The absorption spectrum of $Fe^{3+}$ solution covers most of the emission spectrum of **1**, while in the absorption spectra of other metal ions no such spectral overlap have been observed. So, the competitive absorption of excitation wavelength between aqueous solution of $Fe^{3+}$ and **1** may be plausible reason for the quenching in photoluminescnece (Tang et al., 2013; Yang et al., 2013; Hu et al., 2014). Furthermore, the fluorescence lifetime of 3.6 ms in **1** was reduced to 1.9 ms using 1.0 mM $Fe^{3+}$ solution (**Figure S32**). Hence, energy transfer is the prime phenomenon because of which loss in photoluminescent intensity is observed. To further explicate the possible mechanism for luminescence quenching in **1** by $Fe^{3+}$ ion, the X-ray photoelectron spectroscopy (XPS) on $Fe^{3+}@1$ showed that the energy of Fe 2p1 shifts to 712.6 eV, which may demonstrate the weak interaction between them (**Figure S33**) (Buragohain et al., 2016; Santra et al., 2016; Wu et al., 2017; Wang et al., 2018). In the time-dependent luminescence

intensity measurement experiment (**Figure S34**), the final results indicated that it follows the first-order exponential decay curve. The character showed that the collision between $Fe^{3+}$ and **1** may be faster than the static process. Hence, the static interaction might be incomplete instantly and acts as a continuous process which leads to a gradual decrease in luminescence intensity.

## CONCLUSION

A new 10-connected Cd(II)-based MOF with $(3^6.4^4.5^{10}.5^{12}.6^8.6^5)$ topology have been synthesized. Moreover, **1** reveals the selective and sensitive photoluminescent quenching by TNP. A combined experimental and mechanistic investigation substantiates that the quenching of the photoluminescent intensity of MOF in presence of analytes can be credited to the simultaneous charge transfer and weak interactions that are operating between **1** and analytes. Additional investigation of **1** to detect metal-ions indicated extremely sensitive luminescent quenching of **1** framework by $Fe^{3+}$ ion over other metal ions. The good quenching constant ($6.05 \times 10^3$ $M^{-1}$) and very low limit of detection (LOD) (1.56 ppm), validates that **1** can be the potential detector for $Fe^{3+}$. The excellent reusability/recyclability of MOF with respect to both TNP and $Fe^{3+}$ sensing is certainly remarkable and this makes **1** as anew dual channel sensor for detection of TNP and $Fe^{3+}$ ions.

## AUTHOR CONTRIBUTIONS

JuW wrote the manuscript. JiW, LL, HX, and MT designed and synthesised the materials. AK, JL, and MZ checked the full materials.

## ACKNOWLEDGMENTS

## SUPPLEMENTARY MATERIAL

The Supplementary Material for this article can be found online at: https://www.frontiersin.org/articles/10.3389/fchem.2019.00244/full#supplementary-material

## REFERENCES

Allendorf, M. D.,Bauer, A., Bhakta, R. K., and Houk, R. J. T. (2009). Luminescent metal-organic frameworks. *Chem. Soc. Rev.* 38, 1330–1352. doi: 10.1039/B802352M

Balamurugan, A., Kumar, V., and Jayakannan, M. (2014). Triple action polymer probe: carboxylic distilbene fluorescent polymer chemosensor for temperature, metal-ions and biomolecules. *Chem.Commun.* 50, 842–845. doi: 10.1039/C3CC45274C

Banerjee, D., Hu, Z. C., and Li, J. (2014). Luminescent metal-organic frameworks as explosive sensors. *Dalton Trans.* 43, 10668–10685. doi: 10.1039/C4DT01196A

Buragohain, A., Yousufuddin, M., Sarma, M., and Biswas, S. (2016). 3D luminescent amide-functionalized cadmium tetrazolate framework for selective detection of 2,4,6-trinitrophenol. *Cryst. Growth Des.* 16, 842–851. doi: 10.1021/acs.cgd.5b01427

Cao, K. L., Xia, Y., Wang, G. X., and Feng, Y. L. (2015). A robust luminescent Ba (II) metal-organic framework based on pyridine carboxylate ligand for sensing of small molecules. *Inorg. Chem. Commun.* 53, 42–45. doi: 10.1016/j.inoche.2015.01.021

Chen, B., Yang, Y., Zapata, F., Lin, G., Qian, G., and Lobkovsky, E. B. (2007). Luminescent open metal sites within a metal-organic framework for sensing small molecules. *Adv. Mater.* 19, 1693–1696. doi: 10.1002/adma.2006 01838

Chen, B. L., Wang, L. B., Xiao, Y. Q., Fronczek, F. R., Xue, M., Cui, Y. J., et al. (2009). A luminescent metal-organic framework with lewis basic pyridyl sites for the sensing of metal ions. *Angew. Chem. Int. Ed.* 48, 508–511. doi: 10.1002/ange.200805101

Chen, W. M., Meng, X. L., Zhuang, G. L., Wang, Z., Kurmoo, M., Zhao, Q. Q., et al. (2017). A superior fluorescent sensor for $Al^{3+}$ and $UO_2^{2+}$ based on a Co(II) metal–organic framework with exposed pyrimidyl Lewis base sites. *J. Mater. Chem. A* 5, 13079–13085. doi: 10.1039/C7TA01546A

Chen, Z., Mi, X., Lu, J., Wang, S., Li, Y., Dou, J., et al. (2018a). From 2D → 3D interpenetration to packing: N coligand-driven structural assembly and tuning

of luminescent sensing activities towards $Fe^{3+}$ and $Cr_2 O_7^{2-}$ ions. *Dalton Trans.* 47, 6240–6249. doi: 10.1039/C8DT00909K

Chen, Z., Mi, X., Wang, S., Lu, J., Li, Y., Li, D., et al. (2018b). Two novel penetrating coordination polymers based on flexible S-containing dicarboxylate acid with sensing properties towards $Fe^{3+}$ and $Cr_2O_7^{2-}$ ions. *J. Solid State Chem.* 261, 75–85. doi: 10.1016/j.jssc.2018.02.008

Chen, Z., Sun, Y. W., Zhang, L. L., Sun, D., Liu, F. L., Meng, Q. G., et al. (2013). A tubular europium-organic framework exhibiting selective sensing of $Fe^{3+}$ and $Al^{3+}$ over mixed metal ions. *Chem. Commun.* 49, 11557–11559. doi: 10.1039/C3CC46613B

Cui, Y. J., Yue, Y. F., Qian, G. D., and Chen, B. L. (2012). Luminescent functional metal–organic frameworks. *Chem. Rev.* 112, 1126–1162. doi: 10.1021/cr200101d

Dang, S., Ma, E., Sun, Z. M., and Zhang, H. J. (2012). A layer-structured Eu-MOF as a highly selective fluorescent probe for $Fe^{3+}$ detection through a cation-exchange approach. *J. Mater. Chem.* 22, 16920–16926. doi: 10.1039/C2JM32661B

Das, P., and Mandal, S. K. (2018). Strategic design and functionalization of an amine-decorated luminescent metal organic framework for selective gas/vapor sorption and nanomolar sensing of 2,4,6-trinitrophenol in water. *ACS Appl. Mater. Interfaces* 10, 25360–25371. doi: 10.1021/acsami.8b06339

Gole, B., Bar, A. K., and Mukherjee, S. (2011). Fluorescent metal–organic framework for selective sensing of nitroaromatic explosives. *Chem. Commun.* 47, 1137–12139. doi: 10.1039/c1cc15594f

Guo, L. Y., Su, H. F., Kurmoo, M., Wang, X. P., Zhao, Q. Q., Lin, S. C., et al. (2017). Multifunctional triple-decker inverse 12-metallacrown-4 sandwiching halides. *ACS Appl. Mater. Interfaces* 9, 19980–19987. doi: 10.1021/acsami.7b05191

Heine, J., and Buschbaum, K. M. (2013). Engineering metal-based luminescence in coordination polymers and metal–organic frameworks. *Chem. Soc. Rev.* 42, 9232–9242. doi: 10.1039/c3cs60232j

Hou, Y. F., Liu, B., Yue, K. F., Zhou, C. S., Wang, Y. M., Yan, N., et al. (2014a). Five solvent-induced cadmium coordination polymers (CPs) based on the same mixed ligands. *CrystEngComm* 16, 9560–9567. doi: 10.1039/C4CE01359J

Hou, Y. F., Yan, N., Yue, K. F., Shi, J. T., He, T., and Li, X. Y. (2014b). Syntheses and characterization of Co(II) and Cu(II) coordination polymers (CPs) based on mixed flexible and rigid ligands. *Inorg. Chem.Commun.* 48, 44–47. doi: 10.1016/j.inoche.2014.08.011

Hu, X. L., Liu, F. H., Qin, C., Shao, K. Z., and Su, Z. M. (2015). A 2D bilayered metal–organic framework as a fluorescent sensor for highly selective sensing of nitro explosives. *Dalton. Trans.* 44, 7822–7827. doi: 10.1039/C5DT00515A

Hu, Y., Ding, M., Liu, X., Sun, L., and Jiang, H. (2016). Rational synthesis of an exceptionally stable Zn(II) metal-organic framework for the highly selective and sensitive detection of picric acid. *Chem. Commun.* 52, 5734–5737. doi: 10.1039/C6CC01597B

Hu, Z. C., Deibert, B. J., and Li, J. (2014). Luminescent metal–organic frameworks for chemical sensing and explosive detection. *Chem. Soc. Rev.* 43, 5815–5840. doi: 10.1039/C4CS00010B

Hua, J. A., Zhao, Y., Kang, Y. S., Lu, Y., and Sun, W. Y. (2015). Solvent-dependent zinc(II) coordination polymers with mixed ligands: selective sorption and fluorescence sensing. *Dalton Trans.* 44, 11524–11532. doi: 10.1039/C5DT01386K

Jayaramulu, K., Narayanan, R. P., George, S. J., and Maji, T. K. (2012). Luminescent microporous metal-organic framework with functional lewis basic sites on the pore surface: specific sensing and removal of metal ions. *Inorg. Chem.* 51, 10089–10091. doi: 10.1021/ic3017547

Jin, J. C., Wu, X. R., Luo, Z. D., Deng, F. Y., Liu, J. Q., Singh, A., et al. (2017). Luminescent sensing and photocatalytic degradation properties of an uncommon (4,5,5)-connected 3D MOF based on 3,5-di(3′,5′-dicarboxylphenyl)benzoic acid. *CrystEngComm* 19, 4368–4377. doi: 10.1039/C7CE01012E

Kent, C. A., Mehl, B. P., Ma, L., Papanikolas, J. M., Meyer, T. J., and Lin, W. (2010). Energy transfer dynamics in metal-organic frameworks. *J. Am. Chem. Soc.* 132, 12767–12769. doi: 10.1021/ja102804s

Kim, T. K., Lee, J. H., Moon, D., and Moon, H. R. (2013). Luminescent Li-based metal–organic framework tailored for the selective detection of explosive nitroaromatic compounds: direct observation of interaction sites. *Inorg. Chem.* 52, 589–595. doi: 10.1021/ic3011458

Kreno, L. E., Leong, K., Farha, O. K., Allendorf, M., Van Duyne, R. P., and Hupp, J. T. (2012). Metal-organic framework materials as chemical sensors. *Chem. Rev.* 112, 1105–1125. doi: 10.1021/cr200324t

Lan, A., Li, K., Wu, H., Olson, D. H., Emge, T. J., Ki Hong, W., et al. (2009). A Luminescent Microporous Metal-Organic Framework for the Fast and Reversible Detection of High Explosives. *Angew. Chem. Int. Ed.* 48, 2370–2374. doi: 10.1002/ange.200804853

Li, B. H., Wu, J., Liu, J. Q., Gu, C. Y., Xu, J. W., Luo, M. M., et al. (2016). A luminescent zinc(II) metal-organic framework for selective detection of nitroaromatics, $Fe^{3+}$ and $CrO_4^{2-}$: a versatile threefold fluorescent sensor. *ChemPlusChem* 81, 885–892. doi: 10.1002/cplu.201600304

Li, J., Yang, G. P., Hou, L., Cui, L., Li, Y. P., Wang, Y. Y., et al. (2013). Three new solvent-directed 3D lead(II)-MOFs displaying the unique properties of luminescence and selective $CO_2$ sorption. *Dalton Trans.* 42, 13590–13598. doi: 10.1039/c3dt51203g

Li, X. Y., Liu, M., Yue, K. F., Wu, Y. P., He, T., Yan, N., et al. (2015). A series of reaction-controlled coordination polymers constructed from bis(imidazole) and tetrafluoroterephthalic acid ligands: syntheses, structural diversities, properties. *CrystEngComm* 17, 8273–8281. doi: 10.1039/C5CE01423A

Li, Y., Song, H., Chen, Q., Liu, K., Zhao, F. Y., Ruan, W. J., et al. (2014). Two coordination polymers with enhanced ligand-centered luminescence and assembly imparted sensing ability for acetone. *J. Mater. Chem. A* 2, 9469–9473. doi: 10.1039/c4ta00944d

Lin, R. B., Liu, S. Y., Ye, J. W., Li, X. Y., and Zhang, J. P. (2016). Photoluminescent metal-organic frameworks for gas sensing. *Adv. Sci.* 3:1500434. doi: 10.1002/advs.201500434

Liu, B., Wu, W. P., Hou, L., and Wang, Y. Y. (2014). Four uncommon nanocage-based Ln-MOFs: highly selective luminescent sensing for $Cu^{2+}$ ions and selective $CO_2$ capture. *Chem. Commun.* 50, 8731–8734. doi: 10.1039/c4cc03049d

Liu, J. Q., Li, G. P., Liu, W. C., Li, Q. L., Li, B. H., Gable, R. W., et al. (2016b). Two unusual nanocage-based Ln-MOFs with triazole sites: highly fluorescent sensing for $Fe^{3+}$ and $Cr_2O_7^{2-}$, and selective $CO_2$ capture. *ChemPlusChem* 81, 1299–1304. doi: 10.1002/cplu.201600289

Liu, J. Q., Liu, G. L., Gu, C. Y., Liu, W. C., Xu, J. W., Li, B. H., et al. (2016a). Rational synthesis of a novel 3,3,5-c polyhedral metal-organic framework with high thermal stability and hydrogen storage capability. *J. Mater. Chem. A* 4, 11630–11634. doi: 10.1039/C6TA03675A

Liu, J. Q., Wang, W. J., Luo, Z. D., Li, B. H., and Yuan, D. Q. (2017). Microporous metal-organic framework based on ligand-truncation strategy with high performance for gas adsorption and separation. *Inorg. Chem.* 56, 10215–10219. doi: 10.1021/acs.inorgchem.7b00851

Liu, J. Q., Wu, J., Li, F. M., Liu, W. C., Li, B. H., Wang, J., et al. (2016c). Luminescent sensing from a new Zn(II) metal–organic framework. *RSC. Adv.* 6, 31161–31166. doi: 10.1039/C6RA01709F

Lu, L., Wu, J., Wang, J., Liu, J. Q., Li, B. H., Singh, A., et al. (2017). An uncommon 3D 3,3,4,8-c Cd(II) metal-organic framework for highly efficient luminescent sensing and organic dye adsorption: experimental and theoretical insight. *CrystEngComm* 19, 7057–7067. doi: 10.1039/C7CE01638G

Ma, D. X., Li, B. Y., Zhou, X. J., Zhou, Q., Liu, K., Zeng, G., et al. (2013). A dual functional MOF as a luminescent sensor for quantitatively detecting the concentration of nitrobenzene and temperature. *Chem. Commun.* 49, 8964–8966. doi: 10.1039/c3cc44546a

Ma, R., Chen, Z., Wang, S., Yao, Q., Li, Y., Lu, J., et al. (2017). Solvent-induced assembly of two helical Eu(III) metal-organic frameworks and fluorescence sensing activities towards nitrobenzene and $Cu^{2+}$ ions. *J. Solid State Chem.* 252, 142–151. doi: 10.1016/j.jssc.2017.05.018

Marin, V., Holder, E., Hoogenboom, R., Tekin, E., and Schubert, U. S. (2006). Light-emitting iridium(III) and ruthenium(II) polypyridyl complexes containing quadruple hydrogen-bonding moieties. *Dalton Trans.* 13, 1636–1644. doi: 10.1039/b513957k

Park, I. H., Mulijanto, C. E., Lee, H. H., Kang, Y., Lee, E., Chanthapally, A., et al. (2016). Influence of interpenetration in diamondoid metal-organic frameworks on the photoreactivity and sensing properties. *Cryst. Growth Des.* 16, 2504–2508. doi: 10.1021/acs.cgd.6b00354

Park, S., and Lee, S. Y. (2015). Significant enhancement of curcumin photoluminescence by a photosensitizing organogel: an optical sensor for pyrrole detection. *Sens. Actuators B* 220, 318–325. doi: 10.1016/j.snb.2015.05.078

Pramanik, S., Zheng, C., Zhang, X., Emge, T. J., and Li, J. (2011). New microporous metal-organic framework demonstrating unique selectivity for detection of high explosives and aromatic compounds. *J. Am. Chem. Soc.* 133, 4153–4155. doi: 10.1021/ja106851d

Qin, J. S., Bao, S. J., Li, P., Xie, W., Du, D. Y., Zhao, L., et al. (2014). A stable porous anionic metal-organic framework for luminescence sensing of Ln3+ ions and detection of nitrobenzene. *Chem. Asian J.* 9, 749–753. doi: 10.1002/asia.201301531

Rocha, J., Carlos, L. D., Paz, F. A. A., and Ananias, D. (2011). Luminescent multifunctional lanthanides-based metal-organic frameworks. *Chem. Soc. Rev.* 40, 926–940. doi: 10.1039/C0CS00130A

Saini, R. K., and Das, K. J. (2012). Picosecond spectral relaxation of curcumin excited state in a binary solvent mixture of toluene and methanol. *Phys. Chem. B* 116, 10357–10363. doi: 10.1021/jp305447y

Sanchez, J. C., and Trogler, W. C. (2008). Efficient blue-emitting silafluorene-fluorine-conjugated copolymers: selective turn-off/turn-on detection of explosives. *J. Mater. Chem.* 18, 3143–3156. doi: 10.1039/B802623H

Sanchez, J. C., Urbas, S. A., Toal, S. J., DiPasquale, A. G., Rheingold, A. L., and Trogler, W. C. (2008). Catalytic hydrosilylation routes to divinylbenzene bridged silole and silafluorene polymers. Applications to surface imaging of explosive particulates. *Macromolecules* 41, 1237–1245. doi: 10.1021/ma702274c

Santra, D. C., Bera, M. K., Sukul, P. K., and Malik, S. (2016). Charge-transfer-induced fluorescence quenching of anthracene derivatives and selective detection of picric acid. *Chem. Eur. J.* 22, 2012–2019. doi: 10.1002/chem.201504126

Shen, J., Wang, Z., Sun, D., Xia, C., Yuan, S., Sun, P., et al. (2018). pH-responsive nanovesicles with enhanced emission co-assembled by Ag(I) nanoclusters and polyethyleneimine as a superior sensor for $Al^{3+}$. *ACS Appl. Mater. Interfaces* 10, 3955–3963. doi: 10.1021/acsami.7b16316

Shi, B. B., Zhong, Y. H., Guo, L. L., and Li, G. (2015). Two dimethylphenyl imidazole dicarboxylate-based lanthanide metal-organic frameworks for luminescence sensing of benzaldehyde. *Dalton Trans.* 44, 4362–4369. doi: 10.1039/C4DT03326D

Shi, J. T., Yue, K. F., Liu, B., Zhou, C. S., Liu, Y. L., Fang, Z. G., et al. (2014). Two porous metal-organic frameworks (MOFs) based on mixed ligands: synthesis, structure and selective gas adsorption. *CrystEngComm* 16, 3097–3102. doi: 10.1039/c3ce41557k

Singh, D., and Nagaraja, C. M. (2014). A luminescent 3D interpenetrating metal–organic framework for highly selective sensing of nitrobenzene. *Dalton Trans.* 43, 17912–17915. doi: 10.1039/C4DT02841D

Son, H. J., Jin, S., Patwardhan, S., Wezenberg, S. J., Jeong, N. C., So, M., et al. Hupp, J. T. (2013). Light-harvesting and ultrafast energy migration in porphyrin-based metal–organic frameworks. *J. Am. Chem. Soc.* 135, 862–869. doi: 10.1021/ja310596a

Song, X. Z., Song, S. Y., Zhao, S. N., Hao, Z. M., Zhu, M., Meng, X., et al. (2014). Single-crystal-to-single-crystal transformation of a europium(III) metal-organic framework producing a multi-responsive luminescent sensor. *Adv. Funct. Mater.* 24, 4034–4041. doi: 10.1002/adfm.201303986

Spek, A. L. (2003). Single-crystal structure validation with the program PLATON. *J. Appl. Crystallogr.* 36, 7–13. doi: 10.1107/S0021889802022112

Tang, Q., Liu, S. X., Liu, Y. W., Miao, J., Li, S. J., Zhang, L., et al. (2013). Cation sensing by a luminescent metal-organic framework with multiple lewis basic sites. *Inorg. Chem.* 52, 2799–2801. doi: 10.1021/ic400029p

Tian, D., Li, Y., Chen, R. Y., Chang, Z., Wang, G. Y., and Bu, X. H. (2014). A luminescent metal-organic framework demonstrating ideal detection ability for nitroaromatic explosives. *J. Mater. Chem. A* 2, 1465–1470. doi: 10.1039/C3TA13983B

Toal, S. J., and Trogler, W. C. (2006). Polymer sensors for nitroaromatic explosives detection. *J. Mater. Chem.* 116, 2871–2883. doi: 10.1039/b517953j

Wang, G. Y., Yang, L. L., Li, Y., Song, H., Ruan, W. J., Chang, Z., et al. (2013). A luminescent 2D coordination polymer for selective sensing of nitrobenzene. *Dalton Trans.* 42, 12865–12868. doi: 10.1039/c3dt51450a

Wang, J., Wu, X. R., Liu, J. Q., Li, B. H., Singh, A., Kumar, A., et al. (2017). An uncommon (5,5)-connected 3D metal organic material for selective and sensitive sensing of nitroaromatics and ferric ion: experimental studies and theoretical analysis. *CrystEngComm* 19, 3519–3525. doi: 10.1039/C7CE00912G

Wang, X. L., Luan, J., Lin, H. Y., Lu, Q. L., Le, M., Liu, G. C., et al. (2015). Metal(II)-Organic coordination polymers modulated by two isomeric semirigid Bis-Pyridyl-Bis-Amide ligands: structures, fluorescent sensing behavior, and selective photocatalysis. *ChemPlusChem* 79, 1691–1702. doi: 10.1002/cplu.201402193

Wang, X. P., Han, L. L., Wang, Z., Guo, L. Y., and Sun, D. (2016). Microporous Cd(II) metal-organic framework as fluorescent sensor for nitroaromatic explosives at the sub-ppm level. *J. Mol. Struct.* 1107, 1–6. doi: 10.1016/j.molstruc.2015.11.018

Wang, X. S., Li, L., Yuan, D., Huang, Q. Y. B., and Cao, R. (2018). Fast, highly selective and sensitive anionic metal-organic framework with nitrogen-rich sites fluorescent chemosensor for nitro explosives detection. *J. Hazard Mater.* 344, 283–290. doi: 10.1016/j.jhazmat.2017.10.027

Wen, L. L., Xu, X. Y., Lv, K. L., Huang, Y. M., Zheng, X. F., Zhou, L., et al. (2015). Metal-organic frameworks constructed from d-camphor acid: bifunctional properties related to luminescence sensing and liquid-phase separation. *ACS Appl. Mater. Interfaces* 7, 4449–4455. doi: 10.1021/acsami.5b00160

Wu, Y. L., Yang, G. P., Zhou, X., Li, J., Ning, Y., and Wang, Y. Y. (2015). Three new luminescent Cd(II)-MOFs by regulating the tetracarboxylate and auxiliary co-ligands, displaying high sensitivity for $Fe^{3+}$ in aqueous solution. *Dalton Trans.* 44, 10385–10391. doi: 10.1039/C5DT00492F

Wu, Y. P., Xu, G. W., Dong, W. W., Zhao, J., Li, D. S., Zhang, J., et al. (2017). Anionic lanthanide MOFs as a platform for iron-selective sensing, systematic color tuning, and efficient nanoparticle catalysis. *Inorg. Chem.* 56, 1402–1411. doi: 10.1021/acs.inorgchem.6b02476

Xiang, S., Zhou, W., Zhang, Z., Green, M. A., Liu, Y., and Chen, B. (2010). Open metal sites within isostructural metal–organic frameworks for differential recognition of acetylene and extraordinarily high acetylene storage capacity at room temperature. *Angew. Chem. Int. Ed.* 49, 4719–4722. doi: 10.1002/ange.201000094

Xu, H., Hu, H. C., Cao, C. S., and Zhao, B. (2015). Lanthanide organic framework as a regenerable luminescent probe for $Fe^{3+}$. *Inorg. Chem.* 54, 4585–4587. doi: 10.1021/acs.inorgchem.5b00113

Xu, H., Liu, F., Cui, Y., Chen, B., and Qian, G. (2011). A luminescent nanoscale metal-organic framework for sensing of nitroaromatic explosives. *Chem. Commun.* 47, 3153–3155. doi: 10.1039/c0cc05166g

Xu, X. Y., and Yan, B. (2015). Eu(III)-functionalized MIL-124 as fluorescent probe for highly selectively sensing ions and organic small molecules especially for Fe(III) and Fe(II). *ACS Appl. Mater. Interfaces* 7, 721–729. doi: 10.1021/am5070409

Yang, C. X., Ren, H. B., and Yan, X. P. (2013). Fluorescent metal-organic framework MIL-53(Al) for highly selective and sensitive detection of $Fe^{3+}$ in aqueous solution. *Anal. Chem.* 85, 7441–7446. doi: 10.1021/ac401387z

Yang, Y. J., Wang, M. J., and Zhang, K. L. (2016). A novel photoluminescent Cd(II)–organic framework exhibiting rapid and efficient multi-responsive fluorescence sensing for trace amounts of $Fe^{3+}$ ions and some NACs, especially for 4-nitroaniline and 2-methyl-4 –nitroaniline. *J. Mater. Chem. C* 4, 11404–11418. doi: 10.1039/C6TC04195G

Yi, F. Y., Yang, W. T., and Sun, Z. M. (2012). Highly selective acetone fluorescent sensors based on microporous Cd(II) metal–organic frameworks. *J. Mater. Chem.* 22, 23201–23209. doi: 10.1039/C2JM35273G

Zhan, C., Ou, S., Zou, C., Zhao, M., and Wu, C. D. (2014). A luminescent mixed-lanthanide-organic framework sensor for decoding different volatile organic molecules. *Anal. Chem.* 86, 6648–6653. doi: 10.1021/ac5013442

Zhang, C., Che, Y., Zhang, Z., Yang, X., and Zang, L. (2011). Fluorescent nanoscale zinc(II)-carboxylate coordination polymers for explosive sensing. *Chem. Commun.* 47, 2336–2338. doi: 10.1039/C0CC04836D

Zhang, C., Sun, L., Yan, Y., Li, J., Song, X., Liu, Y., et al. (2015). A luminescent cadmium metal-organic framework for sensing of nitroaromatic explosives. *Dalton Trans.* 44, 230–236. doi: 10.1039/C4DT02227K

Zhang, L. L., Kang, Z. X., Xin, X. L., and Sun, D. F. (2016). Metal-organic frameworks based luminescent materials for nitroaromatics sensing. *CrystEngComm* 18, 193–206. doi: 10.1039/C5CE01917F

Zhang, Z., Xiang, S., Rao, X., Zheng, Q., Fronczek, F. R., Qian, G., et al. (2010). A rod packing microporous metal-organic framework with open metal sites for selective guest sorption and sensing of nitrobenzene. *Chem. Commun.* 46, 7205–7207. doi: 10.1039/c0cc01236j

Zhao, S., Ding, J. G., Zheng, T. R., Li, K., Li, B. L., and Wu, B. (2017). The 3D and 2D cadmium coordination polymers as luminescent sensors for detection of nitroaromatics. *J. Lumin.* 188, 356–364. doi: 10.1016/j.jlumin.2017.04.044

Zhao, S., Lv, X. X., Shi, L. L., Li, B. L., and Wu, B. (2016). An unusual (4,4)-connected 3D porous cadmium metal-organic framework as a luminescent sensor for detection of nitrobenzene. *RSC. Adv.* 6, 56035–56041. doi: 10.1039/C6RA10664A

Zheng, M., Tan, H. Q., Xie, Z. G., Zhang, L. G., Jing, X. B., and Sun, Z. C. (2013). Fast response and high sensitivity europium metal organic framework fluorescent probe with chelating terpyridine sites for $Fe^{3+}$. *ACS Appl. Mater. Interfaces* 5, 1078–1083. doi: 10.1021/am302862k

Zheng, Q., Yang, F., Deng, M., Ling, Y., Liu, X., Chen, Z., et al. (2013). A porous metal–organic framework constructed from carboxylate–pyrazolate shared heptanuclear zinc clusters: synthesis, gas adsorption, and guest-dependent luminescent properties. *Inorg. Chem.* 52, 10368–10374. doi: 10.1021/ic401092j

Zheng, X. F., Zhou, L., Huang, Y. M., Wang, C. G., Duan, J. G., Wen, L. L., et al. (2014). A series of metal-organic frameworks based on 5-(4-pyridyl)-isophthalic acid: selective sorption and fluorescence sensing. *J. Mater. Chem. A* 2, 12413–12422. doi: 10.1039/C4TA01900H

Zhou, Y., Chen, H. H., and Yan, B. (2014). An $Eu^{3+}$ post-functionalized nanosized metal-organic framework for cation exchange-based $Fe^{3+}$-sensing in an aqueous environment. *J. Mater. Chem. A* 2, 13691–13697. doi: 10.1039/C4TA01297F

Check for updates

# Synthesis, Thermal, Structural Analyses, and Photoluminescent Properties of a New Family of Malonate-Containing Lanthanide(III) Coordination Polymers

Sajjad Hussain [1,2]*, Xuenian Chen [1,3]*, William T. A. Harrison [4], Saeed Ahmad [5], Mark R. J. Elsegood [6], Islam Ullah Khan [7] and Shabbir Muhammad [8]

[1] Henan Key Laboratory of Boron Chemistry and Advanced Energy Materials, School of Chemistry and Chemical Engineering, Henan Normal University, Xinxiang, China, [2] Department of Chemistry, Mohi Ud Din Islamic University Nerian Sharif, Azad Jammu and Kashmir, Pakistan, [3] College of Chemistry and Molecular Engineering, Zhengzhou University, Zhengzhou, China, [4] Department of Chemistry, University of Aberdeen, Aberdeen, Scotland, [5] Department of Chemistry, College of Sciences and Humanities, Prince Sattam Bin Abdulaziz University, Al-Kharj, Saudi Arabia, [6] Chemistry Department, Loughborough University, Loughborough, United Kingdom, [7] Department of Chemistry, Government College University, Lahore, Pakistan, [8] Department of Physics, College of Science, King Khalid University, Abha, Saudi Arabia

Five new Lanthanide(III) complexes of malonic acid ($HOOC-CH_2-COOH$); {[Gd($C_3H_2O_4$)($H_2O$)$_4$]·$NO_3$}$_n$ (**1**), {[Tb($C_3H_2O_4$)($H_2O$)$_4$]·$NO_3$}$_n$ (**2**), {[Ho($C_3H_2O_4$)($H_2O$)$_4$]·$NO_3$}$_n$ (**3**), [Er($C_3H_2O_4$)($C_3H_3O_4$)($H_2O$)$_2$]$_n$ (**4**), and {[Eu$_2$($C_3H_2O_4$)$_2$($C_3H_3O_4$)$_2$($H_2O$)$_6$]·$4H_2O$}$_n$ (**5**) were synthesized and characterized by elemental, infrared spectral, and thermal analyses. The structures of compounds **1**–**5** were determined by single crystal X-ray diffraction technique. The X-ray analysis reveals that compounds **1**, **2**, and **3** are isostructural and crystallized in the orthorhombic space group $Pmn2_1$. The lanthanide(III) ions are coordinated by four carboxylate and four water oxygen atoms adopting a distorted square antiprism geometry. The LnO$_8$ square antiprisms are linked into infinite layers by malonate ($C_3H_2O_4^{2-}$) dianions sandwiching sheets of nitrate counter ions. Compound **4** contains ErO$_8$ square antiprisms linked into a two-dimensional network by hydrogen malonate ($C_3H_3O_4^-$) anions and malonate dianions. The europium complex, **5** is dinuclear having the two europium(III) ions (Eu1 and Eu2) bridged by carboxylate groups of hydrogen malonate ligands. The europium ions in **5** are nine-coordinate and exhibit a distorted monocapped square antiprism geometry. All the structures are consolidated by O–H···O hydrogen bonds. The photoluminescence spectra of **1**–**5** exhibit characteristic emissions in the visible region. The IR spectra and thermal data are consistent with the structural results. The room-temperature effective magnetic moments for **1**–**4** are in good agreement with those expected for the free ions, while the data for **5** indicates that low-lying excited states contribute to the observed moment. The compound **1** was further subjected to quantum computational calculations to explore its optoelectronic properties including; density of states (DOS), dielectric function, refractive index, extinction coefficient, and absorption spectrum, to highlight the possible applications of such materials in the optoelectronics.

**Keywords: lanthanides, malonate, photoluminescence, crystal structure, optoelectronic properties**

**Graphical Abstract |**
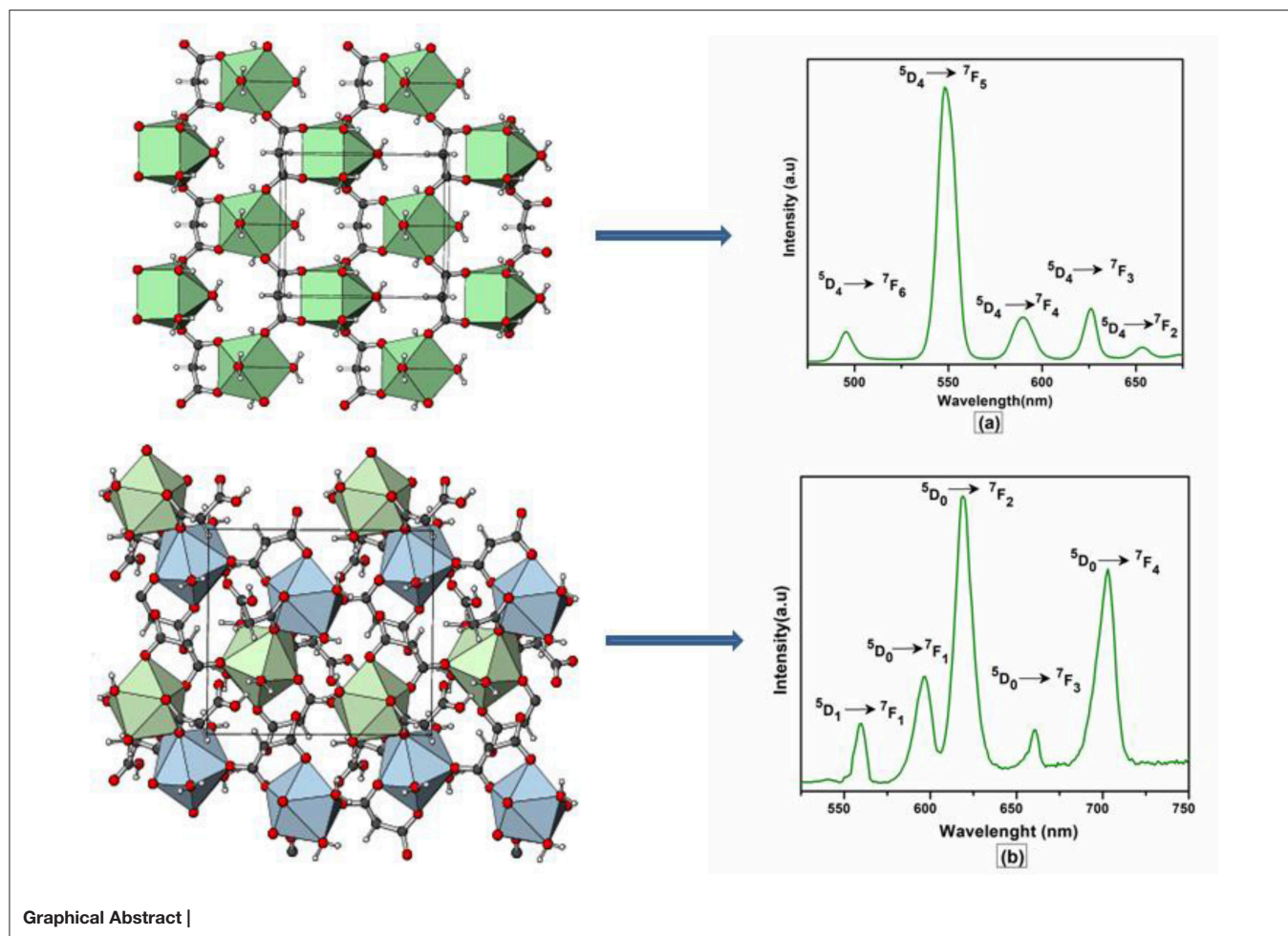
# INTRODUCTION

In the modern hi-tech society, lanthanide-based metal-organic frameworks find a wide range of applications in several cutting-edge scientific fields, such as contrast agents (Caravan et al., 1999; Wahsner et al., 2019), catalysis (Shibasaki and Yoshikawa, 2002; He et al., 2013; Pagis et al., 2016), gas storage and purification (Reineke et al., 1999; He et al., 2013; Roy et al., 2014), magnetism (Woodruff et al., 2013; Zhu et al., 2016; Gao et al., 2018), and optoelectronic devices (Kenyon, 2002; Armelao et al., 2010; Heffern et al., 2013). The study of photo physical properties of lanthanides (Ln) triggered the potential use of these compounds not only in color televisions and fluorescent tubes but also in optical amplifiers, luminescent solar concentrators, active waveguides, organic light emitting diodes, and immunoassays (Bünzli, 2010; Katkova and Bochkarev, 2010; Heffern et al., 2013; Reisfeld, 2015). The optoelectronic properties of lanthanide complexes originate from the inner *f-f* electron transitions. The shielding of 4*f* orbitals confers the excellent luminescence properties of $Ln^{3+}$ ions (Reisfeld and Jorgensen, 2012; Heffern et al., 2013; Reisfeld, 2015). Several reports have appeared in the literature on the physical and optical properties of lanthanide complexes, which demonstrate their significant

technological interest (Kenyon, 2002; Faulkner et al., 2005; Terai et al., 2006; Daiguebonne et al., 2008; Dos Santos et al., 2008; Armelao et al., 2010; Zhuravlev et al., 2011; Räsänen et al., 2014; Buenzli, 2015; Sharma and Narula, 2015; Sun et al., 2015; George et al., 2016).

Lanthanide(III) ions are hard Lewis acids and prefer to combine with hard Lewis bases such as oxygen donors (Bünzli, 2014). On the basis of this fact, carboxylate ligands have been widely applied for the preparation of lanthanide coordination polymers (Hansson, 1973a,b; Wenmei et al., 1992; Marrot and Trombe, 1994; Benmerad et al., 2000; Hernández-Molina et al., 2000, 2002, 2003; Doreswamy et al., 2003, 2005; Thirumurugan and Natarajan, 2004; Cui et al., 2005; Yan et al., 2005; Cañadillas-Delgado et al., 2006; Deacon et al., 2006; Rahahlia et al., 2007; Zhang et al., 2007; Fang et al., 2008; Wang et al., 2009; Chrysomallidou et al., 2010; Silva et al., 2010; Jin et al., 2012; Seidel et al., 2012; Sharif et al., 2012; Calahorro et al., 2013; Tian et al., 2013; Bünzli, 2014; Delgado et al., 2016; Li et al., 2017). The flexible aliphatic dicarboxylates (e.g., malonate and succinate) are more fascinating than the rigid mono or aromatic carboxylates due to many possible conformations (Cui et al., 2005; Rahahlia et al., 2007; Wang et al., 2009; Delgado et al., 2016). The use of multidentate organic linkers together with the high coordination

number of lanthanide ions help to construct diverse structural motifs with unexpected properties. The structural arrangements in the lanthanide dicarboxylate polymers range from one- (Yan et al., 2005; Chrysomallidou et al., 2010; Silva et al., 2010; Li et al., 2017), two- (Hernández-Molina et al., 2000; Cañadillas-Delgado et al., 2006; Li et al., 2017), to three-dimensional (Hansson, 1973a,b; Wenmei et al., 1992; Marrot and Trombe, 1994; Benmerad et al., 2000; Hernández-Molina et al., 2002, 2003; Doreswamy et al., 2003, 2005; Thirumurugan and Natarajan, 2004; Cañadillas-Delgado et al., 2006; Zhang et al., 2007; Fang et al., 2008; Chrysomallidou et al., 2010; Jin et al., 2012; Seidel et al., 2012; Calahorro et al., 2013) coordination networks. Malonic acid, $C_3H_4O_4$, is a simple dicarboxylic acid that exhibits a rather flexible stereochemistry and a variety of coordination modes toward metal ions. It can coordinate as a monodentate, bridging, and chelating ligand in monoanionic (hydrogen malonate, $C_3H_3O_4^-$) or dianionic (malonate, $C_3H_2O_4^{2-}$) form (Rodríguez-Martín et al., 2002; Delgado et al., 2016). A number of reports have been published on the synthesis and structures of malonate-containing lanthanide polymers, which describe the versatility of the bonding modes of the malonate group (Hansson, 1973a,b; Wenmei et al., 1992; Marrot and Trombe, 1994; Benmerad et al., 2000; Hernández-Molina et al., 2000, 2002, 2003; Doreswamy et al., 2005; Cañadillas-Delgado et al., 2006; Zhang et al., 2007; Fang et al., 2008; Chrysomallidou et al., 2010; Silva et al., 2010; Jin et al., 2012; Delgado et al., 2016). Delgado et al. reported a detailed overview on the crystal structures and topologies of these systems, as well as the molecular structures assembled by hydrogen-bonding from low-dimensional entities to higher-dimensional supramolecular architectures. The study describes that most of the $Ln^{3+}$-malonate ($mal^{2-}$) complexes exist as dinuclear species (Delgado et al., 2016), while the reports about the mononuclear complexes are rare (Wenmei et al., 1992; Marrot and Trombe, 1994; Chrysomallidou et al., 2010; Silva et al., 2010).

In order to enhance the fundamental knowledge of structural chemistry of lanthanide-carboxylate frameworks and in view of our continuous interest in this direction (Hussain et al., 2014, 2015a,b, 2018), we report here the syntheses, characterization, crystal structures, photoluminescence, and magnetic properties of five novel lanthanide coordination polymers involving malonate ligand. They include; $\{[M(C_3H_2O_4)(H_2O)_4] \cdot NO_3\}_n$ (M = Gd, Tb, Ho) (1-3), $[Er(C_3H_2O_4)(C_3H_3O_4)(H_2O)_2]_n$ (4), and $\{[Eu_2(C_3H_2O_4)_2(C_3H_3O_4)_2(H_2O)_6] \cdot 4H_2O\}_n$ (5). The optoelectronic properties including density of states, dielectric function, refractive index, extinction coefficient, and absorption spectrum, were also investigated for complex 1 with the help of DFT calculations. Owing to the bigger size of lanthanide complexes, they are very difficult to deal quantum chemically. Nonetheless, there are some previous computational studies including the structures and reactions (Eisenstein and Maron, 2002), bonding characteristics (Adamo and Maldivi, 1997), determination of ligand-field parameters (Ishikawa et al., 2003), effective core potential studies (Cundari et al., 1995), and details of computational methods applied in lanthanide and actinide chemistry etc (Dolg, 2015). To the best of our knowledge, this is the first report that describes the formation of lanthanide complexes including a nitrate ion and dinuclear $Eu^{3+}$ or $Er^{3+}$ complexes containing a hydrogen malonate anion, and their photoluminescent properties.

## EXPERIMENTAL

## Reagents and Measurements

The nitrate salts of Gd, Tb, and Ho$\{M(NO_3)_3 \cdot 6H_2O\}$, $ErCl_3 \cdot 6H_2O$, and $EuCl_3 \cdot 6H_2O$ were purchased from Alfa Aesar, a Johnson Matthey Company, USA. Malonic acid was obtained from Merck Chemical Co. Germany.

## Synthesis of Complexes

### Synthesis of $\{[M(C_3H_2O_4)(H_2O)_4] \cdot NO_3\}_n$(M = Gd, Tb, Ho) (1–3)

The compounds 1–3 were synthesized by reacting 0.225 g (0.5 mmol) of $M(NO_3)_3 \cdot 6H_2O$ (M = Gd, Tb, Ho) dissolved in 5 mL de-ionized water and 0.156 g (1.5 mmol) of malonic acid in 20 mL ethanol. The solutions were stirred for 2 h at room temperature. The pH of the reaction mixture was adjusted between 5 and 6 with 0.1 M NaOH solution. The solutions were filtered and kept at ambient temperature (or in the refrigerator) for crystallization. The crystals appeared in the solution after 2–3 weeks. The complexes 1, 2, and 3 were obtained as light yellow, colorless, and light pink crystals, respectively. They were separated by vacuum filtration and rinsed with ethanol. Yield: ~50%.

### Synthesis of $[Er(C_3H_2O_4)(C_3H_3O_4)(H_2O)_2]_n$ (4)

Malonic acid (0.104 g, 1 mmol) and $ErCl_3 \cdot 6H_2O$ (0.137 g, 0.5 mmol) were separately dissolved in 20 mL ethanol and 10 mL deionized water, respectively. The solutions were mixed and stirred for 2 h in a round-bottom flask at room temperature. During stirring, 0.1 M NaOH solution was used to maintain the pH of the mixture between 5 and 6. After 10 days, pink crystals of 4 appeared in solution, which were isolated by filtration and rinsed with methanol. Yield: 49%.

### Synthesis of $\{[Eu_2(C_3H_2O_4)_2(C_3H_3O_4)_2(H_2O)_6] \cdot 4H_2O\}_n$ (5)

To a solution of 0.183 g (0.5 mmol) of $EuCl_3 \cdot 6H_2O$ in 10 mL deionized water was added 0.104 g (1 mmol) of malonic acid dissolved in 25 mL ethanol. The solutions were mixed in round bottom flask and stirred for 3 h at room temperature at a pH of 5–6 maintained by using 0.1 M NaOH solution. After 2 weeks, colorless crystals of 5 were recovered by filtration and rinsed with methanol. Yield: 43%.

### Analytical and spectroscopic data

$C_3H_{10}NO_{11}Gd$ (1): Calc. (%) C 9.16, H 2.55, N 3.56; Found (%): C 9.25, H 2.59, N 3.50.IR ($cm^{-1}$): $\nu$ = 3583, 3369 (O-H), 2927 (C-H), 1582 $(COO)_{as}$, 1384,1370 $(COO)_s$, 276 (Gd-O); $\delta$ = 1463, 1149 (C-H),953 (COO), 819 $(NO_3)$; $\rho$ = 836 $(H_2O)$, 735 $(CH_2)$.

$C_3H_{10}NO_{11}Tb$ (2): Calc. (%) C 9.13; H 2.55; N 3.55; Found (%): C 9.25, H 2.62, N 3.45. IR ($cm^{-1}$): $\nu$ = 3585, 3369 (O-H), 2926 (C-H), 1583 $(COO)_{as}$, 1384,1370 $(COO)_s$, 285 (Tb-O); $\delta$ = 1463, 1149 (C-H), 954 (COO), 819 $(NO_3)$; $\rho$ = 837 $(H_2O)$, 735 $(CH_2)$.

**TABLE 1 |** Crystal data for compounds **1–5**.

| | 1 | 2 | 3 | 4 | 5 |
|---|---|---|---|---|---|
| Empirical formula | $C_3H_{10}NO_{11}Gd$ | $C_3H_{10}NO_{11}Tb$ | $C_3H_{10}NO_{11}Ho$ | $C_6H_9O_{10}Er$ | $C_6H_{15}O_{13}Eu$ |
| $M_r$ | 393.37 | 395.04 | 401.05 | 408.39 | 447.14 |
| $T$ (K) | 150(2) | 150(2) | 150(2) | 150(2) | 150(2) |
| $\lambda$ (Å) | 0.71073 | 0.71073 | 0.71073 | 0.71073 | 0.71073 |
| Crystal system | Orthorhombic | Orthorhombic | Orthorhombic | Orthorhombic | Monoclinic |
| Space group | $Pmn2_1$ (No. 31) | $Pmn2_1$ (No. 31) | $Pmn2_1$ (No. 31) | $Fdd2$ (No. 43) | $P2_1/n$ (No. 14) |
| $a$ (Å) | 8.0955 (8) | 8.0863 (6) | 8.0652 (12) | 15.2618 (16) | 10.7945 (5) |
| $b$ (Å) | 6.7470 (6) | 6.7359 (5) | 6.7123 (9) | 10.0290 (10) | 12.3934 (6) |
| $c$ (Å) | 9.3030 (9) | 9.2562 (7) | 9.1895 (11) | 13.9992 (15) | 20.2839 (10) |
| $\beta$ (°) | 90 | 90 | 90 | 90 | 100.3900 (7) |
| $V$ (Å$^3$) | 508.13 (8) | 504.17 (7) | 497.48 (12) | 2142.7 (4) | 2669.1 (2) |
| $Z$ | 2 | 2 | 2 | 8 | 8 |
| $F(000)$ | 374 | 376 | 380 | 1,544 | 1,744 |
| $\rho_{calc}$ (g cm$^{-3}$) | 2.571 | 2.602 | 2.677 | 2.532 | 2.225 |
| $\mu$ (mm$^{-1}$) | 6.58 | 7.07 | 8.01 | 7.88 | 4.77 |
| Total data, $2\theta_{max}$ (°) | 5901, 63.8 | 5802, 61.2 | 5384, 61.2 | 6299, 63.8 | 31194, 61.2 |
| $R_{Int}$ | 0.031 | 0.020 | 0.025 | 0.035 | 0.036 |
| Merged, observed [$I> 2\sigma(I)$] data | 1747, 1732 | 1642, 1635 | 1612, 1594 | 1742, 1562 | 8180, 7533 |
| $R(F)[I> 2\sigma(I)]$ | 0.018 | 0.012 | 0.016 | 0.019 | 0.025 |
| $wR(F^2)$ (all data) | 0.043 | 0.029 | 0.033 | 0.038 | 0.063 |
| Absolute structure parameter | 0.036 (11) | 0.025 (15) | 0.026 (9) | 0.045 (12) | — |
| min., max.$\Delta\rho$ ($e$ Å$^{-3}$) | −1.79, +0.71 | −0.83, +0.75 | −0.49, +1.19 | −1.12, +0.87 | −1.55, +1.38 |
| CCDC deposition number | 1555502 | 1555503 | 1555504 | 1555505 | 1555506 |

$C_3H_{10}NO_{11}Ho$ (**3**): Calc. (%): C 8.96, H 2.49, N 3.49; Found (%): C 8.81, H 2.52, N 3.45. IR (cm$^{-1}$): $\nu$ = 3591, 3369 (O-H), 2928 (C-H), 1586 (COO)$_{as}$, 1384,1372 (COO)$_s$, 290 (Ho-O); $\delta$ = 1463, 1149 (C-H), 955 (COO), 819 (NO$_3$); $\rho$ = 838 (H$_2$O), 739 (CH$_2$).

$C_6H_9O_{10}Er$ (**4**): Calc. (%): C 17.65, H 2.22; Found (%): C 17.01, H 2.11. IR (cm$^{-1}$): $\nu$ = 3573, 3338 (O-H), 2921 (C-H), 1697, 1566 (COO)$_{as}$, 1383, 1279 (COO)$_s$; $\delta$ = 1449, 1186 (C-H), 967 (COO); $\rho$ = 803 (H$_2$O), 712 (CH$_2$).

$C_6H_{15}O_{13}Eu$ (**5**): Calc. (%): C 16.11, H 3.38; Found (%): C 16.72, H 3.92. IR (cm$^{-1}$): $\nu$ = 3401 (O-H), 1714, 1570 (COO)$_{as}$, 1384(COO)$_s$; $\delta$ =1440, 1206 (C-H), 964 (COO); $\rho$ = 711 (CH$_2$). (Malonic acid, $\nu$ = 3398 (O-H), 2992, 2948 (C-H), 1737, 1706 (COO)$_{as}$, 1418, 1398 (COO)$_s$; $\delta$ = 1438, 1174 (C-H), 920 (COO); $\rho$ = 804 (H$_2$O), 771 (CH$_2$)).

## Physical Measurements

Elemental analyses were carried out on a Varion Micro Cube, Elementar, Germany. FTIR spectra were recorded over the frequency range 4,000–250 cm$^{-1}$ on a Perkin Elmer FTIR 180 spectrophotometer using KBr pellets. Thermal analyses were performed from room temperature to 1,000°C at heating rate of 10°C min$^{-1}$ in air on a Thermo-gravimeter Analyzer/Differential Scanning Calorimeter model SDT Q 600 (TA Instruments, USA). The excitation and emission spectra were recorded on photoluminescence spectrometer FLS 180 (Edinburg Instruments). The magnetic susceptibility measurements were conducted on Evans balance (Sherwood Scientific Ltd. UK) at room temperature and Hg[Co(SCN)$_4$] was used as a calibrant. The diamagnetic corrections for the component atoms were determined using Pascal constant (Kahn, 1993; Earnshaw, 2013) and details of the method is given the **Supporting Information**.

## Crystal Structure Determinations

Intensity data for compounds **1–5** were collected on a Bruker APEXII CCD diffractometer at 150 K using MoK$\alpha$ radiation ($\lambda$ = 0.71073 Å). An empirical absorption correction was carried out using SADABS (Sheldrick, 2014). The crystal structures were solved by direct methods with SHELXS-97 (Sheldrick, 2008) and refined by full-matrix least-squares on $F^2$ using SHELXL-2014 (Sheldrick, 2015). For molecular graphics, ORTEP 3 was used (Farrugia, 2012). The C-bound H atoms were geometrically placed (C–H = 0.99 Å) and refined as riding atoms. The O-bound H atoms were located in difference maps and refined freely as riding atoms in their as-found relative positions or with gentle restrains. One of the water molecules of crystallization in **5** is disordered over two adjacent locations and its H atoms could not be located. The constraint $U$iso(H) = 1.2$U_{eq}$(carrier) was applied in most of the cases. Details of the data collection and refinement details are summarized in **Table 1**.

## RESULTS AND DISCUSSION

### Synthesis

The reaction of $M(NO_3)_3 \cdot 6H_2O$ (M = Gd, Tb, Ho) with three equivalents of malonic acid ($C_3H_4O_4$) in the presence of NaOH in water-ethanol medium afforded the crystals of $\{[M(C_3H_2O_4)(H_2O)_4] \cdot NO_3\}_n$ complexes (**1–3**). The presence of nitrate was not detected in any of the previously reported structures of lanthanide-malonate complexes. Similar reactions of $MCl_3 \cdot 6H_2O$ (M = Er, Eu) and malonic acid in 1:2 molar ratio gave the crystalline complexes $[Er(C_3H_2O_4)(C_3H_3O_4)(H_2O)_2]_n$ (**4**) and $\{[Eu_2(C_3H_2O_4)_2(C_3H_3O_4)_2(H_2O)_6] \cdot 4H_2O\}_n$ (**5**). The chloride ion did not participate in coordination demonstrating the greater affinity of Ln(III) ions for O than Cl. In every case, the pH of the reaction solution was adjusted to 5–6 in order to avoid the isolation of insoluble hydroxides. The compounds were isolated by slow evaporation of the reaction solution. The composition of the complexes was established from elemental and thermal analyses and verified by X-ray crystallography. All five complexes crystallized as polymeric substances.

### IR Spectroscopy

The FTIR spectra of **1–5** are shown in **Figures S1–S5**. In the IR spectrum of malonic acid two intense bands at 1,737 and 1,706 cm$^{-1}$ are observed due to $\nu_{as}$(COO), while the symmetric stretches of carboxylate groups appear at 1,418 and 1,398 cm$^{-1}$. The signals at 2,992, 2,948, and 3,398 cm$^{-1}$ are associated with C-H and O-H stretching vibrations, respectively. The $CH_2$ rock is detected at 771 cm$^{-1}$.

In the IR spectra of all complexes the asymmetric and symmetric stretching bands of the carboxylate groups were observed around 1,600 and 1,300 cm$^{-1}$, respectively (Deacon and Phillips, 1980; Rodríguez-Martín et al., 2002; Chrysomallidou et al., 2010; Hussain et al., 2018). There is a significant drop in frequencies of these bands relative to that of free malonic acid indicating the coordination of malonate ions. The broad peaks near 3,600 and 3,400 cm$^{-1}$ correspond to the O-H stretching modes. The rocking vibration of coordinated $H_2O$ ($\rho$($H_2O$)) was found at 837 cm$^{-1}$ in complexes **1–3** and at 803 cm$^{-1}$ in **4** and **5**. The medium band around 950 cm$^{-1}$ is ascribed to bending vibration, $\delta$(O–C–O) of the carboxylate group. The M-O bonds absorbed at 276, 285, and 290 cm$^{-1}$ for complexes **1, 2,** and **3,** respectively, which prabably represent the $\nu$(M-O$_{water}$) vibrations (Chrysomallidou et al., 2010). These absorptions confirmed the formation of complexes as they were not observed in the ligand spectra. The spectral results are in agreement with the reported literature (Marrot and Trombe, 1994; Doreswamy et al., 2003; Chrysomallidou et al., 2010; Mathew et al., 2012).

The bands at 819 cm$^{-1}$ in **1–3** mark the presence of nitrate ions (Alhoshani et al., 2019). The absence of a band around 1,700 cm$^{-1}$ for complexes **1–3** indicates the deprotonation of COOH and coordination of carboxylate dianions to the metal ions. However, the peaks at 1,697 and 1,714 cm$^{-1}$ in **4** and **5,** respectively, correspond to C=O stretches of protonated carboxylic acid (COOH) (Chrysomallidou et al., 2010) as it is evident from crystal structures that the hydrogen malonate ions are present in these compounds.
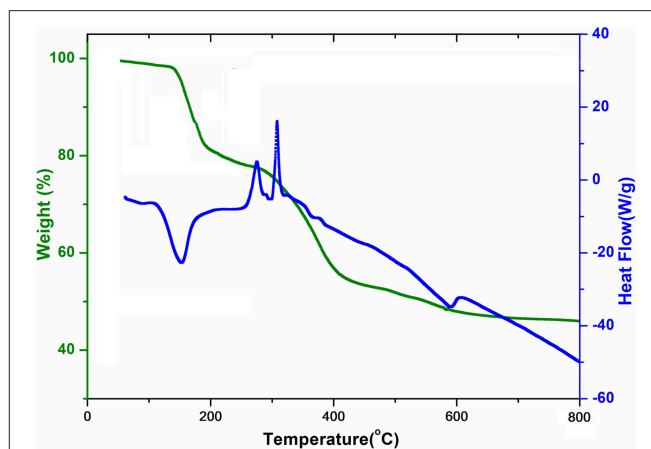


**FIGURE 1 |** TGA curve and DSC curve of $\{[Gd(C_3H_2O_4)(H_2O)_4] \cdot NO_3\}_n$ (**1**).

### Thermal Analysis

The simultaneous TG-DSC curves for complex **1** are shown in **Figure 1**. These curves express the mass losses in three consecutive steps. The first decomposition step occurs between 100 and 200°C that is attributed to the departure of four coordinated water molecules (experimental weight loss = 19%, calculated = 18.3%). This is evidenced by an endothermic peak of DSC at about 160°C. After the removal of water, the complex does not show sufficient thermal stability and starts releasing malonate ligand around 200°C. The decomposition of the malonic group is completed at 400°C with a weight loss of about 27% (calculated value 25.9%). The combustion of malonate is accompanied by two exothermic transitions in DSC. In the third stage nitrate is lost (as a nitrogen oxide) in the range of 400–650°C leaving behind ½Gd$_2$O$_3$ as a residue (experimental = 46%, calculated = 46.1%). The DSC plot shows an endothermic dip at about 600 °C attributable to the removal of nitrate.

A close similarity to **1** is noted concerning the TG-DSC profiles of compounds **2** and **3**, presented in **Figures S6, S7**, respectively. However, instead of 650°C for **1**, the decomposition is completed at 900 and 600°C for **2** and **3,** respectively. The DSC curves show endothermic and exothermic peaks that all are in agreement with the mass losses observed in the TG curves. The final residues in case of **2** and **3** correspond to 46 % ½Tb$_2$O$_3$ (calculated = 46.3%) and 47% ½Ho$_2$O$_3$ (calculated value 47.1%), respectively. The similarity of the thermal patterns suggests that the decomposition mechanism is the same for the three compounds.

As illustrated in **Figure S8**, for compound **4** the first mass loss of 8% occurs between 140 and 170°C, attributed to dehydration (calculated weight loss = 8.8 % for the removal of two water molecules) and is associated with an endothermic peak at 168°C. The loss of water at relatively higher temperature indicates the absence of water molecules of crystallization in the complex. After exclusion of coordinated water molecules, the anhydrous compound is stable up to 370°C. The second weight loss of 45% occurs due to the removal of two malonic groups in the temperature range of 370–900°C (calculated 50.2%), leaving

**TABLE 2 |** Selected bond lengths (Å), bond angles (°), and torsion angles (°) for **1**.

| Gd1–O1 | 2.330(3) | O1–Gd1–O1$^i$ | 115.8(2) |
|---|---|---|---|
| Gd1–O2$^i$ | 2.378(3) | O1–Gd1–O2 | 77.37(11) |
| Gd1–O3 | 2.454(5) | O1–Gd1–O3 | 72.00(11) |
| Gd1–O4 | 2.415(3) | O2–Gd1–O3 | 80.41(13) |
| Gd1–O5 | 2.421(5) | O2–Gd1–O4 | 112.51(12) |
| C1–O1 | 1.245(4) | O4–Gd1–O3 | 144.61(9) |
| C1–O1 | 1.264(5) | O5–Gd1–O3 | 117.72(16) |
| O1–C1–C2–C1$^{ii}$ | 125.1(4) | O2–C1–C2–C1 ii | −55.4(6) |

*Symmetry codes: (i) x–½, 1–y, z–½; (ii) –x+2, y, z; (iii) x, y-1, z; (iv) –x+3/2, -y+2, z+1/2.*



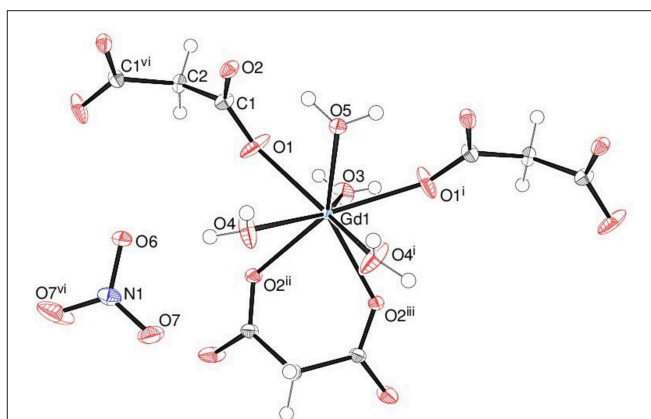**FIGURE 2 |** The asymmetric unit of **1** (50% displacement ellipsoids) expanded to show the full metal coordination sphere.

behind 47% ½Er$_2$O$_3$ as residue (calculated = 46.8%). The DSC curve depicts two exotherms presumably due to combustion of organic moieties at 400 and 625°C.

The thermal behavior of complex **5** is described in **Figure S9**. The decomposition begins with the loss of two water molecules of crystallization in the temperature range 90–130°C (experimental weight loss = 8%; calculated = 8.1%). The second weight loss of 12% was observed in the range of 150–200°C and is ascribed to the elimination of three water molecules coordinated with metal atom. Thus, the thermogram clearly distinguishes the presence of uncoordinated and coordinated water molecules in the complex. After 225°C, the malonate ligands are lost reducing the mass by 41% (calculated = 45.8%). The final residue is 39% that is associated with ½Eu$_2$O$_3$ (calculated 39.4%). In the DSC plot an endotherm at about 150°C corresponds to the dehydration step, while the exotherms at about 300 and 410°C represent the combustion of the malonate ligands. The shapes of the TGA curves for **1**–**5** are similar to those of the other malonate-containing Ln$^{3+}$ complexes described in the literature (Muraishi et al., 1991; Doreswamy et al., 2003; Chrysomallidou et al., 2010; Delgado et al., 2016) suggesting that the stability of the complexes is comparable to the reported ones.

## Description of Crystal Structures

Single-crystal X-ray structural analysis revealed that compounds **1, 2,** and **3** crystallize in the polar, orthorhombic space group $Pmn2_1$ and are isostructural. Therefore, complex **1** is taken as an example to present and discuss the structures in detail with any significant differences for **2** and **3** noted, where ever applicable. Selected bond distances and bond angles for **1** are presented in **Table 2**, while for **2**–**5** in **Tables S1**–**S4**, respectively. The hydrogen bonding details for **1**–**5** are given in **Tables S5**–**S9**, respectively.

The asymmetric unit of **1** shown in **Figure 2** consists of a Gd$^{3+}$ ion (site symmetry *m*), a malonate (C$_3$H$_2$O$_4^{2-}$) ligand (with the central C atom lying on a crystallographic mirror plane), four water molecules (two lying on a mirror plane) and a nitrate counter ion (the N atom and one of the O atoms have *m* site symmetry). The cationic complex is polymeric with each Gd$^{3+}$ ion coordinated by four O atoms from three different malonate groups and by four water molecules adopting a fairly regular square anti-prismatic geometry. Each square face of GdO$_8$ coordination polyhedron consists of two malonate
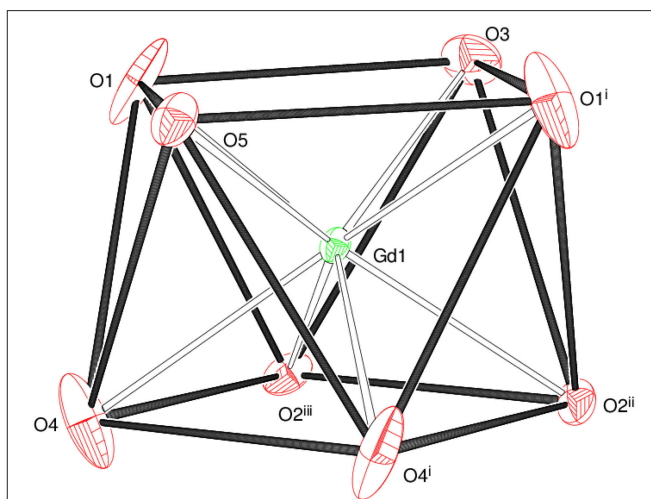


**FIGURE 3 |** The square anti-prismatic metal coordination geometry in **1**.

O atoms and two O atoms of water molecules, but their dispositions are different (**Figure 3**). In the O1/O1$^i$/O3/O5 face, the water O atoms are "*trans*" (lying across the square diagonal), whereas in the other, O2$^{ii}$/O2$^{iii}$/O4/O4$^i$, they are "*cis*" (adjacent). The angles subtended at the Gd atom by them vary in the range 72.01 to 144.61°. The malonate ligand is bonded to three different symmetry-related metal atoms yielding a two dimensional coordination polymer. It forms a six-membered chelate ring with one Gd$^{3+}$ ion, while the remaining two carboxyl oxygen atoms bind in a unidentate mode to the other two metal ions. In this way, the coordination mode of the bridging malonate group can be described as μ$_3$-κ$^2$O,O'κO",κO''' (Delgado et al., 2016). The six-membered chelate ring is well described as a boat conformation, with C1 × 2 and O2 × 2 exactly coplanar by symmetry and C2 and Gd1 displaced in the same sense by 0.610 (6) Å and 0.623 (7) Å, respectively.

The mean Gd–O bond distance in **1** is 2.390(4) Å (**Table 2**). The comparable distances for Tb in **2** (**Table S1**) and for Ho
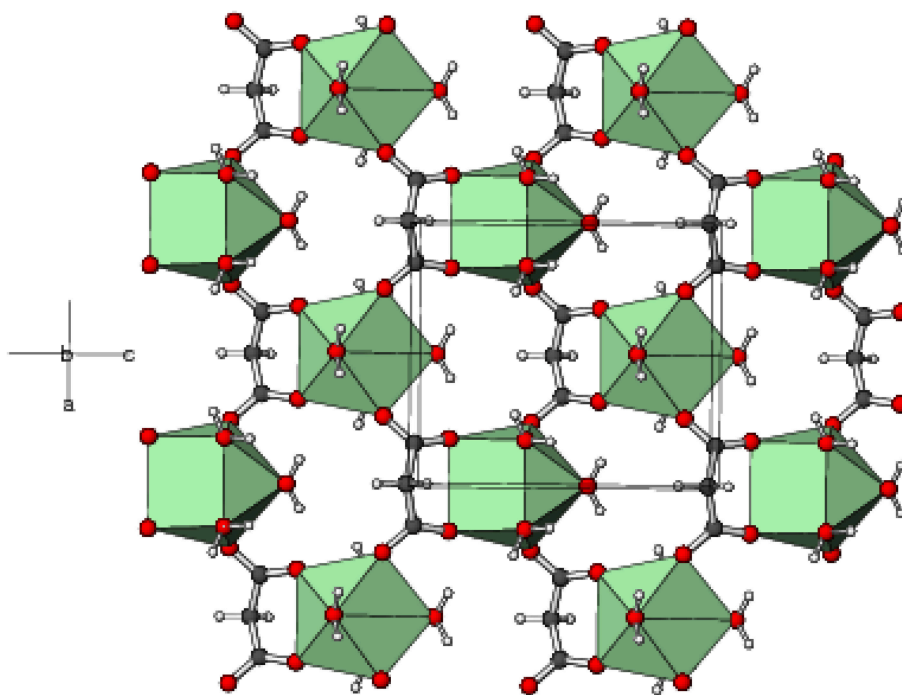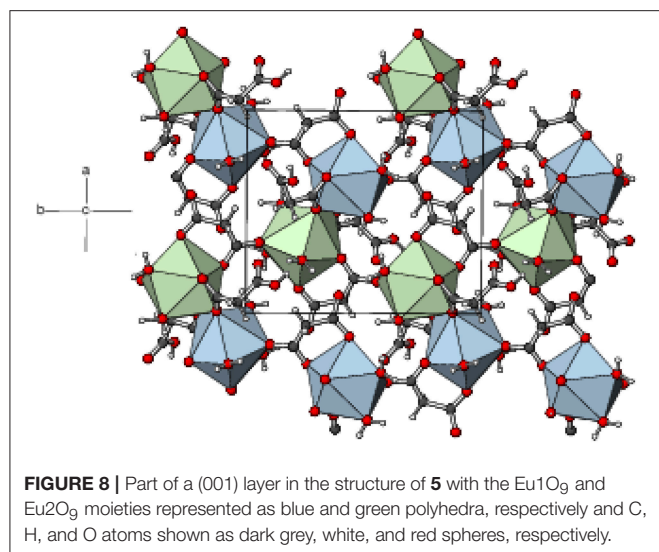
**FIGURE 4 |** Part of a (010) layer in the structure of **1** with the GdO$_8$ moieties represented as green polyhedra and C, H, and O atoms shown as dark grey, white, and red spheres, respectively.

in **3** (**Table S2**) are 2.377(3) and 2.352(4) Å, respectively. This trend agrees well with that expected in terms of the lanthanide contraction effect (Bünzli, 2014). In each case, the M–O$_m$ (m = malonate) bonds are shorter than the M–O$_w$ (w = water) bonds, which can be explained electrostatically in terms of stronger attraction to the delocalized negative charge on the malonate O atoms. The M-O bond lengths fall within the range observed for other Ln$^{3+}$ complexes of malonate (Hernández-Molina et al., 2003; Cañadillas-Delgado et al., 2006; Delgado et al., 2016). The C1–O1 and C1–O2 bond lengths (**Table 2**) in the malonate ligand are almost equal, indicating delocalization of charge. The dihedral angle between the square planes is 2.84(16)° and the metal ion is displaced from the O1 and O2 planes by 1.248(2) and −1.330(2) Å, respectively.

In the extended structure of **1**, the ligands bridge the metal ions into infinite cationic sheets of the formula [Gd(C$_3$H$_2$O$_4$)(H$_2$O)$_4$]$^+$ propagating in the (010) plane (**Figure 4**). Each malonate ligand links with three metal ions and the shortest Gd···Gd separation within a layer is 6.1705(9) Å, slightly less than the shortest inter-layer separation of 6.7470(7) Å [The corresponding data for **2** = 6.1498(7) and 6.7359(5) Å, respectively, and for **3** = 6.1179(11) and 6.7123(10) Å, respectively]. The nitrate counter ions occupy the inter-layer sites and the inter-sheet bonding is consolidated by O–H···O hydrogen bonds (**Table S5**), with malonate O atoms, water molecules and nitrate-O atoms all acting as acceptors. The hydrogen-bonding patterns in the terbium (**Table S6**) and holmium (**Table S7**) compounds are essentially identical to that in **1**.

Complex **4** crystallizes in the unusual orthorhombic space group *Fdd*2. The asymmetric unit of **4** depicted in **Figure 5** contains one erbium(III) ion (site symmetry 2), a malonate ligand, a hydrogen malonate anion and two water molecules. To balance the charge of Er$^{3+}$, the malonate species must represent statistically disordered malonate (C$_3$H$_2$O$_4^{2-}$) and hydrogen malonate (C$_2$H$_3$O$_4^-$) ions, with half of the O2 oxygen atoms in the crystal bearing a proton. The coordination polyhedra of Er$^{3+}$ ion is a square antiprism defined by two chelating ligands (bonding *via* O1 and O3), two monodentate malonate ligands (*via* O4) and two water molecules. In both square faces (O1/O1$^i$/O3/O3$^i$ and O4$^{ii}$/O4$^{iii}$/O5/O5$^i$), the water molecules are located at "*trans*" positions (**Figure S10**). The dihedral angle between these planes is 0° (by symmetry) and the metal ion is displaced from them by −1.303(2) and 1.186(2) Å, respectively. The average Er–O bond length is 2.334(4) Å (**Table S3**) that agrees well with the reported values (Delgado et al., 2016). The chelate conformation is an asymmetric boat, with C2 and Er1 deviating from C1/O1/C3/O3 (r.m.s. deviation = 0.001 Å) by 0.324(6) and 0.827(6) Å, respectively. The C3–O3 and C3–O4 bond lengths in the ligand are almost the same, indicating the delocalization of charge. However, C1–O2 is much longer than C1–O1 as a result of its disordered protonation, as described above. It is notable that O2 (the protonated O atom) does not coordinate to the metal ion. The coordination mode of the C1/O1/O2 carboxyl group is η$^1$ (monodentate) and that of C3/O3/O4 is μ$_2$-η$^1$:η$^1$ (bridging). In the extended structure of **4** the malonate ligands are bound in chelating form on one side (through O1 and O3) and as a bridging entity (*via* O4) from the

FIGURE 5 | The asymmetric unit of **4** (50% displacement ellipsoids) expanded to show the full metal coordination sphere.



FIGURE 7 | The asymmetric unit of **5** (50% displacement ellipsoids) with the non-coordinated water molecules of crystallization omitted for clarity.



FIGURE 6 | Part of a (110) chain in the structure of **4** with the $ErO_8$ moieties represented as pink polyhedra and C, H, and O atoms shown as dark grey, white, and red spheres, respectively.

other side ($\mu_2$-$\kappa^2$O,O'$\kappa$O" coordination mode). The repeating units are cross-linked to generate a dense two-dimensional network, with no evidence of channels or pores. A part of the chain propagating in the (110) direction is expressed in **Figure 6**.

The structure of the compound does not match with any of the earlier reported structures of $Ln^{3+}$ complexes involving the hydrogen malonate ligand (Wenmei et al., 1992; Marrot and Trombe, 1994; Delgado et al., 2016).

Complex **5** is a 2D polymer consisting of neutral dinuclear asymmetric units (**Figure 7**) composed of two $Eu^{3+}$ ions, two malonate dianions, two hydrogen malonate ions, six coordinated water molecules, and four water molecules of crystallization (one of which is disordered over two adjacent sites). In each dinuclear unit the two europium centers (Eu1 and Eu2) are bridged by the carboxylate groups of two hydrogen malonate ions to form a four membered Eu-O-Eu-O ring. Both metal ions are nine-coordinated by six carboxylate and three water oxygen atoms. The increase in coordination number from

eight (for $Gd^{3+}$ - $Er^{3+}$) to nine (for $Eu^{3+}$) is due to its larger size as compared with the others (Bünzli, 2014). The coordination polyhedron around Eu1 can be described as a distorted capped square antiprism (**Figure S11**) with O1/O3/O4$^i$/O5 and O9/O10/O17/O18 sets (two water molecules *cis*) forming the square faces and O19 (water molecule) as the cap. The dihedral angle between the squares is 2.8(1)° and Eu1 is displaced from them by 0.7244(12) and −1.6269(12) Å, respectively. Eu2 possesses a similar coordination polyhedron, the squares of which are defined by O9/O13/O14$^{ii}$/O15$^{ii}$ and O5/O6/O21/O22 (water molecules *cis*) [dihedral angle between them = 4.61(9)°] and the cap by O20. Eu2 is displaced from these squares by −0.7270(11) and 1.6413(12) Å, respectively. The malonate dianions behave as bridging as well as chelating (forming a six-membered chelating ring through O1 and O3) ligands adopting $\mu_2$-$\kappa^2$O,O'$\kappa$O" coordination mode. The hydrogen malonate ions bind only on one side in a $\mu_2$-$\kappa$O,$\kappa^2$O' manner. The carboxylate bonding modes in **5** are more varied than in **1–4**: C1/O1/O2 is monodentate to Eu1 ($\eta$1 mode); C3/O3/O4 is bridging to two Eu1 atoms ($\mu_2$-$\eta^1$:$\eta^1$ mode); C4/O5/O6 bonds to both Eu1 and Eu2 in chelating-bridging $\mu_2$-$\eta^2$:$\eta^1$ mode; C7/O9/O10 is chelating-bridging ($\mu_2$-$\eta^2$:$\eta^1$ mode); C6/O7/O8 and C9/O11/O12 are protonated at O8 and O12, respectively and these two groups do not coordinate to the metal ion; C10/O13/O14 is bridging ($\mu_2$-$\eta^1$:$\eta^1$); C12/O15/O16 is monodentate ($\eta^1$ mode). The ligands have different conformations as indicated by the following dihedral angles between the carboxylate groups: C1/O1/O2 + C3/O3/O4 = 34.4(3)°; C4/O5/O6 + C6/O7/O8 = 72.9(3)°; C7/O9/O10 + C9/O11/O12 = 87.0(3)°; C10/O13/O14 + C12/O15/O16 = 28.5(3)°.

The mean Eu–O distances are 2.454(2) and 2.457(2) Å for Eu1 and Eu2, respectively (**Table S4**), which are comparable to the literature data (Hansson, 1973a; Hernández-Molina et al., 2002; Zhang et al., 2007; Jin et al., 2012). For both metal ions, the charge-assisted Eu–O bonds from the deprotonated carboxylate groups tend to be the shortest. In the extended structure of

**FIGURE 8 |** Part of a (001) layer in the structure of **5** with the Eu1O$_9$ and Eu2O$_9$ moieties represented as blue and green polyhedra, respectively and C, H, and O atoms shown as dark grey, white, and red spheres, respectively.

**5**, the europium polyhedra share an edge, *via* O5 and O9, resulting in a Eu1···Eu2 separation of 4.3486 (4) Å. The ligands bridge the dinuclear species into (001) 2D sheets (**Figure 8**). Numerous O–H···O hydrogen bonds (**Table S9**) consolidate the packing: the bonds from the O8 and O11 carboxyl groups (one to another ligand O atom and one to a water molecule) have notably shorter H···O separations than the bonds arising from the water molecules.

## Comparative Structural Analysis

The crystal structures of several lanthanide compounds containing malonate ligand have been reported, which describe the ability of the malonate ion to adopt monodentate, chelating, and bridging coordination modes. The six-membered chelate ring through the two carboxylate groups is quite common in the lanthanide complexes (Delgado et al., 2016). In the present series of complexes, the malonate$^{2-}$ ligand adopts two types of coordination modes; $\mu_3$-$\kappa^2$O,O'$\kappa$O",$\kappa$O''' (**1–3**) and $\mu_2$-$\kappa^2$O,O'$\kappa$O" (**4,5**) leading to 2D network structures.

A closer look at the previously reported structures of the Ln(III)-malonate (mal$^{2-}$) compounds shows that most of them are dinuclear having the general formula, [Ln$_2$(mal)$_3$(H$_2$O)$_6$]$_n$·xH$_2$O (Delgado et al., 2016), (Ce, Sm) (Doreswamy et al., 2003; Chrysomallidou et al., 2010) (Pr), (Hansson, 1973b; Doreswamy et al., 2005), (Nd) (Hernández-Molina et al., 2002; Zhang et al., 2007), (Eu) (Hernández-Molina et al., 2003; Cañadillas-Delgado et al., 2006) (Gd), (Fang et al., 2008), (Dy), or [Ln$_2$(mal)$_3$(H$_2$O)$_5$]$_n$·xH$_2$O (Delgado et al., 2016) (Ho, Tb, Dy, Er, Yb) (Hernández-Molina et al., 2003; Cañadillas-Delgado et al., 2006) (Gd) (Hansson, 1973a), (Eu). Some of them exist in the mononuclear form (Wenmei et al., 1992; Marrot and Trombe, 1994; Chrysomallidou et al., 2010; Silva et al., 2010). The trivalent lanthanide cations (because of their high charge and small size) have high affinity for water and therefore, the coordination sphere is usually completed by water molecules. Most of the structures are assembled into 3D

coordination frameworks, while some as 1D or 2D polymers. The richness of structural architectures could be related to the versatility of malonate coordination modes and high values of the coordination number and flexibility of geometries of the Ln(III) ions.

In the majority of the complexes, the metal ions exhibit the coordination number nine, and the common geometries are tri-capped trigonal prism and distorted monocapped square antiprism (Delgado et al., 2016). In [Pr$_2$(mal)$_3$(H$_2$O)$_6$] and its dihydrate, the coordination environment is distorted capped tetragonal antiprism (Chrysomallidou et al., 2010). [Gd$_2$(mal)$_3$(H$_2$O)$_5$]$_n$·2nH$_2$O is eight-coordinated in which the Gd environment is distorted square antiprismatic (Cañadillas-Delgado et al., 2006). Complexes with coordination number of ten are also known. For example, in 1D polymeric [CeCl(mal)(H$_2$O)$_3$]·0.5(H$_2$O), the cerium center adopts a highly distorted dodecahedron (Silva et al., 2010). The coordination polyhedra of metal ions in [La(H$_2$O)$_2$(mal)(mal-H)]·H$_2$O and [PrCl(mal)(H$_2$O)$_3$]$_n$·0.5nH$_2$O are best described as distorted tetracapped trigonal prism (Marrot and Trombe, 1994) and bicapped tetragonal antiprism (Chrysomallidou et al., 2010), respectively. The extensive network of hydrogen bonds in the polymers enhances their structural stability.

The structures of the complexes presented here (**1–5**) do not possess similarity to any of the previously reported structures. Four of the five complexes exist as mononuclear 2D polymers, while the fifth (**5**) is dinuclear. Two complexes (**4** and **5**) are non-ionic as usual, but three (**1–3**) contain nitrate as a counter ion, which are so far unprecedented. In complexes **1–4**, the metal ions are eight-coordinated. The increase in coordination number from eight (for Gd$^{3+}$-Er$^{3+}$) to nine (for Eu$^{3+}$) is due to its larger size compared with the others. The change in coordination number from nine to eight can be related to the lanthanide contraction (Bünzli, 2014).

## Photoluminescence Properties

The excitation and emission spectra of **1–5** were recorded in the solid state at room temperature. All these compounds **1–5** exhibited luminescence in the visible region but most excellent results were obtained for compounds **2** and **5.** The excitation spectrum of **2** was recorded to monitor the strongest emission of terbium ($^5$D$_4$ → $^7$F$_5$) at 548 nm. The spectrum of **2** (**Figure 9A**) exhibited ligand excited peaks between 230 and 270 nm which correspond to the S$_0$ → S$_3$, S$_2$ of the ligand transitions. The peaks in the terbium spectrum were observed at 318, 341, 351, 365, and 379 nm which correspond to the $^7$F$_6$ → $^5$H$_7$, $^5$D$_{0,1}$, $^7$F$_6$ → $^5$D$_2$, $^7$F$_6$ → $^5$D$_3$, $^7$F$_6$ → $^5$L$_{10}$, and $^7$F$_6$ → $^5$G$_6$ transitions, respectively. The excitation spectrum of **5** was recorded to monitor the strongest emission of europium ($^5$D$_0$ → $^7$F$_2$) at 619 nm. The spectrum of **5** (**Figure 9B**) also exhibited broad band between 230 and 275 nm that represents the ligand excitations S$_0$ → S$_3$ and S$_0$ → S$_2$. The excitation peaks of europium are located at 300, 317, 360, 381, 393, 413, and 461 nm attributed to the $^7$F$_0$ → $^5$F$_J$, $^7$F$_0$ → $^5$H$_J$, $^7$F$_0$ → $^5$D$_4$, $^7$F$_0$ → $^5$L$_7$, $^7$F$_0$ → $^5$L$_6$, $^7$F$_0$ → $^5$D$_3$, and $^7$F$_0$ → $^5$D$_3$ transitions, respectively. The major ligand excitation signal S$_0$ → S$_1$ expected at 370 nm might be superimposed on strong peaks $^7$F$_6$ → $^5$L$_{10}$ and $^7$F$_0$
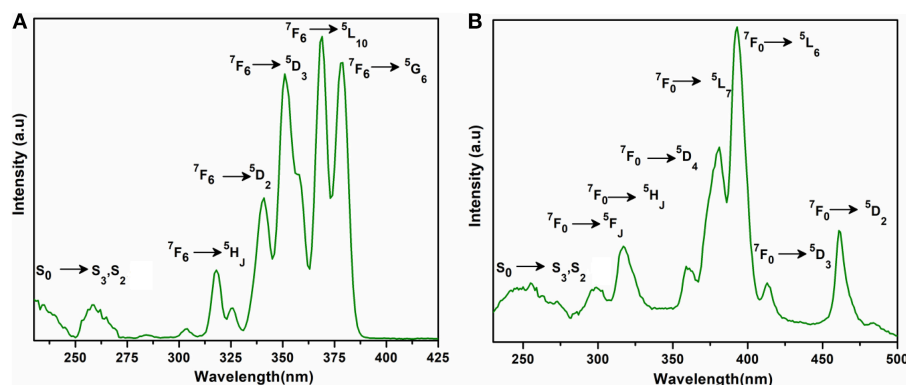
**FIGURE 9 |** Solid state excitation spectra of **2 (A)** and **5 (B)** to monitor emission wavelength at 548 and 619 and respectively.
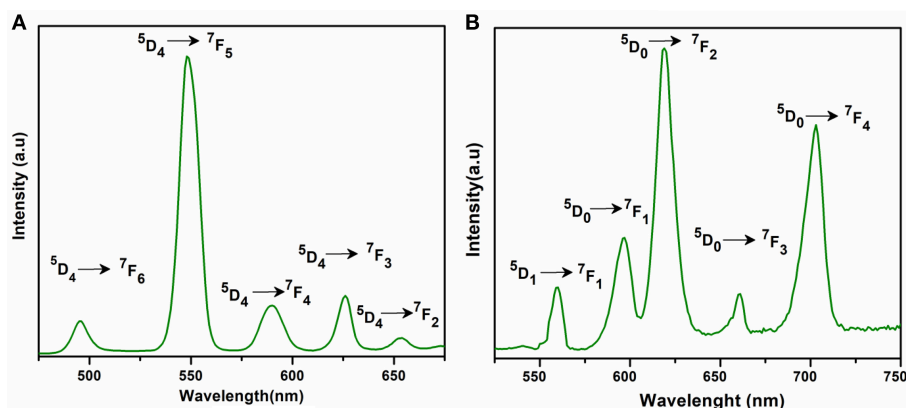


**FIGURE 10 |** Solid state emission spectra of **2 (A)** and **5 (B)** excited at 365 and 381 nm respectively.

$\rightarrow {}^5L_7$ in **2** and **5**, respectively. The excitation spectra of **2** and **5** depict that the ligand absorbs at shorter wavelength (230–280 nm) for excitation which helps to sensitize the symmetry forbidden *f-f* transition of Tb(III) and Eu(III) ions, respectively. The emission spectrum of **2** under the excitation wavelength of 365 nm is shown in **Figure 10A** which exhibits five characteristic *f–f* emission peaks of terbium at 496, 548, 584, 626, and 654 nm attributed to the ${}^5D_4 \rightarrow {}^7F_6$, ${}^5D_4 \rightarrow {}^7F_5$, ${}^5D_4 \rightarrow {}^7F_4$, ${}^5D_4 \rightarrow 7F_3$, and ${}^5D_4 \rightarrow 7F_2$ transitions, respectively. The strongest emission is observed by electric dipole transition at 548 nm (${}^5D_4 \rightarrow {}^7F_5$) due to the induced effect of the coordinated ligand, which confers to the intense green luminescence output from the solid sample when irritated under UV light (Hou et al., 2013; Bogale et al., 2017a,b). In some previously reported terbium carboxylate polymers, the intensity of this emission is quenched in the presence of $Fe^{3+}$ and nitroaromatics, and can be used as a sensor for the detection of metal ions and nitro compounds (Bogale et al., 2017a,b). The magnetic transition at 490 nm (${}^5D_4 \rightarrow {}^7F_6$) is relatively very weak with intensity ratio 1:6 (${}^5D_4 \rightarrow {}^7F_6$: ${}^5D_4 \rightarrow {}^7F_5$) that is almost insensitive to the coordinated environments (Bogale et al., 2017a,b). These peaks have been observed in other terbium complexes (Zhao et al., 2004; Hou et al., 2013, 2014). The

emission spectrum of **5** under the excitation of 381 nm is shown in **Figure 10B** which exhibits five characteristic *f–f* emission peaks of europium 560 nm (${}^5D_1 \rightarrow {}^7F_1$), 597nm (${}^5D_0 \rightarrow {}^7F_1$), 619 nm (${}^5D_0 \rightarrow {}^7F_2$), 661 nm (${}^5D_0 \rightarrow {}^7F_3$), and 560 nm (${}^5D_0 \rightarrow {}^7F_4$). Among them an induced electric dipole transition ${}^5D_0 \rightarrow {}^7F_2$ is the most intense which is hypersensitive to the chemical environment in the vicinity of Eu(III) ion and responsible for the strong red emission when irradiated under UV light (Hou et al., 2014). The magnetic dipole transition at 597 nm (${}^5D_0 \rightarrow {}^7F_1$) that is less sensitive to the coordinated environment is relatively weak compared with the electric dipole transition. The Eu(III) transition rule states that the magnetic dipole transition (${}^5D_0 \rightarrow {}^7F_1$) will be more intense when there exists a center of inversion. The intensity of electric dipole transition ${}^5D_0 \rightarrow {}^7F_2$ transition will be decreased as the site symmetry of Eu(III) ion increases (Hou et al., 2014). By comparing the intensity of ${}^5D_0 \rightarrow {}^7F_2$ (619 nm) and ${}^5D_0 \rightarrow {}^7F_1$(597nm) for **5**, the intensity ratio is about 4:1 which suggests that europium ion exists in the low symmetry environment and there is no center of inversion as revealed by the X-ray structural analysis of compound **5** (Gu and Xue, 2006). The excitation and emission spectra of **3** (**Figure S12**) exhibited sharp peaks with broad bases at 370 (${}^5I_8 \rightarrow {}^3G_6$) and

| Complex | Trivalent ion | Configuration $4f^n$ | $\mu(\mu B)$ (Van Vleck) | $\mu(\mu B)$ (Hund) | $\mu_{eff}(\mu B)$ Experimental |
|---------|---------------|---------------------|------------------------|------------------|------------------------------|
| **1** | Gd | $4f^7$ | 7.94 | 7.94 | 8.38 |
| **2** | Tb | $4f^8$ | 9.70 | 9.70 | 9.82 |
| **3** | Ho | $4f^{10}$ | 10.60 | 10.60 | 9.95 |
| **4** | Er | $4f^{11}$ | 9.60 | 9.60 | 9.53 |
| **5** | Eu | $4f^6$ | 3.40–351 | 0.00 | 3.98 |

$\mu B$ = Bohr magneton

570 nm ($^5S_2$, $^5F_4 \rightarrow {}^5I_8$.), respectively. In addition, few broad peaks are observed between 400 and 500 nm in the emission spectrum of **3** which are difficult to designate. The emission spectra of **1** (**Figure S13B**) and **4** (**Figure S14B**) are different from **2**, **3**, and **5**. No characteristic peaks of gadolinium and erbium are observed in the emission spectra of **1** and **4** except broad emission bands at 560 and 470 nm, respectively.

Plush and Gunnlaugsson reported that a dinuclear europium(III) bismacrocyclic complex (Plush and Gunnlaugsson, 2007) showed significant enhancement in europium(III) emission when titrated with malonic acid at pH 6.5. When this dinuclear complex was titrated with other dicarboxylates such acetate, succinate, aspartate, and glutarate acids at the same pH, the Eu(III) emission on all occasions was quenched (Plush and Gunnlaugsson, 2007). Thus, we believe that malonic acid is most suitable to produce excited states that help to sensitize the lanthanide luminescence compared with the other aliphatic dicarboxylates.

## Magnetic Properties

The room temperature magnetic moments of complexes **1–5** are provided in **Table 3**. The experimental $\mu_{eff}$ values for these complexes are near to the Hund (except for **5**) and Van Vleck (Van Vleck, 1932) values for the applicable free Ln(III) ion. The non-zero moment for **5** can be ascribed to the contribution of low-lying excited states to the magnetism, as observed in other europium(III) complexes (Ferenc et al., 2013a,b). These data indicate that the energies of the $4f$ orbitals in the title compounds differ a little from the free lanthanide(III) ions due to the fact that $5s^2$ and $5p^6$ orbitals are completely filled and strongly shield the $4f$ orbitals. Thus, it supports the assumption of the electrostatic nature of metal-ligand bonding in these compounds (Sinha, 2012; Kettle, 2013).

## Computational Study of Optoelectronic Properties of [Gd($C_3H_2O_4$)($H_2O$)$_4$]$_n$·NO$_3$}$_n$ (1)

The optoelectronic properties of compound **1** were explored using first principle methods (**Supporting Information**). The theoretical calculations have been performed within periodic boundary conditions (PBC) using DFT functional called PBE (in generalized gradient approximation) in solid-state calculations. Further details about computational
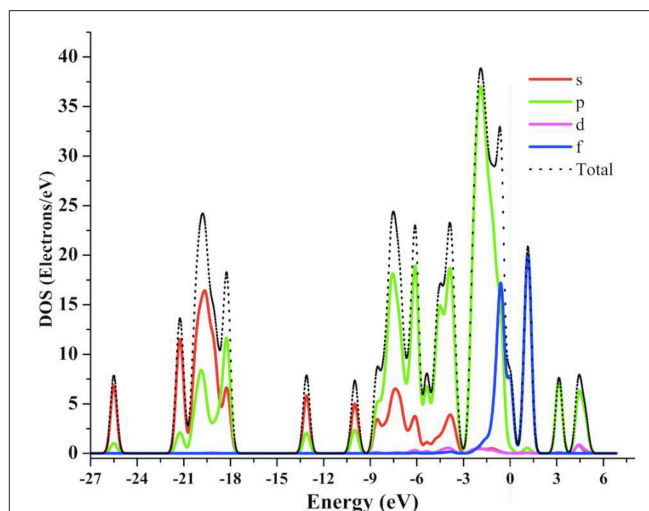


FIGURE 11 | The calculated TDOS and PDOS graph for **1** at GGA-PBE level of theory.

parameters including Brillouin Zone (BZ) sampling and energy cut-offs are given in the **Supporting Information**. All the computational calculations were performed using Cambridge Serial Total Energy Package (CASTEP) in Material Studio (Carter et al., 2006). A detailed comparison of optimized geometry and experimental single crystal geometry of compound **1** is presented in **Table S10** and **Figure S16**, which indicates the reliability of our chosen geometry in the present investigation.

## Density of States (DOS)

In order to understand the structure-property relationship, we have calculated total density of states (TDOS) and partial density of states (PDOS) for compound 1. The TDOS and PDOS projected into individual states contributions of the molecule were calculated for compound 1 as shown in **Figure 11**. The total DOS shows a lot of structural patterns that can be better understood by looking at the PDOS. It can be seen that in deep valence band the contributions of $s$- and $p$-states from oxygen atoms are significant in the range of −25 to −3 eV, which indicates significant ligand contributions in the molecular structure. On the other hand, around the Fermi-level the contributions from $p$- and $f$-states are significant. Hybridization effects can also be analyzed using PDOSs from **Figure 10**. The significant contributions of $p$-states of O atoms and $f$-states of Gd atoms around −0.5 eV indicates the strong bonding character or energy states hybridization of gadolinium atoms with oxygen atoms of ligands.

## Optical Properties

In the past, the photophysical and electroluminescence properties of rare earth metals have been studied very keenly because of their many technological applications i.e., optical amplifiers, luminescent solar concentrators, and active waveguides (Kenyon, 2002; Kido and Okamoto, 2002;
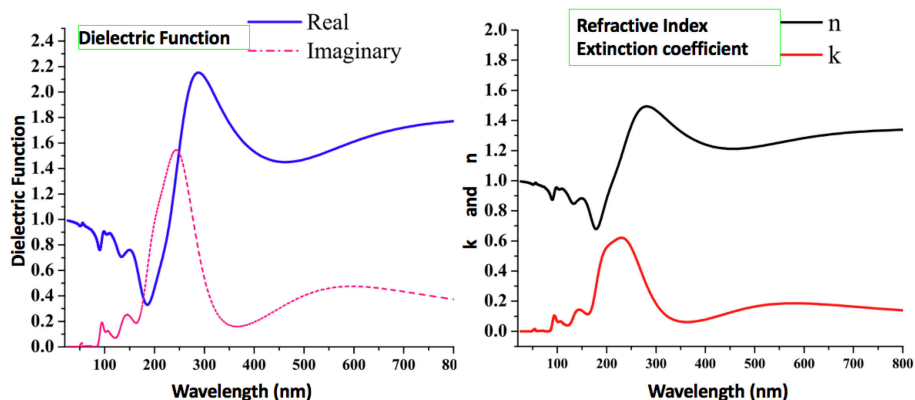
**FIGURE 12 |** The calculated optical properties of **1**, including real and imaginary parts of the dielectric function, refractive index, and extinction.
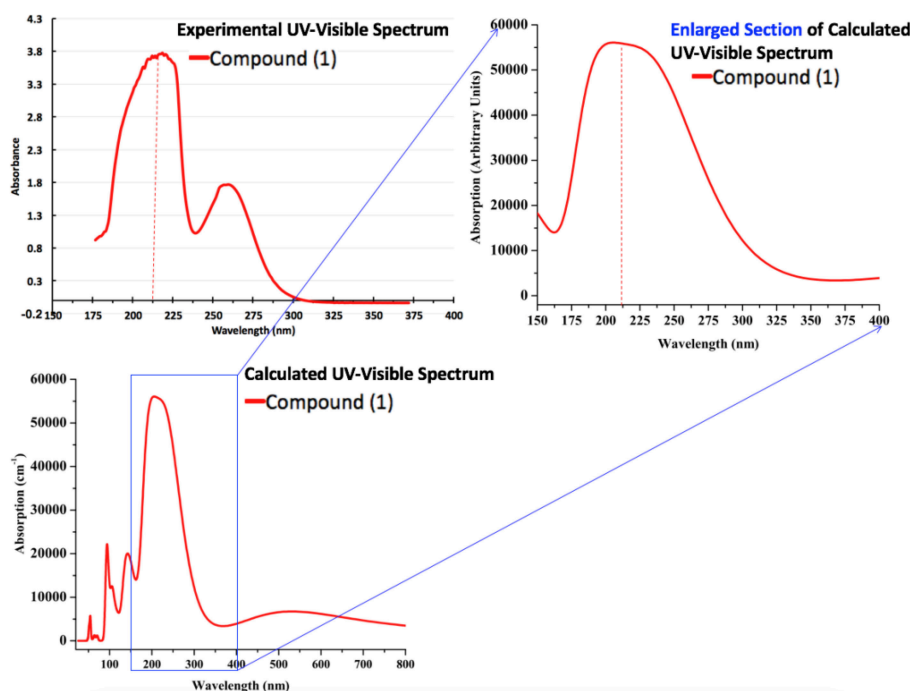


**FIGURE 13 |** The calculated (PBE-GGA) and experimental (in ethanol) absorption spectra of compound **1**.

Armelao et al., 2010; Katkova and Bochkarev, 2010; Heffern et al., 2013; Reisfeld, 2015). Along similar lines, we have calculated some important optical parameters, including real and imaginary parts of dielectric function, refractive index, extinction coefficient and absorption spectrum in the solid-state for **1** using periodic boundary conditions. The real and imaginary parts of the dielectric function are presented in **Figure 12**. The dielectric function is the response of the material to the alternating electric field. Experimentally, dielectric function is calculated using dielectric techniques e.g., dielectric relaxation spectroscopy (DRS). In the present investigation, the optical functions of compound (**1**) are calculated for photon

wavelength up to 800 nm to the direction of polarization vector [100]. For compound **1**, its real and imaginary parts of the dielectric function show peaks of maximum dielectric function values (real = 2.2 and imaginary = 1.5) in the range of 200 nm to 300 nm, which indicates that the maximum interaction of light occurs in this range. The refractive index and extinction coefficients also show the highest values of $n$ (1.52) and $k$ (0.64) at similar wavelengths as that of dielectric function in the UV region. These values indicate by how much the value is bent when entering the material.

Moreover, we have also calculated the UV-Visible spectrum for compound **1** by using the PBE-GGA method for solid-state

crystal structure. In addition to the commutated UV-Visible spectrum, we have also experimentally recorded the UV-Visible spectrum in ethanol solution. Both the calculated and experimental spectra are illustrated in **Figure 13**. It is important to mention that the experimental spectrum is only available in the range of 190–400 nm due to the limits of our spectrophotometer. Owing to the above situation and to make a comprehensive comparison of computed and experimental UV-Visible spectra, we have also presented the enlarged part of the computationally generated UV-Visible spectrum in the range of 150–400 nm as shown in **Figure 13**. A comparison of computationally generated and experimental UV-Visible spectra shows that they are in reasonable agreement with each other. The maximum absorption wavelengths in both spectra are found to be around ∼215 nm. Moreover, the absorption ranges for both the spectra are between 175 and 300 nm. The experimental spectrum for compound **1** shows one shoulder peak which might be due to the fact that it has been measured in ethanol while the computationally generated spectrum is in the solid state. The absorption values display maximum amplitudes in the range of 200–250 nm with good absorption coefficients in the ultraviolet region that could be valuable for the possible application of compound **1** as a UV sensor. Thus, we believe that these optical properties can be very helpful to offer a theoretical basis for the experimental analysis of photophysical properties in future, and to get new physical insights from the molecules to materials.

## CONCLUSIONS

Five new lanthanide-malonate coordination polymers (1–5) with two- or three-dimensional connectivity have been synthesized and their crystal structures were determined by X-ray crystallography. The complexes **1–4** are monoclear and the central $Ln^{3+}$ ions are eight-coordinate assuming square antiprism geometry. Complex **5** is dinuclear with the nine-coordinated $Eu^{3+}$ ions possessing the mono-capped square antiprism polyhedra. The malonate and hydrogen malonate ligands show typical versatility in their chelating, bridging, and combined bonding modes to the different metal ions. So far as we are aware, all three are new crystal structure types. Most of the known compounds such as, $[Gd_2(C_3H_2O_4)_3(H_2O)_6]n\cdot2nH_2O$ (Cañadillas-Delgado et al., 2006) $[Er_2(C_3H_2O_4)_3(H_2O)_5]n\cdot2nH_2O$, (Delgado et al., 2016), and $[Eu_2(C_3H_2O_4)_3(H_2O)_6]n\cdot2nH_2O$ (Hernández-Molina et al., 2002) contain dianionic malonate ligands, while only a few reports are available on the hydrogen malonate complexes (Wenmei et al., 1992; Marrot and Trombe, 1994). The IR spectra also indicate the presence of hydrogen malonate ligand

in **4** and **5**. The results of the thermogravimetric analysis verified the composition of the investigated complexes. The photoluminescence spectra of **2** and **5** exhibit characteristic emission of Tb(III) and Eu(III), respectively. Additionally, we have used the first principle calculations for compound **1** to explore its optoelectronic properties. The prediction of dielectric function, refractive index, extinction coefficient and absorption spectrum shed light on prospective applications as optical materials. The maximum dielectric function and other absorption coefficients in the UV region for compound **1** indicate its potential application as a UV sensor. A comparison of computationally generated and experimental UV-Visible spectra shows that they are in reasonable agreement with each other having maximum absorption around ∼215 nm. Thus, we strongly believe that the present set of synthesis, characterization, and computational insights will evoke the significant interests of scientific community in the chemistry of rare-earth coordination polymers.

## AUTHOR CONTRIBUTIONS

XC, SA, and IK devised the project, the main conceptual ideas, and proof outline. SH synthesized the compounds, performed analyses and wrote the manuscript. SM carried out the computational and theoretical work. ME collected the crystal date and helped in structure solutions. WH refined and drew images of the structures and wrote the crystal description.

## FUNDING

## ACKNOWLEDGMENTS

## SUPPLEMENTARY MATERIAL

The Supplementary Material for this article can be found online at: https://www.frontiersin.org/articles/10.3389/fchem.2019.00260/full#supplementary-material

## REFERENCES

Adamo, C., and Maldivi, P. (1997). Ionic versus covalent character in lanthanide complexes. A hybrid density functional study. *Chem. Phys. Lett.* 268, 61–68. doi: 10.1016/S0009-2614(97)00177-2

Alhoshani, A., Seliman, A. A., Altoum, A. O., Abuelizz, H. A., Ahmad, S., Altaf, M., et al. (2019). Synthesis, X-ray structure and *in vitro* cytotoxicity of trans-diammineplatinum(II) complexes of selenones, trans-[Pt (NH_3)_2 (selenone)_2](NO_3)_2. *Polyhedron* 158, 234–240. doi: 10.1016/j.poly.2018.09.010

Armelao, L., Quici, S., Barigelletti, F., Accorsi, G., Bottaro, G., Cavazzini, M., et al. (2010). Design of luminescent lanthanide complexes: from molecules to highly efficient photo-emitting materials. *Coord. Chem. Rev.* 254, 487–505. doi: 10.1016/j.ccr.2009.07.025

Benmerad, B., Guehria-Laidoudi, A., Bernardinelli, G., and Balegroune, F. (2000). Polymeric tetraaquatris (malonato) dilanthanum(III) monohydrate. *Acta. Crystallogr. C Cryst. Struct. Chem.* 56, 321–323. doi: 10.1107/S0108270199016182

Bogale, R. F., Chen, Y., Ye, J., Yang, Y., Rauf, A., Duan, L., et al. (2017a). Highly selective and sensitive detection of 4-nitrophenol and $Fe^{3+}$ ion based on a luminescent layered terbium(III) coordination polymer. *Sens. Actuators B. Chem.* 245, 171–178. doi: 10.1016/j.snb.2017.01.177

Bogale, R. F., Chen, Y., Ye, J., Zhang, S., Li, Y., Liu, X., et al. (2017b). A terbium(III)-based coordination polymer for selective and sensitive sensing of nitroaromatics and ferric ion: synthesis, crystal structure and photoluminescence properties. *New J. Chem.* 41, 12713–12720. doi: 10.1039/C7NJ02492D

Buenzli, J. C. G. (2015). On the design of highly luminescent lanthanide complexes. *Coord. Chem. Rev.* 293, 19–47. doi: 10.1016/j.ccr.2014.10.013

Bünzli, J. C. G. (2010). Lanthanide luminescence for biomedical analyses and imaging. *Chem. Rev.* 2110, 2729–2755. doi: 10.1021/cr900362e

Bünzli, J. C. G. (2014). Lanthanide coordination chemistry: from old concepts to coordination polymers. *J. Coord. Chem.* 67, 3706–3733. doi: 10.1080/00958972.2014.957201

Calahorro, A. J., Fairen-Jiménez, D., Salinas-Castillo, A., López-Viseras, M. E., and Rodríguez-Diéguez, A. (2013). Novel 3D lanthanum oxalate metal-organic-framework: Synthetic, structural, luminescence and adsorption properties. *Polyhedron* 52, 315–320. doi: 10.1016/j.poly.2012.09.018

Cañadillas-Delgado, L., Pasan, J., Fabelo, O., Hernandez-Molina, M., Lloret, F., Julve, M., et al. (2006). Two-and three-dimensional networks of gadolinium(III) with dicarboxylate ligands: synthesis, crystal structure, and magnetic properties. *Inorg. Chem.* 45, 10585–10594. doi: 10.1021/ic061173d

Caravan, P., Ellison, J. J., Mcmurry, T. J., and Lauffer, R. B. (1999). Gadolinium(III) chelates as MRI contrast agents: structure, dynamics, and applications. *Chem. Rev.* 99, 2293–2352. doi: 10.1021/cr980440x

Carter, R., Sloan, J., Kirkland, A. I., Meyer, R. R., Lindan, P. J., Lin, G., et al. (2006). Correlation of structural and electronic properties in a new low-dimensional form of mercury telluride. *Phys. Rev. Lett.* 96:215501. doi: 10.1103/PhysRevLett.96.215501

Chrysomallidou, K. E., Perlepes, S. P., Terzis, A., and Raptopoulou, C. P. (2010). Synthesis, crystal structures and spectroscopic studies of praseodymium(III) malonate complexes. *Polyhedron* 29, 3118–3124. doi: 10.1016/j.poly.2010.08.020

Cui, G.-H., Li, J.-R., Zhang, R.-H., and Bu, X.-H. (2005). Hydrothermal synthesis, crystal structures and luminescent properties of two new Ln(III)–succinate (Ln = Eu, Tb) complexes exhibiting three dimensional networks. *J. Mol. Struct.* 740, 187–191. doi: 10.1016/j.molstruc.2005.01.049

Cundari, T. R., Sommerer, S. O., Strohecker, L. A., and Tippett, L. (1995). Effective core potential studies of lanthanide complexes. *J. Chem. Phys.* 103, 7058–7063. doi: 10.1063/1.470333

Daiguebonne, C., Kerbellec, N., Guillou, O., Bünzli, J. C., Gumy, F., Catala, L., et al. (2008). Structural and luminescent properties of micro-and nanosized particles of lanthanide terephthalate coordination polymers. *Inorg. Chem.* 47, 3700–3708. doi: 10.1021/ic702325m

Deacon, G., and Phillips, R. (1980). Relationships between the carbon-oxygen stretching frequencies of carboxylato complexes and the type of carboxylate coordination. *Coord. Chem. Rev.* 33, 227–250. doi: 10.1016/S0010-8545(00)80455-5

Deacon, G. B., Forsyth, M., Junk, P. C., Leary, S. G., and Moxey, G. J. (2006). Synthesis and structural diversity of rare earth anthranilate complexes. *Polyhedron* 25, 379–386. doi: 10.1016/j.poly.2005.07.005

Delgado, F. S., Lorenzo-Luís, P., Pasán, J., Cañadillas-Delgado, L., Fabelo, O., Hernández-Molina, M., et al. (2016). Crystal growth and structural remarks on malonate-based lanthanide coordination polymers. *Cryst. Eng. Comm.* 18, 7831–7842. doi: 10.1039/C6CE01360K

Dolg, M. (2015). *Computational Methods in Lanthanide and Actinide Chemistry*. John Wiley & Sons. doi: 10.1002/9781118688304

Doreswamy, B., Mahendra, M., Sridhar, M., Prasad, J. S., Varughese, P., George, J., et al. (2005). A novel three-dimensional polymeric structure of crystalline neodymium malonate hydrate. *Mater. Lett.* 59, 1206–1213. doi: 10.1016/j.matlet.2004.12.029

Doreswamy, B., Mahendra, M., Sridhar, M., Prasad, J. S., Varughese, P., Saban, K., et al. (2003). Structural studies on praseodymium malonate hydrate. *J. Mol. Struct.* 659, 81–88. doi: 10.1016/j.molstruc.2003.08.001

Dos Santos, C. M., Harte, A. J., Quinn, S. J., and Gunnlaugsson, T. (2008). Recent developments in the field of supramolecular lanthanide luminescent sensors and self-assemblies. *Coord. Chem. Rev.* 252, 2512–2527. doi: 10.1016/j.ccr.2008.07.018

Earnshaw, A. (2013). *Introduction to Magnetochemistry*. London; New York, NY: Elsevier; Academic Press.

Eisenstein, O., and Maron, L. (2002). DFT studies of some structures and reactions of lanthanides complexes. *J. Organomet. Chem.* 647, 190–197. doi: 10.1016/S0022-328X(01)01407-3

Fang, Z.-Q., Zeng, R.-H., Song, Z.-F., and Yang, M. (2008). Poly [hexaaquatri-μ-malonato-didysprosium (III)]. *Acta Crystallogr. Sect. E, Struct. Rep. Online* 64, m877–m877. doi: 10.1107/S1600536808015961

Farrugia, L. J. (2012). WinGX and ORTEP for Windows: an update. *J. Appl. Cryst.* 45, 849–854. doi: 10.1107/S0021889812029111

Faulkner, S., Pope, S. J., and Burton-Pye, B. P. (2005). Lanthanide complexes for luminescence imaging applications. *Appl. Spectrosc. Rev.* 40, 1–31. doi: 10.1081/ASR-200038308

Ferenc, W., Cristóvão, B., and Sarzynski, J. (2013a). Magnetic, thermal and spectroscopic properties of lanthanide (III) 2-(4-chlorophenoxy) acetates, Ln $(C_8H_6ClO_3)_3 \bullet n H_2O$. *J. Serb. Chem. Soc.* 78, 1335–1349. doi: 10.2298/JSC121203043F

Ferenc, W., Sadowski, P., Cristovao, B., and Sarzynski, J. (2013b). Investigation of some physicochemical properties of 4-nitrocinnamates of lanthanides (III). *J. Chil. Chem. Soc.* 58, 1753–1758. doi: 10.4067/S0717-97072013000200025

Gao, H.-L., Huang, S.-X., Zhou, X.-P., Liu, Z., and Cui, J.-Z. (2018). Magnetic properties and structure of tetranuclear lanthanide complexes based on 8-hydroxylquinoline Schiff base derivative and β-diketone coligand. *Dalton Trans.* 47, 3503–3511. doi: 10.1039/C8DT00063H

George, T., Varughese, S., and Reddy, M. (2016). Near-infrared luminescence of Nd 3+ and Yb 3+ complexes using a polyfluorinated pyrene-based β-diketonate ligand. *RSC Adv.* 6, 69509–69520. doi: 10.1039/C6RA12220E

Gu, X., and Xue, D. (2006). Selected controlled synthesis of three-dimensional 4d–4f heterometallic coordination frameworks by lanthanide carboxylate subunits and silver centers. *Cryst. Growth Des.* 6, 2551–2557. doi: 10.1021/cg060485o

Hansson, E. (1973a). The crystal and molecular structure of penta-aquo Tris-malonato Di-Europiumum(III) Tri-hydrate. *Acta. Chem. Scand.* 27, 2827–2840. doi: 10.3891/acta.chem.scand.27-2827

Hansson, E. (1973b). Structural studies on the rare earth carboxylates. *Acta. Chem. Scand.* 27, 823–834. doi: 10.3891/acta.chem.scand.27-0823

He, H., Ma, H., Sun, D., Zhang, L., Wang, R., and Sun, D. (2013). Porous lanthanide–organic frameworks: control over interpenetration, gas adsorption, and catalyst properties. *Cryst. Growth Des.* 13, 3154–3161. doi: 10.1021/cg400531j

Heffern, M. C., Matosziuk, L. M., and Meade, T. J. (2013). Lanthanide probes for bioresponsive imaging. *Chem. Rev.* 114, 4496–4539. doi: 10.1021/cr400477t

Hernández-Molina, M., Lorenzo-Luis, P., Ruiz-Pérez, C., López, T., Martín, I. R., Anderson, K. M., et al. (2002). A phase transition in the novel three-dimensional compound [$Eu_2(mal)_3$ $(H_2O)_6$]($H_2mal$= malonic acid). *J. Chem. Soc., Dalton Trans.* 3462–3470. doi: 10.1039/B202649J

Hernández-Molina, M., Lorenzo-Luis, P. A., López, T., Ruiz-Pérez, C., Lloret, F., and Julve, M. (2000). Generation of lanthanide coordination polymers with dicarboxylate ligands: synthesis, structure, thermal decomposition, and magnetic properties of the two-dimensional triaquatris (malonato) dipraseodymium(III) dihydrate {[$Pr_2(C_3H_2O_4)_3(H_2O)_3$]·$2H_2O$}. *Cryst. Eng. Comm.* 2, 169–173. doi: 10.1039/B006256L

Hernández-Molina, M., Ruiz-Pérez, C., López, T., Lloret, F., and Julve, M. (2003). Ferromagnetic coupling in the three-dimensional malonato-bridged gadolinium (III) complex [$Gd_2(mal)_3$ $(H_2O)_6$]($H_2mal$= Malonic Acid). *Inorg. Chem.* 42, 5456–5458. doi: 10.1021/ic034175w

Hou, Y. L., Cheng, R. R., Xiong, G., Cui, J. Z., and Zhao, B. (2014). Structures, luminescent and magnetic properties of a series of (3, 6)-connected lanthanide–organic frameworks. *Dalton Trans.* 43, 1814–1820. doi: 10.1039/C3DT52305E

Hou, Y. L., Xiong, G., Shen, B., Zhao, B., Chen, Z., and Cui, J. Z. (2013). Structures, luminescent and magnetic properties of six lanthanide–organic frameworks: observation of slow magnetic relaxation behavior in the Dy III compound. *Dalton Trans.* 42, 3587–3596. doi: 10.1039/c2dt32390g

Hussain, S., Khan, I., Akkurt, M., Ahmad, S., and Tahir, M. (2014). Synthesis and structural characterization of binuclear ytterbium (III) complexes with 2-amino and 3-amino benzoic acid. *Russ. J. Coord. Chem.* 40, 686–694. doi: 10.1134/S107032841409005X

Hussain, S., Khan, I., Harrison, W. T., and Tahir, M. (2015a). Crystal structures and characterization of two rare-earth-glutarate coordination networks: One-dimensional $[Nd(C_5H_6O_4)(H_2O)_4]\cdot Cl$ and three-dimensional $[Pr(C_5H_6O_4)(C_5H_7O_4)(H_2O)]\cdot H_2O$. *J. Struct. Chem.* 56, 934–941. doi: 10.1134/S0022476615050169

Hussain, S., Khan, I., Harrison, W. T., Tahir, M., and Ahmad, S. (2015b). Crystal structures and characterization of two one-dimensional coordination polymers containing $Ln^{3+}$ ions and anthranilate $(C_7H_6NO_2^-)$ anions. *J. Struct. Chem.* 56, 126–133. doi: 10.1134/S0022476615010187

Hussain, S., Khan, I. U., Elsegood, M. R., Jabeen, N., Tahir, M. N., Ahmad, S., et al. (2018). Synthesis and structural characterization of dinuclear cerium(III) and erbium (III) complexes of nicotinic acid or 2-aminobenzoic acid. *Polyhedron* 151, 452–457. doi: 10.1016/j.poly.2018.05.057

Ishikawa, N., Sugita, M., Okubo, T., Tanaka, N., Iino, T., and Kaizu, Y. (2003). Determination of ligand-field parameters and f-electronic structures of double-decker bis (phthalocyaninato) lanthanide complexes. *Inorg. Chem.* 42, 2440–2446. doi: 10.1021/ic026295u

Jin, J., Wang, X., Li, Y., Chi, Y., and Niu, S. (2012). Synthesis, structure, and photophysical property of series of Ln (III) coordination polymers with different carboxylato ligands (Ln = Sm, Eu). *Struct. Chem.* 23, 1523–1531. doi: 10.1007/s11224-012-9957-6

Kahn, O. (1993). *Molecular Magnetism.* New York, NY: VCH Publishers, Inc.(USA).

Katkova, M. A., and Bochkarev, M. N. (2010). New trends in design of electroluminescent rare earth metallo-complexes for OLEDs. *Dalton Trans.* 39, 6599–6612. doi: 10.1039/c001152e

Kenyon, A. (2002). Recent developments in rare-earth doped materials for optoelectronics. *Prog. Quant. Electron.* 26, 225–284. doi: 10.1016/S0079-6727(02)00014-9

Kettle, S. F. A. (2013). *Physical Inorganic Chemistry: A Coordination Chemistry Approach.* Heidelberg: Springer.

Kido, J., and Okamoto, Y. (2002). Organo lanthanide metal complexes for electroluminescent materials. *Chem. Rev.* 102, 2357–2368. doi: 10.1021/cr010448y

Li, Z. Y., Cao, Y. Q., Li, J.-Y., Zhang, X. F., Zhai, B., Zhang, C., et al. (2017). Three types of lanthanide coordination polymers with methylmalonate and isonicotinate as coligands: structures, luminescence, and magnetic properties. *Cryst. Growth Des.* 17, 6752–6761. doi: 10.1021/acs.cgd.7b01341

Marrot, F., and Trombe, J. C. (1994). Synthesis, characterization and structure of a diaqua lanthanum bimalonate malonate monohydrate. *Polyhedron* 13, 1931–1935. doi: 10.1016/0277-5387(94)80017-0

Mathew, V., Jacob, S., Xavier, L., and Abraham, K. (2012). Spectroscopic studies of gel-grown lanthanum malonate crystals. *J. Rare Earth.* 30, 245–249. doi: 10.1016/S1002-0721(12)60039-8

Muraishi, K., Yokobayashi, H., and Nagase, K. (1991). Systematics on the thermal reactions of lanthanide malonates $Ln_2(C_3H_2O_4)_3\cdot nH_2O$ in the solid state. *Thermochim. Acta.* 182, 209–217. doi: 10.1016/0040-6031(91)80006-5

Pagis, C., Ferbinteanu, M., Rothenberg, G., and Tanase, S. (2016). Lanthanide-based metal organic frameworks: synthetic strategies and catalytic applications. *ACS Catal.* 6, 6063–6072. doi: 10.1021/acscatal.6b01935

Plush, S. E., and Gunnlaugsson, T. (2007). Luminescent Sensing of Dicarboxylates in Water by a bismacrocyclic dinuclear Eu(III) Conjugate. *Org. Lett.* 9, 1919–1922. doi: 10.1021/ol070339r

Rahahlia, N., Benmerad, B., Guehria-Laïdoudi, A., Dahaoui, S., and Lecomte, C. (2007). Three-dimensional ionic frameworks built up from La(III)

and Ce(III) succinates. *J. Mol. Struct.* 833, 42–48. doi: 10.1016/j.molstruc.2006.08.029

Räsänen, M., Takalo, H., Rosenberg, J., Mäkelä, J., Haapakka, K., and Kankare, J. (2014). Study on photophysical properties of Eu (III) complexes with aromatic β-diketones–Role of charge transfer states in the energy migration. *J. Lumin.* 146, 211–217. doi: 10.1016/j.jlumin.2013. 09. 076

Reineke, T. M., Eddaoudi, M., O'keeffe, M., and Yaghi, O. M. (1999). A microporous lanthanide–organic framework. *Angew. Chem. Int. Ed.* 38, 2590–2594. doi: 10.1002/(SICI)1521-3773(19990903)38:17<2590::AID-ANIE2590>3.0.CO;2-H

Reisfeld, R. (2015). Optical properties of lanthanides in condensed phase, theory and applications. *AIMS Mater. Sci.* 2, 37–60. doi: 10.3934/matersci.2015.2.37

Reisfeld, R., and Jorgensen, C. K. (2012). *Lasers and Excited States of Rare Earths.* Springer Science & Business Media.

Rodríguez-Martín, Y., Hernández-Molina, M., Delgado, F. S., Pasán, J., Ruiz-Pérez, C., Sanchiz, J., et al. (2002). Structural versatility of the malonate ligand as a tool for crystal engineering in the design of molecular magnets. *Cryst. Eng. Comm.* 4, 522–535. doi: 10.1039/B202166H

Roy, S., Chakraborty, A., and Maji, T. K. (2014). Lanthanide–organic frameworks for gas storage and as magneto-luminescent materials. *Coord. Chem. Rev.* 273, 139–164. doi: 10.1016/j.ccr.2014.03.035

Seidel, C., Lorbeer, C., Cybinska, J., Mudring, A. V., and Ruschewitz, U. (2012). Lanthanide coordination polymers with tetrafluoroterephthalate as a bridging ligand: thermal and optical properties. *Inorg. Chem.* 51, 4679–4688. doi: 10.1021/ic202655d

Sharif, S., Khan, I. U., Sahin, O., Ahmad, S., Büyükgüngör, O., and Ali, S. (2012). Synthesis and crystal structures of a lanthanum(III) 1D polymer and a mixed-ligand cerium (III) binuclear complex derived from pyridine-2, 6-dicarboxylic acid. *J. Inorg. Organomet. Polym.* 22, 1165–1173. doi: 10.1007/s10904-012-9715-7

Sharma, G., and Narula, A. K. (2015). Synthesis and optoelectronic properties of three Eu(III)-dipicolinate complexes based on α-picolinic acid, 2-aminopyridine and 2-hydroxypyridine as secondary ligands. *J. Mater. Sci. Mater. Electron.* 26, 1009–1017. doi: 10.1007/s10854-014-2497-7

Sheldrick, G. M. (2008). A short history of SHELX. *Acta Cryst. A. Found. Crystallogr.* 64, 112–122. doi: 10.1107/S0108767307043930

Sheldrick, G. M. (2014). *"SADABS v. 2014/5". Bruker/Siemens Area Detector Absorption Correction Program.* Madison, WI: Bruker AXS Inc.

Sheldrick, G. M. (2015). Crystal structure refinement with SHELXL. *Acta Crystallogr. Sect. C. Struct. Chem.* 71, 3–8. doi: 10.1107/S2053229614024218

Shibasaki, M., and Yoshikawa, N. (2002). Lanthanide complexes in multifunctional asymmetric catalysis. *Chem. Rev.* 102, 2187–2210. doi: 10.1021/cr010297z

Silva, P., Fernandes, J. A., and Almeida Paz, F. A. (2010). Catena-poly [[triaquachlorido-μ₃-malonato-cerium(III)] hemihydrate]. *Acta Crystallogr. Sect. E Struct. Rep. Online.* 66, m1514–m1515. doi: 10.1107/S1600536810044727

Sinha, S. P. (2012). *Systematics and the Properties of the Lanthanides.* Dordrecht: Springer Science & Business Media

Sun, Q., Yan, P., Niu, W., Chu, W., Yao, X., An, G., et al. (2015). NIR luminescence of a series of benzoyltrifluoroacetone erbium complexes. *RSC Adv.* 5, 65856–65861. doi: 10.1039/C5RA12954K

Terai, T., Kikuchi, K., Iwasawa, S.-Y., Kawabe, T., Hirata, Y., Urano, Y., et al. (2006). Modulation of luminescence intensity of lanthanide complexes by photoinduced electron transfer and its application to a long-lived protease probe. *J. Am. Chem. Soc.* 128, 6938–6946. doi: 10.1021/ja060729t

Thirumurugan, A., and Natarajan, S. (2004). Inorganic– organic hybrid compounds: synthesis and structures of new metal organic polymers synthesized in the presence of mixed dicarboxylates. *Eur. J. Inorg. Chem.* 2004, 762–770. doi: 10.1002/ejic.200300594

Tian, J., Li, B., Zhang, X., Li, X., Li, X., and Zhang, J. (2013). Three novel 1D lanthanide-carboxylate polymeric complexes: syntheses, crystal structures and magnetic analyses. *Dalton Trans.* 42, 8504–8511. doi: 10.1039/c3dt50782c

Van Vleck, J. (1932). *The Theory of Electronic and Magnetic Susceptibility.* London: Oxford University Press.

Wahsner, J., Gale, E. M., Rodríguez-Rodríguez, A., and Caravan, P. (2019). Chemistry of MRI contrast agents: current challenges and new frontiers. *Chem. Rev.* 119, 957–1057. doi: 10.1021/acs.chemrev.8b00363

Wang, C. G., Xing, Y. H., Li, Z. P., Li, J., Zeng, X. Q., Ge, M. F., et al. (2009). Synthesis, crystal structures and properties of a series of three-dimensional lanthanide coordination polymers with the rigid and flexible mixed dicarboxylate ligands of 1, 4-benzene dicarboxylic acid and succinic acid. *J. Mol. Struct.* 921, 126–131. doi: 10.1016/j.molstruc.2008.12.057

Wenmei, X., Qiguang, W., Lan, Y., and Rudong, Y. (1992). Synthesis, characterization and crystal structure of tri-aquo bimalonate malonate samarium (III) monohydrate. *Polyhedron* 11, 2051–2054. doi: 10.1016/S0277-5387(00)83161-7

Woodruff, D. N., Winpenny, R. E., and Layfield, R. A. (2013). Lanthanide single-molecule magnets. *Chem. Rev.* 113, 5110–5148. doi: 10.1021/cr400018q

Yan, B., Bai, Y., and Chen, Z. (2005). Synthesis, structure and luminescence of novel 1D chain coordination polymers [Ln(isophth)(Hisophth)(H$_2$O)$_4$·4H$_2$O]$_n$ (Ln= Sm, Dy). *J. Mol. Struct.* 741, 141–147. doi: 10.1016/j.molstruc.2005.02.004

Zhang, C. Z., Mao, H. Y., Wang, Y. L., Zhang, H. Y., and Tao, J. C. (2007). Syntheses of two new hybrid metal-organic polymers using flexible aliphatic dicarboxylates and pyrazine: crystal structures and magnetic studies. *J. Phys. Chem. Solids.* 68, 236–242. doi: 10.1016/j.jpcs.2006.11.001

Zhao, B., Chen, X. Y., Cheng, P., Liao, D. Z., Yan, S.-P., and Jiang, Z. H. (2004). Coordination polymers containing 1D channels as selective luminescent probes. *J. Am. Chem. Soc.* 126, 15394–15395. doi: 10.1021/ja047141b

Zhu, W. H., Li, S., Gao, C., Xiong, X., Zhang, Y., Liu, L., et al. (2016). Lanthanide dinuclear complexes constructed from mixed oxygen-donor ligands: the effect of substituent positions of the neutral ligand on the magnetic dynamics in Dy analogues. *Dalton Trans.* 45, 4614–4621. doi: 10.1039/C5DT04850H

Zhuravlev, K. P., Tsaryuk, V. I., Pekareva, I. S., Sokolnicki, J., and Klemenkova, Z. S. (2011). Europium and terbium ortho-, meta-, and para-methoxybenzoates: Structural peculiarities, luminescence, and energy transfer. *J. Photoch. Photobio. A* 219, 139–147. doi: 10.1016/j.jphotochem.2011.02.003

# Synthesis and Structures of Ruthenium Carbonyl Complexes Bearing Pyridine-Alkoxide Ligands and Their Catalytic Activity in Alcohol Oxidation

*Xinlong Yan[†], Xiaohui Yue[†], Kang Liu, Zhiqiang Hao\*, Zhangang Han and Jin Lin\**

*Hebei Key Laboratory of Organic Functional Molecules, College of Chemistry and Material Science, Hebei Normal University, Shijiazhuang, China*

Reaction of $Ru_3(CO)_{12}$ with two equiv of 6-bromopyridine alcohols 6-bromopyCHROH [(R = $C_6H_5$ (**L1**); R = $4-CH_3C_6H_4$ (**L2**); R = $4-OMeC_6H_4$ (**L3**); R = $4-ClC_6H_4$ (**L4**); (R = $4-CF_3C_6H_4$ (**L5**); R = $2-OMeC_6H_4$ (**L6**); R = $2-CF_3C_6H_4$ (**L7**)] and 6-bromopyC(Me)$_2$OH (**L8**) in refluxing xylene afforded novel trinuclear ruthenium complexes [6-bromopyCHRO]$_2$Ru$_3$(CO)$_8$ (**1a-1g**) and [6-bromopyC(Me)$_2$O]$_2$Ru$_3$(CO)$_8$ (**1h**). These complexes were characterized by FT-IR and NMR spectroscopy as well as elemental analysis. The structures of all the complexes were further confirmed by X-ray crystallographic analysis. In the presence of *tert*-butyl hydroperoxide (TBHP) as the source of oxidant, complexes **1a**-**1h** displayed high catalytic activities for oxidation of primary and secondary alcohols and most of oxidation reactions could be completed within 1 h at room temperature.

Keywords: ruthenium carbonyl complexes, alcohols oxidation, *t*-butyl hydroperoxide, pyridine alcohols, chemoselectivity

## INTRODUCTION

As a class of common starting materials, alcohols can beeasily converted into a variety of useful compounds via organic synthesis methods (Salvatore et al., 2001; Crabtree, 2017). Among all transfer strategies, oxidation of alcohols into their corresponding carbonyl compounds is one of the fundamental and important chemical reactions (Sheldon et al., 2000, 2002; Mallat and Baiker, 2004; Vazylyev et al., 2005; Parmeggiani and Cardona, 2012; Cao et al., 2014; Wang et al., 2017) and the oxidation products, including aldehydes, ketones and carboxylic acids, are important building blocks for synthesis of pharmaceuticals and fine chemicals (Caron et al., 2006; Bianchini and Shen, 2009; Simon and Li, 2012; Balaraman et al., 2013). Conventional oxidation methods to access these compounds usually require stoichiometric amounts of inorganic oxidants, such as chromium(VI) compounds (Canielli and Cardillo, 1984; Tojo and Fernández, 2007), hypervalent iodine reagents (Uyanik and Ishihara, 2009) or radical oxidants i.e., *N*-methylmorpholine-*N*-oxide (NMO) (Kumar et al., 2007; Gunasekaran et al., 2011; Saleem et al., 2013), 2,2,6,6-tetramethyl-1-piperidinyloxyl (TEMPO) (Dijksman et al., 2001; Wang et al., 2008; Allen et al., 2013). Such reactions often result in the generation of numerous wastes which caused serious environment problems. To ease this issue, great efforts have been devoted to the development of atom-economic and green methods.

Molecular oxygen is one of the green oxidants and the $H_2O$ is the only by-product (Punniyamurthy et al., 2005). But in most aerobic alcohol oxidation systems, the additives e.g., TEMPO and large amounts of base are also needed, which makes the reaction system more complicated (Wang et al., 2005; Kumpulainen and Koskinen, 2009; Hoover et al., 2012). In addition, $H_2O_2$ is also used as an environmentally benign oxidant (Campestrini et al., 2004; Zhou et al., 2013; Ren et al., 2015; Vermaak et al., 2018). However, due to its limited oxidation capacity, the catalytic system should be assisted by carboxylic acid or $H_2SO_4$ as an additive to achieve a high efficiency (Dai et al., 2015; Miao et al., 2017). Compared with above oxidants, *tert*-butyl hydroperoxide (TBHP) is an alternative suitable oxidant and widely used in oxidation reactions, particularly in olefin epoxidation (Chen and Luck, 2016; Kashani et al., 2018) and C–H bond oxidation (Murahashi et al., 2000; Kudrik and Sorokin, 2017; Sarma et al., 2018). There are also some successful examples of using TBHP as an external oxidant in alcohol oxidation (Sarkar et al., 2014; Annunziata et al., 2018; Borah et al., 2018). In spite of this progress, less attention has been paid to this research area. Therefore, it is in an urgent demand to develop mild and efficient oxidation systems using TBHP as an oxidant.

It is well-known that transition metal complexes play a crucial role in oxidation process. Many transition metal catalysts including ruthenium (Shapley et al., 2000; Lybaert et al., 2017; Sarbajna et al., 2017; Moore et al., 2019), palladium (Stahl, 2004; Sigman and Jensen, 2006; Ho et al., 2018), copper (Velusamy et al., 2006; Jehdaramarn et al., 2018; Lagerspets et al., 2019), and iron (Coleman et al., 2010; Stanje et al., 2018) have been reported for promoting the oxidation of alcohols. Among them, ruthenium compounds are intensively studied because of their rich structures and various valence states. For example, Ramesh and co-workers reported that ruthenium(II) carbonyl 2-(arylazo)phenolate complexes could oxidize sensitive group-contained alcohols with moderate to high conversion (Kumar et al., 2007). The group of Zhang synthesized several ruthenium complexes containing 2-(biphenylazo)phenolate ligands that successfully achieved high catalytic activity in the presence of NMO without diminishing chemoselectivity (Tang et al., 2018). However, very few examples were focused on di-or tri-nuclear ruthenium complexes and their applications in organic reactions were limited. Recently, we have reported a series of triruthenium carbonyl complexes and their efficient oxidation behavior toward secondary alcohols, while these Ru compounds showed poor reactivity in oxidation of primary alcohols (Hao et al., 2018a,b, 2019). As part of our continuing efforts in developing novel ruthenium carbonyl complexes and their applications in alcohol oxidation, herein, we reported the synthesis and characterization of several ruthenium carbonyl complexes supported by pyridine-alkoxide ligands and their catalytic properties in the oxidation of primary and secondary alcohols using TBHP as an oxidant.

# EXPERIMENTAL

## Materials and Methods

All manipulations were performed under a nitrogen atmosphere using standard Schlenk techniques. Solvents for reaction were distilled from appropriate drying agents under $N_2$ before use. All the chemical reagents were purchased from commercial sources. $Ru_3(CO)_{12}$ was prepared by literature methods (Fauré et al., 2003). NMR spectra were measured using a Bruker Avance III-500 NMR spectrometer at room temperature with TMS as internal standard. Melting points were determined using an SGW X-4A Digital Melting Point Apparatus. IR spectra were recorded as KBr disks on a Thermo Fisher iS 50 spectrometer in the range 4,000–600 $cm^{-1}$ and elemental analyses were performed on a Vario EL III analyzer.

## Preparation of 6-bromopyCH(2-CF$_3$C$_6$H$_4$)OH (L7)

To a dried $Et_2O$ (30 mL) of 2, 6-dibromopyridine (3.55 g, 15 mmol) at $-78°C$, *n*-BuLi (9.5 mL, 15 mmol) was added dropwise via a syringe in 10 min and the solution was stirred at $-78°C$ for 1 h. After addition of 2-(trifluoromethy)benzaldehyde (2.61 g, 15 mmol), the mixture was allowed to warm to room temperature and stirred overnight. The reaction solution was neutralized with aqueous $NH_4Cl$ and the organic phase was separated. The aqueous layer was extracted with $CH_2Cl_2$ (3 × 10 mL), and combined organic fractions were dried over $MgSO_4$ and the residue was placed in an $Al_2O_3$ column with ethyl acetate/petroleum ether as an eluent to give **L7** as a off-white powders (2.04 g, 46%). $^1H$ NMR ($CDCl_3$, 500 MHz, 298 K): δ 7.69 (d, *J* = 7.9 Hz, 1 H, Py-H), 7.53 (t, *J* = 7.7 Hz, 1 H, Py-H), 7.45–7.49 (m, 2 H, $C_6H_4$), 7.41 (d, *J* = 8.2 Hz, 2 H, $C_6H_4$), 6.96



**SCHEME 1 |** Synthetic routes of Ru complexes.
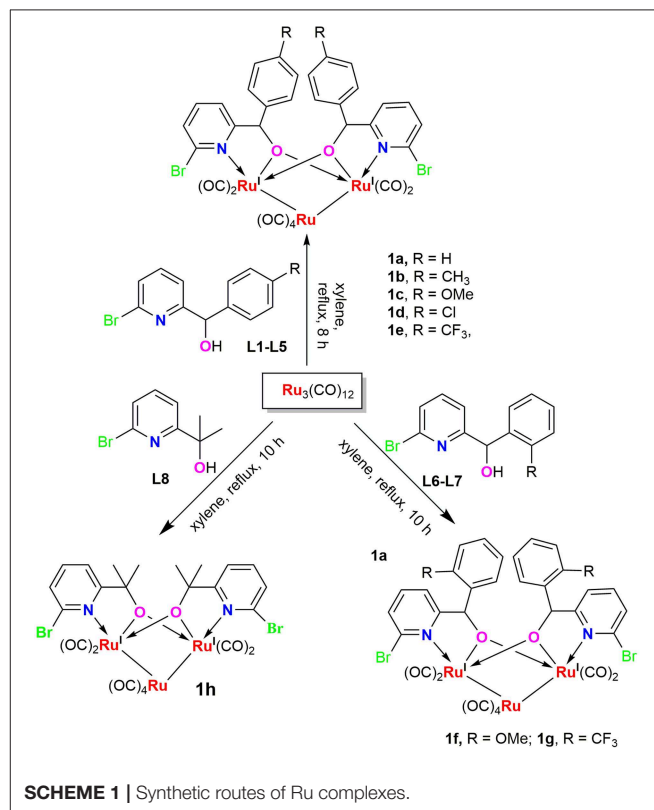
(d, $J = 7.7$ Hz, 1 H, Py-H), 6.15 (s, 1 H, CH), 4.93 (s, 1 H, OH). $^{13}$C NMR (CDCl$_3$, 125 MHz, 298 K): δ 161.9, 141.1, 140.8, 139.5, 132.6, 129.9, 128.4, 128.2, 127.2, 125.5 (q, $J_{C-F} = 5.5$ Hz), 123.1 (q, $J_{C-F} = 272$ Hz), 120.6, 69.5 ppm.

## Preparation of (6-bromopyCHC$_6$H$_5$O)$_2$Ru$_3$(CO)$_8$ (1a)

A solution of ligand precursor **L1** (0.248 g, 0.938 mmol) and Ru$_3$(CO)$_{12}$ (0.300 g, 0.469 mmol) in 30 mL of xylene was refluxed for 10 h. After evaporation of the solvent in vacuo, the residue was placed in an Al$_2$O$_3$ column. Elution with ethyl acetate/petroleum ether gave **1a** as orange crystals (yield 0.307 g, 62%). Mp: 168–169°C. Anal. Calc. for C$_{32}$H$_{18}$Br$_2$N$_2$O$_{10}$Ru$_3$: C, 36.48; H, 1.72; N, 2.66. Found (%): C, 36.30; H, 1.85; N, 2.71. $^1$H NMR (CDCl$_3$, 500 MHz, 298 K): δ 7.61 (d, $J = 7.7$ Hz, 2 H, Py-H), 7.25–7.29 (m, 8 H, Py-H, C$_6$H$_4$), 7.15 (d, $J = 6.5$ Hz, 4 H, C$_6$H$_4$), 6.62 (d, $J = 7.7$ Hz, 2 H, Py-H), 5.58 (s, 2 H, CH) ppm. $^{13}$C NMR (CDCl$_3$, 125 MHz, 298 K): δ 205.9, 202.9, 200.8, 190.1, 170.8, 144.8, 143.4, 138.2, 128.7, 128.4, 128.3, 128.0, 120.0, 91.7 ppm. IR (υ$_{CO}$, KBr, cm$^{-1}$): 2081(s), 2015(s), 1998(vs), 1909(s).

## Preparation of [6-bromopyCH(4-MeC$_6$H$_4$O)]$_2$Ru$_3$(CO)$_8$ (1b)

Complex **1b** was prepared in a similar procedure to that described above for preparation of **1a**. Reaction of **L2** (0.261 g, 0.938 mmol) with Ru$_3$(CO)$_{12}$ (0.300 g, 0.469 mmol) in 30 mL of xylene generated complex **1b** as orange crystals (yield 0.358 g, 70%). Mp: 173–175°C. Anal. Calc. for C$_{34}$H$_{22}$Br$_2$N$_2$O$_{10}$Ru$_3$: C, 37.76; H, 2.05 N, 2.59. Found (%): C, 37.91; H, 2.19, N, 2.45. $^1$H NMR (CDCl$_3$, 500 MHz, 298 K): δ 7.60 (d, $J = 7.7$ Hz, 2 H, Py-H), 7.26 (t, $J = 7.7$ Hz, 2 H, Py-H), 7.09 (d, $J = 7.9$ Hz, 4 H, C$_6$H$_4$), 7.04 (d, $J = 8.0$ Hz, 4 H, C$_6$H$_4$), 6.60 (d, $J = 7.7$ Hz, 2 H, Py-H), 5.54 (s, 2 H, CH), 2.30 (s, 6 H, CH$_3$) ppm. $^{13}$C NMR (CDCl$_3$, 125 MHz, 298 K): δ 206.0, 203.0, 200.9, 190.2, 171.0, 144.7, 140.5, 138.1, 138.0, 129.3, 128.2, 127.9, 119.9, 91.5, 21.4 ppm. IR (υ$_{CO}$, KBr, cm$^{-1}$): 2085(s), 2015(s), 2000(s), 1909(s).
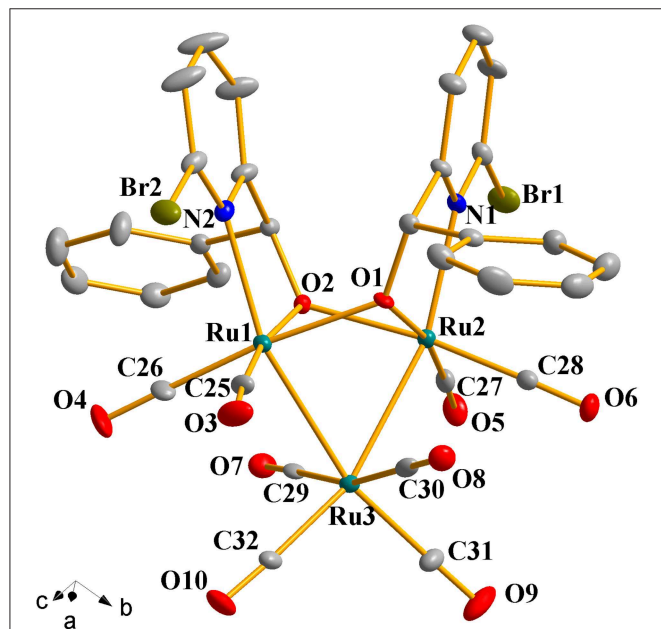


**FIGURE 1 |** Perspective view of **1a** with thermal ellipsoids are drawn at the 30% probability level. Hydrogens have been omitted for clarity. The selected bond lengths (Å) and angles (°): Ru(1)-Ru(3) 2.7743(10), Ru(2)-Ru(3) 2.7625(10), Ru(1)-O(1) 2.140(5), Ru(2)-O(1) 2.084(6), Ru(1)-N(2) 2.237(7), Ru(2)-N(1) 2.252(7); N(2)-Ru(1)-Ru(3) 157.9(2), N(2)-Ru(1)-Ru(2) 102.2(2), Ru(2)-O(1)-Ru(1) 91.4(2), Ru(1)-O(2)-Ru(2) 91.1(2), Ru(2)-Ru(3)-Ru(1) 66.20(3).



**FIGURE 2 |** Perspective view of **1c** with thermal ellipsoids are drawn at the 30% probability level. Hydrogens and solvent have been omitted for clarity. The selected bond lengths (Å) and angles (°): Ru(1)-O(1) 2.083(3), Ru(2)-O(1) 2.132(3), Ru(1)-Ru(3) 2.7649(5), Ru(2)-Ru(3) 2.7552(5), Ru(1)-N(1) 2.258(4), Ru(2)-N(2) 2.240(4); Ru(2)-O(1)-Ru(2) 92.33(12), Ru(2)-O(3)-Ru(1) 92.00(12), N(1)-Ru(1)-Ru(3) 157.10(10), N(2)-Ru(2)-Ru(3) 157.01(12), Ru(2)-Ru(3)-Ru(1) 66.848(15).



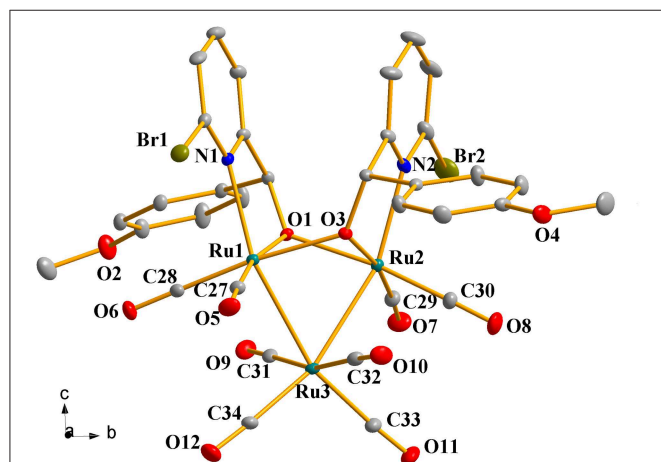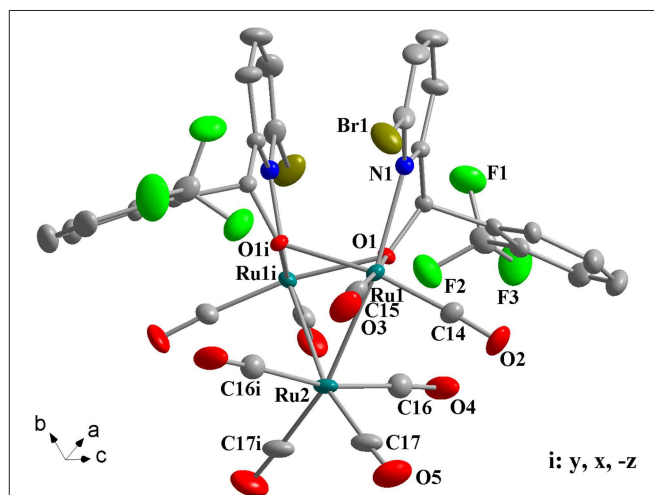**FIGURE 3 |** Perspective view of **1g** with thermal ellipsoids are drawn at the 30% probability level. Hydrogens have been omitted for clarity. The selected bond lengths (Å) and angles (°): Ru(1)-O(1) 2.089(4), Ru(1)-O(1i) 2.147(4), Ru(1)-N(1) 2.313(5), Ru(2)-Ru(1) 2.7560(7), Ru(2)-Ru(1i) 2.7560(7), Ru(1)-O(1)-Ru(1i) 92.06(15), N(1)-Ru(1)-Ru(1i) 97.72(13), Ru(1)-Ru(2)-Ru(1i) 67.17(2).

## Preparation of [6-bromopyCH(4-OMeC$_6$H$_4$O)]$_2$Ru$_3$(CO)$_8$ (1c)

Complex **1c** was prepared in a similar procedure to that described above for preparation of **1a**. Reaction of **L3** (0.276 g, 0.938 mmol) with Ru$_3$(CO)$_{12}$ (0.300 g, 0.469 mmol) in 30 ml of xylene generated complex **1c** as orange crystals (yield 0.337 g, 65%). Mp: 176–177°C. Anal. Calc. for C$_{34}$H$_{22}$Br$_2$N$_2$O$_{12}$Ru$_3$: C, 36.67; H, 1.99, N, 2.52. Found (%): C, 36.53; H, 2.10, N, 2.44. $^1$H NMR (CDCl$_3$, 500 MHz, 298 K): δ 7.59 (d, $J = 7.7$ Hz, 2 H, Py-H), 7.26 (t, $J = 7.7$ Hz, 2 H, Py-H), 7.07 (d, $J = 8.6$ Hz, 4 H, C$_6$H$_4$), 6.81 (d, $J = 8.6$ Hz, 4 H, C$_6$H$_4$), 6.60 (d, $J = 7.7$ Hz, 2 H, Py-H), 5.55 (s, 2 H, CH), 3.76 (s, 6H, OCH$_3$) ppm. $^{13}$C NMR (CDCl$_3$, 125 MHz, 298 K): δ 206.0, 203.0, 200.9, 190.2 171.1, 159.6, 144.7, 138.1, 135.9, 129.3, 128.2, 120.0, 114.1, 91.2, 55.4 ppm. IR (υ$_{CO}$, KBr, cm$^{-1}$): 2078(s), 2004(s), 1993(vs), 1912(s).

## Preparation of [6-bromopyCH(4-ClC$_6$H$_4$O)]$_2$Ru$_3$(CO)$_8$ (1d)

Complex **1d** was prepared in a similar procedure to that described above for preparation of **1a**. Reaction of **L4** (0.281 g, 0.938 mmol) with Ru$_3$(CO)$_{12}$ (0.300 g, 0.469 mmol) in 30 mL of

xylene generated complex **1d** as orange crystals (yield 0.267 g, 51%). Mp: 182–183°C. Anal. Calc. for C$_{32}$H$_{16}$Br$_2$Cl$_2$N$_2$O$_{10}$Ru$_3$: C, 34.24; H, 1.44, N, 2.50. Found (%): C, 34.34; H, 1.52, N, 2.48. $^1$H NMR (CDCl$_3$, 500 MHz, 298 K): δ 7.64 (d, $J = 7.5$ Hz, 2 H, Py-H), 7.31 (t, $J = 7.7$ Hz, 2 H, Py-H), 7.29 (d, $J = 8.3$ Hz, 4 H, C$_6$H$_4$), 7.08 (d, $J = 8.3$ Hz, 4 H, C$_6$H$_4$), 6.61 (d, $J = 7.7$ Hz, 2 H, Py-H), 5.54 (s, 2 H, CH) ppm. $^{13}$C NMR (CDCl$_3$, 125 MHz, 298 K): δ 205.8, 202.8, 200.9,189.7, 170.1,144.9, 141.8, 138.3, 134.2, 129.3, 129.0, 128.6, 119.9, 90.9 ppm. IR (υ$_{CO}$, KBr, cm$^{-1}$): 2084(s), 2012(s), 1998(s), 1915(s).

## Preparation of [6-bromopyCH(4-CF$_3$C$_6$H$_4$O)]$_2$Ru$_3$(CO)$_8$ (1e)
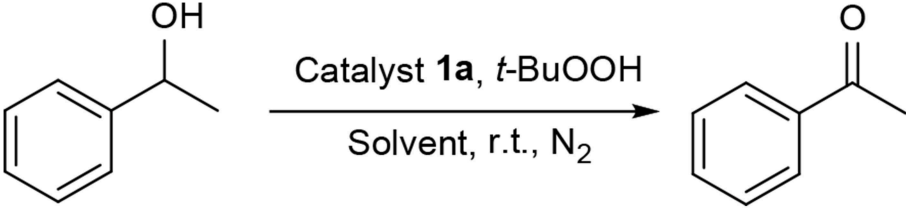
Complex **1e** was prepared in a similar procedure to that described above for preparation of **1a**. Reaction of **L5** (0.339 g, 0.938 mmol) with Ru$_3$(CO)$_{12}$ (0.300 g, 0.469 mmol) in 30 mL of xylene generated complex **1e** as orange crystals (yield 0.267 g, 48%). Mp: 177–179°C. Anal. Calc. for C$_{34}$H$_{16}$Br$_2$F$_6$N$_2$O$_{10}$Ru$_3$: C, 34.33; H, 1.36, N, 2.36. Found (%): C, 34.44; H, 1.30, N, 2.43. $^1$H NMR (CDCl$_3$, 500 MHz, 298 K): δ 7.67 (d, $J = 7.7$ Hz, 2 H, Py-H), 7.57 (d, $J = 8.1$ Hz, 4 H, C$_6$H$_4$), 7.35 (t, $J = 7.8$ Hz, 2 H, Py-H), 7.29

**TABLE 1 |** Oxidation of 1-phenylethanol catalyzed by complex 1a under various conditions[a].



| Entry | Cat. (mol%) | TBHP (mmol) | Solvent | Yield[b] (%) | TOF[c] (h$^{-1}$) |
|---|---|---|---|---|---|
| 1 | 1.0 | 2.0 | Toluene | 64 | 113 |
| 2 | 1.0 | 2.0 | Acetone | 77 | 120 |
| 3 | 1.0 | 2.0 | CH$_3$CN | 85 | 138 |
| 4 | 1.0 | 2.0 | CH$_2$Cl$_2$ | 53 | 69 |
| 5 | 1.0 | 2.0 | THF | 44 | 60 |
| 6 | 1.0 | 2.0 | Dioxide | 40 | 31 |
| 7 | 2.0 | 2.0 | CH$_3$CN | 88 | 90 |
| 8 | 1.5 | 2.0 | CH$_3$CN | 86 | 102 |
| 9 | 0.5 | 2.0 | CH$_3$CN | 85 | 228 |
| 10 | 0.5 | 1.0 | CH$_3$CN | 80 | 129 |
| 11 | 0.5 | 1.5 | CH$_3$CN | 84 | 164 |
| 12 | 0.5 | 2.5 | CH$_3$CN | 90 | 240 |
| 13 | 0.5 | 3.0 | CH$_3$CN | 91 | 257 |
| 14[d] | 0.5 | 2.5 | CH$_3$CN | 72 | 206 |
| 15[e] | 0.5 | 2.5 | CH$_3$CN | 54 | 72 |
| 16 | – | 2.5 | CH$_3$CN | Trace | – |
| 17 | 0.5 | – | CH$_3$CN | – | – |

[a] *Reaction conditions: 1-phenylethanol (1.0 mmol), solvent (2.0 mL), reaction time 1 h.*
[b] *Yield was determined by GC.*
[c] *TOF was calculated at 30% conversion of 1-phenylethanol.*
[d] *T = 50°C.*
[e] *T = 80°C.*

(d, $J = 8.0$ Hz, 4 H, $C_6H_4$), 6.64 (d, $J = 7.6$ Hz, 2 H, Py-H), 5.61 (s, 2 H, CH) ppm. $^{13}$C NMR (CDCl$_3$, 125 MHz, 298 K): δ 205.6, 202.7, 200.9, 189.5, 169.7, 146.9, 145.0, 138.5, 130.7, 128.9, 128.2, 125.8 (q, $J_{C-F} = 2.7$ Hz), 123.1 (q, $J_{C-F} = 270.5$ Hz), 120.0, 91.1 ppm. IR ($\upsilon_{CO}$, KBr, cm$^{-1}$): 2083(s), 2017(s), 1993(s), 1912(s).

## Preparation of [6-bromopyCH(2-OMeC$_6$H$_4$O)]$_2$Ru$_3$(CO)$_8$ (1f)

Complex **1f** was prepared in a similar procedure to that described above for preparation of **1a**. Reaction of **L6** (0.276 g, 0.938 mmol) with Ru$_3$(CO)$_{12}$ (0.300 g, 0.469 mmol) in 30 mL of xylene generated complex **1f** as orange crystals (yield 0.298 g, 57%). Mp:
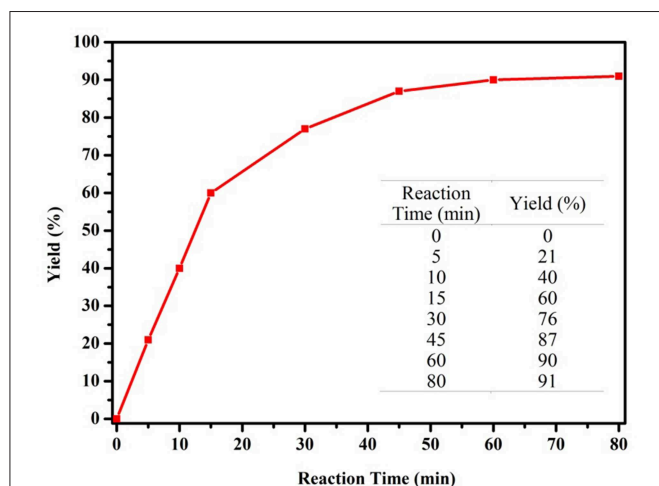


**FIGURE 4** | Influence of the reaction time on catalytic performance of complex **1a** (1-phenylethanol 1.0 mmol, complex **1a** 0.5 mol%, TBHP 2.5 mmol, CH$_3$CN 2.0 mL).

**TABLE 2** | Comparison of catalytic activity of Ru complexes[a].



| Entry | Catalyst | TBHP (mmol) | Solvent | Yield[b] (%) | TOF[c] (h$^{-1}$) |
|---|---|---|---|---|---|
| 1 | **1a** | 2.5 | CH$_3$CN | 91 | 240 |
| 2 | **1b** | 2.5 | CH$_3$CN | 93 | 273 |
| 3 | **1c** | 2.5 | CH$_3$CN | 96 | 281 |
| 4 | **1d** | 2.5 | CH$_3$CN | 87 | 228 |
| 5 | **1e** | 2.5 | CH$_3$CN | 85 | 220 |
| 6 | **1f** | 2.5 | CH$_3$CN | 90 | 243 |
| 7 | **1g** | 2.5 | CH$_3$CN | 74 | 210 |
| 8 | **1h** | 2.5 | CH$_3$CN | 92 | 256 |
| 9 | Ru$_3$(CO)$_{12}$ | 2.5 | CH$_3$CN | 30 | – |

[a]*Reaction conditions: 1-phenylethanol (1.0 mmol), catalyst (0.5 mol%), solvent (2.0 mL), reaction time 1 h.*
[b]*Yield was determined by GC.*
[c]*TOF was calculated at 30% conversion of 1-phenylethanol.*

183–184°C. Anal. Calc. for $C_{34}H_{22}Br_2N_2O_{12}Ru_3$: C, 36.67; H, 1.99, N, 2.52. Found (%): C, 36.75; H, 2.12, N, 2.45. $^1$H NMR (CDCl$_3$, 500 MHz, 298 K): δ 7.59 (d, $J = 7.7$ Hz, 2 H, Py-H), 7.24–7.19 (m, 4 H, $C_6H_4$, Py-H), 6.85 (d, $J = 8.2$ Hz, 2 H, $C_6H_4$), 6.76 (t, $J = 7.4$ Hz, 2 H, $C_6H_4$), 6.61 (d, $J = 7.6$ Hz, 2 H, Py-H), 6.50 (d, $J = 7.5$ Hz, 2 H, $C_6H_4$), 6.04 (s, 2 H, CH), 3.94 (s, 6 H, OCH$_3$) ppm. $^{13}$C NMR (CDCl$_3$, 125 MHz, 298 K): δ 206.2, 203.1, 201.1, 190.7, 171.2, 157.3, 144.9, 138.0, 131.7, 129.4, 128.3, 128.1, 120.0, 119.2, 110.3, 84.9, 55.2 ppm. IR ($\upsilon_{CO}$, KBr, cm$^{-1}$): 2086 (s), 2020 (vs), 1995 (s), 1960 (s), 1905 (s).

## Preparation of [6-bromopyCH(2-CF$_3$C$_6$H$_4$O)]$_2$Ru$_3$(CO)$_8$ (1g)

Complex **1g** was prepared in a similar procedure to that described above for preparation of **1a**. Reaction of **L7** (0.339 g, 0.938 mmol) with Ru$_3$(CO)$_{12}$ (0.300 g, 0.469 mmol) in 30 mL of xylene generated complex **1g** as orange crystals (yield 0.212 g, 38%). Mp: 186–188°C. Anal. Calc. for $C_{34}H_{16}Br_2F_6N_2O_{10}Ru_3$: C, 34.33; H, 1.36, N, 2.36. Found (%): C, 34.25; H, 1.41, N, 2.43. $^1$H NMR (CDCl$_3$, 500 MHz, 298 K): δ 7.69 (d, $J = 7.8$ Hz, 2 H, Py-H), 7.62 (d, $J = 7.9$ Hz, 2 H, $C_6H_4$), 7.43 (t, $J = 7.6$ Hz, 2 H, Py-H), 7.35–7.30 (m, 6 H, $C_6H_4$), 6.51 (d, $J = 7.7$ Hz, 2 H, Py-H), 5.61 (s, 2 H, CH) ppm. $^{13}$C NMR (CDCl$_3$, 125 MHz, 298 K): δ 204.9, 203.1, 200.8, 190.0, 169.9, 145.3, 141.9, 138.5, 132.3, 129.9, 128.7, 127.9, 126.4, 125.7 (q, $J_{C-F} = 4.6$ Hz), 123.0 (q, $J_{C-F} = 273.8$ Hz), 119.8, 85.5 ppm. IR ($\upsilon_{CO}$, KBr, cm$^{-1}$): 2089(m), 2022(s), 2001(s), 1969(s), 1914(s).
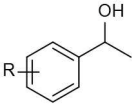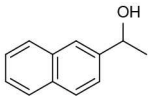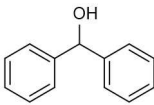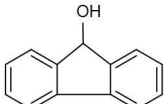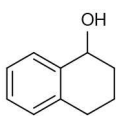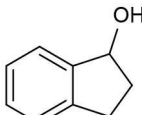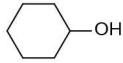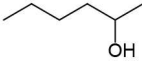
## Preparation of [6-bromopyCH(Me)$_2$O]$_2$Ru$_3$(CO)$_8$ (1h)

Complex **1h** was prepared in a similar procedure to that described above for preparation of **1a**. Reaction of **L8** (0.202 g, 0.938 mmol) with Ru$_3$(CO)$_{12}$ (0.300 g, 0.469 mmol) in 30 mL of xylene generated complex **1h** as orange crystals (yield 0.305 g, 68%). Mp: 171–172°C. Anal. Calc. for $C_{24}H_{18}Br_2N_2O_{10}Ru_3$: C, 30.11; H, 1.89; N, 2.93. Found (%): C, 30.25; H, 1.99; N, 2.81. $^1$H NMR (CDCl$_3$, 500 MHz, 298 K): δ 7.51 (d, $J = 7.6$ Hz, 2 H, Py-H), 7.41 (t, $J = 7.7$ Hz, 2 H, Py-H), 6.89 (d, $J = 7.6$ Hz, 2 H, Py-H), 1.37 (s, 6 H, CH$_3$), 1.18 (s, 6 H, CH$_3$) ppm. $^{13}$C NMR (CDCl$_3$, 125 MHz, 298 K) δ 206.9, 202.9, 202.7, 191.0, 175.7, 145.6, 138.8, 128.2, 118.7, 87.7, 34.7, 31.1 ppm. IR ($\upsilon_{CO}$, KBr, cm$^{-1}$): 2080(s), 2007(s), 1966(s), 1906(s).

## General Procedure for Catalytic Oxidation of Alcohols

An alcohol substrate (1.0 mmol), complex **1c** (0.005 mmol) and TBHP (2.5 mmol) was placed in a 2-neck 25 mL round bottom flask and degassed 2 times. Two millili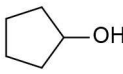ter of dried CH$_3$CN was then added and the resulting mixture was reacted at room temperature for 1 h under an N$_2$ atmosphere. After the reaction was complete, the solvent was removed under reduced pressure and the residue was purified by Al$_2$O$_3$ column chromatography (eluent ethylacetate/petroleum ether v/v = 1/15) to afford the desired product, which was identified by comparison with the authentic sample through NMR and GC analyses.

**TABLE 3 |** Oxidation of various of secondary alcohols to ketones catalyzed by 1c[a].



| Entry | Alcohol | Conv.[b] (%) | Yield[c] (%) | TOF[d] (h$^{-1}$) |
|-------|---------|--------------|--------------|--------------------|
| |  | | | |
| 1 | R = 4-Me | 96 | 92 | 286 |
| 2 | R = 3-Me | 99 | 93 | 290 |
| 3 | R = 4-OMe | 97 | 94 | 305 |
| 4 | R = 4-Cl | 96 | 93 | 270 |
| 5 | R = 4-Br | 94 | 90 | 256 |
| 6 | R = 3-Br | 91 | 85 | 250 |
| 7 | R = 4-CF$_3$ | 90 | 87 | 243 |
| 8 |  | 96 | 90 | 285 |
| 9 |  | 97 | 91 | 275 |
| 10 |  | 99 | 96 | 292 |
| 11 |  | 97 | 93 | 274 |
| 12 |  | 98 | 92 | 280 |
| 13[e] |  | 94 | 90 | 88 |
| 14[e] |  | 92 | 88 | 85 |
| 15[e] |  | 91 | 90 | 80 |

*(Continued)*

**TABLE 3 |** Continued

| Entry | Alcohol | Conv.[b] (%) | Yield[c] (%) | TOF[d] (h$^{-1}$) |
|---|---|---|---|---|
| 16[e] | (structure: OH on a secondary carbon of a hexyl chain) | 93 | 91 | 81 |

[a] *Reaction conditions: alcohol (1.0 mmol), catalyst 1c (0.5 mol%), solvent (2.0 mL).*
[b] *Conversion was determined by GC.*
[c] *Isolated yields.*
[d] *TOF was calculated at 30% conversion of alcohol.*
[e] *Reaction time 3 h, yield was determined by GC.*

## Crystal Structural Determination

Single crystals of complexes **1a-1h** suitable for X-ray crystal structural analysis were obtained from a $CH_2Cl_2/n$-hexane mixed solvent system. Data collection was performed on a Bruker SMART 1000 diffractometer, using graphite-monochromated Mo-K radiation ($\omega$-$\varphi$ scans, $\lambda = 0.71073$ Å). The structures were solved by direct methods and refined by full-matrix least squares. All calculations were using SHELXTL crystallographic software packages (Sheldrick, 1997). The crystal data and summary of X-ray data collection are presented in **Tables S2, S3**.

## RESULTS AND DISCUSSION

### Synthesis of Ligands and Ruthenium Complexes

6-bromopyridine alcohol ligands **L1**-**L6 and L8** were synthesized according to the literature procedure (Tsukahara et al., 1997; Song and Morris, 2004) and identified by NMR and elemental analysis prior to use. **L7** was synthesized following similar methods. 2,6-Dibromopyridine reacted with *n*-BuLi and 1 equiv of *o*-substituted aldehydes was added to the reaction mixture, then hydrolysis led to the target ligand.

Ruthenium clusters were prepared in moderate to high yields from $Ru_3(CO)_{12}$ by treating with 2.0 equiv of ligands **L1**-**L8** in refluxing xylene, respectively. The general synthetic route for these new compounds is depicted in **Scheme 1**. These trinuclear Ru complexes were identified by FI-IR, NMR spectroscopy and elemental analysis. The FT-IR spectra of all the complexes exhibit several absorption peaks around 1906–1950 cm$^{-1}$, which can be assigned to the characteristic stretching vibration of the terminally coordinated CO. In the $^1$H NMR spectra of **1a-1g**, the characteristic signal of –OH disappeared and the singlets resonance for the methyne adjacent to oxygen were observed at 5.5–6.1 ppm, which were shifted upfield when compared to those in the free ligands (L1-L7). In the $^{13}$C NMR spectra, the resonance signals around 85–92 ppm correspond to the methynes mentioned above, which are in good accordance with compound $[pyC(Me)_2O]_2Ru_3(CO)_8$ ($\delta$ 87.6 ppm) and $[pyCHC_6H_5O]_2Ru_3(CO)_8$ ($\delta$ 89.3 ppm), which were previously reported in the literature (Hao et al., 2018b).

### Crystal Structures of Complexes 1a-1h

Complexes **1a-1h** were further characterized by X-ray crystallography. The molecular structures of **1a**, **1c**, and **1g**

**TABLE 4 |** Oxidation of various primary alcohols to aldehydes catalyzed by 1c[a].

| Entry | Alcohol | Conv.[b] (%) | Yield[c] (%) | TOF[d] (h$^{-1}$) |
|---|---|---|---|---|
| 1 | R = H | 94 | 88 | 279 |
| 2 | R = 4-Me | 95 | 90 | 286 |
| 3 | R = 3-Me | 97 | 90 | 290 |
| 4 | R = 4-OMe | 99 | 93 | 302 |
| 5 | R = 4-Cl | 94 | 85 | 271 |
| 6 | R = 4-Br | 95 | 90 | 276 |
| 7 | R = 4-NO$_2$ | 97 | 91 | 277 |
| 8 | (2-naphthylmethanol) | 98 | 92 | 300 |
| 9 | (cinnamyl alcohol) | 95 | 90 | 287 |
| 10[e] | (furfuryl alcohol) | 87 | 82 | 88 |
| 11[e] | (2-thiophenemethanol) | 89 | 85 | 92 |
| 12[e] | (2-pyridinemethanol) | 84 | 81 | 83 |

[a] *Reaction conditions: alcohol (1.0 mmol), catalyst 1c (0.5 mol%), solvent (2.0 mL).*
[b] *Conversion was determined by GC.*
[c] *Isolated yields.*
[d] *TOF was calculated at 30% conversion of alcohol.*
[e] *1.5 mol% of 1c was used.*

are shown in **Figures 1–3** with selected bond lengths and angles, respectively. Those of **1b**, **1d-1f**, and **1h** are shown in **Figures S1–S5**, respectively. Details of the structural parameters are also given in **Tables S2, S3**. X-ray diffraction analysis shows that all the complexes **1a-1h** are trinuclear ruthenium clusters accompanied by two pyridylalkoxo ligands simultaneously via their pyridyl N and hydroxy O atoms. Three Ru atoms adopt a pseudooctahedral coordinated mode. The unit cell of **1a**
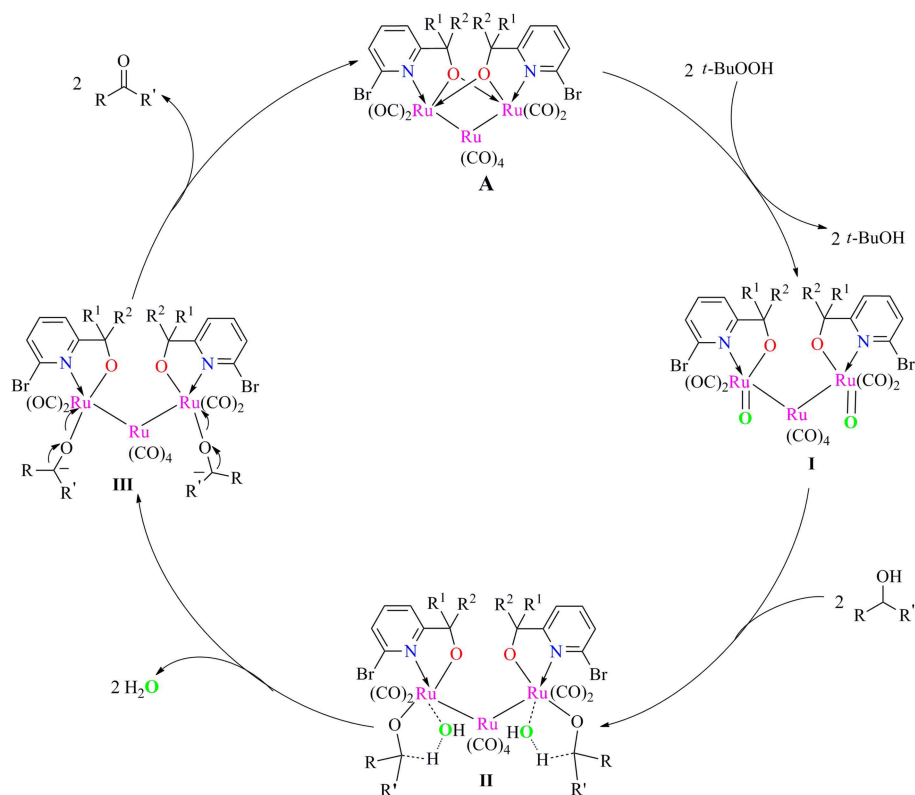
**SCHEME 2** | Proposed mechanism for alcohol oxidation catalyzed by Ru/TBHP system.

contains two crystallographically-independent molecules which possess similar connectivity and only one molecular structure is depicted in **Figure 1** for clarity. In complexes **1a-1h**, the distances between the two Ru atoms directly connected to the ligands are in the range of 3.0236(10)-3.0516(10) Å, which are comparable to the Ru–Ru bond distances in complexes $(\mu\text{-OC}_6\text{H}_4\text{OMe-2})_2\text{Ru}_3(\text{CO})_8$ (3.012(1) Å) (Santini et al., 1987) and $[\text{PyCH}=\text{C(Ph)O}]_2\text{Ru}_3(\text{CO})_8$ (3.0693(6) Å) (Ma et al., 2017). The bond lengths of Ru(1)–N(1) varying from 2.252(7) Å to 2.330(14) Å observed in all complexes are slightly longer than those Ru–N bond lengths found in complexes $\{\mu_2\text{-}\mu^5\text{:}\eta^1\text{-}(\text{C}_5\text{H}_4\text{N})(\text{C}_9\text{H}_5)\}\text{Ru}_3(\text{CO})_9$ [2.164(3) Å] (Chen et al., 2010) and $(6\text{-bromopyCMeC}_6\text{H}_5\text{O})\text{Ru}_3(\text{CO})_9$ (2.229(4) Å) (Hao et al., 2018b). The Ru(1)–O(1) bond lengths for **1a-1h** are all similar and are in the range of 2.072(3)-2.093(5) Å, showing that the substitutions at 2- or 4- positions of benzene ring have no significant effect on bond lengths.

## Catalytic Activity on Oxidation of Alcohols

We commenced our study by using complex **1a** as precatalyst and 1-phenylethanol as a simple substrate to obtain the appropriate conditions. Initially, various oxidants (NMO, $H_2O_2$, *t*-BuOOH, TEMPO) were tested to oxidize 1-phenylethanol. Among different oxidants applied in this studies, *t*-BuOOH was found to be the best oxidant and acetophenone can be obtained in a high yield of 75% (**Table S1**). The effect of solvent on

this oxidation process was then evaluated (**Table 1**, entries 1–6). When the reaction was performed in $CH_2Cl_2$, THF or dioxide, the oxidation product was obtained in low yields (<55%). When using toluene or acetone as solvent, the the yield was enhanced slightly. To our delight, the yield of the desired ketone in $CH_3CN$ was 85%, which is higher than that in other solvents. Thus, acetonitrile was selected as the optimal solvent. The subsequent lowering the loading of **1a** from 2.0 to 0.5 mol% did not significantly affect the yield, thus only 0.5 mol% catalyst **1a** is sufficient for catalyzing the present reaction (**Table 1**, entries 3 and 7–9). Subsequently, the effect of TBHP on the reaction was examined. Upon increasing the amounts of TBHP from 1.0 to 3.0 mmol, the yield of acetophenone was gradually improved to 91%, and 2.5 mmol of TBHP was selected as the most suitable amount from the view of cost-saving (**Table 1**, entries 10–13). It was found that the reaction temperature had an obvious impact on the reaction efficiency. As shown in **Table 1**, when elevating the temperature from room temperature to 50 or 80°C, the yield of product decreased dramatically to 72 and 54%, respectively (**Table 1**, entries 14 and 15). Furthermore, the effect of reaction time on the rate of oxidation was investigated (**Figure 4**). When the reaction time was extended from 0 to 20 min, an almost linear increase of the yield was observed during the oxidation of 1-phenylethanol. After 40 min, the yield increased slightly, and further extension of the time after 60 min could hardly increase the yield. Finally, control experiments indicated that only traces

(8%) of the desired product was formed without using complex **1a** and almost no oxidation product was generated in the absence of TBHP (**Table 1**, entries 16 and 17).

The above interesting results encouraged us to continue the optimization study using different ruthenium complexes and the obtained results are summaried in **Table 2**. The complexes containing electronically rich ligands (**1a-c**, **1f**, and **1h**) exhibited higher catalytic activity than those bearing electronically poor ligands (**1d**, **1e**, and **1g**), suggesting that the catalytic behavior of Ru complexes was influenced by the electronic nature of the ligands. Catalysts **1f** and **1g** with *ortho*-substituents in the phenyl ring exhibited lower catalytic activity than their *para*-substituted analogs **1c** and **1e** (**Table 2**, entries 3–4 vs. 6–7). This difference is likely due to the fact that substitutions at 2-position of ligands caused more steric hindrance around the metal centers, thus influencing the coordination of metals with substrates. Besides, catalytic oxidation of 1-phenylethanol was also carried out in the presence of $Ru_3(CO)_{12}$ and the yield of the desired product was only 30% (**Table 2**, entry 9). Thus, the optimized reaction conditions are as follows: alcohol (1.0 mmol), TBHP (2.5 mmol), catalyst **1c** (0.5 mol%), reaction time (1 h) at room temperature.

Under optimized conditions, we set out to test the catalytic performance of complex **1c** in oxidation of different secondary alcohols. As listed in **Table 3**, a diverse array of functional groups including methyl-, chloro-, and trifluoromethyl-etc. on the phenyl ring of substituted 1-phenylethanol were tolerated (**Table 3**, entries 1–7). Additionally, several sterically encumbered substrates undergo oxidation in >90% yields (**Table 3**, entries 8–10). The fused-ring alcohols, that are 1,2,3,4-tetrahydro-1-naphthol and 1-indanol could be also converted to target product in 93 and 92% yields, respectively (**Table 3**, entries 11 and 12). As for secondary aliphatic alcohols, a prolonged reaction time (3h) was required to achieve high yields (**Table 3**, entries 13–16).

Moreover, the oxidation of primary alcohols was also tested in the standard conditions and the results were summarized in **Table 4**. The reaction of benzyl alcohols bearing electron-rich or electron-deficient substituents in the aromatic ring proceeded efficiently to furnish the corresponding benzaldehyde derivatives in excellent yields (**Table 4**, entries 1–7). Only trace amount of benzoic acids were detected, which demonstrated the superiority of the present catalytic system in terms of chemoselectivity. 2-Naphthalenemethanol showed satisfactory reactivity to provide 2-naphthaldehyde in >90% yield (**Table 4**, entry 8). The substrate having sensitive group (internal alkene) was also tolerated in this system, the carbon-carbon double was preserved in the final product (**Table 4**, entry 9). While the catalytic system displayed a diminished activity for oxidation of heterocyclic primary alcohols such as 2-furanmethanol and 2-thiophenemethanol, and <70% yields of the target products were obtained under optimized condition. This outcome can be explained by the strong coordination ability of heteroatoms with Ru centers, which led to the deactivation of the catalyst. Delightfully, decent yields of the heterocyclic products could be obtained by simply increasing the catalyst loading of **1c** to 1.5 mol% (**Table 4**, entries 10–12).

Based on our preliminary data and related Ru-catalyzed alcohol oxidation processes, a plausible inner-sphere mechanism for alcohol oxidation catalyzed by present ruthenium carbonyl complexes/TBHP system is proposed in **Scheme 2**. First, the catalyst **A** reacted with two molecules of TBHP to give Ru-oxide species **I** and *t*BuOH. Subsequent reaction of intermediate **I** with alcohol to form a five-membered ring transient state **II**, which then released water to give the alkoxide species **III**. Finally, the break of Ru-O bond in this intermediate occurred to regenerate catalyst **A** for next catalytic cycle and afforded the target carbonyl product.

## CONCLUSIONS

In summary, a series of ruthenium carbonyl complexes bearing pyridine-alkoxide ligands were synthesized and exhibited excellent catalytic activity for the oxidation of both primary and secondary alcohol substrates, showing broad substrate scope. Of particular note was the effective oxidation of primary alcohols to desired aldehydes without over-oxidation, displaying good chemoselectivity. A striking advantage associated with this catalytic system is that the oxidation reaction can be completed within only 1 h at room temperature for most cases, which is far more efficient than previously reported Ru/TBHP or Ru/NMO systems.

## DATA AVAILABILITY

The raw data supporting the conclusions of this manuscript will be made available by the authors, without undue reservation, to any qualified researcher.

## AUTHOR CONTRIBUTIONS

XYa and XYu were response for the synthesis and characterization of Ru complexes and catalytic experiment. KL conducted the synthesis of pyridine alcohol ligands. ZHan solved the single crystals and drew figures for the complexes. ZHao and JL supervised the whole work, drafted and revised the manuscript.

## FUNDING

## SUPPLEMENTARY MATERIAL

The Supplementary Material for this article can be found online at: https://www.frontiersin.org/articles/10.3389/fchem.2019.00394/full#supplementary-material

# REFERENCES

Allen, S. E., Walvoord, R. R., Padilla-Salinas, R., and Kozlowski, M. C. (2013). Aerobic copper-catalyzed organic reactions. *Chem. Rev.* 113, 6234–6458. doi: 10.1021/cr300527g

Annunziata, A., Esposito, R., Gatto, G., Cucciolito, M. E., Tuzi, A., Macchioni, A., et al. (2018). Iron (III) complexes with cross-bridged cyclams: synthesis and use in alcohol and water oxidation catalysis. *Eur. J. Inorg. Chem.* 2018, 3304–3311. doi: 10.1002/ejic.201800451

Balaraman, E., Khaskin, E., Leitus, G., and Milstein, D. (2013). Catalytic transformation of alcohols to carboxylic acid salts and $H_2$ using water as the oxygen atom source. *Nat. Chem.* 5, 122–125. doi: 10.1038/nchem.1536

Bianchini, C., and Shen, P. K. (2009). Palladium-based electrocatalysts for alcohol oxidation in half cells and in direct alcohol fuel cells. *Chem. Rev.* 109, 4183–4206. doi: 10.1021/cr9000995

Borah, B. J., Mahanta, A., Mondal, M., Gogoi, H., Yamada, Y., and Bharali, P. (2018). Cobalt-copper nanoparticles catalyzed selective oxidation reactions: efficient catalysis at room temperature. *Chem. Select* 3, 9826–9832. doi: 10.1002/slct.201801140

Campestrini, S., Carraro, M., Ciriminna, R., Pagliaro, M., and Tonellato, U. (2004). Alcohols oxidation with hydrogen peroxide promoted by TPAP-doped ormosils. *Tetrahedron Lett.* 45, 7283–7286. doi: 10.1016/j.tetlet.2004.08.020

Canielli, G., and Cardillo, G. (1984). *Chromium Oxidation in Organic Chemistry*. Berlin: Springer Verlag.

Cao, Q., Dornan, L. M., Rogan, L., Hughes, N. L., and Muldoon, M. J. (2014). Aerobic oxidation catalysis with stable radicals. *Chem. Commun.* 50, 4524–4543. doi: 10.1039/C3CC47081D

Caron, S., Dugger, R. W., Ruggeri, S. G., Ragan, J. A., and Ripin, D. H. B. (2006). Large-scale oxidations in the pharmaceutical industry. *Chem. Rev.* 106, 2943–2989. doi: 10.1021/cr040679f

Chen, D., Zhang, X., Xu, S., Song, H., and Wang, B. (2010). Pyridyl-substituted indenyl ruthenium complexes: synthesis, structures, and reactivities. *Organometallics* 29, 3418–3430. doi: 10.1021/om100556y

Chen, Z., and Luck, R. L. (2016). Oxidation of olefins using atmospheric oxygen atoms initiated by tert-butylhydroperoxide or hydrogen peroxide with silver nanoparticles deposited on MCM-41 as catalysts. *Green Chem.* 18, 3354–3359. doi: 10.1039/C5GC03110A

Coleman, M. G., Brown, A. N., Bolton, B. A., and Guan, H. (2010). Iron-catalyzed oppenauer-type oxidation of alcohols. *Adv. Synth. Catal.* 352, 967–970. doi: 10.1002/adsc.200900896

Crabtree, R. H. (2017). Homogeneous transition metal catalysis of acceptorless dehydrogenative alcohol oxidation: applications in hydrogen storage and to heterocycle synthesis. *Chem. Rev.* 117, 9228–9246. doi: 10.1021/acs.chemrev.6b00556

Dai, W., Lv, Y., Wang, L., Shang, S., Chen, B., Li, G., et al. (2015). Highly efficient oxidation of alcohols catalyzed by a porphyrin-inspired manganese complex. *Chem. Commun.* 51, 11268–11271. doi: 10.1039/C5CC03657G

Dijksman, A., Marino-González, A., Mairata I Payeras, A., Arends, I. W. C. E., and Sheldon, R. A. (2001). Efficient and selective aerobic oxidation of alcohols into aldehydes and ketones using ruthenium/TEMPO as the catalytic system. *J. Am. Chem. Soc.* 123, 6826–6833. doi: 10.1021/ja0103804

Fauré, M., Saccavini, C., and Lavigne, G. (2003). New insight into a convenient base-promoted synthesis of $Ru_3(CO)_{12}$. *Chem. Commun.* 1578–1579. doi: 10.1039/B303884J

Gunasekaran, N., Remya, N., Radhakrishnan, S., and Karvembu, R. (2011). Ruthenium (II) carbonyl complexes with N-[di(alkyl/aryl) carbamothioyl] benzamide derivatives and triphenylphosphine as effective catalysts for oxidation of alcohols. *J. Coord. Chem.* 64, 491–501. doi: 10.1080/00958972.2010.548007

Hao, Z., Li, N., Yan, X., Li, Y., Zong, S., Liu, H., et al. (2018a). Ruthenium carbonyl complexes with pyridylalkanol ligands: synthesis, characterization and catalytic properties for aerobic oxidation of secondary alcohols. *New J. Chem.* 42, 6968–6975. doi: 10.1039/C8NJ00329G

Hao, Z., Li, Y., Li, C., Wu, R., Ma, Z., Li, S., et al. (2019). Synthesis of a series of new ruthenium organometallic complexes derived from pyridine-imine ligands and their catalytic activity in oxidation of secondary alcohols. *Appl. Organomet. Chem.* 33:e4750. doi: 10.1002/aoc.4750

Hao, Z., Yan, X., Liu, K., Yue, X., Han, Z., and Lin, J. (2018b). Ruthenium carbonyl complexes with pyridine-alkoxide ligands: synthesis, characterization and catalytic application in dehydrogenative oxidation of alcohols. *New J. Chem.* 42, 15472–15478. doi: 10.1039/C8NJ03706J

Ho, W. C., Chung, K., Ingram, A. J., and Waymouth, R. M. (2018). Pd-catalyzed aerobic oxidation reactions: strategies to increase catalyst lifetimes. *J. Am. Chem. Soc.* 140, 748–757. doi: 10.1021/jacs.7b11372

Hoover, J. M., Steves, J. E., and Stahl, S. S. (2012). Copper (I)/TEMPO-catalyzed aerobic oxidation of primary alcohols to aldehydes with ambient air. *Nat. Protoc.* 7, 1161–1166. doi: 10.1038/nprot.2012.057

Jehdaramarn, A., Pornsuwan, S., Chumsaeng, P., Phomphrai, K., and Sangtrirutnugul, P. (2018). Effects of appended hydroxyl groups and ligand chain length on copper coordination and oxidation activity. *New J. Chem.* 42, 654–661. doi: 10.1039/C7NJ03113K

Kashani, S. H., Moghadam, M., Tangestaninejad, S., Mirkhani, V., and Mohammadpoor-Baltork, I. (2018). Ruthenium nanoparticles immobilized on nano-silica functionalized with thiol-based dendrimer: a nanocomposite material for oxidation of alcohols and epoxidation of alkenes. *Catal. Lett.* 148, 1110–1123. doi: 10.1007/s10562-018-2313-8

Kudrik, E. V., and Sorokin, A. B. (2017). Oxidation of aliphatic and aromatic CH bonds by *t*-BuOOH catalyzed by μ-nitrido diiron phthalocyanine. *J. Mol. Catal. A Chem.* 426, 499–505. doi: 10.1016/j.molcata.2016.08.013

Kumar, K. N., Ramesh, R., and Liu, Y. (2007). Synthesis, structure and catalytic activity of cycloruthenated carbonyl complexes containing arylazo phenolate ligands. *J. Mol. Catal. A Chem.* 265, 218–226. doi: 10.1016/j.molcata.2006.10.015

Kumpulainen, E. T., and Koskinen, A. M. (2009). Catalytic activity dependency on catalyst components in aerobic copper-TEMPO oxidation. *Chem. Eur. J.* 15, 10901–10911. doi: 10.1002/chem.200901245

Lagerspets, E., Lagerblom, K., Heliövaara, E., Hiltunen, O.-M., Moslova, K., Nieger, M., et al. (2019). Schiff base Cu (I) catalyst for aerobic oxidation of primary alcohols. *Mol. Catal.* 468, 75–79. doi: 10.1016/j.mcat.2019.02.003

Lybaert, J., Trashin, S., Maes, B. U., De Wael, K., and Abbaspour Tehrani, K. (2017). Cooperative electrocatalytic and chemoselective alcohol oxidation by Shvo's catalyst. *Adv. Synth. Catal.* 359, 919–925. doi: 10.1002/adsc.201600783

Ma, Z.-H., Liu, Q., Qin, M., Han, Z.-G., and Lin, J. (2017). Synthesid, structure and reactivity of a trinuclear ruthenium cluster compound $[PyCH=C(Ph)O]_2Ru_3(CO)_8$. *Chin. J. Inorg. Chem.* 2017, 1293–1298. doi: 10.11862/CJIC.2017.135

Mallat, T., and Baiker, A. (2004). Oxidation of alcohols with molecular oxygen on solid catalysts. *Chem. Rev.* 104, 3037–3058. doi: 10.1021/cr0200116

Miao, C., Li, X.-X., Lee, Y.-M., Xia, C., Wang, Y., Nam, W., et al. (2017). Manganese complex-catalyzed oxidation and oxidative kinetic resolution of secondary alcohols by hydrogen peroxide. *Chem. Sci.* 8, 7476–7482. doi: 10.1039/C7SC00891K

Moore, P. W., Zerk, T. J., Burns, J. M., Bernhardt, P. V., and Williams, C. M. (2019). Hydrogen-bonding interactions in the ley-griffith oxidation: practical considerations for the synthetic chemist. *Eur. J. Org. Chem.* 2019, 303–308. doi: 10.1002/ejoc.201800860

Murahashi, S.-I., Komiya, N., Oda, Y., Kuwabara, T., and Naota, T. (2000). Ruthenium-catalyzed oxidation of alkanes with tert-butyl hydroperoxide and peracetic acid. *J. Org. Chem.* 65, 9186–9193. doi: 10.1021/jo001348f

Parmeggiani, C., and Cardona, F. (2012). Transition metal based catalysts in the aerobic oxidation of alcohols. *Green Chem.* 14, 547–564. doi: 10.1039/c2gc16344f

Punniyamurthy, T., Velusamy, S., and Iqbal, J. (2005). Recent advances in transition metal catalyzed oxidation of organic substrates with molecular oxygen. *Chem. Rev.* 105, 2329–2364. doi: 10.1021/cr050523v

Ren, L., Wang, L., Lv, Y., Shang, S., Chen, B., and Gao, S. (2015). Synthesis of 6, 7-dihydro-5H-cyclopenta[b]pyridin-5-one analogues through manganese-catalyzed oxidation of the $CH_2$ adjacent to pyridine moiety in water. *Green Chem.* 17, 2369–2372. doi: 10.1039/C4GC02471K

Saleem, F., Rao, G. K., Kumar, A., Mukherjee, G., and Singh, A. K. (2013). Half-sandwich ruthenium (II) complexes of click generated 1, 2, 3-triazole based organosulfur/-selenium ligands: structural and donor site dependent catalytic oxidation and transfer hydrogenation aspects. *Organometallics* 32, 3595–3603. doi: 10.1021/om400057e

Salvatore, R. N., Yoon, C. H., and Jung, K. W. (2001). Synthesis of secondary amines. *Tetrahedron* 57, 7785–7812. doi: 10.1016/S0040-4020(01)00722-0

Santini, C. C., Basset, J.-M., Fontal, B., Krause, J., Shore, S., and Charrier, C. (1987). Surface organometallic chemistry: synthesis and X-ray structure of Ru3(CO)8(μ-OC6H4OMe-2)2, an oxygen stabilized triruthenium cluster. *J. Chem. Soc. Chem. Commun.* 512–513. doi: 10.1039/C39870000512

Sarbajna, A., Dutta, I., Daw, P., Dinda, S., Rahaman, S. W., Sarkar, A., et al. (2017). Catalytic conversion of alcohols to carboxylic acid salts and hydrogen with alkaline water. *ACS Catal.* 7, 2786–2790. doi: 10.1021/acscatal.6b03259

Sarkar, S. K., Jana, M. S., Mondal, T. K., and Sinha, C. (2014). Alcohol oxidation reactions catalyzed by ruthenium-carbonyl complexes of thioarylazoimidazoles. *Appl. Organomet. Chem.* 28, 641–651. doi: 10.1002/aoc.3174

Sarma, D., Majumdar, B., and Sarma, T. K. (2018). Carboxyl-functionalized carbon dots as competent visible light photocatalysts for aerobic oxygenation of alkyl benzenes: role of surface functionality. *ACS Sustain. Chem. Eng.* 6, 16573–16585. doi: 10.1021/acssuschemeng.8b03811

Shapley, P. A., Zhang, N., Allen, J. L., Pool, D. H., and Liang, H.-C. (2000). Selective alcohol oxidation with molecular oxygen catalyzed by Os-Cr and Ru-Cr complexes. *J. Am. Chem. Soc.* 122, 1079–1091. doi: 10.1021/ja982171y

Sheldon, R., Arends, I., Ten Brink, G.-J., and Dijksman, A. (2002). Green, catalytic oxidations of alcohols. *Acc. Chem. Res.* 35, 774–781. doi: 10.1021/ar010075n

Sheldon, R. A., Arends, I., and Dijksman, A. (2000). New developments in catalytic alcohol oxidations for fine chemicals synthesis. *Catal. Today* 57, 157–166. doi: 10.1016/S0920-5861(99)00317-X

Sheldrick, G. H. (1997). *SHELX 97, A Software Package for the Solution and Refinement of X-ray Data.* Göttingen: University of Göttingen.

Sigman, M. S., and Jensen, D. R. (2006). Ligand-modulated palladium-catalyzed aerobic alcohol oxidations. *Acc. Chem. Res.* 39, 221–229. doi: 10.1021/ar040243m

Simon, M.-O., and Li, C.-J. (2012). Green chemistry oriented organic synthesis in water. *Chem. Soc. Rev.* 41, 1415–1427. doi: 10.1039/C1CS15222J

Song, D., and Morris, R. H. (2004). Cyclometalated tridentate CNN ligands with an amine or amido donor in platinum (II) and palladium (II) complexes and a novel potassium alkoxide aggregate. *Organometallics* 23, 4406–4413. doi: 10.1021/om0496232

Stahl, S. S. (2004). Palladium oxidase catalysis: selective oxidation of organic chemicals by direct dioxygen-coupled turnover. *Angew. Chem. Int. Ed.* 43, 3400–3420. doi: 10.1002/anie.200300630

Stanje, B., Traar, P., Schachner, J., Belaj, F., and Mösch-Zanetti, N. (2018). Iron catalyzed oxidation of benzylic alcohols to benzoic acids. *Dalton Trans.* 47, 6412–6420. doi: 10.1039/C8DT00819A

Tang, L.-H., Wu, F., Lin, H., Jia, A.-Q., and Zhang, Q.-F. (2018). Synthesis, structure and catalytic alcohol oxidation by ruthenium (III) supported by schiff base and triphenylphosphine ligands. *Inorg. Chim. Acta* 477, 212–218. doi: 10.1016/j.ica.2018.03.017

Tojo, G., and Fernández, M. (2007). *Oxidation of Primary Alcohols to Carboxylic Acids. A Guide to Current Common Practice* (New York, NY: Springer).

Tsukahara, T., Swenson, D. C., and Jordan, R. F. (1997). Neutral and cationic zirconium benzyl complexes containing bidentate pyridine-alkoxide ligands. synthesis and olefin polymerization chemistry of (pyCR2O)2Zr(CH2Ph)2 and (pyCR2O)2Zr (CH2Ph) complexes. *Organometallics* 16, 3303–3313. doi: 10.1021/om9702439

Uyanik, M., and Ishihara, K. (2009). Hypervalent iodine-mediated oxidation of alcohols. *Chem. Commun.* 16, 2086–2099. doi: 10.1039/b823399c

Vazylyev, M., Sloboda-Rozner, D., Haimov, A., Maayan, G., and Neumann, R. (2005). Strategies for oxidation catalyzed by polyoxometalates at the interface of homogeneous and heterogeneous catalysis. *Top. Catal.* 34, 93–99. doi: 10.1007/s11244-005-3793-5

Velusamy, S., Srinivasan, A., and Punniyamurthy, T. (2006). Copper (II) catalyzed selective oxidation of primary alcohols to aldehydes with atmospheric oxygen. *Tetrahedron Lett.* 47, 923–926. doi: 10.1016/j.tetlet.2005.11.149

Vermaak, V., Young, D. A., and Swarts, A. J. (2018). Catalytic oxidation of alcohols with novel non-heme N 4-tetradentate manganese (ii) complexes. *Dalton Trans.* 47, 16534–16542. doi: 10.1039/C8DT03808B

Wang, N., Liu, R., Chen, J., and Liang, X. (2005). NaNO2-activated, iron–TEMPO catalyst system for aerobic alcohol oxidation under mild conditions. *Chem. Commun.* 42, 5322–5324. doi: 10.1039/b509167e

Wang, Q., Chai, H., and Yu, Z. (2017). Dimeric ruthenium (II)-NNN complex catalysts bearing a pyrazolyl-pyridylamino-pyridine ligand for transfer hydrogenation of ketones and acceptorless dehydrogenation of alcohols. *Organometallics* 36, 3638–3644. doi: 10.1021/acs.organomet.7b00587

Wang, X., Liu, R., Jin, Y., and Liang, X. (2008). TEMPO/HCl/NaNO2 catalyst: a transition-metal-free approach to efficient aerobic oxidation of alcohols to aldehydes and ketones under mild conditions. *Chem. Eur. J.* 14, 2679–2685. doi: 10.1002/chem.200701818

Zhou, X.-T., Ji, H.-B., and Liu, S.-G. (2013). Solvent-free selective oxidation of primary and secondary alcohols catalyzed by ruthenium-bis (benzimidazole) pyridinedicarboxylate complex using hydrogen peroxide as an oxidant. *Tetrahedron Lett.* 54, 3882–3885. doi: 10.1016/j.tetlet.2013.05.055

# Effect of $Mn^{2+}$ on Upconversion Emission, Thermal Sensing and Optical Heater Behavior of $Yb^{3+}$ - $Er^{3+}$ Codoped $NaGdF_4$ Nanophosphors

Qinping Qiang [1,2] and Yuhua Wang [1,2]*

[1] Department of Materials Science, School of Physical Science and Technology, Lanzhou University, Lanzhou, China, [2] Key Laboratory for Special Function Materials and Structural Design of the Ministry of Education, Lanzhou University, Lanzhou, China

In thiswork, we investigate the influence of $Mn^{2+}$ on the emission color, thermal sensing and optical heater behavior of $NaGdF_4$: Yb/Er nanophosphors, which the nanoparticles were synthesized by a hydrothermal method using oleic acid as both a stabilizing and a chelating agent. The morphology and crystal size of upconversion nano particles (UCNPs) can be effectively controlled through the addition of $Mn^{2+}$ dopant contents in $NaGdF_4$: Yb/Er system. Moreover, an enhancement in overall UCL spectra of $Mn^{2+}$ doped UCNPs for $NaGdF_4$ host compared to the UCNPs is observed, which results from a closed back-energy transfer between $Er^{3+}$ and $Mn^{2+}$ ions ($^4S_{3/2}$ ($Er^{3+}$) → $^4T_1$ ($Mn^{2+}$) → $^4F_{9/2}$ ($Er^{3+}$)). The temperature sensitivity of $NaGdF_4$:$Yb^{3+}$/$Er^{3+}$ doping with $Mn^{2+}$ based on thermally coupled levels ($^2H_{11/2}$ and $^4S_{3/2}$) of $Er^{3+}$ is similar to that particles without $Mn^{2+}$ in the 303–548 K range. And the maximum sensitivity is 0.0043 $K^{-1}$ at 523 K for $NaGdF_4$:$Yb^{3+}$/$Er^{3+}$/$Mn^{2+}$. Interestingly, the $NaGdF_4$:$Yb^{3+}$/$Er^{3+}$/$Mn^{2+}$ shows preferable optical heating behavior, which is reaching a large value of 50 K. These results indicate that inducing of $Mn^{2+}$ ions in $NaGdF_4$:$Yb^{3+}$/$Er^{3+}$ nanophosphors has potential in colorful display, temperature sensor.

Keywords: $NaGdF_4$:$Yb^{3+}$/$Er^{3+}$, $Mn^{2+}$, upconversion luminescence, temperature sensing, optical heater

## INTRODUCTION

Owing to the virtues of non-invasion, rapid response, high spatial resolution and signal to noise ratio, rare earth ions ($Ln^{3+}$) doped up-conversion luminescent (UCL) material as an optical thermometer have been a subject of particular interest now a day, which can be applicable in life sciences, industrial production, aerospace and military (Fischer et al., 2011; Sedlmeier et al., 2012; Chen et al., 2013; Liu et al., 2015; Yang et al., 2015; Zheng et al., 2015). Trivalent lanthanide ion has abundant ladder-like levels, which can convert two or more low energy photons to a higher energy photon (Dong et al., 2012; Niu et al., 2012; Xu et al., 2015). Erbium ion ($Er^{3+}$) is one of the most significant activator, whose luminescence ranges from visible to ultraviolet under near infrared (NIR) excitation (Gai et al., 2013; Wang et al., 2016).

Among temperature dependent optical performance, such as peak position (Jiang et al., 2014), luminescent lifetime (Peng et al., 2010), emission intensity (Zhou et al., 2016), and bandwidth (Walsh and Di Bartolo, 2015), fluorescence intensity ratio (FIR) technique (Liu et al., 2017; Xu et al., 2017) can achieve accurate temperature measurement, which is independent of external interferences, spectral losses, as well as fluctuations in the excitation density (Wade et al., 2003; Wawrzynczyk et al., 2012; Zhou et al., 2014; Pandey et al., 2015; Wang et al., 2015). Using this ratiometric technique, the sensitivity of sensor is strongly dependent on the energy gap of thermally coupled levels (TCL), which is confined in the range of 200–2,000 cm$^{-1}$ (Zheng et al., 2016; Du et al., 2017; Tong et al., 2017; Wang et al., 2017). Generally, the larger energy gap of TCL leads to the higher sensitivity (Du et al., 2016). Therefore, the TCL $^2H_{11/2}$ and $^4S_{3/2}$ of $Er^{3+}$ have been used in FIR thermometry due to their larger energy gap ($\sim$800 cm$^{-1}$) (Zheng et al., 2014; Chen et al., 2017), intense green emissions and minor overlap between two green emission peaks (León-Luis et al., 2013). It has been reported that the sensing sensitivity of $Er^{3+}$ doped up-conversion nanocrystals is mainly depended on the host matrix, exciting power and nanocrystal size (Dong et al., 2014, 2015; Marciniak et al., 2016).

Notably, the host is one of the most important factors to determine UC efficiency since the phonon energy of host has a significant impact on the probability of non-radiative transitions for the incorporated $Ln^{3+}$ dopants (Wang and Liu, 2009). Yb/Er co-doped $NaLnF_4$ (Ln = Y, La, Lu, Yb, Gd) hosts are considered as the most efficient UCL systems (Zeng et al., 2014). However, it is still a challenge to achieve multi-color output and enhanced red UCL in a single fixed composition of Yb/Er co-doped system. Recently, some dopants, such as divalent manganese ($Mn^{2+}$), have been recognized as effective elements which can decrease the short-wavelength green emission and enhance the long-wavelength red emission because of the energy transfer between $Er^{3+}$ and $Mn^{2+}$ ions (Tian et al., 2012; Liu et al., 2019).

Here, we construct an energy transfer bridge to achieve high sensitivity for the temperature sensing. The hexagonal phase $NaGdF_4$ is selected as the matrix material due to its low phonon energy and remarkable chemical stability. Compared with $NaGdF_4$:$Yb^{3+}$/$Er^{3+}$ phosphor, the luminescence of $NaGdF_4$:$Yb^{3+}$/$Er^{3+}$/$Mn^{2+}$ phosphor is illustrated under 980 nm excitation. Importantly, the $Mn^{2+}$ doping in phosphor could be result in energy transfer between $^4S_{3/2}$ and $^4F_{9/2}$ ($Er^{3+}$). Meanwhile, the temperature sensing behaviors of two phosphors are investigated in the temperature 303–523 K based on TCL. The internal heating of the developed phosphors has been computed employing temperature dependent FIR study at the same time. The influences of energy transfer induced by $Mn^{2+}$ ions are discussed for temperature sensing and optical heating.

## EXPERIMENTAL

### Synthesis of β-NaGdF4: 20 mol% Yb3+/1 mol% Er3+/x mol% Mn2+(0 ≤ x ≤ 40) Nanoparticles

$NaGdF_4$: 20 mol% $Yb^{3+}$/1 mol% $Er^{3+}$/$x$ $Mn^{2+}$ ($x$ = 0, 5, 10, 20, 30, and 40 mol%) nanocrystals were synthesized by a hydrothermal method using oleic acid as both a stabilizing and a chelating agent. The typical synthesis involved the addition of 10 mL of ethanol to 2 mL of an aqueous solution containing 1.2 g of NaOH under stirring to form a homogeneous solution. Then, 20 mL of oleic acid was added to form a sodium-oleic acid complex. Subsequently, 1 mmol $RE(NO_3)_3$ (RE = Gd, Yb, and Er with designed molar ratios) and 8 mL of 1.0 M NaF aqueous and stoichiometric ratio of $Mn(NO_3)_2$ solutions were added under constant vigorous stirring for 10–20 min. The resulting solution was transferred into a 50 mL stainless Teflon-lined autoclave, which was operated at 170°C for 24 h. After reaction completion, the system was naturally cooled to room temperature. The resulting samples were washed several times with ethanol and de-ionized water to remove oleic acid and other residual solvents, and then dried at 60°C for 10 h. The $NaGdF_4$: 20 mol% $Yb^{3+}$/1 mol% $Er^{3+}$ nanoparticle is labeled as $NaGdF_4$: Yb/Er, and the $NaGdF_4$: 20 mol% $Yb^{3+}$/1 mol% $Er^{3+}$/$x$ mol% $Mn^{2+}$ sample is labeled as $NaGdF_4$: Yb/Er/$x$ Mn.

### Characterization

The X-ray diffraction (XRD) patterns were obtained on a Rigaku D/Max-2400 X-ray diffractometer with Ni-filter Cu K α radiation at 40 kV and 60 mA. The size, shape and structure of the as-prepared microcrystals were characterized by scanning electron microscopy (SEM) (S-4800), transmission electron microscopy (TEM) (JSM-1200EX) and high-resolution transmission electron microscopy (HRTEM) (FEI Tecnai F30, operated at 300 kV). The elemental analysis identified by energy dispersive X-ray spectroscopy (EDX) was attached with the same TEM. In the measurements of UC emission, a continuous 980 nm laser diode (LD) with a power maximum of 1.5 W was used for excitation sources. The samples used in the upconversion measurement and Pump Power dependence measurements are powder samples. The powder samples are pressed on a sample tray which is cover with a quartz glass sheet, then the output laser beam collimated and focused on the samples to test. All measurements were performed at room temperature.

## RESULTS AND DISCUSSION

### Phase Identification and Crystal Structure of β-NaGdF4

The structure of all samples is typical hexagonal phase. As shown in **Figure 1A**, XRD studies show peak positions and intensities that can be well-indexed in accordance with β-$NaGdF_4$ crystals (JCPDS file no. 27-0699). It is worth noting that, the diffraction peak shifts slightly toward higher angle side as an addition of $Mn^{2+}$. This is mainly attributed to the decrease in unit-cell volume of $NaGdF_4$ host because of $Mn^{2+}$ replace of $Gd^{3+}$. Moreover, energy dispersive X-ray spectrometer (EDX) analysis (**Figure 1B**) shows the presence of Na, Gd and doped Yb, Mn elements, further verifying the substitution by $Mn^{2+}$. In addition, with increasing $Mn^{2+}$ doping content in the product, as shown in **Figure 1A**. $Gd^{3+}$ content decreases gradually, and the value of Gd/Mn ratio shows a gradual decline compared with the nominal one, whereas Na content keeps unchanged. Because of the incorporation of $Mn^{2+}$ into $NaGdF_4$ by substituting $Gd^{3+}$. It should be noted that charge balance in $NaGdF_4$ is disturbed

after $Mn^{2+}$ replacing $Gd^{3+}$. To maintain charge balance, $F^-$ vacancies are formed (**Figures 1C,D**), which subsequently induce lattice contraction. On the other hand, the ionic radius difference between $Gd^{3+}$ (1.05 Å) and $Mn^{2+}$ (0.96 Å) also results in lattice contraction (Shannon, 1976). Due to these two positive effects, a little shifting to large degree of the diffraction peaks is observed after $Mn^{2+}$ doping.
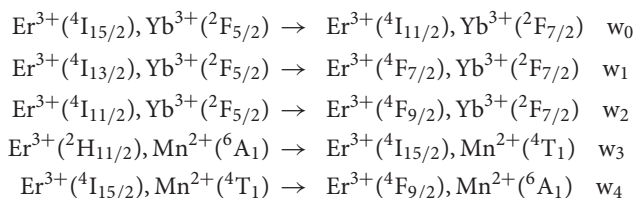
## Effect on Morphology and Crystal Size of the Products

To reveal the morphology and size control, we performed transmission electron microscopy (TEM) analyses. As demonstrated in **Figure 2**, the $NaGdF_4$: Yb/Er exhibit irregular shapes (**Figures 2a,c**), while the $NaGdF_4$: Yb/Er/5Mn samples are almost uniformly hexagonal-shaped (**Figures 2e,f**). High resolution TEM (HRTEM) image (**Figure 2b**) of a single particle taken from **Figure 2c** shows the measured interplanar spacing of 5.16 Å, matching well with the (100) crystal plane of β-phase. In the presence of $Mn^{2+}$, the $NaGdF_4$ products become hexagonal prisms besides the sphere-shaped NPs, while keeping their hexagonal lattice structure as evidenced by selected-area electron diffraction (SAED) analysis (**Figure 2d**) taken from **Figure 2f**. Besides, the average size of products is changed from 23.64 to 36.49 nm/20.52 nm (L/D) (**Figures 2g–i**) by adding $Mn^{2+}$ with 5 mol% content. A fundamental understanding of the crystal growth process in this work could be mainly ascribed to the substitution of large sized $Gd^{3+}$ ($r = 1.05$ Å) by relative smaller sized $Mn^{2+}$ ($r = 0.96$ Å) (Shannon, 1976). The substitution of $Gd^{3+}$ by $Mn^{2+}$ could generate positive vacancies on the grain surface for the charge balance, subsequently forming transient electric dipoles with the positive poles pointing outward (Chen et al., 2010), which can greatly accelerate the diffusion of F ions from the solution to the grain, therefore promote the growth of $NaGdF_4$ UCNPs with increasing $Mn^{2+}$ content.

## Effects of $Mn^{2+}$ on UC Emission Properties of $Ln^{3+}$, $Mn^{2+}$ Doped $NaGdF_4$ Nanocrystals

**Figure 3A** displays the room-temperature UC emission spectra of the irradiated $NaGdF_4$: Yb/Er/$x$ Mn ($x$ = 0, 5, 10, 20, 30, and 40 mol%) nanocrystals under 980 nm excitation, the pump power density is as low as 1.6 W/cm$^2$, demonstrating an efficiency of the UC process. All the nanoparticles exhibit three distinct bands in the range of 500–700 nm. Two green emissions ranging from 515 to 535 nm and from 535 to 557 nm were attributed to the $^2H_{11/2} \rightarrow {}^4I_{15/2}$ and $^4S_{3/2} \rightarrow {}^4I_{15/2}$ transitions of $Er^{3+}$, respectively. A narrow-band visible emission centered at 654 nm was due to the $^4F_{9/2} \rightarrow {}^4I_{15/2}$ transition of $Er^{3+}$. Since a close proximity and effective mixing of wave functions of the $Er^{3+}$ and $Mn^{2+}$ ions, there is a high possibility of energy transfer between $Mn^{2+}$ and $Er^{3+}$ ions. And $Mn^{2+}$ itself can't absorb the 980 nm photon, other experimental conditions didn't change. It can be ascribed to non-radiative energy transfer from the $^4F_{7/2}$ and ($^2H_{11/2}$, $^4S_{3/2}$) levels of $Er^{3+}$ to the $^4T_1$ level of $Mn^{2+}$, followed by back-energy transfer (BET) to the $^4F_{9/2}$ level of $Er^{3+}$ (**Figure 3B**) (Sell et al., 1967; Flaherty and Di Bartolo, 1973; Wang et al., 2011; Dan et al., 2016). The BET and

cross relaxation (CR) process reduce the population at the $^4F_{7/2}$ state which supplies carriers to realize radiative recombination between ($^2H_{11/2}$, $^4S_{3/2}$) and $^4I_{15/2}$ states (i.e., green emission). Evidently, the UC emission intensity initially increases with increasing $Mn^{2+}$ doping content under 10 mol%. And then starts to decrease when the $Mn^{2+}$ content is further increased to 40 mol%, which is due to the quenching effect of concentration, and the excess Mn ions increases the distance between Yb and Er ions, thus greatly reducing the effective energy transfer efficiency between Yb and Er. In addition, the up-conversion emission spectra and absorption spectra of $NaGdF_4$: Mn, $NaGdF_4$: Yb, Er and $NaGdF_4$: Mn, Yb, Er in the supplementary document can also assist in proving the energy transfer mechanism between $Er^{3+}$ and $Mn^{2+}$ (**Figures S1, S2**). The increased ratio of red to green emissions of $Er^{3+}$ suggests a relatively efficient energy transfer process between the $Er^{3+}$ and $Mn^{2+}$ ions, which can be largely attributed to the close proximity and effective mixing of wave functions of the $Er^{3+}$ and $Mn^{2+}$ ions in the crystal host lattices.

In light of all these observations, the following mechanism can be proposed for the upconversion emission in these materials (**Figure 3B**). $Yb^{3+}$ absorbs the excitation energy and transfers it to $Er^{3+}$ ions, which can be represented as $Er^{3+}(^4I_{15/2})$, $Yb^{3+}(^2F_{5/2}) \rightarrow Er^{3+}(^4I_{11/2})$, $Yb^{3+}(^2F_{7/2})$, with the excess energy being transferred to the surrounding matrix. $Er^{3+}(^4I_{11/2})$ can undergo phonon relaxation to $Er^{3+}(^4I_{13/2})$. $Er^{3+}(^4I_{11/2})$ and $Er^{3+}(^4I_{13/2})$ could populate $Er^{3+}(^4F_{7/2})$ and $Er^{3+}(^4F_{9/2})$, respectively, either by excited-state absorption or by energy transfer from another $Yb^{3+}$ ion. What is noteworthy is that $Mn^{2+}(^4T_1)$ and $Er^{3+}(^4F_{9/2})$ could be populated through two energy transfer processes, that is (Sell et al., 1967; Flaherty and Di Bartolo, 1973; Wang et al., 2011),

$$Er^{3+}(^4I_{15/2}), Yb^{3+}(^2F_{5/2}) \rightarrow Er^{3+}(^4I_{11/2}), Yb^{3+}(^2F_{7/2}) \quad w_0$$
$$Er^{3+}(^4I_{13/2}), Yb^{3+}(^2F_{5/2}) \rightarrow Er^{3+}(^4F_{7/2}), Yb^{3+}(^2F_{7/2}) \quad w_1$$
$$Er^{3+}(^4I_{11/2}), Yb^{3+}(^2F_{5/2}) \rightarrow Er^{3+}(^4F_{9/2}), Yb^{3+}(^2F_{7/2}) \quad w_2$$
$$Er^{3+}(^2H_{11/2}), Mn^{2+}(^6A_1) \rightarrow Er^{3+}(^4I_{15/2}), Mn^{2+}(^4T_1) \quad w_3$$
$$Er^{3+}(^4I_{15/2}), Mn^{2+}(^4T_1) \rightarrow Er^{3+}(^4F_{9/2}), Mn^{2+}(^6A_1) \quad w_4$$

The radiative transfer of the $Er^{3+}(^2H_{11/2})$ and $(^4S_{3/2})$ to the ground-state $(^4I_{15/2})$ level gives 522 and 541 nm emissions, respectively, while that of $Er^{3+}(^4F_{9/2})$ to the ground state yields red emission (**Figure 3A**).

Non-radiative deactivation of $Er^{3+}$ could happen in two ways (**Figure 3B**). Which could be contribute to the red to green upconversion emission ratio in different samples.

Pathway 1 Phonon relaxation of $Er^{3+}(^4S_{3/2}, {}^2H_{11/2})$ to $Er^{3+}(^4F_{9/2})$ β1;

Pathway 2 Phonon relaxation of $Er^{3+}(^4I_{11/2})$ to $Er^{3+}(^4I_{13/2})$ β2.

The concentration of $Mn^{2+}$ increases in the appropriate range, the value of $w_3$ and $w_4$ will increase too. Therefore, R/G will increase. This result indicates that the back energy transfer process of $^4T_1$ ($Mn^{2+}$) $\rightarrow {}^4F_{9/2}$ ($Er^{3+}$) is efficient.

To demonstrate the existence of BET and the upconversion mechanism, the excitation power-dependent UC emissions were measured. And the power densities have already been calculated
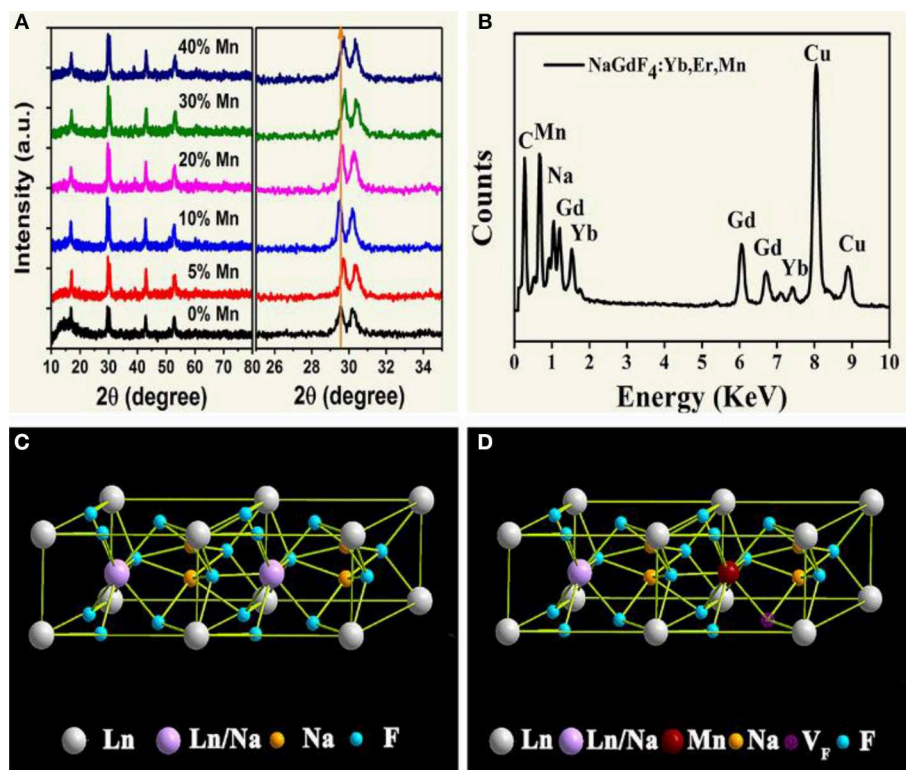
**FIGURE 1 | (A)** XRD patterns of $NaGdF_4$: Yb/Er/$x$ Mn NCs ($0 \leq x \leq 40$); **(B)** EDX spectrum of the corresponding sample, all the signals are normalized to Gd one, and Cu signals come from copper grid; **(C)**, **(D)** schematic illustrations of the crystal structures for pure and $Mn^{2+}$ doped $NaGdF_4$, respectively.

to normalize the UC results. For the unsaturated upconversion process, the number of photons which are required to populate the upper emitting level can be described by the following relationship (Li et al., 2012; Ramasamy et al., 2013):

$$I_{UP} \propto I_{NIR}{}^{n}$$

Where $I_{UP}$ is the upconversion luminescence intensity, $I_{NIR}$ is the pump laser intensity, and n is the number of pump photons required. As shown in **Figures 4A,B**, the slopes of the linear fit of $\ln(I_{UP})$ vs. $\ln(I_{NIR})$ for the 522, 541, and 654 nm emissions in the $NaGdF_4$: Yb/ Er co-doped with 0, 5 mol% of $Mn^{2+}$ ions are all below 2, indicating that two photon processes are involved to produce the green and red UC emissions both in nanocrystals with and without $Mn^{2+}$ ions. Notably, for 5 mol% $Mn^{2+}$ doped $NaGdF_4$: Yb/Er nanoparticles (**Figure 4B**), the slope (n) values for the 522, 541, and 654 nm emissions were $1.94 \pm 0.02$, $1.75 \pm 0.03$, and $1.82 \pm 0.03$, respectively. These values are slightly lower than the values for $NaGdF_4$: Yb/Er NPs (**Figure 4A**). It was reported that a realistic upconversion system that produces detectable upconversion luminescence will exhibit an intensity-vs.-power dependence, which is less than the assumed $P^n$. Competition between the upconversion process and linear decay by luminescence to the ground state or relaxation into the next lower-lying state for the depletion of the intermediate excited states results in a significantly reduced slope (Pollnau et al., 2000). A larger upconversion rate means a smaller slope. The

result indicates that introducing $Mn^{2+}$ ions can increase the upconversion transition rate leading to the enhancement of upconversion luminescence.

To provide further evidence on the role that $Mn^{2+}$ plays in the enhanced UC emission, the decay curves of the UCNPs with and without $Mn^{2+}$ doping are also drawn in **Figures 4C,D**, which deviate from single exponential and thus are fitted with the equation proposed by Nakazawa et al. (1999):

$$\tau_m = \frac{\int_0^\infty tI(t)dt}{\int_0^\infty I(t)dt}$$

Where $\tau_m$ is the effective decay time constant, and I(t) is the intensity at time t. It is noted that the decay times of the $^2H_{11/2} \rightarrow {}^4I_{15/2}$ (@522 nm) transition of the UCNPs have been increased by $\sim$35% after $Mn^{2+}$ doping. Increases of decay lifetime for $^4S_{3/2} \rightarrow {}^4I_{15/2}$ (@541 nm) and $^4F_{9/2} \rightarrow {}^4I_{15/2}$ (@654 nm) transition by $\sim$19% and $\sim$13% respectively are also observed after $Mn^{2+}$ doping. For UC materials, a long lifetime usually means a high-efficiency UC luminescence, i.e., a low non-radiative deactivation probability of $Ln^{3+}$ activators. That agrees with the result of UC emission spectra. In this case, the enhancement of BET and prolonged carrier lifetimes indicates that the removal of amorphous surface and the improvement of surface crystallinity (Bian et al., 2018).
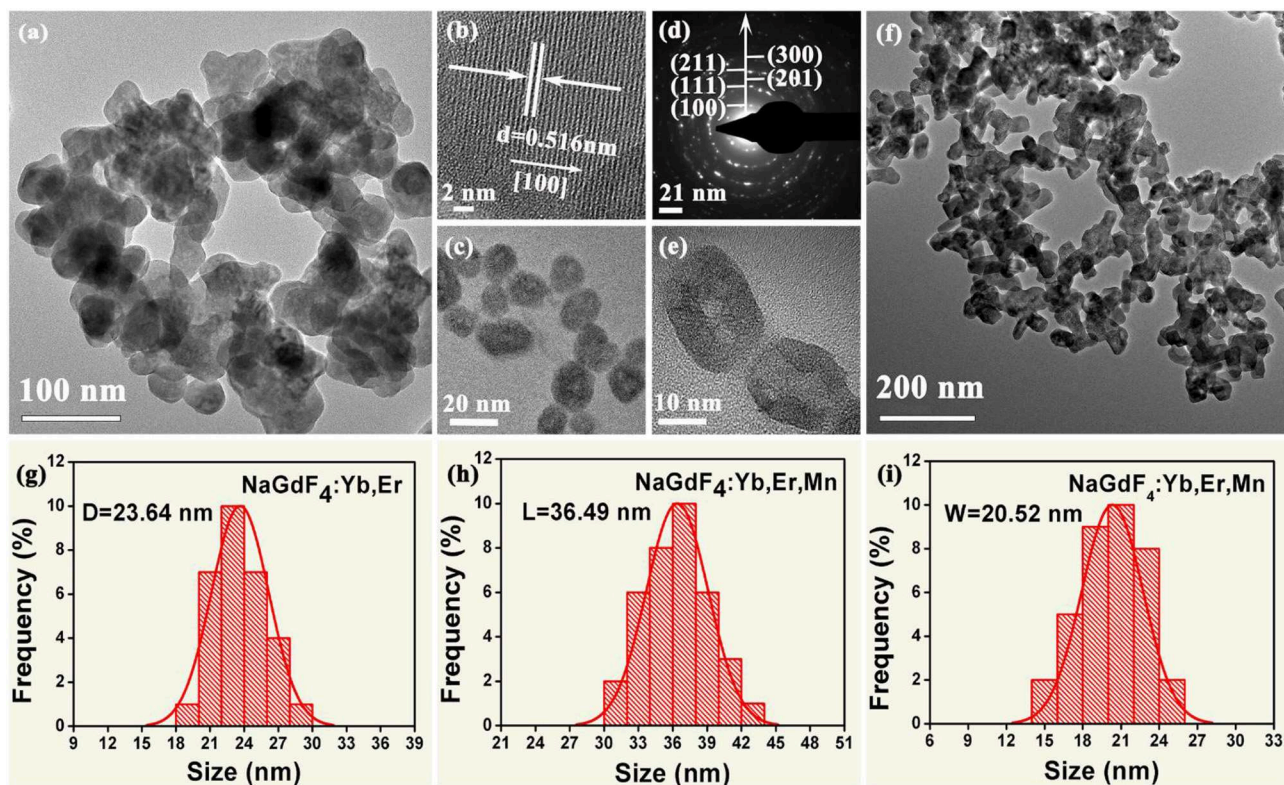
**FIGURE 2** | **(a, c)** Low-resolution and High-magnification TEM images of the as-synthesized NaGdF$_4$:Yb/Er nanocrystals; **(b)** The corresponding High-resolution TEM (HRTEM) image of a single nanocrystal; **(d)** The selected-area electron diffraction (SAED) patterns of the TEM image shown in **(f)**; **(e)** High-magnification TEM image of the as-synthesized NaGdF$_4$: Yb/Er/5 Mn nanocrystals; **(f)** Low-resolution TEM image of the as-synthesized NaGdF$_4$: Yb/Er/5 Mn nanocrystals; **(g)** Histograms of particle size distributions for the NaGdF$_4$: Yb/Er NCs; **(h)** and **(i)** show histograms of length and width distributions of the NaGdF$_4$: Yb/Er/5 Mn NCs, respectively.
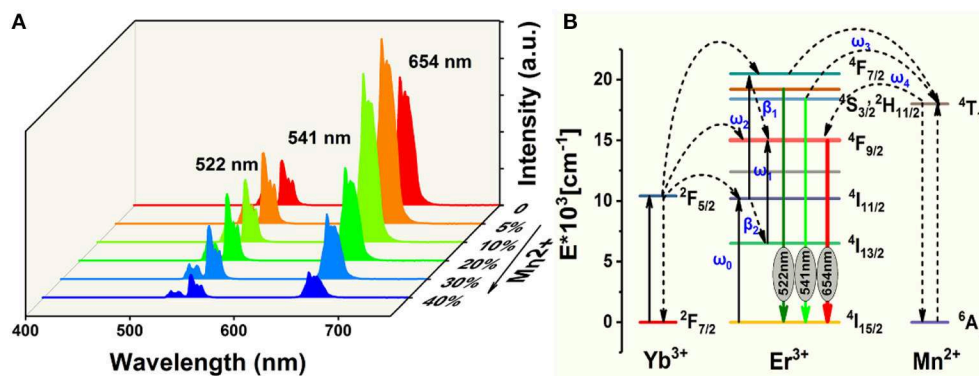


**FIGURE 3** | **(A)** Room-temperature UC emission spectra of NaGdF$_4$: Yb/Er/$x$ Mn (0 mol%$\leq x \leq$40 mol%) nanocrystals under an excitation irradiance of 980 nm laser; **(B)** Simplified energy level diagrams of Er$^{3+}$, Yb$^{3+}$, and Mn$^{2+}$ ions and proposed energy transfer mechanism in NaGdF$_4$.

We know that the variation in FIR of two close lying levels of rare earth (RE) ions is due to change in their populations (Wade et al., 2003; Rai, 2007; Brites et al., 2012; Jaque and Vetrone, 2012; Verma and Rai, 2012; Carlos and Palacio, 2016). Due to the energy difference between the $^4$S$_{3/2}$ and $^4$F$_{9/2}$ states is ~2,700 cm$^{-1}$ and follows Boltzmann's distribution (Dong et al., 2007; Dey et al., 2014; Nigoghossian et al., 2017a). The

observed FIR variation corresponding to the $^4$S$_{3/2} \rightarrow$ $^4$I$_{15/2}$ and $^4$F$_{9/2} \rightarrow$ $^4$I$_{15/2}$ transitions of Er$^{3+}$–Yb$^{3+}$ and Mn$^{2+}$–Er$^{3+}$– Yb$^{3+}$ codoped NaGdF$_4$ samples due to change in laser power density generates an idea of optical heating (Debasu et al., 2013, 2016). For experimental verification of the concept of optical heating induced by laser power density, the FIR technique for the same UC emission bands have been used and obtained
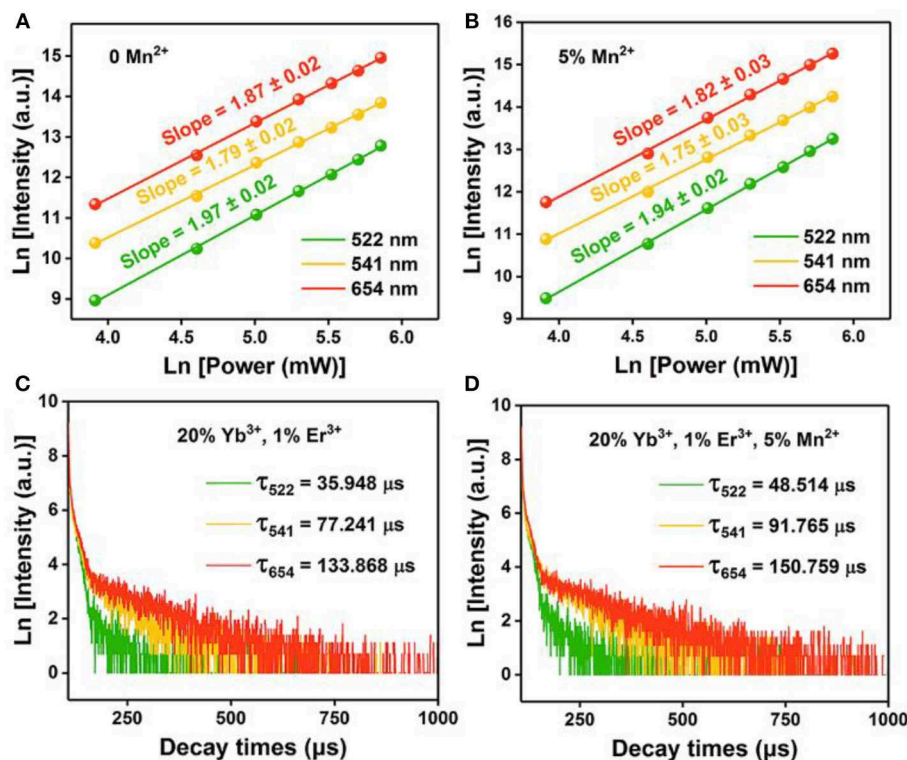
**FIGURE 4 |** Pump power dependence of the UC emissions in **(A)** NaGdF$_4$: Yb/Er UCNPs; **(B)** NaGdF$_4$: Yb/Er/5 Mn UCNPs; **(C)**, **(D)** Corresponding decay curves of $^2H_{11/2} \rightarrow {}^4I_{15/2}$ transition (@522 nm), $^4S_{3/2} \rightarrow {}^4I_{15/2}$ transition (@541 nm), and $^4F_{9/2} \rightarrow {}^4I_{15/2}$ transition (@654 nm) of the UCNPs, respectively.

the factors which affect the change in the intensity ratio. As shown in **Figure 5**, the UC emission intensity of the two samples are significantly improved with the increase of power density. Moreover, the power-dependent red-to-green ratio increases with Mn$^{2+}$ doping. We can deduce that the red-to-green ratio increases with the increasing of BET process between Er$^{3+}$ and Mn$^{2+}$ ($^4S_{3/2}$ (Er$^{3+}$) $\rightarrow$ $^4T_1$ (Mn$^{2+}$) $\rightarrow$ $^4F_{9/2}$ (Er$^{3+}$)). That is owe to the increasing power density generate an optical heating along with the electrons are largely accumulating at $^4F_{9/2}$ state. This result also supports the standpoint that BET process takes part in the up-conversion emissions.

## Temperature Sensor Characterization

Finally, to explore the possible application of the present investigated NaGdF$_4$ in optical thermometry, UC emission spectra of 0 and 5 mol% Mn$^{2+}$ co-doped NaGdF$_4$: Yb$^{3+}$/Er$^{3+}$ under 980 nm excitation ranging from 500 to 590 nm are recorded at different temperatures from 303 to 548 K, as depicted in **Figures 6A,E**. It can observe that these spectra exhibit two distinct emission bands around 522 nm and 541 nm assigned to the $^2H_{11/2} \rightarrow {}^4I_{15/2}$ and $^4S_{3/2} \rightarrow {}^4I_{15/2}$ transitions of Er$^{3+}$ ion, respectively. The FIR of these two UC emissions show a remarkable dependence on the temperature (**Figures 6C,G**), owing to the thermal coupling between $^2H_{11/2}$ and $^4S_{3/2}$ states of Er$^{3+}$. Based on Boltzmann distribution theory, FIR of two thermally coupled states can be expressed as the

following equation: (Chen et al., 2015; Pandey et al., 2015; Nigoghossian et al., 2017a)

$$\text{FIR} = \frac{I_{522}}{I_{541}} = C exp(\frac{-\Delta E}{k_B T}) \tag{1}$$

$$\ln{(FIR)} = \ln C - (\frac{-\Delta E}{k_B})/T \tag{2}$$

where I$_{522}$ and I$_{541}$ are the integrated UC intensities corresponding to the $^2H_{11/2} \rightarrow {}^4I_{15/2}$ and $^4S_{3/2} \rightarrow {}^4I_{15/2}$ transitions, respectively, C is the constant, $\Delta E$ is the energy gap between $^2H_{11/2}$ and $^4S_{3/2}$ states, k$_B$ is the Boltzmann constant, and T is the absolute temperature. According to the expression of the FIR, the value of Ln(I$_{522}$/I$_{541}$) vs. the inverse absolute temperature (1/T) is plotted in **Figures 6B,F**. The slope is fitted to be 1,072 and 1,057, respectively. As a consequence, the energy gap $\Delta E$ and the pre-exponential constant are evaluated to be about 745 cm$^{-1}$, 734 cm$^{-1}$ and 8.316, 8.422, respectively. These two parameters are vital factors for the sensor sensitivity (S) of temperature detection, as defined by the following equation (Chen et al., 2015; Pandey et al., 2015; Nigoghossian et al., 2017a):

$$S_A = \frac{d(FIR)}{dT} = FIR\left(\frac{\Delta E}{k_B T^2}\right) = C(\frac{\Delta E}{k_B T^2}) \exp(\frac{-\Delta E}{k_B T}) \tag{3}$$

The calculated curve of sensor sensitivity as a function of absolute temperature is plotted in **Figures 6D,H**. It can be seen that
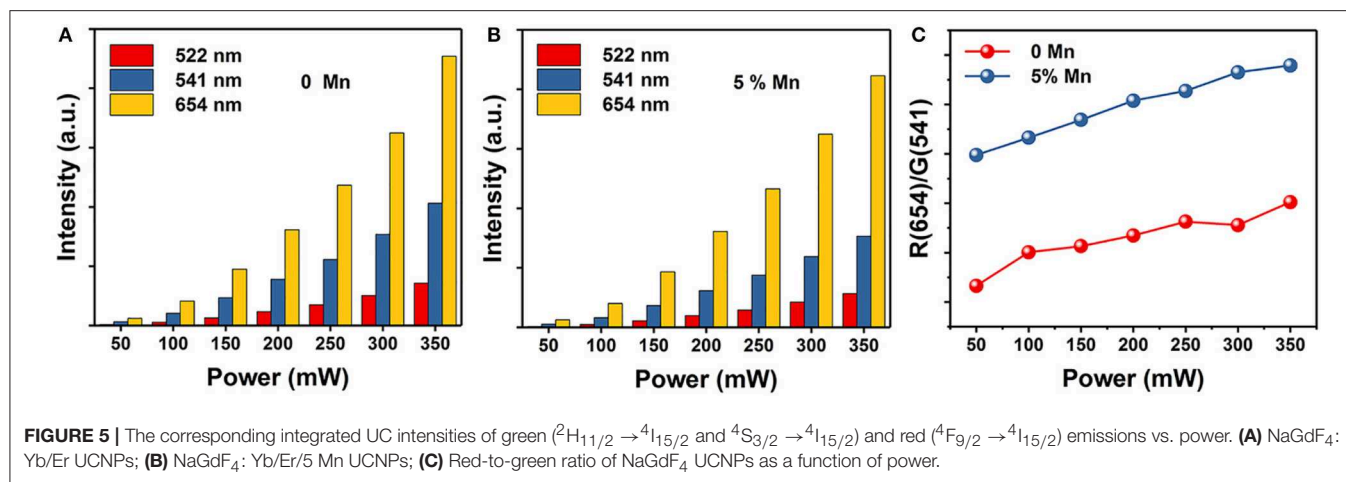
**FIGURE 5 |** The corresponding integrated UC intensities of green ($^2H_{11/2} \rightarrow {}^4I_{15/2}$ and $^4S_{3/2} \rightarrow {}^4I_{15/2}$) and red ($^4F_{9/2} \rightarrow {}^4I_{15/2}$) emissions vs. power. **(A)** NaGdF$_4$: Yb/Er UCNPs; **(B)** NaGdF$_4$: Yb/Er/5 Mn UCNPs; **(C)** Red-to-green ratio of NaGdF$_4$ UCNPs as a function of power.
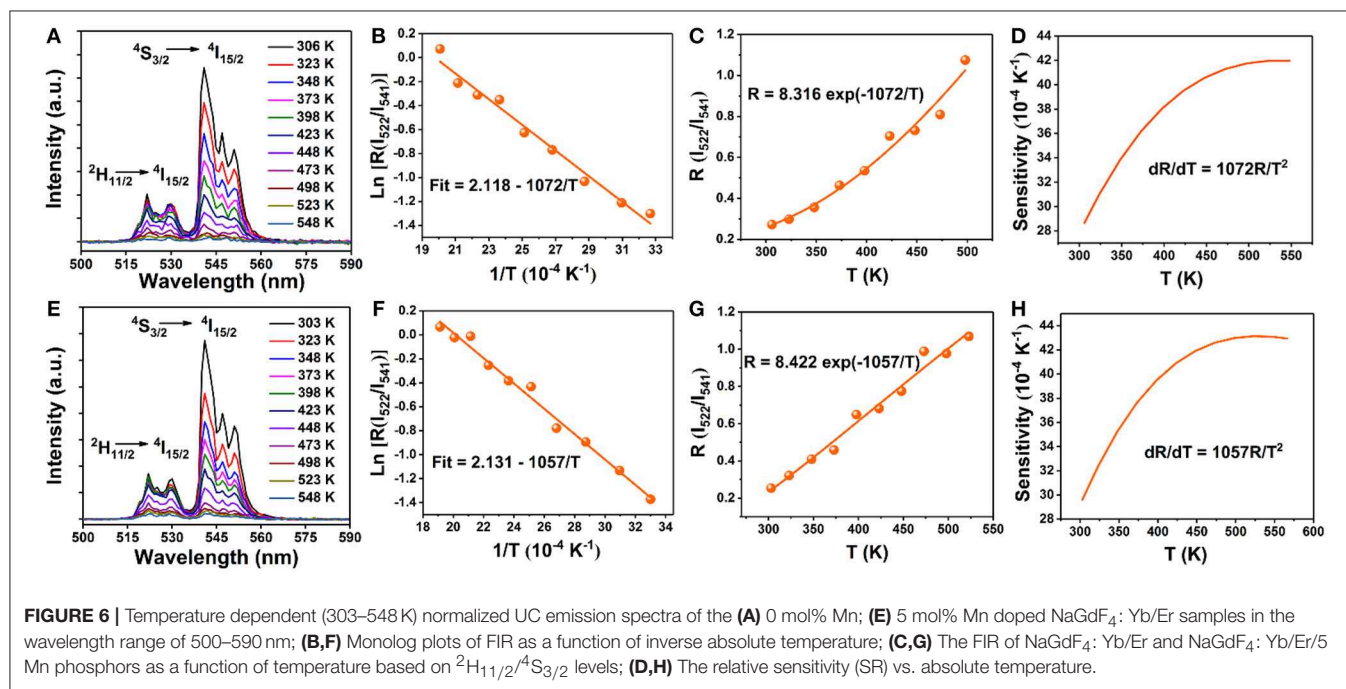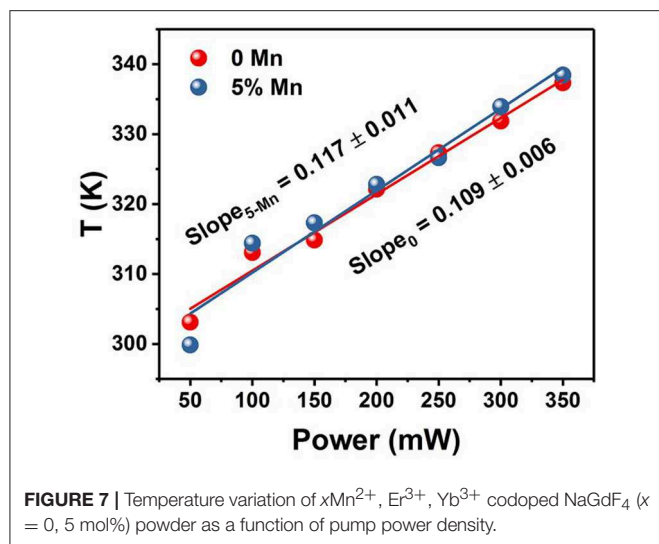


**FIGURE 6 |** Temperature dependent (303–548 K) normalized UC emission spectra of the **(A)** 0 mol% Mn; **(E)** 5 mol% Mn doped NaGdF$_4$: Yb/Er samples in the wavelength range of 500–590 nm; **(B,F)** Monolog plots of FIR as a function of inverse absolute temperature; **(C,G)** The FIR of NaGdF$_4$: Yb/Er and NaGdF$_4$: Yb/Er/5 Mn phosphors as a function of temperature based on $^2H_{11/2}/^4S_{3/2}$ levels; **(D,H)** The relative sensitivity (SR) vs. absolute temperature.

the sensitivity keeps increasing in our experimental temperature range, and the maximal value of about 0.0043 K$^{-1}$ and 0.0042 K$^{-1}$ is realized at the temperature of 523 K, respectively. The FIR of NaGdF$_4$: Yb/ Er doping with Mn$^{2+}$ is similar to that without Mn$^{2+}$ based on thermally coupled levels (TCL), indicating that the energy transfer between Er$^{3+}$ and Mn$^{2+}$ has a small impact on FIR.

## Optical Heater Properties

The temperatures at different power densities are calculated through Equation (2). As shown in **Figure 7**, the temperature exhibits a linearly increasing tendency with the power density increase (Rohani et al., 2015; Nigoghossian et al., 2017b). The slopes of without and with Mn$^{2+}$ doped powders are 0.109 and 0.117, respectively. It could be concluded that optical heat generated by laser power density is mildly more in the

Mn$^{2+}$ participate in Er$^{3+}$–Yb$^{3+}$ codoped NaGdF$_4$ phosphor than the Er$^{3+}$–Yb$^{3+}$ codoped NaGdF$_4$ phosphor. Due to the energy absorbed by the sample may slightly increase as Mn$^{2+}$ doping. As we know, the heat generation inside the samples is due to the non-radiative relaxation involved and the crystalline nature of the synthesized materials. When the energy could not be entirely utilized in the radiative transitions, the excess energy will lead to phonon-assisted non-radiative transitions process, resulting in elevated temperature (Xiang et al., 2014; Hao et al., 2017). The outstanding capability of quickly photo-thermal conversion makes the Mn$^{2+}$ participate in Er$^{3+}$–Yb$^{3+}$ codoped NaGdF$_4$ NPs not only a potential candidate as optical heater, but also useful in local hyperthermia based cancer treatment as the temperature were produced within the required range for hyperthermia based treatment (Van der Zee, 2002; Xiang et al., 2014; Lyu et al., 2018).

**FIGURE 7 |** Temperature variation of $x$Mn$^{2+}$, Er$^{3+}$, Yb$^{3+}$ codoped NaGdF$_4$ ($x$ = 0, 5 mol%) powder as a function of pump power density.

## CONCLUSIONS

In conclusion, a method of transition metal Mn$^{2+}$ doping for the simultaneous morphology/size control, and multi-color output in NaGdF$_4$: Yb/Er UCNPs with fixed composition of both host and dopants of lanthanides is demonstrated. The Mn$^{2+}$ dopant makes an enhanced UCL intensity, and larger power-dependent R/G ratio compared to Mn$^{2+}$ free UCNPs. It could be ascribed to the increasing of BET process between Er$^{3+}$ and Mn$^{2+}$ ($^4$S$_{3/2}$ (Er$^{3+}$) → $^4$T$_1$ (Mn$^{2+}$) → $^4$F$_{9/2}$ (Er$^{3+}$)). Furthermore, the samples show high sensing sensitivities and the maximal sensing sensitivities reach 0.0043 K$^{-1}$ at 523 K. In addition, the input excitation power density induced FIR change and the optical

heating of the phosphors have been studied eventually by varying the input excitation power density of the 980 nm NIR diode laser. More importantly, the near-infrared laser induced elevated temperatures ($\Delta$T) reach ~50 K (5 mol% Mn$^{2+}$) when the power density was changed, which is attributed to the increasing phonon-assisted non-radiative transitions process. The internal heat produced from the samples is within the range required for hyperthermia treatment, too. These results provide guidance for the application of Mn$^{2+}$ participate in Yb$^{3+}$–Er$^{3+}$ codoped NaGdF$_4$ UCNPs in color modulation, temperature sensing and optical heating.

## AUTHOR CONTRIBUTIONS

All experimental work was performed by QQ under guidance of YW. All authors contributed to the analysis of the results and to the writing of the paper.

## ACKNOWLEDGMENTS

## SUPPLEMENTARY MATERIAL

The Supplementary Material for this article can be found online at: https://www.frontiersin.org/articles/10.3389/fchem. 2019.00425/full#supplementary-material

## REFERENCES

Bian, W., Lin, Y., Wang, T., Yu, X., Qiu, J., Zhou, M., et al. (2018). Direct Identification of surface defects and their influence on the optical characteristics of upconversion nanoparticles. *ACS nano* 12, 3623–3628. doi: 10.1021/acsnano.8b00741

Brites, C. D., Lima, P. P., Silva, N. J., Millán, A., Amaral, V. S., Palacio, F., et al. (2012). Thermometry at the nanoscale. *Nanoscale* 4, 4799–4829. doi: 10.1039/c2nr30663h

Carlos, L. D., and Palacio, F. (eds.) (2016). *Thermometry at the Nanoscale: Technique and Selected Applications.* Oxfordshire: Royal Society of Chemistry.

Chen, D., Liu, S., Li, X., Wan, Z., and Li, S. (2017). Gd-based oxyfluoride glass ceramics: phase transformation, optical spectroscopy and upconverting temperature sensing. *J. Eur. Ceramic Soc.* 37, 4083–4094. doi: 10.1016/j.jeurceramsoc.2017. 05.006

Chen, D., Wan, Z., Zhou, Y., Zhou, X., Yu, Y., Zhong, J., et al. (2015). Dual-phase glass ceramic: structure, dual-modal luminescence, and temperature sensing behaviors. *ACS Appl. Mater. Interfaces* 7, 19484–19493. doi: 10.1021/acsami.5b06036

Chen, D., Yu, Y., Huang, F., Huang, P., Yang, A., and Wang, Y. (2010). Modifying the size and shape of monodisperse bifunctional alkaline-earth fluoride nanocrystals through lanthanide doping. *J. Am. Chem. Soc.* 132, 9976–9978. doi: 10.1021/ja10 36429

Chen, G., Seo, J., Yang, C., and Prasad, P. N. (2013). Nanochemistry and nanomaterials for photovoltaics. *Chem. Soc. Rev.* 42, 8304–8338. doi: 10.1039/C3CS60054H

Dan, H. K., Zhou, D., Wang, R., Jiao, Q., Yang, Z., Song, Z., et al. (2016). Effect of Mn$^{2+}$ ions on the enhancement red upconversion emission and energy transfer of Mn$^{2+}$/Tm$^{3+}$/Yb$^{3+}$ tri-doped transparente glass-ceramics. *Mater. Res. Bull.* 73, 357–361. doi: 10.1016/j.materresbull.2015.09.019

Debasu, M. L., Ananias, D., Pastoriza-Santos, I., Liz-Marzán, L. M., Rocha, J., and Carlos, L. D. (2013). All-in-one optical heater-thermometer nanoplatform operative from 300 to 2000 K based on Er$^{3+}$ emission and blackbody radiation. *Adv. Mater.* 25, 4868–4874. doi: 10.1002/adma.201300892

Debasu, M. L., Brites, C. D., Balabhadra, S., Oliveira, H., Rocha, J., and Carlos, L. D. (2016). Nanoplatforms for plasmon-induced heating and thermometry. *Chem. Nano Mat.* 2, 520–527. doi: 10.1002/cnma.201600061

Dey, R., Pandey, A., and Rai, V. K. (2014). Er3+-Yb3+ and Eu3+-Er3+-Yb3+ codoped Y2O3 phosphors as optical heater. *Sensors Actuators B Chem.* 190, 512–515. doi: 10.1016/j.snb.2013.09.025

Dong, B., Cao, B., He, Y., Liu, Z., Li, Z., and Feng, Z. (2012). Temperature sensing and in vivo imaging by molybdenum sensitized visible upconversion luminescence of rare-earth oxides. *Adv. Mater.* 24, 1987–1993. doi: 10.1002/adma.201200431

Dong, B., Hua, R. N., Cao, B. S., Li, Z. P., He, Y. Y., Zhang, Z. Y., et al. (2014). Size dependence of the upconverted luminescence of NaYF4: Er, Yb microspheres for use in ratiometric thermometry. *Phys. Chem. Chem. Phys.* 16, 20009–20012. doi: 10.1039/C4CP01966K

Dong, B., Yang, T., and Lei, M. K. (2007). Optical high temperature sensor based on green up-conversion emissions in $Er^{3+}$ doped $Al_2O_3$. *Sensors Actuators B Chem.* 123, 667–670. doi: 10.1016/j.snb.2006.10.002

Dong, H., Sun, L. D., and Yan, C. H. (2015). Energy transfer in lanthanide upconversion studies for extended optical applications. *Chem. Soc. Rev.* 44, 1608–1634. doi: 10.1039/C4CS00188E

Du, P., Luo, L., Park, H. K., and Yu, J. S. (2016). Citric-assisted sol-gel based $Er^{3+}/Yb^{3+}$-codoped $Na_{0.5}Gd_{0.5}MoO_4$: a novel highly-efficient infrared-to-visible upconversion material for optical temperature sensors and optical heaters. *Chem. Eng. J.* 306, 840–848. doi: 10.1016/j.cej.2016.08.007

Du, P., Luo, L., and Yu, J. S. (2017). Tunable color upconverison emissions in erbium (III)-doped BiOCl microplates for simultaneous thermometry and optical heating. *Microchim. Acta*, 184, 2661–2669. doi: 10.1007/s00604-017-2278-0

Fischer, L. H., Harms, G. S., and Wolfbeis, O. S. (2011). Upconverting nanoparticles for nanoscale thermometry. *Angew. Chem. Int. Ed.* 50, 4546–4551. doi: 10.1002/anie.201006835

Flaherty, J. M., and Di Bartolo, B. (1973). Radiative and radiationless processes of $Er^{3+}$ in $MnF_2$. *J. Luminescence*, 8, 51–70. doi: 10.1016/0022-2313(73)90035-5;

Gai, S., Li, C., Yang, P., and Lin, J. (2013). Recent progress in rare earth micro/nanocrystals: soft chemical synthesis, luminescent properties, and biomedical applications. *Chem. Rev.* 114, 2343–2389. doi: 10.1021/cr4001594

Hao, H., Lu, Z., Lu, H., Ao, G., Song, Y., Wang, Y., and Zhang, X. (2017). $Yb^{3+}$ concentration on emission color, thermal sensing and optical heater behavior of $Er^{3+}$ doped $Y_6O_5F_8$ phosphor. *Ceramics Int.* 43, 10948–10954. doi: 10.1016/j.ceramint.2017.05.133

Jaque, D., and Vetrone, F. (2012). Luminescence nanothermometry. *Nanoscale* 4, 4301–4326. doi: 10.1039/c2nr30764b

Jiang, G., Wei, X., Zhou, S., Chen, Y., Duan, C., and Yin, M. (2014). Neodymium doped lanthanum oxysulfide as optical temperature sensors. *J. Luminesc.* 152, 156–159. doi: 10.1016/j.jlumin.2013.10.027

León-Luis, S. F., Rodríguez-Mendoza, U. R., Martín, I. R., Lalla, E., and Lavín, V. (2013). Effects of $Er^{3+}$ concentration on thermal sensitivity in optical temperature fluorotellurite glass sensors. *Sensors Actuators B Chem.* 176, 1167–1175. doi: 10.1016/j.snb.2012.09.067

Li, D., Wang, Y., Zhang, X., Dong, H., Liu, L., Shi, G., et al. (2012). Effect of $Li^+$ ions on enhancement of near-infrared upconversion emission in $Y_2O_3$: $Tm^{3+}/Yb^{3+}$ nanocrystals. *J. Appl. Phys.* 112:094701. doi: 10.1063/1.4764028

Liu, B. T., Wu, C. G., Chen, G., Chen, W. B., Peng, L. L., Yao, Y. C., et al. (2019). All-in-one surface engineering strategy on nickel phosphide arrays towards a robust electrocatalyst for hydrogen evolution reaction. *J. Power Sources* 429, 46–54. doi: 10.1016/j.jpowsour.2019.04.119

Liu, G., Sun, Z., Fu, Z., Ma, L., and Wang, X. (2017). Temperature sensing and bio-imaging applications based on polyethylenimine/$CaF_2$ nanoparticles with upconversion fluorescence. *Talanta* 169, 181–188. doi: 10.1016/j.talanta.2017.03.054

Liu, X., Deng, R., Zhang, Y., Wang, Y., Chang, H., Huang, L., et al. (2015). Probing the nature of upconversion nanocrystals: instrumentation matters. *Chem. Soc. Rev.* 44, 1479–1508. doi: 10.1039/C4CS00356J

Lyu, L., Cheong, H., Ai, X., Zhang, W., Li, J., Yang, H., et al. (2018). Near-infrared light-mediated rare-earth nanocrystals: recent advances in improving photon conversion and alleviating the thermal effect. *NPG Asia Mater.* 10, 685–702. doi: 10.1038/s41427-018-0065-y

Marciniak, L., Waszniewska, K., Bednarkiewicz, A., Hreniak, D., and Strek, W. (2016). Sensitivity of a nanocrystalline luminescent thermometer in high and low excitation density regimes. *J. Phys. Chem. C* 120, 8877–8882. doi: 10.1021/acs.jpcc.6b01636

Nakazawa, E., Shionoya, S., and Yen, W. M. (1999). *Phosphor Handbook*. Boca Raton, Boston, London, New York, Washington, DC: CRC Press, 102.

Nigoghossian, K., Messaddeq, Y., Boudreau, D., and Ribeiro, S. J. (2017a). UV and temperature-sensing based on NaGdF4: $Yb^{3+}$: $Er^{3+}$@ $SiO_2$-Eu (tta)$_3$. *ACS Omega* 2, 2065–2071. doi: 10.1021/acsomega.7b00056

Nigoghossian, K., Ouellet, S., Plain, J., Messaddeq, Y., Boudreau, D., and Ribeiro, S. J. L. (2017b). Upconversion nanoparticle-decorated gold nanoshells for near-infrared induced heating and thermometry. *J. Mater. Chem. B* 5, 7109–7117. doi: 10.1039/c7tb01621b

Niu, N., Yang, P., He, F., Zhang, X., Gai, S., Li, C., et al. (2012). Tunable multicolor and bright white emission of one-dimensional NaLuF4: $Yb^{3+}$, $Ln^{3+}$ (Ln= Er,

Tm, Ho, Er/Tm, Tm/Ho) microstructures. *J. Mater. Chem.* 22, 10889–10899. doi: 10.1039/C2JM31256E

Pandey, A., Rai, V. K., Kumar, V., Kumar, V., and Swart, H. C. (2015). Upconversion based temperature sensing ability of $Er^{3+}$-$Yb^{3+}$ codoped $SrWO_4$: an optical heating phosphor. *Sensors Actuators B Chem.* 209, 352–358. doi: 10.1016/j.snb.2014.11.126

Peng, H., Stich, M. I., Yu, J., Sun, L. N., Fischer, L. H., and Wolfbeis, O. S. (2010). Luminescent europium (III) nanoparticles for sensing and imaging of temperature in the physiological range. *Adv. Mater.* 22, 716–719. doi: 10.1002/adma.200901614

Pollnau, M., Gamelin, D. R., Lüthi, S. R., Güdel, H. U., and Hehlen, M. P. (2000). Power dependence of upconversion luminescence in lanthanide and transition-metal-ion systems. *Phys. Rev. B* 61:3337. doi: 10.1103/PhysRevB.61.3337

Rai, V. K. (2007). Temperature sensors and optical sensors. *Appl. Phys. B* 88, 297–303. doi: 10.1007/s00340-007-2717-4

Ramasamy, P., Chandra, P., Rhee, S. W., and Kim, J. (2013). Enhanced upconversion luminescence in NaGdF4: Yb, Er nanocrystals by Fe3+ doping and their application in bioimaging. *Nanoscale* 5, 8711–8717. doi: 10.1039/C3NR01608K

Rohani, S., Quintanilla, M., Tuccio, S., De Angelis, F., Cantelar, E., Govorov, A. O., et al. (2015). Enhanced luminescence, collective heating, and nanothermometry in an ensemble system composed of lanthanide-doped upconverting nanoparticles and gold nanorods. *Adv. Opt. Mater.* 3, 1606–1613. doi: 10.1002/adom.201500380

Sedlmeier, A., Achatz, D. E., Fischer, L. H., Gorris, H. H., and Wolfbeis, O. S. (2012). Photon upconverting nanoparticles for luminescent sensing of temperature. *Nanoscale* 4, 7090–7096. doi: 10.1039/C2NR32314A

Sell, D. D., Greene, R. L., and White, R. M. (1967). Optical Exciton-Magnon Absorption in $MnF_2$. *Phys. Rev.* 158:489. doi: 10.1103/PhysRev.158.489

Shannon, R. D. (1976). Revised effective ionic radii and systematic studies of interatomic distances in halides and chalcogenides. *Acta Cryst.* 32, 751–767. doi: 10.1107/S0567739476001551

Tian, G., Gu, Z., Zhou, L., Yin, W., Liu, X., Yan, L., et al. (2012). $Mn^{2+}$ dopant-controlled synthesis of NaYF4: Yb/Er upconversion nanoparticles for in vivo imaging and drug delivery. *Adv. Mater.* 24, 1226–1231. doi: 10.1002/adma.201104741

Tong, L., Li, X., Zhang, J., Xu, S., Sun, J., Zheng, H., et al. (2017). NaYF4: $Sm^{3+}/Yb^{3+}$@ NaYF4: $Er^{3+}/Yb^{3+}$ core-shell structured nanocalorifier with optical temperature probe. *Optics Express* 25, 16047–16058. doi: 10.1364/OE.25.016047

Van der Zee, J. (2002). Heating the patient: a promising approach? *Ann. Oncol.* 13, 1173–1184. doi: 10.1093/annonc/mdf280

Verma, R. K., and Rai, S. B. (2012). Laser induced optical heating from $Yb^{3+}/Ho^{3+}$: $Ca_{12}Al_{14}O_{33}$ and its applicability as a thermal probe. *J. Q. Spectr. Radiative Transfer* 113, 1594–1600. doi: 10.1016/j.jqsrt.2012.04.001

Wade, S. A., Collins, S. F., and Baxter, G. W. (2003). Fluorescence intensity ratio technique for optical fiber point temperature sensing. *J. Appl. Phys.* 94, 4743–4756. doi: 10.1063/1.1606526

Walsh, B. M., and Di Bartolo, B. (2015). On the analysis of the thermal line shift and thermal line width of ions in solids. *J. Luminesc.* 158, 265–267. doi: 10.1016/j.jlumin.2014.10.015

Wang, F., and Liu, X. (2009). Recent advances in the chemistry of lanthanide-doped upconversion nanocrystals. *Chem. Soc. Rev.* 38, 976–989. doi: 10.1039/B809132N

Wang, J., Wang, F., Wang, C., Liu, Z., and Liu, X. (2011). Single-band upconversion emission in lanthanide-doped KMnF3 nanocrystals. *Angew. Chem.* 123, 10553–10556. doi: 10.1002/ange.201104192

Wang, R., Zhang, X., Liu, F., Xiao, L., Chen, Y., and Liu, L. (2016). Upconversion mechanisms of $Er^{3+}$: NaYF4 and thermal effects induced by incident photon on the green luminescence. *J. Luminesc.* 175, 35–43. doi: 10.1016/j.jlumin.2016.02.018

Wang, R., Zhang, X., Zhang, Z., Zhong, H., Chen, Y., Zhao, E., et al. (2017). Modified FIR thermometry for surface temperature sensing by using high power laser. *Optics Express* 25, 848–856. doi: 10.1364/OE.25.000848

Wang, X., Liu, Q., Bu, Y., Liu, C. S., Liu, T., and Yan, X. (2015). Optical temperature sensing of rare-earth ion doped phosphors. *Rsc Adv.* 5, 86219–86236. doi: 10.1039/C5RA16986K

Wawrzynczyk, D., Bednarkiewicz, A., Nyk, M., Strek, W., and Samoc, M. (2012). Neodymium (III) doped fluoride nanoparticles as non-contact optical temperature sensors. *Nanoscale* 4, 6959–6961. doi: 10.1039/C2NR32203J

Xiang, S., Chen, B., Zhang, J., Li, X., Sun, J., Zheng, H., et al. (2014). Microwave-assisted hydrothermal synthesis and laser-induced optical heating effect of NaY(WO$_4$)$_2$: Tm$^{3+}$/Yb$^{3+}$ microstructures. *Optical Mater. Express* 4, 1966–1980. doi: 10.1364/OME.4.001966

Xu, H., Yan, L., Nguyen, V., Yu, Y., and Xu, Y. (2017). One-step synthesis of nitrogen-doped carbon nanodots for ratiometric pH sensing by femtosecond laser ablation method. *Appl. Surface Sci.* 414, 238–243. doi: 10.1016/j.apsusc.2017.04.092

Xu, X., Wang, Z., Lei, P., Yu, Y., Yao, S., Song, S., et al. (2015). α-NaYb(Mn)F$_4$:Er$^{3+}$/Tm$^{3+}$@NaYF$_4$ UCNPs as "band-shape" luminescent nanothermometers over a wide temperature range. *ACS Appl. Mater. Interfaces* 7, 20813–20819. doi: 10.1021/acsami.5b05876

Yang, D., Hou, Z., Cheng, Z., Li, C., and Lin, J. (2015). Current advances in lanthanide ion (Ln$^{3+}$)-based upconversion nanomaterials for drug delivery. *Chem. Soc. Rev.* 44, 1416–1448. doi: 10.1039/C4CS00155A

Zeng, S., Yi, Z., Lu, W., Qian, C., Wang, H., Rao, L., et al. (2014). Simultaneous realization of phase/size manipulation, upconversion luminescence enhancement, and blood vessel imaging in multifunctional nanoprobes through transition metal Mn$^{2+}$ doping. *Adv. Functional Mater.* 24, 4051–4059. doi: 10.1002/adfm.201304270

Zheng, H., Chen, B., Yu, H., Li, X., Zhang, J., Sun, J., et al. (2016). Rod-shaped NaY(MoO$_4$)$_2$:Sm$^{3+}$/Yb$^{3+}$ nanoheaters for photothermal conversion: influence of doping concentration and excitation power density. *Sensors Actuators B Chem.* 234, 286–293. doi: 10.1016/j.snb.2016.04.162

Zheng, H., Chen, B., Yu, H., Zhang, J., Sun, J., Li, X., et al. (2014). Microwave-assisted hydrothermal synthesis and temperature sensing application of Er$^{3+}$/Yb$^{3+}$ doped NaY(WO$_4$)$_2$ microstructures. *J. Colloid Interface Sci.* 420, 27–34. doi: 10.1016/j.jcis.2013.12.059

Zheng, W., Huang, P., Tu, D., Ma, E., Zhu, H., and Chen, X. (2015). Lanthanide-doped upconversion nano-bioprobes: electronic structures, optical properties, and biodetection. *Chem. Soc. Rev.* 44, 1379–1415. doi: 10.1039/C4CS00178H

Zhou, S., Jiang, S., Wei, X., Chen, Y., Duan, C., and Yin, M. (2014). Optical thermometry based on upconversion luminescence in Yb$^{3+}$/Ho$^{3+}$ co-doped NaLuF$_4$. *J. Alloys Compounds* 588, 654–657. doi: 10.1016/j.jallcom.2013.11.132

Zhou, S., Li, X., Wei, X., Duan, C., and Yin, M. (2016). A new mechanism for temperature sensing based on the thermal population of $^7F_2$ state in Eu$^{3+}$. *Sensors Actuators B Chem.* 231, 641–645. doi: 10.1016/j.snb.2016.03.082

# Oxygen Reduction Reaction Activity of Microwave Mediated Solvothermal Synthesized CeO$_2$/g-C$_3$N$_4$ Nanocomposite

Siba Soren[1], Ipsha Hota[1], A. K. Debnath[2], D. K. Aswal[2], K. S. K. Varadwaj[1] and Purnendu Parhi[1]*

[1] Department of Chemistry, Ravenshaw University, Cuttack, India, [2] Technical Physics Division, Bhabha Atomic Research Center, Mumbai, India

Electrocatalytic active species like transition metal oxides have been widely combined with carbon-based nanomaterials for enhanced Oxygen Reduction Reaction (ORR) studies because of the synergistic effect arising between different components. The aim of the present study is to synthesize CeO$_2$/g-C$_3$N$_4$ system and compare the ORR activity with bare CeO$_2$. Ceria (CeO$_2$) embedded on g-C$_3$N$_4$ nanocomposite was synthesized by a single-step microwave-mediated solvothermal method. This cerium oxide-based nanocomposite displays enhanced ORR activity and electrochemical stability as compared to bare ceria.

**Keywords: g-C$_3$N$_4$, CeO$_2$, cyclic voltammogram, linear sweep voltammetry, rotating disk electrode, rotating ring disk electrode**

## INTRODUCTION

Metal–air batteries and fuel cells are alternative energy transfer devices designed to meet the requirements of sustainable energy (Sun et al., 2017). Direct Methanol Fuel Cells (DMFCs) are documented as an ideal candidate for laptop, mobile, and digital camera applications. Efficient reduction of O$_2$ to water is a major challenge in energy conversion in DMFCs. The Oxygen Reduction Reaction (ORR) in alkaline DMFCs proceeds via a 4-electron pathway, (O$_2$ + 2H$_2$O + 4e$^-$ → 4OH$^-$) which is preferable over the 2-electron pathway (O$_2$ + H$_2$O + 2e$^-$ → HO$_2^-$ + OH$^-$) (Zhang and Song, 2008). The 2-electron process is unfavorabl because of the production of corrosive peroxide species, which can cause degradation of electrochemical cells. The precious metal catalysts such as Pt and Pt- based alloys used to catalyze the ORR process are expensive and available in limited quantity (Peng and Yang, 2009; Kim et al., 2010). These Pt-based catalysts are also intolerant to methanol, which is used as fuel in DMFCs. Design of new non-precious electrocatalyst with improved ORR activity is still a challenge before the scientific community. First row transition metal oxides (TMOs) (Bashyam and Zelenay, 2006; Cheng et al., 2009; Jaouen et al., 2011; Cheng and Chen, 2012) have already been used as robust alternatives for promoting the ORR in alkaline conditions. The low electrical conductivity of the TMOs influences the electron transfer process in ORR (Soren et al., 2016).

Carbon materials possess a specific place for the ORR in DMFCs. Various carbon materials like graphite (Jiao et al., 2014), carbon black, carbon nanotube, and activated carbon are mostly used as supporting materials in the preparation of electrocatalysts due to their high electrical conductivity, corrosion resistance, porous structure and specific surface area (Liang et al., 2011). TMOs when

embedded with reduced graphene oxide show enhanced catalytic performance because of a synergetic effect between TMOs and graphene oxide (Liang et al., 2011, 2012; Wang et al., 2011; Guo and Sun, 2012; Guo et al., 2012; Wu et al., 2015).

Hetero atoms (e.g., N, B, P, S, and I) were also doped in the reduced graphene oxide in order to improve the catalytic active sites in reduced graphene oxide (Behnam, 2017). In the recent past, nitrogen-doped graphene oxide has become a potential carbon-based electrocatalyst for ORR because of its low cost, high stability, and high efficiency (Qu et al., 2010; Geng et al., 2011; Yang et al., 2012; Paraknowitsch and Thomas, 2013). The electronic environment of doping nitrogen on a reduced graphene sheet in three configurations (e.g., pyridynic, pyrrolic, and graphitic nitrogen) induces an uneven charge distribution in adjacent sites, and as a result it alters the local spin or charge density. It promotes oxygen adsorption and helps in the enhancement of ORR performance (Ikeda et al., 2008; Niwa et al., 2009; Liu et al., 2010; Qu et al., 2010; Rao et al., 2010; Kim et al., 2011; Li et al., 2011, 2013; Sheng et al., 2011; Zhang and Xia, 2011; Lai et al., 2012; Parvez et al., 2012; Sharifi et al., 2012; Wang et al., 2012; Zhang et al., 2013; Zheng et al., 2013; Bag et al., 2014). Transition metal oxide embedded in N doped carbon systems is reported as a promoter of ORR catalytic activity by facilitating electron transfer (Bag et al., 2014). Rare earth oxide-based systems are now extensively studied for ORR due to their unique electronic structure, bonding characteristics and variable oxidation states. There are very few reports available in the literature where rare earth oxides such as lanthanum oxide, samarium oxide, and cerium oxide have been studied for their ORR properties (Soren et al., 2016; Wang et al., 2016, 2017). The unique structural properties of CeO$_2$ have contributed toward the promising electrocatalytic activity of CeO$_2$. However, poor electronic conductivity of CeO$_2$ limits its application toward ORR. Thus, in order to enhance the electrocatalytic activity, CeO$_2$ is doped with different metals or embedded with a conductive active framework. Recently, our group has published an article on ORR activity of the CeO$_2$/NrGO system (Soren et al., 2016).

Researchers have found a new material analogy to N-doped rGO called graphitic carbon nitride (g-C$_3$N$_4$) (Qiao et al., 2016). It is a carbon- and nitrogen-based polymeric material. Graphitic carbon nitride (g-C$_3$N$_4$) is a nitrogen-rich carbon-based material. But as reported in the literature g-C$_3$N$_4$ is an inert electrocatalyst (Liu and Zhang, 2013; Zou et al., 2013). However, g-C$_3$N$_4$ with metal doping or metal oxide doping has already been reported as a promising electrocatalyst for ORR and OER (Oxygen Evolution Reaction), when embedded with transition metal/metal oxide (Liu and Zhang, 2013; Zou et al., 2013).

It is expected that CeO$_2$/g-C$_3$N$_4$ composite can enhance the ORR in fuel cells. In this paper, we have investigated the ORR activity of CeO$_2$ embedded with g-C$_3$N$_4$ to show whether it follows a 2-electron or 4-electron pathway in the ORR process. The hybrid CeO$_2$/g-C$_3$N$_4$ nanostructures were prepared by the microwave mediated polyol method.

## MATERIALS AND METHODS

### Chemicals

Melamine, Ammonium Cerium (IV) Nitrate and 1, 4-Butanediol were procured from HIMEDIA. All the chemicals were used as received.

### Synthesis of g-C$_3$N$_4$

About 3 g of melamine was taken in china crucible and was heated for 4 h at 520°C with a moderate heating rate of 10°C/min inside the muffle furnace. The product obtained was cooled to room temperature. The prepared g-C$_3$N$_4$ was characterized for further work.

### Synthesis of CeO$_2$/g-C$_3$N$_4$ Composite

In typical synthesis 50 mg of the above-prepared g-C$_3$N$_4$ was added to 20 ml of 1, 4-butanediol. The solution was stirred at 300 rpm in a 50 ml beaker to make a heterogeneous mixture. A total of 250 mg of ammonium cerium (IV) nitrate was added to this heterogeneous solution and again stirred at the same rpm for 10 min until the color of the solution changed from light yellow to orange red. The entire solution was transferred to a Teflon vessel. The vessel was tightly sealed and irradiated with microwave radiation (MDS 6) for 10 min at 180°C. The reaction mixture was allowed to cool to room temperature after completion of the reaction. The obtained light yellow-colored precipitate was centrifuged several times with distilled water, ethanol, and acetone to remove the impurities. Finally, the product was kept for drying in an oven over night at 60°C.

### Characterization

The crystallographic phases were identified by XRD measurements using a Rigaku Ultima-IV Advance X-ray Diffractometer operating at 40 KV (radiation source Cu Kα, wavelength = 1.5418 Å). FTIR analysis was carried out with the help of Thermo Fischer Nicolet iS5 FTIR instrument. The XPS measurement was performed using DESA-150 electron analyzer (Staib (1253.6 eV) as radiation source. Transmission Electron Microscope (TEM) and High Resolution Transmission Electron Microscope (HRTEM) images were obtained by the Model FEI Technai G2 S-Twin (Benson et al., 2014). Electrochemical Impedance Spectroscopic analysis was recorded CH660E electrochemical work station.

### Electrochemical Measurements

The electrochemical measurements were conducted in a conventional three-electrode system using a Metrohm Autolab 204 B.V. (Metrohm Autolab, Netherland). During the measurements, saturated Ag/AgCl electrode, Pt wire, and modified glassy carbon (GC) electrode were used as reference, counter, and working electrode respectively. Synthesized electrocatalyst material was loaded on a pre-cleaned GC electrode during preparation of the working electrode. For the preparation of catalytic ink 5 mg of as synthesized electrocatalyst was dispersed in 2 ml isopropanol, 3 ml double distilled H$_2$O, and 25 micro liter Nafion solution (as binder) in an ultrasonic bath for 30 min (Soren et al., 2016). About 12 μl of well-dispersed catalytic ink (∼0.012 mg) was drop casted onto the polished GC
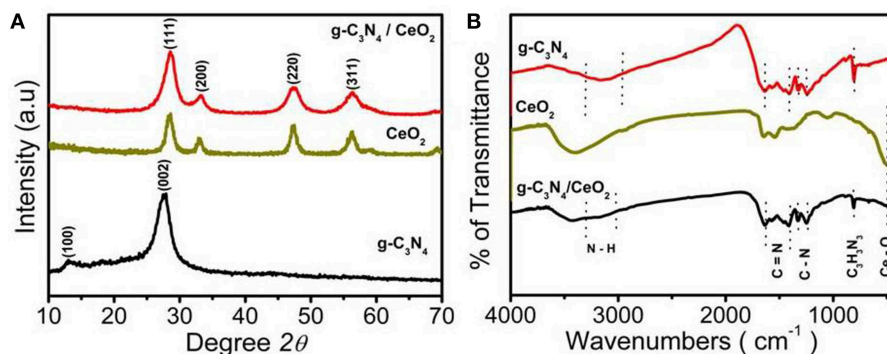
**FIGURE 1 | (A)** XRD of g-C$_3$N$_4$, CeO$_2$, CeO$_2$/ g-C$_3$N$_4$ and **(B)** FTIR spectra of g-C$_3$N$_4$, CeO$_2$, CeO$_2$/g-C$_3$N$_4$.
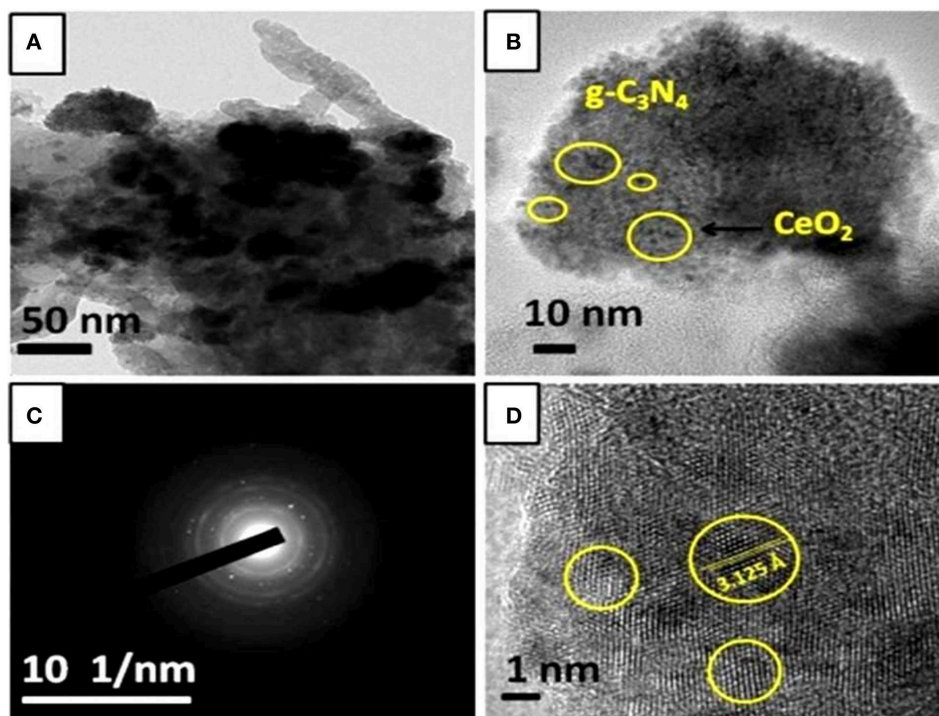


**FIGURE 2 | (a)** TEM, **(b)** HRTEM at 10 nm, **(c)** SAED, and **(d)** HRTEM at 1 nm of CeO$_2$/g-C$_3$N$_4$.

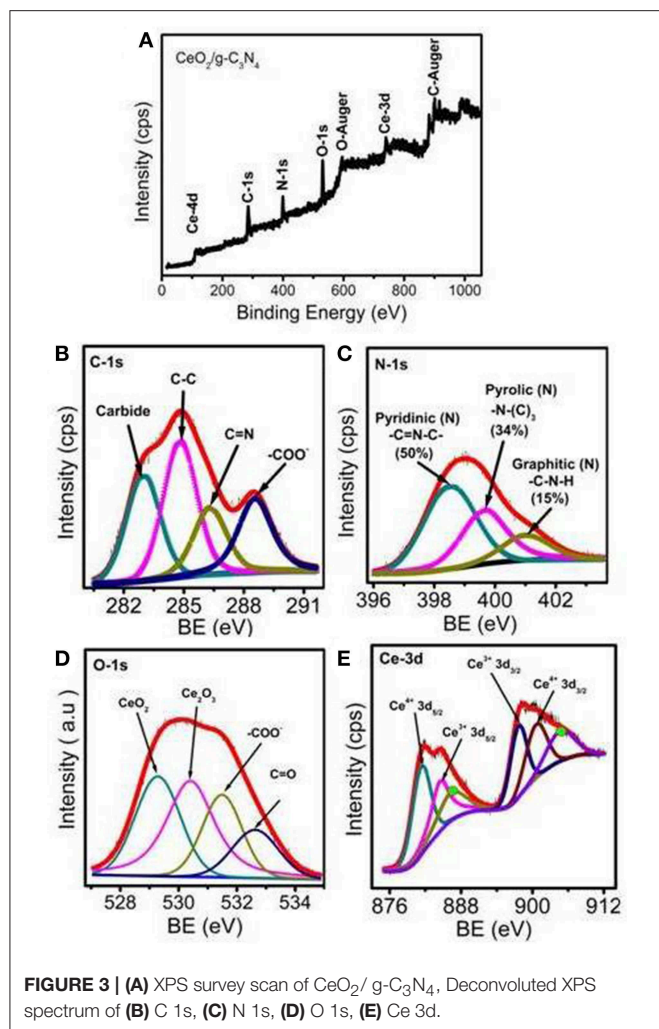electrode of surface area (0.07067 cm$^2$). The modified glassy carbon electrode was dried in a vacuum oven for 3 h. About 33.3 μl of previously prepared catalyst ink was drop casted on RRDE electrode (GC disk electrode) with 5 mm diameter (S = 0.196 cm$^2$) to make the loading the same as in RDE studies.

## RESULT AND DISCUSSION

### Composition and Structure Characterization of CeO$_2$/gC$_3$N$_4$ Hybrid

XRD patterns of the synthesized composite (1:1) were studied and compared with the XRD pattern of individual CeO$_2$ and g-C$_3$N$_4$ (Ferrero et al., 2016). In the case of a pure g-C$_3$N$_4$ sample,

a strong diffraction peak appears at 27.61° that corresponds to the (002) plane. The strong diffraction peak arises because of the stacking of the conjugated aromatic system (Wang et al., 2009). The sharp peak at 27.61° indicates tight packing in g-C$_3$N$_4$, which is because of the strong binding between the layers and large localization of electrons. Another small peak at 13.12° can be assigned to the (100) plane. The diffraction peaks of the pure cubic fluorite structure of CeO$_2$ were indexed to the (111), (200), (220), and (311) planes (JCPDS 81-0792) (Soren et al., 2015). After the incorporation of CeO$_2$ into the g-C$_3$N$_4$ network, the XRD pattern shows an absence of peak at 13.12° even though the weight ratio of g-C$_3$N$_4$ and CeO$_2$ are nearly 1:1 in the composite (Liu and Zhang, 2013). The peak corresponding to the (111) plane of CeO$_2$, which coincides with the highest intensity peak of

FIGURE 3 | (A) XPS survey scan of CeO$_2$/ g-C$_3$N$_4$, Deconvoluted XPS spectrum of (B) C 1s, (C) N 1s, (D) O 1s, (E) Ce 3d.

bare g-C$_3$N$_4$, has been shifted to higher 2θ value, and the intensity of the peak has also been increased. From these findings it can be concluded that CeO$_2$ nanoparticles are successfully embedded into in-planes of g-C$_3$N$_4$ sheets (Thomas et al., 2008; Zhang et al., 2008; Xu et al., 2013) (**Figure 1A**).

The chemical structures of the samples were evaluated by the FTIR analysis. A broad band between 3,000 and 3,500 cm$^{-1}$ was noticed in the composite, which can be attributed to stretching vibration of N-H and surface adsorbed water molecules. The absorption peaks at 1,572 and 1,632 cm$^{-1}$ (Li et al., 2015) were due to C=N stretching (Bojdys et al., 2008; Yan et al., 2009) while for aromatic C-N stretching, peaks at 1,253, 1,320, and 1,425 cm$^{-1}$ were observed. The main structural peaks at 808 cm$^{-1}$ corresponded to the breathing mode of triazine units of g-C$_3$N$_4$ (Xu et al., 2013), which reveals that the graphitic C-N network of g-C$_3$N$_4$ was not affect even after the inclusion of CeO$_2$ in the g-C$_3$N$_4$ layer (**Figure 1B**).

CeO$_2$/g-C$_3$N$_4$ composite showed a layered structure of g-C$_3$N$_4$ (**Figure 2a**), and several small dark images of CeO$_2$ nanoparticle appeared in the TEM image

(**Figure 2b**). The appearance of some bright spots and the diffuse rings in the SAED pattern of CeO$_2$/g-C$_3$N$_4$ corresponds to the growth of crystalline CeO$_2$ nanoparticle on the amorphous g-C$_3$N$_4$ sheet (**Figure 2c**). The fringe spacing was measureed to be 3.125 Å, which corresponds to the (111) lattice plane of the cubic fluorite CeO$_2$ structure (**Figure 2d**).

The composition and chemical structure of the synthesized material were established by X-ray photoelectron spectroscopy. The high resolution XPS survey spectra of C 1s, N 1s, O 1s, and Ce 3d XPS spectra of CeO$_2$/g-C$_3$N$_4$ (1:1) composite is shown in **Figure 3A**. The XPS spectra of the C 1s core level for CeO$_2$/g-C$_3$N$_4$ can be deconvoluted into four components including the standard reference carbon (283 eV) (Xing et al., 2014). The peak at 284.8 eV corresponds to sp$^2$-bonded C-C (Raymundo-Pinero et al., 2002). The peaks at 286.3 and 288.5 eV (Guan et al., 2018) are ascribed to C=N and N-C-N in g-C$_3$N$_4$ respectively (**Figure 3B**) (Yan et al., 2012). The main peak of N 1s at 398.5 eV is assigned to sp$^2$ nitrogen (C=N-C) (pyridinic) present in triazine rings, while the peak at 399.6 eV arises from the tertiary nitrogen bonded to carbon atoms in the form of N–(C)$_3$ (pyrollic). The peak at 401.1 eV can be ascribed to g (C-N-H) (ghaphitic) (**Figure 3C**) (Raymundo-Pinero et al., 2002). The % of N in total spectrum is calculated to be 7.09%. The percentages of different levels of nitrogen in the system were 50.6, 34.48, and 15.05% for pyridinic, pyrrolic, and graphitic nitrogen, respectively. The O 1s spectrum is deconvoluted at 529.2, 531.0, and 533.2 eV for CeO$_2$, COOH and OH respectively. These spectrums suggest the formation of CeO$_2$ on g-C$_3$N$_4$ (**Figure 3D**). The oxidation states of Ce in g-C$_3$N$_4$/CeO$_2$ composites were examined by deconvolution of Ce 3d peaks. The two peaks at 881.6 and 884.7 eV can be attributed to 3d$_{5/2}$ of Ce$^{4+}$ and Ce$^{3+}$ core electrons respectively. Further peaks at 897.5 and 900.1 eV can be ascribed to 3d$_{3/2}$ of Ce$^{3+}$ and Ce$^{4+}$, respectively (**Figure 3E**) (Zheng et al., 2017).

## Electrochemical Performance of CeO$_2$/gC$_3$N$_4$ Hybrid

The cyclic voltammogram (CV) was performed in N$_2$ as well as O$_2$ saturated 0.1 M KOH solution for the three materials (g-C$_3$N$_4$, CeO$_2$ and CeO$_2$/ g-C$_3$N$_4$) in the potential range of −0.8 to 0.2 V at various scan rates (Ferrero et al., 2016). No reduction peaks were observed in the N$_2$-saturated condition. After O$_2$ was introduced for 30 min, intense reduction peaks of g-C$_3$N$_4$ (Jiao et al., 2014), CeO$_2$, and CeO$_2$/g-C$_3$N$_4$ at E$_{onset}$ −0.3, −0.24, and −0.17 V vs. Ag/AgCl, respectively, were recorded (**Figure 4A**). To investigate ORR performance, linear sweep voltammetry (LSV) was recorded for the prepared materials together with commercial 20 wt% Pt/C, in O$_2$ saturated 0.1 M KOH solution using Rotating Disk Electrode (RDE) at 1,600 RPM (Wu X. et al., 2017). From the LSV, plot the onset potential was observed to be −0.3, −0.23, and −0.2 V vs. Ag/AgCl for g-C$_3$N$_4$, CeO$_2$, and CeO$_2$/g-C$_3$N$_4$, respectively (**Figure 4B**). The shift in onset potential of 30 mV for CeO$_2$/g-C$_3$N$_4$ as compared to CeO$_2$ indicates a synergetic interaction between CeO$_2$ and g-C$_3$N$_4$ in
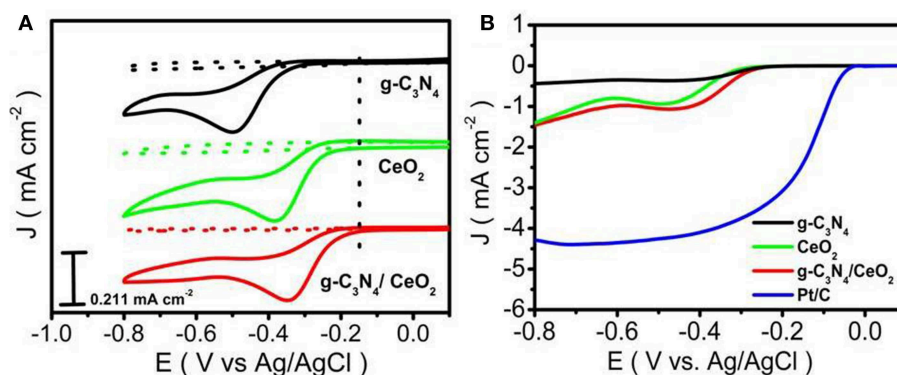
FIGURE 4 | (A) CV study of g-C$_3$N$_4$, CeO$_2$, CeO$_2$/g-C$_3$N$_4$, (B) LSV study of g-C$_3$N$_4$, CeO$_2$, CeO$_2$/g-C$_3$N$_4$ and Pt/C at 1,600 rpm.
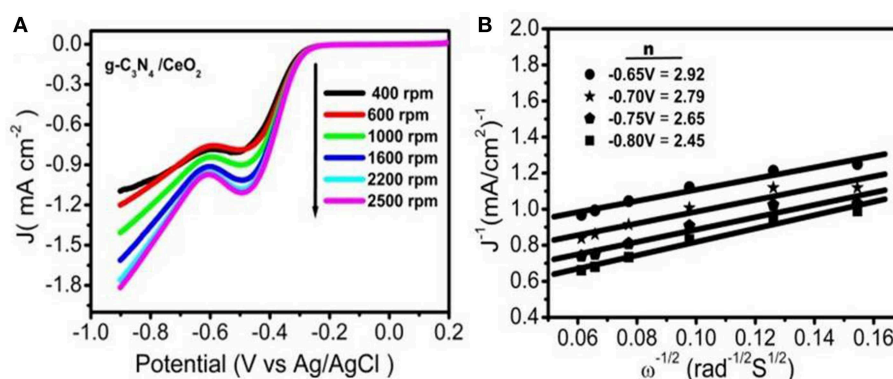


FIGURE 5 | (A) RDE of CeO$_2$/g-C$_3$N$_4$ at various rotation rates, (B) K-L plot of CeO$_2$/g-C$_3$N$_4$ at different potentials.

the composite which facilitates ORR, but the constancy in the current value of CeO$_2$/g-C$_3$N$_4$ composite with CeO$_2$ indicates a slow ORR rate. A positive shift of onset potential (100 mV) between CeO$_2$/g-C$_3$N$_4$ (E$_{onset}$ = −0.2V vs. Ag/AgCl) and g-C$_3$N$_4$ (E$_{onset}$ = −0.3V vs. Ag/AgCl) suggests a strong interaction between CeO$_2$ and g-C$_3$N$_4$. We observed a small improvement in the E$_{1/2}$ for CeO$_2$/g-C$_3$N$_4$ composite (E$_{1/2}$ is −0.383 V) as compared to their individual counterparts (E$_{1/2}$ is −0.383 V and −0.388 V for bare CeO$_2$ and g-C$_3$N$_4$, respectively) (Ferrero et al., 2016). LSVs of CeO$_2$/g-C$_3$N$_4$ at different rotation speeds from 400 to 2,500 rpm were carried out with Rotating Disk Electrode (RDE) to study electron transfer kinetics during ORR process (**Figure 5A**). It is observed that with an increase in rotation rate the diffusion rate of oxygen molecules also increases, which leads to a gradual increase in current density value. Koutecky–Levich (K–L) plots were plotted (**Figure 5B**) in order to gain better insight into the electron transfer process during ORR. The Koutecky–Levich (K–L) equation is given as follows:

$$1/J = 1/J_L + 1/J_K = (1/B)\omega^{-1/2} + 1/J_K \tag{1}$$

$$B = 0.62nFC_0(D_0)^{2/3}\nu^{1/6} \tag{2}$$

Here J is the measured current density, J$_L$ and J$_K$ are the diffusion and kinetic current densities, respectively, n is the transferred electron number per O$_2$ molecule, $\omega$ is the angular velocity, F is the Faraday constant (F = 96,485 C mol$^{-1}$), D$_0$ is the O$_2$ diffusion coefficient (1.9 × 10$^{-5}$ cm$^2$ s$^{-1}$), C$_0$ is the bulk concentration of O$_2$ (1.2 × 10$^{-3}$ mol L$^{-1}$), $\nu$ is the kinematic viscosity of the electrolyte (0.01 m$^2$ s$^{-1}$) (Soren et al., 2016). At various electrode potentials J$^{-1}$ vs. $\omega^{-1/2}$ graphs were plotted for CeO$_2$/g-C$_3$N$_4$ (**Figure 5B**). The number of electrons transferred per O$_2$ molecule (n) was calculated from the slopes of the best fit lines (Soren et al., 2016). The n value for the CeO$_2$/g-C$_3$N$_4$ nano-composite was calculated around 3, which suggests the ORR kinetics proceeds through the 2-electron pathway.

To gain more information on the ORR mechanism, the electron transfer number '$n$' and the rate of peroxide formation can be determined from the RRDE analysis (Ge et al., 2015). In RRDE, the ORR takes place at the GC disk (where the different catalysts were deposited) and the concentric Pt ring detects the peroxide production. **Figure 6** shows the disk and ring currents for the CeO$_2$ and CeO$_2$/g-C$_3$N$_4$ systems. Both catalysts generate ring current at the onset potential for the ORR. All three electrodes display large disk currents with relatively low ring current. Here, n is the

number of electrons transferred, I$_D$ is the current measured at the GC disk, and I$_R$ is the current measured at the Pt ring obtained through RRDE (Qiao et al., 2016). The value of "*N*" is 0.25, denoting the collection efficiency which is a design parameter provided by the RRDE manufacturer. The following two equations are used to determine electron transfer number and amount of peroxide produced during ORR (Ge et al., 2015).

$$n = \frac{4I_D}{I_D + (I_R/N)} \tag{3}$$

$$\%HO_2^- = \frac{200\,(I_R/N)}{I_D + (I_R/N)} \tag{4}$$

At lower over potential regions (−0.4 V vs. Ag/AgCl), the average value of "n" for CeO$_2$, CeO$_2$/g-C$_3$N$_4$ were 2.71, 3.2, respectively. The peroxide formation follows the reverse trend (CeO$_2$ > CeO$_2$/g-C$_3$N$_4$). At higher over potential regions (−0.6 V vs. Ag/AgCl) the "n" of CeO$_2$ and CeO$_2$/g-C$_3$N$_4$ remains constant, i.e., 2.57 and 3.2 respectively (**Figure 7A**). This indicates at the quasi-4-electron process followed CeO$_2$/g-C$_3$N$_4$. The peroxide

formation follows the reverse trend (CeO$_2$ > CeO$_2$/g-C$_3$N$_4$) at higher over potential regions (**Figure 7B**).

An enhancement of reaction kinetics toward the 4-electron ORR pathway is clearly observed from CeO$_2$ to CeO$_2$/ g-C$_3$N$_4$. The ORR activity can be ascribed to the oxygen vacancies in the CeO$_2$ lattice, which originated from the mixed valence states. The defects can be easily healed by oxygen adsorption when exposed to oxygen environment (Soren et al., 2016). The improved ORR activity of CeO$_2$/gC$_3$N$_4$ can be explained by considering the synergistic effect between CeO$_2$ and carbon network containing different types of nitrogen (Pyridinc, pyrolic, and graphitic). Ruoff's group in their recent publication has confirmed the effect of nitrogen doping on the ORR activity (Lai et al., 2012). They have concluded that the catalytic activity is dependent on the nature and amount of nitrogen present in the matrix. It has been established that presence of graphitic nitrogen increases the limiting current whereas the pyridinic nitrogen alters the onset potential of ORR (Soren et al., 2016). Li et al. have shown that the direct reduction pathway for ORR is favored by the presence of pyridinic nitrogen (Li et al., 2013). Bag et al. also confirmed the vital role of pyridinic nitrogen in the enhancement of ORR activity (Bag et al., 2014). In this paper the XPS analysis reveals that CeO$_2$/g-C$_3$N$_4$ has 50.6% pyridinic nitrogen. This explains the shift in onset potential while going from CeO$_2$ to CeO$_2$/gC$_3$N$_4$ composite (as discussed in **Figure 4B**)

Stability of electrocatalysts is another key parameter in the evaluation of their catalytic performance. The catalytic stability of CeO$_2$/g-C$_3$N$_4$ along with commercial Pt/C and bare CeO$_2$ were measured and compared by the Chronoamperometric response method at −0.35 V vs. Ag/AgCl in 0.1 M KOH solution for 12,500 s at 1,000 rpm, and the results are shown in **Figure 8** (Soren et al., 2016). As expected, CeO$_2$/g-C$_3$N$_4$ exhibited better stability as compared to both Pt/C as well as bare CeO$_2$. Moreover, after 12,500 s, relative current value for bare CeO$_2$ and Pt/C decreased by 53 and 40% respectively, while in case of CeO$_2$/g-C$_3$N$_4$ composite a 24% decrease in the relative current was observed.

Methanol poisoning of the cathode impacts the ORR process. As a result, it is very much essential to address another important
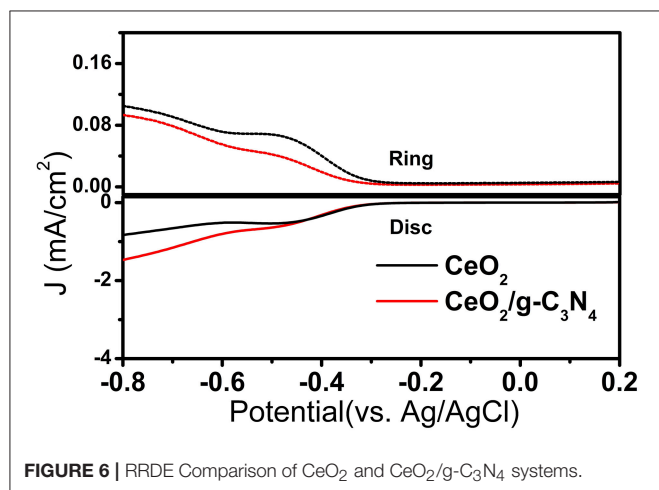
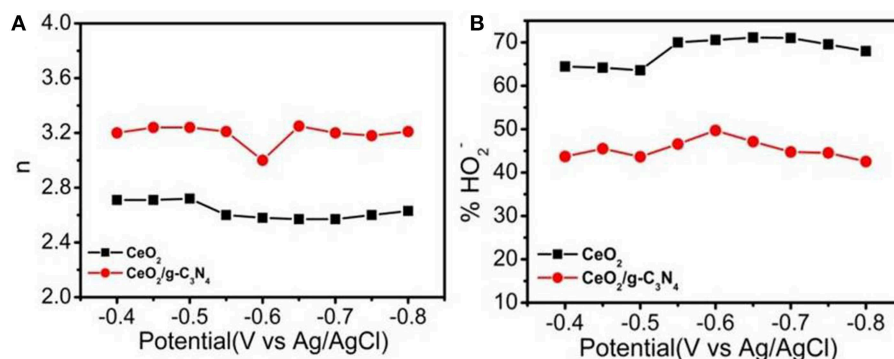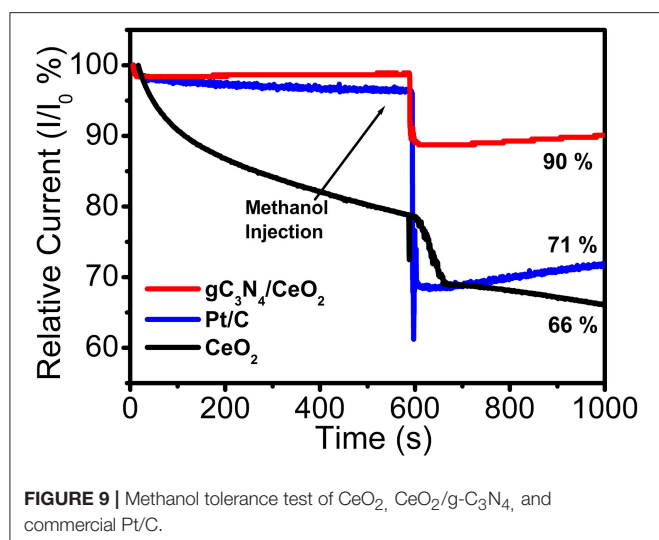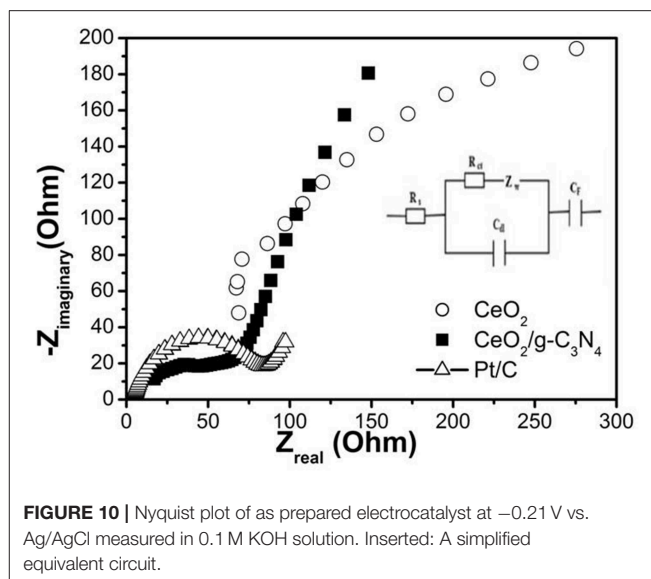

**FIGURE 6 |** RRDE Comparison of CeO$_2$ and CeO$_2$/g-C$_3$N$_4$ systems.



**FIGURE 7 | (A)** Electron transfer number, **(B)** % of HO$_2^-$ formation of CeO$_2$ and CeO$_2$/g-C$_3$N$_4$.

FIGURE 8 | (Current–time) chronoamperometric responses for ORR on CeO$_2$, CeO$_2$/g-C$_3$N$_4$ and commercial Pt/C at −0.35 V at a rotational rate of 1,000 rpm.



FIGURE 10 | Nyquist plot of as prepared electrocatalyst at −0.21 V vs. Ag/AgCl measured in 0.1 M KOH solution. Inserted: A simplified equivalent circuit.



FIGURE 9 | Methanol tolerance test of CeO$_2$, CeO$_2$/g-C$_3$N$_4$, and commercial Pt/C.
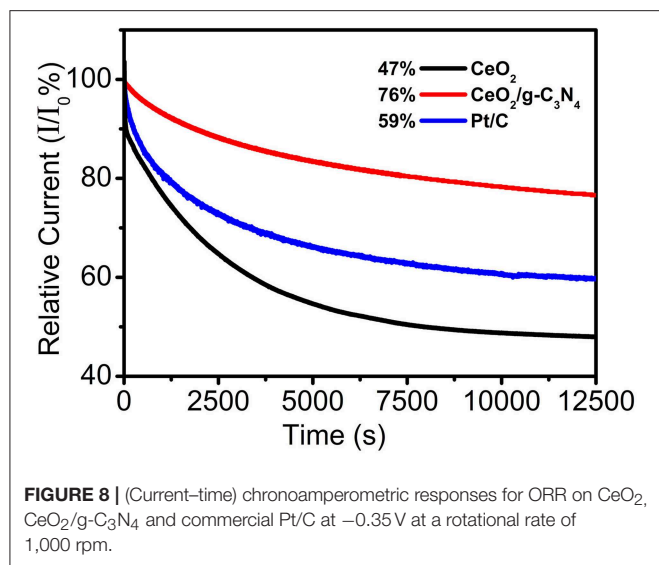
factor of ORR catalysis—i.e., methanol tolerant capability (Bag et al., 2014). For methanol tolerance, test chronoamperometric measurements were performed at −0.35V vs. Ag/AgCl at 1,000 rpm in O$_2$ saturated 0.1 M KOH solution to investigate the methanol crossover effect of CeO$_2$, CeO$_2$/g-C$_3$N$_4$ composite as well as of commercial Pt/C. A total of 25 mL of (10 wt%) 3 M methanol was injected at 600 s. It was observed that there was a 34% and 29% decrease in relative current for CeO$_2$, Pt/C, respectively, whereas only a 10% decrease in relative current was observed for the CeO$_2$/g-C$_3$N$_4$ composite system (**Figure 9**). This result demonstrates the better methanol tolerance ability of CeO$_2$/g-C$_3$N$_4$ as compared to Pt/C.

## Impedance Measurement

Electrochemical impedance spectroscopy (EIS) is another potent technique to describe the electrocatalyst kinetics and interface properties in ORR (Perini et al., 2015). EIS analysis

through Nyquist plots is generally used to examine interfacial charge transport behavior of the electrode-electrolyte interface. The Nyquist plots demonstrate variation of impedance with frequency reflected as imaginary component vs. real component of impedance. **Figure 10** shows the Nyquist plots over the frequency range 100–1 MHz for the CeO$_2$/g-C$_3$N$_4$ modified electrode in 0.1 M KOH solution with an AC amplitude of 0.1 V at an initial potential of −0.210 V. The Nyquist plot is represented at high frequency by a semicircular arc and at low frequency the plot is represented by a straight line. In this plot, the charge transfer resistance at the electrode-electrolyte interface is represented by the diameter of the semicircular arc whereas the diffusion nature of the electrolyte at the electrode surface is represented by a straight line (Parwaiz et al., 2017). The impedance data was fitted to an equivalent circuit (inset of **Figure 10**). The equivalent circuit consists of charge transfer resistance (R$_{ct}$), solution resistance (R$_s$), pseudocapacitance (C$_F$), Warburg impedance (Z$_w$), and double layer capacitance (C$_{dl}$) (Tan and Ren, 2016). The semicircle intercepting the real axis is a combination of both charge transfer resistance R$_{ct}$ (Guan et al., 2018) and ionic resistance of electrolyte R$_s$ (Maheswari and Muralidharan, 2016). R$_s$ consists of bulk electrolyte solution resistance and electron transfer resistance whereas R$_{ct}$ can be ascribed to change transfer resistance at the electrode-electrolyte boundary (Maheswari and Muralidharan, 2015).

The calculated R$_s$ for the CeO$_2$/g-C$_3$N$_4$ composite is 36.5 Ω. The value of R$_s$ of the electrodes can be attributed to the dissimilar conductivities and morphologies of the materials in their construction. A faster electron-transfer rate can be designated by a smaller R$_{ct}$ (Wu Q. et al., 2017). Based on the observations, the diameter of the semicircle and the calculated R$_{ct}$ of the CeO$_2$/g-C$_3$N$_4$ is 150 Ω whereas the R$_{ct}$ for CeO$_2$ and Pt/C was found to be 534.4 and 77.3 Ω, respectively. The lower R$_{ct}$ value of CeO$_2$/g-C$_3$N$_4$ can be assigned to active electron transfer kinetics which in turn favor ORR catalytic activity.

## CONCLUSION

In accordance with the study report, CeO$_2$/g-C$_3$N$_4$ was successfully synthesized by a facile microwave mediated polyol route. The synergic effect of CeO$_2$ after interacting g-C$_3$N$_4$ leads to the enhancement of ORR activity of the CeO$_2$/g-C$_3$N$_4$ modified system as compared to bare CeO$_2$. The XPS and ORR kinetics study results reveal that CeO$_2$/g-C$_3$N$_4$ with high levels of pyridinic nitrogen performs better ORR catalytic activity, implying a vital role of pyridinic nitrogen as promoter of ORR. The composites have shown excellent ORR stability and methanol tolerance behavior than commercial Pt/C. The low cost and facile synthesis procedure predict the future utility of the CeO$_2$/g-C$_3$N$_4$ composite in energy conversion system.

## DATA AVAILABILITY

The datasets generated for this study are available on request to the corresponding author.

## AUTHOR CONTRIBUTIONS

The project is designed by PP. Scientific contributions in term of knowledge and discussion given by KV. SS and IH did the experimental work. DA and AD did the XPS analysis.

## REFERENCES

Bag, S., Roy, K., Gopinath, C. S., and Raj, C. R. (2014). Facile single-step synthesis of nitrogen-doped reduced graphene oxide-Mn$_3$O$_4$ hybrid functional material for the electrocatalytic reduction of oxygen. *ACS Appl. Mater. Interf.* 6, 2692–2699. doi: 10.1021/am405213z

Bashyam, R., and Zelenay, P. (2006). A class of non-precious metal composite catalysts for fuel cells. *Nat. Lett.* 443, 63–66. doi: 10.1038/nature05118

Behnam, S. (2017). Bio-inspired iron metal–carbon black based nano-electrocatalyst for the oxygen reduction reaction. *Pigment Resin Technol.* 46, 267–275. doi: 10.1108/PRT-07-2016-0081

Benson, J., Xu, Q., Wang, P., Shen, Y., Sun, L., Wang, T., et al. (2014). Tuning the catalytic activity of graphene nanosheets for oxygen reduction reaction via size and thickness reduction. *ACS Appl. Mater. Interf.* 6 19726–19736. doi: 10.1021/am5048202

Bojdys, M. J., Muller, J. O., Antonietti, M., and Thomas, A. (2008). Ionothermal synthesis of crystalline, condensed, graphitic carbon nitride. *Chem. Eur. J.* 14, 8177–8182. doi: 10.1002/chem.200800190

Cheng, F., and Chen, J. (2012). Metal–air batteries: from oxygen reduction electrochemistry to cathode catalysts. *Chem. Soc. Rev.* 41, 2172–2192. doi: 10.1039/c1cs15228a

Cheng, F., Shen, J., Ji, W., Tao, Z., and Chen, J. (2009). Selective synthesis of manganese oxide nanostructures for electrocatalytic oxygen reduction. *ACS Appl. Mater. Interf.* 2, 460–466. doi: 10.1021/am800131v

Ferrero, G. A., Antonio, B. F., Marta, S., and Maria-Magdalena, T. (2016). Efficient metal-free N-doped mesoporous carbon catalysts for ORR by a template-free approach. *Carbon* 106, 179–187. doi: 10.1016/j.carbon.2016.04.080

Ge, X., Sumboja, A., Wu, D., Wuu, T., An, T., Li, B., et al. (2015). Oxygen reduction in alkaline media: from mechanisms to recent advances of catalysts. *ACS Catal.* 5, 4643–4667. doi: 10.1021/acscatal.5b00524

Geng, D., Chen, Y., Li, Y., Li, R., Sun, X., Ye, S., et al. (2011). High oxygen-reduction activity and durability of nitrogen-doped grapheme. *Energ. Environ. Sci.* 4, 11760–11764. doi: 10.1039/c0ee00326c

Guan, W., Sun, G., Yin, L., Zhang, Z., and Tian, S. (2018). Ti$_4$O$_7$/g-C$_3$N$_4$ Visible light photocatalytic performance on hypophosphite oxidation: effect of annealing temperature. *Front. Chem.* 6, 37–47. doi: 10.3389/fchem.2018.00037

Guo, J. S., and Sun, H. S. (2012). FePt nanoparticles assembled on graphene as enhanced catalyst for oxygen reduction reaction. *J. Am. Chem. Soc.* 134, 2492–2495. doi: 10.1021/ja2104334

Guo, J. S., Zhang, S., Wu, H. L., and Sun, H. S. (2012). Co/CoO nanoparticles assembled on graphene for electrochemical reduction of oxygen. *Angew. Chem. Int. Ed.* 51, 11770–11773. doi: 10.1002/anie.201206152

Ikeda, T., Boero, M., Huang, F. S., Terakura, K., Oshima, M., and Ozaki, I. J. (2008). Carbon alloy catalysts: active sites for oxygen reduction reaction. *J. Phys. Chem. C* 112, 14706–14709. doi: 10.1021/jp806084d

Jaouen, F., Proietti, E., Lefevre, M., Chenitz, R., Dodelet, J., Wu, P. G., et al. (2011). Recent advances in non-precious metal catalysis for oxygen-reduction reaction in polymer electrolyte fuel cells. *Ener. Environ. Sci.* 4, 114–130. doi: 10.1039/C0EE00011F

Jiao, Y., Zheng, Y., Jaroniec, M., and Qiao, S. Z. (2014). Origin of the electrocatalytic oxygen reduction activity of graphene-based catalysts: a roadmap to achieve the best performance. *J. Am. Chem. Soc.* 136, 4394–4403. doi: 10.1021/ja500432h

Kim, H., Lee, K., Woo, I. S., and Jung, Y. (2011). On the mechanism of enhanced oxygen reduction reaction in nitrogen-doped graphene nanoribbon. *Phys. Chem.* 13, 17505–17510. doi: 10.1039/c1cp21665a

Kim, J., Lee, Y., and Sun, S. (2010). Structurally ordered Fe Pt nanoparticles and their enhanced catalysis for oxygen reduction reaction. *J. Am. Chem. Soc.* 132, 4996–4997. doi: 10.1021/ja1009629

Lai, L., Potts, R. J., Zhan, D., Wang, L., Poh, K. C., Tang, C., et al. (2012). Exploration of the active center structure of nitrogen-doped graphene-based catalysts for oxygen reduction reaction. *Energy Environ. Sci.* 5, 7936–7942. doi: 10.1039/c2ee21802j

Li, H., Kang, W., Wang, L., Yue, Q., Xu, S., Wang, H., et al. (2013). Synthesis of three-dimensional flowerlike nitrogen-doped carbons by a copyrolysis route and the effect of nitrogen species on the electrocatalytic activity in oxygen reduction reaction. *Carbon* 54, 249–257. doi: 10.1016/j.carbon.2012.11.036

Li, L., Xianghong, F., Yao, N., Siguo, C., Feng, S., Kun, X., et al. (2015). Insight into the effect of oxygen vacancy concentration on the catalytic performance of MnO$_2$. *ACS Catal.* 5 4825–4832. doi: 10.1021/acscatal.5b00320

Li, Y., Zhao, Y., Cheng, H., Hu, Y., Shi, G., Dai, L., et al. (2011). Nitrogen-doped graphene quantum dots with oxygen-rich functional groups. *J. Am. Chem. Soc.* 134, 15–18. doi: 10.1021/ja206030c

Liang, Y., Li, Y., Wang, H., Zhou, G. J., Wang, and, J., and Dai, H. (2011). Co$_3$O$_4$ nanocrystals on graphene as a synergistic catalyst for oxygen reduction reaction. *J. Nat. Mater.* 10, 780–786. doi: 10.1038/nmat3087

Liang, Y., Wang, H., Zhou, J., Li, Y., Wang, J., Regier, T., et al. (2012). Covalent hybrid of spinel manganese–cobalt oxide and graphene as advanced oxygen reduction electrocatalysts. *J. Am. Chem. Soc.* 134, 3517–3523. doi: 10.1021/ja210924t

Liu, Q., and Zhang, J. (2013). Graphene supported Co-g-C$_3$N$_4$ as a novel metal–macrocyclic electrocatalyst for the oxygen reduction reaction in fuel cells. *Langmuir* 29, 3821–3828. doi: 10.1021/la400003h

Liu, R., Wu, D., Feng, X., and Mullen, K. (2010). Nitrogen-doped ordered mesoporous graphitic arrays with high electrocatalytic activity for oxygen reduction. *Angew. Chem. Int. Ed.* 122, 2619–2623. doi: 10.1002/ange.200907289

Maheswari, N., and Muralidharan, G. (2015). Supercapacitor behaviour of cerium oxide nanoparticles in nuteral aqueous electrolutes. *Energy Fuels* 29, 8246–8253. doi: 10.1021/acs.energyfuels.5b02144

Maheswari, N., and Muralidharan, G. (2016). Hexagonal CeO$_2$ nanostructures: an efficient electrode material for supercapacitors. *Dalton Trans.* 45, 14352–14362. doi: 10.1039/C6DT03032G

Niwa, H., Horiba, K., Harada, Y., Oshima, M., Ikeda, T., Terakura, K., et al. (2009). X-ray absorption analysis of nitrogen contribution to oxygen reduction reaction in carbon alloy cathode catalysts for polymer electrolyte fuel cells. *J. Power Sources* 187, 93–97. doi: 10.1016/j.jpowsour.2008.10.064

Paraknowitsch, P. J., and Thomas, A. (2013). Doping carbons beyond nitrogen: an overview on advanced heteroatom doped carbons with boron, sulphur and phosphorus for energy applications. *Energy. Environ. Sci.* 6, 2839–2855. doi: 10.1039/c3ee41444b

Parvez, K., Yang, B. S., Hernandez, Y., Winter, A., Turchanin, A., Feng, L. X., et al. (2012). Nitrogen-doped graphene and its iron-based composite as efficient electrocatalysts for oxygen reduction reaction. *ACS Nano* 6, 9541–9550. doi: 10.1021/nn302674k

Parwaiz, S., Bhunia, K., Das, A. K., Khan, M. M., and Pradhan, D. (2017). Cobalt-doped ceria/reduced graphene oxide nanocomposite as an efficient oxygen reduction reaction catalyst and supercapacitor material. *J. Phys. Chem. C.* 121, 20165–20176. doi: 10.1021/acs.jpcc.7b06846

Peng, Z. M., and Yang, H. (2009). Synthesis and oxygen reduction electrocatalytic property of Pt-on-Pd bimetallic heteronanostructures. *J. Am. Chem. Soc.* 131, 7542–7543. doi: 10.1021/ja902256a

Perini, L., Durante, C., Favaro, M., Perazzolo, V., Agnoli, S., Granozzi, G., et al. (2015). Metal-support interaction in platinum and palladium nanoparticles loaded on nitrogen doped mesoporous carbon for oxygen reduction reaction. *ACS Appl. Mater. Interf.* 7, 1170–1179. doi: 10.1021/am506916y

Qiao, X., Shijun, L., Guanghua, W., Ruiping, Z., Huiyu, S., and Xiuhua, L. (2016). Simultaneous doping of nitrogen and fluorine into reduced graphene oxide: a highly active metal-free electrocatalyst for oxygen reduction, Carbon, 2016.*Carbon.* 99, 272–279. doi: 10.1016/j.carbon.2015.12.034

Qu, L., Liu, Y., Baek, B. J., and Dai, L. (2010). Nitrogen-doped graphene as efficient metal-free electrocatalyst for oxygen reduction in fuel cells. *ACS Nano* 4, 1321–1326. doi: 10.1021/nn901850u

Rao, V. C., Cabrera, R. C., and Ishikawa, Y. (2010). In Search of the active site in nitrogen-doped carbon nanotube electrodes for the oxygen reduction reaction. *J. Phys. Chem. Lett.* 1, 2622–2627. doi: 10.1021/jz100971v

Raymundo-Pinero, E., Cazorla-Amoros, D., Linares-Solano, A., Find, J., Wild, U., and Schlogl, R. (2002). Structural characterization of N-containing activated carbon fibers prepared from a low softening point petroleum pitch and a melamine resin. *Carbon* 40, 597–608. doi: 10.1016/S0008-6223(01)00155-5

Sharifi, T., Hu, G., Jia, X., and Wagberg, T. (2012). Formation of active sites for oxygen reduction reactions by transformation of nitrogen functionalities in nitrogen-doped carbon nanotubes. *ACS Nano* 6, 8904–8912. doi: 10.1021/nn302906r

Sheng, H. Z., Shao, L., Chen, J. J., Bao, W. J., Wang, B. F., and Xia, H. X. (2011). Catalyst-free synthesis of nitrogen-doped graphene via thermal annealing graphite oxide with melamine and its excellent electrocatalysis. *ACS Nano* 5, 4350–4358. doi: 10.1021/nn103584t

Soren, S., Bessoi, M., and Parhi, P. (2015). A rapid microwave initiated polyol synthesis of cerium oxide nanoparticle using different cerium precursors. *Ceram. Int.* 41, 8114–8118. doi: 10.1016/j.ceramint.2015.03.013

Soren, S., Mohapatra, B. D., Mishra, S., Debnath, A. K., Aswal, D. K., Varadwaj, K. S. K., et al. (2016). Nano ceria supported nitrogen doped graphene as a highly stable and methanol tolerant electrocatalyst for oxygen reduction. *RSC Adv.* 6, 77100–77104. doi: 10.1039/C6RA13218A

Sun, S., Xue, Y., Wang, Q., Li, S., Huang, H., Miao, H., et al. (2017). Electrocatalytic activity of silver decorated ceria microsphere for oxygen reduction reaction and its application in aluminium-air battery. *Chem. Comm.* 53, 7921–7924. doi: 10.1039/C7CC03691D

Tan, H., and Ren, Z. (2016). Facile Synthesis of Co$_3$O$_4$/Nitrogen-doped graphene Composite with enhanced electrochemical performance. *Mater. Sci. Forum* 847, 14–21. doi: 10.4028/www.scientific.net/MSF.847.14

Thomas, A., Fischer, A., Goettmann, F., Antonietti, M., Müller, J. O., Schlögl, R., et al. (2008). Graphitic carbon nitride materials: variation of structure and morphology and their use as metal-free catalysts. *J. Mater. Chem.* 18, 4893–4908. doi: 10.1039/b800274f

Wang, H., Liang, Y., Li, G. Y., and Dai, J. H. (2011). Co$_{1-x}$ S–graphene Hybrid: a high-performance metal chalcogenide electrocatalyst for oxygen reduction. *Angew. Chem. Int. Ed.* 50, 10969–10972. doi: 10.1002/anie.201104004

Wang, N., Liu, J., Gu, W., Song, Y., and Wang, F. (2016). Toward synergy of carbon and La$_2$O$_3$ in their hybrid as efficient catalyst for oxygen reduction reaction. *RSC Adv.* 6, 77786–77795. doi: 10.1039/C6RA17104D

Wang, S., Zhang, L., Xia, Z., Roy, A., D. W., Chang, J. B., et al. (2012). BCN graphene as efficient metal-free electrocatalyst for the oxygen reduction reaction. *Angew. Chem Int. Ed.* 51, 4209–4212. doi: 10.1002/anie.201109257

Wang, W., Song, J., Kang, Y., Chai, D., Zhao, R., and Lei, Z. (2017). Sm$_2$O$_3$ embedded in nitrogen doped carbon with mosaic structure: an effective catalyst for oxygen reduction reaction. *Energy* 133,115–120. doi: 10.1016/j.energy.2017.05.095

Wang, X., Maeda, K., Thomas, A., Takanabe, K., Xin, G., Carlsson, J. M., et al. (2009). A metal-free polymeric photocatalyst for hydrogen production from water under visible light. *Nat. Mater.* 8, 76–80. doi: 10.1038/nmat2317

Wu, H. K., Zeng, Q., Zhang, B., Leng, X., Su, S. D., Gentle, R. I., et al. (2015). Structural origin of the activity in Mn$_3$O$_4$-graphene oxide hybrid electrocatalysts for the oxygen reduction reaction. *Chem. Sus. Chem.* 8, 3331–3339. doi: 10.1002/cssc.201500372

Wu, Q., Jiang, M., Zhang, X., Cai, J., and Lin, S. (2017). A novel octahedral MnO/RGO composite prepared by thermal decomposition as a noble-metal free electrocatalyst for ORR. *J. Mater. Sci.* 52, 6656–6669. doi: 10.1007/s10853-017-0901-4

Wu, X., Zhu, C., Wang, L., Guo, S., Zhang, Y., Li, H., et al. (2017). Control strategy on two-/four-electron pathway of water splitting by multidoped carbon based catalysts. *ACS Catal.* 3, 1637–1645. doi: 10.1021/acscatal.6b03244

Xing, T., Zheng, Y., Li, H. L., Cowie, C. C. B., Gunzelmann, D., Qiao, S. Z., et al. (2014). Observation of active sites for oxygen reduction reaction on nitrogen-doped multilayer graphene. *ACS Nano* 8, 6856–6862. doi: 10.1021/nn501506p

Xu, M., Han, L., and Dong, S. (2013). Facile fabrication of highly efficient g-C$_3$N$_4$/Ag$_2$O heterostructured photocatalysts with enhanced visible-light photocatalytic activity. *ACS Appl. Mater. Interf.* 5, 12533–12540. doi: 10.1021/am4038307

Yan, H., Chen, Y., and Xu, S. (2012). Synthesis of graphitic carbon nitride by directly heating sulfuric acid treated melamine for enhanced photocatalytic H$_2$ production from water under visible light. *Int. J. Hydrogen Energy* 37, 125–133. doi: 10.1016/j.ijhydene.2011.09.072

Yan, S. C., Li, Z. S., and Zou, Z. G. (2009). Photodegradation performance of g-C$_3$N$_4$ fabricated by directly heating melamine. *Langmuir* 25, 10397–10401. doi: 10.1021/la900923z

Yang, Z., Yao, Z., Li, G., Fang, G., Nie, H., Liu, Z., et al. (2012). Sulfur-doped graphene as an efficient metal-free cathode catalyst for oxygen reduction. *ACS Nano* 6, 205–211. doi: 10.1021/nn203393d

Zhang, C., Hao, R., Liao, H., and Hou, Y. (2013). Synthesis of amino-functionalized graphene as metal-free catalyst and exploration of the roles of various nitrogen states in oxygen reduction reaction. *Nano Energy* 2, 88–97. doi: 10.1016/j.nanoen.2012.07.021

Zhang, J., and Song, C. (2008). Electrocatalytic oxygen reduction reaction, PEM fuel cell electrocatalysts and catalyst layers(springer) 2008, 189–134. doi: 10.1007/978-1-84800-936-3

Zhang, L., and Xia, Z. (2011). Mechanisms of oxygen reduction reaction on nitrogen-doped graphene for fuel cells. *J. Phys. Chem. C* 115, 11170–11176. doi: 10.1021/jp201991j

Zhang, Y., Thomas, A., Antonietti, M., and Wang, X. C. (2008). Activation of carbon nitride solids by protonation: morphology changes, enhanced ionic conductivity, and photoconduction experiments. *J. Am. Chem. Soc.* 131, 50–51. doi: 10.1021/ja808329f

Zheng, B., Wang, J., Wang, B. F., and Xia, H. X. (2013). Synthesis of nitrogen doped graphene with high electrocatalytic activity toward oxygen reduction reaction. *Electrochem. Commun.* 28, 24–26. doi: 10.1016/j.elecom.2012.11.037

Zheng, Y., Jiao, Y., Zhu, Y., Cai, Q., Vasileff, A., Li, L. H., et al. (2017). Molecule-level g-C$_3$N$_4$ coordinated transition metals as a new class of electrocatalysts for oxygen electrode reactions. *J. Am. Chem. Soc.* 139, 3336–3339. doi: 10.1021/jacs.6b13100

Zou, X., Su, J., Silva, R., Goswami, A., Sathe, B. R., and Asefa, T. (2013). Efficient oxygen evolution reaction catalyzed by low-density Ni-doped Co$_3$O$_4$ nanomaterials derived from metal-embedded graphitic C$_3$N$_4$. *Chem. Commun.* 49, 7522–7524. doi: 10.1039/c3cc42891e

# Rhenium (I) Complexes as Probes for Prokaryotic and Fungal Cells by Fluorescence Microscopy: Do Ligands Matter?

Carolina Otero[1], Alexander Carreño[2]*, Rubén Polanco[3], Felipe M. Llancalahuen[1], Ramiro Arratia-Pérez[2], Manuel Gacitúa[4] and Juan A. Fuentes[5]*

[1] Facultad de Medicina, Escuela de Química y Farmacia, Universidad Andres Bello, Santiago, Chile, [2] Center for Applied Nanosciences (CANS), Universidad Andres Bello, Santiago, Chile, [3] Facultad de Ciencias de la Vida, Centro de Biotecnología Vegetal, Universidad Andres Bello, Santiago, Chile, [4] Facultad de Química y Biología, Universidad de Santiago de Chile (USACH), Santiago, Chile, [5] Laboratorio de Genética y Patogénesis Bacteriana, Facultad de Ciencias de la Vida, Universidad Andres Bello, Santiago, Chile

Re(I) complexes have exposed highly suitable properties for cellular imaging (especially for fluorescent microscopy) such as low cytotoxicity, good cellular uptake, and differential staining. These features can be modulated or tuned by modifying the ligands surrounding the metal core. However, most of Re(I)-based complexes have been tested for non-walled cells, such as epithelial cells. In this context, it has been proposed that Re(I) complexes are inefficient to stain walled cells (i.e., cells protected by a rigid cell wall, such as bacteria and fungi), presumably due to this physical barrier hampering cellular uptake. More recently, a series of studies have been published showing that a suitable combination of ligands is useful for obtaining Re(I)-based complexes able to stain walled cells. This review summarizes the main characteristics of different fluorophores used in bioimage, remarking the advantages of $d^6$-based complexes, and focusing on Re(I) complexes. In addition, we explored different structural features of these complexes that allow for obtaining fluorophores especially designed for walled cells (bacteria and fungi), with especial emphasis on the ligand choice. Since many pathogens correspond to bacteria and fungi (yeasts and molds), and considering that these organisms have been increasingly used in several biotechnological applications, development of new tools for their study, such as the design of new fluorophores, is fundamental and attractive.

Keywords: rhenium (I) tricarbonyl complexes, Equatorial ligand, ancillary ligand, bacteria, fungi, yeasts, molds

## CELL IMAGING METHODS

Cell imaging has become a powerful tool to reveal particular biological structures and explore molecular mechanisms, unraveling dynamics, and functions of many different cellular processes (Rabuka et al., 2008; Hensle and Blum, 2013; Hananya et al., 2016; Majumder et al., 2016; Cui et al., 2017; Yoshimura, 2018). Accordingly, development of diverse transmitted light microscopy approaches, including fluorescence microscopy, is increasingly contributing to improve this technique (Roeffaers et al., 2008; Hauser et al., 2017). Fluorescence microscopy has been considered to be one of the most important advances to observe biological structures, but also to explore physiological processes or even characterize new compartments

(Phimphivong and Saavedra, 1998; Bullok et al., 2002; Heintzmann and Huser, 2017). In this sense, research about new, improved fluorescent indicators (simply known as fluorophores) clearly constitutes a new challenge (Frederiksen et al., 2016; Yang et al., 2016; Xue et al., 2017; Bourassa et al., 2018).

Fluorescence microscopy relies upon the use of fluorescent agents, or those parts of a sample that are naturally emissive, to generate a detectable emitted light signal upon excitation (Borman, 2010; Vendrell et al., 2012; Kim et al., 2015; Tian et al., 2017). This allows for greater contrast between sections of the specimen and greater signal-to-noise ratios than conventional microscopy, which uses detection of reflected or transmitted light (Cheng et al., 2017; Gao et al., 2017; More et al., 2018).

Nevertheless, overall limitations of fluorescence microscopy, as an imaging technique, include low resolution to approximately half the wavelength of the light involved in the experiment, and the limited depth of tissue penetration of the light used. This limits visible light fluorescence microscopy to sample depths of a few millimeters and near IR microscopy to a few centimeters (Li et al., 2017; Taylor et al., 2018). For these reasons, it is necessary to develop new and improved luminescent fluorophores, suitable to be used with fluorescence microscopy.

# LUMINESCENT MARKERS FOR FLUORESCENCE MICROSCOPY

In fluorescence microscopy, image quality depends largely on the physicochemical properties of the luminescent marker. For these reasons, markers should be carefully chosen to fulfill the requirements of a particular technique (Shaner, 2014). It has been considered that a good luminescent marker for imaging applications must exhibit some desirable properties, such as good stability and solubility in aqueous solvents (including buffer and culture media); low cytotoxicity, including low phototoxicity (i.e., toxicity generated upon light exposure) (Haas et al., 2014); differential affinity (i.e., specificity) for certain cell structures; and an efficient cellular uptake, hopefully in absence of other chemical or physical agents that artificially increase membrane permeability (Fernandez-Moreira et al., 2010). Other photophysical properties are also important. Accordingly, luminescent fluorophores must exhibit an efficient sample penetration to create high quality images. For instance, fluorophores with red shifted emission and excitation profiles, particularly in the near-infrared region, have shown a suitable penetration for biological systems (Zhao et al., 2014). In addition, luminescent markers should be easily distinguishable from the background, showing high brightness. In this context, background autofluorescence from biological systems generally reduce resolution of a luminescent marker. Since autofluorescence, produced by DNA, NADPH, and other biomolecules, normally presents small Stokes shift (Santoro et al., 2012; Balasubramaniam et al., 2015; Coda et al., 2015), it is desirable that luminescent markers present large Stokes shift, a property that contributes to preventing self-quenching (i.e., dimmer images) (Moriarty et al., 2014). Finally, markers must also show a relatively long luminescent lifetime ($\tau$, from

$\sim 10^2$ to $10^6$ ms), a useful feature that also contributes to distinguish the desired signal from the biological system, which shows mostly short-lived autofluorescence ($\sim 10$ ns). Thus, since different cellular structures present different $\tau$ with respect to autofluorescence, it is possible to remove this autofluorescence background or even use it to provide further information through fluorescence lifetime imaging microscopy/mapping (FLIM) (Coda et al., 2015).

At present, a wide variety of fluorophores for bioimaging applications have been reported. Among these, genetically encoded fluorescent proteins (FPs) (Enterina et al., 2015); organic dyes; quantum dots (Baker, 2010; Doane and Burda, 2012); and metal-based systems (Shang et al., 2011; Echeverría et al., 2012) are the most important.

## Fluorescent Proteins (FPs)

A wide variety of fluorescent proteins have been engineered, with several adaptations and characteristics to suit diverse applications, including presentation in different colors, from blue to far-red. FPs can be genetically encoded, a major advantage over other systems, thereby allowing direct labeling of many proteins in a living cell; albeit this advantage must be contrasted against poor quantum yield, low photon yield (i.e., FPs exhibit poor brightness), and a large size that impairs cellular uptake when they are heterologously produced, particularly in prokaryotic cells (bacteria) and eukaryotic walled cells such as yeasts or molds (Baird et al., 2000; Kubitscheck et al., 2000; Shaner et al., 2004). Moreover, not all FPs are stable; some of them exhibiting high degradation rates (Haas et al., 2014). Even more so, several chimeric proteins containing an FP moiety lack their original functions and/or do not exhibit luminescence due to inappropriate protein folding (Stepanenko et al., 2013). Another consideration when using FPs is the maturation time, i.e., time necessary to properly fold and emission. Typical maturation times are around 40 min, but depending on pH, temperature, and the specific FP, some may take several hours to mature (Baird et al., 2000; Shaner et al., 2004; Chudakov et al., 2010). Moreover, it is important to remark that the chromophore formation step requires the presence of oxygen in many FPs (including green fluorescence protein GFP), making these markers incompatible with obligate anaerobes (Haas et al., 2014). Furthermore, it is important to consider that the use of FPs is restricted to cellular systems that have well-established transformation protocols or availability of appropriate expression vectors.

## Organic Molecules

Most fluorophores used in confocal microscopy are organic molecules, normally a series of fused, heterocyclic rings (Wood, 1994). While extinction coefficients and quantum yield of many of these fluorophores are high, they exhibit small Stokes shift, and short luminescence lifetime compared to metal-based systems (see below). Unlike FPs, organic dyes are not genetically encodable, consequently they must be incorporated into the cell through the plasma membrane by diffusion, endocytosis or microinjection. Nevertheless, not all organic dyes can permeate cell membranes. For instance, rhodamine dyes

can poorly diffuse across bacterial membranes, while sulfonated cyanine dyes are completely unable to enter into bacterial cells (Fernandez-Suarez and Ting, 2008). This is an especially critical point since endocytosis and microinjection are not available for prokaryotic cells. Instead, membrane permeabilization is normally used; albeit this procedure can produce misleading or confusing alterations in data (artifacts) due to the presence of organic solvents affecting membranes and other cell structures (Sochacki et al., 2011). In addition, considering that organic dyes usually bind non-specifically in the cell, most staining is limited regarding their specificity, needing several washing steps to remove excess, unbound dye from the cell (Fernandez-Suarez and Ting, 2008).

## Quantum Dots

Quantum dots have also been used for fluorescence microscopy, although they are much less common in applications due to their usual large size, requirement for surface passivation, and unpredictable blinking properties (Antelman et al., 2009; Wang et al., 2009; Mutavdzic et al., 2011; Ritchie et al., 2013). As well as with exogenous proteins and organic dyes, many quantum dots are difficult to be incorporated into cells, restricting their use to the outer membrane and cell surface in prokaryotic cells (Chalmers et al., 2007; Zhang et al., 2011; Ritchie et al., 2013). Although quantum dots commonly exhibit much longer photobleaching lifetimes compared to FPs, the presence of blinking constitutes a clear disadvantage to obtain high quality images (Michalet et al., 2005; Mahler et al., 2008; Omogo et al., 2016; Osborne and Fisher, 2016). Furthermore, another important disadvantage is the high toxicity of the semiconducting materials used in the fabrication of quantum dots like CdQ (Q = Se or Te) (Khalili Fard et al., 2015; Li et al., 2016; Silva et al., 2016). To address this issue, numerous studies have explored the development of non-toxic quantum dots. Nevertheless, only less-toxic quantum dots have been produced (Das and Snee, 2016). For that reason, they must be coated with organic molecules, a complex, and expensive procedure, to render them soluble and biocompatible by preventing the leaching of toxic ions (Fernandez-Moreira et al., 2010). Even though extinction coefficients and quantum yield of many quantum dots are high, these fluorophores exhibit normally smaller Stokes shift, shorter luminescence lifetime and higher susceptibility to photobleaching compared with metal-based systems (see below).

## Metal-Based Systems

Metal-based systems are comparatively smaller (1–2 nm), and often possess excellent optical properties such as high brightness, narrow emission bands, multiple emission wavelengths, emission tunability, long fluorescence lifetime, large Stokes shift, resistance to photobleaching, and high stability, compared with other fluorophores (Baird et al., 2000; Shaner et al., 2004; Ranjan et al., 2015). Due to all these properties, especially small size, the position of these dyes in a sample can be determined with high precision, a useful feature to perform super-resolution microscopy (Thompson et al., 2002; Agrawal et al., 2013; Haas et al., 2014). Some complexes of certain 4f elements (i.e.,

lanthanides) show extremely long luminescence lifetime ($10^6$ ns) and, in some cases, they emit in the NIR region of the spectrum, which are features that make them attractive targets for applications in fluorescence microscopy (Song et al., 2008; Montgomery et al., 2009; Amoroso and Pope, 2015). Despite all these promising advantages, the presence of an additional chromophore must be incorporated into the complex (i.e., an antenna) to allow sufficient absorption and subsequent transfer of energy to the lanthanide; in other words, lanthanide ions are difficult to excite (Liu et al., 2013). In addition, lanthanide complexes must exhibit high stability to avoid the release of highly toxic lanthanide ions, a process demanding the synthesis of intricate macrocyclic ligands (Montgomery et al., 2009). Besides 4f elements (lanthanides), $d^6$ metal-based systems, in combination with a relatively high amount of ligand-field dinitrogenated and/or organometallic ligands, present attractive features to be used as fluorophore for applications in fluorescence microscopy.

# D⁶ METAL-BASED COMPLEXES

Over the last few years, luminescent $d^6$ complexes have attracted considerable interest for applications in microscopy as synthetic fluorescent dyes, mainly due to their attractive photophysical properties (Haas and Franz, 2009; Patra and Gasser, 2012). Typical $d^6$ complexes of Re(I), Ru(II), Os(II), and Ir(III) (Lee et al., 2017), in combination of a relatively high diversity of ligands (e.g., ruthenium trisbipyridyls, rhenium *fac* tricarbonyl polypyridyls, osmium bipyridyl, and iridium cyclometallates complexes), have been used as fluorophores for fluorescent microscopy and related applications (**Table 1**) (Virel et al., 2009; Langdon-Jones et al., 2014; You et al., 2014; Gupta et al., 2016). In general, $d^6$ complexes share common features making them suitable for microscopy applications. For instance, as well as luminescent lanthanide complexes, $d^6$ complexes have large Stokes shift (hundreds of nm), which allow clear differentiation between autofluorescence and signal luminescence; long excited-state lifetimes, which can permit elimination of short-lived autofluorescence (ns) (Fernandez-Moreira et al., 2010; Li et al., 2011); enhanced photostability (leading to lower photobleaching) (Stufkens and Vlcek, 1998; Lowry et al., 2004); high chemical stability; and cellular uptake, at least for eukaryotic non-walled cells (Haas and Franz, 2009; Langdon-Jones et al., 2014).

Photophysical properties of $d^6$ complexes depend directly on the nature of the whole molecule itself, with an emission explained by the triplet metal-to-ligand-charge-transfer ($^3$MLCT) as the most important in most molecules (Bonello et al., 2014). $^3$MLCT involves excitation by a photo-induced electron transfer from metal-based orbital (i.e., from Re, Ru, Ir) to a conjugated π-system normally located on an aromatic heterocyclic ligand (often a dinitrogenated ligand) (Long and Wong, 2015). Since excited $d^6$ metal-based orbitals must transfer electrons to emit light, $d^6$ complexes usually include high-field ancillary ligands (i.e., π acceptors) in order to improve charge transfer (Mitoraj and Michalak, 2010; Lambic et al., 2018; Munoz-Osses et al., 2018). For these reasons, due to low

**TABLE 1** | Examples of d[6] complexes used as fluorophores in biological applications.

| Complex | Structure | Comment | References |
|---------|-----------|---------|-----------|
| Re(I) |  | Soft staining of walled cells (yeasts, *Candida albicans,* and *Cryptococcus* spp.) | Carreño et al., 2017a |
| |  | Differential staining of the nucleus in walled cells (yeasts, *Candida albicans,* and *Cryptococcus* spp.) | Carreño et al., 2015b, 2017a |
| Ru(II) |  | Differential staining of a structure presumably corresponding to the nucleus in walled cells (yeasts, *Candida albicans*) | Carreño et al., 2019b |
| |  | Differential staining of a structure corresponding to the cell envelop (presumably the cell wall) in walled cells (yeasts, *Candida albicans*) | Carreño et al., 2019b |
| Os(II) |  | Universal luminescent probe for enzymatic reactions | Virel et al., 2009 |
| Ir(III) |  | Complexes for phosphorescence sensing of biological metal Ions. This complex is useful to detect Zn (II) ion. | You et al., 2014 |

oxidation state of metals [i.e., Re(I), Ru(II), Ir(III)], highly conjugated ligands that can easily accept electronic density are desirable for the development of good fluorescent probes (Cameron et al., 2018; Isik Buyukeksi et al., 2018; Zanoni et al., 2018). In this sense, it is possible to modulate both excitation and emission wavelengths of $d^6$ complexes according to the nature of the ligand involved in charge transfer. Thus, the choice of the ligand can directly affect the band gap, impacting, in turn, in the emitting light and remarking the possibility to design complexes with particular luminescent properties (Fernandez-Moreira et al., 2010; Atoini et al., 2017; Ward et al., 2018). All these features contribute to easy excitation and increased quantum yield of $d^6$ complexes, in comparison with lanthanide complexes, producing brighter images at lower concentrations and few cytotoxicity, without the need of antennae (Fernandez-Moreira et al., 2010; Thorp-Greenwood, 2012; Thorp-Greenwood et al., 2012).

Besides good luminescent properties, $d^6$ complexes must exhibit other additional properties to be suitable for imaging applications in biology. Among these properties, cellular uptake (e.g., by modulating lipophilicity), low cytotoxicity, and specific intracellular localization are crucial, thereby engineering of $d^6$ complexes by the presence of different ligands must be explored in order to obtain improved luminescent fluorophores. Since emission comes mainly from the charge transfer between the metal and ligand, exhibiting sensitivity to their electronic levels (Lowry et al., 2004), modifications of the ligands will allow for the designing of new fluorophores with different photophysical properties, but also fluorophores that could be conjugated to other biomolecules (e.g., antibodies) to allow localization-control of the sample.

## RE(I) TRICARBONYL COMPLEXES

As stated, properties exhibited by $d^6$ complexes make them attractive for bioimaging applications using fluorescence microscopy (Thorp-Greenwood and Coogan, 2011; Morais et al., 2012). $d^6$-based complexes have shown remarkable properties in cellular imaging, especially with epithelial cells, showing specific intracellular localization patterns (Amoroso et al., 2007; Botchway et al., 2008; Li et al., 2011). In particular, Re(I) tricarbonyl complexes have luminescent properties that have long been postulated, but have only been demonstrated relatively recently as being useful as *in vivo* probes (Amoroso et al., 2007, 2008).

In the first fluorescence studies, Re(I) tricarbonyl complexes with bisquinoline (**bqi**) as substituted trinitrogenated ligand were conjugated to fMLF, a small peptide-based targeting agent used to specifically recognize the formyl peptide receptor (FPR) found in neutrophils (Stephenson et al., 2004), producing a *fac*-[Re(CO)$_3$(**bqi**)fMLF]$^+$ complex. At low temperatures, fluorescent complexes were located at the same position than the fluorescein-labeled probe, showing that the presence of Re(I) tricarbonyl complexes did not affect neither the recognizing nor localization of fMLF receptor (Stephenson et al., 2004). Although Re(I) **bqi** complexes were the first rhenium species reported as fluorophores for cell imaging, more recent studies

demonstrated that dinitrogenated complexes such as 2,2′-bipyridine (**bpy**), 1,10-phenanthroline (**phen**), or derivatives, require longer wavelength excitation compared with **bqi** (i.e., trinitrogenated) ligands, producing low cellular damage but good penetration (Maggioni et al., 2012). In this sense, facial isomers of type *fac*-[Re(CO)$_3$(**N,N**)**L**]$^n$ (where n is 0, +,or -), preferably monocationic complexes where **N,N** corresponds to a substituted dinitrogenated ligand and **L** is the ancillary ligand (**Figure 1**), have been extensively studied due to their photophysical attributes, especially with non-walled eukaryotic cells (Langdon-Jones et al., 2014; North et al., 2015). The relatively lipophilic nature of *fac*-[Re(CO)$_3$(**N,N**)**L**]$^n$ complexes (e.g., they can be dissolved in DMSO) seems also suitable for cell imaging, showing that the choice of the dinitrogenated ligand modulates some photophysical properties (e.g., excitation and emission ranges) (Amoroso et al., 2007), but also some properties as biomarkers (Carreño et al., 2017a).

Most common Re(I) luminescent markers are based on the *fac*-[Re(CO)$_3$(**bpy**)**L**]$^+$ core, which have been modified in order to develop imaging and sensing agents with diverse properties. These complexes are usually synthesized from parent pentacarbonyl halides, [Re(CO)$_5$**X**] (**X** = Cl/Br), to obtain neutral tricarbonyl dinitrogenated halides (e.g., *fac*-[Re(CO)$_3$(**bpy**)**X**]) (Kurz et al., 2006; Ranasinghe et al., 2016). In this case, it is important to include a reflux step under an inert atmosphere for 2–3 h (Kurz et al., 2006; Ranasinghe et al., 2016). Nevertheless, more recently a synthesis procedure has been reported that requires only stirring without the need of reflux and inert atmosphere, with a high yield and purity, in only 15–30 min (Carreño et al., 2015b, 2017a). After the synthesis of neutral *fac*-[Re(CO)$_3$(**bpy**)**X**], the halide (i.e., **X**) can be substituted by the required ancillary ligand (**L**) to produce the final complexes (i.e., *fac*-[Re(CO)$_3$(**bpy**)**L**]$^{(0,+,or-)}$), where total charge depends on the nature of the ancillary ligand **L** (Amoroso et al., 2008; Thorp-Greenwood et al., 2012; Carreño et al., 2016; Carreño et al., 2017a).

Thus, as discussed before, it has been demonstrated that the Re(I) tricarbonyl complexes can be engineered by choosing the ancillary ligand, in order to modulate some properties related to bioimage, including wavelength emission, subcellular localization, and/or cellular uptake. The ancillary ligand can determine lipophilicity, but also other properties such as global charge of the Re(I) tricarbonyl complexes. For example, there are differences in neutral, cationic and anionic forms of Re(I) tricarbonyl complexes. Neutral complexes (e.g., *fac*-[Re(CO)$_3$(**N,N**)**L**], where **L** is a halogen as substituent) normally exhibit relatively low quantum yield and short lifetime, along with relatively low cellular uptake (Fernandez-Moreira et al., 2010; Carreño et al., 2019). By contrast, cationic *fac*-[Re(CO)$_3$(**bpy**)**L**]$^+$ complexes normally present more desirable photophysical properties, including increased lifetime and better quantum yield. In addition, several Re(I) tricarbonyl complexes can be up taken by non-walled eukaryotic cells by passive diffusion, facilitating the staining procedure. Specifically, some cationic lipophilic complexes, e.g., *fac*-[Re(CO)$_3$(bpy)(Py-CH$_2$OCO(CH$_2$)nCH$_3$)]$^+$ (Py = pyridine; n
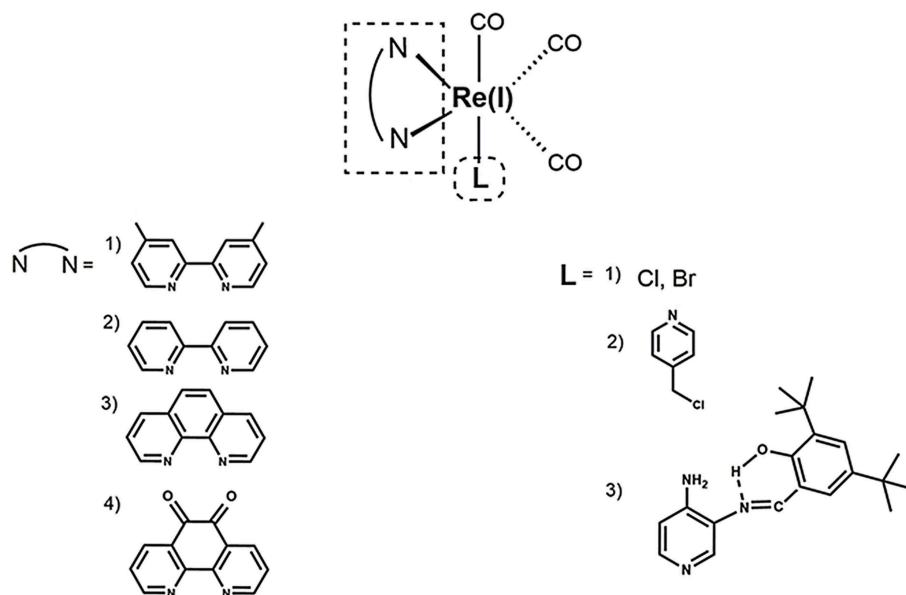
**FIGURE 1 |** Structural scheme of Re(I) tricarbonyl complexes and their different functional groups [i.e., substituted dinitrogenated ligand (**N**, **N**); ancillary ligand (**L**)]. Some examples of (**N**, **N**) ligands include (1) 4,4′-dimethyl-2,2′-bpy (**dmb**); (2) 2,2′-bipyridine (**bpy**); (3) 1,10-phenanthroline (**phen**); (4) 5,6-dione-1,10-phenanthroline (**dione**). Some examples of ancillary ligands (**L**) include (1) halogens; (2) 3-chloromethylpyridyl; (3) (*E*)-2-{[(3-aminopyridin-4-yl)imino]-methyl}-4,6-di-*tert*-butyl-phenol (a pyridine Schiff base harboring an intramolecular hydrogen bond) (Carreño et al., 2014, 2015a,b, 2017a).

= 6, 12, 16), co-localize in internal membranes of organelles, or other lipophilic cytoplasmic structures (Stufkens and Vlcek, 1998; Coogan and Fernandez-Moreira, 2014). On the other hand, anionic complexes (e.g., *fac*-[Re(CO)$_3$((SO$_3$-phenyl)$_2$-**phen**)(Py-R)]$^-$(Py: pyridine; R: H, CH$_2$OH, CH$_2$OCOC$_{13}$H$_{27}$) accumulate only on the outer face of the plasma membrane, or show no cellular uptake at all despite the presence of very lipophilic substituents (Amoroso et al., 2007), showing that a suitable combination of both the dinitrogenated and the ancillary ligand must be performed in order to develop an adequate biomarker.

Besides contributing to the global charge of the complex, ancillary ligands can also modulate other properties, showing this moiety was not as irrelevant, as previously suggested (Sacksteder et al., 1990). For instance, a group of *fac*-[Re(CO)$_3$(**N**,**N**)**L**]$^+$ (where **N**,**N** is **bpy** or **phen** derivatives) complexes, where **L** corresponds to a highly lipophilic series including esters of 3-hydroxymethylpyridine, i.e., Py-3-CH$_2$O$_2$CR′ (Py = pyridine; R′ = octyl, merystyl, or steryl), were tested as biomarkers in both liposomes and *Spironucleus vortens*, a unicellular eukaryotic fish parasite related to *Giardia* spp. (Amoroso et al., 2007). Results showed that lipophilic *fac*-[Re(CO)$_3$(**subs-bpy**)**L**]$^+$ complexes (where **subs-bpy** is a substituted **bpy**, and **L** is a highly hydrophobic ligand) were associated to cell membranes, internal membranes of organelles and cell debris. Interestingly, the neutral compound *fac*-[Re(CO)$_3$(**phen**)Cl] was mainly found in aqueous fractions and not in membranes, suggesting that high lipophilicity and/or a cationic nature are required for an efficient uptake and staining, as stated above (Amoroso et al., 2007). Thus, apparently, the use of lipophilic

complexes could lead to an improved luminescent staining in cells. Nevertheless, highly lipophilic *fac*-[Re(CO)$_3$(**N**, **N**)**L**]$^+$ exhibit cytotoxicity, mainly due to membrane disruption that ultimately led to cell lysis. In this sense, it has been stated that *fac*-[Re(CO)$_3$(**N**, **N**)**L**]$^+$ complexes are not toxic *per se*, but toxicity can be a problem depending on the chosen ancillary ligand (**L**) (Amoroso et al., 2007; Hallett et al., 2018), indicating that experimental research is necessary to establish biocompatibility in each case. Besides cytotoxicity, ancillary ligands can also modify other properties in Re(I) tricarbonyl complexes involved in bioimaging. In this regard, it was stated that chloride used as an ancillary ligand promotes high cell-depending photobleaching when used in these complexes (Amoroso et al., 2007). Nevertheless, other similar neutral Re(I) tricarbonyl complexes harboring bromide as ancillary ligand, instead of chloride, seem to be resistant to photobleaching, exhibiting an efficient stain of different cell models and reinforcing the need of an experimental approach in each case to assess the complexes as biomarkers (Carreño et al., 2017a).

Ligands can also modify other properties with potential use in biological applications. For instance, alkoxy bridged binuclear Re(I) tricarbonyl complexes containing long alkyl chains with photoisomerizable 4-(1-naphthylvinyl) pyridine ligand (1,4-NVP) enhance its fluorescent emission in the presence of β-amyloid fibrils, exhibiting a potential in Alzheimer's disease diagnosis (Sathish et al., 2014), remarking an eventual use of Re(I) tricarbonyl complexes as novel differential probes and opening new windows in medical approaches.

# RE(I)-BASED FLUOROPHORES FOR WALLED CELLS

As stated above, several fluorophores have been extensively studied regarding their use for non-walled cells (e.g., cell lines, usually epithelial cells). However, in the last years, the use of Re(I)-based fluorophores in walled cells, in particular bacteria and fungi, have been explored. Many pathogens correspond to bacteria and fungi (yeasts and molds). In addition, these organisms have been increasingly used in innumerable biotechnological applications, underlining the importance of developing new tools for their study, such as the design of new fluorophores. Nevertheless, development of Re(I)-based fluorophores for walled cells has encountered some troubles. Both bacteria and fungi possess a rigid structure found in their respective envelop, called cell wall (Sanz et al., 2017; Caveney et al., 2018). The presence of the cell wall could impair incorporation of foreign molecules, including Re(I)-based complexes, as previously proposed (Amoroso et al., 2007, 2008). According to our experience, the development of Re(I)-based fluorophores for walled cells is possible, but requires systematic experimentation to find suitable ligands surrounding the metallic core. Although much of the evidence showing adequate Re(I)-based fluorophores for walled cells is empirical, we can list some common features that favor their use for these kind of cells.

With respect to substitutions in the denitrogenated ligand in *fac*-Re(I)(CO)$_3$(**N,N**)**X** complexes (where **N,N** is a denitrogenated ligand and **X** is a halide), apparently larger substituents seem to impair the properties as fluorophores in yeasts, showing, for instance, that *fac*-Re(I)(CO)$_3$(**2,2′-bpy**)**Br** exhibit better staining than *fac*-Re(I)(CO)$_3$(**4,4′-diethanoate-2,2′-bpy**)**Br** (Carreño et al., 2017a). Interestingly, it has been stated that some dinitrogenated ligands alone (e.g., 1,10-phenanthroline or derivatives) are highly cytotoxic toward different cell types, including walled cells such yeasts and bacteria (Coyle et al., 2003; Roy et al., 2008; Kaplanis et al., 2014; Carreño et al., 2019). Nevertheless, it has been shown that, when these dinitrogenated ligands are coordinated through their two nitrogens with the metal, cytotoxicity is strongly diminished (Carreño et al., 2017a, 2019). Low cytotoxicity is fundamental for fluorophores, indicating that the most common dinitrogenated ligands, such as 1,10-phenanthroline derivatives, can be used to develop luminescent fluorophores for walled cells.

Regarding the total charge, a cationic nature of *fac*-[Re(CO)$_3$(**2,2′-bpy**)**L**)]$^+$ complexes is desirable for the generation of luminescent fluorophores, even for walled cells, due to advantageous photophysical properties and improved uptake (Coogan and Fernandez-Moreira, 2014; Carreño et al., 2016, 2017a, 2019,a). This is apparently true for other d$^6$-based complexes used to stain walled cells. For instance, prototypical *cis*-Ru(II)(**N,N**)$_3^{2+}$ complexes (where **N,N** is a dinitrogenated ligand) were reported to be useful to stain yeasts (Carreño et al., 2019b). However, it is necessary to be cautious since highly charged cationic d$^6$-based complexes are apparently unable to penetrate walled cells. This is the case for ruthenium

red ([(NH$_3$)$_5$Ru(II)–O–Ru(II)(NH$_3$)$_4$–O–Ru(II)(NH$_3$)$_5$]$^{6+}$), used as a dense material to stain extracellular components in yeasts, a compound that is unable to penetrate cells (Farrington and Sannes, 2015).

As stated above, the choice of both the dinitrogenated ligand and the total charge of the complex are important to generate a suitable fluorophores for walled cells. In this context, the ancillary ligand also plays a relevant role, albeit the choice of the right ligand is not trivial. Amoroso et al. tested different ancillary ligands in *fac*-Re(I)(CO)$_3$(**2,2′-bpy**)**L**$^+$, where **L** is a *meta*-substituted pyridine with ester aliphatic chains (from 6 to 16 carbons), and found that these complexes were toxic for different cell kinds, inducing cell disruption and affecting the image obtained by fluorescence microscopy (Amoroso et al., 2007). Later, Amoroso et al. explored a different ancillary ligand using the same *fac*-Re(I)(CO)$_3$(**2,2′-bpy**)**L**$^+$ core, but using 3-chloromethylpyridyl instead of *meta*-substituted pyridine with ester aliphatic chains (from 6 to 16 carbons) as **L**. Although these new complexes were significantly less toxic than complexes harboring long aliphatic chains, producing better images, the use of 3-chloromethylpyridyl as ancillary ligand seems to be useful only for non-walled cells (i.e., breast cancer cell line). By contrast, when this same complex was used to stain yeasts, poor results were obtained, showing only a small proportion of cells that retained the fluorophore (Amoroso et al., 2008). These findings remark the fact that, although the cationic nature has been proposed as being important for the uptake by non-walled cells (Langdon-Jones et al., 2014), it is also necessary to find suitable ancillary ligands to allow uptake by walled cells. In this way, it has been reported that one particular kind of pyridine Schiff base harboring an intramolecular hydrogen bond is useful to act as ancillary ligands to generate Re(I) complexes useful to stain walled cells (Carreño et al., 2015b, 2016, 2017a, 2019a). Schiff bases are aldehyde- or ketone-like compounds, where the carbonyl group is replaced by an azomethine (–C=N–) group (Da Silva et al., 2011). In general, Schiff bases have been used for diverse applications, including antimicrobial compounds, due to their high cytotoxicity against bacteria or fungi (Jarrahpour et al., 2007; Justin Dhanaraj and Sivasankaran Nair, 2009). At a first sight, an ancillary ligand exhibiting cytotoxic activity is not desirable. Nevertheless, it has been established that pyridine Schiff bases harboring an intramolecular hydrogen bond depend on the non-coordinated nitrogen found in the pyridine ring to exert their antimicrobial activity (Carreño et al., 2015a,b, 2018a,b). Considering that coordination of Re(I) core occurs through the pyridine nitrogen in this kind of Schiff bases, the resulting *fac*-Re(I)(CO)$_3$(**N,N**)(**pyridine Schiff Base**)$^+$ complexes exhibit lower cytotoxicity for walled cells, when compared with the respective free ancillary ligand (Carreño et al., 2015a,b, 2016, 2017a,b, 2018a,b). More importantly, *fac*-Re(I)(CO)$_3$(**N,N**)(**pyridine Schiff Base**)$^+$ complexes are useful to observe walled cells, including bacteria and fungi, through fluorescence microscopy. Thus, an efficient staining can be achieved with a simple protocol, with short incubation times (15–30 min), at 37°C, and in absence of an additional permeabilizer agent (Carreño et al., 2016, 2017a). Interestingly, these same complexes were also useful to stain non-walled cells (i.e.,
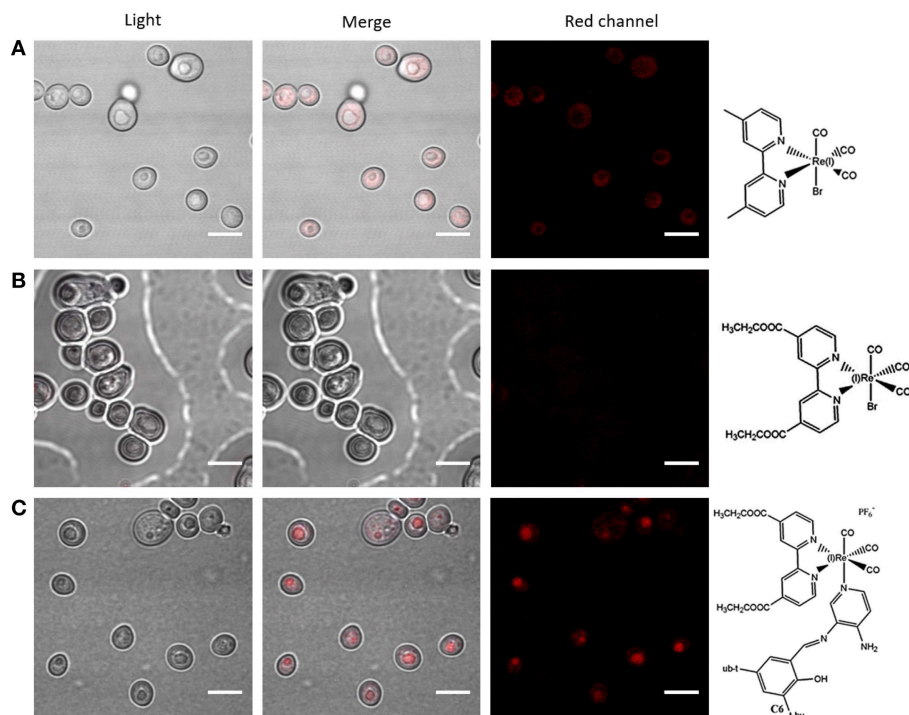
FIGURE 2 | Effect of ligands in the use of *fac*-Re(I)(CO)$_3$(**N,N**)**L**$^{(0,+)}$ complexes in walled cells (yeasts). Fluorescence confocal microscopy images of *Candida albicans* (yeasts) stained with *fac*-Re(I)(CO)$_3$(**4,4′-dimethyl-2,2′-bpy**)**Br (A)**, *fac*-Re(I)(CO)$_3$(**4,4′-diethanoate-2,2′-bpy**)**Br (B)**, or *fac*-Re(I)(CO)$_3$ (**4,4′-diethanoate-2,2′-bpy**) [(***E***)-2-((3-amino-pyridin-4-ylimino)-methyl)-4,6-di-***tert***-butylphenol]$^+$ **(C)** were compared. "Red channel" corresponds to excitation of 405 nm and emission collected in a range of 555 to 625 nm. In all cases, microorganisms were observed fresh, immobilized with 1% agarose, using a 100× objective. DMSO alone was used to set the detection threshold (not shown). White bars represent 5 μm. The complete protocol for staining and other examples of how ligand choice impacts on staining properties of d$^6$ complexes were previously reported (Carreño et al., 2016, 2017a, 2019b).

epithelial cell line), but only after long incubations periods (48–72 h) (Carreño et al., 2016), suggesting that these Re(I) complexes could be considered as being especially designed for walled cells.

A combination of different features in the Re(I)-based fluorophores, such as a cationic nature, a dinitrogenated ligand and a suitable ancillary ligand (e.g., as a pyridine Schiff base such as (*E*)-2-((3-amino-pyridin-4-ylimino)-methyl)-4,6-di-*tert*-butylphenol)) (Carreño et al., 2016, 2017a) are useful to develop new fluorophores for walled cells. Remarkably, small modifications in the nature of these components, such as the substituent groups in the dinitrogenated ligand, can even allow for obtaining differential fluorophores. For instance, *fac*-Re(I)(CO)$_3$(**2,2′-bpy**)((***E***)-2-((3-amino-pyridin-4-ylimino)-methyl)-4,6-di-***tert***-butylphenol))$^+$ can differentially stain bud-like structures when used to stain *Candida albicans* or *Cryptococcus* spp. (yeasts). By contrast, a small change in the dinitrogenated ligand, with the addition of a polar group (*fac*-Re(I)(CO)$_3$(**4,4′-diethanoate-2,2′-bpy**)((***E***)-2-((3-amino-pyridin-4-ylimino)-methyl)-4,6-di-***tert***-butylphenol**$^+$**)) produces a fluorophore that specifically stains the cell nucleus in these same fungi (Carreño et al., 2016, 2017a). This phenomenon was also observed with other d$^6$-based fluorophores, where *cis*-Ru(II)(**4,4′-diethanoate-2,2′-bipyridine**)$_3^{2+}$ was useful to stain yeasts, remaining retained in a structure consistent with

the nucleus, whereas *cis*-Ru(II)(**1,10-phenanthroline**)$_3^{2+}$ was retained in a peripheric structure of the yeast, probably cell membrane or cell wall (Carreño et al., 2019b). This evidence supports that relatively small substitutions, not necessarily involving long aliphatic chains, are enough to change the properties of other d$^6$-based fluorophores, including Re(I) and Ru(II) complexes. In this regard, potential intermolecular interactions that these substituents could form with biological systems, is a fundamental property to be considered in the development of d$^6$-based differential luminescent dyes (Carreño et al., 2017a). Some examples of how ligands affect staining properties of Re(I) complexes in walled cells are shown in **Figure 2**. High versatility of the d$^6$-based fluorophores will plausibly allow the generation of diverse biological probes, even in the absence of other moieties aimed to provide specificity, such as antibodies.

Regarding filamentous fungi (mold, walled cells), Re(I) complexes harboring a pyridine Schiff base have been shown to be useful to stain both spores and hyphae of *Botrytis cinerea*, a ubiquitous necrotrophic filamentous fungal pathogen causing the "gray mold" disease in a wide range of plants. Since hyphae and conidia from *Botrytis cinerea* present a dynamic multilayer cell wall that varies the composition during normal growth (Cantu et al., 2009), it is difficult to

develop suitable fluorophores to stain these structures. Recently, it has been reported that cationic Re(I) complexes with a dinitrogenated ligand and a pyridine Schiff base as ancillary ligand (e.g., *fac*-Re(I)(CO)$_3$(**2,2′-bpy**)((*E*)-**2-((3-amino-pyridin-4-ylimino)-methyl)-4,6-di-*tert*-butylphenol**)$^+$) were useful to stain *Botrytis cinerea* structures, including conidia and juvenile hyphae. In that work, a new protocol was proposed as incubation at higher temperatures (65°C) can be useful to stain this kind of fungal structures. Furthermore, evidence of selective staining of living conidia was provided, opening a new focus for the generation of Re(I)-based fluorophores with potential use for vital staining (Carreño et al., 2019a).

## CONCLUSION

Use of Re(I)-based complexes as fluorophores is increasingly gaining attention. Development of new applications in walled cells, such as bacteria and fungi, has underlined that systematic research of the best molecular features is fundamental to engineer new, improved fluorophores. Accordingly, *fac*-Re(I)(CO)$_3$(**N,N**)**L**$^+$ complexes should fulfill some desirable structural features:

1) Charge: Monocationic nature.
2) **N,N**: the presence of a **bpy** or **phen** with relatively small substituents (e.g., methyl, ethyl ester). Changes in these substituents can produce complexes for differential staining.
3) Ancillary ligand: An ancillary ligand lacking long aliphatic chains but preferentially presenting groups favoring the formation of hydrogen bonds. Hydrogen bonds potentially could improve interactions with biomolecules found in biological systems, improving retention.

A combination of these three features provides high plasticity to develop new Re(I) complexes with specific properties, adapted for a particular purpose regarding the generation of fluorophores for walled cells. It also important to remark that it is necessary to establish a suitable staining protocol since, depending on the organisms, increasing temperature or incubation time could greatly improve results.

Finally, it is possible to conclude that d$^6$-based complexes exhibit a high versatility, allowing the development of new molecules for diverse applications, including fluorophores especially designed for walled cells, showing low cytotoxicity, cellular uptake and differential staining properties.

## AUTHOR CONTRIBUTIONS

CO contributed with bibliographic research of eukaryotic, non-walled cells, and critical reading. AC contributed with the whole chemical section (**Table 1**), general discussion, review organization, and paper writing. RP contributed with bibliographic research of molds and critical reading. FL contributed with critical reading and **Figure 1**. RA-P contributed with critical reading, with emphasis on rhenium chemistry. MG contributed with critical reading, with emphasis on chemical properties. JF contributed with the whole biological section (**Table 1**; **Figure 2**), general discussion, review organization, and paper writing.

## REFERENCES

Agrawal, U., Reilly, D. T., and Schroeder, C. M. (2013). Zooming in on biological processes with fluorescence nanoscopy. *Curr. Opin. Biotechnol.* 24, 646–653. doi: 10.1016/j.copbio.2013.02.016

Amoroso, A. J., Arthur, R. J., Coogan, M. P., Court, J. B., Fernandez-Moreira, V., Hayes, A. J., et al. (2008). 3-Chloromethylpyridyl bipyridine fac-tricarbonyl rhenium: a thiol-reactive luminophore for fluorescence microscopy accumulates in mitochondria. *N. J. Chem.* 32, 1097–1102. doi: 10.1039/b802215a

Amoroso, A. J., Coogan, M. P., Dunne, J. E., Fernández-Moreira, V., Hess, J. B., Hayes, A. J., et al. (2007). Rhenium fac tricarbonyl bisimine complexes: biologically useful fluorochromes for cell imaging applications. *Chem. Commun.* 2007, 3066–3068. doi: 10.1039/B706657K

Amoroso, A. J., and Pope, S. J. (2015). Using lanthanide ions in molecular bioimaging. *Chem. Soc. Rev.* 44, 4723–4742. doi: 10.1039/C4CS00293H

Antelman, J., Wilking-Chang, C., Weiss, S., and Michalet, X. (2009). Nanometer distance measurements between multicolor quantum dots. *Nano Lett.* 9, 2199–2205. doi: 10.1021/nl901163k

Atoini, Y., Prasetyanto, E. A., Chen, P. K., Jonckheere, D., De Vos, D., and De Cola, L. (2017). Tuning luminescent properties of a metal organic framework by insertion of metal complexes. *Supramol. Chem.* 29, 758–767. doi: 10.1080/10610278.2017.1290249

Baird, G. S., Zacharias, D. A., and Tsien, R. Y. (2000). Biochemistry, mutagenesis, and oligomerization of DsRed, a red fluorescent protein from coral. *Proc. Natl. Acad. Sci. U.S.A.* 97, 11984–11989. doi: 10.1073/pnas.97.22.11984

Baker, M. (2010). Nanotechnology imaging probes: smaller and more stable. *Nat. Methods* 7, 957–962. doi: 10.1038/nmeth1210-957

Balasubramaniam, A. M., Sriraman, R., Sindhuja, P., Mohideen, K., Parameswar, R. A., and Muhamed Haris, K. T. (2015). Autofluorescence based diagnostic techniques for oral cancer. *J. Pharm. Bioallied Sci.* 7, S374–377. doi: 10.4103/0975-7406.163456

Bonello, R. O., Morgan, I. R., Yeo, B. R., Jones, L. E. J., Kariuki, B. M., Fallis, I. A., et al. (2014). Luminescent rhenium(I) complexes of substituted imidazole [4,5-f]-1,10-phenanthroline derivatives. *J. Organomet. Chem.* 749, 150–156. doi: 10.1016/j.jorganchem.2013.08.031

Borman, S. T. U. (2010). Illuminating tumor cells. *Chem. Eng. News* 88:12. doi: 10.1021/cen-v088n019.p012

Botchway, S. W., Charnley, M., Haycock, J. W., Parker, A. W., Rochester, D. L., Weinstein, J. A., et al. (2008). Time-resolved and two-photon emission imaging microscopy of live cells with inert platinum complexes. *Proc. Natl. Acad. Sci. USA.* 105, 16071–16076. doi: 10.1073/pnas.0804071105

Bourassa, D., Elitt, C. M., Mccallum, A. M., Sumalekshmy, S., Mcrae, R. L., Morgan, M. T., et al. (2018). Chromis-1, a ratiometric fluorescent probe optimized for two-photon microscopy reveals dynamic changes in labile Zn(II) in differentiating oligodendrocytes. *ACS Sens.* 3, 458–467. doi: 10.1021/acssensors.7b00887

Bullok, K. E., Dyszlewski, M., Prior, J. L., Pica, C. M., Sharma, V., and Piwnica-Worms, D. (2002). Characterization of novel histidine-tagged tat-peptide complexes dual-labeled with99mtc-tricarbonyl and fluorescein for scintigraphy and fluorescence microscopy. *Bioconjug. Chem.* 13, 1226–1237. doi: 10.1021/bc025573a

Cameron, J. M., Wales, D. J., and Newton, G. N. (2018). Shining a light on the photo-sensitisation of organic-inorganic hybrid polyoxometalates. *Dalton Trans.* 47, 5120–5136. doi: 10.1039/C8DT00400E

Cantu, D., Greve, L. C., Labavitch, J. M., and Powell, A. L. (2009). Characterization of the cell wall of the ubiquitous plant pathogen *Botrytis cinerea*. *Mycol. Res.* 113, 1396–1403. doi: 10.1016/j.mycres.2009.09.006

Carreño, A., Aros, A. E., Otero, C., Polanco, R., Gacitúa, M., Arratia-Pérez, R., et al. (2017a). Substituted bidentate and ancillary ligands modulate the bioimaging properties of the classical Re(i) tricarbonyl core with yeasts and bacteria. *N. J. Chem.* 41, 2140–2147. doi: 10.1039/C6NJ03792E

Carreño, A., Fernández, K., Sáez-Cortez, F., Otero, C., Arratia-Pérez, R., Fuentes, J. A., et al. (2019a). Confocal microscopy studies of living fungal hyphae and conidia using rhenium (I) tricarbonyl complexes as fluorescent dyes. *J. Chilean Chem. Soc.* 92, 216–221. doi: 10.1080/00275514.2000.12061147

Carreño, A., Gacitúa, M., Fuentes, J. A., Páez-Hernández, D., Peñaloza, J. P., Otero, C., et al. (2016). Fluorescence probes for prokaryotic and eukaryotic cells using Re(CO)3+ complexes with an electron withdrawing ancillary ligand. *N. J. Chem.* 40, 7687–7700. doi: 10.1039/C6NJ00905K

Carreño, A., Gacitúa, M., Molins, E., and Arratia-Pérez, R. (2017b). X-ray diffraction and relativistic DFT studies on the molecular biomarker fac-Re(CO)3(4,4′-dimethyl-2,2′-bpy)(E-2-((3-amino-pyridin-4-ylimino)-methyl)-4,6-di-tert-butylphenol)(PF6). *Chem. Papers* 71, 2011–2022. doi: 10.1007/s11696-017-0196-6

Carreño, A., Gacitua, M., Paez-Hernandez, D., Polanco, R., Preite, M., Fuentes, J. A., et al. (2015a). Spectral, theoretical characterization and antifungal properties of two phenol derivative Schiff bases with an intramolecular hydrogen bond. *N. J. Chem.* 39, 7822–7831. doi: 10.1039/C5NJ01469G

Carreño, A., Gacitua, M., Schott, E., Zarate, X., Manriquez, J. M., Preite, M., et al. (2015b). Experimental and theoretical studies of the ancillary ligand (E)-2-((3-amino-pyridin-4-ylimino)-methyl)-4,6-di-tert-butylphenol in the rhenium(I) core. *N. J. Chem.* 39, 5725–5734. doi: 10.1039/C5NJ00772K

Carreño, A., Páez-Hernández, D., Zúñiga, C., Ramírez-Osorio, A., Nevermann, J., Rivera-Zaldívar, M. M., et al. (2019b). Prototypical *cis*-Ruthenium (II) complexes present differential fluorescent staining in walled-cell models (yeasts). *Chemical Papers.* 73, 1629–1637. doi: 10.1007/s11696-019-00714-z

Carreño, A., Rodriguez, L., Paez-Hernandez, D., Martin-Trasanco, R., Zuniga, C., Oyarzun, D. P., et al. (2018a). Two new fluorinated phenol derivatives pyridine schiff bases: synthesis, spectral, theoretical characterization, inclusion in epichlorohydrin-beta-cyclodextrin polymer, and antifungal effect. *Front. Chem.* 6:312. doi: 10.3389/fchem.2018.00312

Carreño, A., Solis-Cespedes, E., Zuniga, C., Nevermann, J., Rivera-Zaldivar, M. M., Gacitua, M., et al. (2019). Cyclic voltammetry, relativistic DFT calculations and biological test of cytotoxicity in walled-cell models of two classical rhenium (I) tricarbonyl complexes with 5-amine-1,10-phenanthroline. *Chem. Phys. Lett.* 715, 231–238. doi: 10.1016/j.cplett.2018.11.043

Carreño, A., Vega, A., Zarate, X., Schott, E., Gacitúa, M., Valenzuela, N., et al. (2014). Synthesis, characterization and computational studies of (E)-2-{[(2-Aminopyridin-3-Yl) Imino]-Methyl}-4,6-Di-tert-Butylphenol. *Quím. Nova* 37, 584–588. doi: 10.5935/0100-4042.20140098

Carreño, A., Zúñiga, C., Páez-Hernández, D., Gacitúa, M., Polanco, R., Otero, C., et al. (2018b). Study of the structure–bioactivity relationship of three new pyridine Schiff bases: synthesis, spectral characterization, DFT calculations and biological assays. *N. J. Chem.* 42, 8851–8863. doi: 10.1039/C8NJ00390D

Caveney, N. A., Li, F. K., and Strynadka, N. C. (2018). Enzyme structures of the bacterial peptidoglycan and wall teichoic acid biogenesis pathways. *Curr. Opin. Struct. Biol.* 53, 45–58. doi: 10.1016/j.sbi.2018.05.002

Chalmers, N. I., Palmer, R. J. Jr., Du-Thumm, L., Sullivan, R., Shi, W., and Kolenbrander, P. E. (2007). Use of quantum dot luminescent probes to achieve single-cell resolution of human oral bacteria in biofilms. *Appl. Environ. Microbiol.* 73, 630–636. doi: 10.1128/AEM.02164-06

Cheng, M. H. Y., Savoie, H., Bryden, F., and Boyle, R. W. (2017). A convenient method for multicolour labelling of proteins with BODIPY fluorophores via tyrosine residues. *Photochem. Photobiol. Sci.* 16, 1260–1267. doi: 10.1039/C7PP00091J

Chudakov, D. M., Matz, M. V., Lukyanov, S., and Lukyanov, K. A. (2010). Fluorescent proteins and their applications in imaging living cells and tissues. *Physiol. Rev.* 90, 1103–1163. doi: 10.1152/physrev.00038.2009

Coda, S., Siersema, P. D., Stamp, G. W., and Thillainayagam, A. V. (2015). Biophotonic endoscopy: a review of clinical research techniques for optical imaging and sensing of early gastrointestinal cancer. *Endosc. Int. Open* 3, E380–392. doi: 10.1055/s-0034-1392513

Coogan, M. P., and Fernandez-Moreira, V. (2014). Progress with, and prospects for, metal complexes in cell imaging. *Chem. Commun.* 50, 384–399. doi: 10.1039/C3CC45229H

Coyle, B., Kavanagh, K., Mccann, M., Devereux, M., and Geraghty, M. (2003). *Biometals* 16, 321–329. doi: 10.1023/A:1020695923788

Cui, Q., Xu, J., Shen, G., Zhang, C., Li, L., and Antonietti, M. (2017). Hybridizing carbon nitride colloids with a shell of water-soluble conjugated polymers for tunable full-color emission and synergistic cell imaging. *ACS Appl. Mater. Interfaces* 9, 43966–43974. doi: 10.1021/acsami.7b13212

Da Silva, C. M., Da Silva, D. L., Modolo, L. V., Alves, R. B., De Resende, M. A., Martins, C. V. B., et al. (2011). Schiff bases: a short review of their antimicrobial activities. *J. Adv. Res.* 2, 1–8. doi: 10.1016/j.jare.2010.05.004

Das, A., and Snee, P. T. (2016). Synthetic developments of nontoxic quantum dots. *Chemphyschem.* 17, 598–617. doi: 10.1002/cphc.201500837

Doane, T. L., and Burda, C. (2012). The unique role of nanoparticles in nanomedicine: imaging, drug delivery and therapy. *Chem. Soc. Rev.* 41, 2885–2911. doi: 10.1039/c2cs15260f

Echeverría, C., Becerra, Á., Nuñez-Villena, F., Muñoz-Castro, A., Stehberg, J., Zheng, Z., et al. (2012). The paramagnetic and luminescent $[Re_6Se_8I_6]^{3-}$ cluster. Its potential use as an antitumoral and biomarker agent. *N. J. Chem.* 36, 927–932. doi: 10.1039/c2nj21016a

Enterina, J. R., Wu, L., and Campbell, R. E. (2015). Emerging fluorescent protein technologies. *Curr. Opin. Chem. Biol.* 27, 10–17. doi: 10.1016/j.cbpa.2015.05.001

Farrington, J. E., and Sannes, P. L. (2015). "Basement membranes and the extracellular matrix," in *Comparative Biology of the Normal Lung, 2nd edn.*, ed R. A. Parent (London, UK: Academic Press), 119–128. doi: 10.1016/B978-0-12-404577-4.00010-2

Fernandez-Moreira, V., Thorp-Greenwood, F. L., and Coogan, M. P. (2010). Application of d6 transition metal complexes in fluorescence cell imaging. *Chem. Commun.* 46, 186–202. doi: 10.1039/B917757D

Fernandez-Suarez, M., and Ting, A. Y. (2008). Fluorescent probes for super-resolution imaging in living cells. *Nat. Rev. Mol. Cell Biol.* 9, 929–943. doi: 10.1038/nrm2531

Frederiksen, R. S., Alarcon-Llado, E., Krogstrup, P., Bojarskaite, L., Buch-Månson, N., Bolinsson, J., et al. (2016). Nanowire-aperture probe: local enhanced fluorescence detection for the investigation of live cells at the nanoscale. *ACS Photonics* 3, 1208–1216. doi: 10.1021/acsphotonics.6b00126

Gao, T., He, H., Huang, R., Zheng, M., Wang, F.-F., Hu, Y.-J., et al. (2017). BODIPY-based fluorescent probes for mitochondria-targeted cell imaging with superior brightness, low cytotoxicity and high photostability. *Dyes Pigments* 141, 530–535. doi: 10.1016/j.dyepig.2017.03.009

Gupta, G., Das, A., Ghate, N. B., Kim, T., Ryu, J. Y., Lee, J., et al. (2016). Novel BODIPY-based Ru(ii) and Ir(iii) metalla-rectangles: cellular localization of compounds and their antiproliferative activities. *Chem. Commun.* 52, 4274–4277. doi: 10.1039/C6CC00046K

Haas, B. L., Matson, J. S., Dirita, V. J., and Biteen, J. S. (2014). Imaging live cells at the nanometer-scale with single-molecule microscopy: obstacles and achievements in experiment optimization for microbiology. *Molecules* 19, 12116–12149. doi: 10.3390/molecules190812116

Haas, K. L., and Franz, K. J. (2009). Application of metal coordination chemistry to explore and manipulate cell biology. *Chem. Rev.* 109, 4921–4960. doi: 10.1021/cr900134a

Hallett, A. J., Placet, E., Prieux, R., Mccafferty, D., Platts, J. A., Lloyd, D., et al. (2018). Exploring the cellular uptake and localisation of phosphorescent rhenium fac-tricarbonyl metallosurfactants as a function of lipophilicity. *Dalton Trans.* 47, 14241–14253. doi: 10.1039/C8DT00669E

Hananya, N., Eldar Boock, A., Bauer, C. R., Satchi-Fainaro, R., and Shabat, D. (2016). Remarkable enhancement of chemiluminescent signal by dioxetane-fluorophore conjugates: turn-ON chemiluminescence probes with color modulation for sensing and imaging. *J. Am. Chem. Soc.* 138, 13438–13446. doi: 10.1021/jacs.6b09173

Hauser, M., Wojcik, M., Kim, D., Mahmoudi, M., Li, W., and Xu, K. (2017). Correlative super-resolution microscopy: new dimensions and new opportunities. *Chem. Rev.* 117, 7428–7456. doi: 10.1021/acs.chemrev.6b00604

Heintzmann, R., and Huser, T. (2017). Super-resolution structured illumination microscopy. *Chem. Rev.* 117, 13890–13908. doi: 10.1021/acs.chemrev.7b00218

Hensle, E. M., and Blum, S. A. (2013). Phase separation polymerization of dicyclopentadiene characterized by in operando fluorescence microscopy. *J. Am. Chem. Soc.* 135, 12324–12328. doi: 10.1021/ja405283k

Isik Buyukeksi, S., Sengul, A., Erdonmez, S., Altindal, A., Orman, E. B., and Ozkaya, A. R. (2018). Spectroscopic, electrochemical and photovoltaic properties of Pt(ii) and Pd(ii) complexes of a chelating 1,10-phenanthroline appended perylene diimide. *Dalton Trans.* 47, 2549–2560. doi: 10.1039/C7DT04713D

Jarrahpour, A., Khalili, D., De Clercq, E., Salmi, C., and Brunel, J. M. (2007). Synthesis, antibacterial, antifungal and antiviral activity evaluation of some new bis-Schiff bases of isatin and their derivatives. *Molecules* 12, 1720–1730. doi: 10.3390/12081720

Justin Dhanaraj, C., and Sivasankaran Nair, M. (2009). Synthesis, characterization, and antimicrobial studies of some Schiff-base metal(II) complexes. *J. Coord. Chem.* 62, 4018–4028. doi: 10.1080/00958970903191142

Kaplanis, M., Stamatakis, G., Papakonstantinou, V. D., Paravatou-Petsotas, M., Demopoulos, C. A., and Mitsopoulou, C. A. (2014). Re(I) tricarbonyl complex of 1,10-phenanthroline-5,6-dione: DNA binding, cytotoxicity, anti-inflammatory and anti-coagulant effects towards platelet activating factor. *J. Inorg. Biochem.* 135, 1–9. doi: 10.1016/j.jinorgbio.2014.02.003

Khalili Fard, J., Jafari, S., and Eghbal, M. A. (2015). A review of molecular mechanisms involved in toxicity of nanoparticles. *Adv. Pharm. Bull.* 5, 447–454. doi: 10.15171/apb.2015.061

Kim, E., Yang, K. S., Kohler, R. H., Dubach, J. M., Mikula, H., and Weissleder, R. (2015). Optimized near-IR fluorescent agents for *in vivo* imaging of Btk expression. *Bioconjug. Chem.* 26, 1513–1518. doi: 10.1021/acs.bioconjchem.5b00152

Kubitscheck, U., Kuckmann, O., Kues, T., and Peters, R. (2000). Imaging and tracking of single GFP molecules in solution. *Biophys. J.* 78, 2170–2179. doi: 10.1016/S0006-3495(00)76764-6

Kurz, P., Probst, B., Spingler, B., and Alberto, R. (2006). Ligand variations in [ReX(diimine)(CO)(3)] complexes: effects on photocatalytic CO2 reduction. *Eur. J. Inorg. Chem.* 2006, 2966–2974. doi: 10.1002/ejic.200600166

Lambic, N. S., Sommer, R. D., and Ison, E. A. (2018). High-valent nitridorhenium(v) complexes containing PNP ligands: implications of ligand flexibility. *Dalton Trans.* 47, 758–768. doi: 10.1039/C7DT03615A

Langdon-Jones, E. E., Symonds, N. O., Yates, S. E., Hayes, A. J., Lloyd, D., Williams, R., et al. (2014). Fluorescent rhenium-naphthalimide conjugates as cellular imaging agents. *Inorg. Chem.* 53, 3788–3797. doi: 10.1021/ic500142z

Lee, L. C., Leung, K. K., and Lo, K. K. (2017). Recent development of luminescent rhenium(i) tricarbonyl polypyridine complexes as cellular imaging reagents, anticancer drugs, and antibacterial agents. *Dalton Trans.* 46, 16357–16380. doi: 10.1039/C7DT03465B

Li, C., Yu, M., Sun, Y., Wu, Y., Huang, C., and Li, F. (2011). A nonemissive iridium(III) complex that specifically lights-up the nuclei of living cells. *J. Am. Chem. Soc.* 133, 11231–11239. doi: 10.1021/ja202344c

Li, K.-B., Chen, F.-Z., Zhang, S., Shi, W., Han, D.-M., Cai, C., et al. (2017). A nile red-based near-infrared fluorescent probe for endogenous hydrogen polysulfides in living cells. *Anal. Methods* 9, 6443–6447. doi: 10.1039/C7AY02376F

Li, X., Yang, X., Yuwen, L., Yang, W., Weng, L., Teng, Z., et al. (2016). Evaluation of toxic effects of CdTe quantum dots on the reproductive system in adult male mice. *Biomaterials* 96, 24–32. doi: 10.1016/j.biomaterials.2016.04.014

Liu, Y., Tu, D., Zhu, H., and Chen, X. (2013). Lanthanide-doped luminescent nanoprobes: controlled synthesis, optical spectroscopy, and bioapplications. *Chem. Soc. Rev.* 42, 6924–6958. doi: 10.1039/c3cs60060b

Long, N., and Wong, W. (2015). *The Chemistry of Molecular Imaging.* Hoboken, NJ: Wiley. doi: 10.1002/9781118854754

Lowry, M. S., Hudson, W. R., Pascal, R. A. Jr., and Bernhard, S. (2004). Accelerated luminophore discovery through combinatorial synthesis. *J. Am. Chem. Soc.* 126, 14129–14135. doi: 10.1021/ja047156+

Maggioni, D., Fenili, F., D'alfonso, L., Donghi, D., Panigati, M., Zanoni, I., et al. (2012). Luminescent rhenium and ruthenium complexes of an amphoteric poly(amidoamine) functionalized with 1,10-phenanthroline. *Inorg. Chem.* 51, 12776–12788. doi: 10.1021/ic301616b

Mahler, B., Spinicelli, P., Buil, S., Quelin, X., Hermier, J. P., and Dubertret, B. (2008). Towards non-blinking colloidal quantum dots. *Nat. Mater.* 7, 659–664. doi: 10.1038/nmat2222

Majumder, S., Demott, C. M., Reverdatto, S., Burz, D. S., and Shekhtman, A. (2016). Total cellular RNA modulates protein activity. *Biochemistry* 55, 4568–4573. doi: 10.1021/acs.biochem.6b00330

Michalet, X., Pinaud, F. F., Bentolila, L. A., Tsay, J. M., Doose, S., Li, J. J., et al. (2005). Quantum dots for live cells, *in vivo* imaging, and diagnostics. *Science* 307, 538–544. doi: 10.1126/science.1104274

Mitoraj, M. P., and Michalak, A. (2010). Sigma-donor and pi-acceptor properties of phosphorus ligands: an insight from the natural orbitals for chemical valence. *Inorg. Chem.* 49, 578–582. doi: 10.1021/ic901736n

Montgomery, C. P., Murray, B. S., New, E. J., Pal, R., and Parker, D. (2009). Cell-penetrating metal complex optical probes: targeted and responsive systems based on lanthanide luminescence. *Acc. Chem. Res.* 42, 925–937. doi: 10.1021/ar800174z

Morais, G. R., Paulo, A., and Santos, I. (2012). Organometallic complexes for SPECT imaging and/or radionuclide therapy. *Organometallics* 31, 5693–5714. doi: 10.1021/om300501d

More, K. N., Lim, T.-H., Kim, S.-Y., Kang, J., Inn, K.-S., and Chang, D.-J. (2018). Characteristics of new bioreductive fluorescent probes based on the xanthene fluorophore: detection of nitroreductase and imaging of hypoxic cells. *Dyes Pigments* 151, 245–253. doi: 10.1016/j.dyepig.2018.01.008

Moriarty, R. D., Martin, A., Adamson, K., O'reilly, E., Mollard, P., Forster, R. J., et al. (2014). The application of water soluble, mega-Stokes-shifted BODIPY fluorophores to cell and tissue imaging. *J. Microsc.* 253, 204–218. doi: 10.1111/jmi.12111

Munoz-Osses, M., Godoy, F., Fierro, A., Gomez, A., and Metzler-Nolte, N. (2018). New organometallic imines of rhenium(i) as potential ligands of GSK-3beta: synthesis, characterization and biological studies. *Dalton Trans* 47, 1233–1242. doi: 10.1039/C7DT04344A

Mutavdzic, D., Xu, J., Thakur, G., Triulzi, R., Kasas, S., Jeremic, M., et al. (2011). Determination of the size of quantum dots by fluorescence spectroscopy. *Analyst* 136, 2391–2396. doi: 10.1039/c0an00802h

North, A. J., Hayne, D. J., Schieber, C., Price, K., White, A. R., Crouch, P. J., et al. (2015). Toward hypoxia-selective rhenium and technetium tricarbonyl complexes. *Inorg. Chem.* 54, 9594–9610. doi: 10.1021/acs.inorgchem.5b01691

Omogo, B., Gao, F., Bajwa, P., Kaneko, M., and Heyes, C. D. (2016). Reducing blinking in small core-multishell quantum dots by carefully balancing confinement potential and induced lattice strain: the "Goldilocks" effect. *ACS Nano* 10, 4072–4082. doi: 10.1021/acsnano.5b06994

Osborne, M. A., and Fisher, A. A. (2016). Charge-tunnelling and self-trapping: common origins for blinking, grey-state emission and photoluminescence enhancement in semiconductor quantum dots. *Nanoscale* 8, 9272–9283. doi: 10.1039/C6NR00529B

Patra, M., and Gasser, G. (2012). Organometallic compounds: an opportunity for chemical biology? *Chembiochem* 13, 1232–1252. doi: 10.1002/cbic.201200159

Phimphivong, S., and Saavedra, S. S. (1998). Terbium chelate membrane label for time-resolved, total internal reflection fluorescence microscopy of substrate-adherent cells. *Bioconjug. Chem.* 9, 350–357. doi: 10.1021/bc9701609

Rabuka, D., Forstner, M. B., Groves, J. T., and Bertozzi, C. R. (2008). Noncovalent cell surface engineering: incorporation of bioactive synthetic glycopolymers into cellular membranes. *J. Am. Chem. Soc.* 130, 5947–5953. doi: 10.1021/ja710644g

Ranasinghe, K., Handunnetti, S., Perera, I. C., and Perera, T. (2016). Synthesis and characterization of novel rhenium(I) complexes towards potential biological imaging applications. *Chem. Cent. J.* 10:71. doi: 10.1186/s13065-016-0218-4

Ranjan, S., Jayakumar, M. K., and Zhang, Y. (2015). Luminescent lanthanide nanomaterials: an emerging tool for theranostic applications. *Nanomedicine.* 10, 1477–1491. doi: 10.2217/nnm.14.229

Ritchie, K., Lill, Y., Sood, C., Lee, H., and Zhang, S. (2013). Single-molecule imaging in live bacteria cells. *Philos. Trans. R. Soc. Lond. B Biol. Sci.* 368:20120355. doi: 10.1098/rstb.2012.0355

Roeffaers, M. B., Ameloot, R., Baruah, M., Uji, I. H., Bulut, M., De Cremer, G., et al. (2008). Morphology of large ZSM-5 crystals unraveled by fluorescence microscopy. *J. Am. Chem. Soc.* 130, 5763–5772. doi: 10.1021/ja7113147

Roy, S., Hagen, K. D., Maheswari, P. U., Lutz, M., Spek, A. L., Reedijk, J., et al. (2008). Phenanthroline derivatives with improved selectivity as DNA-targeting anticancer or antimicrobial drugs. *ChemMedChem* 3, 1427–1434. doi: 10.1002/cmdc.200800097

Sacksteder, L., Zipp, A. P., Brown, E. A., Streich, J., Demas, J. N., and Degraff, B. A. (1990). Luminescence studies of pyridine alpha-diimine rhenium(I) tricarbonyl complexes. *Inorg. Chem.* 29, 4335–4340. doi: 10.1021/ic00346a033

Santoro, G., Blacque, O., and Zobi, F. (2012). Post-protein binding metal-mediated coupling of an acridine orange-based fluorophore. *Metallomics* 4, 253–259. doi: 10.1039/c2mt00175f

Sanz, A. B., Garcia, R., Rodriguez-Pena, J. M., and Arroyo, J. (2017). The CWI pathway: regulation of the transcriptional adaptive response to cell wall stress in yeast. *J. Fungi* 4:E1. doi: 10.3390/jof4010001

Sathish, V., Babu, E., Ramdass, A., Lu, Z. Z., Velayudham, M., Thanasekaran, P., et al. (2014). Alkoxy bridged binuclear rhenium (I) complexes as a potential sensor for beta-amyloid aggregation. *Talanta* 130, 274–279. doi: 10.1016/j.talanta.2014.06.070

Shaner, N. C. (2014). Fluorescent proteins for quantitative microscopy: important properties and practical evaluation. *Methods Cell Biol.* 123, 95–111. doi: 10.1016/B978-0-12-420138-5.00006-9

Shaner, N. C., Campbell, R. E., Steinbach, P. A., Giepmans, B. N., Palmer, A. E., and Tsien, R. Y. (2004). Improved monomeric red, orange and yellow fluorescent proteins derived from *Discosoma* sp. red fluorescent protein. *Nat. Biotechnol.* 22, 1567–1572. doi: 10.1038/nbt1037

Shang, L., Dong, S. J., and Nienhaus, G. U. (2011). Ultra-small fluorescent metal nanoclusters: synthesis and biological applications. *Nano Today* 6, 401–418. doi: 10.1016/j.nantod.2011.06.004

Silva, B. F., Andreani, T., Gavina, A., Vieira, M. N., Pereira, C. M., Rocha-Santos, T., et al. (2016). Toxicological impact of cadmium-based quantum dots towards aquatic biota: effect of natural sunlight exposure. *Aquat. Toxicol.* 176, 197–207. doi: 10.1016/j.aquatox.2016.05.001

Sochacki, K. A., Shkel, I. A., Record, M. T., and Weisshaar, J. C. (2011). Protein diffusion in the periplasm of *E. coli* under osmotic stress. *Biophys. J.* 100, 22–31. doi: 10.1016/j.bpj.2010.11.044

Song, B., Vandevyver, C. D., Chauvin, A. S., and Bunzli, J. C. (2008). Time-resolved luminescence microscopy of bimetallic lanthanide helicates in living cells. *Org. Biomol. Chem.* 6, 4125–4133. doi: 10.1039/b811427g

Stepanenko, O. V., Kuznetsova, I. M., Verkhusha, V. V., and Turoverov, K. K. (2013). Beta-barrel scaffold of fluorescent proteins: folding, stability and role in chromophore formation. *Int. Rev. Cell Mol. Biol.* 302, 221–278. doi: 10.1016/B978-0-12-407699-0.00004-2

Stephenson, K. A., Banerjee, S. R., Besanger, T., Sogbein, O. O., Levadala, M. K., Mcfarlane, N., et al. (2004). Bridging the gap between *in vitro* and *in vivo* imaging: isostructural Re and 99mTc complexes for correlating fluorescence and radioimaging studies. *J. Am. Chem. Soc.* 126, 8598–8599. doi: 10.1021/ja047751b

Stufkens, D. J., and Vlcek, A. (1998). Ligand-dependent excited state behaviour of Re(I) and Ru(II) carbonyl-diimine complexes. *Coord. Chem. Rev.* 177, 127–179. doi: 10.1016/S0010-8545(98)00132-5

Taylor, A., Barlow, N., Day, M. P., Hill, S., Martin, N., and Patriarca, M. (2018). Atomic spectrometry update: review of advances in the analysis of clinical and biological materials, foods and beverages. *J. Anal. At. Spectrom.* 33, 338–382. doi: 10.1039/C8JA90005A

Thompson, R. E., Larson, D. R., and Webb, W. W. (2002). Precise nanometer localization analysis for individual fluorescent probes. *Biophys. J.* 82, 2775–2783. doi: 10.1016/S0006-3495(02)75618-X

Thorp-Greenwood, F. L. (2012). An introduction to organometallic complexes in fluorescence cell imaging: current applications and future prospects. *Organometallics* 31, 5686–5692. doi: 10.1021/om3004477

Thorp-Greenwood, F. L., Balasingham, R. G., and Coogan, M. P. (2012). Organometallic complexes of transition metals in luminescent cell imaging applications. *J. Organomet. Chem.* 714, 12–21. doi: 10.1016/j.jorganchem.2012.01.020

Thorp-Greenwood, F. L., and Coogan, M. P. (2011). Multimodal radio-(PET/SPECT) and fluorescence imaging agents based on metallo-radioisotopes: current applications and prospects for development of new agents. *Dalton Trans.* 40, 6129–6143. doi: 10.1039/c0dt01398f

Tian, H., Furstenberg, A., and Huber, T. (2017). Labeling and single-molecule methods to monitor G protein-coupled receptor dynamics. *Chem. Rev.* 117, 186–245. doi: 10.1021/acs.chemrev.6b00084

Vendrell, M., Zhai, D., Er, J. C., and Chang, Y. T. (2012). Combinatorial strategies in fluorescent probe development. *Chem. Rev.* 112, 4391–4420. doi: 10.1021/cr200355j

Virel, A., Sanchez-Lopez, J., Saa, L., Garcia, A. C., and Pavlov, V. (2009). Use of an osmium complex as a universal luminescent probe for enzymatic reactions. *Chemistry* 15, 6194–6198. doi: 10.1002/chem.200900498

Wang, X., Ren, X., Kahen, K., Hahn, M. A., Rajeswaran, M., Maccagnano-Zacher, S., et al. (2009). Non-blinking semiconductor nanocrystals. *Nature* 459, 686–689. doi: 10.1038/nature08072

Ward, C. L., Dimarco, B. N., O'donnell, R. M., and Meyer, G. J. (2018). Dye excited states oriented relative to TiO2 surface electric fields. *J. Phys. Chem. C.* 122, 13863–13871. doi: 10.1021/acs.jpcc.8b01010

Wood, E. J. (1994). Molecular probes: handbook of fluorescent probes and research chemicals. *Biochem. Educ.* 22:83. doi: 10.1016/0307-4412(94)90083-3

Xue, Z., Zhao, H., Liu, J., Han, J., and Han, S. (2017). Imaging Lysosomal pH alteration in stressed cells with a sensitive ratiometric fluorescence sensor. *ACS Sens* 2, 436–442. doi: 10.1021/acssensors.7b00035

Yang, X., Zhanghao, K., Wang, H., Liu, Y., Wang, F., Zhang, X., et al. (2016). Versatile application of fluorescent quantum dot labels in super-resolution fluorescence microscopy. *ACS Photonics* 3, 1611–1618. doi: 10.1021/acsphotonics.6b00178

Yoshimura, H. (2018). Live cell imaging of endogenous RNAs using pumilio homology domain mutants: principles and applications. *Biochemistry* 57, 200–208. doi: 10.1021/acs.biochem.7b00983

You, Y., Cho, S., and Nam, W. (2014). Cyclometalated iridium(III) complexes for phosphorescence sensing of biological metal ions. *Inorg. Chem.* 53, 1804–1815. doi: 10.1021/ic4013872

Zanoni, K. P. S., Ito, A., Gruner, M., Murakami Iha, N. Y., and De Camargo, A. S. S. (2018). Photophysical dynamics of the efficient emission and photosensitization of [Ir(pqi)2(NN)](+) complexes. *Dalton Trans.* 47, 1179–1188. doi: 10.1039/C7DT03930A

Zhang, R., Rothenberg, E., Fruhwirth, G., Simonson, P. D., Ye, F., Golding, I., et al. (2011). Two-photon 3D FIONA of individual quantum dots in an aqueous environment. *Nano Lett.* 11, 4074–4078. doi: 10.1021/nl201225r

Zhao, C., Li, X., and Wang, F. (2014). Target-triggered NIR emission with a large stokes shift for the detection and imaging of cysteine in living cells. *Chem. Asian J.* 9, 1777–1781. doi: 10.1002/asia.201402043

# The Zn(II)-1,4,7-Trimethyl-1,4,7-Triazacyclononane Complex: A Monometallic Catalyst Active in Two Protonation States

Marta Diez-Castellnou[1]*, Giovanni Salassa[2], Fabrizio Mancin[3] and Paolo Scrimin[3]

[1] EaStCHEM School of Chemistry, University of St Andrews, St. Andrews, United Kingdom, [2] Département de Chimie Physique, Université de Genève, Genève, Switzerland, [3] Dipartimento di Scienze Chimiche, Università di Padova, Padova, Italy

In this paper, the unusual reactivity of the complex Zn(II)-1,4,7-trimethyl-1, 4,7-triazacyclononane (**2**) in the transesterification of the RNA-model substrate, *HPNP* (**3**), is reported. The dependence of the reactivity ($k_2$) with pH does not follow the characteristic bell-shape profile typical of complexes with penta-coordinated metal centers. By the contrary, two reactive species, featuring different deprotonation states, are present, with the tri-aqua complex being more reactive than the mono-hydroxy-diaqua one. Apparently, such a difference arises from the total complex charge which plays an important role in the stability of the transition state/s of the reactions. Relevant insight on the reaction mechanism were hence obtained.

Keywords: RNA, monometallic Zn(II)-complexes, azacrown, phosphate cleavage, phosphoesterase models, kinetics

## INTRODUCTION

Phosphate diesters have a fundamental importance in the chemistry of life in particular because they constitute the backbone of essential biomolecules as DNA and RNA. Their hydrolytic stability is very high. When the sole P-O cleavage by water is considered, the half-life of DNA is estimated to be in the order of magnitude of millions of years, at 25°C and pH 7, and that of RNA is around a hundred years (Wolfenden et al., 1998; Schroeder et al., 2006). Still, the hydrolytic processing of nucleic acids occurs in living organism in few milliseconds, thanks to the enzymes devoted to this task, as nucleases and phosphatases (Westheimer, 1987; Kamerlin et al., 2013). Most of them contain metal ions, as Mg(II), Ca(II), and Zn(II), in their active sites.

In the attempt to reproduce the activity, and possibly the proficiency of enzymes, chemists have focused their attention on the creation of artificial nucleases (Morrow et al., 2008; Aiba et al., 2011; Lassila et al., 2011; Lönnberg, 2011; Mancin et al., 2012; Diez-Castellnou et al., 2017a). Despite the significant effort invested in understanding the mechanism of the enzyme catalyzed reaction (Korhonen et al., 2013; Erxleben, 2019) and, therefore, in creating efficient artificial hydrolytic agents, the enzyme reactivity is still unrivaled and several questions remain to be addressed.

A better understanding of the roles played by the metal ion in promoting the hydrolytic cleavage of phosphate esters could be achieved using simple mono- or bi-metallic complexes as models. In particular Zn(II), while not being Nature's first choice, is likely the metal ion most widely employed in artificial systems (Mancin and Tecilla, 2007). This is due to several reasons: (i) the possibility to produce well defined and relatively stable complexes with neutral ligands; (ii) the absence of a

relevant redox chemistry; (iii) a good Lewis acid acidity; (iv) a modest field effect that allow the easy reorganization of the ligand shell to match the ligand or reaction requirements.

Design and investigation of bimetallic systems is often difficult since the possible formation of μ-hydroxo bridges may affect and even cancel their reactivity (Mancin and Tecilla, 2007). Mono-metallic Zn(II) complexes, on the other hand, produce usually modest rate accelerations when compared to the corresponding bimetallic ones. Still, they allow more detailed investigations of the cleavage reaction providing a simple and better defined model (Bonfá et al., 2003).

In this perspective, we report here a detailed investigation of the reactivity of the Zn(II) complexes of 1,4,7-triazacyclononane (**1**) and of its methyl derivative 1,4,7-trimethyl-1,4,7-triazacyclo-nonane (**2**) toward the hydrolysis of the RNA model 2-hydroxypropyl-p-nitrophenylphosphate (*HPNP*, **3**) (see **Scheme 1**). We found that the reactivity of **2** follows an unprecedented behavior featuring three pH dependent reactivity breaks, providing new insight on the reactivity of these systems.

## RESULTS

HPNP cleavage rate in the presence of the two Zn(II) complexes was measured at 40°C. Kinetic experiments were performed in pseudo-first order conditions (i.e., in the presence of an excess of metal complex over the substrate, whose concentration was fixed at 20 μM) by monitoring the formation of 4-nitrophenolate by its UV-Vis absorption at 400 nm.

The complexes were prepared *in situ* by mixing a solution of $Zn(NO_3)_2$ with the corresponding ligand, in buffer. TACN and his derivatives have a high affinity for Zn(II). Indeed, the values reported in literature for the complex formation constants assure that, in the experimental condition here used, the complexes are fully formed (Yang and Zompa, 1976).

With both the complexes **1** and **2**, the pseudo-firsts order rate constants ($k_{obs}$) measured increase linearly with the Zn(II) complex concentration in the interval investigated (0–0.4 mM). Apparent second order rate constants (i.e., $k_2 = k_{cat}/K_M$ in the Michaelis-Menten formalism) can be obtained by linear regression fitting of the $k_{obs}$ vs. [complex] data.

**Figure 1** reports the pH dependence of the apparent second order rate constants measured for the two complexes. As expected, the pH has a strong influence on the reaction rates suggesting, as generally observed with similar systems, that the deprotonation of metal bound-species has a relevant role in the reaction.

At a first sight, both the profiles show the bell-shape characteristic of metal complexes with two metal bound water molecules. Indeed, kinetic data for complex **1** were fitted with Equation (1), which accounts for the reactivity of a species with three protonation states where only the second one is active (**Supplementary Material**). The fit provides the pKa values of 8.13 and 11.28, respectively for the first and second deprotonation. The second order rate constant ($k_{Zn}$) for the reaction of the active
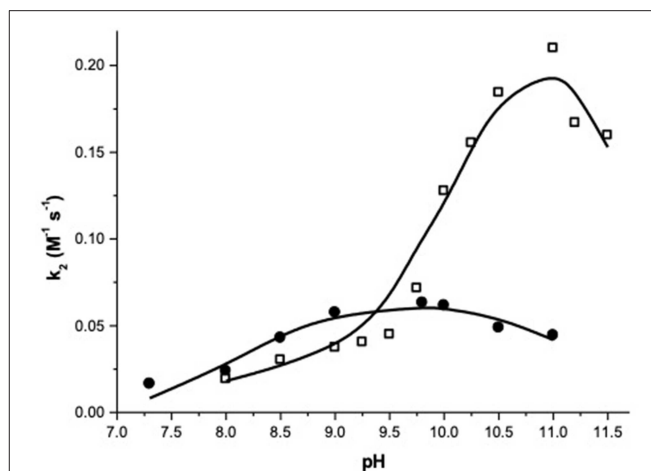
---

**Abbreviations:** HPNP, 2-hydroxypropyl-p-nitrophenylphosphate.



**FIGURE 1 |** pH dependence of the second order rate constants ($k_2$) for the transesterification of HPNP catalyzed by complex 1 (●) and 2 (□) at 40°C.
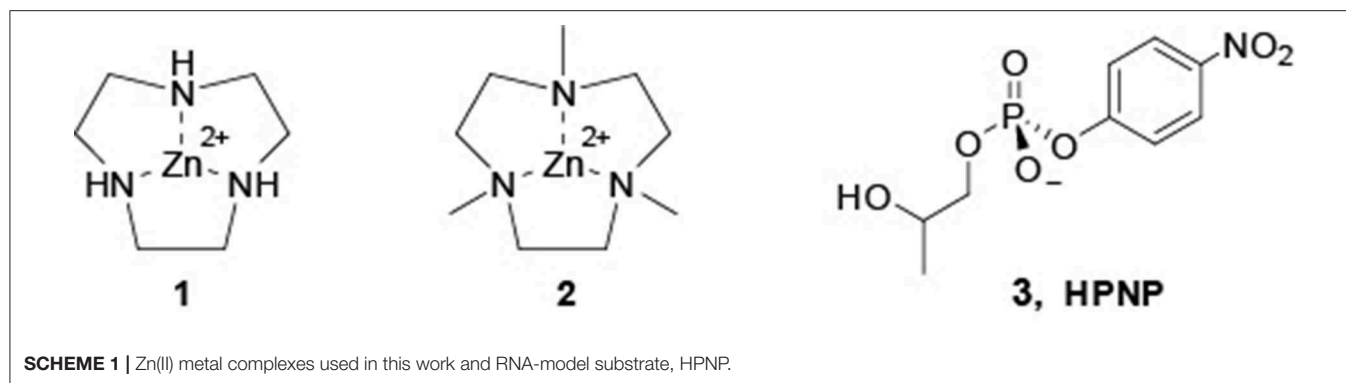
mono-deprotonated catalyst's species with the substrate is $0.064\,M^{-1}\,s^{-1}$.

The values of $pK_a^1$ and $k_{Zn}$ obtained are in line with those reported in literature for complex **1** (Bonfá et al., 2003). The formation of the bis-deprotonated species and the consequent drop of the catalysts reactivity at higher pH have never been reported for **1**, but a similar behavior is well-known for similar complexes of tridentate ligands, as 1,5,9-triazacyclododecane (Livieri et al., 2007).

The fitting of the kinetic data for complex **2** with Equation (1) gives very poor results (see **Supplementary Information**). A closer inspection of the profile of complex **2** reveals that it does not follow exactly a bell-shape. Indeed, $k_2$ smoothly increases from pH 8 to pH 9.5, with a reactivity similar to that of complex **1**, suggesting that the first deprotonation is occurring in this range. When the pH reaches the value of 9.5, a stronger, reactivity increase is observed and $k_2$ reaches values 4-fold larger than the maximum one reached by complex **1**. Eventually, the reactivity starts to drop above pH 11.0. A good fit of the data was obtained by using Equation (2), which was written for a reactivity model that involves a species with four protonation states and with two of them, the second and the third, reactive (**Supplementary Material**). Note, one of the referees pointed out that highly correlated parameters are obtained in the case of 5 variables fitting. As discussed, reliability of the reactivity and acidity parameters obtained is however supported by the comparison with the pH reactivity profile of complex **1**.

The results of the fittings are reported in **Table 1**. The three pKa values obtained (7.7, 10.2, and 11.6) are separated respectively by 2.5 and 1.4 pKa units, with the first pKa value quite close to the corresponding one measured for **1**. Also the $k_{Zn}$ value for the mono-deprotonated species is on the same order of magnitude to that measured for **1** ($0.025\,M^{-1}\,sec^{-1}$) but that of the bis-deprotonated species ($k'_{Zn}$) is considerably larger ($0.27\,M^{-1}\,sec^{-1}$).

**SCHEME 1 |** Zn(II) metal complexes used in this work and RNA-model substrate, HPNP.

**TABLE 1 |** Kinetic parameters from pH rate profiles.

| Complex | $pK_a^1$ | $pK_a^2$ | $pK_a^3$ | $k_{Zn}$ ($M^{-1} \cdot s^{-1}$) | $k'_{Zn}$ ($M^{-1} \cdot s^{-1}$) |
|---------|----------|----------|----------|-------------------------------|--------------------------------|
| **1** | 8.13 | 11.28 | - | 0.064 | - |
| **2** | 7.71 | 10.18 | 11.6 | 0.025 | 0.27 |

Conditions: [HPNP] = $2.0 \cdot 10^{-5}$ M, [buffer] = $5.0 \cdot 10^{-2}$ M, at 40 °C.

# DISCUSSION

The presence of a third metal bound water molecule in complex **2** is confirmed by the crystal structure obtained by Trogler and coworkers (Silver et al., 1995) for the complex $[Zn(Me_3tacn)(H_2O)_3]^{2+}$ $(\mathbf{2 \cdot 3H_2O})^{2+}$ where the Zn(II) ion adopts an octahedral environment, coordinated to three nitrogens of the macrocycle and also to three aqua ligands. In addition, Spiccia and coworkers (Fry et al., 2003) reported the crystal structure for the related complex $[Zn_2(Me_3tacn)_2(H_2O)_4(PhOPO_3)]^{2+} (\mathbf{2_2} \cdot \mathbf{4H_2O \cdot PhPO_4})^{2+}$ where the Zn(II) ion is coordinated to three nitrogen atoms from N,N,N-trimethyl-1,4,7,-triazacyclononane, two water molecules and one oxygen from phenyl phosphate. These structures support our hypothesis that in complex **2**, formed by Zn(II) with the ligand 1,4,7-trimethyl-1,4,7-triazacyclononane, the coordination number of the metal ion is 6, as the accessible surface of the metal ion is large enough to allow coordination of two water molecules and of the substrate simultaneously. Unfortunately, no crystal structures are available for complex **1** to confirm its preference for the coordination number 5 at the metal ion, as suggested by kinetic experiments. The *flexibility* of the Zn(II) ion, which does not have a defined coordination geometry, is well-known (Sigel and Bruce Martin, 1994).

Potentiometric titration data available are also quite scarce. In the case of complex **1**, precipitation above pH 8 prevented the determination of the acidity of the metal bound water molecules. Kinetic experiments, as already mentioned, confirm a $pK_a$ value around 8 for the first water molecule (Bonfá et al., 2003). In the case of complex **2**, Trogler and coworkers reported the values of 10.9 and 12.3 (Silver et al., 1995). Such values appear surprisingly high when compared with complex **1** and with other Zn(II) complexes of macrocyclic polyamides (Kimura et al., 1990; Koike et al., 1990, 1991, 1992; Kimura and Koike, 1991). Indeed, one would expect that electron-donating methyl group will lower

the acidity of the substituted metallic complex with respect to the unsubstituted one (Canary et al., 1995). Interestingly, the similarity of these values with those here reported for the second and third $pK_a$ is clear (Fry et al., 2005).

Focusing the attention on the hydrolytic reactivity of the two complexes, it is relevant to note that the pH profiles obtained confirm the coordination of the substrate to the complex. No other possible mechanism, as general base catalysis or nucleophile catalysis, would account for the reactivity decrease observed at high pH values. There are three kinetically equivalent mechanisms that have been proposed to explain the pH dependence observed for the metal catalyzed HPNP transesterification (Korhonen et al., 2013; Diez-Castellnou et al., 2017a). In the first, the reaction involves the deprotonation of the substrate's hydroxyl group by a metal bound hydroxide, which acts as a general base, simultaneously to the nucleophilic attack on the phosphorus atom (**Scheme 2A**). In the second, the substrate alcoholic group is bound to the metal ion and deprotonates before the nucleophilic attack (**Scheme 2B**). This mechanism is indistinguishable from the others because the $pK_a$ values of metal bound water molecules and alcoholic hydroxyls are similar (Kimura et al., 1995; Livieri et al., 2007). In the third mechanism (**Scheme 2C**) the substrate deprotonation occurs before metal coordination and the deprotonation of a metal bound water molecules decreases (or hamper) the interaction of the metal with the substrate.

Several experimental evidences strongly support the last mechanism (2C) in the case of catalysts that have coordination sites available on the metal ion to accommodate only the substrate (Morrow et al., 2008; Korhonen et al., 2013; Diez-Castellnou et al., 2017a). On the other hand, it is quite likely that when the catalyst have more coordination sites, the substrate alkoxide will bind to the metal ion, turning the reaction mechanism into path 2B (Livieri et al., 2007). In this mechanism, the metal ion plays two opposite roles: (i) it increases the reactivity of the substrate toward the nucleophilic attack, acting as a Lewis acid, (ii) it decreases the reactivity of the nucleophile, by decreasing its $pK_a$.

A few years ago, we calculated the $k_{Zn}$ values for the HPNP cleavage promoted by several mononuclear Zn(II) complexes of polyamine ligands (**Figure 2**) (Bonfá et al., 2003; Bonomi et al., 2013). In the case of triamine complexes, we found a positive correlation of the reactivity with the $pK_a$ of the first deprotonation of a metal bound species.
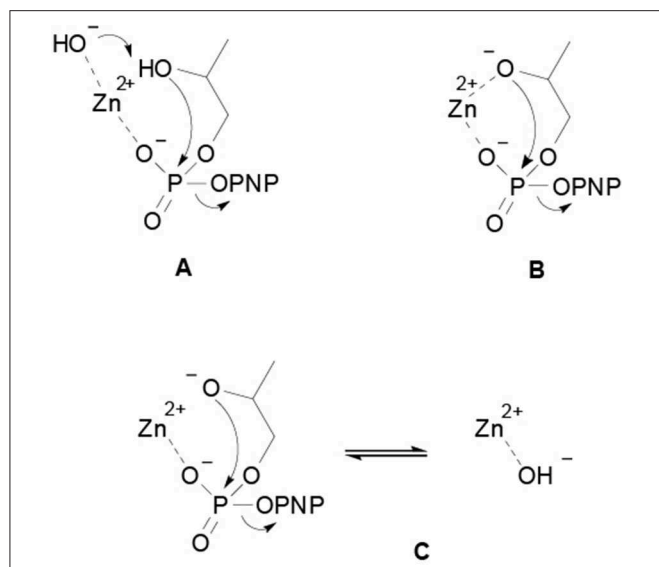
SCHEME 2 | Proposed mechanisms for the metal catalyzed HPNP transesterification reaction: **(A)** the substrate deprotonation by a metal bound hydroxide occurs simultaneously to the nucleophilic attack on the phosphorus atom; **(B)** the substrate alcoholic group is bound to the metal ion and deprotonates before the nucleophilic attack; **(C)** the substrate deprotonation occurs before metal coordination and the deprotonation of a metal bound water molecule decreases the interaction of metal with the substrate.
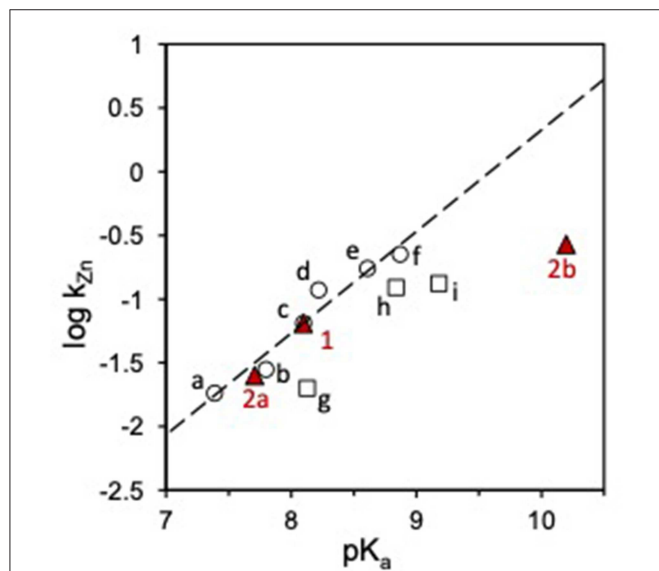


FIGURE 2 | Plot of log $k_{Zn}$ vs. $pK_a$ for the transesterification of HPNP catalyzed by Zn(II) complexes in water. Red triangles represent the reactivity of complexes **1** and **2**, circles (○) are cyclic triamine ligands (a-f), squares (□) linear triamine ligands (g-i), see ref Bonfá et al. (2003) and Bonomi et al. (2013). The dashed line shows the linear fit of the reactivity data for the complexes of cyclic triamines (slope = 0.80). The reactivity of **1** and **2** was corrected to account for the temperature difference by matching the reactivity of **1** with the reported data (ref. Bonfá et al., 2003).

Such a behavior suggested that, among the two concomitant and counterbalancing effects active, the loss of reactivity of

the nucleophile prevails over the Lewis acid activation of the substrate.

When the reactivity of complexes **1** and **2** is analyzed in this perspective, interesting insight is provided. The reactivity of complexes **1** and **2a** (**Scheme 3**) is in line with that of other triamine complexes (**Figure 2**). On the other hand, the reactivity of mono-deprotonated complex **2b** is about 10 times smaller than that expected for a complex of a triamine ligand with that $pK_a$. This suggest that a further effect is at play in this case besides substrate Lewis acid activation and nucleophile reactivity modulation. Significant modifications of the coordination geometries in the two complexes **2a** and **2b**, which could justify their different reactivity, are unlikely as confirmed by DFT optimization of the complex geometries (see **Supplementary Material**). The other relevant differences between the reactive protonation states of complex **2** are essentially two. First, in complex **2a** there is a metal bound water molecule, which could provide intramolecular H-bonds or acid catalysis. Since this water molecule is turned into an hydroxide in **2b**, its positive effect on reactivity would be canceled. If this was the case (or if a general base catalysis mechanism was active), however, reactivity of **2a** would be greater than that of **1** and of the other triamine complexes. The second difference is in the total charge of the reactive species, which is 0 in the ternary complex of **2a** with HPNP and $-1$ in the case of **2b**. Upon the nucleophilic attack of the substrate alkoxide, additional negative charge builds up in the phosphoryl group and this is electrostatically disfavored by the overall complex charge, resulting into a lower reactivity. Indeed, we earlier reported as the insertion of an additional positive charge in the ligand structure, located in close proximity to the reaction site, can increase the reactivity of a mononuclear Zn(II) complex up to one order of magnitude. This is in good agreement with the 10-fold rate decrease estimated for complex **2b** (Bonomi et al., 2009).

## CONCLUSIONS

In conclusion, in this paper we have demonstrated as even small modifications in the structure of the ligands, as the insertion of methyl groups in the nitrogen atoms of triazacyclononane, may have a relevant effect on the ability of the corresponding Zn(II) complex in promoting the phosphoryl transfer reaction. The complex **2** is, at the best of our knowledge, the only monometallic Zn(II) catalyst of HPNP cleavage that is active in two different protonation states. Such a reactivity is due to the peculiar ability of 1,4,7-trimethyl-1,4,7-triazacyclononane to increase the number of coordination sites to 6 on the metal ion with respect of other similar ligands. The most relevant result of this study is however the mechanistic information obtained. The reactivity of complex **2** further supports mechanism 2B as the most likely in the case of complexes where enough solvent-occupied coordination sites on the metal are available. It also confirms that hydrolytic reactivity of these systems is the result of a delicate counterbalance between Lewis acid and electrostatic activation of the substrate (and stabilization of the transition state) and the decrease of the nucleophile reactivity. Several evidences obtained
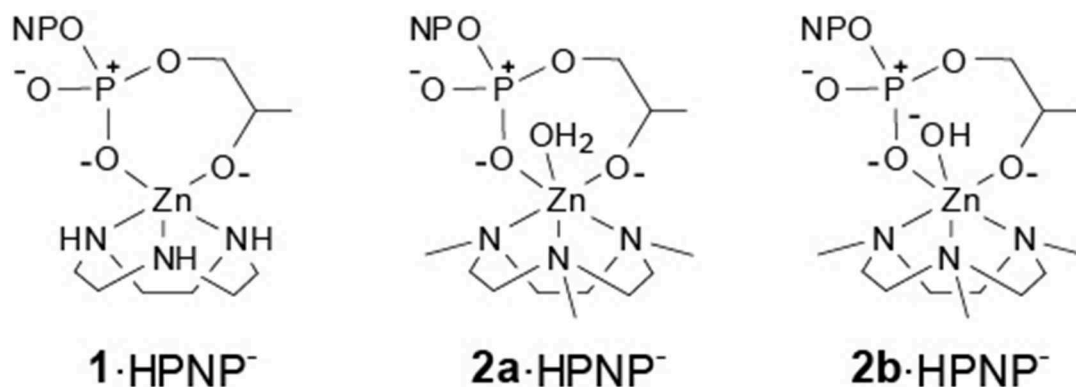
**SCHEME 3 |** Proposed structure of the pre-reactive complexes of 1 and 2 with HPNP.

with model systems, and confirmed by our results, suggest that optimum reactivity should be obtained when the nucleophile is not bound to the metal ion and the overall complex charge is as great as possible (Tirel et al., 2014; Tirel and Williams, 2015). This explains also the greater reactivity usually observed with trivalent cations, as well as the detrimental effect of negatively charged ligands (Mancin et al., 2012). Metal ion coordination of the nucleophile may however be necessary to increase the fraction of nucleophile available at physiological pH and to provide a better preorganization of the latter for the attack to the phosphorous atom. The need to consider of all these factors explains the difficulties in reproducing enzymes' proficiency with simple models. Indeed only a precise spatial organization of multiple active species can optimize the positive effects while minimizing the detrimental one. It is hence not surprising the fact that only by using sophisticated supramolecular architectures, where several beneficial factors can be implemented, remarkable reactivities were obtained (Manea et al., 2004; Feng et al., 2006; Bonomi et al., 2008; Gruber et al., 2011; Diez-Castellnou et al., 2014).

## Equations
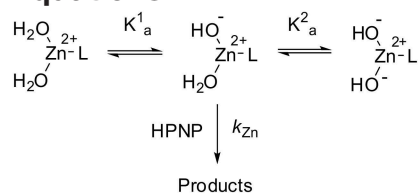


$$k_2 = k_{Zn} \left( \frac{[\mathbf{1}]_{total}}{\frac{[H^+]}{K_a^1} + 1 + \frac{K_a^2}{[H^+]}} \right) \qquad (1)$$
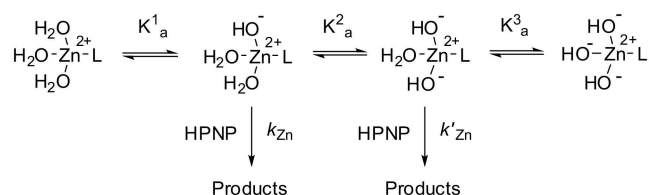


$$k_2 = \left[ \frac{k_{Zn}}{\left( \frac{[H^+]}{K_a^2} + 1 + \frac{K_a^2}{[H^+]} + \frac{K_a^2 K_a^3}{[H^+]^2} \right)} + \frac{k'_{Zn}}{\left( \frac{[H^+]^2}{K_a^1 K_a^2} + \frac{[H^+]}{K_a^2} + 1 + \frac{K_a^3}{[H^+]} \right)} \right] \qquad (2)$$

## DATA AVAILABILITY

All datasets generated for this study are included in the manuscript and/or the **Supplementary Files**.

## AUTHOR CONTRIBUTIONS

MD-C contributed conception and design of the present work, collected and analyzed the kinetic data, and wrote the manuscript. GS performed the DFT calculations. FM and PS supervised this project. All authors contributed to manuscript revision, read, and approved the submitted version.

## FUNDING

## ACKNOWLEDGMENTS

## SUPPLEMENTARY MATERIAL

The Supplementary Material for this article can be found online at: https://www.frontiersin.org/articles/10.3389/fchem.2019.00469/full#supplementary-material

DFT calculations and additional kinetic experiments.

# REFERENCES

Aiba, Y., Sumaoka, J., and Komiyama, M. (2011). Artificial DNA cutters for DNA manipulation and genome engineering. *Chem. Soc. Rev.* 40, 5657–5668. doi: 10.1039/c1cs15039a

Bonfá, L., Gatos, M., Mancin, F., Tecilla, P., and Tonellato, U. (2003). The ligand effect on the hydrolytic reactivity of Zn(II) complexes toward phosphate diesters. *Inorgan. Chem.* 42, 3943–3949. doi: 10.1021/ic034139x

Bonomi, R., Saielli, G., Scrimin, P., and Mancin, F. (2013). An experimental and theoretical study of the mechanism of cleavage of an RNA-model phosphate diester by mononuclear Zn(II) complexes. *Supramol. Chem. Taylor Francis.* 25, 665–671. doi: 10.1080/10610278.2013.830724

Bonomi, R., Saielli, G., Tonellato, U., Scrimin, P., and Mancin, F. (2009). Insights on nuclease mechanism: the role of proximal ammonium group on phosphate esters cleavage. *J. Am. Chem. Soc.* 131, 11278–11279. doi: 10.1021/ja9033236

Bonomi, R., Selvestrel, F., Lombardo, V., Sissi, C., Polizzi, S., Mancin, F., et al. (2008). Phosphate diester and DNA hydrolysis by a multivalent, nanoparticle-based catalyst. *J. Am. Chem. Soc.* 130, 15744–15745. doi: 10.1021/ja801794t

Canary, J. W., Xu, J., Castagnetto, J. M., Rentzeperis, D and Marky, L. A. (1995). Enthalpic control of zinc—water acidity in complexes of Tris(2-Aminoethyl)Amine and Tris(2-(Dimethylamino)Ethyl)Amine. *J. Am. Chem. Soc.* 117, 11545–11547. doi: 10.1021/ja00151a019

Diez-Castellnou, M., Mancin, F., and Scrimin, P. (2014). Efficient phosphodiester cleaving nanozymes resulting from multivalency and local medium polarity control. *J. Am. Chem. Soc.* 136, 1158–1161. doi: 10.1021/ja411969e

Diez-Castellnou, M., Martinez, A., and Mancin, F. (2017a). Phosphate ester hydrolysis: the path from mechanistic investigation to the realization of artificial enzymes. *Adv. Phys. Org. Chem.* 51. 129–186. doi: 10.1016/bs.apoc.2017.09.003

Erxleben, A. (2019). Mechanistic studies of homo- and heterodinuclear zinc phosphoesterase mimics: what has been learned? *Front. Chem.* 7, 1–22. doi: 10.3389/fchem.2019.00082

Feng, G., Natale, D., Prabaharan, R., Mareque-Rivas, J. C., and Williams, N. H. (2006). Efficient phosphodiester binding and cleavage by a ZnII complex combining hydrogen-bonding interactions and double lewis acid activation. *Angew. Chem. Int. Ed.* 45, 7056–7059. doi: 10.1002/anie.200602532

Fry, F. H., Fischmann, A. J., Belousoff, M. J., Spiccia, L., and Brügger, J. (2005). Kinetics and mechanism of hydrolysis of a model phosphate diester by [Cu(Me3tacn)(OH2)2]2+(Me3tacn = 1,4,7-Trimethyl-1,4,7-Triazacyclononane). *Inorg. Chem.* 44, 941–950. doi: 10.1021/ic049469b

Fry, F. H., Jensen, P., Kepert, C. M., and Spiccia, L. (2003). Macrocyclic copper(II) and zinc(II) complexes incorporating phosphate esters. *Inorg. Chem.* 42, 5637–5644. doi: 10.1021/ic026091d

Gruber, B., Kataev, E., Aschenbrenner, J., Stadlbauer, S., and König, B. (2011). Vesicles and micelles from amphiphilic zinc(II)-cyclen complexes as highly potent promoters of hydrolytic DNA cleavage. *J. Am. Chem. Soc.* 133, 20704–20707. doi: 10.1021/ja209247w

Kamerlin, S. C., Sharma, P. K., Prasad, R. B., and Warshel, A. (2013). Why nature really chose phosphate. *Quart. Rev. Biophys.* 46, 1–132. doi: 10.1017/S0033583512000157

Kimura, E., Kimura, E., Shiota, T., Koike, T., Shiro, M., and Kodama, M. (1990). A Zinc(II) Complex of 1,5,9-triazacyclododecane ([12]AneN3 as a model for carbonic anhydrase. *J. Am. Chem. Soc.* 112, 5805–5811. doi: 10.1021/ja00171a020

Kimura, E., Kodama, Y., Koike, T., and Shiro, M. (1995). Phosphodiester hydrolysis by a new zinc(II) macrocyclic tetraamine complex with an alcohol pendant: elucidation of the roles of Ser-102 and Zinc(II) in alkaline phosphatase. *J. Am. Chem. Soc.* 117, 8304–8311. doi: 10.1021/ja00137a002

Kimura, E., and Koike, T. (1991). Macrocyclic polyamines as a probe for equilibrium study of the acid functions of zinc(II) ion in hydrolysis enzymes. *Inorg. Chem.* 11, 285–301. doi: 10.1080/02603599108035829

Koike, T., Kimura, E., and Kimura, E. (1991). Roles of zinc(II) ion in phosphatases. A model study with zinc(II)-macrocyclic polyamine complexes. *J. Am. Chem. Soc.* 113, 8935–8941. doi: 10.1021/ja00023a048

Koike, T., Kimura, E., Nakamura, I., Hashimoto, Y., and Shiro, M. (1992). The first anionic sulfonamide-binding zinc(II) complexes with a macrocyclic triamine:

chemical verification of the sulfonamide inhibition of carbonic anhydrase. *J. Am. Chem. Soc.* 114, 7338–7345. doi: 10.1021/ja00045a002

Koike, T., Shiota, T., Kimura, E., and Iitaka, Y. (1990). Acid properties of zinc(II) and cadmium(II) in complexation with macrocyclic oxo polyamine ligands. *Inorg. Chem.* 29, 4621–4629. doi: 10.1021/ic00348a009

Korhonen, H., Koivusalo, T., Toivola, S., and Mikkola, S. (2013). There is no universal mechanism for the cleavage of RNA model compounds in the presence of metal ion catalysts. *Org. Biomol. Chem.* 11, 8324–8339. doi: 10.1039/c3ob41554f

Lassila, J. K., Zalatan, J. G., and Herschlag, D. (2011). Biological phosphoryl-transfer reactions: understanding mechanism and catalysis. *Annu. Rev. Biochem.* 80, 669–702. doi: 10.1146/annurev-biochem-060409-092741

Livieri, M., Mancin, F., Saielli, G., Chin, J., and Tonellato, U. (2007). Mimicking enzymes: cooperation between organic functional groups and metal ions in the cleavage of phosphate diesters. *Chem. A Eur. J.* 13, 2246–2256. doi: 10.1002/chem.200600672

Lönnberg, H. (2011). Cleavage of RNA phosphodiester bonds by small molecular entities: a mechanistic insight. *Org. Biomol. Chem.* 9, 1687–1703. doi: 10.1039/c0ob00486c

Mancin, F., Scrimin, P., and Tecilla, P. (2012). Progress in artificial metallonucleases. *Chem. Commun.* 48, 5545–5559. doi: 10.1039/c2cc30952a

Mancin, F., and Tecilla, P. (2007). Zinc(II) complexes as hydrolytic catalysts of phosphate diester cleavage: from model substrates to nucleic acids. *New J. Chem.* 31, 800. doi: 10.1039/b703556j

Manea, F., Houillon, F. B., Pasquato, L., and Scrimin, P. (2004). Nanozymes: gold-nanoparticle-based transphosphorylation catalysts. *Angew. Chem. Int. Ed.* 43, 6165–6169. doi: 10.1002/anie.200460649

Morrow, J. R., Amyes, T. L., and Richard, J. P. (2008). Phosphate binding energy and catalysis by small and large molecules. *Acc. Chem. Res.* 41, 539–548. doi: 10.1021/ar7002013

Schroeder, G. K., Lad, C., Wyman, P., Williams, N. H., and Wolfenden, R. (2006). The time required for water attack at the phosphorus atom of simple phosphodiesters and of DNA. *Proc. Nat. Acad. Sci. U.S.A.*103, 4052–4055. doi: 10.1073/pnas.0510879103

Sigel, H., and Bruce Martin, R. (1994). The colourless 'chameleon' or the peculiar properties of Zn2+ in complexes in solution. Quantification of equilibria involving a change of the coordination number of the metal ion. *Chem. Soc. Rev.* 23, 83–91. doi: 10.1039/CS9942300083

Silver, G. C., Gantzel, P., and Trogler, W. C. (1995). Characterization of (Trimethyltriazacyclononane)triaquozinc(II) nitrate. A Nonbridged Isomer. *Inorg. Chem.* 34, 2487–2489. doi: 10.1021/ic00113a038

Tirel, E. Y., Bellamy, Z., Adams, H., Duarte, F., and Williams, N. H. (2014). Catalytic zinc complexes for phosphate diester hydrolysis. *Angew. Chem. Int. Ed.* 53, 8246–50. doi: 10.1002/anie.201400335

Tirel, E. Y., and Williams, N. H. (2015). Enhancing phosphate diester cleavage by a zinc complex through controlling nucleophile coordination. *Chem. Eur. J.* 21, 7053–7056. doi: 10.1002/chem.201500619

Westheimer, F. H. (1987). Why nature chose phosphates. *Science* 235, 1173–1178.

Wolfenden, R., Ridgway, C., Young G., Chapel Hill, and North Carolina. (1998). Spontaneous hydrolysis of ionized phosphate monoesters and diesters and the proficiencies of phosphatases and phosphodiesterases as catalysts. *J. Am. Chem. Soc.* 120, 833–834.

Yang, R., and Zompa, L. J. (1976). Metal complexes of cyclic triamines. 1. complexes of 1,4,7-triazacyclononane ([9]AneN3) with Nickel(II), Copper(II), and Zinc(II). *Inorg. Chem.* 15, 1499–1502. doi: 10.1021/ic50161a007

Check for updates

# Different Strategies of Stabilization of Vanadium Oxidation States in Lagao₃ Nanocrystals

*Karolina Kniec\* and Lukasz Marciniak\**

*Institute of Low Temperature and Structure Research, Polish Academy of Sciences, Wroclaw, Poland*

The spectroscopic properties of $LaGaO_3$, doped with V ions, were examined in terms of the possibility of the stabilization of particular vanadium oxidation states. It was shown that three different approaches may be applied in order to control the ionic charge of vanadium, namely, charge compensation, via incorporation of $Mg^{2+}/Ca^{2+}$ ions, citric acid (CA)-assisted synthesis, with various CA concentrations and grain size tuning through annealing temperature regulation. Each of utilized method enables the significant reduction of $V^{5+}$ emission band at 520 nm associated with the $V^{4+} \rightarrow O^{2-}$ CT transition in respect to the $^2E \rightarrow {}^2T_2$ emission band of $V^{4+}$ at 645 nm and $^1E_2 \rightarrow {}^3T_{1g}$ emission band of $V^{3+}$ at 712 nm. The most efficient V oxidation state stabilization was obtained by the use of grain size modulation, which bases on fact of different localization of the V ions of given charge in the nanoparticles. Moreover, the CA-assisted synthesis of $LaGaO_3$:V determines V valence states but also provides significant separation of the nanograins. It was found that superior charge compensation was achieved when $Mg^{2+}$ ions were introduced in the matrix, due the more efficient lability, resulting from the comparable ionic radii between $Mg^{2+}$ and V ions.

Keywords: vanadium, charge compensation, citric acid, luminescence, nanocrystals

## INTRODUCTION

It is well-known that the electronic configuration of optically active ions and thus their spectroscopic properties depend strongly on the their oxidation state (Weber and Riseberg, 1971; Felice et al., 2001; Gupta et al., 2014; Matin et al., 2017; Drabik et al., 2018; Kniec and Marciniak, 2018a,b; Trejgis and Marciniak, 2018). These features may in turn be influenced by many factors, such as type of the lattice, in which the ions are embedded and coordination number of the substituted ion, synthesis method, size of phosphor grain etc. (McKittrick et al., 1999; Azkargorta et al., 2016; Marciniak et al., 2017; Kniec and Marciniak, 2018b; Zhang et al., 2018). The difference in the spectroscopic properties of optically active ions depending on the oxidation state in the case of lanthanides in especially well-manifested for europium ions, which may occur in two $2+$ and $3+$ oxidation states. Emission spectra of its trivalent ions consist of narrow lines attributed to intraconfigurational f-f electronic transitions whose spectral position is almost independent on the type of host material. On the other hand emission of $Eu^{2+}$ is characterized by broad d-d emission band of maxima which can be tuned by the modification of the crystal field strength (Peng and Hong, 2007; Mao et al., 2009; Mao and Wang, 2010; Sato et al., 2014; Zhang et al., 2015). Similar differences can be found in the case of transition metal (TM) ions, where electronic transitions between d states are responsible for luminescence.

In turn the luminescence of TM on different oxidation state is conditioned by presence of either octahedral or tetrahedral local site symmetries, where the optically active ion is substituted (Grinberg et al., 2017; Cao et al., 2018; Elzbieciak et al., 2018). This points to the importance of the appropriate choice of the local ion's environment and thus the host material to obtain efficient luminescence. The valence state of TM influences their output color, what is the most frequently encountered in case of manganese and chromium ions (Brik et al., 2011; Cao et al., 2016, 2018; Elzbieciak et al., 2018). $Cr^{3+}$ ions may reveal red and NIR luminescence ascribed to the $^2E_g \rightarrow \quad ^4A_{2g}$ spin-forbidden and $^4T_{2g} \rightarrow \quad ^4A_{2g}$ spin-allowed transition and (Struve and Huber, 1985; Brik et al., 2016; Elzbieciak et al., 2018), whereas $Cr^{4+}$ ions exhibit emission in NIR region (around 1,100 nm), which is attributed to the $^3A_2 \rightarrow \quad ^3T_1$ transition (Devi et al., 1996). Different emission color is also observed for manganese ions, where $Mn^{2+}$, $Mn^{3+}$ and $Mn^{4+}$ ions show blue ($^4A_2 \rightarrow \quad ^4T_1$), yellow-orange ($^4T_{1g} \rightarrow \quad ^6A_{1g}$) or red ($^5T_2 \rightarrow \quad ^5E$) luminescence, respectively (Trejgis and Marciniak, 2018). This phenomenon is also observed for titanium ions, where $Ti^{4+}$ and $Ti^{3+}$ possess blue and red emission color, which related to the $O^{2-} \rightarrow \quad T_2$ (CT, $\lambda_{em} \sim 450$ nm) and $^2E_g \rightarrow \quad ^2T_{2g}$ ($\lambda_{em} \sim 800$ nm) transitions, respectively (Martínez-Martínez et al., 2005; Pathak and Mandal, 2011; Drabik et al., 2018). The possibility of charge modulation is not only interesting in terms of spectroscopic tunability but also to get rid of some valence states, being marked by toxic properties and reducing the potential biological deployment, which is very important in case of chromium and cobalt ions (Buzea et al., 2007; Chowdhury and Yanful, 2010; Wang et al., 2012; Scharf et al., 2014).

One of the least known transition metal ion, whose optical properties strongly depend on the oxidation state is vanadium. Several oxidation states of vanadium can be found like $V^{5+}$, $V^{4+}$, $V^{3+}$, $V^{2+}$ of the $3d^0$, $3d^1$, $3d^2$, $3d^3$ electronic configuration, respectively. Recently we presented the potential application of V ions emission for luminescent nanothermometry, where V ions were incorporated into inorganic hosts, such as YAG ($Y_3Al_5O_{12}$) (Kniec and Marciniak, 2018b) and $LaGaO_3$ (Kniec and Marciniak, 2018a). As it was shown its high susceptibility to the thermal changes enables to detect the local temperatures with satisfactory sensitivity (Kniec and Marciniak, 2018a,b). Depending on the host material different V oxidation states were found, namely $V^{5+}$, $V^{3+}$ and $V^{5+}$, $V^{4+}$, $V^{3+}$, for YAG and $LaGaO_3$ lattices, respectively. What is more, an immense impact of synthesis method and annealing temperature on crystalline size, dispersion factor of the particles, size distribution were presented (Kniec and Marciniak, 2018a,b), which in turn lead to the presence of different V valence states, characterized by distinct luminescent properties and susceptibility to changes of local ion environment. Due to good spectral separation of emission bands of particular oxidation states of vanadium ions the qualitatively verification of their presence can be done basing on the analysis of the luminescent properties of vanadium doped phosphor. The $V^{5+}$, $V^{4+}$, and $V^{3+}$ luminescence is related with $V^{4+} \rightarrow \quad O^{2-}$ CT transition ($\lambda_{em} = 520$ nm), broad band $^2E \rightarrow \quad ^2T_2$ d-d electronic transition ($\lambda_{em} = 645$ nm) and narrow line $^1E_2 \rightarrow \quad ^3T_{1g}$ d-d electronic transition

($\lambda_{em} = 712$ nm), respectively (Ryba-Romanowski et al., 1999a; Kniec and Marciniak, 2018a,b).

In the course of our previous studies it was found that broad emission band of $V^{5+}$ with the maxima at around 497 nm ($V^{4+} \rightarrow \quad O^{2-}$ CT emission) predominates in the emission spectra (Kniec and Marciniak, 2018a,b). However, as it was already proved the $^2E \rightarrow \quad ^2T_2$ emission of $V^{4+}$ ions is characterized by higher susceptibility to luminescence thermal quenching and hence reveals the best performance to non-contact readout. As it was already shown in the case of YAG nanocrystals, due to the spatial segregation of different vanadium oxidation states within the nanoparticle, the emission intensity ratio of $V^{5+}$ to $V^{3+}$ can be easily modulated through size of the nanoparticles. Moreover, the involvement of CA during the synthesis caused the reduction of oxidation state of vanadium substrate, namely from pentavalent to trivalent valence states, being observed by the changes of color of the solution, from yellow to blue, respectively (Kniec and Marciniak, 2018a,b). Citric acid is a complexing agent, which is highly soluble in polar solvents and widely used in the synthesis of nanoparticles, guaranteeing the incorporation of each metal into the material, maintaining local stoichiometry (Davar et al., 2013), which is possible due the presence of three carboxylic group (−COOH) and one hydroxyl group (−OH) in the CA chain (Gutierrez et al., 2015; Kniec and Marciniak, 2018a,b). It is well-known as a reducing and capping agent, providing possibility of charge modulation, nano-sized particles and relatively good size distribution, due the high chemical stability, steric impediment and generation of electrostatic repulsive forces (Zhang and Gao, 2004; Thio et al., 2011; Davar et al., 2013; Gutierrez et al., 2015; Shinohara et al., 2018). However, the addition of PEG, entering into polyesterification with CA, leads to discoloration of the solution (Kniec and Marciniak, 2018a,b). This phenomenon may be explained as a decrease of reducing properties of CA, resulting from the interaction between carboxylic and hydroxyl group of CA and PEG, respectively. Another approach which was frequently used in terms of stabilization of oxidation state of vanadium ions in the crystals but never in the case of nanocrystals is charge compensation. In this paper the potential possibilities of the modulation of vanadium oxidation states by varying charge compensation process, annealing temperature and the choice of appropriate synthesis conditions have been presented. Employment of these modifications leads to the changes in vanadium valence states and in consequence modify spectroscopic properties, such as emission color.

## EXPERIMENTAL

### LaGaO$_3$:V Synthesis With Different Amounts of Citric Acid

The LaGaO$_3$:xV nanocrystals have been successfully synthesized by the use of citric acid assisted sol-gel method. The first steps of preparation were carried out analogously to the previous synthesis of LaGaO$_3$ (see **Table S1**) (Kniec and Marciniak, 2018a). Lanthanum oxide (La$_2$O$_3$ with 99.999% purity from Stanford Materials Corporation), gallium nitrate nonahydrate
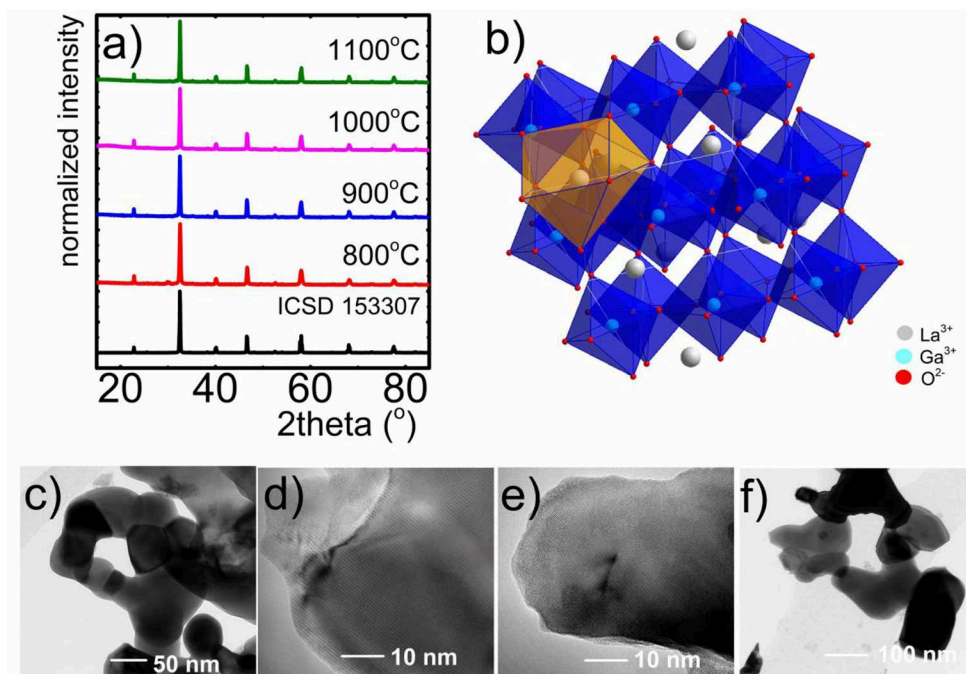
**FIGURE 1 |** XRD patterns of LaGaO$_3$:V nanocrystals synthesized by citric acid-assisted sol-gel method (M:CA 1:1) annealed at different temperatures **(a)**; visualization of LaGaO$_3$ perovskite structure **(b)**; respective TEM images of LaGaO$_3$:V nanocrystals with the 10-fold excess of citric acid, annealed at 800°C **(c)**, 900°C **(d)**, 1,000°C **(e)**, and 1,100°C **(f)**.

[Ga(NO$_3$)$_3$·9H$_2$O with 99.999% purity from Alfa Aesar], ammonium metavanadate (NH$_4$VO$_3$ with 99% purity from Alfa Aesar) and citric acid (CA, C$_6$H$_8$O$_7$, 99.5+% purity from Alfa Aesar,) were used as substrates of the reaction. Stoichiometric amount of lanthanum oxide was dissolved in distilled water and ultrapure nitric acid (96%). The created lanthanum nitrate was recrystallized three times using small quantities of distilled water. After this, adequate quantities of Ga(NO$_3$)$_3$·9H$_2$O and NH$_4$VO$_3$ were diluted in distilled water and added to aqueous solution of obtained lanthanum nitrate. The mixture was stirred with citric acid using magnetic stirrer and heated up to 90°C for 1 h to provide the metal complexation process. Afterwards, the solution was dried for 1 week at 90°C to create a resin. Finally, the nanocrystals were received by annealing the resin in air for 8 h at 800, 900, 1,000, and 1,100°C, respectively. The vanadium dopant was used in the amount of x = 0.1% in respect to number of moles of Ga$^{3+}$ ions. The CA were used in different molar ratio in respect to all metals (M), namely 1:1, 2:1, 4:1, 6:1, 8:1, and 10:1.

## LaGaO$_3$:V Synthesis With the Charge Compensation Using Mg$^{2+}$ and Ca$^{2+}$ ions

The LaGaO$_3$:V nanocrystals with Mg$^{2+}$ and Ca$^{2+}$ ions as a charge compensators have been successfully obtained using the same Pechini method, which was exploited to synthesized the previous presented LaGaO$_3$:V powders (Kniec and Marciniak, 2018a). The lanthanum oxide was recrystallized. Appropriate quantities of Ga(NO$_3$)$_3$·9H$_2$O, NH$_4$VO$_3$, magnesium nitrate heksahydrate [Mg(NO$_3$)$_2$·6H$_2$O with 99.999% purity from Alfa

Aesar] or calcium nitrate tetrahydrate [Ca(NO$_3$)$_2$·4H$_2$O with 99.995% purity from Alfa Aesar] were added to the mixture of all reactants and stirred with citric acid for 1 h at 90°C, where the citric acid was used in the 6-fold excess in respect to total amount of metals moles. Than appropriate volume of PEG-200 (1 PEG-200: 1 CA) was dropped to the solution. The reaction was carried out for 2 h with simultaneous heating. After this synthesis the received solutions were dried for 1 week at 90°C. The powders of LaGaO$_3$:V, Mg$^{2+}$(Ca$^{2+}$) were finally obtained by annealing in air for 8 h at 800°C. The concentration of V ions was 0.1% in respect to number of moles of Ga$^{2+}$ ions, whereas the total amount of Mg$^{2+}$ (Ca$^{2+}$) was used in the ratio of 1:1, 2:1, 4:1, and 8:1 in respect to the vanadium ions.

## Characterization

Powder diffraction studies were carried out on PANalytical X'Pert Pro diffractometer equipped with Anton Paar TCU 1000 N Temperature Control Unit using Ni-filtered Cu *K$\alpha$* radiation ($V = 40$ kV, $I = 30$ mA).

Transmission electron microscopy images were obtained using the Tecnai G2 20 S/TEM Microscope from FEI Company. The microscope was equipped with a thermionic LaB6 emitter and EDS detector for elemental analysis. The study was conducted in the TEM mode at maximum voltage of 200 kV. Micrographs were taken at various magnifications, including high resolution images with lattice fringes.

The emission spectra were measured using the 266 nm excitation line from a laser diode (LD) and a Silver-Nova
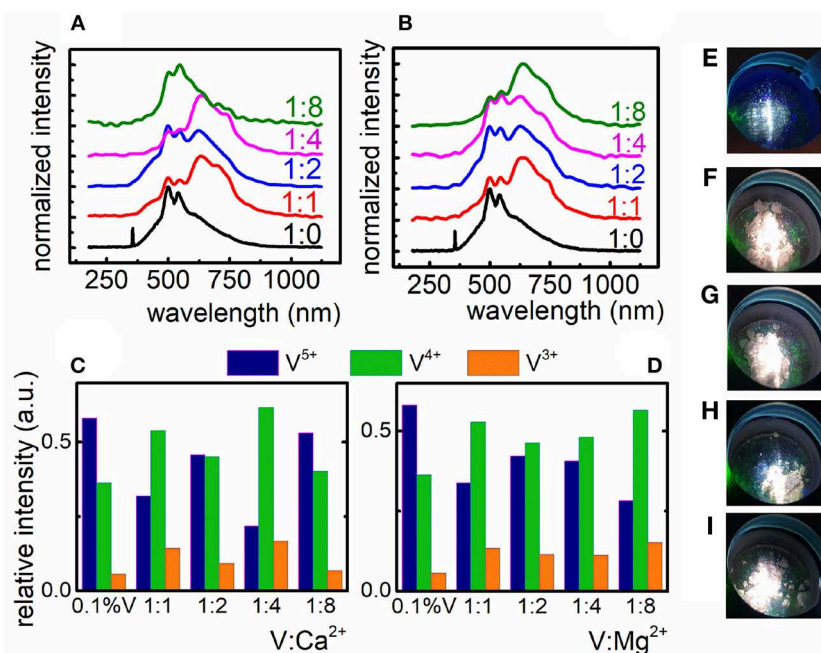
**FIGURE 2** | Influence of the $Ca^{2+}$ **(A)** and $Mg^{2+}$ **(B)** compensating ions on the V emission spectrum in $LaGaO_3$ nanocrystals; relative emission intensity of the V ions after charge compensation with $Ca^{2+}$ **(C)** and $Mg^{2+}$ ions **(D)**; emission color of uncompensated $LaGaO_3$:V nanocrystals **(E)** and compensated $LaGaO_3$:V nanocrystals with the V:$Mg^{2+}$ ratio of 1:1, 1:2, 1:4, and 1:8 **(F–I)**, respectively.

Super Range TEC Spectrometer form Stellarnet (1 nm spectral resolution) as a detector.
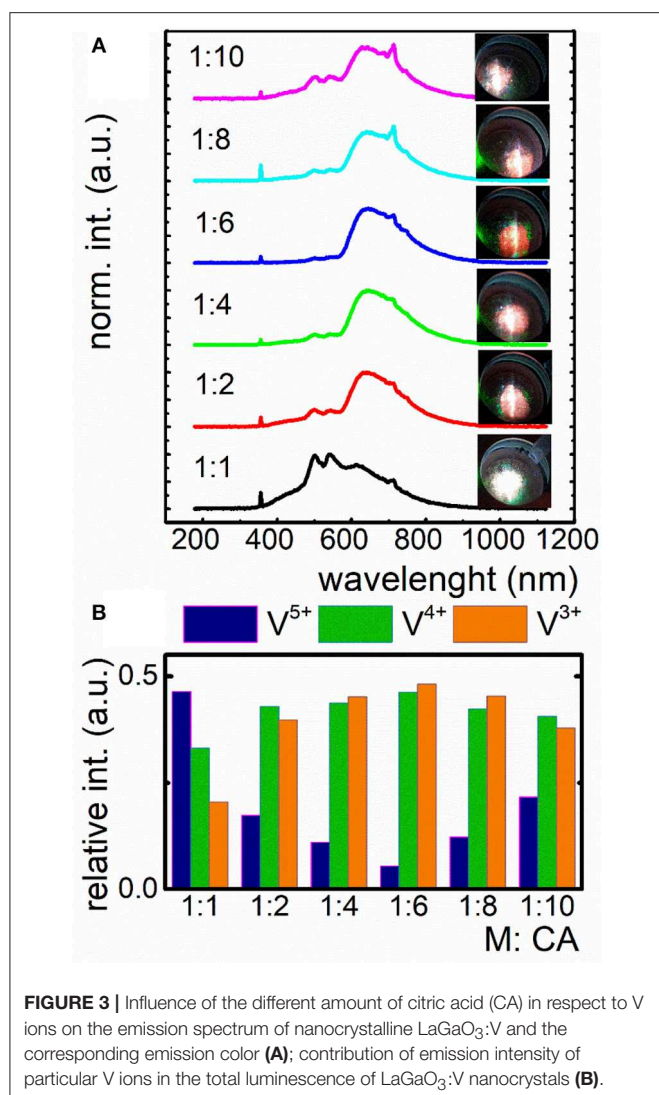
## RESULTS AND DISCUSSION

The phase purity and crystalline structure of obtained $LaGaO_3$:V powders with different amounts of CA and the employment of charge compensating ions was examined using the XRD analysis (**Figure 1a**, see also **Figures S1, S2**). Moreover, the influence of annealing temperature on the $LaGaO_3$ structure, especially on the grain size, was analyzed (**Figures 1a,c-f**). Comparing the reference peaks (ICSD 153307) with measured XRD patterns it was confirmed that obtained phosphors crystalized in orthorhombic structure and centrosymmetric Pbnm space group. Additional reflection peaks found for the sample annealed at 800°C, without charge compensation, originate from $La_2O_3$ and $Ga_2O_3$ impurities. These results confirm that the sol-gel citric acid-assisted synthesis with and without charge compensation allows to obtain the $LaGaO_3$:V nanocrystals of high structural purity. The analyzed structure consists of 6-fold coordinated $Ga^{3+}$ $(GaO_6)^{9-}$ and 8-fold coordinated $La^{3+}$ ions, where $La^{3+}$ sites are situated between slightly tilted and distorted $(GaO_6)^{9-}$ layers (Marti et al., 1994; Ryba-Romanowski et al., 1999a,b; Kamal et al., 2017; Kniec and Marciniak, 2018a) (**Figure 1b**). As it was mentioned in the previous work (Kniec and Marciniak, 2018a), due the similarities in valence states and ionic radii between $Ga^{3+}$ and V ions (0.76, 0.78, 0.72, and 0.54 Å Kniec and Marciniak, 2018a, for $Ga^{3+}$, $V^{3+}$, $V^{4+}$, and $V^{5+}$, respectively) V occupy octahedral site of $Ga^{3+}$ ions in the $LaGaO_3$ matrix.

Representative TEM images of the nanocrystals (**Figures 1c–f**), which were synthesized using the citric acid-assisted sol-gel method reveal well-crystalized agglomerated nanoparticles. Additionally it can be noticed that this synthesis method provides higher degree of grains dispersion and their separation in respect to the previously described modified Pechini method (Kniec and Marciniak, 2018a). According to our predictions the increase of annealing temperature results in the enlargement of the average grain size: from 66 nm for 800°C, 79 for 900°C, 114 nm for 1,000°C to 145 nm for 1,100°C. It is worth mentioning, that the highest grain size of $LaGaO_3$:V annealed at 1,100°C is more than 2-fold smaller in respect to the counterpart synthesized using Pechini method (381.8 nm) (Kniec and Marciniak, 2018a). However, the increase of CA does not cause the evident changes in grain size.

The first approach employed by us to control the valence state of vanadium ions was compensation method. Two series of nanocrystals with different molar ratio of $Mg^{2+}$ and $Ca^{2+}$ ions in respect to the V ions were prepared. Proposed charge compensation can be written as follows:

$$2 \times Ga^{3+} \rightarrow 1 \times V^{4+} + 1 \times Ca^{2+}/Mg^{2+} \quad (1)$$
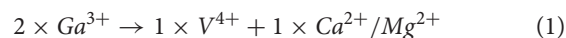
Two $Ga^{3+}$ sites were substituted by one $V^{4+}$ ion and one $Ca^{2+}/Mg^{2+}$ ion so that the excess electron could be transferred to the compensating ion. Taking into consideration the structural properties of compensated material, it is worth mentioning, that the introduction of even large excess of $Ca^{2+}/Mg^{2+}$ ions does not

**FIGURE 3 |** Influence of the different amount of citric acid (CA) in respect to V ions on the emission spectrum of nanocrystalline LaGaO$_3$:V and the corresponding emission color **(A)**; contribution of emission intensity of particular V ions in the total luminescence of LaGaO$_3$:V nanocrystals **(B)**.

influence the changes of XRD patterns (**Figure S1**). According to our predictions, the introduction of Mg$^{2+}$ and Ca$^{2+}$ in the crystal structure caused the rise of the V$^{4+}$ emission intensity ($\lambda_{em}$ = 633 nm) in respect to the uncompensated counterpart (**Figures 2A–D**). Due to the fact that no structural changes can be found in the XRD pattern even for high Ca$^{2+}$/Mg$^{2+}$, the observed changes are the confirmation of the successful charge compensation and thus the increase of V$^{4+}$ concentration. One can notice that even a small addition of Mg$^{2+}$ and Ca$^{2+}$ ions to the LaGaO$_3$:0.1%V crystal lattice affects the shape of emission spectra (**Figures 2C,D**) significantly. It can be found that Mg$^{2+}$ ions revealed better, in respect to the Ca$^{2+}$ ions, performance to charge compensation which is reflected in the dominant emission of V$^{4+}$ ions over the emission of V$^{3+}$ and V$^{5+}$ ions for each amount of compensating ion. However, the most satisfactory charge compensation was found in the case of incorporation of 8-fold excess of Mg$^{2+}$ in respect to V (**Figures 2B,D**). This effect may be explained in terms of superior lability of Mg$^{2+}$ ions in the lattice, which results from their smaller ionic radius

(0.78 Å) compared to Ca$^{2+}$ ions (1.06 Å). The impact of the amount of compensating ions on the emission intensity of the particular oxidation state of vanadium ions is presented in **Figures 2C,D**. In the case of Mg$^{2+}$ gradual increase of its concentration causes gradual decrease of V$^{5+}$ emission intensity and enhancement of V$^{4+}$ intensity while V$^{3+}$ becomes almost constant. The changes observed in the case of Ca$^{2+}$ are rather irregular. The consequence of observed charge compensation is the modulation of emission color (**Figures 2E–I**). It is also worth noting that in the case of calcium ions there is a concentration limit (1:8), above which V$^{5+}$ emission intensity becomes anew dominant (**Figures 2A,C**).

The incorporation of compensating ions caused the enhancement of V$^{4+}$ emission intensity, however the luminescence of both V$^{5+}$ and V$^{3+}$ ions is still observed and cannot be completely reduced. The contribution of V$^{5+}$ emission intensity in the emission spectra of LaGaO$_3$:V is relevant and that is why the emission color does not changes significantly (**Figures 2E–I**) indicating that charge compensation does not provide sufficient ability to modulation of vanadium oxidation states. Based on these results new approach to charge modulation was proposed.

Taking advantage from the fact that PEG, which was used in the case of previously described Pechini method is well-known from its oxidizing properties and may lead to the increase of V$^{5+}$ concentration, in the second approach we decided to use sol-gel method to eliminate PEG as a reagent, being involved in the resin creation. The issue was to involve all COOH groups to reduction reaction. Cit$^{3-}$ ions were used in different molar quantity in respect to the total amount of metal ions (M) in the lattice (**Figure 3**). To verify the capability of V oxidation states modulation by the CA concentration, the emission spectra of LaGaO$_3$:V nanocrystals were recorded at −150°C under 266 nm excitation. Low measurement temperature provides the highest emission intensity, being to a lesser extent affected by lattice vibrations, reducing the luminescence temperature quenching (Kniec and Marciniak, 2018a,b). The employment of the same molar amounts of ions and CA caused the presence of three emitting V oxidation states, namely V$^{5+}$, V$^{4+}$, and V$^{3+}$, with the predominant emission intensity of V$^{5+}$. This phenomenon indicates that this molar ratio is insufficient to provide significant reduction of V$^{5+}$. The employment of 2-fold excess of CA (1:2) leads to the apparent domination of V$^{4+}$ emission and thereby the change of emission color (**Figures 3A,B**), pointing to the immense impact on the V luminescence properties. Increasing the quantity of capping agent to 6-fold excess in respect to metal ions, the V$^{5+}$ emission intensity decreases with the simultaneously rise of V$^{4+}$ and V$^{3+}$ luminescence (**Figure 3B**), being a limit value, above which a reversed dependence occurs. This phenomenon determines the color output of LaGaO$_3$:V, which changes from white to red, while the emission is being red-shifted (V$^{4+}$ and V$^{3+}$) and becomes whitish as the V$^{5+}$ amount increases (**Figure 3A**, see also **Figures S3, S5**). It is worth noting that although initially with the increase of CA concentration the emission intensity of V$^{5+}$ decreases in respect to the V$^{4+}$ and V$^{3+}$, above 1:8 ratio the V$^{5+}$ emission band appears anew. The enhancement of V$^{5+}$ luminescence may be due the fact,
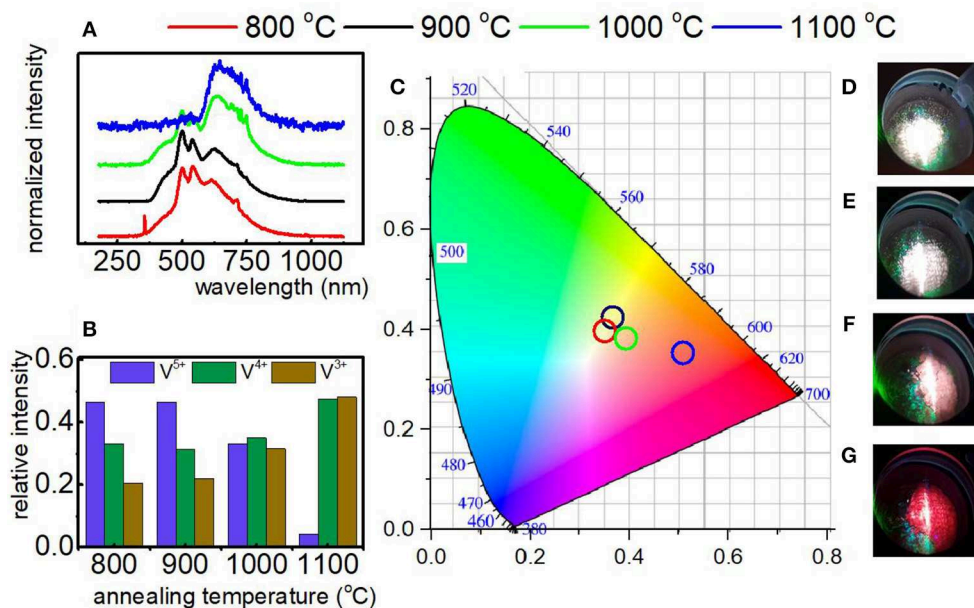
**FIGURE 4 |** Emission spectrum of LaGaO$_3$:V nanocrystals as a function of annealing temperature recorded at $-150°$C under 266 nm excitation **(A)**; the relative emission of each V ions in the LaGaO$_3$ nanocrystals annealed at different temperatures **(B)**; the CIE 1,931 chromatic coordinates calculated for LaGaO$_3$:V nanocrystals annealed at different temperatures **(C)**; LaGaO$_3$:V emission colors at $-150°$C after annealing at 800, 900, 1,000, and 1,100°C **(D–G)**, respectively.

that higher content of Cit$^{3-}$ provides the stabilization of more positive charge on V. In turn the V charge lowering confirms the reducing properties of CA even in the nanoscale materials. On the other hand, as it was already proved in the case of nanocrystalline phosphors doped with vanadium ions the V$^{5+}$ ions are mainly located in the surface part of the grains, while V$^{4+}$ and V$^{3+}$ in the core part (Kniec and Marciniak, 2018b). Therefore, the enhancement of the V$^{5+}$ emission at higher CA concentration may be related with the higher dispersion of the LaGaO$_3$ nanocrystals leading also to the higher separation of the grains. This is in agreement with the TEM images presented in **Figure S4**. The observed changes of the relative emission intensity of particular V oxidation state causes modulation of the emission color (**Figures 3A,B**).

In the course of our studies it was found that in the case of YAG:V and LaGaO$_3$:V nanocrystals the vanadium on its higher oxidation state is mainly located at the surface part of the grain. Therefore, in the last approach we verified either size of the nanocrystals may enable the reduction of the V$^{5+}$ emission intensity in respect to the V$^{4+}$ and V$^{3+}$. The size of the nanocrystals was controlled by the annealing temperature for constant molar ratio of CA:V (1:1). As it can be observed the increase of grain size causes gradual increase of bands associated with the $^2$E $\rightarrow$ $^2$T$_2$ and $^1$E$_2$ $\rightarrow$ $^3$T$_{1g}$ electronic transitions of V$^{4+}$ and V$^{3+}$, respectively in respect to the V$^{4+}$ $\rightarrow$ O$^{2-}$ band of V$^{5+}$ (**Figure 4A**). This is due to the fact that the rise of grain size causes a decrease in the surface-to-volume ratio of the nanocrystals and thus a drop of the amount of emitting V$^{5+}$ ions compared to the V$^{4+}$ and V$^{3+}$ ions. The most apparent emission changes take part by the annealing temperature increase from 1,000 to 1,100°C, whereas

least relevant are between 800 and 900°C (**Figure 4B**), being strictly related to enlargement of the grain size by 42.94 and 2.53 nm, respectively. Therefore, the emission color changes can be observed, ranging from white, connected with the domination of V$^{5+}$ luminescence, trough pinkish, related to the presence of each V ions, ending on red color, originating from predominant V$^{4+}$ and V$^{3+}$ luminescence (**Figures 4B,D–G**). This in turn enables the modulation of color output of LaGaO$_3$:V, which varies depending on the total contribution of each V ions in the luminescence (**Figures 4B,D–G**). The contribution of each V$^{n+}$ ions into total emission spectra was estimated by the calculation of the integrals in the range of 400–570, 580–675, and 680–750 nm integral emission intensity for V$^{3+}$, V$^{4+}$, and V$^{5+}$, respectively. In addition, knowing the average grain size of LaGaO$_3$:V nanocrystals, the possibility of establishment of the emission spectrum and, consequently, predict the color output was affirmed (**Figure 4C**). The same dependence, concerning the size effect on the V oxidation states was also observed for LaGaO$_3$:V nanocrystals, where citric acid was incorporated in higher concentration (see **Figure S3**).

As it can be observed, that all presented approaches led to the decrease of V$^{5+}$ emission intensity, however the last method, based on the modification of the sizes of the LaGaO$_3$ nanocrystals, is the most efficient.

## CONCLUSION

In this paper three approaches to stabilize and modulate the V oxidation states in LaGaO$_3$ nanocrystals and thus their emission color have been demonstrated. It was found that in this perovskite lattice three different V valence states are present, namely V$^{5+}$,

$V^{4+}$, and $V^{3+}$, showing the emission, being related to the $V^{4+} \rightarrow O^{2-}$ CT transition ($\lambda_{em} = 520$ nm), $^2E \rightarrow \; ^2T_2$ ($\lambda_{em} = 645$ nm) and narrow line $^1E_2 \rightarrow \; ^3T_{1g}$ ($\lambda_{em} = 712$ nm) d-d electronic transition, respectively.

Furthermore it was concluded that at $-150°C$ under 266 irradiation $V^{4+}$ ions exhibit broad band emission, whereas $V^{3+}$ ions reveals narrow line luminescence. It was presented that three different approaches including the implementation of compensating ions, by altering the ratio of citric acid to metal ions and the tuning of the size of the nanocrystals in range 66–145 nm through change of annealing temperature in 800–1,100°C range may provide the ability to regulate the valence state of vanadium ions. It was found that in the case of charge compensation method the introducing of $Mg^{2+}$ ions is much more efficient, due the similar ionic radius to V ions and higher lability of compensating ions in respect to $Ca^{2+}$. In turn the citric acid-assisted synthesis, where CA was used in the excess in respect to total amount of metals in the lattice, leads to the significant increase of $V^{4+}$ and $V^{3+}$ luminescent intensity with the simultaneous improvement of nanocrystals separation and narrower size distribution in respect to the powders obtained using Pechini method. Basing on the fact, that particular oxidation states of V ions are localized in different part of the $LaGaO_3$ nanocrystals, namely $V^{5+}$ in the surface, $V^{4+}$ and $V^{3+}$ in the core part, respectively, the influence of the grain size of V emission intensity was investigated. The increase of the annealing temperature and thereby the size of the nanocrystals, leads to the decrease of $V^{5+}$ luminescence and simultaneously causing the enhancement of $V^{4+}$ and $V^{3+}$ ones. The most significant $V^{5+}$ emission changes are observed when the annealing temperature increase from 1,000 to 1,100°C, which corresponds to the enlargement of the grain size by 43 nm. All of the presented approaches provide the differences of V emission intensity, however the most efficient method based on the modification of the grain size, which is confirmed by the most apparent changes in $LaGaO_3$:V color output. Taking into account that different oxidation states of vanadium ions possess favorable optical properties for i.e., lightning and luminescent thermometry, we believe that this study may be of relevant importance for further application of vanadium based nanocrystalline phosphors.

## DATA AVAILABILITY

All datasets generated for this study are included in the manuscript and the **Supplementary Files**.

## AUTHOR CONTRIBUTIONS

All authors listed have made a substantial, direct and intellectual contribution to the work, and approved it for publication.

## ACKNOWLEDGMENTS

## SUPPLEMENTARY MATERIAL

The Supplementary Material for this article can be found online at: https://www.frontiersin.org/articles/10.3389/fchem.2019.00520/full#supplementary-material

## REFERENCES

Azkargorta, J., Marciniak, L., Iparraguirre, I., Balda, R., Strek, W., Barredo-Zuriarrain, M., et al. (2016). Influence of grain size and Nd3+ concentration on the stimulated emission of LiLa$_{1-x}$Nd$_x$P$_4$O$_{12}$ crystal powders. *Opt. Mater. (Amst).* 63, 3–8. doi: 10.1016/j.optmat.2016.07.016

Brik, M. G., Pan, Y. X., and Liu, G. K. (2011). Spectroscopic and crystal field analysis of absorption and photoluminescence properties of red phosphor CaAl$_{12}$O$_{19}$:Mn$^{4+}$ modified by MgO. *J. Alloys Compd.* 509, 1452–1456. doi: 10.1016/j.jallcom.2010.11.117

Brik, M. G., Papan, J., Jovanović, D. J., and Dramićanin, M. D. (2016). Luminescence of Cr$^{3+}$ ions in ZnAl$_2$O$_4$ and MgAl$_2$O$_4$ spinels: correlation between experimental spectroscopic studies and crystal field calculations. *J. Lumin.* 177, 145–151. doi: 10.1016/j.jlumin.2016.04.043

Buzea, C., Pacheco, I. I., and Robbie, K. (2007). Nanomaterials and nanoparticles: sources and toxicity. *Biointerphases* 2, MR17–MR71. doi: 10.1116/1.2815690

Cao, R., Ceng, X., Huang, J., Xia, X., Guo, S., and Fu, J. (2016). A double-perovskite Sr$_2$ZnWO$_6$:Mn$^{4+}$ deep red phosphor: synthesis and luminescence properties. *Ceram. Int.* 42, 16817–16821. doi: 10.1016/j.ceramint.2016.07.173

Cao, R., Zhang, F., Xiao, H., Chen, T., Guo, S., Zheng, G., et al. (2018). Perovskite La$_2$LiRO$_6$:Mn$^{4+}$ (R = Nb, Ta, Sb) phosphors: synthesis and luminescence properties. *Inorganica Chim. Acta* 483, 593–597. doi: 10.1016/j.ica.2018.09.015.

Chowdhury, S. R., and Yanful, E. K. (2010). Arsenic and chromium removal by mixed magnetite-maghemite nanoparticles and the effect of phosphate on removal. *J. Environ. Manage.* 91, 2238–2247. doi: 10.1016/j.jenvman.2010.06.003

Davar, F., Hassankhani, A., and Loghman-Estarki, M. R. (2013). Controllable synthesis of metastable tetragonal zirconia nanocrystals using citric acid assisted sol-gel method. *Ceram. Int.* 39, 2933–2941. doi: 10.1016/j.ceramint.2012.09.067

Devi, P. S., Gafney, H. D., Petricevic, V., and Alfano, R. R. (1996). Synthesis and spectroscopic properties of (Cr$^{4+}$) doped sol-gels. *J. Non Cryst. Solids* 203, 78–83. doi: 10.1016/0022-3093(96)00336-5

Drabik, J., Cichy, B., and Marciniak, L. (2018). New type of nanocrystalline luminescent thermometers based on Ti$^{3+}$/Ti$^{4+}$ and Ti$^{4+}$/Ln$^{3+}$ (Ln$^{3+}$ = Nd$^{3+}$, Eu$^{3+}$, Dy$^{3+}$) luminescence intensity ratio. *J. Phys. Chem. C* 122, 14928–14936. doi: 10.1021/acs.jpcc.8b02328

Elzbieciak, K., Bednarkiewicz, A., and Marciniak, L. (2018). Temperature sensitivity modulation through crystal field engineering in Ga$^{3+}$ co-doped Gd$_3$Al$_{5-x}$Ga$_x$O$_{12}$:Cr$^{3+}$, Nd$^{3+}$ nanothermometers. *Sens. Actuators B Chem.* doi: 10.1016/j.snb.2018.04.157

Felice, V., Dussardier, B., Jones, J. K., Monnom, G., and Ostrowsky, D. B. (2001). Chromium-doped silica optical fibres: influence of the core composition on the Cr oxidation states and crystal field. *Opt. Mater.* 16, 269–277. doi: 10.1016/S0925-3467(00)00087-2

Grinberg, M., Lesniewski, T., Mahlik, S., and Liu, R. S. (2017). 3d$^3$ system–comparison of Mn$^{4+}$ and Cr$^{3+}$ in different lattices. *Opt. Mater.* 74, 93–100. doi: 10.1016/j.optmat.2017.03.057

Gupta, S. K., Kadam, R. M., Natarajan, V., and Godbole, S. V. (2014). Oxidation state of manganese in zinc pyrophosphate: probed by luminescence and EPR studies. *AIP Conf. Proc.* 1591, 1699–1701. doi: 10.1063/1.4873082

Gutierrez, L., Aubry, C., Cornejo, M., and Croue, J. P. (2015). Citrate-coated silver nanoparticles interactions with effluent organic matter: influence of capping agent and solution conditions. *Langmuir* 31, 8865–8872. doi: 10.1021/acs.langmuir.5b02067

Kamal, C. S., Rao, T. K. V., Samuel, T., Reddy, P. V. S. S. S. N., Jasinski, J. B., Ramakrishna, Y., et al. (2017). Blue to magenta tunable luminescence from LaGaO3: $Bi^{3+}$, $Cr^{3+}$ doped phosphors for field emission display applications. *RSC Adv.* 7, 44915–44922. doi: 10.1039/C7RA08864G

Kniec, K., and Marciniak, L. (2018a). Spectroscopic properties of LaGaO3:V, $Nd^{3+}$ nanocrystals as a potential luminescent thermometer. *Phys. Chem. Chem. Phys.* 20, 21598–21606. doi: 10.1039/C8CP04080J

Kniec, K., and Marciniak, L. (2018b). The influence of grain size and vanadium concentration on the spectroscopic properties of YAG:$V^{3+}$, $V^{5+}$ and YAG: V, $Ln^{3+}$ ($Ln^{3+}$ = $Eu^{3+}$, $Dy^{3+}$, $Nd^{3+}$) nanocrystalline luminescent thermometers. *Sensors Actuators B Chem.* doi: 10.1016/j.snb.2018.02.189

Mao, Z. Y., and Wang, D. J. (2010). Color tuning of direct white light of lanthanum aluminate with mixed-valence europium. *Inorg. Chem.* 49, 4922–4927. doi: 10.1021/ic902538a

Mao, Z. Y., Wang, D. J., Lu, Q. F., Yu, W. H., and Yuan, Z. H. (2009). Tunable single-doped single-host full-color-emitting LaAlO3:Eu phosphor via valence state-controlled means. *Chem. Commun.* 2009, 346–348. doi: 10.1039/b814535k

Marciniak, L., Bednarkiewicz, A., and Strek, W. (2017). The impact of nanocrystals size on luminescent properties and thermometry capabilities of Cr, Nd doped nanophosphors. *Sens. Actuators B Chem.* 238, 381–386. doi: 10.1016/j.snb.2016.07.080

Marti, W., Fischer, P., Altorfer, F., Scheel, H. J., and Tadin, M. (1994). Crystal structures and phase transitions of orthorhombic and rhombohedral RGaO3 (R = La, Pr, Nd) investigated by neutron powder diffraction. *J. Phys. Condens. Matter* 6, 127–135. doi: 10.1088/0953-8984/6/1/014

Martínez-Martínez, R., García-Hipólito, M., Ramos-Brito, F., Hernández-Pozos, J. L., Caldiño, U., and Falcony, C. (2005). Blue and red photoluminescence from Al2O3:$Ce^{3+}$:$Mn^{2+}$ films deposited by spray pyrolysis. *J. Phys. Condens. Matter* 17, 3647–3656. doi: 10.1088/0953-8984/17/23/016

Matin, M. A., Islam, M. M., Bredow, T., and Aziz, M. A. (2017). The effects of oxidation states, spin states and solvents on molecular structure, stability and spectroscopic properties of fe-catechol complexes: a theoretical study. *Adv. Chem. Eng. Sci.* 7, 137–153. doi: 10.4236/aces.2017.72011

McKittrick, J., Shea, L. E., Bacalski, C. F., and Bosze, E. J. (1999). Influence of processing parameters on luminescent oxides produced by combustion synthesis. *Displays* 19, 169–172. doi: 10.1016/S0141-9382(98)00046-8

Pathak, C. S., and Mandal, M. K. (2011). Yellow light emission from $Mn^{2+}$ doped ZnS nanoparticles. *Optoelectron. Adv. Mater. Rapid Commun.* 5, 211–214. doi: 10.1016/j.physe.2008.04.013

Peng, M., and Hong, G. (2007). Reduction from $Eu^{3+}$ to $Eu^{2+}$ in BaAl2O4:Eu phosphor prepared in an oxidizing atmosphere and luminescent properties of BaAl2O4:Eu. *J. Lumin.* 127, 735–740. doi: 10.1016/j.jlumin.2007.04.012

Ryba-Romanowski, W., Golab, S., Dominiak-Dzik, G., and Berkowski, M. (1999a). Optical spectra of a LaGaO3 crystal singly doped with chromium, vanadium and cobalt. *J. Alloys Compd.* 288, 262–268. doi: 10.1016/S0925-8388(99)00117-6

Ryba-Romanowski, W., Golab, S., Dominiak-Dzik, G., Sokolska, I., and Berkowski, M. (1999b). "Growth and optical properties of chromium doped LaGaO3 crystal," in *Proceedings of SPIE–The International Society for Optical Engineering*, 43–46. Available online at: https://www.scopus.com/inward/record.uri?eid=2-s2.0-0032669535&partnerID=40&md5=318115d07d121bfee5802f921a39653c

Sato, Y., Kato, H., Kobayashi, M., Masaki, T., Yoon, D. H., and Kakihana, M. (2014). Tailoring of deep-red luminescence in Ca2SiO4:$Eu^{2+}$. *Angew. Chem. Int. Ed.* 53, 7756–7759. doi: 10.1002/anie.201402520

Scharf, B., Clement, C. C., Zolla, V., Perino, G., Yan, B., Elci, S. G., et al. (2014). Molecular analysis of chromium and cobalt-related toxicity. *Sci. Rep.* 4:5729. doi: 10.1038/srep05729

Shinohara, S., Eom, N., Teh, E. J., Tamada, K., Parsons, D., and Craig, V. S. J. (2018). The Role of citric acid in the stabilization of nanoparticles and colloidal particles in the environment: measurement of surface forces between hafnium oxide surfaces in the presence of citric acid. *Langmuir* 34, 2595–2605. doi: 10.1021/acs.langmuir.7b03116

Struve, B., and Huber, G. (1985). The effect of the crystal field strength on the optical spectra of $Cr^{3+}$ in gallium garnet laser crystals. *Appl. Phys. B Photophys. Laser Chem.* 36, 195–201. doi: 10.1007/BF00704574

Thio, B. J., Montes, M. O., Mahmoud, M. A., Lee, D. W., Zhou, D., and Keller, A. A. (2011). Mobility of capped silver nanoparticles under relevant conditions. *Environ. Sci. Technol.* 46, 6985–6991. doi: 10.1021/es203596w

Trejgis, K., and Marciniak, L. (2018). The influence of manganese concentration on the sensitivity of bandshape and lifetime luminescent thermometers based on Y3Al5O12:$Mn^{3+}$, $Mn^{4+}$, $Nd^{3+}$ nanocrystals. *Phys. Chem. Chem. Phys.* 20, 9574–9581. doi: 10.1039/c8cp00558c

Wang, M. Q., Li, H., He, Y. D., Wang, C., Tao, W. J., and Du, Y. J. (2012). Efficacy of dietary chromium (III) supplementation on tissue chromium deposition in finishing pigs. *Biol. Trace Elem. Res.* 148, 316–321. doi: 10.1007/s12011-012-9369-x

Weber, M. J., and Riseberg, L. A. (1971). Optical spectra of vanadium ions in yttrium aluminum garnet. *J. Chem. Phys.* 55, 2032–2038. doi: 10.1063/1.1676370

Zhang, J., and Gao, L. (2004). Synthesis and characterization of nanocrystalline tin oxide by sol-gel method. *J. Solid State Chem.* 177, 1425–1430. doi: 10.1016/j.jssc.2003.11.024

Zhang, J., Zhang, G. X., Cai, G. M., and Jin, Z. P. (2018). Reduction of Ce(IV) to Ce(III) induced by structural characteristics and performance characterization of pyrophosphate MgIn2P4O14-based phosphors. *J. Lumin.* 203, 590–598. doi: 10.1016/j.jlumin.2018.07.015

Zhang, Y., Li, X., Li, K., Lian, H., Shang, M., and Lin, J. (2015). Crystal-site engineering control for the reduction of $Eu^{3+}$ to $Eu^{2+}$ in CaYAlO4: structure refinement and tunable emission properties. *ACS Appl. Mater. Interfaces* 7, 2715–2725. doi: 10.1021/am508859c

# *In situ* Preparation of Chitosan/ZIF-8 Composite Beads for Highly Efficient Removal of U(VI)

Lijuan Liu[1], Weiting Yang[1*], Dongxu Gu[1], Xiaojun Zhao[1] and Qinhe Pan[1,2*]

[1] Key Laboratory of Advanced Materials of Tropical Island Resources, Ministry of Education, School of Science, Hainan University, Haikou, China, [2] Hainan Policy and Industrial Research Institute of Low-Carbon Economy, Hainan University, Haikou, China

With the rapid growth of nuclear power generation and fuel processing, the treatment of nuclear industry wastewater has become a major problem, and if not handled properly, it will pose a potential threat to the ecological environment and human health. Herein, a chitosan (CS)/ZIF-8 composite monolithic beads with ZIF-8 loading up to 60 wt% for U(VI) removal was prepared, which can be easily removed after use. It possesses a very high adsorption capacity of 629 mg•g$^{-1}$ at pH = 3 for U(VI) and a well recyclability is demonstrated for at least four adsorption/desorption cycles. X-ray photoelectron spectroscopy (XPS) was carried out to study the adsorption mechanism between uranium and adsorbent, and the chelation of U(VI) ions with imidazole, hydroxyl, and amino groups was revealed. This work shows that CS/ZIF-8 composite can be used as an effective adsorbent for uranium extraction from aqueous solution, and has a potential application value in wastewater treatment.

Keywords: chitosan, ZIF-8, composite, uranium, adsorption

## INTRODUCTION

Along with the continuous development of industrial modernization, the demand for nuclear energy is rapidly increasing owing to its high energy density and greenhouse gas-free emission. Uranium is a typical core resource in nuclear reaction. It is radioactive and highly toxic, and has a high carcinogenicity (Li et al., 2016). Once discharged into the environment, it will lead to serious pollution to the water body (Fu et al., 2017). While getting inside the human body, it will cause irreversible damage to the internal organs (Zhang M. C. et al., 2018). Therefore, from the perspective of environmental protection and human health, it is particularly important to recover uranium efficiently from aqueous solution. At present, many techniques for uranium recovery from aqueous solution have been developed, such as photocatalytic method (Li Z. J. et al., 2017; Deng et al., 2019), chemical extraction (Sadeghi et al., 2012; Carboni et al., 2013; Wang et al., 2015), chemical flocculation method (Newsome et al., 2015), and adsorption method (Huang et al., 2018). Among these, adsorption method is one of the most extensive technologies because of low cost, simple operation, high efficiency, and good removal effect (Li et al., 2018a; Wang L. et al., 2018). The adsorbents adopted in the uranium adsorption technique include oxides (Yu et al., 2013), sulfides (Manos and Kanatzidis, 2012), hydroxides (Li R. et al., 2017), poly (amid oxime) and its derivatives (Wang D. et al., 2018), carbon nanotubes (Chen et al., 2018), phosphates (Zheng et al., 2015; Cai et al., 2017), porous silica (Huynh et al., 2017), and porous carbon (Starvin and Rao, 2004) etc. However, most of the adsorbents have some disadvantages, like low adsorption capacity, poor

stability, or inability to circulate etc. So developing highly efficient uranium adsorbent materials is still in needed.

Recently, metal-organic frameworks (MOFs), as a class of novel porous material with high surface area (He et al., 2016; Zhao et al., 2018; Li et al., 2019a), adjustable pore size (Zou et al., 2009; Luo et al., 2016; Cheng et al., 2018), and high porosity (Luo et al., 2018; Sun et al., 2018; Li et al., 2019b), have attracted extensive attentions in various fields (Fang et al., 2007; Banerjee et al., 2008). Regarding to uranium separation and recovery, some MOFs and MOF-based composites have been developed (Liu et al., 2018; Yang et al., 2019). For example, Wang et al. demonstrated, for the first time, that the multilayered $V_2CTx$ MXene could be used as a potential and efficient adsorbent for uranium capture from aqueous solution (Wang et al., 2016). Yang et al. reported using a rare earth-based MOF material, MOF-76, for luminescent sensing and adsorption of uranium (Yang et al., 2013). The adsorption was evaluated up to 298 mg•g$^{-1}$ at a relatively low pH of 3.0 ± 0.1. In general, such crystalline materials always lack flexibility and process ability, which limits their application to actual uranium adsorption (Kitao et al., 2017). Combining MOFs and polymers to prepare composite monoliths will provide beneficial and significant improvement while maintaining high adsorption capacity and providing convenient recycling. Wang et al. processed MOFs into nanofiber filters, which can selectively adsorb toxic $SO_2$ gas when exposed in a $SO_2/N_2$ mixture stream (Zhang et al., 2016). Li et al. fabricated a high-quality ZIF-8/PSS membrane, which showed excellent performance in the nanofiltration and separation of dyes from water (Zhang et al., 2014). For uranium separation, Wang et al. prepared the only example of a ZIF-8 based polyacrylonitrile (PAN) fibrous filter, which removed uranyl ions efficiently (Wang C. H. et al., 2018). Thus, more detailed investigations for this target are desirable.

Natural polymers are widely concerned by various industries due to their biocompatibility, biodegradability, non-toxicity, adsorption performance, low cost, etc. (Lee et al., 2011). Chitosan (CS) is an important renewable natural biomass. There are lots of free amino and hydroxyl groups in its structure, which is advantageous to various chemical modifications and hybridization. Owing to such features, chitosan and its composites have been widely used for anti-bacterial coating, drug delivery, wound dressing, and cartilage regeneration (Mohammadzadeh Pakdel and Peighambardoust, 2018). For example, Wang et al. investigated the U(VI) adsorption behavior on cross-linked chitosan (Wang et al., 2009). Zhang et al. developed an impregnation-gelation-hydrothermal technique to prepare hybrid microspheres and hollow fibers consisting of zeolites and chitosan, which could serve as effective absorbents to remove Cu(II) (Zhang Y. Y. et al., 2018). To the best of our knowledge, there is no report on chitosan composites with MOF for uranium adsorption or separation.

Based on the above considerations, in this paper, the *in situ* synthesis of a CS/ZIF-8 composite was developed (**Scheme 1**). Chitosan/zinc ions beads were prepared using a peristaltic pump firstly. When the zinc ions-containing chitosan beads were in contact with the 2-methylimidazole solution, ZIF-8 nanocrystals grew to form the CS/ZIF-8 composite beads, which could recover U(VI) from aqueous solution. The effects of pH, concentration, and adsorption time on its adsorption performances were studied as well as the probable mechanism.

## EXPERIMENT

### Materials
Chitosan (CS) was purchased from Shanghai Aladdin Biochemical Technology Co., Ltd. (Shanghai, China); $UO_2(NO_3)_2 \cdot 6H_2O$ was purchased from Hubei Chu Sheng Wei Chemistry Co., Ltd.; Deionized water was used in all experiments.
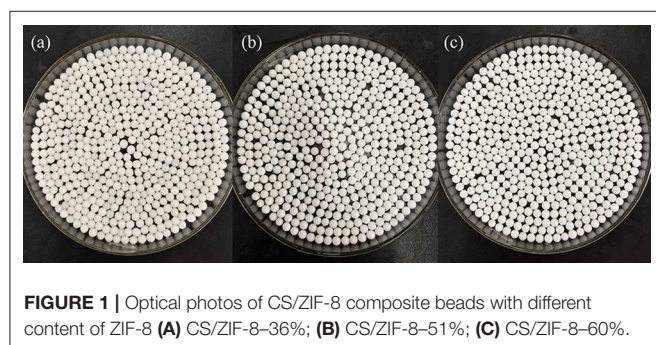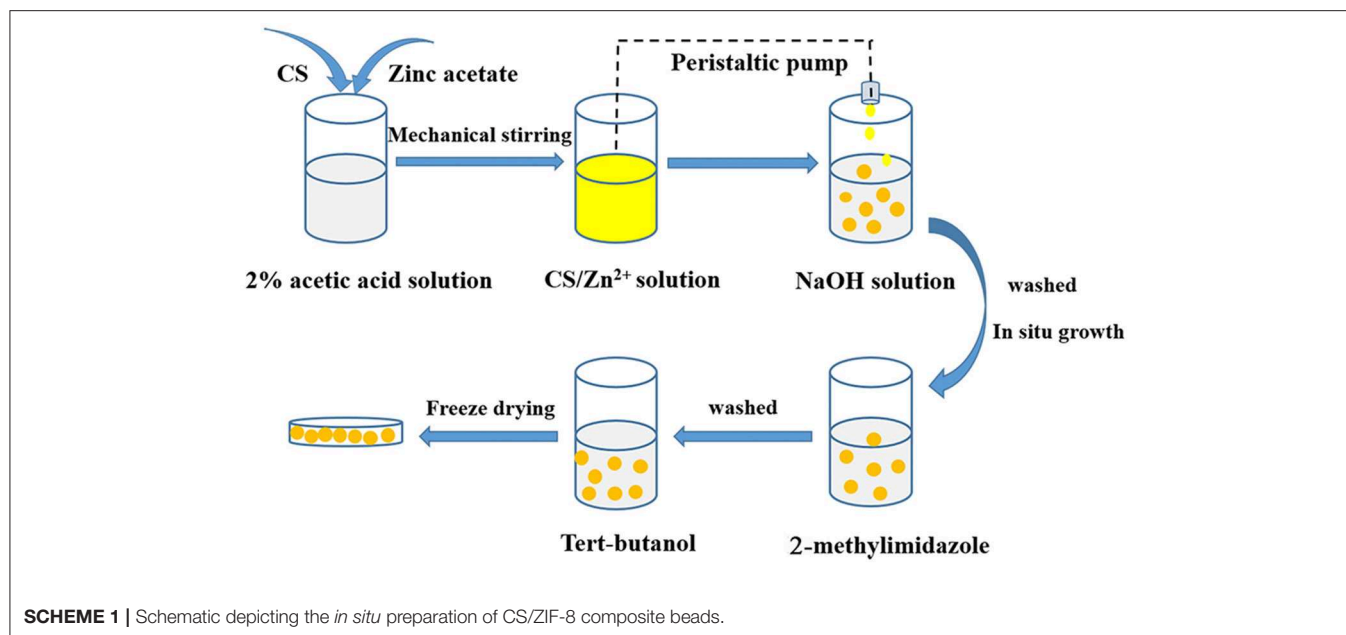
### Preparation of CS/ZIF-8 Composite Beads
The preparation process of CS/ZIF-8 composite beads is shown in **Scheme 1**. 3.0 g chitosan and 1.487 g zinc acetate were dissolved into 0.1 L acetic acid solution (2.0%, v/v) with stirring at 550 rpm for 4 h to form a homogeneous solution. Then, the solution was dripped into 1 M NaOH with a peristaltic pump. After 20 min, the CS/Zn$^{2+}$ microspheres were taken out and washed for 3 times with deionized water to remove away excess NaOH, and then they were soaked in an aqueous solution containing 2.315 g (0.15 mol) 2-methylimidazole. At this time, Zn$^{2+}$ would react with 2-methylimidazole to form ZIF-8 in the microsphere matrix. Next, the obtained CS/ZIF-8 hydrogel composite beads were washed with deionized water for 3 times, soaked in tert-butanol, changed fresh solution every 20 min, subsequently freeze-dried for 12 h to get CS/ZIF-8 composite beads (**Figure 1**). The average dimension of the prepared composite beads is about 2.5 mm in diameter. The ZIF-8 content in the CS/ZIF-8 composites can be adjusted by changing the initial $Zn(CH_3COO)_2$ amounts.

### Characterization
Fourier transform infrared (FT-IR) spectroscopy was conducted by Bruker TENSOR27. The morphology was investigated by a scanning electron microscope (Hitachi S-4800). Powder X-ray diffraction (PXRD) data were obtained by Miniflex-600, with Cu Kα radiation at 40 kV and 15 mA. The thermos gravimetric (TG) curves within 30–800°C were collected on a TA Q600 instrument under air flow. The concentration of U(VI) was determined by the arsenazo III spectrophotometric method, which was measured on a UV spectrophotometer (UV-1801, Beijing Beifen Rayleigh Analytical Instruments (Group) Co., Ltd.). The uranium and the interfering elements concentration were measured by ICP-OES (X Series, Thermo Fisher, USA). The nitrogen adsorption/desorption experiment was conducted at 77 K (ASAP2020M+c, Micromeritics Instrument Corporation, USA). The X-ray photoelectron spectroscopy (XPS) spectra were obtained by using ESCALAB 250Xi (Thermo Fisher, USA) with Al Kα radiation at 1,253.6 eV.

### Batch Adsorption Experiments
In a general procedure, 0.02 g of $UO_2(NO_3)_2 \cdot 6H_2O$ was dissolved in 0.1 L deionized water to obtain a stock solution. The test solutions were prepared by diluting the U(VI) stock solution. The pH was adjusted by 0.1 M NaOH or HCl solution. CS/ZIF-8 composite beads (0.002 g) were added into 0.01 L

**SCHEME 1 |** Schematic depicting the *in situ* preparation of CS/ZIF-8 composite beads.



**FIGURE 1 |** Optical photos of CS/ZIF-8 composite beads with different content of ZIF-8 **(A)** CS/ZIF-8–36%; **(B)** CS/ZIF-8–51%; **(C)** CS/ZIF-8–60%.

solution of U(VI). The mixture was shaken at room temperature for desired reaction time. The concentration of U(VI) was determined by the arsenazo III spectrophotometry. The control experiments were conducted under similar conditions: only ZIF-8 powder or CS replaced the CS/ZIF-8 composites. The U(VI) adsorption capacity ($q_e$) of the samples was calculated according to Equation 1 (Song et al., 2018):

$$q_e = \frac{(C_0 - C_e) \, V}{m} \qquad (1)$$

where $C_0$ refers to the U(VI) initial concentration (mg•L$^{-1}$), $C_e$ is the equilibrium concentration (mg•L$^{-1}$), $V$ (L) refers to the solution volume, and $m$ (g) is the weight of the adsorbent.

After adsorption, the uranium-loaded CS/ZIF-8 adsorbents were used directly for the elution test. The eluate was collected after shaking for 20 min on a shaker using 0.02 L of a solution containing 0.1 M NaHCO$_3$ as an eluent, then the uranium concentration in the eluate was analyzed. Then the CS/ZIF-8 adsorbents were washed with circulating deionized water once

before being used next for uranium adsorption-desorption cycles, which followed the same procedure as described above.

# RESULTS AND DISCUSSION

## Characterization of the CS/ZIF-8 Composite Beads

The prepared composite beads are uniform with average size of 2.5 mm in diameter, which are very stable and easy to store. Scanning electron microscopy (SEM) images show the surface features and interfacial interactions of pure CS and CS/ZIF-8 composites. As shown in **Figure 2A**, the surface of pure CS material exhibits a smooth and evenly porous pattern. After composition with ZIF-8, the surface becomes rough due to the attachment of many ZIF-8 nanoparticles (**Figure 2B**), whose dodecahedral morphologies are clearly visible. As the content of Zn$^{2+}$ increases in the initial reaction mixture, more ZIF-8 nanoparticles grow on the surface and internal of chitosan, and the size is getting smaller (**Figures 2C,D**).

The PXRD patterns further confirm the successful growth of ZIF-8 within the CS beads (**Figure 3A**). Due to the small content of ZIF-8 in the early stage, the peak of ZIF-8 is relatively weak. With the content of ZIF-8 increasing, the peak intensity gradually enhanced. In order to determine the stability of the CS/ZIF-8 composites under acidic or alkaline conditions, the composite beads were soaked in the solution with different pH (3 to 13). Three days later, the PXRD patterns of the composite beads were measured and no change was found, revealing the good stability at the pH condition (**Figure S1**).

In order to know the content of ZIF-8 in the composite beads, ICP analysis was performed, giving the ZIF-8 content of 36, 51, and 60 wt% corresponding to zinc acetate initial amount of 1.487, 2.975, and 4.462 g, respectively. For convenience, the samples

with these different ZIF-8 loading are denoted as CS/ZIF-8–36%, CS/ZIF-8–51%, CS/ZIF-8–60%. As shown in **Figure 3B**, the thermal degradation of chitosan occurs in three steps: before 100°C, there is a small weight loss process about 10%, which is caused by the bound water and crystal water contained
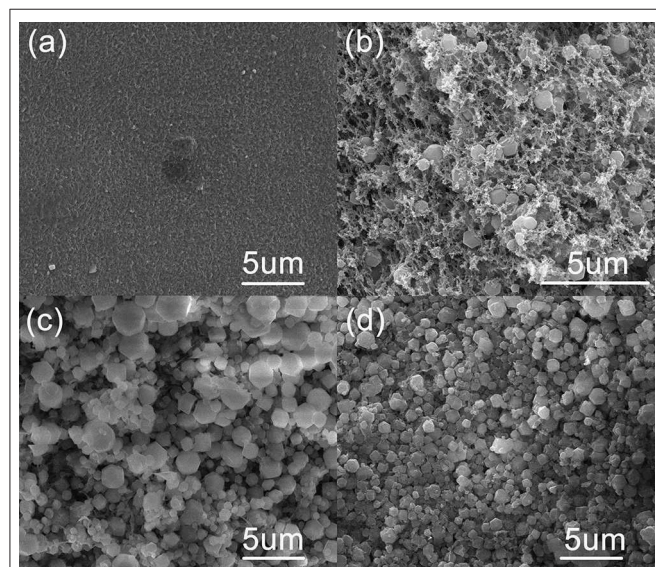


**FIGURE 2 |** SEM images of CS/ZIF-8 composite beads with different content of ZIF-8. **(A)** pure CS; **(B)** CS/ZIF-8–36%; **(C)** CS/ZIF-8–51%; **(D)** CS/ZIF-8–60%.

in the material. This process is an endothermic reaction. At 220–300°C, chitosan is strongly degraded, with a weight loss of about 50%. At 300–600°C, the degradation is slow, the weight loss is about 40%. Both steps of thermal degradation are exothermic reactions and the thermal degradation ends at 600°C. ZIF-8 has a residual of 33% at 600°C, which is consistent with the theoretical value (35%). With the increase of ZIF-8 content, the thermal decomposition temperature gradually rises, indicating the existence of some interaction between CS and ZIF-8 (**Figure S2**). Together with the TG analyses of CS/ZIF-8 composites, we can also verify the loading of ZIF-8 in CS/ZIF-8 composite beads, that is in agreement with ICP results.

FT-IR spectroscopy is shown in **Figure 3C**. For CS, -OH groups vibrate at a wide band of $3,433 \, cm^{-1}$, overlapping with -NH stretching vibration. The characteristic peak at $1,660 \, cm^{-1}$ corresponds to the vibrations of the $-NH_2$ group. Specifically, the absorption peak at $2,929 \, cm^{-1}$ is ascribed to the C-H bond stretching vibration from the methyl imidazole ring of ZIF-8. The absorption peak at $1,584 \, cm^{-1}$ belongs to the $C = N$ vibrations, while peaks at 1,146 and $990 \, cm^{-1}$ are from C-N stretching vibration. In addition, from these spectra, we can see that with the increasing of ZIF-8 content, the characteristic absorption peaks of ZIF-8 in composites are enhanced.

The specific surface areas of the CS/ZIF-8 composites were determined by nitrogen adsorption. The $N_2$ absorption/desorption isotherms show that all materials exhibit a typical I-type isotherm with micropore character (**Figure 3D**). With the increase of ZIF-8 content, the specific surface area also increases sequentially, which is 184.93, 279.24,
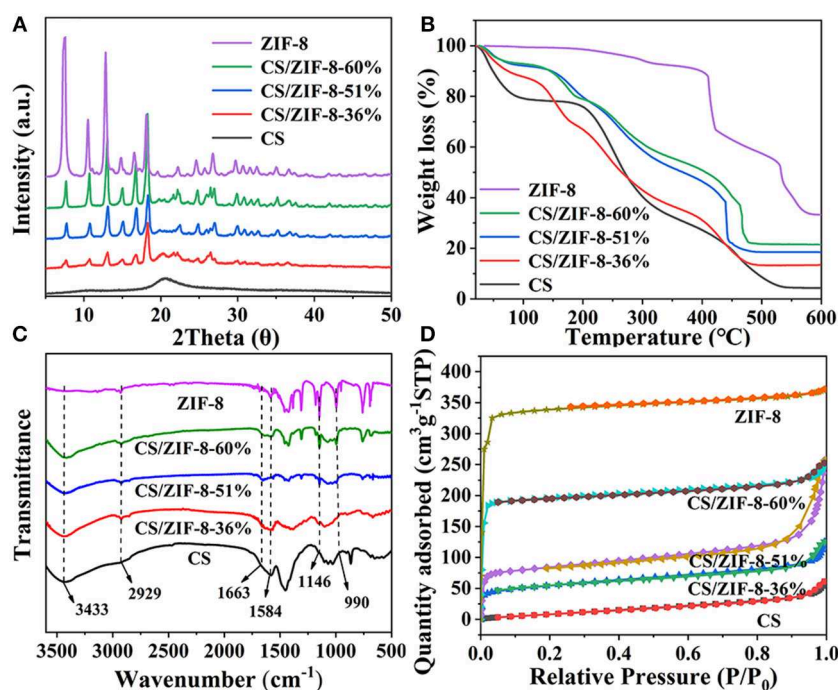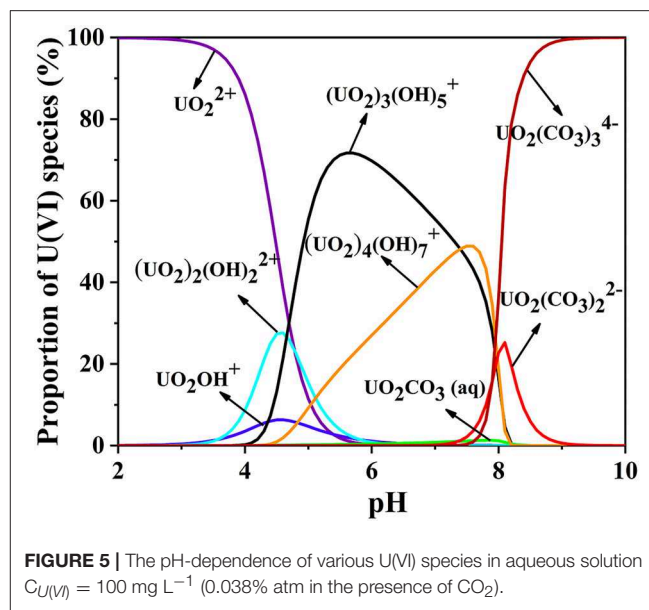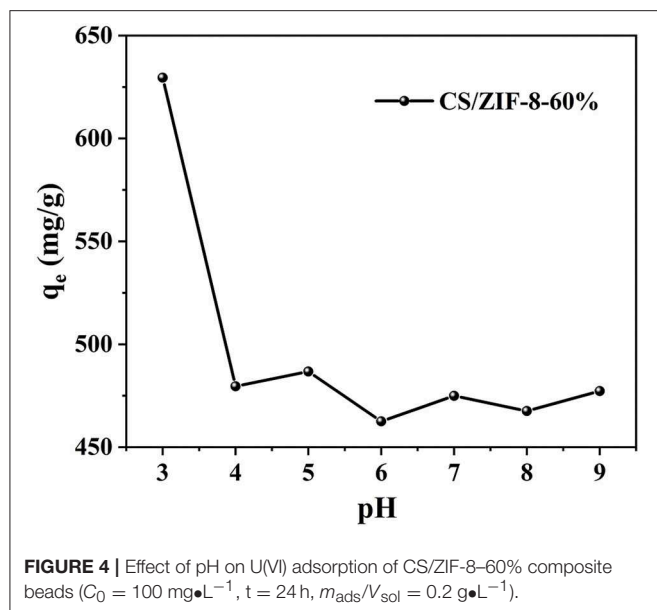


**FIGURE 3 | (A)** PXRD patterns, **(B)** TG curves, **(C)** FT-IR spectra, **(D)** Nitrogen adsorption/desorption isotherms of CS, ZIF-8, CS/ZIF-8–36%, CS/ZIF-8–51%, CS/ZIF-8–60%.

**FIGURE 4 |** Effect of pH on U(VI) adsorption of CS/ZIF-8–60% composite beads ($C_0$ = 100 mg•L$^{-1}$, t = 24 h, $m_{ads}/V_{sol}$ = 0.2 g•L$^{-1}$).



**FIGURE 5 |** The pH-dependence of various U(VI) species in aqueous solution $C_{U(VI)}$ = 100 mg L$^{-1}$ (0.038% atm in the presence of $CO_2$).

and 628.80 m$^2$•g$^{-1}$, respectively, for three different ZIF-8 loading composites. The specific surface area of pure ZIF-8 is 1080.91 m$^2$•g$^{-1}$, while only 40.07 m$^2$•g$^{-1}$ for pure CS beads. This provides possibility of the CS/ZIF-8 composite beads for efficient adsorption of U(VI).

# Evaluation of U(VI) Adsorption Performance

## Effect of Initial pH

pH is an important parameter in uranium batch adsorption experiments (Zhang et al., 2017), due to its dramatic influence on the charge and active site of the sorbent and the speciation of U(VI) in solution (Min et al., 2017). Chitosan dissolves under acidic condition of pH = 2. Therefore, a series of experiments have been performed on the CS/ZIF-8 composite beads under pH values ranging from 3 to 9. As shown in **Figure 4**, the maximum adsorption capacity of U(VI) is obtained as 629 mg•g$^{-1}$ at pH = 3.0, and then gradually decreases as the pH increases. This is a similar trend to the work reported previously where Fe$_3$O$_4$@ZIF-8 (Min et al., 2017) and ZIF-8/PAN (Wang C. H. et al., 2018) were investigated for the adsorption of uranium. As shown in **Figure 5**, at pH of 3, U(VI) mainly exits in the form of UO$_2^{2+}$ cation, as the pH increases, it will be hydrolyzed to oligomeric or colloidal species, such as (UO$_2$)$_3$(OH)$_5^+$, (UO$_2$)$_4$(OH)$_7^+$, (UO$_2$)$_2$(OH)$_2^{2+}$, and UO$_2$(OH)$^+$ etc. (Chen et al., 2018). Due to the increased dimensions of these species, a decrease of adsorption efficiency is resulted with pH increasing (Wang C. H. et al., 2018). In addition, the decreased uptake trends at pH > 6.5 may also arise from the electronic repulsion between the negative charged U(VI) species including UO$_2$(CO$_3$)$_2^{2-}$ and UO$_2$(CO$_3$)$_3^{4-}$ and the adsorbent surfaces (Cai et al., 2017). So pH of 3 is the optimal adsorption value, and following adsorption investigations were performed at this condition.

## Adsorption Kinetics of the CS/ZIF-8 Composite Beads

The adsorption kinetics of CS, ZIF-8 and CS/ZIF-8 composite were studied with different contact time. As shown in **Figure 6A**, several curves have similar trends where a fast adsorption of uranium is observed at the initial 60 min, and followed by a slower adsorption period until an equilibrium of uranium adsorption is reached. It could be explained from this: U(VI) ions first diffuse into the porous CS/ZIF-8 composite beads and they are adsorbed by interior active sites with a slow process until most surface active sites are occupied (Wang C. H. et al., 2018); To further investigate the mechanism of adsorption process, the U(VI) adsorption behavior are fitted using kinetic models as shown in Equation (2) and (3) (Yang et al., 2013):

Pseudo - first - order:

$$\ln\left(q_e - q_t\right) = \ln q_e - k_1 t \tag{2}$$

Pseudo - second - order:

$$\frac{t}{q_t} = \frac{1}{k_2 q_e{}^2} + \frac{t}{q_e} \tag{3}$$

where $q_e$ and $q_t$ (mg•g$^{-1}$) refer to the U(VI) maximum adsorption capacity and the adsorption capacity at $t$ (min), respectively, $t$ is contact time (min), and $k$ (g•mmol$^{-1}$•min$^{-1}$) is the kinetic constant. The fitting results (**Figure 6A**) show that the degrees of linearity of fitted curves of pseudo-second-order model are more suitable than those of pseudo-first-order model, and the values of correlation coefficient ($R^2$) of U(VI) fitted by pseudo-second-order model are higher than those of pseudo-first-order model (**Table S1**), indicating that the adsorption process is mainly chemical adsorption. The calculated $q_e$ is close to the experimental value. With the increase of ZIF-8 content, the adsorption amount gradually increases, the adsorption amount
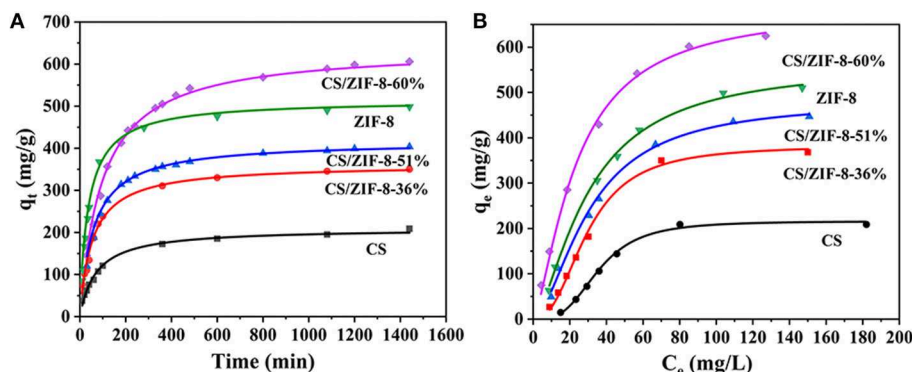
**FIGURE 6 |** Kinetic and isothermal studies of U(VI) adsorption process, fitted with second-order kinetics **(A)** and Langmuir models **(B)** respectively ($C_0 = 100$ mg•L$^{-1}$, pH = 3, t = 24 h, $m_{ads}/V_{sol}$ = 0.2 g•L$^{-1}$).

**TABLE 1 |** Comparison of the maximum adsorption capacity of CS/ZIF-8–60% with other MOF-based adsorbents.

| Absorbents | pH | $q_m$(mg/g) | Refs |
|---|---|---|---|
| GO-COOH/UiO-66 | 8.0 | 1002 | Yang et al., 2017 |
| CS/ZIF-8–60% | 3.0 | 629 | This work |
| GO/ZIF-67-Ag | 7.0 | 602.41 | Guo et al., 2019 |
| PPy@ZIF-8 | 3.5 | 534 | Li et al., 2018b |
| ZIF-8/PAN | 3.0 | 530.3 | Wang C. H. et al., 2018 |
| Fe$_3$O$_4$@ZIF-8 | 3.0 | 523.5 | Min et al., 2017 |



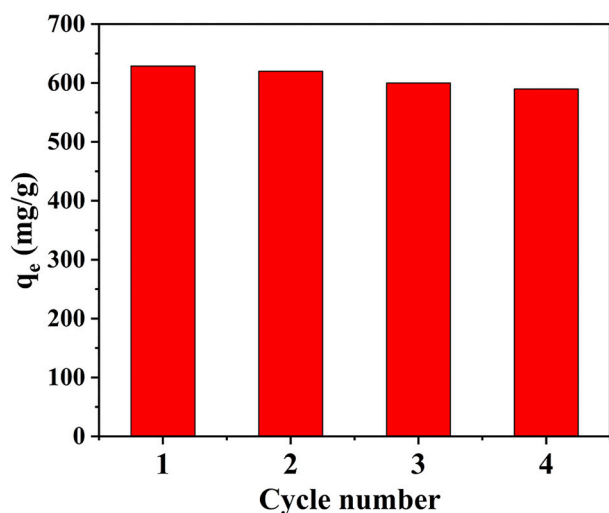**FIGURE 7 |** Elution cycle experiment of CS/ZIF-8–60% for U(VI) adsorption.

of CS/ZIF-8–60% reaches to 608 mg•g$^{-1}$, which is superior evidently to the ZIF-8 powder (498 mg•g$^{-1}$) and CS (208 mg•g$^{-1}$). This better adsorption performance of the CS/ZIF-8–60% composite for U(VI) may be ascribed to its pore structures (Wang C. H. et al., 2018).

## Adsorption Isotherms of the CS/ZIF-8 Composite Beads

In order to investigate the maximum adsorption capacity of the CS/ZIF-8 composites to uranium, the adsorption isotherm experiments with various initial concentrations of uranium (20–200 mg•L$^{-1}$) were carried out at room temperature. As shown in **Figure 6B**, the Langmuir and Freundlich models are used to quantitatively analyze the adsorption isotherms. The equations are as follows (Aguila et al., 2017):

Langmuir models

$$\frac{1}{q_e} = \frac{1}{q_m} + \frac{1}{q_m K_L C_e} \tag{4}$$

Freundlich models

$$\log q_e = \frac{\log C_e}{n} + \log K_F \tag{5}$$

where $q_m$ (mg•g$^{-1}$) refers to the maximum adsorption capacity, $q_e$ is the amount of adsorbed uranium at equilibrium (mg•g$^{-1}$), $C_e$ is the equilibrium concentration (mg•L$^{-1}$), $K_L$ (mL•g$^{-1}$) is involved in the affinity of the adsorbate with the adsorbent, $K_F$ refers to the Freundlich constant, and $n$ is the Freundlich exponent. The results suggest that equilibrium isotherm experimental data is well-described by the Langmuir model with higher correlation coefficient ($R^2$; **Table S2**), demonstrating that this adsorption process is a monolayer chemical adsorption. The theoretical maximum adsorption capacity of 625 mg•g$^{-1}$ for CS/ZIF-8–60% is consistent with experimental value 629 mg•g$^{-1}$. Compared with other reported MOF-based composite materials, the CS/ZIF-8–60% exhibits a very high adsorption capacity in uranium extraction (**Table 1**).

## The Recyclability of the CS/ZIF-8 Composite Beads

Reusability is a very important index for an adsorbent. A solution of NaHCO$_3$ (0.1 M) was used as an eluent to evaluate the reusability of CS/ZIF-8 adsorbents. As shown in **Figure 7**, the CS/ZIF-8–60% can maintain a high adsorption performance after four adsorption/desorption cycles, specifying a good durability
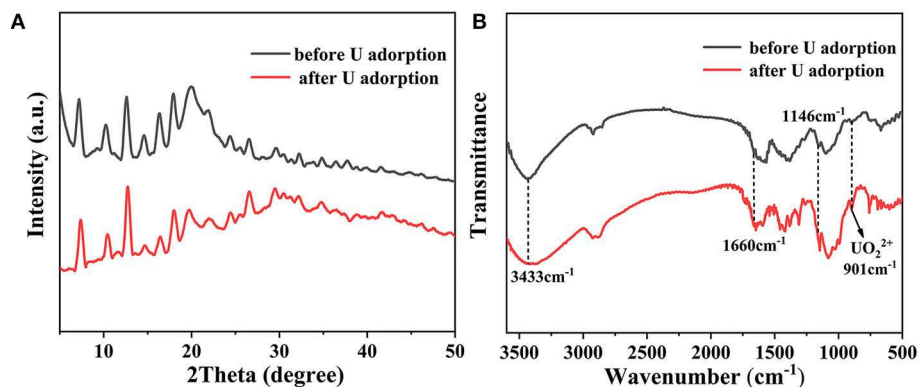
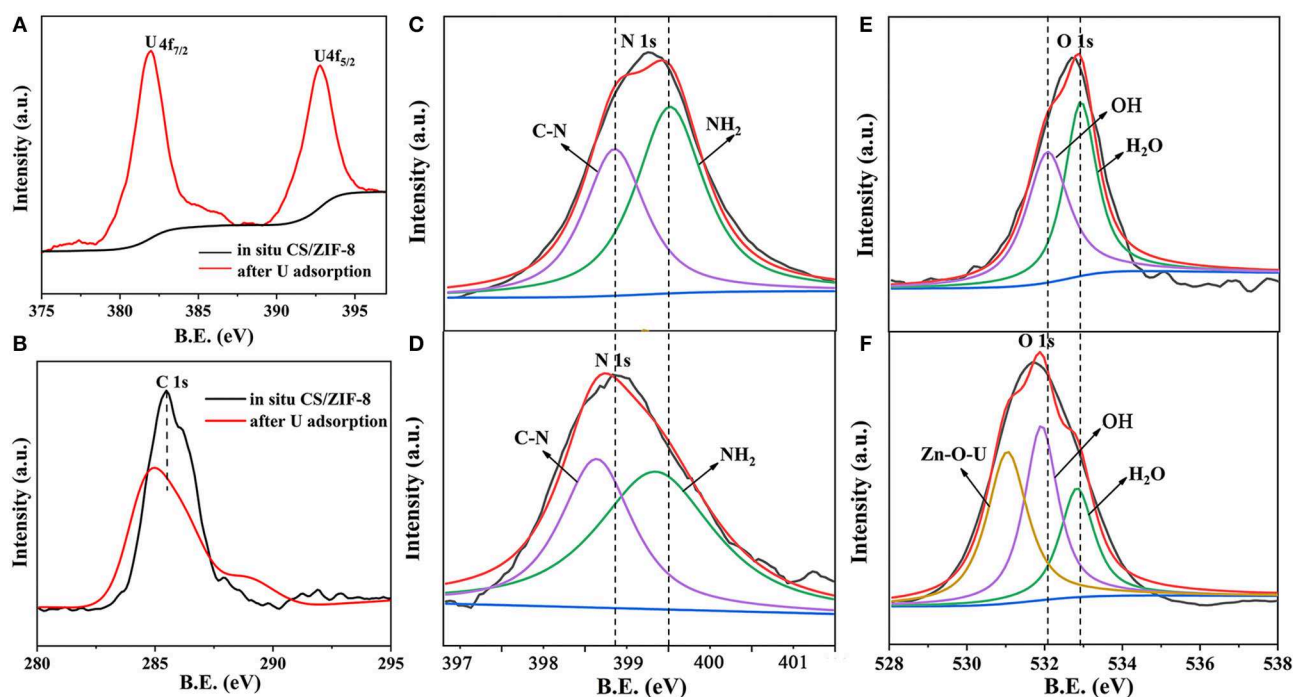**FIGURE 8 | (A)** PXRD patterns and **(B)** FT-IR spectra of CS/ZIF-8–60% before and after U(VI) uptake.



**FIGURE 9 |** XPS survey scans of CS/ZIF-8–60% before and after U(VI) uptake; high-resolution XPS spectra of U 4f **(A)**, C 1s **(B)**, N 1s **(C,D)**, O 1s **(E,F)** before and after U(VI) uptake.

and recyclability, which is critical for the reduction of cost in practical uranium recovery applications. The slight decrease of the adsorption capacity could be caused by the inevitable mass loss of adsorbent during regeneration process. In addition, the structure of CS and ZIF-8 remained intact after the cycle experiment for uranium adsorption (**Figure S3**). Hence, the CS/ZIF-8 composite possess an excellent reusability and can serve as an economical and efficient adsorbent for the removal of U(VI) from aqueous solution.

## Potential Adsorption Mechanism

Additional characterization approaches were adopted to identify the underlying removal mechanism of U(VI). As shown in

**Figure 8A**, the PXRD patterns before and after adsorption of uranium are consistent, indicating that no phase change occurs after adsorption. FT-IR studies show a characteristic absorption peak of uranyl appears at 901 $cm^{-1}$ after uranium adsorption (**Figure 8B**). Moreover, both the vibrations of C-N at 1,146 $cm^{-1}$ and $NH_2$ at 1,660 $cm^{-1}$ exhibit obvious red shifts after U(VI) uptake. Especially at 3,340 $cm^{-1}$, the apparent broad peak is attributed to the stretching vibration of the hydroxyl group and the amino group, which suggests that there are a large amount of Zn-OH and N-H bonds through the water decomposition on the composite material surface. They are involved in the interaction with U(VI), proving the chelation of U(VI) ions with imidazole and chitosan (Cai et al., 2017).

In order to better understand the adsorption mechanism of U(VI), XPS analysis was further carried out. The broad scan XPS spectrum of CS/ZIF-8–60% composite exhibits peaks of O 1s, C 1s, N 1s, and Zn 2p at 532.08, 281.08, 401.08, and 1022.08 eV, respectively (**Figure S4**). In addition, two distinct peaks of U 4f appear at 383.08 and 392.08 eV after U(VI) ingestion (**Figure 9A**). To verify the interaction between U(VI) and CS/ZIF-8 composite, narrow scans of C 1s, N 1s, and O 1s peaks are recorded and analyzed (**Figures 9B–D**). The spectral fitting shows that the energy peaks of C 1s and N 1s all exhibit a significant red shift after U(VI) adsorption, indicating the chelation of U(VI) with nitrogen from chitosan and imidazole (Wang C. H. et al., 2018). **Figures 9E,F** indicate an obviously difference of oxygen spectra. A new peak occurs with a binding energy of 530.75 eV representing Zn-O-U after uranium adsorption (Su et al., 2018). In addition, O-H has a weak red shift. These prove that hydroxyl groups on chitosan and Zn-OH moiety in ZIF-8 complex with uranyl (Su et al., 2018). The analysis of XPS is consistent with the above infrared experiment result.

## CONCLUSION

In summary, CS/ZIF-8 composite beads with different ZIF-8 loadings were synthesized by *in situ* growth for uranium removal. The maximum uranium adsorption capacity of CS/ZIF-8–60% is higher than most reported MOF-based composite adsorbents. In addition, the micron scale spherical adsorbent exhibits outstanding recyclability and is easy to recover. Based on the results of desorption experiments and spectroscopic analysis, the highly efficient removal mechanism of U(VI) is predominantly controlled by the -OH, -NH₂, and C-N groups

chelating with U(VI) ions. The results show that CS/ZIF-8 composite is a promising absorbent for uranium recovery from aqueous solution. The findings in this work will pave the way for the development of practical adsorbents for irradiative wastewater treatment.

## DATA AVAILABILITY

All datasets Synthesis procedure, uranium adsorption experiments and/or data processing, PXRD, SEM, TG, IR, ICP and XPS investigations for this study are included in the manuscript and/or the **Supplementary Files**.

## AUTHOR CONTRIBUTIONS

WY and QP supervised the project. LL performed the experiments. DG participated the data analysis. XZ helped to analyze the results. LL wrote the manuscript with support from WY. All authors contributed to the general discussion.

## FUNDING

## SUPPLEMENTARY MATERIAL

The Supplementary Material for this article can be found online at: https://www.frontiersin.org/articles/10.3389/fchem.2019.00607/full#supplementary-material

## REFERENCES

Aguila, B., Sun, Q., Perman, J. A., Earl, L. D., Abney, C. W., Elzein, R., et al. (2017). Efficient mercury capture using functionalized porous organic polymer. *Adv. Mater.* 29:1700665. doi: 10.1002/adma.201700665

Banerjee, R., Phan, A., Wang, B., Knobler, C., Furukawa, H., O'Keeffe, M., et al. (2008). High-throughput synthesis of zeolitic imidazolate frameworks and application to CO₂ capture. *Science* 319, 939–943. doi: 10.1126/science.1152516

Cai, Y. W., Wu, C. F., Liu, Z. Y., Zhang, L. J., Chen, L. H., Wang, J. Q., et al. (2017). Fabrication of a phosphorylated graphene oxide–chitosan composite for highly effective and selective capture of U(VI). *Environ. Sci. Nano* 4, 1876–1886. doi: 10.1039/c7en00412e

Carboni, M., Abney, C. W., Liu, S. B., and Lin, W. B. (2013). Highly porous and stable metal–organic frameworks for uranium extraction. *Chem. Sci.* 4, 2396–2402. doi: 10.1039/c3sc50230a

Chen, H. J., Zhang, Z. B., Wang, X. X., Chen, J., Xu, C., Liu, Y. H., et al. (2018). Fabrication of magnetic Fe/Zn layered double oxide@Carbon nanotube composites and their application for U(VI) and ²⁴¹Am(III) removal. *ACS Appl. Nano Mater.* 1, 2386–2396. doi: 10.1021/acsanm.8b00528

Cheng, Y. J., Wang, R., Wang, S., Xi, X. J., Ma, L. F., and Zang, S. Q. (2018). Encapsulating [Mo₃S₁₃]⁽²⁻⁾ clusters in cationic covalent organic frameworks: enhancing stability and recyclability by converting a homogeneous photocatalyst to a heterogeneous photocatalyst. *Chem. Commun.* 54, 13563–13566. doi: 10.1039/c8cc07784c

Deng, H., Li, Z. J., Wang, L., Yuan, L. Y., Lan, J. H., Chang, Z. Y., et al. (2019). Nanolayered Ti₃C₂ and SrTiO₃ composites for photocatalytic reduction and removal of uranium(VI). *ACS Appl. Nano Mater.* 2, 2283–2294. doi: 10.1021/acsanm.9b00205

Fang, Q. R., Zhu, G. S., Jin, Z., Xue, M., Wei, X., Wang, D. J., et al. (2007). A novel metal-organic framework with the diamondoid topology constructed from pentanuclear zinc-carboxylate clusters. *Cryst. Growth Des.* 7, 1035–1037. doi: 10.1021/cg060829a

Fu, Q. S., Wen, L., Zhang, L., Chen, X. D., Pun, D., Ahmed, A., et al. (2017). Preparation of ice-templated MOF-polymer composite monoliths and their application for wastewater treatment with high capacity and easy recycling. *ACS Appl. Mater. Interfaces* 9, 33979–33988. doi: 10.1021/acsami.7b10872

Guo, X. J., Chen, R. R., Liu, Q., Liu, J. Y., Zhang, H. S., Yu, J., et al. (2019). Graphene oxide and silver ions coassisted zeolitic imidazolate framework for antifouling and uranium enrichment from seawater. *ACS Sustain. Chem. Eng.* 7, 6185–6195. doi: 10.1021/acssuschemeng.8b06391

He, H. M., Han, H. B., Shi, H., Tian, Y. Y., Sun, F. X., Song, Y., et al. (2016). Construction of thermophilic lipase-embedded metal-organic frameworks via biomimetic mineralization: a biocatalyst for ester hydrolysis and kinetic resolution. *ACS Appl. Mater. Interfaces* 8, 24517–24524. doi: 10.1021/acsami.6b05538

Huang, Z. W., Li, Z. J., Wu, Q. Y., Zheng, L. R., Zhou, L. M., Chai, Z. F., et al. (2018). Simultaneous elimination of cationic uranium(VI) and anionic rhenium(VII) by graphene oxide–poly(ethyleneimine) macrostructures: a

batch, XPS, EXAFS, and DFT combined study. *Environ. Sci. Nano* 5, 2077–2087. doi: 10.1039/c8en00677f

Huynh, J., Palacio, R., Safizadeh, F., Lefevre, G., Descostes, M., Eloy, L., et al. (2017). Adsorption of uranium over $NH_2$-functionalized ordered silica in aqueous solutions. *ACS Appl. Mater. Interfaces* 9, 15672–15684. doi: 10.1021/acsami.6b16158

Kitao, T., Zhang, Y. Y., Kitagawa, S., Wang, B., and Uemura, T. (2017). Hybridization of MOFs and polymers. *Chem. Soc. Rev.* 46, 3108–3133. doi: 10.1039/c7cs00041c

Lee, K. P., Arnot, T. C., and Mattia, D. (2011). A review of reverse osmosis membrane materials for desalination—Development to date and future potential. *J. Membr. Sci.* 370, 1–22. doi: 10.1016/j.memsci.2010.12.036

Li, J., Wang, X. X., Zhao, G. X., Chen, C. L., Chai, Z. F., Alsaedi, A., et al. (2018a). Metal-organic framework-based materials: superior adsorbents for the capture of toxic and radioactive metal ions. *Chem. Soc. Rev.* 47, 2322–2356. doi: 10.1039/c7cs00543a

Li, J., Wu, Z., Duan, Q. Y., Alsaedi, A., Hayat, T., and Chen, C. L. (2018b). Decoration of ZIF-8 on polypyrrole nanotubes for highly efficient and selective capture of U(VI). *J. Clean. Prod.* 204, 896–905. doi: 10.1016/j.jclepro.2018.09.050

Li, L. N., Ma, W., Shen, S. S., Huang, H. X., Bai, Y., and Liu, H. W. (2016). A combined experimental and theoretical study on the extraction of uranium by amino-derived metal-organic frameworks through post-synthetic strategy. *ACS Appl. Mater. Interfaces* 8, 31032–31041. doi: 10.1021/acsami.6b11332

Li, M. L., Ren, G. J., W, F. X., Li, Z. M., Yang, W. T., Gu, D. X., et al. (2019a). Two metal-organic zeolites for highly sensitive and selectivesensing of $Tb^{3+}$. *Inorg. Chem.* 6, 1129–1134. doi: 10.1039/C8QI01406J

Li, M. L., Yang, W. T., Qiu, P. F., Ren, G. J., Li, C. Y., Chen, Z. Y., et al. (2019b). Two efficient pH sensors based on heteronuclear metal-organic frameworks. *J. Lumin.* 205, 380–384. doi: 10.1016/j.jlumin.2018.09.056

Li, R., Che, R., Liu, Q., Su, S. Z., Li, Z. H., Zhang, H. S., et al. (2017). Hierarchically structured layered-double-hydroxides derived by ZIF-67 for uranium recovery from simulated seawater. *J. Hazard. Mater.* 338, 167–176. doi: 10.1016/j.jhazmat.2017.04.075

Li, Z. J., Huang, Z. W., Guo, W. L., Wang, L., Zheng, L. R., Chai, Z. F., et al. (2017). Enhanced photocatalytic removal of uranium(VI) from aqueous solution by magnetic $TiO_2/Fe_3O_4$ and its graphene composite. *Environ. Sci. Technol.* 51, 5666–5674. doi: 10.1021/acs.est.6b05313

Liu, R., Wang, Z. Q., Liu, Q. Y., Luo, F., and Wang, Y. L. (2018). A zinc-MOF with carboxylate oxygen-functionalized pore channels for U(VI) sorption. *Eur. J. Inorg. Chem.* 2019, 735–739. doi: 10.1002/ejic.201801295

Luo, F., Li, J. Q., Xiong, Y. Y., Yan, C. S., Gao, H. Y., Zhou, J. P., et al. (2016). MOF catalysis of FeII-to-FeIII reaction for an ultrafast and one-step generation of the $Fe_2O_3$@MOF composite and uranium(VI) reduction by iron(II) under ambient conditions. *Chem. Commun.* 52, 9538–9541. doi: 10.1039/C6CC04597A

Luo, F., Tao, Y., Wu, H. Q., Li, J. Q., Yang, L. X., Yin, W. H., et al. (2018). Applying $MOF^+$ technique to *in-situ* prepare hybrid material for hydrogenation reaction. *Dalton Trans.* 47, 14889–14892. doi: 10.1039/C8DT03416H

Manos, M. J., and Kanatzidis, M. G. (2012). Layered metal sulfides capture uranium from seawater. *J. Am. Chem. Soc.* 134, 16441–16446. doi: 10.1021/ja308028n

Min, X., Yang, W. Gao, C. Y., Dang, S., Hui, Y-F., and Sun, Z. M. (2017). $Fe_3O_4$@ZIF-8: a magnetic nanocomposite for highly efficient $UO_2^{2+}$ adsorption and selective $UO_2^{2+}/Ln^{3+}$ separation. *Chem. Commun.* 53, 4199–4202. doi: 10.1039/C6CC10274C

Mohammadzadeh Pakdel, P., and Peighambardoust, S. J. (2018). Review on recent progress in chitosan-based hydrogels for wastewater treatment application. *Carbohydr. Polym.* 201, 264–279. doi: 10.1016/j.carbpol.2018.08.070

Newsome, L., Morris, K., Trivedi, D., Bewsher, A., and Lloyd, J. R. (2015). Biostimulation by glycerol phosphate to precipitate recalcitrant uranium(IV) phosphate. *Environ. Sci. Technol.* 49, 11070–11078. doi: 10.1021/acs.est.5b02042

Sadeghi, S., Azhdari, H., Arabi, H., and Moghaddam, A. Z. (2012). Surface modified magnetic $Fe_3O_4$ nanoparticles as a selective sorbent for solid phase extraction of uranyl ions from water samples. *J. Hazard. Mater.* 215–216, 208–216. doi: 10.1016/j.jhazmat.2012.02.054

Song, Y., Wei, G. Y., Kopeć, M., Rao, L. F., Zhang, Z. C., Gottlieb, E., et al. (2018). Copolymer-templated synthesis of nitrogen-doped mesoporous carbons for enhanced adsorption of hexavalent chromium and uranium. *ACS Appl. Nano Mater.* 1, 2536–2543. doi: 10.1021/acsanm.8b00103

Starvin, A. M., and Rao, T. P. (2004). Solid phase extractive preconcentration of uranium(VI) onto diarylazobisphenol modified activated carbon. *Talanta* 63, 225–232. doi: 10.1016/j.talanta.2003.11.001

Su, S. Z., Che, R., Liu, Q., Liu, J. Y., Zhang, H. S., Li, R. M., et al. (2018). Zeolitic Imidazolate Framework-67: a promising candidate for recovery of uranium (VI) from seawater. *Colloid Surf. A* 547, 73–80. doi: 10.1016/j.colsurfa.2018.03.042

Sun, Q., Aguila, B., Earl, L. D., Abney, C. W., Wojtas, L., Thallapally, P. K., et al. (2018). Covalent organic frameworks as a decorating platform for utilization and affinity enhancement of chelating sites for radionuclide sequestration. *Adv. Mater.* 30:e1705479. doi: 10.1002/adma.201705479

Wang, C. H., Zheng, T., Luo, R., Liu, C., Zhang, M., Li, J. S., et al. (2018). *In situ* growth of ZIF-8 on PAN fibrous filters for highly efficient U(VI) removal. *ACS Appl. Mater. Interfaces* 10, 24164–24171. doi: 10.1021/acsami.8b07826

Wang, D., Song, J. N., Wen, J., Yuan, Y. H., Liu, Z. L., Lin, S., et al. (2018). Significantly enhanced uranium extraction from seawater with mass produced fully amidoximated nanofiber adsorbent. *Adv. Energy Mater.* 33:1802607. doi: 10.1002/aenm.201802607

Wang, G. H., Liu, J. S., Wang, X. G., Xie, Z. Y., and Deng, N. S. (2009). Adsorption of uranium (VI) from aqueous solution onto cross-linked chitosan. *J. Hazard. Mater.* 168, 1053–1058. doi: 10.1016/j.jhazmat.2009.02.157

Wang, L., Song, H., Yuan, L. Y., Li, Z. J., Zhang, Y. J., Gibson, J. K., et al. (2018). Efficient U(VI) reduction and sequestration by $Ti_2CTx$ MXene. *Environ. Sci. Technol.* 52, 10748–10756. doi: 10.1021/acs.est.8b03711

Wang, L., Yuan, L. Y., Chen, K., Zhang, Y. J., Deng, Q. H., Du, S. Y.,et al. (2016). Loading actinides in multilayered structures for nuclear waste treatment: the first case study of uranium capture with vanadium carbide MXene. *ACS Appl. Mater. Interfaces* 8, 16396–16403. doi: 10.1021/acsami.6b02989

Wang, L. L., Luo, F., Dang, L. L., Li, J. Q., Wu, X. L., Liu, S. J., et al. (2015). Ultrafast high-performance extraction of uranium from seawater without pretreatment using an acylamide- and carboxyl-functionalized metal–organic framework. *J. Mater. Chem. A* 3, 13724–13730. doi: 10.1039/c5ta01972a

Yang, P. P., Liu, Q., Liu, J. Y., Zhang, H. S., Li, Z. S., Li, R. M., et al. (2017). Interfacial growth of a metal–organic framework (UiO-66) on functionalized graphene oxide (GO) as a suitable seawater adsorbent for extraction of uranium(VI). *J. Mater. Chem. A* 5, 17933–17942. doi: 10.1039/c6ta10022h

Yang, W., Bai, Z. Q., Shi, W. Q., Yuan, L. Y., Tian, T., Chai, Z. F., et al. (2013). MOF-76: from a luminescent probe to highly efficient U(VI) sorption material. *Chem. Commun.* 49, 10415–10417. doi: 10.1039/c3cc44983a

Yang, W., Pan, Q., Song, S., and Zhang, H. (2019). Metal–organic framework-based materials for the recovery of uranium from aqueous solution. *Inorg. Chem. Front.* 6, 1924–1937. doi: 10.1039/C9QI00386J

Yu, J., Bai, H. B., Wang, J., Li, Z. S., Jiao, C. S., Liu, Q., et al. (2013). Synthesis of aluminananosheetsvia supercritical fluid technology with high uranyl adsorptive capacity. *New J. Chem.* 37, 366–372. doi: 10.1039/c2nj40514h

Zhang, M. C., Li, Y., Bai, C. Y., Guo, X. H., Han, J., Hu, S., et al. (2018). Synthesis of microporous covalent phosphazene-based frameworks for selective separation of uranium in highly acidic media based on size-matching effect. *ACS Appl. Mater. Interfaces* 10, 28936–28947. doi: 10.1021/acsami.8b06842

Zhang, N., Yuan, L. Y., Guo, W. L., Luo, S. Z., Chai, Z. F., and Shi, W. Q. (2017). Extending the use of highly porous and functionalized MOFs to Th(IV) capture. *ACS Appl. Mater. Interfaces* 9, 25216–25224. doi: 10.1021/acsami.7b04192

Zhang, R., Ji, S. L., Wang, N. X., Wang, L., Zhang, G. L., and Li, J. R. (2014). Coordination-driven *in situ* self-assembly strategy for the preparation of metal-organic framework hybrid membranes. *Angew. Chem. Int. Ed.* 53, 9775–9779. doi: 10.1002/anie.201403978

Zhang, Y. Y., Cai, J. J., Zhang, D. Y., Ke, X. B., and Zhang, L. X. (2018). Shaping metal-organic framework materials with a honeycomb internal structure. *Chem. Commun.* 54, 3775–3778. doi: 10.1039/c8cc01289j

Zhang, Y. Y., Yuan, S., Feng, X., Li, H. W., Zhou, J. W., and Wang, B. (2016). Preparation of nanofibrous metal-organic framework filters for efficient air pollution control. *J. Am. Chem. Soc.* 138, 5785–5788. doi: 10.1021/jacs.6b02553

Zhao, Y., Wang, L., Fan, N. N., Han, M. L., Yang, G. P., and Ma, L. F. (2018). Porous Zn(II)-based metal–organic frameworks decorated with carboxylate groups exhibiting high gas adsorption and separation of

organic Dyes. *Crystal Growth Design* 18, 7114–7121. doi: 10.1021/acs.cgd.8b0
1290

Zheng, T., Wu, Q. Y., Gao, Y., Gui, D. X., Qiu, S. W., Chen, L. H.,
et al. (2015). Probing the influence of phosphonate bonding modes
to uranium(VI) on structural topology and stability: a complementary
experimental and computational investigation. *Inorg. Chem.* 54, 3864–7384.
doi: 10.1021/acs.inorgchem.5b00024

Zou, X. Q., Zhu, G. S., Hewitt, I. J., Sun, F. X., and Qiu, S. L. (2009).
Synthesis of a metal–organic framework film by direct conversion
techniquefor VOCs sensing. *Dalton Trans.* 16, 3009–3013. doi: 10.1039/b82
2248g

# Synthesis, Crystal Structures and Photoluminescent Properties of One-Dimensional Europium(III)- and Terbium(III)-Glutarate Coordination Polymers, and Their Applications for the Sensing of $Fe^{3+}$ and Nitroaromatics

Sajjad Hussain[1,2]*, Xuenian Chen[1,3]*, William T. A. Harrison[4], Mark R. J. Elsegood[5], Saeed Ahmad[6], Shujun Li[1], Shabbir Muhammad[7] and David Awoyelu[5]

[1] Henan Key Laboratory of Boron Chemistry and Advanced Energy Materials, School of Chemistry and Chemical Engineering, Henan Normal University, Xinxiang, China, [2] Department of Chemistry, Mohi-Ud-Din Islamic University, Azad Jammu and Kashmir, Pakistan, [3] College of Chemistry and Molecular Engineering, Zhengzhou University, Zhengzhou, China, [4] Department of Chemistry, University of Aberdeen, Aberdeen, United Kingdom, [5] Chemistry Department, Loughborough University, Loughborough, United Kingdom, [6] Department of Chemistry, College of Sciences and Humanities, Prince Sattam Bin Abdulaziz University, Al-Kharj, Saudi Arabia, [7] Department of Physics, College of Science, King Khalid University, Abha, Saudi Arabia

Two lanthanide–glutarate coordination polymers, viz. : $\{[Eu(C_5H_6O_4)(H_2O)_4]Cl\}_n$, (**1**) and $[Tb(C_5H_7O_4)(C_5H_6O_4)(H_2O)_2]_n$, (**2**) have been synthesized and characterized by IR spectroscopy, thermogravimetric analysis, and X-ray crystallography. In **1**, the Eu(III) ions are coordinated by four O atoms from two bidentate chelating carboxylate groups, one O atom from a bridging carboxylate group and four O atoms from water molecules adopting an $EuO_9$ distorted tri-capped trigonal prismatic coordination geometry. In **2**, the Tb(III) ions are coordinated by six O atoms from three bidentate chelating carboxylates, one O atom from a bridging carboxylate and two O atoms from water molecules to generate distorted tri-capped trigonal prismatic $TbO_9$ polyhedron. In both compounds, the metal polyhedra share edges, producing centrosymmetric $Ln_2O_2$ diamonds, and are linked into [001] chains by bridging glutarate di-anions. The crystal structures are consolidated by O–H···O and O–H···Cl hydrogen bonds in **1**, and O–H···O hydrogen bonds in **2**. Compound **1** exhibits a red emission attributed to the $^5D_0 \rightarrow {}^7F_J$ ($J = 1$–4) transitions of the Eu(III) ion, whereas **2** displays green emission corresponding to the $^5D_4 \rightarrow {}^7F_J$ ($J = 0$–6) transitions of the Tb(III) ion. Both the compounds exhibit high sensitivity and selectivity for $Fe^{3+}$ ions due to luminescence quenching compared with other metal ions, which include; $Na^+$, $Mg^{2+}$, $Al^{3+}$, $Cr^{3+}$, $Mn^{2+}$, $Fe^{2+}$, $Co^{2+}$, $Ni^{2+}$, $Zn^{2+}$ and $Cd^{2+}$. Compounds **1** and **2** also show high luminescence quenching sensitivity for 4-nitrophenol over the other aromatic and nitroaromatic compounds, namely; bromobenzene, 1,3-dimethylbenzene, nitrobenzene, 4-nitrotolune, 4-nitrophenol, 2,6-dinitrophenol and 2,4,6-trinitrophenol.

Keywords: europium(III), terbium(III), glutarate, X-ray structure, luminescence, sensors

# INTRODUCTION

Lanthanide coordination compounds have attracted great interest from the scientific community in the last two decades due to their potential as an emerging type of multifunctional luminescent materials in areas such as telecommunications, optical amplifiers, immunoassays, and sensors (Werts, 2005; Binnemans, 2009; Armelao et al., 2010; Bünzli, 2010, 2015; Zhang et al., 2010; Azab et al., 2013; Feng and Zhang, 2013; Heffern et al., 2013; Xiang et al., 2017). They exhibit unique optical properties, such as large Stokes, shift, characteristic narrow line-like emission bands, and long lived excited state lifetimes resulting from intra configurational $4f-4f$ transitions (Werts, 2005; Allendorf et al., 2009; Armelao et al., 2010; Bünzli, 2010, 2015; Feng and Zhang, 2013; Heffern et al., 2013; Räsänen et al., 2014; Xiang et al., 2017). The luminescent nature of lanthanide coordination compounds is associated with the organic ligand moieties and lanthanide centers (Xiang et al., 2017). Due to the low molar extinction coefficient of the Laporte forbidden $f$-$f$ transitions, the direct photoexcitation of the lanthanide ions becomes difficult (Werts, 2005; Armelao et al., 2010; Bünzli, 2010, 2015; Heffern et al., 2013; Xiang et al., 2017). The introduction of suitable linkers (ligands) provides an alternative pathway for energy transfer and enriches the lanthanide emitting levels. These ligands transfer energy from the excited triplet state of ligand to the lowest emitting level of the lanthanide ion. The lanthanide ion then relaxes to the ground state by emission of energy (Reinhard and Güdel, 2002; Werts, 2005; Allendorf et al., 2009; Azab et al., 2013; Heffern et al., 2013; Rao et al., 2013; Räsänen et al., 2014; Bünzli, 2015; Xiang et al., 2017). The luminescent properties are not only related to the composition of the materials, but are also heavily dependent on the structure and intermolecular packing for their energy transfer (Cui et al., 2011; Xiang et al., 2017). Choosing appropriate ligands to increase the excited state lifetime and quantum yield (the light output) of lanthanide(III) complexes is thus essential for the development of improved luminescent materials (Li and Yan, 2012). In this regard, aromatic carboxylic acids such as, terephthalic acid (Daiguebonne et al., 2008; Wang et al., 2012) benzene-carboxylic acids (Yan et al., 2005; Wang et al., 2010b, 2012; Zhuravlev et al., 2011; Gai et al., 2013), and pyridine-dicarboxylic acid (Reinhard and Güdel, 2002; Huang et al., 2008; Zhu et al., 2009; Song et al., 2016; Xiang et al., 2017; Kumar et al., 2018) have been particularly used to design luminescent lanthanide coordination polymers. A number of studies also exist on the complexes of aliphatic carboxylic acids such as, malonic acid (Hussain et al., 2019), succinic acid (Cui et al., 2005; De Oliveira et al., 2013), glutaric acid (Głowiak et al., 1987; Legendziewicz et al., 1999; Antic-Fidancev et al., 2002), and adipic acid (Wang et al., 2010b).

From the large number of lanthanide coordination polymers, only some of them have been found active and explored for luminescence changes when brought in contact with some analyte or target molecules, possessing promising application as chemical sensors (Zhao et al., 2004; Zhang et al., 2010; Azab et al., 2013; Wang et al., 2014; Xiang et al., 2017). Thus, the optical properties of lanthanides are a beneficial tool to design new lanthanide based sensors, such as sensing of temperature (Miyata

et al., 2013; Rao et al., 2013), cations (Zhao et al., 2004, 2014a; Chen et al., 2009; Zhang et al., 2010; Bogale et al., 2016, 2017a), anions (Wong et al., 2006; Tan and Wang, 2011) nitroaromatics (Bogale et al., 2016, 2017a) and small molecules (Zhou et al., 2013; Zhao et al., 2014b). Such developments also encouraged us to synthesize new lanthanide coordination polymers with characteristic properties to selectively recognize and sense the specific analyte. Particularly, we are interested to develop a highly effective, quick, and reliable method for the detection of iron and nitroaromatics because of their essentiality in health care and high toxicity/explosiveness, respectively.

Among the luminescent lanthanide complexes, those of europium(III) and terbium(III) (emitting red and green light, respectively) have been especially widely studied because of their efficient luminescent properties (Cui et al., 2005; Bangaru et al., 2010; Tsaryuk et al., 2010; Zhuravlev et al., 2011; Hussain et al., 2019). To further explore the luminescent behavior of such complexes and as a part of our ongoing research on lanthanide complexes (Hussain et al., 2014, 2015a,b, 2018, 2019) herein, we report the structural characterization and photoluminescent properties of two one-dimensional Eu(III) and Tb(III) coordination polymers based on the glutarate ligand. In addition, the possible use of these complexes as sensors for detection of $Fe^{3+}$ and 4-nitrophenol was investigated. Although the crystal structures of a number of lanthanide-glutarate complexes have been reported in the literature (Głowiak et al., 1987; Serpaggi and Férey, 1998; Legendziewicz et al., 1999; Benmerad et al., 2000; Antic-Fidancev et al., 2002; Bromant et al., 2005; Rahahlia et al., 2006; Wang et al., 2010a; Hussain et al., 2015a; Zehnder et al., 2018) the optical properties of only a few of them have been studied (Głowiak et al., 1987; Legendziewicz et al., 1999; Antic-Fidancev et al., 2002). However, the use of none of these has been explored previously for sensing purposes. Thus, the present study would be the first one describing the potential of lanthanide-glutarates for application as sensors. As the exploitation of the new synthetic methods, structures, and properties in this system is still interesting, therefore, the studies of new lanthanide complexes with glutaric acid are important from both fundamental and applied viewpoints.

# EXPERIMENTAL

## Materials and Measurements

The metals salts ($EuCl_3 \cdot 6H_2O$, $TbCl_3 \cdot 6H_2O$) and ethanol were obtained from Alfa Aesar, USA. Glutaric acid was obtained from Merck Chemical Co. Germany. All other metal salts and nitroaromatics were purchased from Sigma Aldrich, a Johnson Matthey Company. Elemental analyses were carried out on a Varion Micro Cube, Elementar, Germany. FTIR spectra were recorded using KBr pellets on a Perkin Elmer FTIR 180 spectrophotometer over the wave number range from 4,000 to 250 $cm^{-1}$. Thermal analyses were carried out under air with a continuous heating rate of $10°C$ $min^{-1}$ from room temperature to 1,000°C on thermo-gravimetric analyzer/differential scanning calorimeter model SDT Q 600 (TA Instruments, USA) by taking 10.459 mg and 8.691 mg of

compound **1** and **2**, respectively. The excitation and emission spectra were measured at room temperature in steady state mode using FLS 180 spectrophotometer equipped with Xenon Arc lamp, photomultiplier detector R928P and Czerny-Turner monochromators having focal length of 300 mm. The excitation and emission were monitored between 250–400 and 400–800 nm, respectively.

## Crystal Structure Determination

The crystal data for compound **1** and **2** were collected on a Bruker Kappa Apex II CCD diffractometer using graphite-monochromated MoKα radiation ($\lambda$ = 0.71073 Å) at a temperature 150 K. The structures were solved by direct methods and the structural models were completed and optimized by refinement against $F^2$ with SHELX-2014 (Sheldrick, 2015). The aliphatic C-bound H atoms were geometrically placed and refined as riding atoms with C–H = 0.99 Å and $U_{iso}$ (H) = 1.2 $U_{eq}$(C). The water molecule H atoms were located in difference maps and coordinates were freely refined with the aid of mild geometrical restraints {target: O–H = 0.84 Å} and the isotropic atomic displacement parameters were fixed to 1.5 × $U_{eq}$ of the parent atom. The key crystallographic data and details of the structure refinements are provided in **Table S1**.

## Preparation of Complexes
### Preparation of {[Eu($C_5H_6O_4$)($H_2O$)$_4$]Cl}$_n$ (1)

EuCl$_3$·6H$_2$O (0.183 g, 0.5 mmol) was dissolved in 15 mL deionized water and glutaric acid (0.132 g, 1.0 mmol) was dissolved in 25 mL ethyl alcohol. The solutions were mixed and stirred in a round-bottomed flask at room temperature for 3 h. 1 M NaOH solution was used to adjust pH 5–6 of the reaction mixture during stirring. The reaction mixture was filtered and left at room temperature for crystallization. Colorless block shape crystals of **1** appeared after 20 days. The crystals were recovered by vacuum filtration, rinsing with ethanol and drying in air. Yield: 51%. Analysis for C$_5$H$_{14}$O$_8$ClEu: calculated (%): C 15.41; H 3.62; found (%): C 15.61; H 3.58.

### Preparation of [Tb($C_5H_7O_4$)($C_5H_6O_4$)($H_2O$)$_2$]$_n$ (2)

TbCl$_3$·6H$_2$O (0.189 g, 0.5 mmol) and glutaric acid (0.132 g, 1 mmol) were dissolved in 15 mL deionized water and 20 mL ethyl alcohol, respectively. The mixture was stirred at room temperature in a round bottomed flask for 4 h. 1 M NaOH solution was added to adjust pH 4–5 of the reaction mixture. The solution was filtered and left at room temperature for crystallization. After 3 weeks, colorless block shape crystals of **2** were recovered as described above. Yield: 47%. Analysis for C$_{10}$H$_{17}$O$_{10}$Tb: calculated (%) C 26.33; H 3.76; found (%): C 26.45; H 3.83.

## Photoluminescence Measurements

To investigate the detection ability of **1** toward the selected metals ions; Na$^+$, Mg$^{2+}$, Al$^{3+}$, Cr$^{3+}$, Mn$^{2+}$, Fe$^{2+}$, Fe$^{3+}$, Co$^{2+}$, Ni$^{2+}$, Zn$^{2+}$ and Cd$^{2+}$ (as chloride salts), equal volumes (130 μL of 1 × 10$^{-3}$ M) of metal solutions were added to **1** suspended in methanol (0.3 mg/3 mL). Likewise, the metal sensing aptitude of **2** was explored by adding equal volumes (160 μL, 1 × 10$^{-3}$

M) of these metals to methanolic suspensions of **2** (0.5 mg / 3 mL). Luminescence titration measurements were performed by stepwise addition of Fe$^{3+}$ solution into 0.35 mg of **1** and 0.51 mg of **2** suspended in 3 mL of methanol. After ultrasonic treatment for 5 min, their emission spectra were recorded under the same conditions at room temperature.

In the same way, to study the detection ability of **1** toward selected aromatics and nitro-aromatics including; bromobenzene (BB), 1,3-dimethylbenzene (DMB), nitrobenzene (NB), 4-nitrotolune (4-NT), 4-nitrophenol (4-NP), 2,6-dinitrophenol (DNP), and 2,4,6-trinitrophenol (TNP), equal volumes (120 μL) of the aromatics and nitroaromatics (0.001 M in ethanol) were added to 0.3 mg of **1** suspended in 3 mL of methanol. Compound **2** was tested by adding 150 μL (0.001 M in ethanol) of these compounds to 0.5 mg of **2** suspended in 3 mL methanol. The luminescence titration measurements on **1** (0.3 mg/ 3 mL methanol) were done by stepwise addition (5–160 μL) of 4-nitrophenol (0.001 M in ethanol). In the same way, **2** was assessed by the gradual addition (10–250 μL) of 4-nitrophenol (0.001 M in ethanol) to 0.5 mg of **2** suspended in 3 mL of methanol.

# RESULTS AND DISCUSSION
## Synthesis

The reaction of EuCl$_3$·6H$_2$O or TbCl$_3$·6H$_2$O with two equivalents of glutaric acid (C$_5$H$_8$O$_4$) in the presence of NaOH in water-ethanol medium yielded the colorless crystals of {[Eu(C$_5$H$_6$O$_4$)(H$_2$O)$_4$]Cl}$_n$, (**1**) and [Tb(C$_5$H$_7$O$_4$)(C$_5$H$_6$O$_4$)(H$_2$O)$_2$]$_n$ (**2**), respectively. The pH value of the medium seems to have a significant influence on the nature of final products. In the preparation of complex **1**, where more amount of NaOH was added as base, the ligand was fully deprotonated to produce glutarate di-anions, while in case of **2**, the lower pH resulted in the partial deprotonatation of the ligand and produced hydrogen-glutarate anion (HGlut$^-$). The proposed formulae of the complexes are in accordance with the elemental analysis. The complexes were further characterized by thermal analysis and X-ray crystallography.

## IR Spectroscopy

The IR spectra of **1** and **2** are shown in **Figures S1**, **S2**, respectively. The IR spectra of both complexes are similar, each showing broad absorption bands in the region 3,400–3,100 cm$^{-1}$ centered at 3,387 and 3,368 cm$^{-1}$ for **1** and **2**, respectively, which correspond to the O-H stretching vibrations of water molecules. The sharp peaks at 1,696 cm$^{-1}$ (with a shoulder at 1,646 cm$^{-1}$) in case of **1** and at 1,695 cm$^{-1}$ (with a shoulder at 1,640 cm$^{-1}$) for **2**, cannot be assigned to the asym(COO) vibration as in the free acid, but represents the O-H bending vibration due to the presence of strong H-bonded water molecules (Rahahlia et al., 2007). The bands at 1,553 and 1,525 cm$^{-1}$ for **1** and 1,555 and 1,527 cm$^{-1}$ for **2** correspond to $\nu_{asym}$(COO) vibrations, while those at 1,436 and 1,407 cm$^{-1}$ for **1** and 1,437 and 1,403 cm$^{-1}$ for **2** are associated with the corresponding symmetric modes (De Oliveira et al., 2013; Hussain et al., 2018, 2019). A difference ($\Delta\nu$) of about 120 cm$^{-1}$ in $\nu_{asym}$ (CO$_2$) and $\nu_{sym}$ (CO$_2$) wavenumbers is indicative of the bidentate coordination

of the carboxylate groups to the metal ions Eu(III) and Tb(III). For monodentate coordination of carboxylates, $\Delta\nu$ is usually more than 200 cm$^{-1}$ (Deacon and Philips, 1980; Zhuravlev et al., 2011; Batool et al., 2015). Monodentate coordination removes the equivalence of two oxygen atoms. If the C–O bond orders are appreciably affected, a pseudo-ester configuration is obtained. This decreases $\nu_{sym}(CO_2)$ and increases $\nu_{asym}(CO_2)$ as well as the separation ($\Delta\nu$) between the $\nu(CO_2)$ values relative to those for the free carboxylate ions, usually taken as sodium salts. Chelation or symmetrical bridging should not alter the bond orders and it has been suggested that bidentate coordination gives separation similar to the ionic values. For sodium and potassium acetates, the asymm and symm modes appear at 1,578–1,571 cm$^{-1}$ and 1,414–1,402 cm$^{-1}$, respectively, and the respective separations are 164 and 171 cm$^{-1}$, respectively (Deacon and Philips, 1980). Thus, the coordination mode proposed for glutarate acid in **1** and **2** is through O, O'-chelation of the carboxylate group. The weak bands appearing around 2,900 cm$^{-1}$, can be assigned to the C–H stretching vibration of the glutarate ligand. The medium band around 900 cm$^{-1}$ is ascribed to bending vibration, $\delta$(O–C–O) of the carboxylate group (Hussain et al., 2019). The spectra also give characteristic C–C stretching vibrations of the glutaric group near 1,200 cm$^{-1}$ (Rahahlia et al., 2007). For both **1** and **2**, the peaks in the low wavenumber region at (495, 303) and (481, 305) cm$^{-1}$, respectively, can be attributed to weak metal–oxygen bonds.

## Thermal Analysis

Thermogravimetric analysis of both complexes reveals the loss of water molecules upon heating. The combined TGA-DSC curves of **1** are presented in **Figure S3**. The compound began to lose coordinated water molecules slowly at 110°C and ended at 200°C (observed weight loss 18.1%; theoretical weight loss 18.5%). The slow decomposition supports the involvement of water molecules in H-bonding. The presence of an endothermic peak at 140°C, indicates the absence of water of crystallization in agreement with the observed formula. After release of water, there is no weight loss up to 320°C, which indicates a thermally metastable product of empirical formula $[Eu(C_5H_6O_4)]^+Cl^-$. Above 320°C, a continuous decomposition occurs slowly until 1,000°C releasing glutarate and chloride ions. At the end ½ $Eu_2O_3$ is left behind as a residue with an overall weight loss of 55% (theoretical 54.8%).

The thermal decomposition of **2** occurs in three stages as shown in **Figure S4**. At the first stage, a 7.8% weight loss occurs in the temperature range of 100 to 180°C, ascribed to the removal of two water molecules (theoretical 7.9%) followed by a plateau up to 290°C. The loss of water is associated with an endothermic transition at about 130°C. In the next stage, a 17.3% weight loss occurs between 290 and 450°C to leave probably two molecules of $CO_2$ (calculated value 19.3%). The remaining fragment of one glutarate and the second ligand are released in the following step with a 35% weight loss in the temperature range of 400–800°C. Some of the oxygen atoms are used in the formation of terbium oxide. The decomposition is completed at about 800°C. The overall weight loss of 60% is in excellent agreement with the theoretical weight loss of 59.9% to leave behind ¼ $Tb_4O_7$ as a

residue, which is in good agreement with that described in the literature (Cui et al., 2005). The TG results show that complex **1** possesses higher thermal stability than **2**.
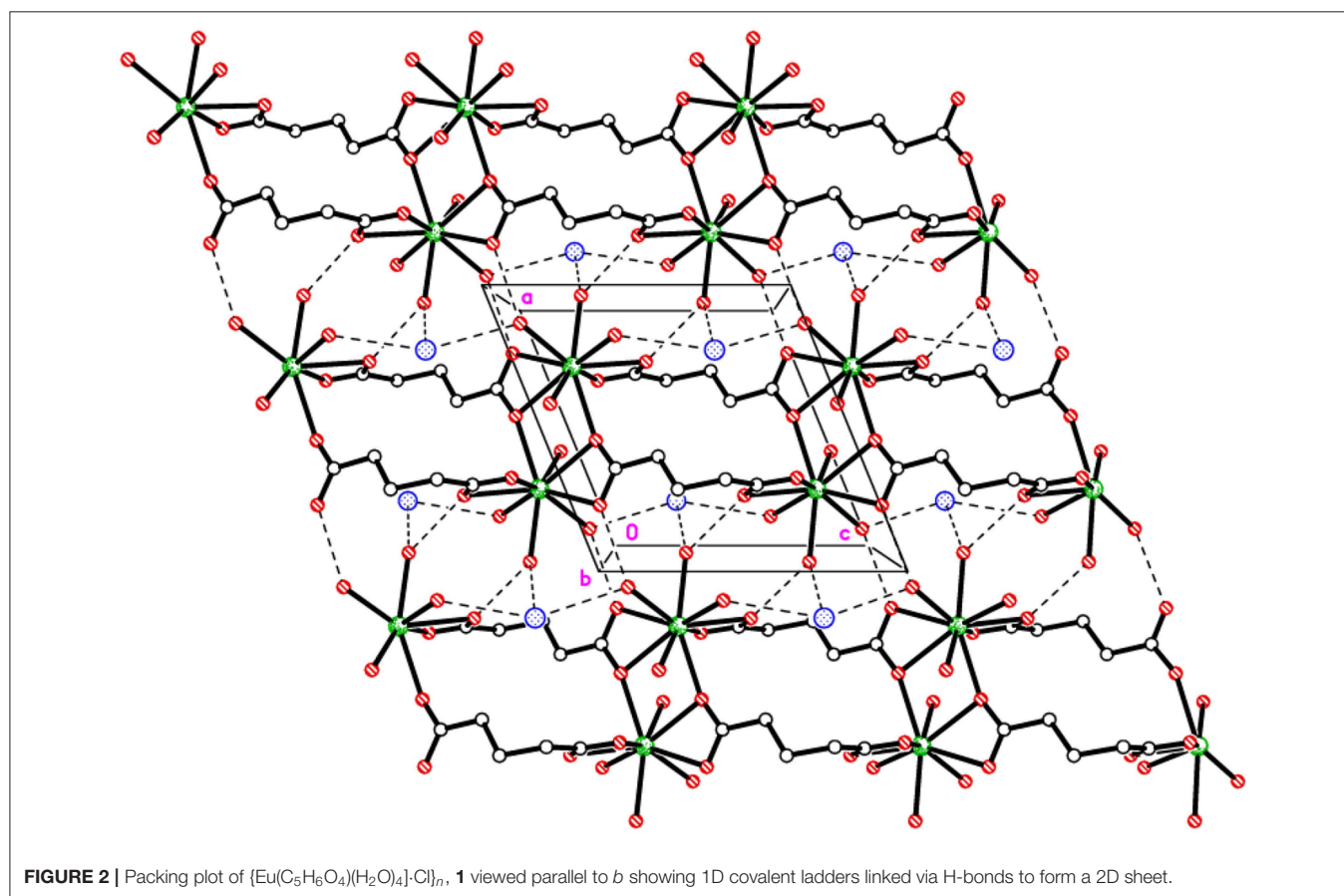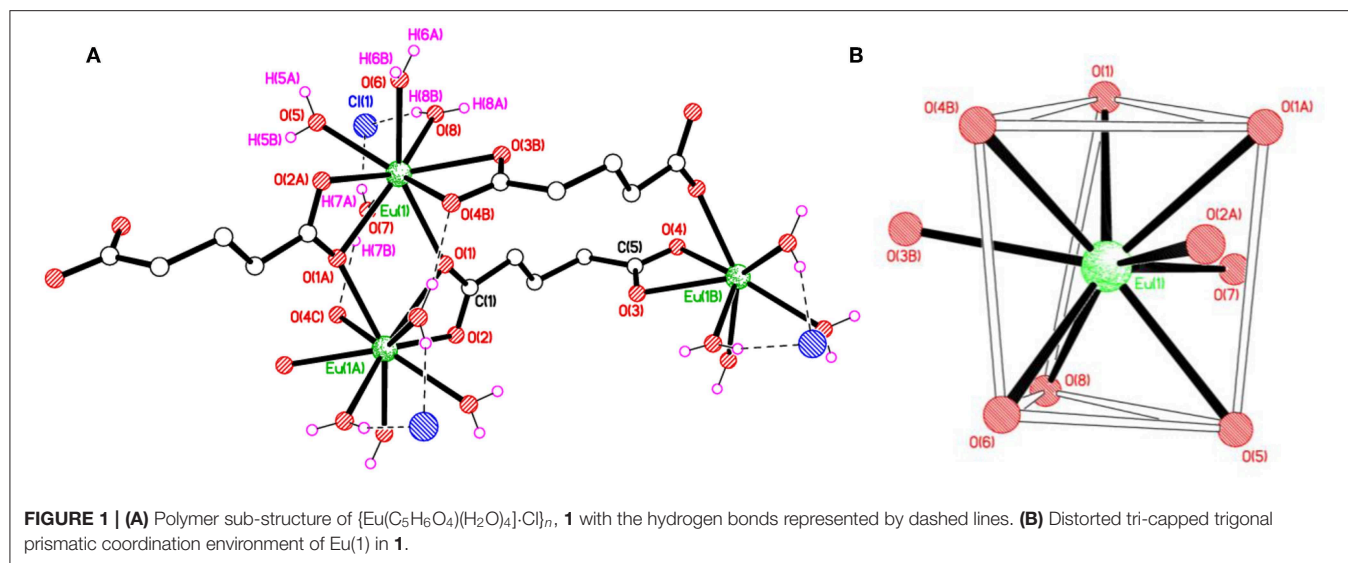
## Crystal Structures

As depicted in **Figure S5**, the asymmetric unit of **1** contains a Eu(III) cation, one completely deprotonated gultarate ligand, four coordinated water molecules and a chloride counter ion. Selected bond lengths and angles concerning the coordination are given in **Table 1**. The complex is polymeric and a segment of the polymeric structure of **1** is shown in **Figure 1A**. Each Eu(III) ion is coordinated by nine oxygen atoms (five from three independent glutarate ligands and four from water molecules) to form an EuO$_9$ distorted tri-capped trigonal prismatic polyhedron around Eu(III) (**Figure 1B**). A pair of europium(III) ions are joined to each other by carboxylate oxygen (O1) atoms of two different glutarate di-anions. The metal-metal separation [Eu1···Eu1$^i$ (i = 1–x, 1–y, 2–z)] in each pair is 4.1074 (3) Å. The dinuclear units are extended in the form of infinite [001] one dimensional chains. A polyhedral view of the chains is shown in **Figure S6**. The glutarate ligands exhibit identical bidentate chelating and chelating-bridging binding modes ($\mu_3$-$\kappa^2 O{:}\kappa O'{:}\kappa O''{:}\kappa O'''$). The C5/O3/O4 carboxyl group adopts a simple chelating bonding mode to a single europium(III) ion (both C–O distances are equal). The other carboxylate side (C1/O1/O2) of glutarate di-anion chelates to one metal ion and bridges to an adjacent metal ion from O1 (C1–O1 and C1–O2 bond lengths are unequal). The aliphatic chain of the glutarate is characterized by C1–C2–C3–C4 and C2–C3–C4–C5 torsion angles of −169.2 (2)° and 68.9 (3)°, respectively, i.e., a *trans–gauche* conformation. The Eu–O distance ranges from 2.3943(17) to 2.5217(16) Å and the average value is 2.455 Å. These distances are comparable to those in the reported nine-coordinated Eu(III)-carboxylate complexes (Cui et al., 2005; Manna et al., 2006; Zhang et al., 2007; Hussain et al., 2019).

Extensive hydrogen bonding involving coordinated water molecules and Cl$^-$ ions adds stability to the coordination

**TABLE 1** | Selected bond lengths (Å) and angles (°) for complex **1**.

| Bond | Distance (Å) | Bond | Angle(°) |
|---|---|---|---|
| Eu1—O1 | 2.4450 (16) | O1—Eu1—O3$^i$ | 76.53 (5) |
| Eu1—O1$^i$ | 2.4879 (16) | O1$^{ii}$—Eu1—O3$^i$ | 128.88 (5) |
| Eu1—O2$^{ii}$ | 2.5217 (16) | O1—Eu1—O4i | 72.85 (5) |
| Eu1—O4$^i$ | 2.4494 (16) | O1—Eu1—O8 | 103.27 (6) |
| Eu1—O3$^i$ | 2.4891 (16) | O4$^i$—Eu1—O3$^i$ | 52.70 (5) |
| Eu1—O5 | 2.4196 (17) | O5—Eu1—O2$^{ii}$ | 73.53 (6) |
| Eu1—O6 | 2.3943 (17) | O5—Eu1—O7 | 69.77 (6) |
| Eu1—O7 | 2.4427 (18) | O6—Eu1—O5 | 72.75 (6) |
| Eu1—O8 | 2.4450 (17) | O6—Eu1—O1 | 149.26 (6) |
| Eu1—Eu1$^{ii}$ | 4.1074 (3) | O6—Eu1—O2$^{ii}$ | 74.76 (5) |
| O1—C1 | 1.288 (3) | O6—Eu1—O7 | 136.59 (6) |
| O2—C1 | 1.253 (3) | O7—Eu1—O8 | 72.98 (6) |
| C5—O4 | 1.270 (3) | O8—Eu1—O3$^i$ | 73.18 (5) |
| C5—O3 | 1.270 (3) | | |

*Symmetry code: (i) −x + 1, −y + 1, −z + 1; (ii) −x + 1, −y + 1, −z + 2.*

**FIGURE 1 | (A)** Polymer sub-structure of {Eu(C$_5$H$_6$O$_4$)(H$_2$O)$_4$)·Cl}$_n$, **1** with the hydrogen bonds represented by dashed lines. **(B)** Distorted tri-capped trigonal prismatic coordination environment of Eu(1) in **1**.



**FIGURE 2 |** Packing plot of {Eu(C$_5$H$_6$O$_4$)(H$_2$O)$_4$)·Cl}$_n$, **1** viewed parallel to *b* showing 1D covalent ladders linked via H-bonds to form a 2D sheet.

polymer by connecting three adjacent metal centers as shown in **Figure 2**. The chloride ion forms hydrogen bonds (O–H···Cl) with five water molecules. Moreover, aqua ligands act as donors to the carboxylic O atoms O2, O3, and O4 as acceptors (O–H···O). The details of hydrogen bonds are provided in **Table S2**. The hydrogen bonds crosslink the 1D covalent polymeric ladders

into a two-dimensional sheet structure. The chloride ions in **1** occupy the regions between the (010) sheets and overall, a H-bonded three-dimensional network arises.

Compound **1** is isostructural with our previously reported neodymium analog, {[Nd(C$_5$H$_6$O$_4$)(H$_2$O)$_4$]Cl}$_n$. (Hussain et al., 2015a). In the closely related hydrated compounds

$\{[Nd(C_5H_6O_4)(H_2O)_4]Cl\cdot2H_2O\}_n$ (Legendziewicz et al., 1999) and $\{[Ce(C_5H_6O_4)(H_2O)_4]Cl\cdot2H_2O\}_n$ (Rahahlia et al., 2006) similar polymeric chains are formed incorporating both chloride ions and two uncoordinated water molecules per formula unit into the inter-chain voids. However, the coordination mode of glutarate ligands is different in these two compounds. The metal atoms are bound by four glutarate ions. Two of the carboxyl groups exhibit the same chelating bridging mode as observed in **1** (having two contacts to the first metal and one contact to the second metal ion). The other two carboxylates bind with two metal ions as bridging ligands instead of chelating with one metal ion as in **1**. In case of the analogous succinic acid complexes, $\{[M(C_4H_4O_4)(H_2O)_4]Cl\cdot2H_2O\}_n$ (M = La, Ce) (Rahahlia et al., 2007), the layer-type polymeric structure is built up from infinite chains of one-edge-sharing $LnO_6(H_2O)_4$ polyhedra (10-coordinate metal atom) and discrete chloride ions. The metal coordination consists of six oxygen atoms belonging to symmetrically equivalent succinate ligands and four aqua ligands. Only one type of carboxylate binding mode was described; the chelating bridging mode as found for (C1/O1/O2) group in **1**. The same bonding pattern of glutarate is found in $[Eu(C_5H_6O_4)(H_2O)_3]ClO_4$ (Głowiak et al., 1987). The europium ions are nine-coordinate with the coordination sphere made up of six oxygen atoms of glutarate ions and three water molecules.

The structure of $[Tb(C_5H_7O_4)(C_5H_6O_4)(H_2O)_2]_n$, **2** can be described as chains of dinuclear terbium(III)-(glutarate) (HGlut) units with two terbium ions linked through the O2 oxygen atoms of bridging glutarate ligands. The C6-monoanions are pendant to the chain (**Figure 3A**). The $Tb(1)\cdots Tb(1^i)$ [(i = 1–x, –y, 1–z)] distance in centrosymmetric, diamond-shaped $Tb_2O_2$ units is 4.0963(5) Å. The asymmetric unit of **2** comprises of one $Tb^{3+}$ ion, one mono-protonated glutarate ion (HGlut), one completely deprotonated gultarate dianion, and two coordinated water molecules. The selected bond parameters are listed in

**Table 2**. Each metal ion in the polymer is coordinated by three bidentate chelating carboxylate groups (two from glutarate di-anion and one from HGlut), one bridging carboxylate O atom and two water molecules. The coordination geometry of $TbO_9$ polyhedron can be described as distorted tri-capped trigonal prismatic (**Figure 3B**). The bond angles around the metal ions are smaller relative to those in **1** leading to a more distorted polyhedron environment for each metal center. A polyhedral view of a [001] chain in **2** showing the edge-sharing $TbO_9$ polyhedra is provided in **Figure S7**.

**TABLE 2 |** Selected bond lengths (Å) and angles (°) for complex **2**.

| Bond | Distance (Å) | Bond | Angles (°) |
|---|---|---|---|
| Tb1—O1 | 2.448 (2) | O1—Tb1—O2 | 51.23 (6) |
| Tb1—O2 | 2.582 (2) | O1—Tb1—O3$^{ii}$ | 91.31 (7) |
| Tb1—O2$^i$ | 2.3585 (19) | O1—Tb1—O4$^{ii}$ | 70.73 (7) |
| Tb1—O3$^{ii}$ | 2.396 (2) | O1—Tb1—O5 | 145.14 (7) |
| Tb1—O4$^{ii}$ | 2.542 (2) | O1—Tb1—O6 | 145.40 (7) |
| Tb1—O5 | 2.4706 (19) | O1—Tb1—O9 | 80.89 (7) |
| Tb1—O6 | 2.443 (2) | O1—Tb1—O10 | 77.57(7) |
| Tb1—O9 | 2.334 (2) | O2—Tb1—O2$^i$ | 68.04 (6) |
| Tb1—O10 | 2.345 (2) | O2—Tb1—O3$^{ii}$ | 74.95 (7) |
| C1—O1 | 1.256 (3) | O2—Tb1—O4$^{ii}$ | 98.49 (6) |
| C1—O2 | 1.273 (3) | O5—Tb1—O6 | 52.86 (7) |
| C5—O4 | 1.264 (3) | O5—Tb1—O9 | 71.87 (7) |
| C5—O3 | 1.270 (3) | O5—Tb1—O10 | 76.94 (7) |
| C6—O5 | 1.269 (3) | O6—Tb1—O3$^{ii}$ | 76.62 (7) |
| C6 —O6 | 1.266 (3) | | |

*Symmetry codes: (i) –x+1, –y, –z+1 (ii) –x+1, –y, –z+2.*
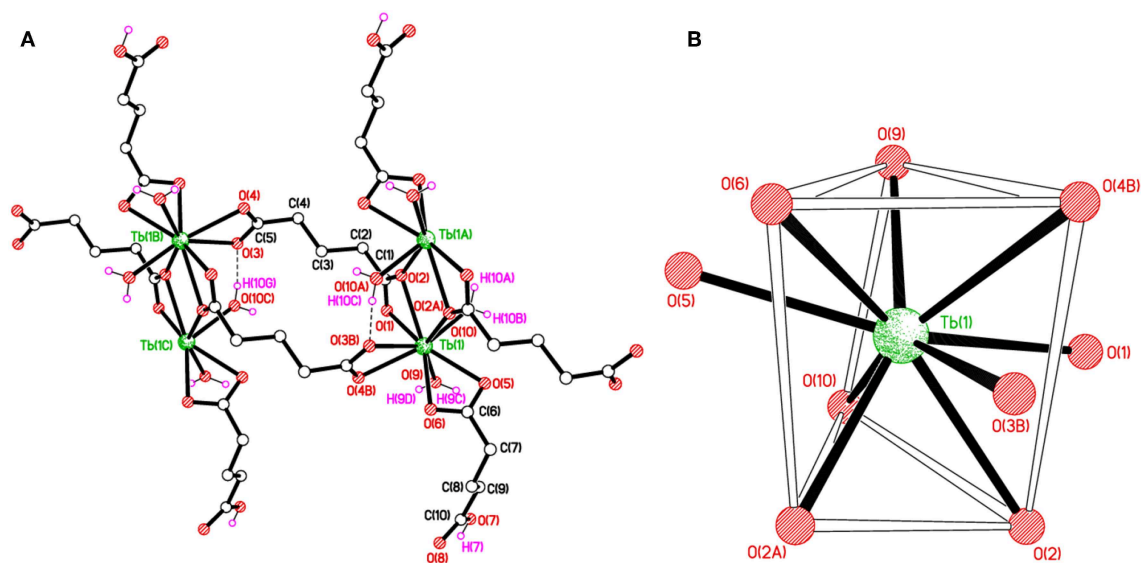


**FIGURE 3 | (A)** Polymer sub-structure of $[Tb(C_5H_7O_4)(C_5H_6O_4)(H_2O)_2]_n$, **2. (B)** Distorted tri-capped trigonal prismatic coordination environment of Tb(1) in **2**.

The glutarate di-anion coordinates in the same way as found in **1**. The C1-containing carboxyl group chelates to a metal ion from the C1/O1/O2 moiety and one of the chelating O atoms O(2) bridges an adjacent metal atom. The C(5)/O3/O(4) moiety follows a chelating bonding mode to Tb1, the next metal along the chain. The carbon-atom chain of the C(1) anion adopts an extended conformation [C1–C2–C3–C4 = 173.4(2)°; C2–C3–C4–C5 = 179.4(2)°]. The mono-anion glutarate chelates to Tb1 through C6/O5/O6 and the other end is protonated carboxylic group C10/O7/O8 does not participate in coordination. The backbone carbon chains have unique *gauche* C6–C7–C8–C9 [74.0(3)°] and *anti.* C7–C8–C9–C10 [−176.9(3)°] conformation. The mean Tb–O distance 2.434 Å is in accordance with the reported literature (Cui et al., 2005; Qiongyan et al., 2008; Hussain et al., 2019). The coordination bond lengths in **2** are slightly shorter, in comparison with **1**, which is in accordance with the slightly smaller ionic radius of Tb$^{3+}$ (Hussain et al., 2019).

The structure of **2** is supported by O–H···O hydrogen bonds including carboxylates and water molecules and details are given in **Table S3**. The carboxylate O7 hydrogen bonds crosslink the 1D polymeric chains into a two-dimensional layer as shown in **Figure 4A**. The layers are further connected to build a three-dimensional network (**Figure 4B**).

## Luminescent Properties

The solid state photoluminescence properties of **1** and **2** were investigated at room temperature.

The excitation spectrum of **1** was measured to monitor the $^5D_0 \rightarrow {}^7F_2$ transitions of europium at 616 nm as shown in **Figure 5A**. The major excitation peaks of europium are observed at 286 nm ($^7F_0 \rightarrow {}^5I_8$), 298 nm ($^7F_0 \rightarrow {}^5F_2$), 318 nm ($^7F_0 \rightarrow {}^5H_3$), 362 nm, 367 nm ($^7F_{0,1} \rightarrow {}^5D_4$), 375 nm, 381 nm, 385 nm ($^7F_0 \rightarrow {}^5L_{7,8,9}$), 395 nm ($^7F_0 \rightarrow {}^5L_6$) and 417 nm ($^7F_0 \rightarrow {}^5D_3$). All the excitation peaks in **1** arise from ground level $^7F_0$ except $^5D_4$ which arises from level $^7F_1$. The most intense among them is $^7F_0 \rightarrow {}^5L_6$. These excitation peaks have been observed in previously reported europium compounds (Baur et al., 2015; Marques et al., 2015). A very weak signal appeared at 268 nm due to transition of the ligand expected to produce luminescence emission. The other ligand transitions are superimposed on the strong $^7F_0 \rightarrow {}^5I_8$ and $^7F_0 \rightarrow {}^5F_2$ transition of europium. The emission spectrum of **1** was recorded under the excitation wavelength of 268 nm and is shown in **Figure 5B**. It exhibits four characteristic peaks in the visible region at 598, 616, 656, and 699 nm, which belong to the $^5D_0 \rightarrow {}^7F_1$, $^5D_0 \rightarrow {}^7F_2$, $^5D_0 \rightarrow {}^7F_3$, and $^5D_0 \rightarrow {}^7F_4$ transitions of the europium(III) ion, respectively. The most intense was the induced electric dipole transition $^5D_0 \rightarrow {}^7F_2$ which is highly sensitive for the chemical bond in the environs of a europium(III) ion, and responsible for the red emission when irradiated under UV light (Cui et al., 2005; Gu and Xue, 2006; Hou et al., 2014).

Whereas $^5D_0 \rightarrow {}^7F_1$ is the magnetic dipole transition, which is rather less sensitive to the coordinated environment and is relatively weak when compared with the electric dipole transition ($^5D_0 \rightarrow {}^7F_2$). The Eu(III) transition rule states that when the center of inversion exists on europium(III), the magnetic dipole transition ($^5D_0 \rightarrow {}^7F_1$) will be more intense emitting orange light instead of red light, emitting electric dipole transition ($^5D_0 \rightarrow {}^7F_2$) (Hou et al., 2014). The crystal field strength acting on europium(III) also affects the intensity of the magnetic dipole transition (Gu and Xue, 2006). As the site
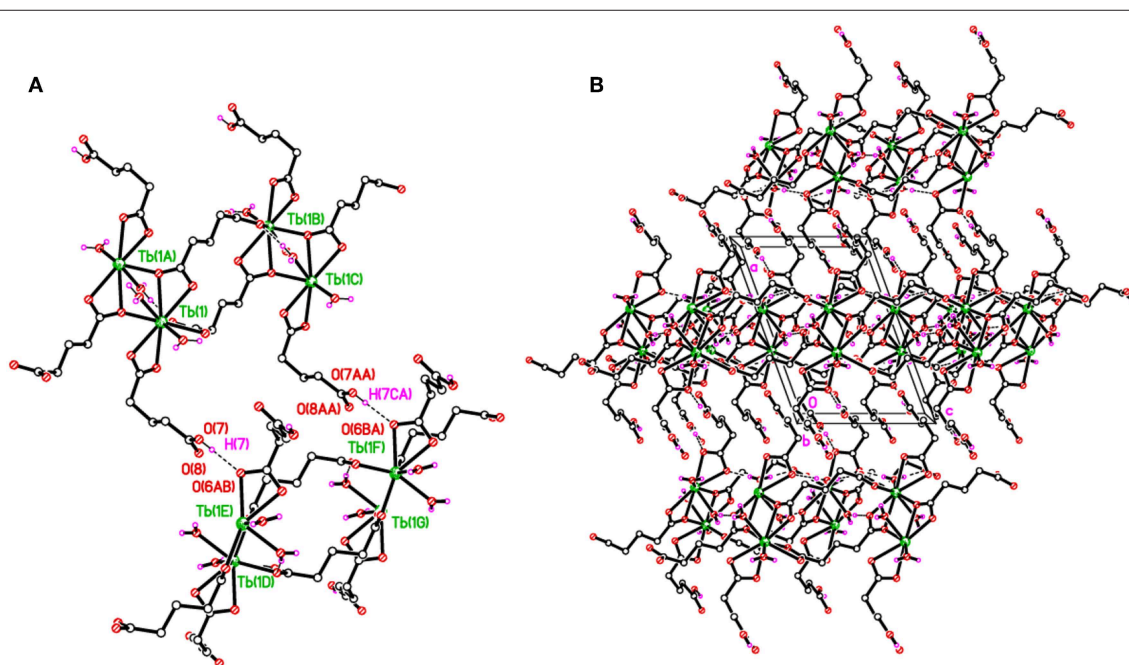


**FIGURE 4 | (A)** Packing plots of **2** showing covalently-bonded 1D chains in the *c* direction. **(B)** An overall 3D H-bonded network. H-bonds shown as dashed lines.
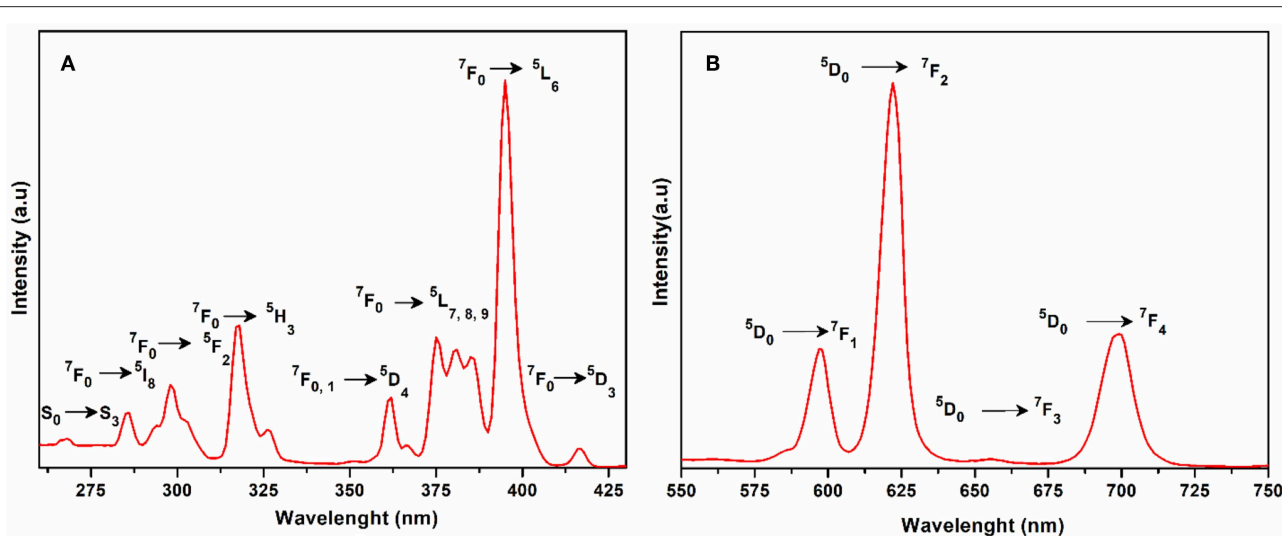
**FIGURE 5 | (A)** Solid state excitation spectrum of **1** to monitor emission at 616 nm. **(B)** Solid state emission spectrum of **1** excited at 268 nm.

symmetry of the Eu(III) ion decreases, the intensity of the electric dipole transition $^5D_0 \rightarrow {}^7F_2$ increases. By comparing the intensity ratio of $^5D_0 \rightarrow {}^7F_1$ (598 nm) and $^5D_0 \rightarrow {}^7F_2$ (616 nm) for **1**, the peak intensity ratio is about 1:3 which suggests that the coordination of the europium ions does not have an inversion center on the local site and exists in a low symmetry environment as is evident by the structural analysis of compound **1** (Hou et al., 2014).

The excitation spectrum of **2** (**Figure 6A**) was measured to observe the $^5D_4 \rightarrow {}^7F_n$ transitions of terbium at 545 nm. The excitation spectrum exhibited the following transitions of terbium; $^7F_6 \rightarrow {}^5H_3$ (266 nm); $^7F_6 \rightarrow {}^5H_4$ (273 nm); $^7F_6 \rightarrow {}^5I_8$ (286 nm); $^7F_6 \rightarrow {}^5H_5$ (296 nm); $^7F_6 \rightarrow {}^5H_6$ (304 nm); $^7F_6 \rightarrow {}^5H_7$ (319 nm); $^7F_6 \rightarrow {}^5D_1$ (327 nm); $^7F_6 \rightarrow {}^5H_{7,8}, {}^5G_3$ (342 nm); $^7F_6 \rightarrow {}^5L_9, {}^5G_5$ (351 nm); $^7F_6 \rightarrow {}^5D_2$ (360 nm); $^7F_6 \rightarrow {}^5L_{10}$ (370 nm); and $^7F_6 \rightarrow {}^5G_5, {}^5D_3$ (380 nm). All these transitions originate from the $^7F_6$ ground state and the strongest of these are: $^7F_6 \rightarrow {}^5L_9, {}^5G_5$ and $^7F_6 \rightarrow {}^5L_{10}$. The weak ligand transitions are superimposed on the $^7F_6 \rightarrow {}^5H_3$ (266 nm), $^7F_6 \rightarrow {}^5H_4$ (273 nm), $^7F_6 \rightarrow {}^5I_8$ (286 nm), and $^7F_6 \rightarrow {}^5H_5$ (296 nm) transition of the terbium, which are more dominant in the excitation spectra. The excitation pattern of **2** closely matches with the previously reported powder MOF of terbium-thenoyltriflourcacetone (Medina-Velazquez et al., 2019). As shown in **Figure 6B** under the excitation wavelength of 268 nm, the emission spectrum of **2** exhibits four intense characteristic transitions of terbium at 494 nm ($^5D_4 \rightarrow {}^7F_6$), 545 nm ($^5D_4 \rightarrow {}^7F_5$), 588 nm ($^5D_4 \rightarrow {}^7F_4$), and 625 nm ($^5D_4 \rightarrow {}^7F_3$). In spite of this, there are also three weak peaks at 652, 672, and 683 nm attributed to the $^5D_4 \rightarrow {}^7F_2$, $^5D_4 \rightarrow {}^7F_1$, and $^5D_4 \rightarrow {}^7F_0$ emissions, respectively. An induced electric dipole transition ($^5D_4 \rightarrow {}^7F_5$) that is sensitive to the coordination environment of the terbium exhibits the strongest emission at 545 nm, which is characterized by the green luminescence output when the solid sample is excited under UV light. The

magnetic transition ($^5D_4 \rightarrow {}^7F_6$), which is less sensitive to the coordination environment is relatively weak when compared with the electric dipole transition ($^5D_4 \rightarrow {}^7F_5$) with intensity ratio close to 1:3 ($^5D_4 \rightarrow {}^7F_6 : {}^5D_4 \rightarrow {}^7F_5$) (Bogale et al., 2017a).

The fluorescence emissions of europium and terbium in different compounds have been reported for sensing metal ions (Zhao et al., 2004; Bogale et al., 2016, 2017a), nitro compounds (Bogale et al., 2016, 2017a), and solvent molecules (Li et al., 2013; Wang et al., 2014). The emission behavior of **1** and **2** were investigated in various solvents, such as methanol, ethanol, THF, DMSO, DMF, water, acetone, and dichloromethane. Complexes **1** and **2** show good luminescence in these solvents (**Figures S8, S9**, respectively) except in acetone and dichloromethane in which they exhibit a strong quenching effect on emission intensity. Thus, **1** and **2** could be used as sensors for acetone and dichloromethane. When **1** and **2** were suspended in methanol they exhibited strong emission peaks as compared with other solvents. The fluorescence life time calculated for compounds **1** and **2** are 2.499 ns and 2.895 ns, respectively.

## Detection of Metals Ions

In order to investigate the sensing properties of complexes **1** and **2** toward various metals ions, such as $Na^+$, $Mg^{2+}$, $Al^{3+}$, $Cr^{3+}$, $Mn^{2+}$, $Fe^{2+}$, $Fe^{3+}$, $Co^{2+}$, $Ni^{2+}$, $Zn^{2+}$ and $Cd^{2+}$, aqueous solutions of chloride salts of these metals were added individually to solutions of **1** and **2** dispersed in methanol under the same conditions. As shown in **Figures 7A,B**, only $Fe^{3+}$ was able to induce significant fluorescence quenching of **1** and **2**, respectively. As compared with the initial solution (control), the fluorescence intensity of **1** and **2** were reduced about 83 and 85%, respectively, by the addition of aqueous solution of $Fe^{3+}$, while the addition of other metals has no appreciable effect on the fluorescence intensity under the same test conditions as shown in **Figures S10, S11**, respectively. These results suggest that **1** and **2** are highly sensitive for the $Fe^{3+}$ ion and induce distinct
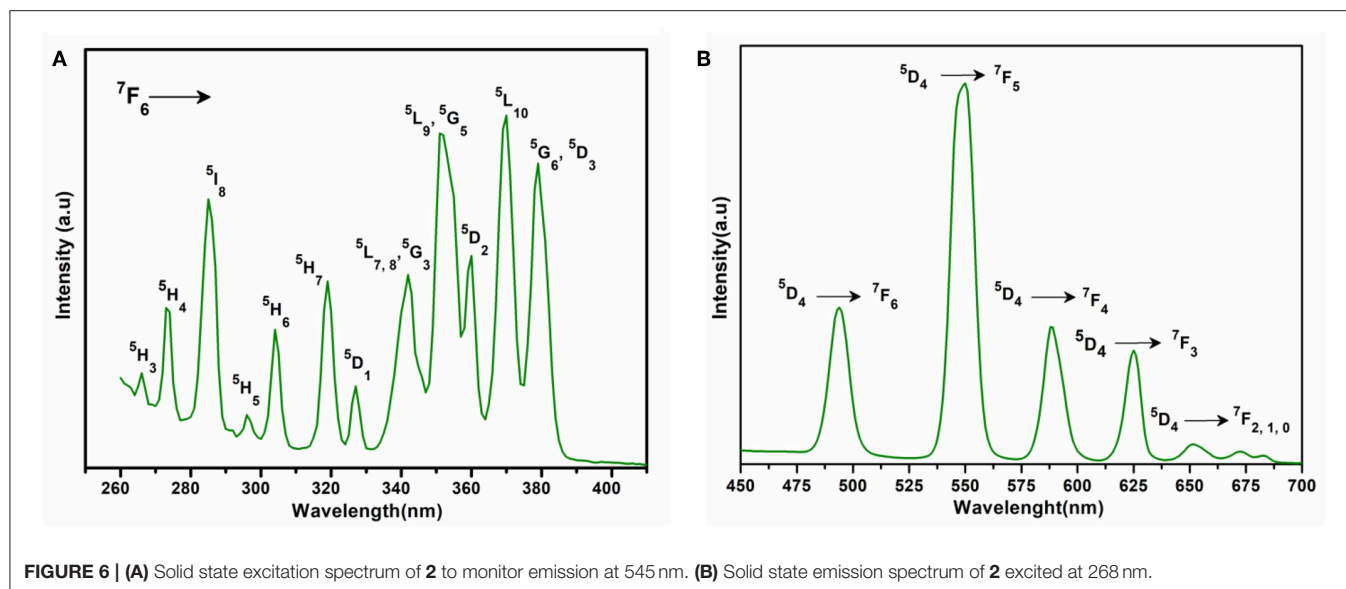
**FIGURE 6 | (A)** Solid state excitation spectrum of **2** to monitor emission at 545 nm. **(B)** Solid state emission spectrum of **2** excited at 268 nm.
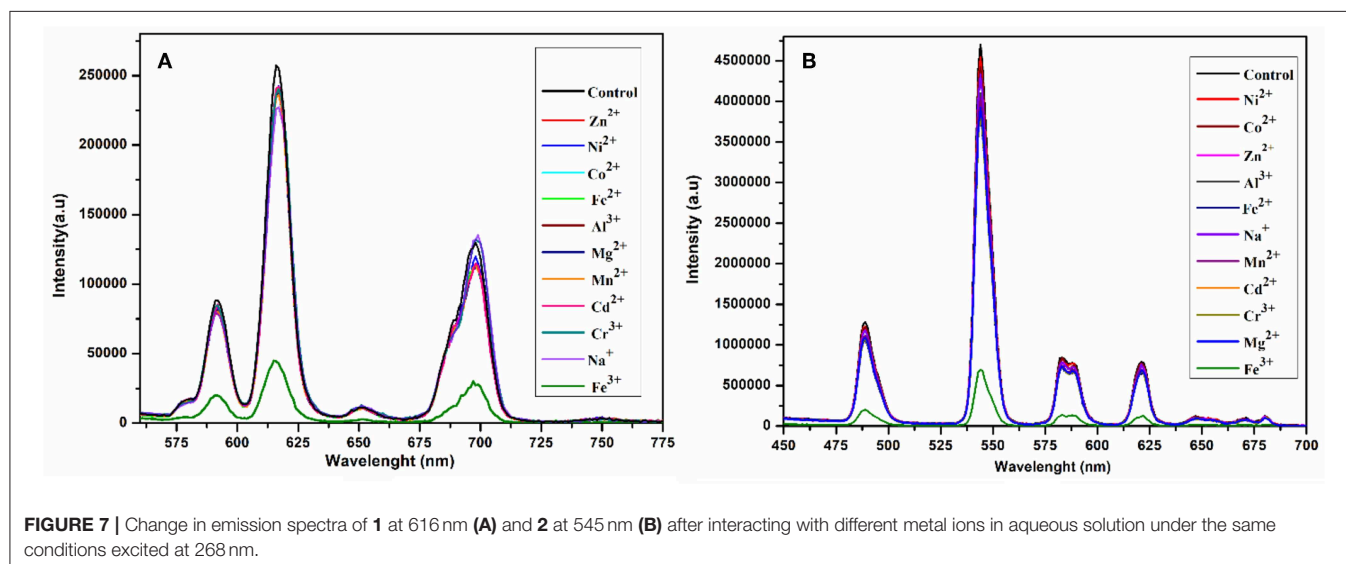


**FIGURE 7 |** Change in emission spectra of **1** at 616 nm **(A)** and **2** at 545 nm **(B)** after interacting with different metal ions in aqueous solution under the same conditions excited at 268 nm.

fluorescence quenching as compared with the other metals ions. Furthermore, the sensitivity tests of **1** and **2** were carried out by progressive addition of an aqueous solution of $Fe^{3+}$ ion to the solutions of **1** and **2** suspended in methanol. The gradual addition of an aqueous solution of $Fe^{3+}$ to the methanolic solution of **1** and **2** produced sequential quenching of fluorescence emission at 616 nm (**Figure 8A**) and 545 (**Figure 8B**) nm, respectively. The **Figures S12, S13** depict that the luminescence quenching efficiencies and concentration of $Fe^{3+}$ are in good agreement with linear proportion with R values of 0.9949 and 0.9734 for **1** and **2**, respectively. The detection limits for and **1** and **2**, estimated from the linear regression curves, were found to be $4.6565 \times 10^{-7}$ M and $1.612 \times 10^{-7}$ M, respectively, which is comparable with the reported terbium and europium coordination polymers for the detection of $Fe^{3+}$ (Bogale et al., 2016, 2017a,b; Gao et al., 2016). The Stern-Volmer equation $\frac{I_0}{I} = (1 + K_{sv}[Q])$ was used; where $I_0$ and $I$ are luminescence intensity before

and after addition of quencher, respectively, $Q$ is the quencher concentration and $K_{sv}$ is the quenching coefficient constant. The value of $K_{sv}$ was found to be $1.31 \times 10^5$ M$^{-1}$ and (for **1**) and $8.07 \times 10^4$ M$^{-1}$ (for **2**), which suggest that the static and dynamic quenching processes are dominant as revealed by the reported studies (Bogale et al., 2016, 2017a,b; Gao et al., 2016).

The sensitivity and selectivity of compounds **1** and **2** toward $Fe^{3+}$ were speculated due to the reason that $Fe^{3+}$ ions diffused into the pores generated by the one-dimensional layers of **1** and **2**, and interact with the carboxylate oxygen and aqua ligands (Dong et al., 2015). Thus, complexation and incorporation of $Fe^{3+}$ may reduce the energy transfer from ligand to $Eu^{3+}$ and $Tb^{3+}$ in **1** and **2**, respectively, and produce efficient fluorescence quenching. Another possible reason for luminescence quenching is exchange of $Eu^{3+}$ and $Tb^{3+}$ with $Fe^{3+}$ in **1** and **2**, respectively (Zheng et al., 2013; Bogale et al., 2016).
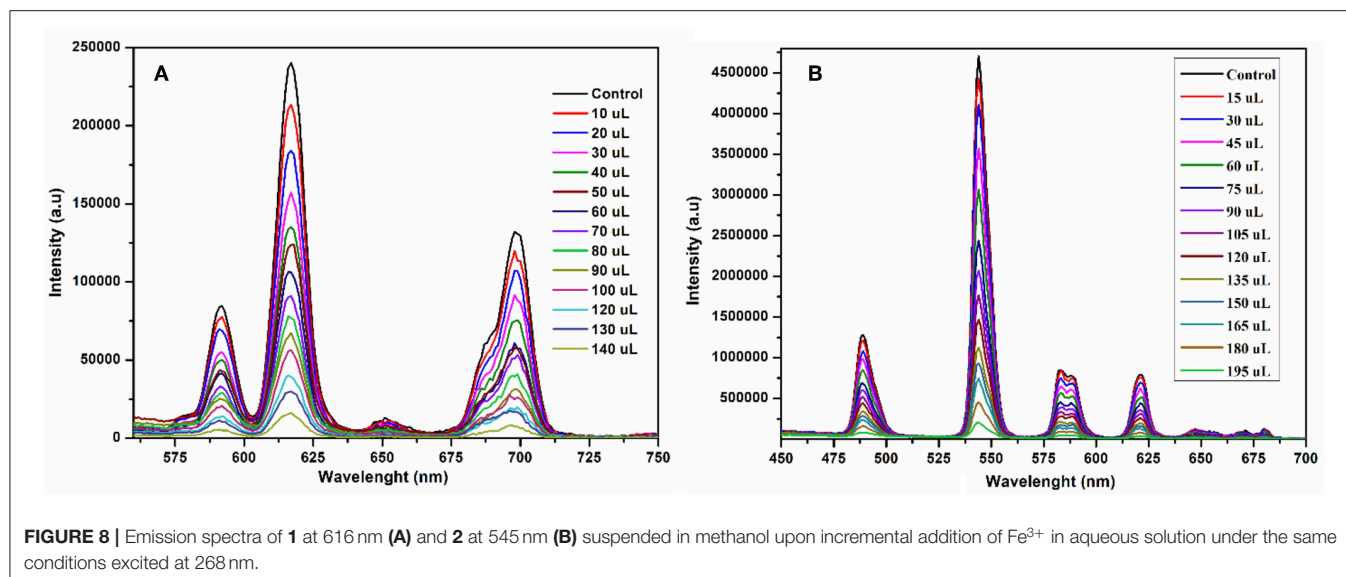
**FIGURE 8 |** Emission spectra of **1** at 616 nm **(A)** and **2** at 545 nm **(B)** suspended in methanol upon incremental addition of $Fe^{3+}$ in aqueous solution under the same conditions excited at 268 nm.

## Detection of Aromatics

To scrutinize the detection capability of **1** toward different aromatic and nitroaromatic compounds; bromobenzene (BB), 1,3-dimethylbenzene (DMB), nitrobenzene (NB), 4-nitrotolune (4-NT), 4-nitrophenol (4-NP), 2,6-dinitrophenol (DNP), and 2,4,6-trinitrophenol (TNP) were selected. In doing so, equal volumes of these compounds were added to the methanolic suspension of **1** and their luminescence spectra were recorded as shown in **Figure 9A**. Interestingly, the emission intensity of **1** was highly reduced after addition of 4-nitrophenol, while the other analogous compounds have negligible quenching effect on the emission intensity. The decreasing potential for quenching efficiency is described as: 4-nitrophenol (4-NP) > 2,4,6-trinitrophenol (TNP) > nitrobenzene (NB) > 2,6-dinitrophenol (DNP) > bromobenzene (BB) > 4-nitrotolune (4 NT) > 1,3-dimethylbenzene (DMB), which deviates a little from the electron deficient trend of these compounds. As shown in **Figure S14**, 4-nitrophenol is the most efficient quencher for **1** with quenching efficiency of 78% as compared to the other electron deficient nitroaromatics, such as 2,4,6-trinitrophenol (27%), nitrobenzene (25%), 2,6-dinitrophenol (21%). The least quenching effect is with 1,3-dimethylbenzene (8%).

The compound **2** was also suspended in methanol to explore the sensing ability toward the above-mentioned aromatics and nitroaromatic compounds. The emission spectra were recorded after addition of aromatics and nitroaromatics into the methanolic suspension of **2**. As shown in **Figure 9B**, 4-nitrophenol exhibits significant fluorescence quenching as compared to the other tested compounds. The decreasing order of reducing emission intensity of **2** is 4-nitrophenol (4-NP) > 2,6-dinitrophenol (DNP) > 2,4,6-trinitrophenol (TNP) > nitrobenzene (NB) > 4-nitrotolune (4-NT) > 1,3-dimethylbenzene (DMB) > bromobenzene (BB). This trend varies from the electron deficient trend of these compounds. The maximum quenching efficiency for 4-nitrophenol (4-NP) was found to be 67.22% and the least quenching is

bromobenzene, found to be 3.37%, while 2,4,6-trinitrophenol and 2,6-dinitrophenol have quenching efficiencies 14.01 and 17.44%, respectively, as shown in **Figure S15**.

The fluorescence quenching titrations were performed by successive addition of 4-nitrophenol into **1** and **2** suspended in methanol. The gradual addition of 4-nitrophenol produced significant fluorescence quenching at 616 nm (for **1**, **Figure 10A**) and 545 nm (for **2**, **Figure 10B**). The **Figures S16**, **S17** depict that the luminescence quenching efficiencies and concentration of 4-nitrophenol are in good agreement with linear proportion with $R^2$ values of 0.9890 and 0.9888 for **1** and **2**, respectively. The detection limits for **1** and **2** from the linear regression curves were found to be $5.0589 \times 10^{-8}$ M and $6.9173 \times 10^{-8}$ M, respectively, which are comparable with the reported europium and terbium coordination polymers for the detection of 4-nitrophenol (Bogale et al., 2016, 2017a,b; Gao et al., 2016). The calculated Ksv values are $9.4792 \times 10^4$ $M^{-1}$ (for **1**) and $4.5295 \times 10^4$ $M^{-1}$ (for **2**), which suggest that the static and dynamic quenching processes are dominant as revealed by the previous studies (Bogale et al., 2016, 2017a,b; Gao et al., 2016).

Therefore, it is surmised that the fluorescence quenching observed in **1** and **2** by the addition of 4-nitrophenol is due to electronic interaction between 4-nitrophenol and the moieties of **1** and **2**, respectively. The other possible reasons for luminescence quenching are the inner filter effect of 4-nitrophenol and competition between absorption energy of 4-nitrophenol and excitation energy of **1** and **2** (Bogale et al., 2017b). The excitation energy absorbed by the ligands is further absorbed by the 4-nitrophenol, which is responsible for fluorescence quenching (Bogale et al., 2016).

## CONCLUSIONS

In summary, two luminescent europium(III)- and terbium(III)-glutarate coordination polymers; $[Eu(C_5H_6O_4)(H_2O)_4]Cl\}_n$ (**1**) and $[Tb(C_5H_7O_4)(C_5H_6O_4)(H_2O)_2]_n$ (**2**) were synthesized and
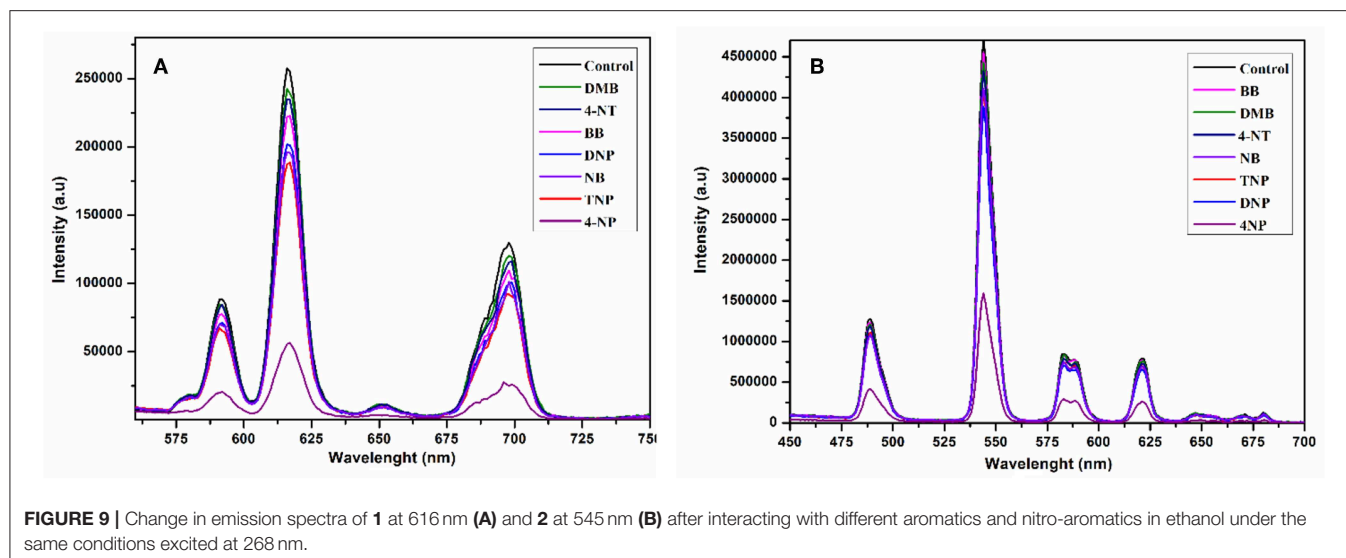
**FIGURE 9 |** Change in emission spectra of **1** at 616 nm **(A)** and **2** at 545 nm **(B)** after interacting with different aromatics and nitro-aromatics in ethanol under the same conditions excited at 268 nm.
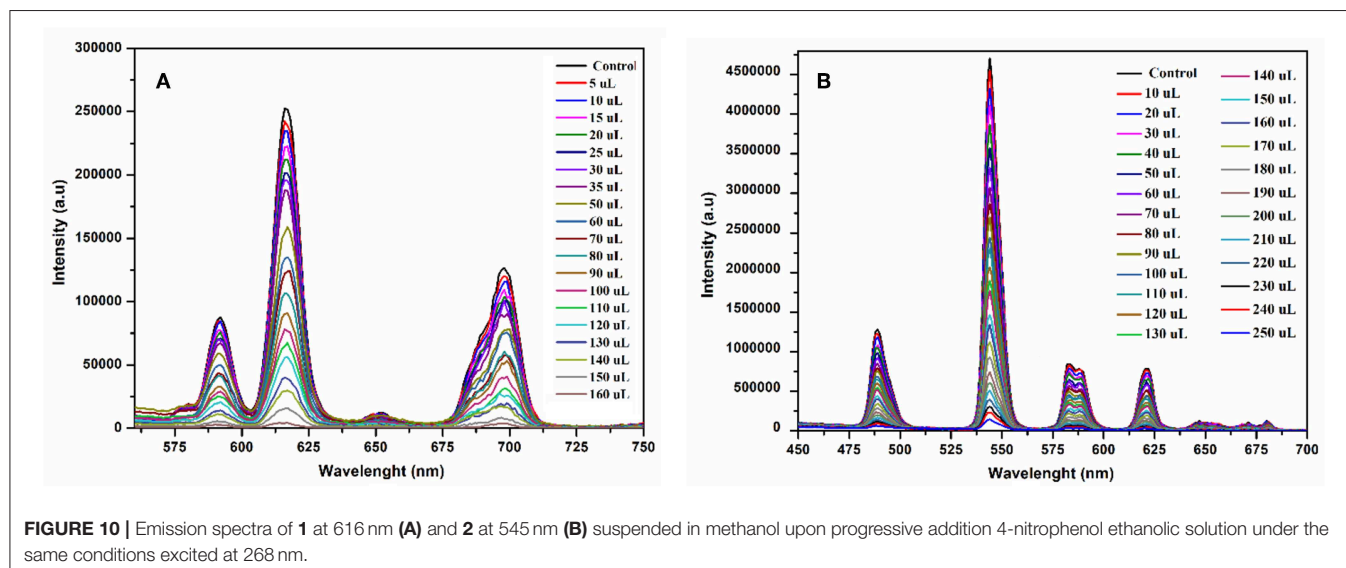


**FIGURE 10 |** Emission spectra of **1** at 616 nm **(A)** and **2** at 545 nm **(B)** suspended in methanol upon progressive addition 4-nitrophenol ethanolic solution under the same conditions excited at 268 nm.

characterized by IR, TGA and X-ray crystallography. The TGA curves show that after the removal of water molecules, compounds **1** and **2** are stable up to about 300°C. The photoluminescence spectra of **1** and **2** depict the characteristic peaks of europium(III) and terbium(III) ions responsible for the intense red and green emissions, respectively, when irradiated under UV light. The appearance of emission bands in the visible region in the luminescent spectra may recommend their use as long-lived luminescent probes in immuno-assays. The compounds also exhibited good luminescence in various solvents except dichloromethane and acetone. Both complexes exhibit a strong quenching effect on emission intensity when brought into contact with $Fe^{3+}$ ions and 4-nitrophenol as compared with the other metal ions and nitroaromatics. Furthermore, fluorescence quenching titrations were performed to investigate the sensitivity of complexes for $Fe^{3+}$ and 4-nitrophenol. By

using quenching titration results, the Stern-Volmer graphs were plotted, which suggested that in all cases both static and dynamic quenching processes are dominant. The $K_{sv}$ values of **1** found for $Fe^{3+}$ and 4-nitrophenol are $1.31 \times 10^5$ $M^{-1}$ and $9.4792 \times 10^4$ $M^{-1}$, respectively. Likewise, for **2** these values for $Fe^{3+}$ and 4-nitrophenol are $8.07 \times 10^4$ $M^{-1}$ and $4.5295 \times 10^4$ $M^{-1}$ respectively. These results suggest that **1** and **2** can be applied as promising sensors for the detection of $Fe^{3+}$ and 4-nitrophenol with excellent sensitivity and selectivity.

## DATA AVAILABILITY STATEMENT

The datasets generated for this study are available on request to the corresponding author. CCDC numbers 1919755 and 1919756

for 1 and 2, respectively, contain the crystal data of this article. These data are available from Cambridge Crystallographic Data Center via: https://www.ccdc.cam.ac.uk/structures/.

## AUTHOR CONTRIBUTIONS

SA and XC conceived the idea and helped in writing and proof outline. SH has a major role in the synthesis and characterization of compounds as well as in manuscript writing. ME and DA helped in data collection, structure solution, and refinement. WH wrote the crystal structure descriptions. SL and SM performed the photoluminescence related experiments.

## SUPPLEMENTARY MATERIAL

The Supplementary Material for this article can be found online at: https://www.frontiersin.org/articles/10.3389/fchem. 2019.00728/full#supplementary-material

## REFERENCES

Allendorf, M., Bauer, C., Bhakta, R., and Houk, R. (2009). Luminescent metal–organic frameworks. *Chem. Soc. Rev.* 38, 1330–1352. doi: 10.1039/b802352m

Antic-Fidancev, E., Serpaggi, F., and Férey, G. (2002). Optical study of praseodymium dicarboxylate $[Pr(H_2O)]_2[O_2C(CH_2)_3CO_2]_3.4H_2O$. *J. Alloys Compd.* 340, 88–94. doi: 10.1016/S0925-8388(02)00052-X

Armelao, L., Quici, S., Barigelletti, F., Accorsi, G., Bottaro, G., Cavazzini, M., et al. (2010). Design of luminescent lanthanide complexes: From molecules to highly efficient photo-emitting materials. *Coord. Chem. Rev.* 254, 487–505. doi: 10.1016/j.ccr.2009.07.025

Azab, H. A., Duerkop, A., Anwar, Z., Hussein, B. H., Rizk, M. A., and Amin, T. (2013). Luminescence recognition of different organophosphorus pesticides by the luminescent Eu(III)–pyridine-2, 6-dicarboxylic acid probe. *Anal. Chim. Acta.* 759, 81–91. doi: 10.1016/j.aca.2012.10.045

Bangaru, S., Muralidharan, G., and Brahmanandhan, G. M. (2010). Thermoluminescence and optical studies on X-irradiated terbium-doped potassium bromide crystals. *J. Lumin.* 130, 618–622. doi: 10.1016/j.jlumin.2009.11.005

Batool, S. S., Ahmad, S., Khan, I. U., and Ejaz, W. T. A. H. (2015). Structural characterization of a new copper(II) complex of 1,10-phenanthroline and benzoate $[Cu(phen)(C_6H_5CO_2^-)_2]$. *J. Struct. Chem.* 56, 387–391. doi: 10.1134/S0022476615020286

Baur, F., Glocker, F., and Jüstel, T. (2015). Photoluminescence and energy transfer rates and efficiencies in $Eu^{3+}$ activated $Tb_2Mo_3O_{12}$. *J. Mater. Chem. C* 3, 2054–2064. doi: 10.1039/C4TC02588A

Benmerad, B., Guehria-Laidoudi, A., Balegroune, F., Birkedal, H., and Chapuis, G. (2000). Polymeric aqua (glutarato)(hydrogen glutarato) lanthanum(III) monohydrate. *Acta Crystallogr. Sect. C Cryst. Struct. Commun.* 56, 789–792. doi: 10.1107/S010827010000500X

Binnemans, K. (2009). Lanthanide-based luminescent hybrid materials. *Chem. Rev.* 109, 4283–4374. doi: 10.1021/cr8003983

Bogale, R. F., Chen, Y., Ye, J., Yang, Y., Rauf, A., Duan, L., et al. (2017a). Highly selective and sensitive detection of 4-nitrophenol and Fe3+ ion based on a luminescent layered terbium(III) coordination polymer. *Sens. Actuat. B Chem.* 245, 171–178. doi: 10.1016/j.snb.2017.01.177

Bogale, R. F., Chen, Y., Ye, J., Zhang, S., Li, Y., Liu, X., et al. (2017b). A terbium (III)-based coordination polymer for selective and sensitive sensing of nitroaromatics and ferric ion: synthesis, crystal structure and photoluminescence properties. *N. J. Chem.* 41, 12713–12720. doi: 10.1039/C7NJ02492D

Bogale, R. F., Ye, J., Sun, Y., Sun, T., Zhang, S., Rauf, A., et al. (2016). Highly selective and sensitive detection of metal ions and nitroaromatic compounds by an anionic europium(III) coordination polymer. *Dalton Trans.* 45, 11137–11144. doi: 10.1039/C6DT01636G

Bromant, C., Nika, W., Pantenburg, I., and Meyer, G. (2005). Selten-erd-metall-koordinationspolymere: synthesen und kristallstrukturen von drei neuen Glutaraten,$[Pr_2(Glu)_3(H_2O)_4]\cdot5H_2O,[Pr$ $(Glu)(H_2O)_2]Cl$

and $[Er(Glu)(GluH)(H_2O)_2]$. *Z. Anorg. Allg. Chem.* 631, 2416–2422. doi: 10.1002/zaac.200500253

Bünzli, J.-C. G. (2010). Lanthanide luminescence for biomedical analyses and imaging. *Chem. Rev.* 110, 2729–2755. doi: 10.1021/cr900362e

Bünzli, J. C. G. (2015). On the design of highly luminescent lanthanide complexes. *Coord. Chem. Rev.* 293, 19–47. doi: 10.1016/j.ccr.2014.10.013

Chen, B., Wang, L., Xiao, Y., Fronczek, F. R., Xue, M., Cui, Y., et al. (2009). A luminescent metal–organic framework with lewis basic pyridyl sites for the sensing of metal ions. *Angew. Chem. Int. Ed.* 48, 500–503. doi: 10.1002/anie.200805101

Cui, G. H., Li, J. R., Zhang, R.-H., and Bu, X.-H. (2005). Hydrothermal synthesis, crystal structures and luminescent properties of two new Ln(III)–succinate (Ln= Eu, Tb) complexes exhibiting three dimensional networks. *J. Mol. Struct.* 740, 187–191. doi: 10.1016/j.molstruc.2005.01.049

Cui, Y., Yue, Y., Qian, G., and Chen, B. (2011). Luminescent functional metal–organic frameworks. *Chem. Rev.* 112, 1126–1162. doi: 10.1021/cr200101d

Daiguebonne, C., Kerbellec, N., Guillou, O., Bünzli, J.-C., Gumy, F., Catala, L., et al. (2008). Structural and luminescent properties of micro-and nanosized particles of lanthanide terephthalate coordination polymers. *Inorg. Chem.* 47, 3700–3708. doi: 10.1021/ic702325m

De Oliveira, C. F., Da Silva, F. F., Malvestiti, I., Malta, V. R. D. S., Dutra, J. D. L., Da Costa, N. B Jr., et al. (2013). Synthesis, characterization, luminescent properties and theoretical study of two new coordination polymers containing lanthanide [Ce(III) or Yb(III)] and succinate ions. *J. Mol. Struct.* 1041, 61–67. doi: 10.1016/j.molstruc.2013.03.001

Deacon, G. B., and Philips, R. J. (1980). Relationship between the carbon-oxygen stretching frequencies of carboxylate complexes and the type of carboxylate coordination. *Coord. Chem. Rev.* 33, 227–250. doi: 10.1016/S0010-8545(00)80455-5

Dong, X. Y., Wang, R., Wang, J. Z., Zang, S. Q., and Mak, T. C. (2015). Highly selective Fe 3+ sensing and proton conduction in a water-stable sulfonate–carboxylate Tb–organic-framework. *J. Mater. Chem. A* 3, 641–647. doi: 10.1039/C4TA04421E

Feng, J., and Zhang, H. (2013). Hybrid materials based on lanthanide organic complexes. *Chem. Soc. Rev.* 42, 387–410. doi: 10.1039/C2CS35069F

Gai, Y. L., Jiang, F. L., Chen, L., Bu, Y., Su, K. Z., Al-Thabaiti, S. A., et al. (2013). Photophysical studies of europium coordination polymers based on a tetracarboxylate ligand. *Inorg. Chem.* 52, 7658–7665. doi: 10.1021/ic400777c

Gao, M. L., Wei, N., and Han, Z. B. (2016). Anionic metal–organic framework for high-efficiency pollutant removal and selective sensing of Fe(III) ions. *RSC Adv.* 6, 60940–60944. doi: 10.1039/C6RA08500H

Głowiak, T., Legendziewicz, J., Dao, C. N., and Huskowska, E. (1987). Crystal structure and spectroscopy of lanthanide complexes with glutaric acid $[Ln(C_5H_6O_4)(H_2O)_3]\cdot ClO_4$. *J. Less Common Met.* 134, 153–168. doi: 10.1016/0022-5088(87)90553-4

Gu, X., and Xue, D. (2006). Selected controlled synthesis of three-dimensional 4d−4f heterometallic coordination frameworks by lanthanide

carboxylate subunits and silver centers. *Cryst. Growth Des.* 6, 2551–2557. doi: 10.1021/cg060485o

Heffern, M. C., Matosziuk, L. M., and Meade, T. J. (2013). Lanthanide probes for bioresponsive imaging. *Chem. Rev.* 114, 4496–4539. doi: 10.1021/cr400477t

Hou, Y. L., Cheng, R. R., Xiong, G., Cui, J. Z., and Zhao, B. (2014). Structures, luminescent and magnetic properties of a series of (3, 6)-connected lanthanide–organic frameworks. *Dalton Trans.* 43, 1814–1820. doi: 10.1039/C3DT52305E

Huang, Y. G., Yuan, D. Q., Gong, Y. Q., Jiang, F. L., and Hong, M. C. (2008). Synthesis, structure and luminescent properties of lanthanide–organic frameworks based on pyridine-2, 6-dicarboxylic acid. *J. Mol. Struct.* 872, 99–104. doi: 10.1016/j.molstruc.2007.02.020

Hussain, S., Chen, X., Harrison, W. T., Ahmad, S., Elsegood, M., and Muhammad, S. (2019). Synthesis, thermal, structural analyses and photoluminescent properties of a new family of malonate-containing lanthanide(III) coordination polymers. *Front. Chem.* 7, 260. doi: 10.3389/fchem.2019.00260

Hussain, S., Khan, I., Harrison, W., and Tahir, M. (2015a). Crystal structures and characterization of two rare-earth-glutarate coordination networks: One-dimensional [Nd $(C_5H_6O_4)(H_2O)_4$]• Cl and three-dimensional [Pr$(C_5H_6O_4)(C_5H_7O_4)(H_2O)$]•$H_2O$. *J. Struct. Chem.* 56, 934–941. doi: 10.1134/S0022476615050169

Hussain, S., Khan, I., Harrison, W. T., Tahir, M., and Ahmad, S. (2015b). Crystal structures and characterization of two one-dimensional coordination polymers containing $Ln^{3+}$ ions and anthranilic ($C_7H_6NO_2^-$) anions. *J. Struct. Chem.* 56, 126–133.doi: 10.1134/S0022476615010187

Hussain, S., Khan, I. U., Akkurt, M., Ahmad, S., and Tahir, M. N. (2014). Synthesis and structural characterization of binuclear ytterbium(III) complexes with 2-amino and 3-amino benzoic acid. *Russ. J. Coord. Chem.* 40, 686–694. doi: 10.1134/S107032841409005X

Hussain, S., Khan, I. U., Elsegood, M. R., Jabeen, N., Tahir, M. N., Ahmad, S., et al. (2018). Synthesis and structural characterization of dinuclear cerium(III) and erbium(III) complexes of nicotinic acid or 2-aminobenzoic acid. *Polyhedron.* 151, 452–457.doi: 10.1016/j.poly.2018.05.057

Kumar, M., Kariem, M., Sheikh, H. N., Frontera, A., Seth, S. K., and Jassal, A. K. (2018). A series of 3D lanthanide coordination polymers decorated with a rigid 3, 5-pyridinedicarboxylic acid linker: syntheses, structural diversity, DFT study, Hirshfeld surface analysis, luminescence and magnetic properties. *Dalton Trans.* 47, 12318–12336. doi: 10.1039/C8DT02429D

Legendziewicz, J., Keller, B., Turowska-Tyrk, I., and Wojciechowski, W. (1999). Synthesis, optical and magnetic properties of homo-and heteronuclear systems and glasses containing them. *New J. Chem.* 23, 1097–1103. doi: 10.1039/a905284d

Li, Q.-P., and Yan, B. (2012). Luminescent hybrid materials of lanthanide β-diketonate and mesoporous host through covalent and ionic bonding with anion metathesis. *Dalton Trans.* 41, 8567–8574. doi: 10.1039/c2dt30364g

Li, Y., Zhang, S., and Song, D. (2013). A luminescent metal–organic framework as a turn-on sensor for DMF vapor. *Angew. Chem. Int. Ed.* 52, 710–713. doi: 10.1002/anie.201207610

Manna, S. C., Zangrando, E., Bencini, A., Benelli, C., and Chaudhuri, N. R. (2006). Syntheses, crystal structures, and magnetic properties of [Ln(III)$_2$ (Succinate)$_3(H_2O)_2$]0.5H$_2$O[Ln= Pr, Nd, Sm, Eu, Gd, and Dy] polymeric networks: unusual ferromagnetic coupling in Gd derivative. *Inorg. Chem.* 45, 9114–9122. doi: 10.1021/ic060807d

Marques, L. F., Correa, C. C., Ribeiro, S. J., Dos Santos, M. V., Dutra, J. D. L., Freire, R. O., et al. (2015). Synthesis, structural characterization, luminescent properties and theoretical study of three novel lanthanide metal-organic frameworks of Ho(III), Gd(III) and Eu(III) with 2, 5-thiophenedicarboxylate anion. *J. Solid State Chem.* 227, 68–78. doi: 10.1016/j.jssc.2015.03.020

Medina-Velazquez, D., Caldiño, U., Morales-Ramirez, A., Reyes-Miranda, J., Lopez, R., Escudero, R., et al. (2019). Synthesis of luminescent terbium-thenoyltriflouroacetone MOF nanorods for green laser application. *Opt. Mater.* 87, 3–10. doi: 10.1016/j.optmat.2018.08.021

Miyata, K., Konno, Y., Nakanishi, T., Kobayashi, A., Kato, M., Fushimi, K., et al. (2013). Chameleon luminophore for sensing temperatures: control of metal-to-metal and energy back transfer in lanthanide coordination polymers. *Angew. Chem. Int. Ed.* 52, 6413–6416. doi: 10.1002/anie.201301448

Qiongyan, Y., Xiuxia, Z., Maosheng, L., Jianqiao, C., Zhengyuan, Z., Xia, Y., et al. (2008). Syntheses, characterization, and luminescence of two lanthanide complexes [Ln$_2$(acetate)$_6$ (H$_2$O)$_4$]·4H$_2$O (Ln= Tb (1), Sm (2). *J. Rare Earth* 26, 178–184. doi: 10.1016/S1002-0721(08)60061-7

Rahahlia, N., Benmerad, B., Guehria-Laidoudi, A., Dahaoui, S., and Lecomte, C. (2006). Poly [[tetraaqua-μ$_4$-glutarato-cerium(III)] chloride dihydrate]. *Acta Crystallogr. E* 62, m2145–m2147. doi: 10.1107/S1600536806030741

Rahahlia, N., Benmerad, B., Guehria-Laïdoudi, A., Dahaoui, S., and Lecomte, C. (2007). Three-dimensional ionic frameworks built up from La(III) and Ce(III) succinates. *J. Mol. Struct.* 833, 42–48. doi: 10.1016/j.molstruc.2006.08.029

Rao, X., Song, T., Gao, J., Cui, Y., Yang, Y., Wu, C., et al. (2013). A highly sensitive mixed lanthanide metal–organic framework self-calibrated luminescent thermometer. *J. Am. Chem. Soc.* 135, 15559–15564. doi: 10.1021/ja407219k

Räsänen, M., Takalo, H., Rosenberg, J., Mäkelä, J., Haapakka, K., and Kankare, J. (2014). Study on photophysical properties of Eu(III) complexes with aromatic β-diketones–Role of charge transfer states in the energy migration. *J. Lumin.* 146, 211–217. doi: 10.1016/j.jlumin.2013.09.076

Reinhard, C., and Güdel, H. U. (2002). High-resolution optical spectroscopy of Na$_3$[Ln(dpa)]·13H$_2$O with Ln = Er$^{3+}$, Tm$^{3+}$, Yb$^{3+}$. *Inorg. Chem.* 41, 1048–1055. doi: 10.1021/ic0108484

Serpaggi, F., and Férey, G. (1998). Hybrid open frameworks (MIL-n). Part 4 Synthesis and crystal structure of MIL-8, a series of lanthanide glutarates with an open framework,[Ln (H$_2$O)]$_2$ O$_2$C(CH$_2$)$_3$CO$_2$]$_3$·4H$_2$O. *J. Mater. Chem.* 8, 2737–2741. doi: 10.1039/a802713g

Sheldrick, G. M. (2015). Crystal structure refinement with SHELXL. *Acta Crystallogr. C Struct. Chem.* 71, 3–8. doi: 10.1107/S2053229614024218

Song, Y., Wang, X., Zhang, S., Wang, J., Gao, S., and Chen, S. (2016). Lanthanide-coordination polymers with pyridinedicarboxylic acids: syntheses, structures, and luminescent properties. *Z. Anorg. Allg. Chem.* 642, 681–691. doi: 10.1002/zaac.201600135

Tan, C., and Wang, Q. (2011). Reversible terbium luminescent polyelectrolyte hydrogels for detection of H$_2$PO$_4^-$ and HSO$_4^-$ in water. *Inorg. Chem.* 50, 2953–2956. doi: 10.1021/ic102366v

Tsaryuk, V. I., Zhuravlev, K. P., Vologzhanina, A. V., Kudryashova, V. A., and Zolin, V. F. (2010). Structural regularities and luminescence properties of dimeric europium and terbium carboxylates with 1,10-phenanthroline (CN = 9). *J. Photochem. Photobiol. A Chem.* 211,7–19. doi: 10.1016/j.jphotochem.2010.01.012

Wang, H. M., Liu, H. P., Chu, T. S., Yang, Y. Y., Hu, Y. S., Liu, W. T., et al. (2014). A luminescent terbium coordination polymer for sensing methanol. *RSC Adv.* 4, 14035–14041. doi: 10.1039/C4RA00745J

Wang, J. L., Hou, K. L., Bai, F. Y., Xing, Y. H., and Shi, Z. (2012). Hydrothermal synthesis, crystal structure, and photoluminescence of novel lanthanide metal organic frameworks constructed from 1, 4-benzene-dicarboxylic acid and 1, 2, 4, 5-benzenetetracarboxylic acid as ligands. *Struct. Chem.* 23, 275–285. doi: 10.1007/s11224-011-9870-4

Wang, Z., Bai, F. Y., Xing, Y. H., Xie, Y., Zeng, X. Q., Ge, M. F., et al. (2010a). Rigid and flexible lanthanide complexes with an infinite Ln–O–Ln framework: synthesis, structure and properties. *J. Inorg. Organomet. Polym. Mater.* 20, 242–249.

Wang, Z., Xing, Y. H., Wang, C. G., Sun, L. X., Zhang, J., Ge, M. F., et al. (2010b). Synthesis, structure and luminescent properties of coordination polymers with 1, 2-benzenedicarboxylic acid and a series of flexible dicarboxylate ligands. *CrystEngComm.* 12, 762–773. doi: 10.1039/B916127A

Werts, M. H. (2005). Making sense of lanthanide luminescence. *Sci. Prog.* 88, 101–131. doi: 10.3184/003685005783238435

Wong, K. L., Law, G. L., Yang, Y. Y., and Wong, W. T. (2006). A highly porous luminescent terbium–organic framework for reversible anion sensing. *Adv. Mater.*18, 1051–1054. doi: 10.1002/adma.200502138

Xiang, S., Bao, D. X., Wang, J., Li, Y. C., and Zhao, X.-Q. (2017). Luminescent lanthanide coordination compounds with pyridine-2, 6-dicarboxylic acid. *J. Lumin.* 186, 273–282. doi: 10.1016/j.jlumin.2017.02.037

Yan, B., Bai, Y., and Chen, Z. (2005). Synthesis, structure and luminescence of novel 1D chain coordination polymers [Ln(isophth)(Hisophth)(H$_2$O)$_4$·4H$_2$O]$_n$ (Ln= Sm, Dy). *J. Mol. Struct.*741, 141–147. doi: 10.1016/j.molstruc.2005.02.004

Zehnder, R. A., Jenkins, J., Zeller, M., Dempsey, C., Kozimor, S. A., Jackson, G., et al. (2018). Conversion of lanthanide glutarate chlorides with interstitial THF

into lanthanide glutarates with unprecedented topologies. *Inorg. Chim. Acta.* 471, 502–512. doi: 10.1016/j.ica.2017.11.050

Zhang, C. Z., Mao, H. Y., Wang, Y. L., Zhang, H. Y., and Tao, J. C. (2007). Syntheses of two new hybrid metal-organic polymers using flexible aliphatic dicarboxylates and pyrazine: crystal structures and magnetic studies. *J. Phys. Chem. Solids* 68, 236–242. doi: 10.1016/j.jpcs.2006.11.001

Zhang, L., Li, B., Su, Z., and Yue, S. (2010). Novel rare-earth(III)-based water soluble emitters for Fe(III) detection. *Sens. Actuat. B Chem.* 143, 595–599. doi: 10.1016/j.snb.2009.09.056

Zhao, B., Chen, X. Y., Cheng, P., Liao, D. Z., Yan, S. P., and Jiang, Z. H. (2004). Coordination polymers containing 1D channels as selective luminescent probes. *J. Am. Chem. Soc.* 126, 15394–15395. doi: 10.1021/ja047141b

Zhao, L., Liu, Y., He, C., Wang, J., and Duan, C. (2014a). Coordination-driven nanosized lanthanide 'Molecular Lanterns' as luminescent chemosensors for the selective sensing of magnesium ions. *Dalton Trans.* 43, 335–343. doi: 10.1039/C3DT51900G

Zhao, X. J., Yang, J. H., Liu, Y., Gao, P. F., and Li, Y. F. (2014b). Metal–organic coordination polymers of $Tb_{2-x} Eu_x(BDC)_3(H_2O)_n$ with tunable fluorescence and smart response toward aldehydes ($0 \leq x \leq 2$, BDC= 1,4-benzenedicarboxylate). *RSC Adv.* 4, 2573–2576. doi: 10.1039/C3RA45725G

Zheng, M., Tan, H., Xie, Z., Zhang, L., Jing, X., and Sun, Z. (2013). Fast response and high sensitivity europium metal organic framework fluorescent probe with chelating terpyridine sites for $Fe^{3+}$. *ACS Appl. Mater. Interfaces*, 5, 1078–1083. doi: 10.1021/am302862k

Zhou, Z., Tan, C., Zheng, Y., and Wang, Q. (2013). Electrochemical signal response for vitamin B1 using terbium luminescent nanoscale building blocks as optical sensors. *Sens. Actuat. B Chem.* 188, 1176–1182. doi: 10.1016/j.snb.2013.08.032

Zhu, T., Ikarashi, K., Ishigaki, T., Uematsu, K., Toda, K., Okawa, H., et al. (2009). Structure and luminescence of sodium and lanthanide(III) coordination polymers with pyridine-2, 6-dicarboxylic acid. *Inorg. Chim. Acta* 362, 3407–3414. doi: 10.1016/j.ica.2009.01.036

Zhuravlev, K. P., Tsaryuk, V. I., Pekareva, I. S., Sokolnicki, J., and Klemenkova, Z. S. (2011). Europium and terbium ortho-, meta-, and para-methoxybenzoates: Structural peculiarities, luminescence, and energy transfer. *J. Photochem. Photobiol. A Chem.* 219, 139–147. doi: 10.1016/j.jphotochem.2011.02.003

# Enhanced Electromagnetic Absorption Properties of Commercial Ni/MWCNTs Composites by Adjusting Dielectric Properties

Pei-Yan Zhao, Hui-Ya Wang* and Guang-Sheng Wang*

School of Chemistry, Beihang University, Beijing, China

In this manuscript, we constructed a Ni/MWCNTs absorber and properly adjusted the permittivity resulted from absorber content in the PVDF to optimize impedance matching properties. Both $\varepsilon'$ and $\varepsilon''$ increase obviously with the increasing content of Ni/MWCNTs in PVDF, demonstrating that dielectric properties are dependent on the conductivity. Moderate dielectric properties and excellent impedance matching can be obtained for the filler content of 20 wt% Ni/MWCNTs. Reasonable impedance matching allows electromagnetic waves to propagate into the materials and finally realize energy dissipation through dielectric loss and interfacial polarization. As expected, the minimum reflection loss (*RL*) of −46.85 dB at 6.56 GHz with a low filler loading (20 wt%) and wide effective bandwidth (*RL*<-10 dB) of 14.0 GHz in the thickness range of 1.5–5.0 mm was obtained for the commercial Ni/MWCNTs composites, which is promising for mass production in industrial applications. Our findings offer an effective and industrialized way to design high-performance material to facilitate the research in microwave absorption.

Keywords: Ni/MWCNTs, dielectric properties, microwave absorption, filling content, impedance matching

## INTRODUCTION

Nowadays, electromagnetic interference and pollution have become a potential hazard to the normal operation of electronic equipment and human health, accompanied by the massive usage of electronic devices in civil and military applications (Yin et al., 2016; Fang et al., 2017; Yang et al., 2018). It is in urgent need to exploit electromagnetic wave absorbers, which possess excellent absorption ability and wide effective band at a relatively thin thickness (Zhou et al., 2017). Based on the loss mechanism, microwave absorbing materials can be usually divided into dielectric loss that mainly attenuated energy through polarization effects and magnetic loss materials, which dissipated energy by resonances and eddy current effects (Yan et al., 2017; Hu P. P. et al., 2019). Carbon materials, dielectric loss materials, have been proved as effective microwave absorption materials due to their superior electronic properties, large specific surface area, and low density (Zhao et al., 2016; Liu Y. et al., 2018; Wang Y. et al., 2019). In particular, carbon nanotubes (CNTs) with unique one-dimensional tubular nanostructure can enhance interface polarization and offer enormous sites for electromagnetic wave scattering, which contributed to electromagnetic wave attenuation (Chen et al., 2017). However, it is difficult for unilateral loss materials to achieve a desired microwave absorption on account of the poor impedance matching, which greatly limits their applications (Wang L. et al., 2019).

Accordingly, incorporation of dielectric loss materials with magnetic loss media may be an ideal method to further enhance the microwave attenuation properties (Xu J. et al., 2018; Xu et al., 2019). Till now, composites based on CNTs and various magnetic nanoparticles have been extensively utilized for microwave absorbing materials (Wang et al., 2016; Kuang et al., 2019). Hu Q. et al. (2019) constructed $NiCo_2O_4$@CNTs hybrid sponges via a facile hydrothermal method and heat treatment. The resultant composites possess a minimum reflection loss of −45.1 dB and an effective absorption bandwidth of 4.1 GHz. Chen et al. (2015) reported a novel 3D $Fe_3O_4$-MWCNTs nanostructures with enhanced tunable microwave absorption. When the thickness was 6.8 mm, the minimum reflection loss value of −23.0 dB and −52.8 dB were observed at 4.1 GHz and 12.8 GHz, which are superior to those of pure MWCNTs as well as other hybrids of $Fe_3O_4$. As expected, the dielectric–magnetic matching components greatly contribute to the improvement of absorbing properties.

Compared with traditional ferrite absorbing materials, transition metal nickel has a higher saturation magnetization value (55 emu/g at room temperature) and Snoek limit (high natural resonance of 8.23 GHz), allowing a high relative permeability in high-frequency range to achieve good impedance matching (Liu D. et al., 2018; Xie P. et al., 2018). Ning et al. (2018) prepared heterostructural Ni/N-CNTs by a modified one-step pyrolysis process, which demonstrated promising candidates in microwave absorption (MWA) application. The minimum reflection loss of as-synthesized samples with 10 wt% loading is up to −34.1 dB and the effective absorption bandwidth is as wide as 4.72 GHz, which benefits from the optimized impedance matching and the intense dielectric relaxation. Zhang et al. (2019c) successfully synthesized special hierarchical yolk-shell ZnO-Ni@CNT microspheres by controlling pyrolysis of the Zn-Ni bimetallic metal-organic framework, which displayed a minimum reflection loss value of −58.6 dB at 2.3 mm, and the effective absorption frequency range of 4.8 GHz. Such superior performance of ZnO-Ni@CNT microspheres benefited from well-matched impedance, special porous hierarchical structure, interfacial polarization, conductive loss, and multiple reflections. Although these works improved the microwave absorption properties to a certain extent, low yield suppresses the development and practical applications. It remains a great challenge to prepare the absorbers with high efficiency and wide bandwidth in large scales.

The commercial Ni/MWCNTs composites with high yield are conducive to prepare the absorbers with high efficiency and wide bandwidth in large scales. In addition, PVDF has been widely utilized in modern electronic appliances because of its compact size, superior hydrophobicity, anticorrosion resistance, and excellent flexibility. Therefore, we purchased Ni/MWCNTs material and adjusted filler loading in PVDF matrix to obtain enhanced microwave absorption property that can be widely used. As known, a moderate conducting material is suitable as an absorbing material, whereas material with high conductivity can be a promising candidate as an electromagnetic shield. In this context, varying the content of Ni/MWCNTs in PVDF is an efficient method to regulate permittivity and impedance matching, thus imparting it with the potential for desired absorbing property. Moreover, the unique one-dimensional tubular nanostructure offers tremendous sites for electromagnetic wave scattering. A remarkable reflection loss of −46.85 dB and a broad bandwidth of 3.2 GHz are achieved by tailoring the filler content with 20 wt%.

# EXPERIMENTAL

## Materials

The Ni/MWCNTs (mean diameter 50 nm, length <10 μm, and Ni content of 60 wt%) were purchased from Nanjing Xianfeng technology co. Ltd and used without further treatment. The commercial Ni/MWCNTs powder was prepared by electroplating nickel on the surface of CNTs prepared by chemical vapor deposition method. Polyvinylidene fluoride (PVDF) and N,N-dimethylformyl (DMF) were supplied by Beijing Chemical Factory (Beijing, China).

## Characterization

The crystalline structure of the Ni/MWCNTs was characterized using X-ray powder diffraction (XRD) on a Rigaku Dmax 2200 diffractometer with Cu Kα radiation (λ = 1.5416 Å). The morphology and microstructures were analyzed by a scanning electron microscope (SEM, Quanta 250 FEG) a field emission scanning electron microscope (FESEM, JEOL JSM-7500F), and a transmission electron microscope (TEM, JEOL JEM-2100F). Raman spectroscopy (Horiba Jobin Yvon, LabRAM HR800) was used to record the properties of samples in the range of 200–2,000 cm$^{-1}$ with an excitation wavelength of 514.5 nm. The chemical composition of the samples was examined by X-ray photoelectron spectroscopy (XPS) using ESCA Lab MKII X-ray photoelectron spectrometer. The magnetic properties were carried out on a Lakeshore Vibrating Sample Magnetometer (VSM, Riken Denshi Co. Ltd, Japan).

## Measurements of Electromagnetic Parameters

The relative complex permeability and permittivity were measured by a vector network analyzer (Agilent, PNA 5244A). Before test, Ni/MWCNTs and PVDF were mixed in DMF with different mass fractions evenly and dried to form a film, which was then being pressed into a ring-like compact structure (with a 3.04-mm inner diameter and a 7.00-mm outer diameter).

# RESULTS AND DISCUSSION

The crystal structure of the Ni/MWCNTs composite was measured by XRD, as displayed in **Figure 1A**. The diffraction peak at 26.1° can be assigned to the (002) reflection of the MWCNTs, indicating that the CNTs structure was not destroyed (Zhao et al., 2010). It is noted that other diffraction peaks located at 2θ = 33.8° and 44.8° can be indexed to the $NiP_2$ and metallic Ni (111) structure, respectively (Kim et al., 2014; Yim et al., 2016). The Raman spectroscopy was also tested to aid in the investigation of the compositions. As can be seen in **Figure 1B**, the existence of MWCNTs is clearly confirmed by

the featured D band at 1,330.3 cm$^{-1}$ and D band at 1,581.9 cm$^{-1}$. D peak is related to disordered structure of amorphous carbon, forbidden in complete graphitization and became active in the presence of disordered or finite size crystals of graphite, while the G peak corresponds to the E$_{2g}$ mode of the telescopic vibration of the $sp^2$ bond (Ferrari and Robertson, 2000; Cheng et al., 2018). Meanwhile, the intensity ratio of D band to G band ($I_D/I_G$) can be utilized to assess the disorder degree of carbon materials. A high $I_D/I_G$ value of the Ni/MWCNTs composite suggested the presence of numerous defects in the graphitized structure or the edges, which may have contributed to induce dipole/electron polarization (Wen et al., 2014). The information and atomic structure were obtained by the XPS technique. The survey scan displayed in **Figure 1C** confirms the presence of Ni, C, and O elements in the composites. In the Ni 2p spectrum of the sample (**Figure 1D**), the two satellite peaks of Ni that are located at 861.8 and 879.8 eV can be observed (Fang et al., 2019). Besides, two peaks with a binding energy of 856.0 and 873.6 eV are assigned to Ni$^{2+}$ $2p_{3/2}$ and Ni$^{2+}$ $2p_{1/2}$, respectively (Zhang et al., 2019a). The result demonstrates that Ni–C or Ni–O–C bonds exist on the Ni/MWCNTs surface, which is

presumably attributed to a partial oxidation of surface metal Ni species (Yang et al., 2019).

To further investigate the microstructure and morphology of Ni/MWCNTs composites, SEM and TEM were conducted and shown in **Figure 2**. As observed from **Figures 2A,B**, Ni nanoparticles were anchored unevenly to the surface of the MWCNTs, indicating the successful synthesis of Ni/MWCNTs composites. The Ni/MWCNTs composites with a diameter of 25–73 nm and length up to several micrometers are aggregated into a porous three-dimensional network. The TEM image in **Figures 2C,D** further indicates that conductive MWCNTs can serve as the skeleton to deposit Ni nanoparticles with an obvious particle accumulation, and then self-assemble into irregular nanoparticles.

Magnetic hysteresis loops of Ni/MWCNTs composite were conducted by a vibrating sample magnetometer (VSM) at room temperature to investigate magnetic properties. As seen from **Figure S1**, typical S-type M-H curve indicates ferromagnetic behavior with a saturating reversible magnetization. The saturation magnetization (*Ms*) of Ni/MWCNTs is 0.76 emu/g, which is lower than bulk nickel (55 emu/g) and elemental nickel
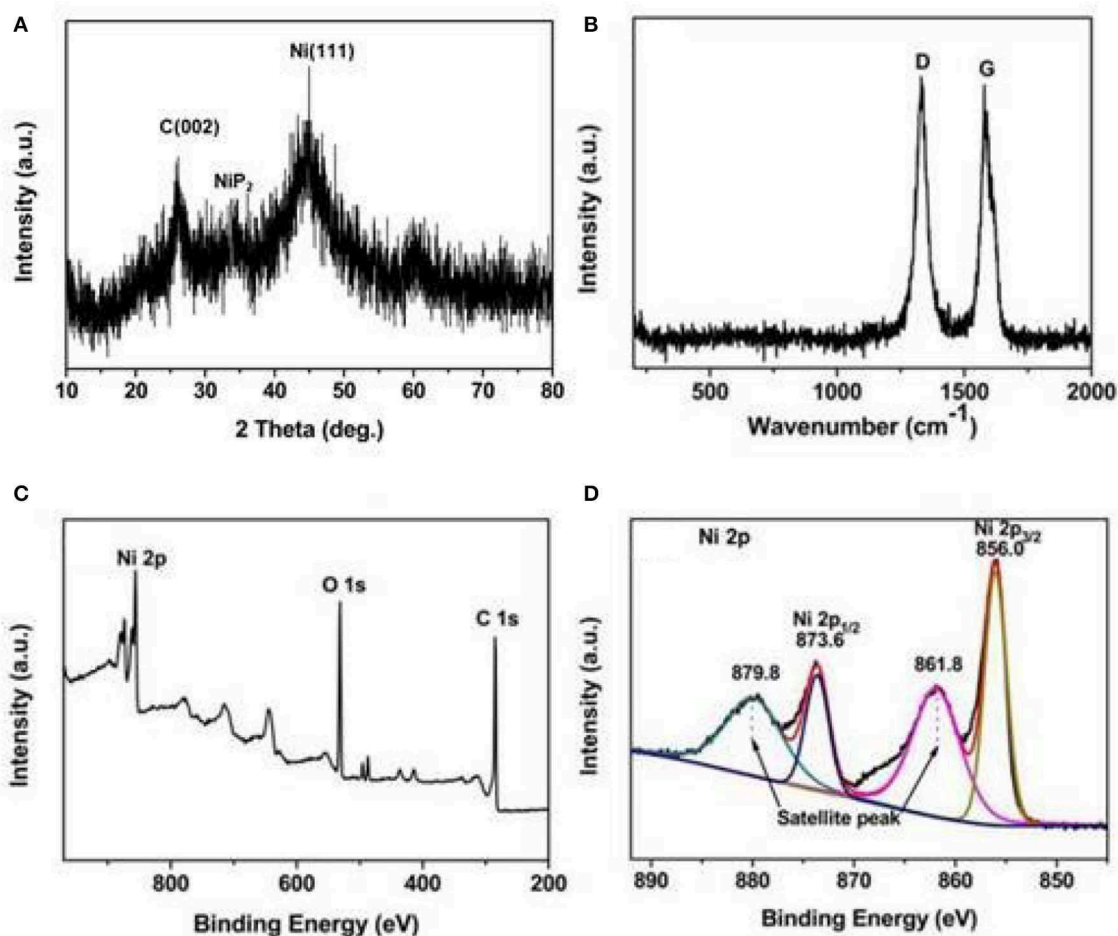


**FIGURE 1 |** XRD patterns **(A)**, Raman spectra **(B)**, and XPS spectra of survey spectrum **(C)**, and Ni 2p **(D)** of Ni/MWCNTs composites.
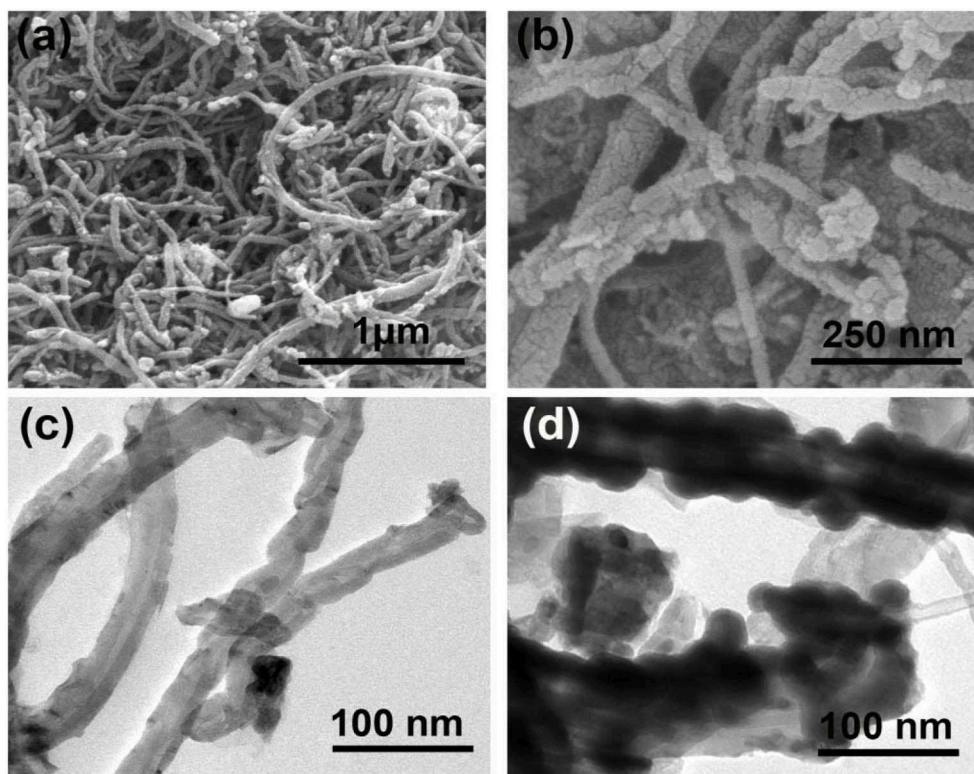
**FIGURE 2 |** SEM **(A,B)** and TEM **(C,D)** image of Ni/MWCNTs composites.

reported in other literatures (42 emu/g) (Liu et al., 2016). Such a decline can be attributed to the existence of nonmagnetic carbon with low crystallinity.

The microwave absorption properties, in terms of reflection loss (*RL*), are calculated from the relative permeability and permittivity through the following transmission line theory (Xie et al., 2017; Wang et al., 2018):

$$RL = 20 \log \left| \frac{Z_{in} - 1}{Z_{in} + 1} \right| \tag{1}$$

$$Z_{in} = Z_0 \sqrt{\frac{\mu_r}{\varepsilon_r}} \tanh \left( j \frac{2\pi f d}{c} \sqrt{\mu_r \varepsilon_r} \right) \tag{2}$$

where $Z_0$ and $Z_{in}$ are the intrinsic impedance of free space and the input impedance of the absorber, respectively. *d*, *c*, and *f* represent the thickness of absorber, the velocity of light, and the frequency of electromagnetic wave, respectively. Commonly, the excellent microwave absorption materials are required to have a *RL* value lower than −10 dB within a wide bandwidth under thin thickness. **Figure 3** presents the *RL* curves of Ni/MWCNTs absorber with different loading contents in the frequency range of 2–18 GHz. It is clear that the microwave absorption property of Ni/MWCNTs composite is significantly enhanced initially and then decreases with the increase of filler loading. The minimum *RL* values shift to a lower-frequency range with the increases of Ni/MWCNTs filler loadings, which can be reasonably ascribed to interfacial polarization that usually

occurs in the low-frequency stage. For the composites containing 1 wt% Ni/MWCNTs (**Figure 3A**), it exhibits poor microwave absorption capacity with the *RL* value of −1.6 dB over the tested frequency of 2–18 GHz. Such poor absorption property also emerges in other filler loading of 5 wt and 10 wt%, which is mainly originated from the weak dielectric loss derived from low conductivity and interfacial polarization (**Figures 3B,C**). However, when the filler loading is 20 wt%, the minimum *RL* value of the materials reaches −46.85 dB at 6.56 GHz with a thickness of 3.7 mm, and the effective bandwidth is up to 3.20 GHz (**Figure 3D**). Besides, the *RL* value exceeding −10 dB can be achieved in the range of 4.0–18.0 GHz by varying thickness from 1.5 to 5.0 mm. As for sample with 30 wt and 40 wt% filler contents shown in **Figures 3E,F**, it exhibits poor absorbing performance because of the high conductivity brought by the formation of a conductive network, which makes electromagnetic waves reflect on the surface of materials. Thus, the samples can achieve better microwave absorption by adjusting the absorber thickness and filler loading.

Moreover, it should be pointed out that the optimal *RL* peaks are shifted toward lower frequency along with the change of thickness from 1.0 to 5.0 mm. This interesting phenomenon is usually expressed by the 1/4 wavelength cancellation equation (Liu H. et al., 2018):

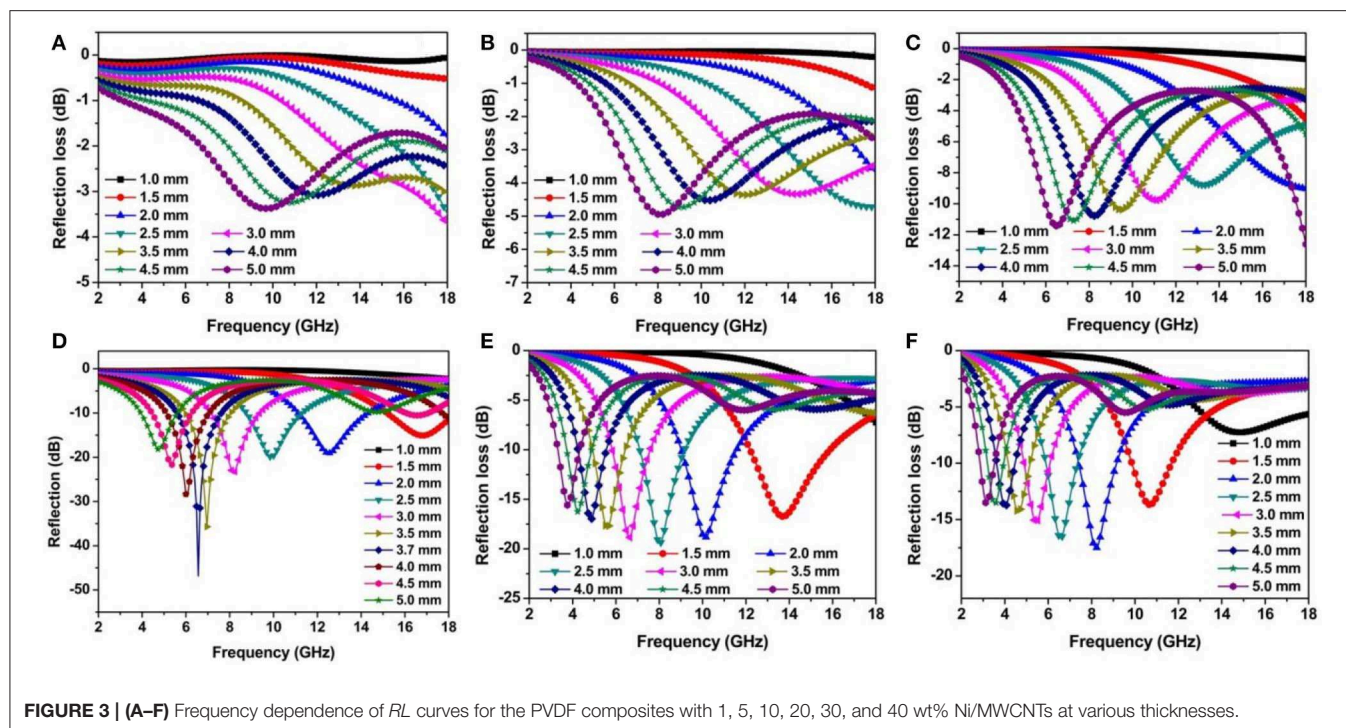$$t_m = \frac{nc}{4f_m \sqrt{\varepsilon_r \mu_r}} \tag{3}$$

**FIGURE 3 | (A–F)** Frequency dependence of *RL* curves for the PVDF composites with 1, 5, 10, 20, 30, and 40 wt% Ni/MWCNTs at various thicknesses.

Obviously, the peak frequency is inversely proportional to the thickness of absorbers. As shown in **Figure S2**, this sample obeys the λ/4 model, meaning the reflected electromagnetic waves from both the air–absorber interface and the absorber–metal background interface are out of phase by 180°, making them cancel out and then resulting in a minimum *RL* value (Lou et al., 2018).

To further investigate the associated wave absorption mechanisms and influence of the filler content on microwave absorption properties, frequency-dependent complex permittivity and permeability were examined in 2–18 GHz for Ni/MWCNTs sample loading from 1 wt to 40 wt%. As known, the complex relative permittivity ($\varepsilon_r$) and permeability ($\mu_r$) highly determine reflection and attenuation characteristics of absorbers. In general, the real permittivity ($\varepsilon'$) and permeability ($\mu'$) stand for the storage capability of the electric and magnetic energy, while the imaginary parts ($\varepsilon''$ and $\mu''$) correspond to the dissipation capability (Xie A. et al., 2018). As shown in **Figures 4A,B**, the $\varepsilon'$ values of six different loading samples over 2–18 GHz present a declining trend with a certain degree of fluctuations from 3.20 to 2.99, 3.99 to 3.86, 6.33 to 5.43, 10.77 to 9.07, 15.49 to 12.32, and 19.81 to 18.78, respectively. Both $\varepsilon'$ and $\varepsilon''$ increase obviously with the increasing content of Ni/MWCNTs in PVDF, demonstrating that dielectric properties are dependent on the conductivity (Duan et al., 2018). The increase is mainly determined by the interfacial polarization and enhanced conductivity resulted from the gradually establishment of a large conductive networks as the increasing filler loading (**Figure S5**), which is beneficial for electron transport and space charge polarization (Xu W. et al., 2018; Wu et al., 2019). Based on the free electron theory (Liang et al., 2016; Guan et al., 2018; Lu et al., 2019): $\sigma = 2\pi f \varepsilon'' \varepsilon_0$, the

frequency-dependent conductivity profiles were characterized in **Figure S3**. The conductivity values of 0.04–0.73 S/m are obtained for the Ni/MWCNTs composite with the loading of 1, 5, and 10 wt% in 2–18 GHz. For the filler content of 40 wt%, it shows much larger values from 0.45 to 0.92 S/m in the same frequency range. Undoubtedly, the ameliorated conductivity will enhance electromagnetic performance, but the high electrical conductivity leads to the imbalance of impedance matching and weakens microwave absorption property. As observed in **Figures 4C,D**, the $\mu'$ and $\mu''$ values of different filler samples exhibit pretty similar variation trends, showing a sharp decrease and then keep relatively flat with a slight fluctuation in 8.0–18.0 GHz. This is mainly ascribed to the stronger eddy current loss in alternating the EM field at high frequency. Furthermore, derivative internal magnetic field can be induced by an alternating current electric field generated by the eddy current (Qiu et al., 2016). At high frequency, the loss capability of Ni nanoparticles may be gradually counteracted with the consolidation of the internal magnetic field, resulting in the decreased complex permeability (Liu et al., 2019).

Meanwhile, the dielectric and magnetic loss tangents of Ni/MWCNT composites with different filler loading are calculated to evaluate the attenuation loss and shown in **Figure S4**. Except for the loading of 40 wt%, the tan$\delta_\varepsilon$ values enhance with the increase of filler proportions (**Figure S4A**). From **Figure 4B**, it is clear that tan$\delta_\mu$ is much lower than that of the dielectric loss, which indicates that the dielectric loss has a major contribution to electromagnetic loss. Besides, negative tan$\delta_\mu$ values appear in the high frequency, which indicates that the magnetic energy is radiated out from the Ni/MWCNTs absorbers and converted into electrical energy to increase tan$\delta_\varepsilon$.
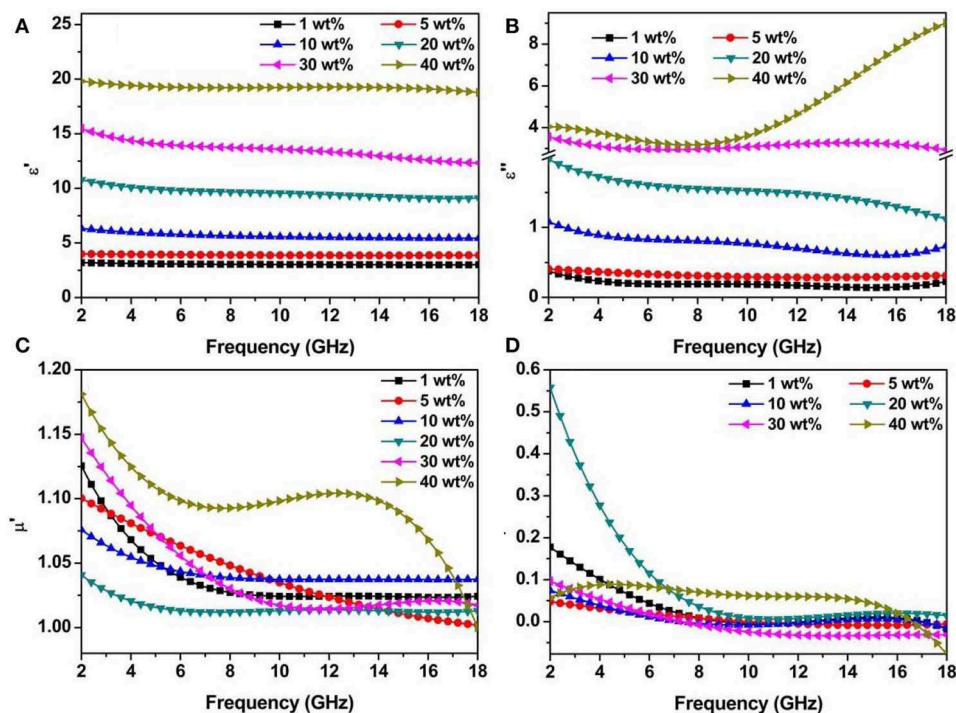
**FIGURE 4 |** Electromagnetic parameters of samples with different filler loading in the frequency range of 2–18 GHz, real part of permittivity **(A)**, imaginary part of permittivity **(B)**, real part of permeability **(C)**, and imaginary part of permeability **(D)**.
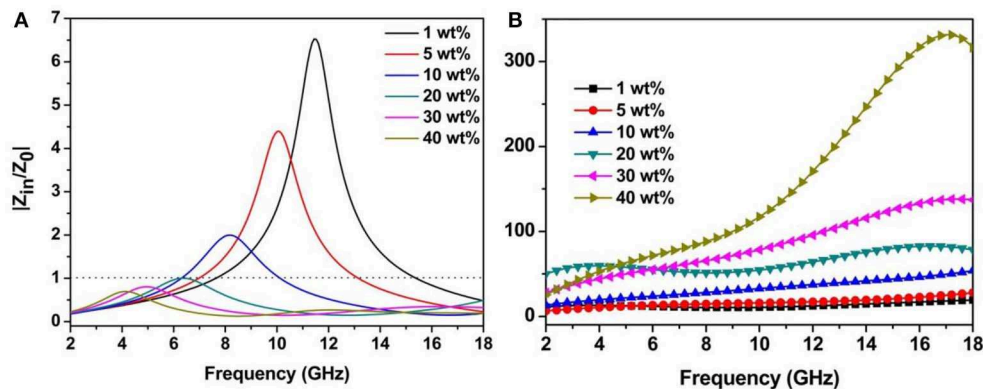


**FIGURE 5 |** Modulus of normalized input impedance Z **(A)** of 3.7 mm and attenuation constant α **(B)** of Ni/MWCNT composites with different filler loading.

Actually, the *RL* values are not simply determined by their dielectric/magnetic loss capability, but more dependent on impedance behavior that is a necessary prerequisite for obtaining excellent microwave absorption performance, as well as overall attenuation ability, which is another key factor to impact the intensity and bandwidth of *RL* peak. Generally, impedance matching and attenuation constant ($\alpha$) can be expressed by the relative input $Z = |Z_{in}/Z_0|$ and deduced using the following equation (Ma et al., 2016; Wu et al., 2018), respectively.

$$\alpha = \frac{\sqrt{2}\pi f}{c}\sqrt{\left(\mu''\varepsilon'' - \mu'\varepsilon'\right) + \sqrt{\left(\mu''\varepsilon'' - \mu'\varepsilon'\right)^2 + \left(\mu'\varepsilon'' + \mu''\varepsilon'\right)^2}} \quad (4)$$

It can be found from **Figure 5** that the *Z* values decrease with the increasing filler contents, whereas the attenuation constant of samples increase as the filler contents increase in PVDF. As for the sample with 20 wt% loading, the $|Z_{in}/Z_0|$ values are the nearest to 1 and even coincide with dot lines in a certain frequency band (**Figure 5A**). These results illustrate that the excellent microwave absorption property has also been caused by the superior impedance matching in the sample with 20 wt% loading. The sample with 40 wt% loading possesses best attenuation property but poor impedance matching behavior, thus leading to that only very limited incident electromagnetic waves can be transmitted into absorber. In this case, no matter

TABLE 1 | Microwave absorption performances of various carbon-based magnetic composites in previous reports compared with this work.

| Absorber | Matrix | Content (wt%) | RL$_{min}$ (dB) | $d$ (mm) | EAB (GHz) (RL < −10 dB) | References |
|---|---|---|---|---|---|---|
| CNTs/NiCo$_2$O$_4$ | Paraffin | 30 | −45.1 | 2.5 | 2.7 | Hu Q. et al., 2019 |
| Fe@NCNTs | Paraffin | 10 | −30.4 | 3.2 | 5.7 | Ning et al., 2018 |
| Ni@NCNTs | Paraffin | 10 | −34.1 | 3.2 | 4.7 | |
| MWCNT/NiFe$_2$O$_4$ | Paraffin | 50 | −42.3 | 1.2 | 3.8 | Zhang et al., 2019b |
| Porous Ni/C composites | Paraffin | 40 | −51.8 | 2.6 | 3.5 | Liu W. et al., 2017 |
| Ni/CNT composites | Paraffin | 20 | −30.0 | 2.0 | 6.5 | Sha et al., 2017 |
| Ni/MWCNT | Paraffin | 30 | −37.9 | 4.0 | 3.6 | Tong et al., 2014 |
| MoO$_3$/MoS$_2$ Hybrid | PVDF | 20 | −38.5 | 2.0 | 2.0 | Li et al., 2019 |
| C-Fe$_3$O$_4$/PVDF | PVDF | 40 | −41.75 | 3.0 | 2.01 | Adebayo et al., 2019 |
| Ni/MWCNTs | PVDF | 20 | −46.85 | 3.7 | 3.2 | This work |

how good the attenuation ability they own, it will not create desirable absorption properties.

Based on these results, it can be concluded that the enhanced microwave absorption mechanism may be the well-matched impedance, conductive loss, multiple reflections and scatterings, and synergistic effect of dielectric loss and magnetic loss. The optimal impedance matching means that most of the incident electromagnetic wave can effectively propagate into the absorbers and further be attenuated by the multiple loss mechanism (Liu P. et al., 2017). Ni/MWCNTs composites with unique one-dimensional tubular nanostructure and appropriate conductivity may generate microcurrent and be beneficial to the enhancement of conduction loss (Zhao et al., 2018). Space charge polarization and interfacial polarization induced by space charge accumulation between various interfaces make a contribution to the dielectric loss (Liang et al., 2019). Furthermore, dipole polarization induced by abundant defects also enhance microwave attenuation capacity (Zhang et al., 2019b). **Table 1** summarizes the MWA performance of various carbon-based magnetic composites reported in literature. Ni/MWCNTs prepared in this work have the advantages of low filler loading, thinner thickness, and broadening efficient absorption bandwidth (EAB).

## CONCLUSIONS

In summary, we created a prominently excellent microwave absorber with moderate conductivity and optimal impedance matching by adjusting the filling content based on purchased Ni/MWCNTs materials. As a result, not only a strong reflection loss (−46.85 dB) but also a broad bandwidth (3.2 GHz)

in frequency of 2–18GHz was achieved in the Ni/MWCNTs composites with only 20 wt% fillers. Its excellent absorbing properties are mainly ascribed to well impedance matching and synergistic effect of dielectric loss and magnetic loss. The aforementioned results provide a novel strategy to obtain a commercially available absorber that can be widely applied in many fields.

## DATA AVAILABILITY STATEMENT

All datasets generated for this study are included in the article/**Supplementary Material**.

## AUTHOR CONTRIBUTIONS

P-YZ performed the main experimental operation and drafted the manuscript. H-YW performed the data analyses. G-SW contributed to the conception of the study and financial support.

## FUNDING

## SUPPLEMENTARY MATERIAL

The Supplementary Material for this article can be found online at: https://www.frontiersin.org/articles/10.3389/fchem.2020.00097/full#supplementary-material

## REFERENCES

Adebayo, L. L., Soleimani, H., Yahya, N., Abbas, Z., Ridwan, A. T., and Wahaab, F. A. (2019). Investigation of the broadband microwave absorption of citric acid coated Fe$_3$O$_4$/PVDF composite using finite element method. *Appl. Sci.* 9:3877. doi: 10.3390/app9183877

Chen, H., Huang, Z., Huang, Y., Zhang, Y., Ge, Z., Qin, B., et al. (2017). Synergistically assembled MWCNT/graphene foam with highly efficient microwave absorption in both C and X bands. *Carbon N. Y.* 124, 506–514. doi: 10.1016/j.carbon.2017.09.007

Chen, Y. H., Huang, Z. H., Lu, M. M., Cao, W. Q., Yuan, J., Zhang, D. Q., et al. (2015). 3D Fe$_3$O$_4$ nanocrystals decorating carbon nanotubes to tune

electromagnetic properties and enhance microwave absorption capacity. *J. Mater. Chem. A* 3, 12621–12625. doi: 10.1039/C5TA02782A

Cheng, Y., Li, Z., Li, Y., Dai, S., Ji, G., Zhao, H., et al. (2018). Rationally regulating complex dielectric parameters of mesoporous carbon hollow spheres to carry out efficient microwave absorption. *Carbon N. Y.* 127, 643–652. doi: 10.1016/j.carbon.2017.11.055

Duan, Y., Xiao, Z., Yan, X., Gao, Z., Tang, Y., Hou, L., et al. (2018). Enhanced electromagnetic microwave absorption property of peapod-like MnO@carbon nanowires. *ACS Appl. Mater. Interfaces* 10, 40078–40087. doi: 10.1021/acsami.8b11395

Fang, J., Shang, Y., Chen, Z., Wei, W., Hu, Y., Yue, X., et al. (2017). Rice husk-based hierarchically porous carbon and magnetic particles composites for highly efficient electromagnetic wave attenuation. *J. Mater. Chem. C* 5, 4695–4705. doi: 10.1039/C7TC00987A

Fang, S., Cui, Z., Zhu, Y., Wang, C., Bai, J., Zhang, X., et al. (2019). In situ synthesis of biomass-derived Ni/C catalyst by self-reduction for the hydrogenation of levulinic acid to γ-valerolactone. *J. Energy Chem.* 37, 204–214. doi: 10.1016/j.jechem.2019.03.021

Ferrari, A. C., and Robertson, J. (2000). Interpretation of Raman spectra of disordered and amorphous carbon. *Phys. Rev. B* 61, 95–107. doi: 10.1103/PhysRevB.61.14095

Guan, H., Wang, H., Zhang, Y., Dong, C., Chen, G., Wang, Y., et al. (2018). Microwave absorption performance of Ni(OH)$_2$ decorating biomass carbon composites from Jackfruit peel. *Appl. Surf. Sci.* 447, 261–268. doi: 10.1016/j.apsusc.2018.03.225

Hu, P. P., Dong, S., Li, X., Chen, J., Zhang, X., Hu, P. P., et al. (2019). A low-cost strategy to synthesize MnO nanorods anchored on 3D biomass-derived carbon with superior microwave absorption properties. *J. Mater. Chem. C* 7, 9219–9228. doi: 10.1039/C9TC02182E

Hu, Q., Yang, R., Mo, Z., Lu, D., Yang, L., He, Z., et al. (2019). Nitrogen-doped and Fe-filled CNTs/NiCo$_2$O$_4$ porous sponge with tunable microwave absorption performance. *Carbon N. Y.* 153, 737–744. doi: 10.1016/j.carbon.2019.07.077

Kim, B. J., Bae, K. M., Lee, Y. S., An, K. H., and Park, S. J. (2014). EMI shielding behaviors of Ni-coated MWCNTs-filled epoxy matrix nanocomposites. *Surf. Coat. Technol.* 242, 125–131. doi: 10.1016/j.surfcoat.2014.01.030

Kuang, D., Hou, L., Wang, S., Luo, H., Deng, L., Mead, J. L., et al. (2019). Large-scale synthesis and outstanding microwave absorption properties of carbon nanotubes coated by extremely small FeCo-C core-shell nanoparticles. *Carbon N. Y.* 153, 52–61. doi: 10.1016/j.carbon.2019.06.105

Li, C. Q., Shen, X., Ding, R. C., and Wang, G. S. (2019). Controllable synthesis of one-dimensional MoO$_3$/MoS$_2$ hybrid composites with their enhanced efficient electromagnetic wave absorption properties. *Chempluschem* 84, 226–232. doi: 10.1002/cplu.201800599

Liang, L., Han, G., Li, Y., Zhao, B., Zhou, B., Feng, Y., et al. (2019). Promising Ti$_3$C$_2$T$_x$ MXene/Ni chain hybrid with excellent electromagnetic wave absorption and shielding capacity. *ACS Appl. Mater. Interfaces* 11, 25399–25409. doi: 10.1021/acsami.9b07294

Liang, X., Zhang, X., Liu, W., Tang, D., Zhang, B., and Ji, G. (2016). A simple hydrothermal process to grow MoS$_2$ nanosheets with excellent dielectric loss and microwave absorption performance. *J. Mater. Chem. C* 4, 6816–6821. doi: 10.1039/C6TC02006B

Liu, D., Du, Y., Li, Z., Wang, Y., Xu, P., Zhao, H., et al. (2018). Facile synthesis of 3D flower-like Ni microspheres with enhanced microwave absorption properties. *J. Mater. Chem. C* 6, 9615–9623. doi: 10.1039/C8TC02931H

Liu, D., Du, Y., Xu, P., Liu, N., Wang, Y., Zhao, H., et al. (2019). Waxberry-like hierarchical Ni@C microspheres with high-performance microwave absorption. *J. Mater. Chem. C* 7, 5037–5046. doi: 10.1039/C9TC00771G

Liu, H., Li, Y., Yuan, M., Sun, G., Li, H., Ma, S., et al. (2018). In situ preparation of cobalt nanoparticles decorated in N-doped carbon nanofibers as excellent electromagnetic wave absorbers. *ACS Appl. Mater. Interfaces* 10, 22591–22601. doi: 10.1021/acsami.8b05211

Liu, J., Cao, M.-S., Luo, Q., Shi, H.-L., Wang, W.-Z., and Yuan, J. (2016). Electromagnetic property and tunable microwave absorption of 3D nets from nickel chains at elevated temperature. *ACS Appl. Mater. Interfaces* 8, 22615–22622. doi: 10.1021/acsami.6b05480

Liu, P., Ng, V. M. H., Yao, Z., Zhou, J., Lei, Y., Yang, Z., et al. (2017). Facile synthesis and hierarchical assembly of flowerlike NiO structures with enhanced

dielectric and microwave absorption properties. *ACS Appl. Mater. Interfaces* 9, 16404–16416. doi: 10.1021/acsami.7b02597

Liu, W., Shao, Q., Ji, G., Liang, X., Cheng, Y., Quan, B., et al. (2017). Metal–organic-frameworks derived porous carbon-wrapped Ni composites with optimized impedance matching as excellent lightweight electromagnetic wave absorber. *Chem. Eng. J.* 313, 734–744. doi: 10.1016/j.cej.2016.12.117

Liu, Y., Zhang, Y., Zhang, C., Huang, B., Wang, X., Li, Y., et al. (2018). Aligned fluorinated single-walled carbon nanotubes as a transmission channel towards attenuation of broadband electromagnetic waves. *J. Mater. Chem. C* 6, 9399–9409. doi: 10.1039/C8TC02522C

Lou, Z., Han, H., Zhou, M., Han, J., Cai, J., Huang, C., et al. (2018). Synthesis of magnetic wood with excellent and tunable electromagnetic wave-absorbing properties by a facile vacuum/pressure impregnation method. *ACS Sustain. Chem. Eng.* 6, 1000–1008. doi: 10.1021/acssuschemeng.7b03332

Lu, S., Xia, L., Xu, J., Ding, C., Li, T., Yang, H., et al. (2019). Permittivity-regulating strategy enabling superior electromagnetic wave absorption of lithium aluminum Silicate/rGO nanocomposites. *ACS Appl. Mater. Interfaces* 11, 18626–18636. doi: 10.1021/acsami.9b00348

Ma, J., Zhang, X., Liu, W., and Ji, G. (2016). Direct synthesis of MOF-derived nanoporous CuO/carbon composites for high impedance matching and advanced microwave absorption. *J. Mater. Chem. C* 4, 11419–11426. doi: 10.1039/C6TC04048A

Ning, M., Li, J., Kuang, B., Wang, C., Su, D., Zhao, Y., et al. (2018). One-step fabrication of N-doped CNTs encapsulating M nanoparticles (M = Fe, Co, Ni) for efficient microwave absorption. *Appl. Surf. Sci.* 447, 244–253. doi: 10.1016/j.apsusc.2018.03.242

Qiu, S., Lyu, H., Liu, J., Liu, Y., Wu, N., and Liu, W. (2016). Facile synthesis of porous nickel/carbon composite microspheres with enhanced electromagnetic wave absorption by magnetic and dielectric losses. *ACS Appl. Mater. Interfaces* 8, 20258–20266. doi: 10.1021/acsami.6b03159

Sha, L., Gao, P., Wu, T., and Chen, Y. (2017). Chemical Ni-C bonding in Ni-carbon nanotube composite by a microwave welding method and its induced high-frequency radar frequency electromagnetic wave absorption. *ACS Appl. Mater. Interfaces* 9, 40412–40419. doi: 10.1021/acsami.7b07136

Tong, G., Liu, F., Wu, W., Du, F., and Guan, J. (2014). Rambutan-like Ni/MWCNT heterostructures: easy synthesis, formation mechanism, and controlled static magnetic and microwave electromagnetic characteristics. *J. Mater. Chem. A* 2, 7373–7382. doi: 10.1039/c4ta00117f

Wang, J., Jia, X., Wang, T., Geng, S., Zhou, C., Yang, F., et al. (2016). Synthesis and microwave absorption property of two-dimensional porous nickel oxide nanoflakes/carbon nanotubes nanocomposites with a threaded structure. *J. Alloys Compd.* 689, 366–373. doi: 10.1016/j.jallcom.2016.07.328

Wang, L., Guan, H., Hu, J., Huang, Q., Dong, C., Qian, W., et al. (2019). Jute-based porous biomass carbon composited by Fe$_3$O$_4$ nanoparticles as an excellent microwave absorber. *J. Alloys Compd.* 803, 1119–1126. doi: 10.1016/j.jallcom.2019.06.351

Wang, Y., Gao, X., Lin, C., Shi, L., Li, X., and Wu, G. (2019). Metal organic frameworks-derived Fe-Co nanoporous carbon/graphene composite as a high-performance electromagnetic wave absorber. *J. Alloys Compd.* 785, 765–773. doi: 10.1016/j.jallcom.2019.01.271

Wang, Y., Wang, W., Sun, J., Sun, C., Feng, Y., and Li, Z. (2018). Microwave-based preparation and characterization of Fe-cored carbon nanocapsules with novel stability and super electromagnetic wave absorption performance. *Carbon N. Y.* 135, 1–11. doi: 10.1016/j.carbon.2018.04.026

Wen, B., Wang, X. X., Cao, W. Q., Shi, H. L., Lu, M. M., Wang, G., et al. (2014). Reduced graphene oxides: the thinnest and most lightweight materials with highly efficient microwave attenuation performances of the carbon world. *Nanoscale* 6, 5754–5761. doi: 10.1039/C3NR06717C

Wu, F., Sun, M., Chen, C., Zhou, T., Xia, Y., Xie, A., et al. (2019). Controllable coating of polypyrrole on silicon carbide nanowires as a core-shell nanostructure: a facile method to enhance attenuation characteristics against electromagnetic radiation. *ACS Sustain. Chem. Eng.* 7, 2100–2106. doi: 10.1021/acssuschemeng.8b04676

Wu, F., Xia, Y., Sun, M., and Xie, A. (2018). Two-dimensional (2D) few-layers WS2 nanosheets: an ideal nanomaterials with tunable electromagnetic absorption performance. *Appl. Phys. Lett.* 113:052906. doi: 10.1063/1.5040274

Xie, A., Wu, F., Jiang, W., Zhang, K., Sun, M., and Wang, M. (2017). Chiral induced synthesis of helical polypyrrole (PPy) nano-structures: a lightweight and high-performance material against electromagnetic pollution. *J. Mater. Chem. C* 5, 2175–2181. doi: 10.1039/C6TC05057C

Xie, A., Zhang, K., Sun, M., Xia, Y., and Wu, F. (2018). Facile growth of coaxial Ag@polypyrrole nanowires for highly tunable electromagnetic waves absorption. *Mater. Des.* 154, 192–202. doi: 10.1016/j.matdes.2018.05.039

Xie, P., Li, H., He, B., Dang, F., Lin, J., Fan, R., et al. (2018). Bio-gel derived nickel/carbon nanocomposites with enhanced microwave absorption. *J. Mater. Chem. C* 6, 8812–8822. doi: 10.1039/C8TC02127A

Xu, C., Sun, M., Yang, Z., Sun, Y., Wu, F., and Xie, A. (2019). Magnetized polypyrrole and its enhanced electromagnetic attenuation performance. *Appl. Phys. Lett.* 115, 1–5. doi: 10.1063/1.5100545

Xu, J., Qi, X., Sun, Y., Wang, Z., Liu, Y., Luo, C., et al. (2018). Tuning the electromagnetic synergistic effects for enhanced microwave absorption via magnetic nickel core encapsulated in hydrogenated anatase $TiO_2$ shell. *ACS Sustain. Chem. Eng.* 6, 12046–12054. doi: 10.1021/acssuschemeng.8b02350

Xu, W., Pan, Y., Wei, W., and Wang, G. (2018). Nanocomposites of oriented nickel chains with tunable magnetic properties for high-performance broadband microwave absorption. *ACS Appl. Nano Mater.* 1, 1116–1123. doi: 10.1021/acsanm.7b00293

Yan, J., Huang, Y., Wei, C., Zhang, N., and Liu, P. (2017). Covalently bonded polyaniline/graphene composites as high-performance electromagnetic (EM) wave absorption materials. *Compos. A Appl. Sci. Manuf.* 99, 121–128. doi: 10.1016/j.compositesa.2017.04.016

Yang, L., Zhao, X., Yang, R., Zhao, P., Li, Y., Yang, P., et al. (2019). In-situ growth of carbon nanotubes on Ni/NiO nanofibers as efficient hydrogen evolution reaction catalysts in alkaline media. *Appl. Surf. Sci.* 491, 294–300. doi: 10.1016/j.apsusc.2019.06.160

Yang, Y., Xia, L., Zhang, T., Shi, B., Huang, L., Zhong, B., et al. (2018). $Fe_3O_4$@LAS/RGO composites with a multiple transmission-absorption mechanism and enhanced electromagnetic wave absorption performance. *Chem. Eng. J.* 352, 510–518. doi: 10.1016/j.cej.2018.07.064

Yim, Y. J., Rhee, K. Y., and Park, S. J. (2016). Electromagnetic interference shielding effectiveness of nickel-plated MWCNTs/high-density polyethylene composites. *Compos. B Eng.* 98, 120–125. doi: 10.1016/j.compositesb.2016.04.061

Yin, Y., Liu, X., Wei, X., Yu, R., and Shui, J. (2016). Porous CNTs/Co composite derived from zeolitic imidazolate framework: a lightweight, ultrathin, and highly efficient electromagnetic wave absorber. *ACS Appl. Mater. Interfaces* 8, 34686–34698. doi: 10.1021/acsami.6b12178

Zhang, J., Jiang, Y., Wang, Y., Yu, C., Cui, J., Wu, J., et al. (2019a). Ultrathin carbon coated mesoporous Ni-NiFe$_2$O$_4$ nanosheet arrays for efficient overall water splitting. *Electrochim. Acta* 321, 134652. doi: 10.1016/j.electacta.2019.134652

Zhang, J., Shu, R., Guo, C., Sun, R., Chen, Y., and Yuan, J. (2019b). Fabrication of nickel ferrite microspheres decorated multi-walled carbon nanotubes hybrid composites with enhanced electromagnetic wave absorption properties. *J. Alloys Compd.* 784, 422–430. doi: 10.1016/j.jallcom.2019.01.073

Zhang, Y., Gao, S., Xing, H., and Li, H. (2019c). *In situ* carbon nanotubes encapsulated metal Nickel as high-performance microwave absorber from Ni–Zn Metal–Organic framework derivative. *J. Alloys Compd.* 801, 609–618. doi: 10.1016/j.jallcom.2019.06.164

Zhao, H., Cheng, Y., Lv, H., Zhang, B., Ji, G., and Du, Y. (2018). Achieving sustainable ultralight electromagnetic absorber from flour by turning surface morphology of nanoporous carbon. *ACS Sustain. Chem. Eng.* 6, 15850–15857. doi: 10.1021/acssuschemeng.8b04461

Zhao, H., Han, X., Han, M., Zhang, L., and Xu, P. (2010). Preparation and electromagnetic properties of multiwalled carbon nanotubes/Ni composites by γ-irradiation technique. *Mater. Sci. Eng. B* 167, 1–5. doi: 10.1016/j.mseb.2010.01.003

Zhao, H. B., Fu, Z. B., Chen, H. B., Zhong, M. L., and Wang, C. Y. (2016). Excellent electromagnetic absorption capability of Ni/carbon based conductive and magnetic foams synthesized via a green one pot route. *ACS Appl. Mater. Interfaces* 8, 1468–1477. doi: 10.1021/acsami.5b10805

Zhou, W., Long, L., Xiao, P., Li, Y., Luo, H., Hu, W., et al. (2017). Silicon carbide nano-fibers *in-situ* grown on carbon fibers for enhanced microwave absorption properties. *Ceram. Int.* 43, 5628–5634. doi: 10.1016/j.ceramint.2017.01.095

# 1D Copper(II)-Aroylhydrazone Coordination Polymers: Magnetic Properties and Microwave Assisted Oxidation of a Secondary Alcohol

Manas Sutradhar[1]*, Elisabete C. B. A. Alegria[1,2], Tannistha Roy Barman[1], M. Fátima C. Guedes da Silva[1], Cai-Ming Liu[3] and Armando J. L. Pombeiro[1]*

[1] Centro de Química Estrutural, Instituto Superior Técnico, Universidade de Lisboa, Lisbon, Portugal, [2] Área Departamental de Engenharia Química, Instituto Superior de Engenharia de Lisboa, Instituto Politécnico de Lisboa, Lisbon, Portugal, [3] National Laboratory for Molecular Sciences, Center for Molecular Science, Institute of Chemistry, Chinese Academy of Sciences, Beijing, China

The 1D Cu(II) coordination polymers $[Cu_3(L^1)(NO_3)_4(H_2O)_2]_n$ (**1**) and $[Cu_2(H_2L^2)(NO_3)(H_2O)_2]_n(NO_3)_n$ (**2**) have been synthesized using the aroylhyrazone Schiff bases $N'^1,N'^2$-bis(pyridin-2-ylmethylene)oxalohydrazide ($H_2L^1$) and $N'^1,N'^3$-bis(2-hydroxybenzylidene)malonohydrazide ($H_4L^2$), respectively. They have been characterized by elemental analysis, infrared (IR) spectroscopy, UV-Vis spectroscopy, electrospray ionization mass spectrometry (ESI-MS), single crystal X-ray diffraction and variable temperature magnetic susceptibility measurements (for **2**). The ligand $(L^1)^{2-}$ coordinates in the *iminol* form in **1**, whereas the *amide* coordination is observed for $(H_2L^2)^{2-}$ in **2**. Either the ligand bridge or the nitrate bridge in **2** mediates weak antiferromagnetic coupling. The catalytic performance of **1** and **2** has been investigated toward the solvent-free microwave-assisted oxidation of a secondary alcohol (1-phenylethanol used as model substrate). At 120°C and in the presence of the nitroxyl radical 2,2,6,6-tetramethylpiperydil-1-oxyl (TEMPO), the complete conversion of 1-phenylethanol into acetophenone occurs with TOFs up to 1,200 h$^{-1}$.

Keywords: Cu(II) complexes, coordination polymer, X-ray structure, magnetism, microwave assisted oxidation of alcohols

## INTRODUCTION

Transition metal complexes derived from multidentate Schiff base ligands received high significance due to their wide dimension of applications in the areas of molecular magnetism (Benelli and Gatteschi, 2002; Sutradhar et al., 2012, 2013, 2014b, 2015a, 2018; Cho et al., 2016; Andruh, 2018), crystal engineering (Dong et al., 2000; Kitaura et al., 2004; Andruh et al., 2009), supramolecular chemistry (Pradeep and Das, 2013; El-Bindary et al., 2016; Dwivedi et al., 2018), catalysis (Sutradhar et al., 2013, 2014b, 2015a,b,c, 2016a,b,c, 2017, 2018, 2019), etc. Molecular magnetism is one of the significant domains determining magneto-structural correlations to design magnetic materials (Benelli and Gatteschi, 2002; Sutradhar et al., 2012, 2013, 2014b, 2015a, 2018; Cho et al., 2016; Andruh, 2018). Single molecule magnets (SMMs) (Karotsis et al., 2010; Glaser et al., 2015; Maniaki et al., 2018) exhibit a large spin ground-state (*S*) value and large negative magnetic anisotropy and are used in potential high-density information storage devices and

**GRAPHICAL ABSTRACT |** Two new aroylhydrazone Cu(II) 1D coordination polymers $[Cu_3(L^1)(NO_3)_4(H_2O)_2]_n$ (**1**) and $[Cu_2(H_2L^2)(NO_3)(H_2O)_2]_n \cdot (NO_3)_n$ (**2**) ($H_2L^1 = N'^1,N'^2$-bis(pyridin-2-ylmethylene)oxalohydrazide and $H_4L^2 = N'^1,N'^3$-bis(2-hydroxybenzylidene)malonohydrazide) have been structurally characterized. Their magnetic properties and the catalytic activity toward the solvent-free microwave-assisted oxidation of 1-phenylethanol have been explored.

quantum computers (Leuenberger and Loss, 2001). Therefore, many efforts have been devoted to rationally establish polynuclear metal complexes and/or clusters elucidating molecular magnetism (Benelli and Gatteschi, 2002; Karotsis et al., 2010; Sutradhar et al., 2012, 2013, 2014b, 2015a, 2018; Glaser et al., 2015; Cho et al., 2016; Andruh, 2018; Maniaki et al., 2018). Coordination polymers and molecular clusters are particular classes of compounds that can display novel magnetic properties including high ground-state spin values and single molecule magnetism behavior (Zheng et al., 2014; Journaux et al., 2018; Yue and Gao, 2019).

The coordination behavior of Cu(II) is versatile, flexible and magnetically attractive. Many Cu(II) complexes are widely explored for magnetic studies focused on the synthesis of polynuclear complexes and/or clusters and their possible application in molecular magnetism (Benelli and Gatteschi, 2002; Sutradhar et al., 2013, 2015a, 2018; Andruh, 2018). Several attempts have been carried out to synthesize polynuclear Cu(II) complexes by designing suitable flexidentate Schiff base ligands to fabricate magnetic properties (Lu et al., 2013; Sutradhar et al., 2013, 2015a, 2018). Moreover, some multinuclear copper complexes show good catalytic performances toward the mild peroxidative oxidation of alkanes and alcohols into more valuable organic products (Pombeiro, 2013, 2019; Sutradhar et al., 2013, 2015a, 2018; Kopylovich et al., 2015) thus contributing to one of the most challenging subjects of modern chemistry. However, such examples are still limited and the study requires further exploration.

Aroylhydrazone Schiff bases are versatile in terms of functionalities, coordination properties and chelating abilities (Sutradhar et al., 2013, 2015a,b,c, 2016a,b,c, 2017, 2018). In continuation of our work in the fields of catalysis and magnetic studies, herein we report the syntheses of two 1D coordination polymers using two different multidentate *N,O* donor aroylhydrazone Schiff bases. The magnetic properties of one of them (complex **2**) are studied using variable temperature magnetic susceptibility measurements. These 1D polymers

are also tested as catalysts toward the microwave assisted peroxidative oxidation of alcohols under mild conditions for the future development of an environment benign catalytic system.

## EXPERIMENTAL

All synthetic work was performed in air. Commercially available reagents and solvents were used as received, without further purification or drying. $Cu(NO_3)_2 \cdot 2.5H_2O$ was used as metal source for the synthesis of the complexes.

C, H, and N elemental analyses were carried out by the Microanalytical Service of Instituto Superior Técnico. Infrared spectra (4,000–400 cm$^{-1}$) were recorded on a Bruker Vertex 70 (Bruker Corporation, Ettlingen, Germany) instrument in KBr pellets; wavenumbers are in cm$^{-1}$. The $^1$H NMR spectra were recorded at room temperature on a Bruker Avance II + 400.13 MHz (UltraShieldTM Magnet, Rheinstetten, Germany) spectrometer. The UV–Vis absorption spectra of methanol solutions of **1** and **2** (*ca.* $2 \times 10^{-5}$M) in 1.00 cm quartz cells were recorded at room temperature on a Lambda 35 UV–Vis spectrophotometer (Perkin–Elmer) by scanning the 200–1000 nm region at a rate of 240 nm min$^{-1}$. Tetramethylsilane was used as the internal reference and the chemical shifts are reported in ppm. Mass spectra were run in a Varian 500-MS LC Ion Trap Mass Spectrometer (Agilent Technologies, Amstelveen, The Netherlands) equipped with an electrospray (ESI) ion source. For electrospray ionization, the drying gas and flow rate were optimized according to the particular sample with 35 p.s.i. nebulizer pressure. Scanning was performed from *m/z* 100 to 1,200 in methanol solution. The compounds were observed in the positive mode (capillary voltage = 80–105 V). The catalytic tests were performed under microwave (MW) irradiation using a focused Anton Paar Monowave 300 microwave (Anton Paar GmbH, Graz, Austria) fitted with a rotational system and an IR temperature detector, using a 10 mL capacity reaction tube with a 13 mm internal diameter. Gas chromatographic (GC) measurements were carried in a FISONS Instrument GC 8000 series gas chromatograph with a capillary DB-WAX column (30 m x 0.32 mm), a FID detector, helium as the carrier gas and using the Jasco-Borwin v.1.50 software. The magnetic susceptibility measurements were carried out on a polycrystalline samples with a Quantum Design MPMS-XL5 SQUID magnetometer in the temperature range of 2–300 K and at an applied field of 2000 Oe. Diamagnetic corrections were estimated from Pascal's constants for all constituent atoms (Kahn, 1993).

## Synthesis of the $N'^1,N'^2$-bis(pyridin-2-ylmethylene)oxalohydrazide ($H_2L^1$)

The aroylhydrazone Schiff base pro-ligand $H_2L^1$ (**Scheme 1**) was prepared by using a similar method reported for the synthesis of $N'^1,N'^3$-bis(2-hydroxybenzylidene)malonohydrazide ($H_4L^2$) (Sutradhar et al., 2014a) upon condensation of the oxalyl dihydrazide with pyridine-2-aldehyde.

Yield: 86%. Anal. Calcd for $H_2L^1$ $C_{14}H_{12}N_6O_2$: C, 56.75; H, 4.08; N, 28.36. Found: C, 56.68; H, 4.04; N, 28.29. IR (KBr
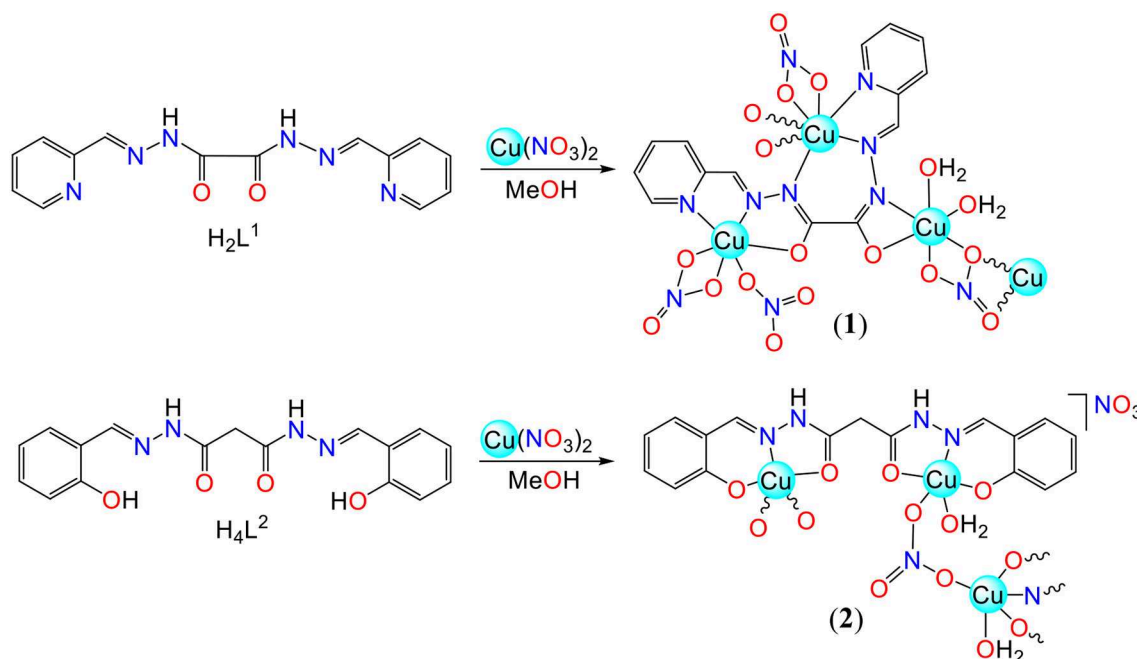
**SCHEME 1 |** Syntheses of **1** and **2**.

pellet, cm$^{-1}$): 3131$\nu$(NH), 1681 $\nu$(C=O) 1185 $\nu$(N–N). $^1$H NMR (DMSO-d6, $\delta$): 12.67 (s, 2H, NH), 7.47 (s, 2H, -CH=N), 8.67–7.89 (m, 8H, C$_5$H$_4$N). UV–Vis $_{max}$ (MeOH, nm ($\epsilon$, LM$^{-1}$ cm$^{-1}$)): 656 (305), 378 (16,478), 285 (23,434), 237 (32,108). ESI-MS(+): $m/z$ 297 [M+H]$^+$ (100%).

## Synthesis of [Cu$_3$(L$^1$)(NO$_3$)$_4$(H$_2$O)$_2$]$_n$ (1)

0.930 g Cu(NO$_3$)$_2$·2.5H$_2$O (4.0 mmol) was added to a 25 mL methanolic suspension of H$_2$L$^1$ (0.302 g, 1.02 mmol). The resultant mixture was stirred at room temperature for 20 min and a dark green solution was obtained. The solution was then filtered and the solvent was allowed to evaporate slowly at room temperature. After 2 d, single crystals suitable for X-ray diffraction were isolated, washed 3 times with cold methanol and dried over silica gel.

Yield: 0.523 g (68%, with respect to Cu). Anal. Calcd for C$_{14}$H$_{14}$Cu$_3$N$_{10}$O$_{16}$: C, 21.87; H, 1.84; N, 18.22. Found: C, 21.83; H, 1.81; N, 18.17. IR (KBr; cm$^{-1}$): 3448 $\nu$(OH), 1610 $\nu$(C=N), 1382 $\nu$(NO$_3$), 1252 $\nu$(C–O)enolic and 1154 $\nu$(N–N). UV–Vis $\lambda_{max}$ (MeOH, nm ($\epsilon$, LM$^{-1}$ cm$^{-1}$)): 752 (309), 820 (286), 390 (16,248), 282 (22,632), 254 (31,818). ESI-MS(+): $m/z$ 770 [M+H]$^+$ (100%).

## Synthesis of [Cu$_2$(H$_2$L$^2$)(NO$_3$)(H$_2$O)$_2$]$_n$(NO$_3$)$_n$ (2)

To a 25 mL methanol solution of H$_4$L$^2$ (0.340 g, 1.00 mmol), a 20 mL methanol solution of Cu(NO$_3$)$_2$·2.5H$_2$O (0.670 g, 3.0 mmol) was added and the reaction mixture was stirred for 20 min at room temperature. The resultant dark green solution was filtered and the filtrate was kept in open air. Dark green single

crystals suitable for X-ray diffraction analysis were isolated after 2 days. Crystals were washed 3 times with cold ethanol and dried over silica gel.

Yield: 0.450 g (72%, with respect to Cu). Anal. Calcd for C$_{17}$H$_{18}$Cu$_2$N$_6$O$_{12}$ (2): C, 32.65; H, 2.90; N, 13.44. Found: C, 32.60; H, 2.86; N, 13.39. IR (KBr; cm$^{-1}$): 3432 $\nu$(OH), 2874 $\nu$(NH), 1607 $\nu$(C=O), 1384 $\nu$(NO3), and 1154 $\nu$(N–N). UV–Vis $\lambda_{max}$ (MeOH, nm ($\epsilon$, LM−1 cm−1)): 756 (296), 359 (14,436), 344 (18,322), 326 (16,862). ESI-MS(+): m/z 581 [(M-NO$_3$)+H$_2$O]$^+$ (100%).

## X-Ray Measurements

Crystals of **1** were unstable at room temperature and without solvent. A good quality single crystal of **1** in the mother liquor was mounted in a capillary tube, sealed and measured at the temperature of *ca.* 150 K. A crystal of **2** was immersed in cryo-oil, mounted in a Nylon loop and measured at the temperature of 296 K. Intensity data were collected using a Bruker AXS PHOTON 100 diffractometer with graphite monochromated Mo-K$\alpha$ ($\lambda$ 0.71073) radiation. Data were collected using omega scans of 0.5° per frame and full sphere of data were obtained. Cell parameters were retrieved using Bruker SMART (Bruker, 2012) software and refined using Bruker SAINT (Bruker, 2012) on all the observed reflections. Absorption corrections were applied using SADABS (Bruker, 2012). Structures were solved by direct methods by using SHELXS (Sheldrick, 2000) and refined with SHELXL 2018 (Sheldrick, 2015). Calculations were performed using WinGX version 2014.1 (Farrugia, 2012). All non-hydrogen atoms were refined anisotropically. The H-atoms bonded to carbons were included in the model at geometrically calculated positions and refined using a riding model. U$_{iso}$(H)

were defined as 1.2$U_{eq}$ of the parent aromatic and methylene groups and 1.5$U_{eq}$ of the parent methyl ones. The hydrogen atoms attached to O were located in the difference Fourier map and refined with their isotropic thermal parameter set at 1.5 times the average thermal parameter of the parent oxygen atom. There was disordered solvent in the structure of **2** that could not be modeled (232 electrons in a void of 471 Å$^3$). Platon Squeeze (Spek, 2009) was used to remove that electron density. Least square refinements with anisotropic thermal motion parameters for all the non-hydrogen atoms and isotropic for the remaining atoms were employed. Crystal structures data are provided in the **Supplementary Material**.

## Typical Procedures and Product Analysis for Catalysis

The catalytic microwave-assisted (MW) peroxidative oxidation of 1-phenylethanol was undertaken in a focused Anton Paar Monowave 300 reactor equipped with a rotational system and an IR temperature detector. To a cylindrical pyrex tube (10 mL), 2.5 mmol alcohol, 5 µmol catalyst **1** or **2** (0.2 mol% *vs.* substrate) and 70% aqueous solution of *tert*-BuOOH (5 mmol) were added. The tube was sealed and placed in the microwave reactor under stirring and irradiation (5 or 20 W) at 80 or 120°C respectively, for 0.5 h. In the end, the reaction mixture was cooled to room temperature, 150 µL of benzaldehyde (internal standard) and 2.5 mL of MeCN (for substrate and organic products extraction) were added. The reaction mixture was stirred for 10 min and in the end a sample (1 µL) was taken from the organic phase and analyzed by GC using a FISONS gas chromatograph (GC 8000) with a FID detector and a capillary column (DB-WAX, column length: 30 m; internal diameter: 0.32 mm) (He as the carrier gas) and the Jasco-Borwin v.1.50 software. The samples were injected at 240°C. Initially the temperature was held at 120°C for 1 min, then elevated 10°C/min up to 200°C and maintained at this temperature for 1 min. Assignment of product peaks was done by comparison with chromatograms of pure commercial samples.

## RESULTS AND DISCUSSION

### Syntheses and Characterization

The aroylhydrazone Schiff base $N'^1,N'^2$-bis(pyridin-2-ylmethylene)oxalohydrazide (H$_2$L$^1$) and $N'^1,N'^3$-bis(2-hydroxybenzylidene)malonohydrazide (H$_4$L$^2$) have been used to synthesize Cu(II) coordination polymers. Reactions of Cu(NO$_3$)$_2$·2.5H$_2$O with those Schiff bases result in the formation of the 1D coordination polymers [Cu$_3$(L$^1$)(NO$_3$)$_4$(H$_2$O)$_2$]$_n$ (**1**) and [Cu$_2$(H$_2$L$^2$)(NO$_3$)(H$_2$O)$_2$]$_n$(NO$_3$)$_n$ (**2**). In **1** and **2** the coordination forms of the ligands are different (**Scheme 1**). Generally, in the presence of a base, aroylhydrazone coordinates to the metal center via the *iminol* (*enol*) form. The *amide* (*keto*) form is typically observed when reacting with a metal salt of the weak conjugated base of strong acid, e.g., nitrate, chloride or sulfate (Sutradhar et al., 2015a, 2016a). The treatment of H$_2$L$^1$ with Cu(NO$_3$)$_2$·2.5H$_2$O yields the 1D polymer **1** with the *iminol* (*enol*) coordination form of the ligand without addition of a base. However, this is probably due to the presence of the basic pyridine moiety in H$_2$L$^1$ which helps to deprotonate the *enolic* hydrogen of another molecule during complex

formation. In accord, the ligand exhibits the usual *amide* (*keto*) coordination in polymer **2**, where no such basic moiety is present in the ligand.

All the characteristic bands of the corresponding coordinated tridentate anionic ligand are found in the IR spectra of **1** and **2**, *viz.*, 3,448, 1,610, 1,252, and 1,154 ν(N–N) cm$^{-1}$ for **1** and 3,432, 2,874, 1,607, 1,384, and 1,154 cm$^{-1}$ for **2**. In addition, the presence of nitrate was found at *ca.* 1,382 cm$^{-1}$. In the UV-Vis spectra, both complexes **1** and **2** exhibit intense ligand to metal charge transfer transitions (LMCT) in the range of 254–390 nm (**Figures S1,S2**). In **1**, less intense absorption bands at 752 and 820 nm are due to d–d transitions attributable to $^2B_{1g} \rightarrow\ ^2A_{1g}$ and $^2B_{1g} \rightarrow\ ^2E_{1g}$ transitions, suggesting a distorted octahedral geometry (**Figure S1**) (Sutradhar et al., 2016b; Sureshbabu et al., 2019). In the case of **2** a less intense absorption band is observed at 756 nm (**Figure S2**) in accord with square pyramidal coordination geometries at the Cu(II) centers (Sutradhar et al., 2016b; Sureshbabu et al., 2019), which is in agreement with the structures obtained by single crystal X-ray analysis. The ESI-MS spectrum of compound **1**, in methanol solution (see experimental section), displays the molecular ion peak at *m/z* = 770 [**1**+H]$^+$ (100%). For **2**, the peak at *m/z* 581 (100%) suggests the absence of the non-coordinated nitrate ion and the addition of one water molecule. The magnetic properties and catalytic activity toward solvent-free microwave-assisted oxidation of 1-phenylethanol of **1** and **2** are discussed in the following sections.

## Description of the Crystal Structures

Single crystals suitable for X-ray analysis were isolated upon slow evaporation of a methanolic solution of **1** or **2** at room temperature. Crystals of **1** are unstable at room temperature and loose crystallinity in the absence of the mother liquor. A special precaution was taken (mentioned in experimental section) to analyze the structure. Crystallographic data for **1** and **2** are summarized in **Table S1** and selected dimensions (bond angle and lengths) are presented in **Table S2**. **Figures 1**, **2** represent the structures of the respective complexes.

The multidentate ligand (L$^1$)$^{2-}$ in **1** is planar and chelates to three Cu(II) ions through the *NNN,* the *NNO* and the *NO* pockets affording one 6-membered and four 5-membered metallacycles (**Figure 1A**). The copper cations are slightly displaced (maximum of 0.197 Å) toward the same side of the least-square plane of the organic ligand. Despite the planarity of (L$^1$)$^{2-}$, its derived 1D coordination polymer has a smoth wave-like shape imposed by the coordination mode of one of the nitrate anions behaving as bridging 1κ*OO'*:2κ*OO"* donors to Cu1 and Cu2; the least-square planes of adjacent (L$^1$)$^{2-}$ ligands make angles of 19.84°. The remaining nitrate ligands work as bidentate (to Cu1 and to Cu3) and as monodentate (to Cu3) ligands. The two water molecules are coordinated to the same copper cation (Cu2). The metal ions assume coordination numbers six (Cu2 and Cu3) and seven (Cu1), with the coordination polyhedron of Cu3 (**Figure 1B**) having no contact atom with the other polyhedra; those of Cu1 and Cu2 share an O$_{nitrate}$ atom. The *intra*chain Cu…Cu distances through the azine bridges are of 4.736 and 4.794 Å, and of 4.451

**FIGURE 1 | (A)** Ellipsoid plot of **1** with partial atom numbering scheme, **(B)** a fragment of its 1D polymeric chain with the metals in polyhedral representations (coordination number six represented in blue, and seven in violet), and **(C)** a view of the smooth wave-like nature of the chain. Symmetry operation to generate equivalent atoms: (i) 1.5–x, –y,1/2+z; (ii) 1.5–x, –y, −1/2+z.

Å through the nitrate bridge. The minimum *inter*chain Cu…Cu distance is of 5.692 Å.

The asymmetric unit of **2** contains two Cu(II) ions, one $(H_2L^2)^{2-}$, one nitrate and two water ligands, and a nitrate counter-ion. The organic ligand in **2** behaves as a hexadentate chelator acting as an *NOO* donor for each of the Cu(II) ions, therefore giving rise to two six- and two five-membered metallacycles (**Figure 1A**). Bridging monodentate nitrate anions connect the $\{Cu_2(H_2L^2)\}^{2-}$ moieties and generate a 1D polymeric chain running along the crystallographic *a* axis (**Figure 1C**). The copper cations adopt square pyramidal geometries ($\tau_5 = 0.04$ for Cu1 and 0.05 for Cu2) and share the $O_{nitrate}$ atom that stands in the axial position (**Figures 2A,C**). In view of the binding mode of the nitrates, the shortest Cu…Cu distance of 4.028 Å is along such ligands, while that along the hydrazone group exclusively (6.469 Å) is much longer than in **1** (see above). Resulting from the presence of a central methylene group in $(H_2L^2)^{2-}$ the ligand is highly twisted at this level, with the least-square planes of the two phenyl(methylene)acetohydrazide moieties making angles of 84.85°.

## Magnetic Properties

The dc magnetic susceptibility of **2** was measured under 2000 Oe field (**Figure 3**). The room temperature $\chi T$ value of 0.775 cm$^3$ K mol$^{-1}$ is a little larger than 0.750 cm$^3$ K mol$^{-1}$ calculated for two isolated Cu$^{2+}$ ions. The $\chi T$ value for **2** decreases gently with decreasing temperature in the range of 300–25 K, and then decreases sharply. The magnetic data at 50–300 K follow the Curie-Weiss law, with $C = 0.785$ cm$^3$.K.mol$^{-1}$ and $\Theta = -3.20$ K (**Figure S3**). The small negative $\Theta$ value suggests existence of weak antiferromagnetic interaction in **2**.

Based on the crystal structure, complex **2** is an alternative copper(II) chain compound, so two $J_1$ and $J_2$ parameters are necessary to describe the magnetic interaction, which are mediated through the ligand bridge and the $O_{nitrate}$ bridge, respectively. The magnetic data could be fitted by MagPack software using a Cu$_{14}$ cluster loop approximation (**Figure 4**). The Hamiltonian of the Cu$_{14}$ cluster loop with alternative $J_1$ and $J_2$ magnetic coupling constants is as follows: $H = -2J_1(S_{Cu1}S_{Cu2}+S_{Cu3}S_{Cu4}+S_{Cu5}S_{Cu6}+S_{Cu7}S_{Cu8}+S_{Cu9}S_{Cu10} + S_{Cu11}S_{Cu12}+S_{Cu13}S_{Cu14})-2J_2(S_{Cu2}S_{Cu3}+S_{Cu4}S_{Cu5}+S_{Cu6}S_{Cu7} + S_{Cu8}S_{Cu9}+S_{Cu10}S_{Cu11}+S_{Cu12}S_{Cu13}+S_{Cu14}S_{Cu1})$. The best
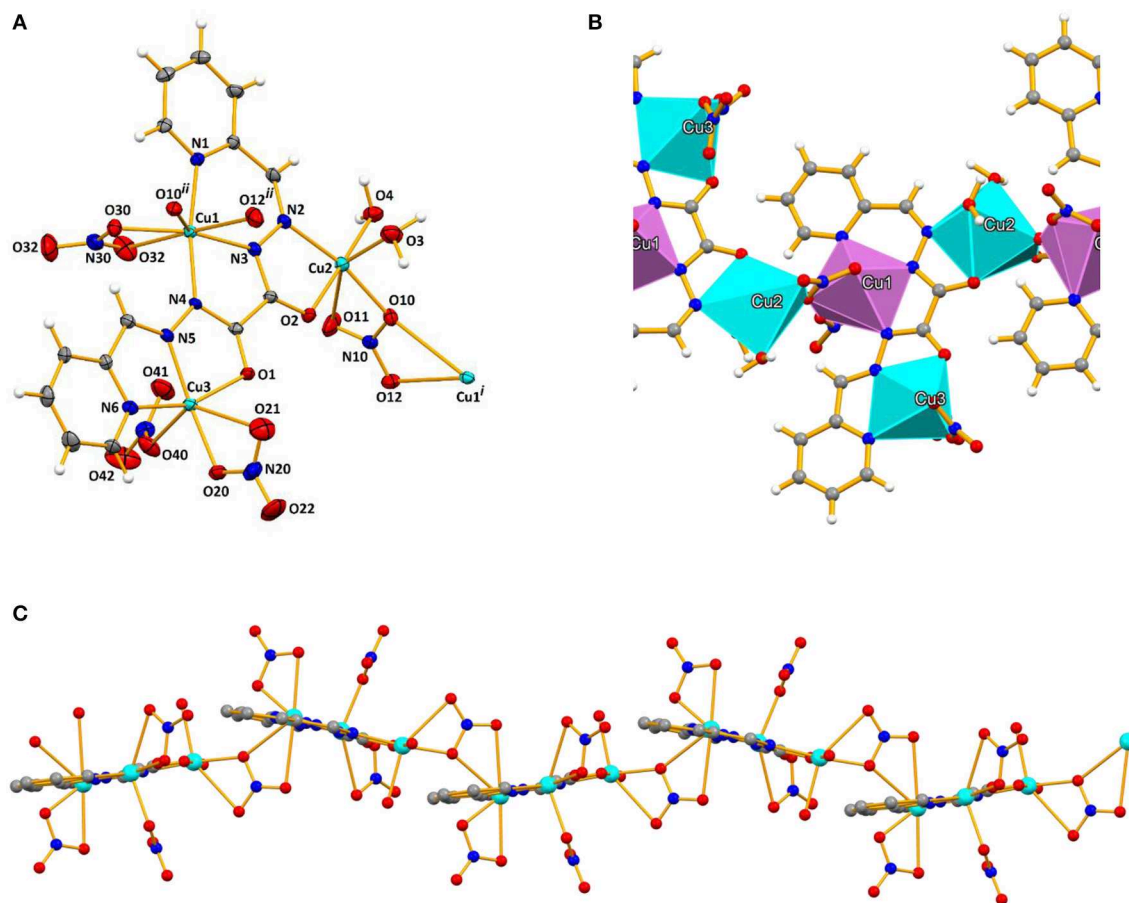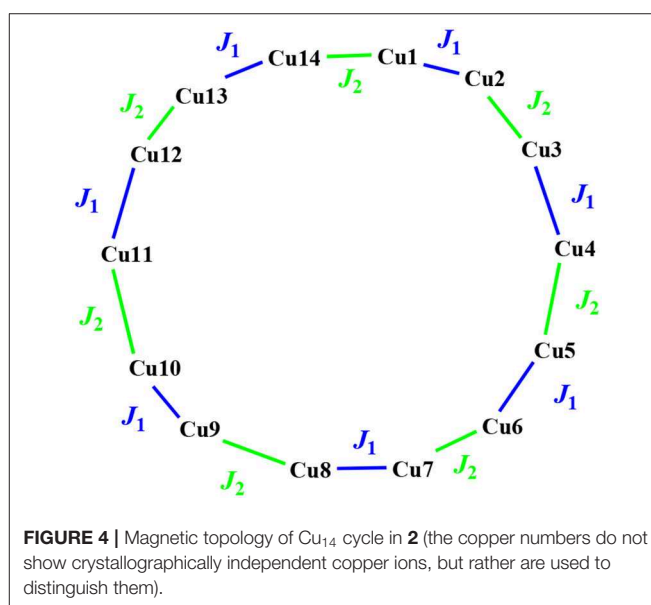
**FIGURE 2 | (A)** Ellipsoid plot of **2** with partial atom numbering scheme; **(B)** a fragment of 1D polymeric chain with the metals in polyhedral representation; **(C)** a view of the 1D chain. The nitrate counter-ions are omitted for clarity. Symmetry operations to generate equivalent atoms: (i) $1+x, y, z$; (ii) $-1+x, y, z$.



**FIGURE 3 |** Plot of $\chi T$ vs. $T$ for **2**. The solid line represents the best theoretical fitting.



**FIGURE 4 |** Magnetic topology of $Cu_{14}$ cycle in **2** (the copper numbers do not show crystallographically independent copper ions, but rather are used to distinguish them).

fitting gave $J_1 = -1.84$ cm$^{-1}$, $J_2 = -4.35$ cm$^{-1}$, $g = 2.10$ and $R = 1.6 \times 10^{-4}$. Both $J_1$ and $J_2$ values are small, suggesting that the antiferromagnetic interaction in **2** is weak. The $J_2$ value is more negative than that of $J_1$, indicating that the antiferromagnetic interaction

**SCHEME 2 |** MW-assisted solvent-free oxidation of 1-phenylethanol to acetophenone.

**TABLE 1 |** Solvent-free MW-assisted oxidation of 1-phenyethanol using **1** and **2** as catalysts precursors (selected data)[a].

| Entry | Substrate | Temperature (°C) | Additive (μmol) | Yield[b] (%) | TON [TOF (h$^{-1}$)]$^c$ |
|---|---|---|---|---|---|
| **1** | | | | | |
| 1 | | 80 | - | 15 | 150 (300) |
| 2 | | 120 | - | 68 | 334 (668) |
| 3 | OH | 80 | TEMPO (30) | 40 | 202 (404) |
| 4 | | 120 | TEMPO (30) | >99 | 588 (1.2 × 10$^3$) |
| 5 | | 80 | TFA (50) | 22 | 111 (222) |
| 6 | | 80 | TFA (100) | 25 | 124 (248) |
| 7 | | 80 | Hpca (50) | 13 | 102 (204) |
| **2** | | | | | |
| 8 | | 80 | - | 11 | 94 (188) |
| 9 | | 120 | - | 47 | 244 (488) |
| 10 | OH | 80 | TEMPO (30) | 33 | 163 (326) |
| 11 | | 120 | TEMPO (30) | >99 | 522 (1.0 × 10$^3$) |
| 12 | | 80 | TFA (50) | 16 | 81 (162) |
| 13 | | 80 | TFA (100) | 20 | 99 (198) |
| 14 | | 80 | Hpca (50) | 6 | 32 (64) |

$^a$Reaction conditions: 2.5 mmol of substrate, 5 μmol (0.2 mol% vs. substrate) catalyst **1** or **2**, 5 mmol of t-BuOOH (70% aq. solution), 0.5 h, 80 or 120°C, MW irradiation (5 or 20 W, respectively).
$^b$Molar yield (%) based on substrate, i.e., moles of product per 100 mol of substrate, determined by GC.
$^c$Turnover number = number of moles of product per mol of metal catalyst; TOF = TON per hour (values in brackets).

## Catalytic Studies Toward Microwave (MW) Assisted Oxidation of a Secondary Alcohol Under Solvent-Free Conditions
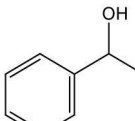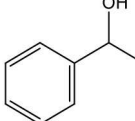
Cu(II) complexes **1** and **2** have been investigated as catalysts for the homogeneous oxidation of a secondary alcohol, 1-phenylethanol, to the corresponding ketone using *tert*-butylhydroperoxide (*tert*-BuOOH, TBHP, aq. 70%, 2 eq.) as oxidizing agent. The oxidation reactions were performed typically at 80 or 120°C, low power (5 or 20 W) microwave irradiation (MW), 0.5 h reaction time without additional solvent (**Scheme 2**). Results are summarized in **Table 1**.

Complexes **1** and **2** proved to be essential for the formation of acetophenone, since under similar reaction conditions and in the absence of these metal catalysts only traces of the desired product were detected. For catalytic tests performed only with the free ligand, no product was detected.

Under the studied conditions, the assays with copper catalysts **1** and **2** have shown comparable yields. For instance, for both **1** and **2** and using TBHP as oxidant at 120 °C, in the presence of TEMPO (2,2,6,6-tetramethylpiperydil-1-oxyl) radical, the almost complete conversion of 1-phenylethanol to the desired product is achieved after the short period of 30 min with a TON of 588 and 522, respectively (**Table 1**, entries 4 and 11, respectively).

For these encouraging results, the effect of temperature and the presence of TEMPO, a chemically stable nitroxyl radical which has emerged as a promoter for the metal catalyzed transformation of alcohols to the corresponding carbonyl products (Gamez et al., 2004; Sheldon and Arends, 2004; Figiel et al., 2007, 2009; Sheldon, 2008; Ahmad et al., 2009), seem to be determinant. Reactions carried out under the same reaction conditions but at 80°C and in the absence of any additive did not go beyond 15 and 11% in the presence of **1** and **2**, respectively



**FIGURE 5 |** Influence of temperature and of presence of TEMPO additive on the yield of acetophenone from oxidation of 1-phenylethanol catalyzed by **1** and **2**. Reaction conditions: 2.5 mmol of substrate, 5 μmol (0.2 mol% vs. substrate) catalyst **1** or **2**, 5 mmol of t-BuOOH, 0.5 h, 80 or 120°C (5 or 20 W, respectively).

(**Table 1**, entries 1 and 8, respectively) whereas when carried out at 120°C it was possible to observe a significant increase in yield to 68 and 47% for **1** and **2**, respectively (**Table 1**, entries 2 and 9, respectively). The combination of these two parameters, temperature at 120°C and presence of TEMPO radical (**Figure 5**), resulted in the complete conversion of 1-phenylethanol into acetophenone and TOFs up to 1200 h$^{-1}$ (**Table 1**, entries 4 and 11, for **1** and **2**, respectively).

**FIGURE 6 |** Influence of different additives on the yield of acetophenone from oxidation of 1-phenylethanol catalyzed by **1** and **2**. Reaction conditions: 2.5 mmol of substrate, 5 μmol (0.2 mol% vs. substrate) catalyst **1** or **2**, 5 mmol of *t*-BuOOH, 0.5 h, 80°C (5 W MW irradiation).
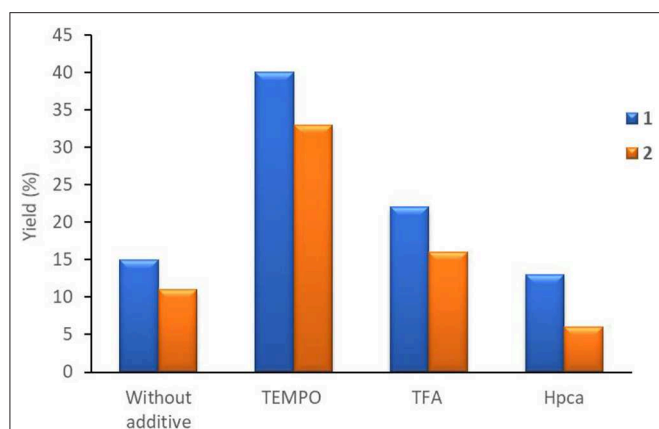
Considering the promoting effect of acid co-catalysts observed for other Cu-catalyzed oxidation systems (Sutradhar et al., 2016a,c, 2018), which are believed to accelerate the oxidation reactions by improving the oxidation properties of the complexes and by creating unsaturated metal centers (Sutradhar et al., 2015c), the influence of acidic additives on the acetophenone product yield was explored. The addition of trifluoroacetic acid (TFA) has a slight beneficial effect on both catalytic systems, resulting, for example, into a maximum yield of 25% (**Table 1**, entry 6), in the presence of **1** (at 80°C) (**Figure 6**). In contrary, the addition of the heteroaromatic 2-pyrazynecarboxylic acid (Hpca) has the opposite effect (**Figure 6**), i.e., a yield drop is observed when 50 μmol was used [$n$(acid)/$n$(catalyst **1** or **2**) = 10] (**Table 1**, entries 7 and 14, for **1** and **2**, respectively).

The promoting effect of TEMPO suggests the involvement of a radical mechanism which possibly involves the formation of *t*-BuOO' and *t*-BuO' radicals by a metal-assisted oxidation or reduction of *t*-BuOOH by a Cu$^{II}$ or a Cu$^{I}$ center, respectively (Gephart et al., 2012; Dronova et al., 2014), the latter behaving as an H-atom abstractor from the alcohol (Rothenberg et al., 1998; Mahdavi and Mardani, 2012; Frija et al., 2016; Sutradhar et al., 2016a,b, 2018; Ma et al., 2019).

## CONCLUSIONS

In this study we have successfully synthesized two 1D Cu(II) coordination polymers using two different multidenate aroylhyrazone Schiff bases. The X-ray crystallographic study indicates that the two ligands show different coordination behaviors. The $N'^1, N'^2$-bis(pyridin-2-ylmethylene)oxalohydrazide (H$_2$L$^1$), having a basic pyridine moiety, coordinates in the *iminol* form, whereas

the *amide* form is observed in the case of **2**. Both the ligand bridge and the nitrate bridge in **2** mediate weak antiferromagnetic interaction. The effects of temperature and of the aditive TEMPO dramatically increase the catalytic efficiency of both Cu(II) compounds in the microwave-assisted oxidation of 1-phenylethanol to acetophenone under solvent-free conditions.

Our study concerns an attempt to design Cu(II) coordination polymers with interesting magnetic properties and also for use as catalyst toward the development of environmentally friendly alcohol oxidation catalytic systems.

## DATA AVAILABILITY STATEMENT

All datasets generated for this study are included in the article/**Supplementary Material**. The crystallographic datasets generated for this study can also be found in the Cambridge Crystallographic Data Center (https://www.ccdc.cam.ac.uk/structures/) under the identifiers 1945551 and 1945552.

## AUTHOR CONTRIBUTIONS

MS: overall planning, synthesis and characterization of catalysts, and manuscript writing. EA: catalytic studies and manuscript writing. TB: catalytic studies, GC analysis and manuscript writing. MG: single crystal X-ray diffraction analysis. C-ML: Magnetic studies and manuscript writing. AP: manuscript reading and correcting.

## FUNDING

## ACKNOWLEDGMENTS

## SUPPLEMENTARY MATERIAL

The Supplementary Material for this article can be found online at: https://www.frontiersin.org/articles/10.3389/fchem.2020.00157/full#supplementary-material

**Data sheet 1 |** Crystal structures data.

# REFERENCES

Ahmad, J. U., Figiel, P. J., Räisänen, M. T., Leskelä, M., and Repo, T. (2009). Aerobic oxidation of benzylic alcohols with bis(3,5-di-tert-butylsalicylaldimine)copper(II) complexes. *Appl. Catal. A* 371, 17–21. doi: 10.1016/j.apcata.2009.09.011

Andruh, M. (2018). Heterotrimetallic complexes in molecular magnetism. *Chem. Commun.* 54, 3559–3577. doi: 10.1039/C8CC00939B

Andruh, M., Branzea, G. D., and Gheorghe, R., Madalan, A. M. (2009). Crystal engineering of hybrid inorganic–organic systems based upon complexes with dissymmetric compartmental ligands. *Cryst. Eng. Comm.* 11, 2571–2584. doi: 10.1039/b909476h

Benelli, C., and Gatteschi, D. (2002). Magnetism of lanthanides in molecular materials with transition-metal ions and organic radicals. *Chem. Rev.* 102, 2369–2388. doi: 10.1021/cr010303r

Bruker (2012). *APEX2*. Madison, Wisconsin: Bruker AXS Inc.,

Cho, Y. I., Ward, M. L., Rose, M. J. (2016). Substituent effects of N4 schiff base ligands on the formation of fluoride-bridged dicobalt(II) complexes via B-F abstraction: structures and magnetism. *Dalton. Trans.* 45, 13466–13476. doi: 10.1039/C6DT02104B

Dong, Y.-B., Smith, M. D., zur Loye, H.-C. (2000). New inorganic/organic coordination polymers generated from bidentate schiff-base ligands. *Inorg. Chem.* 39. 4927–4935. doi: 10.1021/ic0006504

Dronova, M. S., Bilyachenko, A. N., Yalymov, A. I., Kozlov, Y. N., Shul'pina, L. S., Korlyukov, A. A., et al. (2014). Solvent-controlled synthesis of tetranuclear cage-like copper(II) silsesquioxanes. Remarkable features of the cage structures and their high catalytic activity in oxidation with peroxides. *Dalton Trans.* 43, 872–882. doi: 10.1039/C3DT52508B

Dwivedi, N., Sunkari, S. S., Verma, A., Saha, S. (2018). Molecular packing dependent solid state fluorescence response of supramolecular metal-organic frameworks: phenoxo-bridged trinuclear Zn(II) centered schiff base complexes with halides and pseudohalides. *Cryst. Growth Des.* 18, 5628–5637. doi: 10.1021/acs.cgd.8b00948

El-Bindary, A. A., El-Sonbati, A. Z., Diab, M. A., Ghoneim, M. M., Serag, L. S. (2016). Polymeric complexes - LXII. Coordination chemistry of supramolecular schiff base polymer complexes—a review. *J. Mol. Liq.* 216, 318–329. doi: 10.1016/j.molliq.2015.12.113

Farrugia, L. J. (2012). WinGX and ORTEP for windows: an update. *J. Appl. Cryst.* 45, 849–854. doi: 10.1107/S0021889812029111

Figiel, P. J., Leskelä, M., Repo, T. (2007). TEMPO-copper(II) diimine-catalysed oxidation of benzylic alcohols in aqueous media. *Adv. Synth. Catal.* 349, 1173–1179. doi: 10.1002/adsc.200600505

Figiel, P. J., Sibaouih, A., Ahmad, J. U., Nieger, M., Räisänen, M. T., Leskelä, M., et al. (2009). Aerobic oxidation of benzylic alcohols in water by 2,2,6,6-tetramethylpiperidine-1-oxyl (TEMPO)/copper(II) 2-N-arylpyrrolecarbaldimino complexes. *Adv. Synth. Catal.* 351, 2625–2632. doi: 10.1002/adsc.200900478

Frija, L. M. T., Alegria, E. C. B. A., Sutradhar, M., Cristiano, M. L. S., Ismael, A., Kopylovich, M. N., et al. (2016). Copper(II) and cobalt(II) tetrazole-saccharinate complexes as effective catalysts for oxidation of secondary alcohols. *J. Mol. Cat. A Chem.* 425, 283–290. doi: 10.1016/j.molcata.2016.10.023

Gamez, P., Arends, I. W. C. E., Sheldon, R. A., Reedijk J. (2004). Room temperature aerobic copper–catalysed selective oxidation of primary alcohols to aldehydes. *Adv. Synth. Catal.* 346, 805–811. doi: 10.1002/adsc.200404063

Gephart, R. T., McMullin, C. L., Sapiezynski, N. G., Jang, E. S., Aguila, M. J. B., Cundari, T. R., et al. (2012). Reaction of Cu$^I$ with dialkyl peroxides: Cu$^{II}$-alkoxides, alkoxy radicals, and catalytic C–H etherification. *J. Am. Chem. Soc.* 134, 17350–17353. doi: 10.1021/ja3053688

Glaser, T., Hoeke, V., Gieb, K., Schnack, J., Schroder, C., and Muller, P. (2015). Quantum tunneling of the magnetization in [(Mn6M)-M-III](3+) (M = Cr-III, Mn-III) SMMs: impact of molecular and crystal symmetry. *Coord. Chem. Rev.* 289, 261–278. doi: 10.1016/j.ccr.2014.12.001

Journaux, Y., Ferrando-Soria, J., Pardo, E., Ruiz-Garcia, R., Julve, M., Lloret, F., et al. (2018). Design of magnetic coordination polymers built from polyoxalamide ligands: a thirty year story. *Eur. J. Inorg. Chem.* 228–247. doi: 10.1002/ejic.201700984

Kahn, O. (1993). *Molecular Magnetism*. New York: VCH.

Karotsis, G., Kenedy, S., Teat, S. J., Beavers, C. M., Fowler, D. A., Morales, J. J., et al. (2010). [Mn$_4^{III}$Ln$_4^{III}$] Calix[4]arene clusters as enhanced magnetic coolers and molecular magnets. *J. Am. Chem. Soc.* 132, 12983–12990. doi: 10.1021/ja104848m

Kitaura, R., Onoyama, G., Sakamoto, H., Matsuda, R., Noro, S-i., Kitagawa, S. (2004). Immobilization of a metallo schiff base into a microporous coordination polymer. *Angew. Chem. Int. Ed.* 43. 2684–2687. doi: 10.1002/anie.200352596

Kopylovich, M. N., Ribeiro, A. P. C., Alegria, E. C. B., Martins, N. M. R., Martins, L. M. D. R. S., Pombeiro, A. J. L. (2015). Catalytic oxidation of alcohols: recent advances. *Adv. Organomet. Chem.* 63, 91–174. doi: 10.1016/bs.adomc.2015.02.004

Leuenberger, M. N., Loss, D. (2001). Quantum computing in molecular magnets. *Nature* 410, 789–793. doi: 10.1038/35071024

Lu, Z., Fan, T., Guo, W., Lu, Z., Fan, C. (2013). Synthesis, structure and magnetism of three cubane Cu(II) and Ni(II) complexes based on flexible schiff-base ligands. *Inorg. Chim. Acta* 400, 191–196. doi: 10.1016/j.ica.2013.02.030

Ma, Z., Wang, Q., Yang, H., Alegria, E. C. B. A., Guedes da Silva, M. F. C., Martins, L. M. D. R. S., et al. (2019). Synthesis and structure of copper complexes of a N$_6$O$_4$ macrocyclic ligand and catalytic application in alcohol oxidation. *Catalysts* 9:424. doi: 10.3390/catal9050424

Mahdavi, V., Mardani, M. (2012). Selective oxidation of benzyl alcohol with tert-butylhydroperoxide catalysed via Mn (II) 2, 2-bipyridine complexes immobilized over the mesoporous hexagonal molecular sieves (HMS). *J. Chem. Sci.* 124, 1107–1115. doi: 10.1007/s12039-012-0307-4

Maniaki, D., Pilichos, E., Perlepes, S. P. (2018). Coordination clusters of 3d-metals that behave as single-molecule magnets (SMMs): synthetic routes and strategies. *Front. Chem.* 6:461. doi: 10.3389/fchem.2018.00461

Pombeiro, A. J. L. (2013). *Advances in Organometallic Chemistry and Catalysis*. Hoboken, NJ: Wiley, 15–25. doi: 10.1002/9781118742952.ch2

Pombeiro, A. J. L. (2019). "Alkane Functionalization: Introduction and Overview," in *Alkane Functionalization*, eds A. J. L. Pombeiro and M. F. C. Guedes da Silva (Hoboken, NJ: Wiley), 1–15. doi: 10.1002/9781119379256.ch1

Pradeep, C. P., Das, S. K. (2013). Coordination and supramolecular aspects of the metal complexes of chiral N-salicyl-beta-amino alcohol schiff base ligands: towards understanding the roles of weak interactions in their catalytic reactions. *Coord. Chem. Rev.* 257, 1699–1715. doi: 10.1016/j.ccr.2013.01.028

Rothenberg, G., Feldberg, L., Wiener, H., Sasson, Y. J. (1998). Copper-catalyzed homolytic and heterolytic benzylic and allylic oxidation using tert-butyl hydroperoxide. *Chem. Soc. Perkin Trans.* 2, 2429–2434. doi: 10.1039/a805324c

Sheldon, R. A. (2008). E factors, green chemistry and catalysis: an odyssey. *Chem. Commun.* 29, 3352–3365. doi: 10.1039/b803584a

Sheldon, R. A., Arends, I. W. C. E. (2004). Organocatalytic oxidations mediated by nitroxyl radicals. *Adv. Synth. Catal.* 346, 1051–1071. doi: 10.1002/adsc.200404110

Sheldrick, G. M. (2000). *SADABS*. Program for Empirical Absorption Correction. Göttingen: University of Göttingen.

Sheldrick, G. M. (2015). Crystal structure refinement with SHELXL. *Acta Cryst.* C71, 3–8. doi: 10.1107/S2053229614024218

Spek, A. L. (2009). Structure validation in chemical crystallography. *Acta Cryst.* D65, 148–155. doi: 10.1107/S0907444908004362X

Sureshbabu, P., Junaid, Q. M., Upadhyay, C., Victoria, W., Pitchavel, V., Natarajan, S., Sabiah, S. (2019). Di and tetranuclear Cu(II) complexes with simple 2-aminoethylpyridine: magnetic properties, phosphodiester hydrolysis, DNA binding/cleavage, cytotoxicity and catecholase activity. *Polyhedron* 164, 202–218. doi: 10.1016/j.poly.2019.02.015

Sutradhar, M., Alegria, E. C. B. A., Guedes da Silva, M. F. C., Liu, C.-M., Pombeiro, A. J. L. (2018). Peroxidative oxidation of alkanes and alcohols under mild conditions by di- and tetranuclear copper(II) complexes of bis(2-hydroxybenzylidene)isophthalohydrazide. *Molecules* 23:2699. doi: 10.3390/molecules23102699

Sutradhar, M., Alegria, E. C. B. A., Guedes da Silva, M. F. C., Martins, L. M. D. R. S., Pombeiro, A. J. L. (2016b). Aroylhydrazone Cu(II) complexes in keto form: structural characterization and catalytic activity towards cyclohexane oxidation. *Molecules* 21:425. doi: 10.3390/molecules21040425

Sutradhar, M., Alegria, E. C. B. A., Mahmudov, K. T., Guedes da Silva, M. F. C., Pombeiro, A. J. L. (2016a). Iron(III) and cobalt(III) complexes with both tautomeric (keto and enol) forms of aroylhydrazone ligands: catalysts

for the microwave assisted oxidation of alcohols. *RSC Adv.* 6, 8079–8088. doi: 10.1039/C5RA25774C

Sutradhar, M., Alegria, E. C. B. A., Roy Barman, T., Scorcelletti, F., Guedes da Silva, M. F. C., Pombeiro, A. J. L. (2017). Microwave-assisted peroxidative oxidation of toluene and 1-phenylethanol with monomeric keto and polymeric enol aroylhydrazone Cu(II) complexes. *Mol. Catal.* 439, 224–232. doi: 10.1016/j.mcat.2017.07.006

Sutradhar, M., Carrella, L. M., Rentschler, E. (2012). A discrete µ4-oxido tetranuclear iron(III) cluster. *Eur. J. Inorg. Chem.* 2017, 4273–4278. doi: 10.1002/ejic.201200396

Sutradhar, M., Guedes da Silva, M. F. C., Pombeiro, A. J. L. (2014a). A new cyclic binuclear Ni(II) complex as a catalyst towards nitroaldol (Henry) reaction. *Catal. Commun.* 57, 103–106. doi: 10.1016/j.catcom.2014.08.013

Sutradhar, M., Kirillova, M. V., Guedes da Silva, M. F. C., Liu, C. -M., Pombeiro, A. J. L. (2013). Tautomeric effect of hydrazone schiff bases in tetranuclear Cu(II) complexes: magnetism and catalytic activity towards mild hydrocarboxylation of alkanes. *Dalton. Trans.* 42, 16578–16587. doi: 10.1039/c3dt52453a

Sutradhar, M., Martins, L. M. D. R. S., Carabineiro, S. A. C., Guedes da Silva, M. F. C., Buijnsters, J. G., Figueiredo, J. L., et al. (2016c). Oxidovanadium(V) complexes anchored on carbon materials as catalysts for the oxidation of 1-phenylethanol. *ChemCatChem* 8, 2254–2266. doi: 10.1002/cctc.201600316

Sutradhar, M., Martins, L. M. D. R. S., Guedes da Silva, M. F. C., Alegria, E. C. B. A., Liu, C.-M., and Pombeiro, A. J. L. (2014b). Mn(II,II) complexes: magnetic properties and microwave assisted oxidation of alcohols. *Dalton Trans.* 43, 3966–3977. doi: 10.1039/c3dt52774c

Sutradhar, M., Martins, L. M. D. R. S., Guedes da Silva, M. F. C., Mahmudov, K. T., Liu, C.-M., and Pombeiro, A. J. L. (2015a). Trinuclear Cu(II) structural isomers: coordination, magnetism, electrochemistry and catalytic activity toward oxidation of alkanes. *Eur. J. Inorg. Chem.* 2015, 3959–3969. doi: 10.1002/ejic.201500440

Sutradhar, M., Martins, L. M. D. R. S., Guedes da Silva, M. F. C., Pombeiro, A. J. L. (2015b). Vanadium complexes: recent progress in oxidation catalysis. *Coord. Chem. Rev.* 301–302, 200–239. doi: 10.1016/j.ccr.2015.01.020

Sutradhar, M., Martins, L. M. D. R. S., Guedes da Silva, M. F. C., Pombeiro, A. J. L. (2015c). Oxido vanadium complexes with tridentate aroylhydrazone as catalyst precursors for solvent-free microwave-assisted oxidation of alcohol. *Appl. Cat. A Gen.* 493, 50–57. doi: 10.1016/j.apcata.2015.01.005

Sutradhar, M., Roy Barman, T., Pombeiro, A. J. L., Martins, L. M. D. R. S. (2019). Catalytic activity of polynuclear vs. dinuclear aroylhydrazone Cu(II) complexes in microwave-assisted oxidation of neat aliphatic and aromatic hydrocarbons. *Molecules* 24:47. doi: 10.3390/molecules24010047

Yue, Q., Gao, E. Q. (2019). Azide and carboxylate as simultaneous coupler for magnetic coordination polymers. *Coord. Chem. Rev.* 382, 1–31. doi: 10.1016/j.ccr.2018.12.002

Zheng, Y. Z., Zheng, Z. P., Chen, X. M. (2014). A symbol approach for classification of molecule-based magnetic materials exemplified by coordination polymers of metal carboxylates. *Coord. Chem. Rev.* 258, 1–15. doi: 10.1016/j.ccr.2013.08.031

# Metal Oxysulfides: From Bulk Compounds to Nanomaterials

Clément Larquet[1,2] and Sophie Carenco[1]*

[1] Sorbonne Université, CNRS, Collège de France, Laboratoire de Chimie de la Matière Condensée de Paris, LCMCP, Paris, France, [2] Sorbonne Université, CNRS, IRD, MNHN, Institut de Minéralogie, de Physique des Matériaux et de Cosmologie, IMPMC, Paris, France

This review summarizes the syntheses and applications of metal oxysulfides. Bulk compounds of rare earth and transition metals are discussed in the section Introduction. After a presentation of their main properties and applications, their structures are presented and their syntheses are discussed. The section Bulk Materials and Their Main Applications is dedicated to the growing field of nanoscaled metal oxysulfides. Synthesis and applications of lanthanide-based nanoparticles are more mature and are discussed first. Then, works on transition-metal based nanoparticles are presented and discussed. Altogether, this review highlights the opportunities offered by metal oxysulfides for application in a range of technological fields, in relation with the most advanced synthetic routes and characterization techniques.

Keywords: oxysulfide, lanthanides, sulfidation, transition metal, nanoparticles, synthesis, applications

## INTRODUCTION

### Definition

A "metal oxysulfide" is a compound composed of at least a metal, oxygen and sulfur, with negative oxidation states (e.g., –II) for both oxygen and sulfur. The generic formula for ternary oxysulfide is $M_xO_yS_z$. Due to its negative oxidation state, sulfur forms no bounds with oxygen in oxysulfides, in contrast with more common metal sulfates $M_x(S^{VI}O_4)_y$ where the sulfur is +IV.

In 1951, Eastman et al. recommended the following distinction (Eastman et al., 1951): $M_xO_yS_z$ compounds should be designed by the general term "oxide-sulfide" and named after the similarities of their crystalline structure with the corresponding oxide or sulfide. If the oxide-sulfide has the same crystalline structure than the oxide, it should be named "thio-oxide"; if its crystalline structure is the same than the sulfide, it should be called "oxy-sulfide" and if its structure is none of the two, it should be called "sulfoxide."

However, in an article of 1958 published in French, Flahaut et al. questioned this nomenclature (Flahaut et al., 1958). They argued that all the $Ln_2O_2S$ (Ln, lanthanide) compounds crystallize in the same structure and showed similar chemical properties. With Eastman's nomenclature, because $Ln_2O_3$ oxides crystallize in the two different structures $Ce_2O_3$ and $Tl_2O_3$, the $Ln_2O_2S$ compounds would have been named "thioxyde" (French word for thio-oxide) from lanthanum to praseodymium and "sulfoxyde" (sulfoxide) for the others.

Although the terms "thio-oxide" and "oxide-sulfide" are still present in the literature, "oxysulfide" is now employed in a large majority of the works to name any combination on one or several metals to oxygen and sulfur anions.

Altogether, metal oxysulfides represent a class of compounds that is independent from both metal oxides and metal sulfides, though common properties may be punctually identified depending on the metal, the crystal structure, and the anion substitution scheme.

## Discovery and First Phases

Oxysulfides are scarce in nature and are the most often synthetic. One reason for this is the competitive formation of sulfates, which are found in numerous minerals and are more stable toward oxidation. This competition between sulfate and sulfide is also at stake when designing a synthetic route.

To the best of our knowledge, the first occurrence of an oxysulfide compound was reported in 1827 by Mosander, who was working on the sulfidation of $Ce_2O_3$ into $Ce_2S_3$ using $H_2S$ (**Figure 1**). He noticed the presence of oxygen and sulfur combined with the metal in a single product, along with the formation of cerium sulfate. Later, Sterba (1904) and Biltz (1908) also reported this observation. Biltz even proposed the formula $Ce_2S_{2.5}O \cdot S$ as he identified remaining sulfur as polysulfide on its final product. In 1907, Hauser prepared using $H_2S$ on oxides two oxysulfides of tetravalent metal, namely ZrOS and ThOS based on their composition (Hauser, 1907). Hauser indicated that the zirconium and thorium oxysulfides were pyrophoric. Without knowing it, Klemm et al. were probably the first to obtain a pure phase of $Ln_2O_2S$ by heating $Er(SO_4)_3$ in $H_2S$ and consequently getting $Er_2O_2S$, that they only described as pale pink and resistant to other heating treatments in $H_2S$ (Klemm et al., 1930).

The first crystalline oxysulfide structures were elucidated by Pitha et al. (1947) ($La_2O_2S$) and Zachariasen (1949a) ($La_2O_2S$, $Ce_2O_2S$, and $Pu_2O_2S$). The samples often contained impurities and were prepared either by reducing the corresponding sulfate $Ln_2(SO_4)_3$ using $H_2$ or by gently heating in air sesquisulfide compounds ($Ln_2S_3$). The two authors noticed that the metal was coordinated to seven atoms: four atoms of oxygen and three atoms of sulfur. The $Ln_2O_2S$ structure derives from the hexagonal oxide $Ln_2O_3$ and crystallizes in the *P-3m1* space group. This lamellar structure can be described as alternating sheets of $[Ln_2O_2]^{2+}$ and $S^{2-}$ (**Figure 2**). Since this discovery, the entire series of lanthanide oxysulfide $Ln_2O_2S$ (except promethium) was prepared (Flahaut et al., 1958).

In 1948, McCullough et al. established the structure of cubic ZrOS (McCullough et al., 1948) prepared similarly to Hauser and in 1962, Jellinek described a new tetragonal form with the same composition (Jellinek, 1962). In the 1960's and the 1970's, more $M_2O_2S$ compounds were also reported. The work on radioactive elements gave the actinide oxysulfides $Np_2O_2S$ (Marcon, 1967a), $Am_2O_2S$ (Haire and Fahey, 1977), $Cm_2O_2S$ (Haire and Fahey, 1977), $Bk_2O_2S$ (Haire and Fahey, 1977), and $Cf_2O_2S$ (Baybarz et al., 1974). Similarly to $Ln_2O_2S$ compounds, $An_2O_2S$ (An, actinide) materials crystallize in the *P-3m1* space group. On the contrary, $Sc_2O_2S$ crystallizes in the hexagonal $P6_3/mmc$ space group. Its structure remains very close to $Ln_2O_2S$ with a coordinence of seven for scandium atoms and a structure based on alternative layers of $[Sc_2O_2]^{2+}$ and $S^{2-}$ (Julien-Pouzol et al., 1978).

In 1949, Zachariasen described the structure of tetravalent actinide oxysulfides ThOS, UOS, and NpOS as presenting a PbFCl structure type with tetragonal symmetry in *P4/nmm* space group. The tetragonal form of ZrOS described by Jellinek is isostructural of these compounds (Zachariasen, 1949b). On the contrary, cubic HfOS (isostructural to cubic ZrOS) was first identified by Stocks et al. (1980) and prepared as a pure

phase by Eisman and Steinfink (1982). The latter were also able to prepare solid solutions of zirconium and hafnium oxysulfides $Zr_{1-x}Hf_xOS$ ($0 \leq x \leq 1$) such as $Zr_{0.25}Hf_{0.75}OS$ and $Zr_{0.75}Hf_{0.25}OS$.

A few years later, Khodadad et al. and Ballestracci demonstrated the existence of several $Ln_2O_2S_2$ compounds (Ln = La, Pr, and Nd), where the disulfide $[S_2]^{2-}$ anion is present (Khodadad et al., 1965; Ballestracci, 1967; Wichelhaus, 1978a). They have to be distinguished from AnOS (An, actinide) compounds in which the actinide is at the +IV oxidation state while the lanthanide in $Ln_2O_2S_2$ remains at the +III oxidation state.

In 1967, Kupčík reported the kermesite's structure (Kupčík, 1967). The antimony-based compound $Sb_2OS_2$ is a rare crystalline natural oxysulfide mineral, which can form thanks to a partial oxidation of stibnite $Sb_2S_3$. This so-called oxydisulfide $M_2OS_2$ composition was also synthetically obtained for lanthanide compounds $Ln_2OS_2$ [Ln = Sm (Lissner and Schleid, 1992), Gd (Wontcheu and Schleid, 2003), Tb (Schleid, 1991a), Dy (Schleid, 1991b), Er (Range et al., 1990), Tm (Range et al., 1990), Yb (Range et al., 1990), Y (Schleid, 1992)]. The erbium, thulium, and ytterbium compounds were obtained at 10 kbar and 1,600°C.

A sulfur-rich phase was also discovered by trying to solve the crystalline structure of what was thought to be $\beta$-$Ln_2S_3$. It happened to be $Ln_{10}OS_{14}$ (Ln = La, Ce, Pr, Nd, Sm) that formed because of traces of water or oxygen during the reaction (Carré et al., 1970; Besançon, 1973). Besançon et al. showed that the oxygen content of $Ln_{10}S_{14}O_xS_{1-x}$ can be lowered down to a value close to 0.1 mol% for La, Ce, and Pr (Besançon et al., 1970, 1973). Later, Schleid et al. also reported the gadolinium compound $Gd_{10}OS_{14}$ (Schleid and Weber, 1998).

The work of Marcon with actinides led to the first description of more complex compounds, namely $M^{III}_2M^{IV}_2O_4S_3$ ($Pu_4O_4S_3$, $U_2Pu_2O_4S_3$, $U_2Gd_2O_4S_3$, and $Ce_4O_4S_3$), based on composition analysis (Marcon, 1967b). He also completed the work of Zachariasen by obtaining PuOS (Marcon, 1967b). In the same time, based on the work of Marcon, the compositions of cerium oxysulfides $Ce_4O_4S_3$ (Dugué et al., 1978; Wichelhaus, 1978b) and $Ce_6O_6S_4$ (Dugué et al., 1979) were confirmed and their structures were elucidated by X-Ray diffraction on monocrystals by Dugué et al. and Wichelhaus. $Ce_4O_4S_3$ and $Ce_6O_6S_4$ monocrystals were obtained by heating $Ce_2O_2S$ and sulfur or $CeO_2$, $Ce_2S_3$, and sulfur together. In the lanthanide series, only cerium allows both oxidation states +III and +IV. In $Ce^{III}_2O_2S$, partial oxidation of cerium led to $Ce^{III}_2Ce^{IV}_2O_4S_3$ and $Ce^{III}_4Ce^{IV}_2O_6S_4$.

A decade after the discovery of $Bi_2O_2Se$ (Boller, 1973), Koyama et al. published in 1984 a study about the combination of bismuth with chalcogens. They obtained the ternary oxysulfide $Bi_2O_2S$ from $Bi_2O_3$ and $Bi_2S_3$ via a hydrothermal synthesis (Koyama et al., 1984). The $Bi_2O_2S$ structure differs from $Ln_2O_2S$ (Ln, lanthanide), as it crystallizes in the *Pnnm* space group.

The coordination number of the bismuth is eight: bismuth is bound to four atoms of oxygen and four atoms of sulfur (**Figure 3**). In comparison with $Ln_2O_2S$ in which Ln forms four Ln-O and three Ln-S bonds, bismuth-oxygen bonds are in the same length range (between 2.2 and 2.5 Å) but bismuth-sulfur

FIGURE 1 | Key dates and authors of the oxysulfide research with some related structures. Ln stands for lanthanide and An for actinide. $An_2O_2S$ compounds are also known since 1949 ($Pu_2O_2S$) and possess the same structure as $Ln_2O_2S$.



FIGURE 2 | (A) $Ln_2O_2S$ structure: a hexagonal layered structure (Ln = Gd). (B) Lanthanide environment in hexagonal lanthanide oxide $Ln_2O_3$ (JCPDS 02-1878), lanthanide sesquisulfide $Ln_2S_3$ (JCPDS 03-2364) and lanthanide oxysulfide $Ln_2O_2S$ (JCPDS 06-8819) with the example of gadolinium.



FIGURE 3 | Structure of $Bi_2O_2S$ (JCPDS 10-2907) and bismuth coordination in the solid.

## BULK MATERIALS AND THEIR MAIN APPLICATIONS

### Toward More Complex Structures: Quaternary Oxysulfides and Selective Bonding

We already cited the work of Marcon who isolated actinide oxysulfides $U_2Pu_2O_4S_3$ and $U_2Gd_2O_4S_3$ (Marcon, 1967b). These structures contain $U^{IV}$ and $Ln^{III}$. This mixed valence allowed

bonds are significantly longer (3.4 Å for $Bi_2O_2S$, <3 Å for $Ln_2O_2S$). Further works showed that bismuth can form several oxysulfides, leading to superconductive $Bi_4O_4S_3$ (Zhang et al., 2015) (containing both sulfide and sulfate ions) and to $Bi_9O_{7.5}S_6$ (Meng et al., 2015).

the formation of the $An^{IV}_2Ln^{III}_2O_4S_3$ and $An^{IV}_2Ln^{III}_4O_6S_4$ (of general formula $An^{IV}_2Ln^{III}_{2n}O_{2+2n}S_{2+n}$) structures by a shearing mechanism of the $Ln_2O_2S$ structure when similar mixed-valent uranium-lanthanide oxysulfides were obtained (Tien et al., 1988). With Okabe et al. (1988), they also exhibited a series of $U_2La_{2n-2}O_{2n}S_{n+1}$ compounds.

Besides, in the 1980's, a considerable amount of quaternary oxysulfides containing other metals than lanthanides or actinides were synthesized. Firstly, the idea was to insert another metal in the lamellar structure of a lanthanide oxysulfide $Ln_2O_2S$. The easiest way to get a quaternary oxysulfide was to put the other metal in the layer of sulfur anions, and consequently obtain a structure composed by sheets of lanthanide oxide and metal sulfide. This compound, in which oxygen is bound only to the lanthanide and sulfur only to the additional metal, exhibits a particular order that one can call *selective bonding*. As the quaternary oxysulfides can be formed with a large variety of precursors (mainly oxides and sulfides, but also elemental sulfur, $H_2S$, metals, …) and not only using lamellar preformed structures such as $Ln_2O_2S$, this selective bonding can be extended to any resulting oxysulfide in which one of the anions is preferentially bound to one of the metals and conversely. It generally led to layered compounds. On the contrary, when no such order is present in the structure (at least one metal site in the structure is bound to the two anions), the compound exhibits *unselective bonding*.

To illustrate this difference, we chose to study a family of quaternary oxysulfides $Ln_2Ti_2S_2O_5$ (with $Ti^{IV}$) reported in the late 1990's (**Figures 4A–D**). These structures turned out to be defective Ruddlesden-Popper phases which alternate $[Ln_2S_2]^{2+}$

and $[Ti_2O_5]^{2-}$ layers (**Figure 4A**). However, it is also possible to get compounds where both metals are equally bound to both oxygen and sulfur without particular arrangement (unselective bonding). It can be illustrated by the previously reported quaternary titanium oxysulfides $La_4Ti_3O_8S_4$ and $La_6Ti_2S_8O_5$ that do not show any selective bonding (**Figures 4B,D**; Cody and Ibers, 1995). In the 1980's, the study of the $La_wGa_xO_yS_z$ compounds already started the reflexion on the selectivity of the bonds in quaternary oxysulfides (selective bonding for $LaGaOS_2$-α, $La_4Ga_{1.33}O_4S_4$, and $La_3GaOS_5$; unselective bonding for $LaGaOS_2$-β and $La_{3.33}Ga_6O_2S_{12}$, **Table 1**; Guittard et al., 1985).

## Quaternary Oxysulfides: A Large Catalog of Compositions

Using high temperatures and long reaction times, monovalent ($Cu^I$, $Ag^I$), trivalent ($Cr^{III}$, $Ga^{III}$, $As^{III}$, $Sb^{III}$, $Bi^{III}$), tetravalent ($Sn^{IV}$) and pentavalent elements ($Nb^V$) were shown to be able to crystallize along with a lanthanide in various types of oxysulfide compounds (**Table 1**). In some cases, the second metal can also present mixed oxidation states ($Ti^{III,IV}$, $V^{III,IV}$).

More recently, lanthanide-free quaternary oxysulfide compounds CaMOS [M = Fe (Selivanov et al., 2004; Delacotte et al., 2015), Co (Pitha et al., 1947), Zn (McCullough et al., 1948)] and BaM'OS [with M' = Co (Pitha et al., 1947; Valldor et al., 2015), Zn (Broadley et al., 2005)] were synthesized and characterized. This shows the growing interest in obtaining metal oxysulfides without rare earth (which are strategic resources) in order to explore their magnetic and catalytic properties.



**FIGURE 4** | Various quarternary oxysulfide structures containing titanium. **(A)** $Sm_2Ti_2O_5S_2$ (JCPDS 13-1325) exhibits selective bonding as sulfur is preferentially bound to titanium and oxygen to samarium. **(B)** $La_4Ti_3O_8S_4$ (JCPDS 09-7018), **(C)** $La_8Ti_{10}O_4S_{24}$ (JCPDS 09-8085), and **(D)** $La_6Ti_2O_5S_8$ (JCPDS 09-7017) show different structures with unselective bonding.
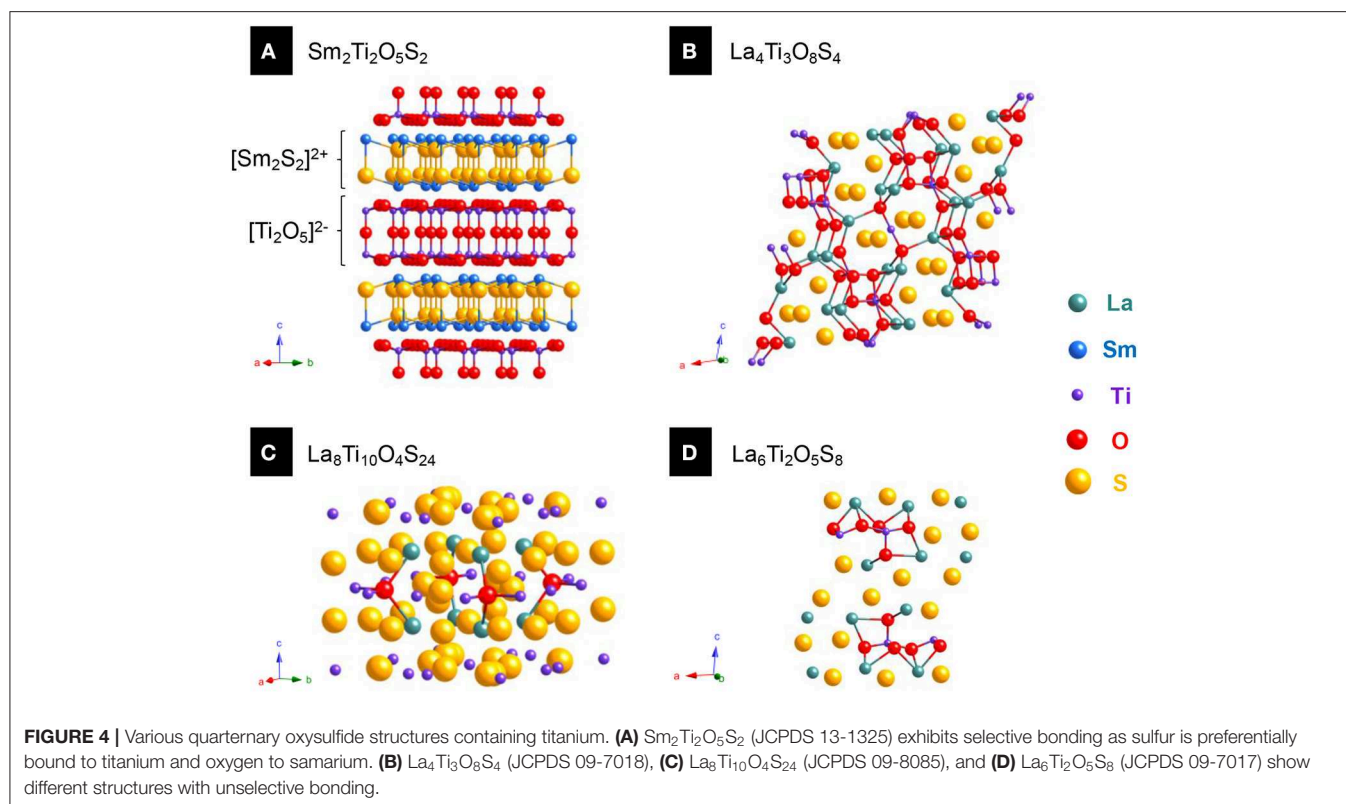
**TABLE 1 |** Quaternary oxysulfides $M^1_w M^2_x O_y S_z$.

| Phase | Space group | Bonding[a] | References |
|---|---|---|---|
| $An_w An_x O_y S_z$ and $An_w Ln_x O_y S_z$ | | | |
| (An, actinide; Ln, lanthanide) | | | |
| $U_{0.5} Pu_{0.5} OS$ | Tetragonal $P/nmm$ | S | Marcon, 1967b |
| $U_2 Pu_2 O_4 S_3$ | Orthorhombic $Pbam$[b] | U | Marcon, 1967b |
| $U_2 Ln_2 O_4 S_3$ | Orthorhombic $Pbam$ | U | Marcon, 1967b; Tien et al., 1988 |
| (Ln = La, Ce, Pr, Nd, Sm, Gd, Tb) | | | |
| $U_2 Ln_4 O_6 S_4$ | Orthorhombic $Pnam$ | U | Tien et al., 1988 |
| (Ln = La, Ce, Pr, Nd, Sm, Gd, Tb) | | | |
| $U_2 La_8 O_8 S_5$ | Orthorhombic | U | Tien et al., 1988 |
| $U_2 La_8 O_{10} S_6$ | | | |
| $U_2 La_{10} O_{12} S_7$ | | | |
| $U_2 Ln O_2 S_3$ | Tetragonal $I4/mmm$ | S | Guittard et al., 1986 |
| (Ln = Gd, Dy, Ho, Er, Tm, Yb, Lu, Y) | | | |
| $U_4 Lu_4 O_4 S_5$ | Tetragonal $I4/mmm$ | S | Jaulmes et al., 1990 |
| $Ln_w M_x O_y S_z$ | | | |
| (Ln, lanthanide or bismuth; M, 1st row transition metal) | | | |
| $Ln_2 Ti_2 O_5 S_2$ | Tetragonal $I4/mmm$ | S | Boyer et al., 1999; Goga et al., 1999 |
| (Ln = Pr, Nd, Sm) | | | |
| $La_{16} Ti_5 O_{17} S_{17+x}$ ($x = 0.75$) | Tetragonal $I4/m$ | U | Meignen et al., 2003 |
| $La_4 Ti_3 O_8 S_4$ | Monoclinic $C2/m$ | U | Cody and Ibers, 1995 |
| $La_6 Ti_2 O_5 S_8$ | Monoclinic $P2_1/m$ | U | Cody and Ibers, 1995 |
| $La_{14} Ti_8 O_4 S_{33}$ | Monoclinic $C2/m$ | U | Tranchitella et al., 1996 |
| $La_8 Ti_{10} O_4 S_{24}$ | Tetragonal $P4/mmm$ | U | Cario et al., 1998 |
| $La_{8.75} Ti_{9.25} O_4 S_{24}$ | Tetragonal $P4/mmm$ | U | Tranchitella et al., 1998 |
| $La_{8.50} Ti_{9.50} O_4 S_{24}$ | | | |
| $La_{8.10} Ti_{8.05} O_4 S_{24}$ | | | |
| $La_{20} Ti_{11} O_6 S_{44}$ | Orthorhombic $Pmmn$ | U | Deudon et al., 1995 |
| $Ce_{20} Ti_{11} O_6 S_{44}$ | Orthorhombic $Pmmn$ | U | Cody et al., 1997 |
| $Nd_{16} Ti_5 O_{17} S_{17}$ | Tetragonal $I4/m$ | U | Boyer-Candalen et al., 2000a |
| $Gd_{6+x} Ti_{4-x} S_{10-y} O_{6+y}$ | Orthorhombic $Pnma$ | U | Meignen et al., 2004a |
| $Ln_5 V_3 O_7 S_6$ | Orthorhombic $Pmnm$ | U | Vovan et al., 1981; Dugué et al., 1985 |
| (Ln = La, Ce, Pr, Nd) | | | |
| $LaCrOS_2$ | Orthorhombic $Pbnm$ | U | Vovan et al., 1978; Dugué et al., 1980a |
| $LnCrOS_2$ | Monoclinic $B2/m$ | U | Vovan et al., 1978; Dugué et al., 1980b |
| (Ln = Ce, Pr, Nd, Sm) | | | |
| $La_4 MnOS_6$ | Hexagonal $P6_3 mc$ | U | Ijjaali et al., 2005 |
| $Ln_2 Fe_2 O_3 S_2$ | Tetragonal $I4/mmm$ | U | Mayer et al., 1992; Charkin et al., 2011 |
| (Ln = La, Ce, Pr) | | | |
| $LaCuOS$ | Tetragonal $P4/nmm$ | S | Palazzi, 1981; Doussier-Brochard et al., 2010 |
| $La_5 Cu_6 O_4 S_7$ | Orthorhombic $Imma$ | U | Huang et al., 2000 |
| $CeCu_x OS$ | Tetragonal $P4/nmm$ | S | Ueda et al., 2003; Chan et al., 2006 |
| ($x = 0.8$; 1) | | | |
| $PrCuOS$ | Tetragonal $P4/nmm$ | S | Lauxmann and Schleid, 2000 |
| $LnCuOS$ | Tetragonal $P4/nmm$ | S | Popovkin et al., 1998 |
| (Ln = Nd, Sm) | | | |
| $BiCuOS$ | Tetragonal $P4/nmm$ | S | Kusainova et al., 1994; Sheets et al., 2007 |
| $Ln_w M_x O_y S_z$ | | | |
| (Ln, lanthanide or bismuth; M, 2nd and 3rd row transition metal in d-block) | | | |
| $La_2 Nb_3 O_8 S_2$ | Orthorhombic $Pnnm$ | U | Brennan and Ibers, 1992; Cario et al., 2003 |
| $La_3 MO_5 S_2$ | Tetragonal $I4/mmm$ | S | Cario et al., 2007 |
| (M = Nb, Ta) | | | |
| $La_{\sim 10.8} Nb_5 O_{20} S_{10}$ | Orthorhombic $Immm$ | U | Boyer-Candalen and Meerschaut, 2000 |
| $Ce_3 NbO_4 S_3$ | Orthorhombic $Pbam$ | U | Altmannshofer and Johrendt, 2008 |
| $Sm_3 NbO_4 S_3$ | Orthorhombic $Pn2_1 a$ | U | Boyer-Candalen et al., 2000b |
| $Gd_3 NbO_4 S_3$ | Orthorhombic $Pn2_1 a$ | U | Kabbour et al., 2003 |
| $La_2 Ta_3 O_8 S_2$ | Orthorhombic $Pnnm$ | U | Brennan and Ibers, 1992 |
| $Sm_2 Ta_3 O_8 S_2$ | Orthorhombic $Pnnm$ | U | Guo et al., 1995 |
| $LaAgOS$ | Tetragonal $P4/nmm$ | S | Palazzi et al., 1980; Palazzi and Jaulmes, 1981 |
| $CeAg_x OS$ | Tetragonal $P4/nmm$ | S | Chan et al., 2006 |
| ($x = 0.8$; 1) | | | |

*(Continued)*

**TABLE 1 |** Continued

| Phase | Space group | Bonding[a] | References |
|---|---|---|---|
| BiAgOS | Tetragonal $P4/nmm$ | S | BaQais et al., 2017 |
| $Ln_wM_xO_yS_z$ (Ln, lanthanide; M, 2nd and 3rd row transition metal in p-block) | | | |
| $LaGaOS_2\alpha$ | Orthorhombic $P2_1ab$ | S | Guittard et al., 1985 |
| $LaGaOS_2\beta$ | Orthorhombic $Pmca$ | U | Jaulmes, 1978 |
| $La_3GaS_5O$ | Orthorhombic $Pnma$ | S | Jaulmes et al., 1983; Guittard et al., 1985 |
| $La_{3.33}Ga_6S_{12}O_2$ | Tetragonal $P42_1m$ | U | Mazurier et al., 1982; Guittard et al., 1985 |
| $Ce_4Ga_2O_4S_5$ | Tetragonal $I4/mmm$ | S | Jaulmes et al., 1982; Guittard et al., 1984 |
| $Ln_4Ga_{1.33}O_4S_4$ (Ln = La, Ce) | Tetragonal $P4/mmm$ | S | Guittard et al., 1985 |
| $Ln_4Ga_2O_4S_5$ (Ln = Pr, Nd, Sm) | Orthorhombic $Pbca$ | S | Guittard et al., 1984 |
| $LaInOS_2$ | Orthorhombic | ND | Kabbour et al., 2004 |
| $La_5In_3O_3S_9$ | Orthorhombic $Pbcm$ | S | Kabbour et al., 2004 |
| $La_{10}In_6O_6S_{17}$ | Orthorhombic $Immm$ | S | Gastaldi et al., 1982 |
| $Ln_4Sn_2O_4S_6$ (Ln = La, Ce, Pr, Nd) | Orthorhombic $Pbnm$ | S | Guittard et al., 1984 |
| $LnBiOS_2$ (Ln = La, Ce, Pr, Nd, Gd, Dy) | Tetragonal $P4/nmm$ | S | Céolin and Rodier, 1976; Pardo et al., 1976; Tanryverdiev et al., 1995 |
| $Ln_wT_xO_yS_z$ and $Ca_wT_xO_yS_z$ (Ln, lanthanide; T, metalloid) | | | |
| $Ln_4Ge_{1.5}O_4S_5$ (Ln = La, Ce, Pr, Nd) | Orthorhombic $Pbca$ | S | Guittard et al., 1984 |
| $La_4As_2O_4S_5$ | Tetragonal $I4/mmm$ | S | Jaulmes et al., 1982 |
| $LnSbOS_2$ (Ln = La, Ce, Pr) | Not described | ND | Pardo et al., 1976 |
| $La_4Sb_2O_4S_5$ | X | X | Aliev and Tanryverdiev, 1997 |
| $La_6Sb_4O_{12}S_3$ | Tetragonal $I4_1/amd$ | U | So et al., 2004 |
| $NdSbOS_2$ | Tetragonal $P4/nmm$ | S | Pardo et al., 1976 |
| $CaSb_{10}O_{10}S_6$ | Monoclinic $C2/c$ | ND | Nakai et al., 1978 |
| $A_wM_xO_yS_z$ (A, alkaline or earth-alkaline; M, transition metal) | | | |
| $K_6Ti_6OS_{18}$ | Triclinic $P1$ | U | Tillinski et al., 2001 |
| $Ba_6Ti_5OS_{15}$ | Orthorhombic $C222_1$ | S | Sutorik and Kanatzidis, 1994 |
| CaFeOS | Hexagonal $P6_3mc$ | S | Selivanov et al., 2004; Delacotte et al., 2015 |
| $Ca_3Fe_4S_3O_6^c$ | Tetragonal | ND | Selivanov et al., 2004 |
| CaCoOS | Hexagonal $P6_3mc$ | S | Salter et al., 2016 |
| BaCoOS | Orthorhombic $Cmcm$ | U | Valldor et al., 2015; Salter et al., 2016 |
| CaZnOS | Hexagonal $P6_3mc$ | S | Petrova et al., 2003; Sambrook et al., 2007 |
| BaZnOS | Orthorhombic $Cmcm$ | U | Broadley et al., 2005 |
| $SrZn_2OS_2$ | Orthorhombic $Pmn2_1$ | U | Tsujimoto et al., 2018 |
| Others | | | |
| $Zr_{1-x}Hf_xOS$ | Cubic $P2_13$ | U | Eisman and Steinfink, 1982 |
| $Pb_{14}Sb_{30}O_5S_{54}$ (scainiite)[d] | Monoclinic $C2/m$ | U | Orlandi et al., 1999 |

[a]S, selective; U, unselective; ND, not described.
[b]Deducted from later works.
[c]Structure not solved, only based on composition.
[d]Natural compound.

In this table are not referenced the quaternary phases reported by Umarji et al. in 1980: $M_2Mo_6S_6O_2$ (M = Co, Ni, Cu) and $PbMo_6S_6O_2$ (Umarji et al., 1980). A few years after this publication, Selwyn et al. tried to obtain the copper-based phase and demonstrated that Umarji et al. reached only a mixture of the Chevrel phase $Cu_{2.7}Mo_6S_8$, Mo, and $MoO_2$ (Selwyn et al., 1987). Then Selwyn et al. also concluded that obtaining the ternary $Mo_6S_6O_2$ oxysulfide from the claimed $M_2Mo_6S_6O_2$ was impossible.

## Quinary Oxysulfides

Quinary oxysulfides also exist, but are not exhaustively listed in this review. Most of them are layered compounds with selective interactions and contain earth-alkaline atoms, as evidenced by Teske in 1985 with $CaLaGa_3OS_6$, $SrLaGa_3OS_6$, $La_2ZnGa_2OS_6$, and $Sr_2ZnGe_2OS_6$ (Teske, 1985). A similar $Sr_2MnGe_2OS_6$ phase was synthesized and studied recently (Endo et al., 2017). Doped phosphors $CaLaGa_3OS_6$ (Yu et al., 2008, 2012; Zhang et al., 2010, 2011, 2012) and $SrLaGa_3OS_6$ (Zhang et al., 2005a, 2016; Yu et al.,

2011, 2012) were extensively studied by Zhang, Yu, and Zhang since 2005. Zhu, Hor, and Otzschi also detailed different quinary oxysulfide families: (i) the $Sr_2Cu_2MO_2S_2$ [M = Mn (Zhu and Hor, 1997a), Co (Zhu et al., 1997; Smura et al., 2011), Zn (Zhu and Hor, 1997a), Ni (Otzschi et al., 1999)] and $Ba_2Cu_2CoO_2S_2$ (Zhu et al., 1997; Smura et al., 2011) family that displays an unusual square planar $MO_2$ layer and the two perovskite-based families (ii) $Sr_3Cu_2M_2O_5S_2$ [M = Sc (Otzschi et al., 1999), Fe (Zhu and Hor, 1997b)] and (iii) $Sr_2CuMO_3S$ [M = Sc (Ogino et al., 2012), Cr (Zhu and Hor, 1997b), Fe (Zhu and Hor, 1997b), Ga (Zhu and Hor, 1997c), In (Zhu and Hor, 1997b)] with the work of Ogino on scandium. Later, Blandy transformed $Sr_2Cu_2MnO_2S_2$ in $Sr_2Cu_{1.5}MnO_2S_2$ by oxidative deintercalation of copper to obtain a mixed-valent perovskite (Blandy et al., 2015).

The study of the quasi-binary system $La_2O_2S$-$AgGaS_2$ ($La_2O_2S$ – 0.75 $Ga_2S_3$ – 0.75 $Ag_2S$) by Carcaly et al. (1981) led to the formation of $La_4Ag_{1.5}Ga_{1.5}O_4S_5$ in which silver and gallium are randomly distributed in the same sites. Along with $La_3MO_5S_2$ (M = Nb, Ta; **Table 1**), Cario et al. reported bilanthanide lamellar $La_2YMO_5S_2$ phases very close to the $Ln_2Ti_2O_5S_2$ structure (Eisman and Steinfink, 1982). The works of Tranchitella on La/Ti quaternary oxysulfide (**Table 1**) led him to the quinary compound $Sr_{5.8}La_{4.4}Ti_{7.8}S_{24}O_4$ with the same $[(Ti_4S_2O_4)(TiS_6)_{4/2}]^{12-}$ layer than $La_{14}Ti_8S_{33}O_4$ (Tranchitella et al., 1996). $La_5Ti_2MS_5O_7$ (M = Cu, Ag), an alkaline-free structure with perovskite layers was also evidenced by Meignen et al. (2004b) and studied for its photocatalytic properties for water reduction and oxidation (Suzuki et al., 2012). Meignen et al. (2005) also prepared $La_5Ti_{\sim 3.25}Zr_{\sim 0.25}S_5O_{9.25}$ with mixed Ti/Zr sites. In 2003, Rutt et al. obtained $KY_2Ti_2O_5S_2$ by topotactic potassium intercalation of potassium in $Y_2Ti_2O_5S_2$ (Rutt et al., 2003). As a perspective, in 2015, Yee et al. designed by DFT modeling a new high-temperature superconductor $Ca_2HgCuO_2S_2$ whose superconducting transition temperature should be close to mercury cuprates' ones (Yee et al., 2015).

## Transition Metal Oxysulfides

For a long time, ternary oxysulfides $M_xO_yS_z$ were limited to lanthanides, actinides, and bismuth. Despite the presence of numerous metals in quaternary oxysulfides, the transition metals did not give any crystalline ternary oxysulfide (except ZrOS and HfOS) until the synthesis of $ZnO_{1-x}S_x$ in the 1990's. This phase is the most often found as crystalline thin films. It is also the case for titanium, tungsten and molybdenum oxysulfides except that they are amorphous.

The first-raw transition metals ternary oxysulfides represent a challenge, because the coordination of the metal commonly does not exceed six, and consequently cannot bear the $M_2O_2S$ structure of $Ln_2O_2S$ (Ln, lanthanide) where the lanthanide coordination is seven or the $Bi_2O_2S$ structure where the coordination of bismuth is eight. Alternative crystal structures may be obtained in the case of first-raw transition metals.

### Crystalline Transition Metal Oxysulfides
#### Copper oxysulfide $Cu_2O_{1-x}S_x$
In 2013, Meyer et al. reported the synthesis of ternary compounds $Cu_2O_{1-x}S_x$ with various compositions (Meyer et al., 2013). These

were obtained using radio-frequency magnetron sputtering (RFS) with a copper target and a flow of $O_2$ and $H_2S$ with various gas ratios. The authors showed that for $x > 0.39$, the compounds did not crystallize in the cubic structure of $Cu_2O$ and became amorphous. The lattice constant of cubic $Cu_2O_{1-x}S_x$ evolved with the composition toward bigger values because of sulfur insertion. The variation was linear only up to $x = 0.13$ and did not follow the Vegard's law. Unfortunately, direct information about the sulfur oxidation state is missing: the oxysulfide nature of the compound remains unsubstantiated.

#### Zinc oxysulfide $ZnO_{1-x}S_x$
Despite their electronegativity and size differences, sulfur atoms are able to replace the oxygen atoms of the wurtzite structure which progressively turns into the ZnS blende structure. It evidences another challenge of metal oxysulfide identification: they could be isostructural of metal sulfides or metal oxides.

Zinc oxysulfide was first reported as thin films grown by atomic layer deposition (ALD) in 1992 by Sanders et al. The oxygen and water traces in the gases were responsible for the oxygen in the resulting film. Since 2010, extensive characterization of $ZnO_{1-x}S_x$ thin films were reported, not only involving ALD (Bakke et al., 2012) but also pulsed-laser deposition (Deulkar et al., 2010), chemical spray pyrolysis (Polat et al., 2011a,b, 2012; Thankalekshmi and Rastogi, 2012) or thioacetate-capped ZnO nanocrystals (Lee and Jeong, 2014). Because of the active research on bandgap engineering, zinc oxysulfide was envisaged as buffer layer in solar cells (Platzer-Björkman et al., 2006; Sinsermsuksakul et al., 2013). X-Ray photoemission spectroscopy (XPS) showed that the sulfur in these films is reduced and thus in agreement with the announced oxysulfide nature (Thankalekshmi and Rastogi, 2012; Lee and Jeong, 2014).

#### Molybdenum oxysulfides $Mo_xO_yS_z$
In 1986, Inoue et al. crystallized two $Mo_xO_yS_z$ compounds while studying the $MoS_2$:$MoS_3$ system (Inoue et al., 1986). The deep-bluish crystal of $MoO_{2.74}S_{0.12}$ (otherwise written as $Mo_4O_{10.96}S_{0.48}$) was isostructural to $\gamma$-$Mo_4O_{11}$ and exhibited charge density wave instabilities similar to these of quasi-2D materials. The similar properties of $MoO_{2.74}S_{0.12}$ and $\gamma$-$Mo_4O_{11}$ supported the hypothesis of a true oxysulfide compound. Also, reddish crystals of $MoO_{1.88}S_{0.15}$ were obtained and presented structural and electronic similarities with monoclinic $MoO_2$.

The decomposition of molybdenum oxodithiocarbamate as a single source precursor also enabled the formation of crystalline thin films (Olofinjana et al., 2010). Rutherford backscattering spectroscopy (RBS) indicated a pure phase. Unfortunately, the final product shared the XRD patterns of $Mo_8O_{23}$, $Mo_9O_{26}$, and $Mo_2S_3$ but the structure was not fully solved.

### Amorphous Titanium, Tungsten, and Molybdenum Oxysulfides
In this section are referenced the oxysulfides of three elements: titanium, tungsten, and molybdenum. In the 1990's, thin films of these oxysulfides were obtained and studied for their electrochemical properties.

In 1993, Tchangbedji et al. announced the formation of a hydrated amorphous phase of vanadium oxysulfide by reacting $Na_2S \cdot 9H_2O$ and $VOCl_2$ (Tchangbedji et al., 1993). The first described formula for this compound was $V_2O_4S \cdot 2H_2O$, but was adjusted to $V_2O_3S \cdot 3H_2O$ in latter studies (electron paramagnetic resonance and XANES at V K-edge demonstrated the presence of $V^{IV}$ species; Tchangbédji et al., 1994; Ouvrard et al., 1995). Water was believed to stabilize the compounds, as its evaporation was accompanied by the loss of the sulfur in the structure. Unfortunately, the authors did not provide enough convincing arguments to justify the oxysulfide nature and the purity of their phase without ambiguity. In particular, the absence of the IR and XANES at S K-edge spectra, which are discussed in the articles, is detrimental. Because of this lack of information, we did not focus on this phase.

### Titanium

Titanium oxysulfides were obtained under the form of thin films to serve as positive electrode material for solid state batteries. Reported for the first time in 1989 by Meunier et al. (1989, 1991) they were extensively characterized in the same group by X-ray photoemission spectroscopy (XPS) that was shown well-adapted for thin films characterization (Levasseur et al., 1999).

Titanium oxysulfides ($TiO_yS_z$) of various compositions were obtained using RFS of hydrolyzed $TiS_2$ targets. The composition can be adjusted via the partial pressure of oxygen during the sputtering process. XPS showed that titanium oxysulfides thin films contain three titanium species ($Ti^{IV}$ as in $TiO_2$, $Ti^{IV}$ as in $TiS_2$ and Ti in mixed environment) and three sulfur species ($S^{-II}$ of $S^{2-}$ anions, $S^{-I}$ in disulfide $S_2^{2-}$ ions and undefined $S_n^{2-}$ ions). For high oxygen contents (TiOS for instance), $S^{VI}$ species of sulfate ions attributed to surface species were also observed, although in a lesser extent due to mechanical erosion (Gonbeau et al., 1991; Dupin et al., 2001; Martinez et al., 2004; Lindic et al., 2005a) Besides, the presence of ordered domains, observed by TEM and XRD, revealed the existence of $TiS_2$ nanocrystals in the amorphous materials (Lindic et al., 2005b). Lithiated titanium oxysulfides thin films were recently obtained with RFS using $LiTiS_2$ targets (Dubois et al., 2017). Their characterization show similar properties than $TiO_yS_z$. Their capacities of around 85 $\mu Ah.cm^{-2}.\mu m^{-1}$ made them usable in a Li-ion cell.

Aside these thin films, "sulfur-doped $TiO_2$" can be obtained by reacting $TiO_2$ with thiourea or hexamethyldisilathiane, for instance. However, in this case, the products should not be named "oxysulfides," because they only contain oxidized sulfur under the form of $S^{IV}$ and $S^{VI}$ species (Yang et al., 2012; Ramacharyulu et al., 2014; Smith et al., 2016).

### Tungsten

Similarly to titanium oxysulfides, amorphous tungsten oxysulfides thin films with adjustable composition were obtained by RFS on $WS_2$ targets and mainly characterized by XPS (Martin et al., 1999). Along with the three species of sulfur described in the titanium section, three different species of tungsten ($W^{VI}$ as in $WO_3$, $W^{IV}$ as in $WS_2$, and $W^V$ in a mixed environment of $O^{2-}$, $S^{2-}$, and $S_2^{2-}$) were observed (Dupin et al., 2001; Martinez et al., 2004). TEM and XRD showed

the presence of nano-crystallites of $WS_2$, but the polymorphs $3R$-$WS_2$ and $2H$-$WS_2$ could not be distinguished (Martin-Litas et al., 2002). The incorporation of lithium in these thin films and their electrochemical properties were studied (Martin et al., 1999; Martin-Litas et al., 2001). It revealed that 1.1 lithium atoms per formula can be incorporated, providing a capacity of 75 $\mu A.cm^{-2}$. XPS also demonstrated that the tungsten ions are reduced to $W^{(0)}$ and that sulfide ions participated to the redox process with irreversible behaviors (Martin-Litas et al., 2003).

### Molybdenum

Abraham, Pasquariello et al. synthesized various $MoO_yS_z$ amorphous compounds from the thermal decomposition of ammonium dithiomolybdate $(NH_4)_2MoO_2S_2$ (Abraham et al., 1989; Pasquariello et al., 1990). This precursor was obtained by bubbling $H_2S$ on ammonium paramolybdate $[(NH_4)_6Mo_7O_{24} \cdot 4H_2O]$ in an ammonia solution. Depending on the thermal treatment (temperature, number of steps), significant amounts of hydrogen and/or nitrogen could be found in the solids. Reacting a mixture of $[(NH_4)_6Mo_7O_{24} \cdot 4H_2O]$ and $(NH_4)_2MoS_4$ also led to a solid precursor whose thermal decomposition yielded $MoO_yS_z$. Based on the electrochemical properties of these amorphous compounds, the authors suggested different structures for them, with different O/S ratios and involving both $S_2^{2-}$ and $S^{2-}$ anions (Abraham and Pasquariello, 1993). Infrared spectroscopy and XPS supported the presence of Mo–O and Mo–S bonds in the solid, but Mo–Mo bonding could not be evidenced.

The solution obtained by reflux of $(NH_4)_2Mo_2S_{12}$ in acetone dispersed in different aqueous electrolyte solutions led to original morphologies of amorphous molybdenum oxysulfides (water/acetone = 1/10 $v/v$; Afanasiev and Bezverkhy, 2003). For instance, tubular morphologies (with the following electrolyte: 10% KCl, 10% $NH_4SCN$), hollow spheres [with 10% $(NH_2OH)H_2SO_4$] and fractal sponge-like solids (with 20% $NH_4SCN$) were obtained. A solid was collected by evaporation of the solvent. EXAFS at Mo K-edge spectra showed one oxygen atom and four sulfur atoms in the first coordination shell of molybdenum atoms. XPS supported the hypothesis of mainly reduced sulfur, even if a broad peak in the region 167–171 eV indicated oxidized species. In the same group, Genuit et al. (2005) performed the condensation in acidic medium of $MoO_2S_2^{2-}$ to amorphous $MoOS_2$. The addition of HCl in a $(NH_4)_2MoO_2S_2$ aqueous solution led to $MoOS_2$.

Similarly to titanium and tungsten, RFS gave amorphous thin films of molybdenum oxysulfides (Schmidt et al., 1994, 1995a). The target was a pellet of $MoS_2$. Pure oxygen was flowed into the chamber to get oxygen-rich oxysulfides ($MoO_{\sim 1.3}S_{\sim 1.9}$), but the traces of oxygen in the glovebox were originally sufficient to get $MoO_yS_z$ thin films. For oxysulfides with a low content of oxygen ($MoO_{\sim 0.5}S_{\sim 2.0}$), TEM showed ordered domains that are isostructural of $MoS_2$, based on electronic diffraction. XRD evidenced both $MoS_2$ and $MoO_2$ phases when the films were annealed under inert atmosphere. As shown by Buck for contaminated $MoS_2$ films, substitution of sulfur by oxygen atoms is likely to explain the changes in lattice parameters observed in the $MoS_2$-like phase (Buck, 1991). Later, XPS analysis provided

clues about the oxidation states of molybdenum and sulfur in $MoO_yS_z$ films which strongly varied with the film composition (Levasseur et al., 1995; Schmidt et al., 1995b; Dupin et al., 2001). For $y < 0.6$ and $z > 2$ (oxygen-poor oxysulfides), $Mo^{IV}$ cations and $S^{-II}$ (as in $MoS_2$) were dominant. For $y > 3$ and $z < 1$ (oxygen-rich oxysulfides), only $Mo^{VI}$ in octahedral sites (as in $MoO_3$) was observed. For $0.6 < y < 3$ and $1 < z < 2$, $Mo^V$ was observed in addition to $Mo^{IV}$ and $Mo^{VI}$ and was likely surrounded by $O^{-II}$ ($O^{2-}$) and $S^{-I}$ ($S_2^{2-}$) species. Moreover, in $MoO_{0.6}S_{1.9}$ thin films, extended X-ray absorption fine structure (EXAFS) at molybdenum K-edge also showed the presence of oxygen atoms in the coordination sphere of molybdenum atoms (Schmidt et al., 1995b).

During the same decade, useful XPS and IR references for molybdenum oxysulfides were established by Muijsers et al. (1995) and Weber et al. (1996) in the study of $MoO_3$ films sulfidation. The formation of oxysulfide intermediate species with their corresponding probable structures was detailed.

## Applications of Bulk and Thin Film Metal Oxysulfides

In the 1980's, potential applications for doped $Ln_2O_2S$ materials were identified and led to their use as lamps, lasers, scintillators, screens, etc. For example, they can be found in X-ray detectors used for tomography or medical imaging. They have also been used for oxygen storage. Often, $Y_2O_2S$, $La_2O_2S$, or $Gd_2O_2S$ are used as the lattice and doped with one or several lanthanide ions to obtain the desirable luminescence features. The oxysulfide was compared with the corresponding oxide $Sm_2Ti_2O_7$ that has a higher bandgap. Also, electrochemical properties of transition metal oxysulfides were investigated for their use in lithium-ion batteries. A brief summary is given below on these applications.

### Screens

Doped oxysulfides were primary employed in cathode ray tubes (CRTs) of television screens and later in computer monitors. In 1968, Royce patented a "family of new cathodoluminescent phosphors" by describing the potential use of doped $Y_2O_2S$ and $Gd_2O_2S$ (Royce, 1968). Lutetium and lanthanum were also envisaged as efficient matrixes for the doping ions (mainly $Sm^{III}$ or $Eu^{III}$).

Three classes of phosphors, respectively, associated to red, blue, and green, are necessary for a proper screen to emit the colors of the visible spectrum. Thanks to their good luminescence properties, lanthanide doping ions equip the main phosphors used for industrial applications (Jüstel et al., 1998). Red color is provided by $Eu^{III}$: $Y_2O_3$:Eu, $Y_2O_2S$:Eu, $YVO_4$:Eu, $Y_2(WO_4)_3$:Eu; blue emission is enabled by $Eu^{II}$ in compounds such as: $Sr_5(PO_4)_3Cl$:Eu, $BaMgAl_{11}O_7$:Eu, $Sr_2Al_6O_{11}$:Eu; and green is emitted thanks to $Tb^{III}$: $CeMgAl_{11}O_{19}$:Tb, $(Ce,Gd)MgB_5O_{10}$:Tb, $(La,Ce)PO_4$:Tb, $Y_2SiO_5$:Tb, $Y_3Al_5O_{12}$:Tb (Ronda et al., 1998). However, for CRTs, blue and green are preferentially obtained with ZnS:Ag and ZnS:(Cu,Au), respectively.

In current computer monitors, the amount of europium-doped yttrium oxysulfide $Y_2O_2S$:Eu (0.73% w/w for Eu, 13.4% w/w for Y) used for red emission has become large enough to

implement and develop the rare-earths recovery (Resende and Morais, 2015).

## Laser: Emission and Absorption
### Stimulated emission in lanthanum oxysulfide
The first study on metal oxysulfides as laser-emitting material was reported in the earliest years of the design of laser devices. "Laser" stands for light amplification by stimulated emission of radiation and is a general term for a device that emits light through a process of optical amplification based on the stimulated emission of electromagnetic radiation. It is characterized and differs from other light sources by the spatial and temporal coherences of the resulting light. Thus, there are countless applications of the laser devices. Two kinds of applications can be distinguished: information transfer (fiber-optic communication, length measurements, fingerprint detection, barcode scanner, thermometers, laser pointers, weapon guidance…) and power transfer (cutting, welding, superficial fusion, marking materials…).

In 1971, while the most famous laser crystal, namely YAG:Nd (neodymium-doped yttrium aluminum garnet), had already been extensively studied, Alves et al. (1971) carried out the first experiments dealing with an oxysulfide-based laser. They grew and studied millimetric $La_2O_2S$:Nd crystals with many defects, but also estimated the properties of crystals with less imperfections. Similarly to YAG:Nd, the stimulated emission takes place between the $^4F_{3/2}$ and $^4I_{11/2}$ energy levels of the $Nd^{III}$ ion in $La_2O_2S$:Nd with an emission wavelength of 1,075 nm (9,300 cm$^{-1}$), while YAG:Nd emits at 1,064 nm (9,400 cm$^{-1}$).

In 1990, Markushev et al. (1990) presented preliminary results on the stimulation emission kinetics at the temperature of liquid nitrogen for 1 mol% of neodymium. In 2012, the stimulated emission properties of $La_2O_2S$:Nd were studied with oxysulfide powders (Iparraguirre et al., 2012). In particular, Iparraguirre et al. (2012) estimated and experimentally investigated the influence of the doping ion concentration and pumping wavelengths on the different laser properties.

### Laser absorption of samarium oxysulfide
The counterpart of laser emission is laser absorption. Because of the coherence of the emitted light, laser devices can be harmful for human skin or eyes. Protecting glasses or clothes are then required for safety issues. Absorption materials must display a low reflectivity and a good thermal stability because of local heating induced by the laser beam.

The research on absorption devices deals with materials that can absorb the 1,064 nm radiation of the widespread YAG:Nd$^{3+}$ laser. In particular, samarium-based compounds were found to be efficient absorption materials because of electronic transitions between the ground state $^6H_{5/2}$ to the $^6F_{9/2}$ excited state.

Undoped $Sm_2O_2S$ was found to absorb a large proportion of the 1,064 nm laser radiation with a reflectivity of around 0.74% and it is stable up to 2,000°C (Zhu et al., 2016). In comparison, $SmBO_3$ presents a reflectivity of 0.6% but endures a phase transition at 1,200°C (He et al., 2009). Doping with erbium or thulium may also be an efficient way to slightly enhance the absorption properties of $Sm_2O_2S$ (Sun et al., 2017).

## Scintillators

A scintillator is a material that emits light when it is excited by an ionizing radiation (X-rays or gamma rays for example). Scintillators are mainly used in the field of medical imaging. Their role is to lower the dose of X-rays endured by a patient during an analysis. To enable a good absorption of the X-ray beam, the requirements for a good scintillator phosphor is the presence of heavy atoms (cadmium, bismuth, lanthanides, tungsten for instance), a high material density ($\geq 4\,g.cm^{-3}$) and a high stability regarding the radiations. The photon must be converted into photons in the visible range (500-800 nm) with a good efficiency, a fast decay and a short afterglow. Moreover, mechanical strength, absence of toxicity, and chemical stability are desired features (Rossner and Grabmaier, 1991).

Thus, a scintillator is generally composed by a dense ceramic and converts X-rays in visible light. It is connected to photodiodes that convert the visible photons in electrons that form an image on a layer of amorphous silica. Considering their efficient absorption of X-rays, $Y_2O_2S$:Tb, $La_2O_2S$:Tb, $Gd_2O_2S$:Tb were considered to replace $CaWO_4$, which was commonly used as scintillator (Brixner, 1987). $Gd_2O_2S$:Tb was finally chosen for its higher density and better absorption properties in comparison to the other lanthanides (Brixner, 1987). Later, $Gd_2O_2S$:Pr was shown to be an efficient scintillator by Rossner et al. They demonstrated that the main differences between the $Pr^{III}$ and the $Tb^{III}$ doping lie in the incident beam conversion efficiency (for a 40-80 keV X-ray beam, 8.5% for $Gd_2O_2S$:Pr, Ce, F, and 15% for $Gd_2O_2S$:Tb) and the luminescence lifetime of the doping ion ($\sim$3 $\mu$s for $Gd_2O_2S$:Pr, Ce, F; 600 $\mu$s for $Gd_2O_2S$:Tb; Rossner and Grabmaier, 1991). $Pr^{III}$ shows a very rapid decay, cerium decreases the trap states and fluorine causes an important decrease of the afterglow. $Gd_2O_2S$:Eu was also studied. Its absorption and luminescence properties were competitive enough and it enables the emission of red photons (instead of green photons for Pr and Tb) which can be useful for compatibility issues with digital imaging systems (Michail et al., 2010).

Nowadays, gadolinium oxysulfides are used as scintillators for Single-Photon Emission Computed Tomography (SPECT), X-ray Computed Tomography (CT), and Positron Emitting Tomography (PET).

## Lithium-ion Batteries

Lithium intercalation and electrochemical properties of bulk metal oxysulfides were discussed because of possible oxido-reduction reactions with transition metals such as titanium or molybdenum. We already mentioned that titanium (Meunier et al., 1989; Lindic et al., 2005a; Dubois et al., 2017) or tungsten (Martin et al., 1999; Martin-Litas et al., 2001, 2003) thin films were studied as cathodes in solid-state lithium-ion batteries. As cathodes, molybdenum oxysulfide thin films were also developed (Abraham et al., 1989; Pasquariello et al., 1990; Gonbeau et al., 1991; Abraham and Pasquariello, 1993; Levasseur et al., 1995; Schmidt et al., 1995a; Yufit et al., 2003; Golodnitsky et al., 2006a,b) More recently, a $TiO_2$@$MoO_yS_z$ composite was investigated as anode material (Qiao et al., 2013). The external

layer of molybdenum oxysulfide was supposed to enhance the conductivity of the hybrid material.

## Conclusion

At the end of this section, we wanted to underline several crucial points:

(i) Oxysulfide materials are mainly reached by chemical synthesis and much fewer compositions were obtained compared to monochalcogenide compounds.
(ii) The lack of oxysulfide compositions is mainly based on the strong differences between oxygen and sulfur. Metals tend to preferentially bind to one compared to the other.
(iii) Transition metals oxysulfides are particularly rare and their crystalline phases even more.

In this context, a periodic table showing the reported oxysulfide compounds is presented in **Figure 5**.

# NANOSCALED TERNARY LANTHANIDE OXYSULFIDES Ln$_2$O$_2$S

## Introduction

Following the hype for nanotechnology in the twenty-first century, researchers have recently worked on producing metal oxysulfide materials as nanoparticles (**Figure 6**). This trend is justified by the applications that could emerge from nanomaterials, especially in the domain of biology and medicine. In particular, nano-scale objects can cross biologic barriers and be metabolized by living beings. Also, because of their wide range of morphologies, compositions, and grafting, the nanoparticles can reach targeted zones using specific interactions to provide local information, deliver drugs at precise places or stimulate organs and tissues with an internal or external stimulus.

Lanthanide oxysulfide nanomaterials present many advantages for imaging in biological medium. They have a good chemical and thermal stability. Their size and shape is highly tunable from very small crystals around 5 nm to micrometer spheres, rods, belts, tubes and so on. Moreover, the Ln$_2$O$_2$S crystalline phase bears many lanthanide/transition metal or lanthanide/lanthanide substitutions, which guarantees a generous variety of luminescent properties.

## Examples of Oxysulfide Nanoparticles' Applications
### Upconversion

In the fields of therapy and *in vivo* imaging, using direct light composed of high energy photons, typically X-rays or gamma rays, leads to potential harmful effects for the patient. Organic dyes, radioisotopes and quantum dots are currently used in order to perform bioimaging. However, toxicity of radioactive isotopes, and quantum dots is problematic. Also, organic fluorophores and quantum dots (QD) are sometimes excited through ultraviolet (UV) irradiation that can lead to autofluorescence (excitation of natural targets, such as elastin, collagen...), photobleaching (destruction of the dye), and luminescence blinking.

Another indirect but efficient way to excite phosphors at low energy for bioimaging is infrared (IR) irradiation, taking advantage of the biological transparency windows: 750–950 nm
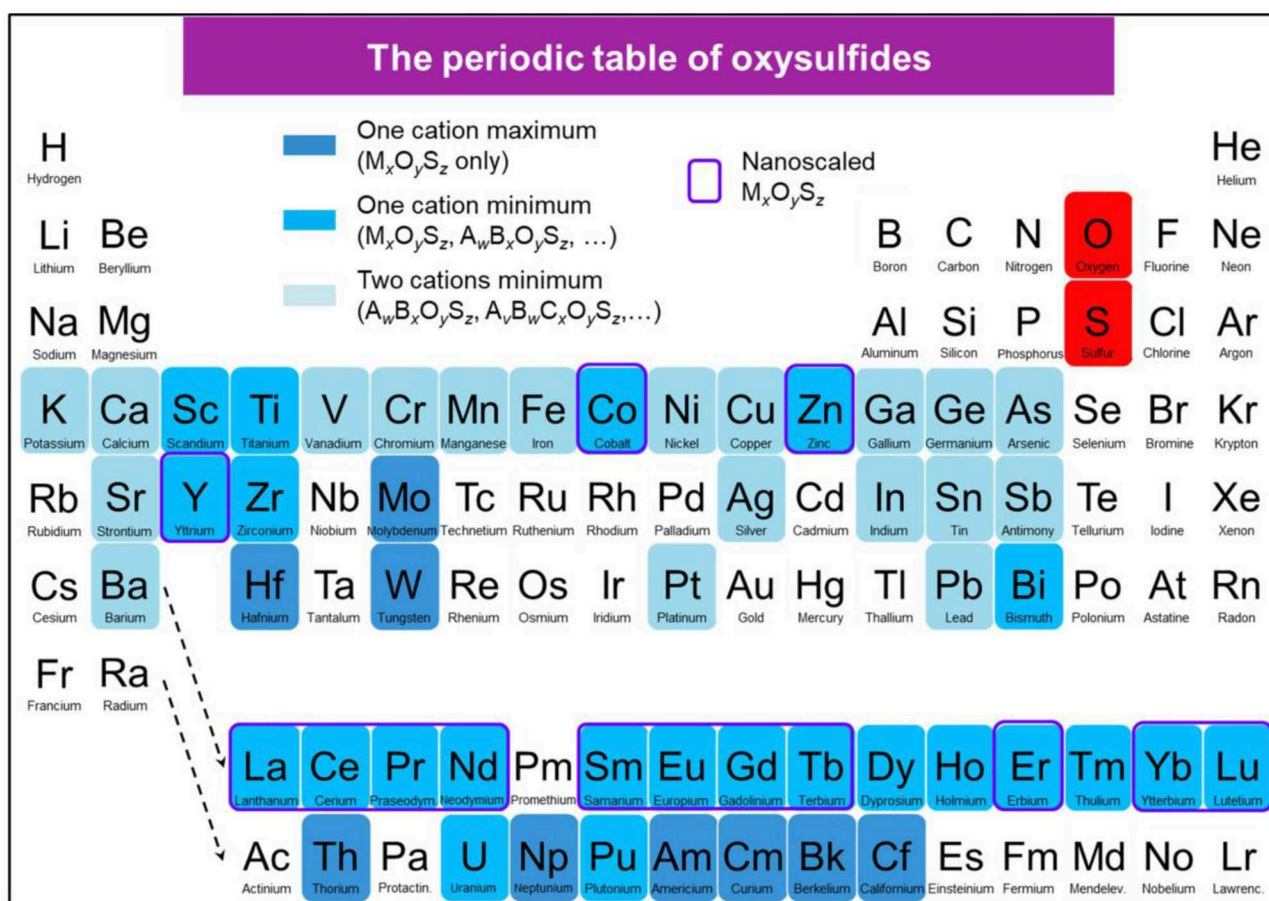
**FIGURE 5** | Periodic table showing the reported oxysulfide compounds. In blue are indicated the elements that can be found in synthetic or natural oxysulfides. Blue shades indicate the compositions (ternary, quaternary, and more) that can be achieved for each element. Surrounded in violet are the elements for which $M_xO_yS_z$ nanoparticles were reported.
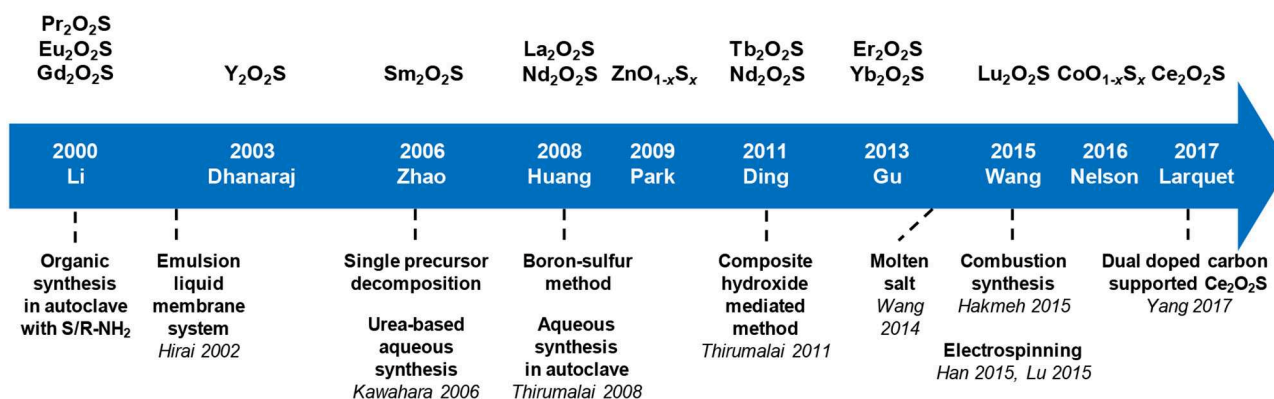


**FIGURE 6** | Key dates, authors, and techniques of the oxysulfide nanoparticles research.

(BW−1), 1,000–1,450 nm (BW–II), and 1,500–1,700 nm (BW–III). The main advantage is the high signal-to-noise ratio, because biological tissues (containing melanin, hemoglobin and water) absorb less light in these spectral ranges (Shi et al., 2016). Consequently, IR bioimaging does not result in parasitic fluorescence. Moreover, it causes low tissue damage and enables local irradiation along with high penetration depth.

Lanthanide-based upconverting phosphors are based (in the simplest case) on the combination of two absorbed low-energy photons in one of a higher energy, resulting for instance in the absorption of IR wavelengths and emission of visible light (Auzel, 2004). This way, many advantages are conferred to the imaging system (Ajithkumar et al., 2013): the chemical stability and low toxicity of rare-earth compounds, the absence of photobleaching, the low and easy available required energy.

Oxysulfide nanomaterials based on the upconverting properties of lanthanide dopants have been studied as potential upconverting phosphors for biomedical imaging. Ytterbium and erbium co-doped materials are being investigated in detail, but other dopants, such as holmium and thulium have also been reported for upconverting materials.

### Persistent luminescence

The phenomenon of persistent luminescence is the emission of light by a material after excitation has stopped. It must be distinguished from fluorescence and phosphorescence. Its mechanism is complex and still debated (Jain et al., 2016). In persistent luminescence, the origin of the extended emission in an insulator or semi-conductor is the entrapment of electrons or holes that are progressively released (Leverenz, 1949). Either an electron is trapped in an energy level near the conduction band or a hole is trapped in an energy level near the valence band.

The traps can be point defects with intrinsic defects of the lattice such as vacancies, interstitial defects, antisite defects, or extrinsic defects when doping ions substitute lattice atoms or occupy interstitial sites. Extended defects (dislocations, surface, or grain boundaries) of the lattice can also play the role of traps.

Oxysulfide materials containing titanium and europium have been developed for persistent luminescence. Here, the doping ions substitute the rare-earth of the matrix and correspond to extrinsic defects. $Y_2O_2S:Ti$ in 2005 was the first example (Zhang et al., 2005b), but numerous articles focused on the promising properties of $Ln_2O_2S:Eu^{3+}, Mg^{2+}, Ti^{4+}$ (Ln = Gd, Y) which will be named $Ln_2O_2S:Eu, Mg, Ti$ for simplification (Mao et al., 2008; Li et al., 2010; Cui et al., 2013a, 2014a; Liu et al., 2014a).

### Magnetic probes

Because of their remaining $4f$ electrons, most of the lanthanide ions present magnetic properties. Lanthanide oxysulfides were found to be paramagnetic in a large range of temperatures, and their magnetic properties at low temperatures were extensively studied (Ballestracci et al., 1968; Quezel et al., 1970; Biondo et al., 2014).

Lanthanides can exhibit high magnetic susceptibility, which is major interest for chemicals that can be injected in a living organism. For instance, $Gd^{III}$ complexes are used as positive contrast agents in magnetic resonance imaging (MRI) due to the

$4f^7$ electronic configuration of the ion ($\mu = 7.94 \mu_B$). The role of a contrast agent is to enhance the MRI signal by locally perturbing the magnetic field. The spin relaxation time of $Gd^{III}$ is long enough to optimize the dipole-dipole interactions of electron and protons (biological tissues, water) in the neighborhood of the contrast agent. The MRI signal is then enhanced by the acceleration of the spin relaxation of the protons caused by these interactions. Gadolinium ions in molecular complexes are toxic because of polarizing effects and competition with calcium. Special hydrosoluble complexes were then developed to prevent the toxicity of $Gd^{III}$ (Tóth et al., 2002).

An alternative to lanthanide complexes is lanthanide nanoparticles. A better detection occurs as the consequence of the concentration of several thousand atoms in a little volume. Iron oxide nanoparticles have been widely studied and used as negative contrast agents, but many artifacts were observed on the resulting images (Bulte and Kraitchman, 2004). $Gd_2O_3$ nanoparticles were found to have a similar or better relaxivity than gadolinium complexes, without the drawbacks of iron oxides. They were then chosen for the precise visualization of locally injected cells (Engström et al., 2006; Petoral et al., 2009).

With doping ions, gadolinium oxide nanoparticles were then applied for bimodal imaging (MRI and luminescence) (Kryza et al., 2011). Because of their very good luminescence properties, similar results are expected for oxysulfide $Gd_2O_2S$ nanoparticles. Bimodal agents are especially useful to get various information of the environment of the nanoparticles from the luminescence properties (wavelength, lifetime, and so on) in short times coupled with long term data and precise localization with magnetic resonance imaging (Cherry, 2006). Ajithkumar et al. (2013) demonstrated the possibility of performing multimodal bioimaging using oxysulfide material choosing the $Gd_2O_2S:Yb$, Er phosphor. Besides, $Gd_2O_2S:Eu$ micronic particles were used as a colloidal solution for X-ray Luminescence Computed Tomograghy (XLCT), a technique that could be applied in vivo (Pratx et al., 2010a,b). Drug delivery can also be tracked in vivo. $Gd_2O_2S:Tb$ nanoparticles coated with $SiO_2$ were employed as radioluminescent markers to evaluate the release of doxorubicin as a function of pH, using X-ray Excited Optical Luminescence (XEOL) (Chen et al., 2013).

### Catalysis

Recently, sub-micronic powder of $Sm_2Ti_2O_5S_2$ was used as a stable photocatalyst for water oxidation and reduction under visible-light irradiation, and this was later further extended to other $Ln_2Ti_2O_5S_2$ (Ln = Pr, Nd, Gd, Tb, Dy, Ho, and Er) phases (Ishikawa et al., 2002, 2004). Moreover, because the majority of lanthanides are often restricted to the +III oxidation state, catalysis based on oxido-reduction reactions is not the preferential application of oxysulfide materials. Nevertheless, cerium ($Ce^{III}$ and $Ce^{IV}$) and europium ($Eu^{II}$ and $Eu^{III}$) are notable exceptions. In particular, $Ce_2O_2S$ nanoparticles on carbon was tested for oxygen reduction reaction (ORR) (Yang et al., 2017). Also, $Eu_2O_2S$ nanoparticles showed catalytic activity for the water-gas shift reaction (reaction of CO with water that yields $CO_2$ and $H_2$) (Tan et al., 2016). They can also act

**FIGURE 7 |** Synthetic strategies toward Ln$_2$O$_2$S.
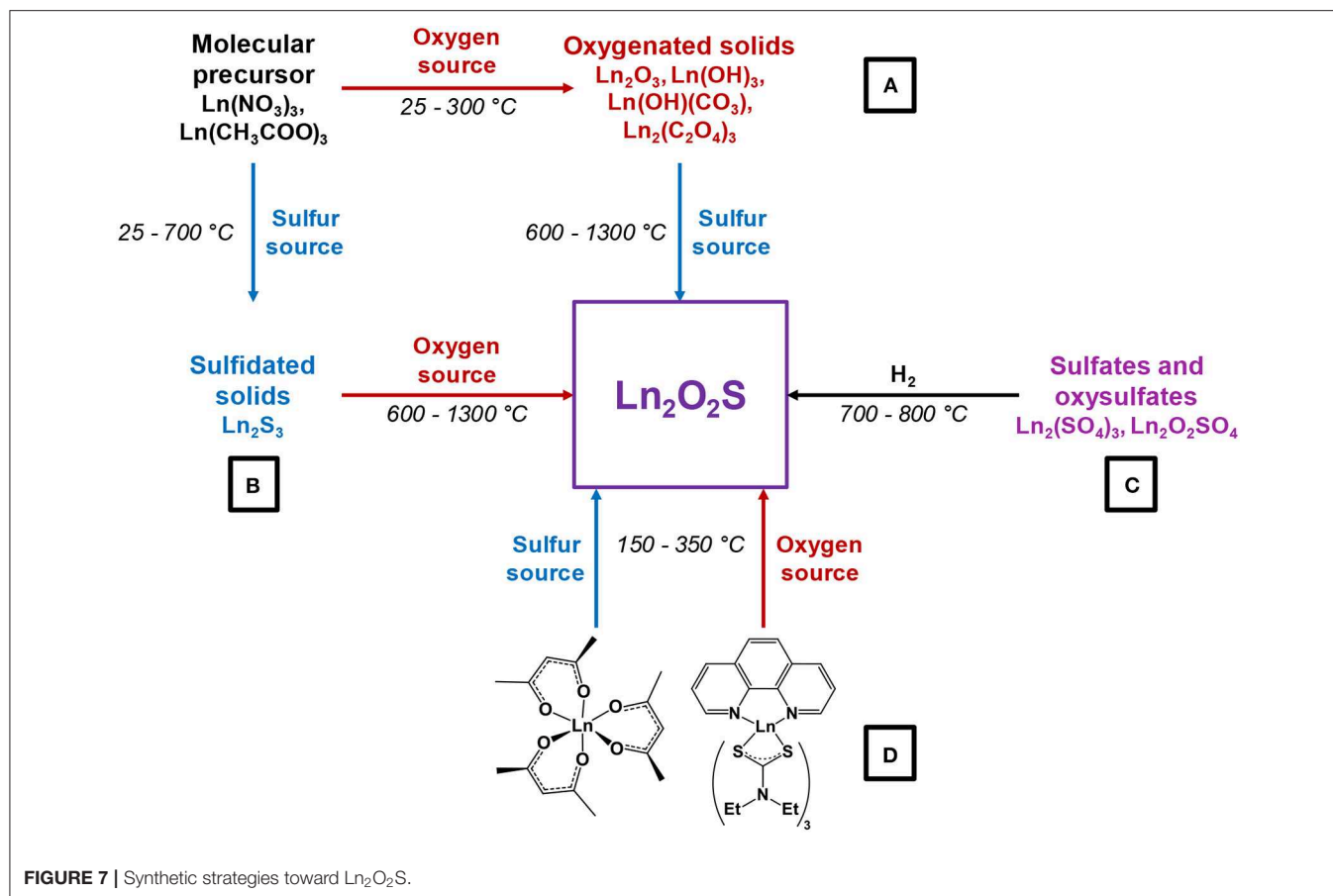
as a peroxidase mimic for the catalytic oxidation of 3,3′,5,5′-tetramethylbenzidine (TMB) (Ghosh et al., 2016).

## Synthetic Strategies for Lanthanide Oxysulfide Nanoparticles

### General pathways toward Ln$_2$O$_2$S nanoparticles

Several strategies can be employed to yield oxysulfides nanoparticles. Historically, bulk oxysulfides were formed by partial sulfidation of oxides, oxidation of sulfides or reduction of sulfates (**Figure 7**). However, solid-gas or solid-solid reactions at high temperatures inevitably lead to sintering and large particles. This should be avoided to control the growth of nanoparticles. Moreover, avoiding sulfates is challenging: their formation is thermodynamically favored.

Four major strategies are employed to yield Ln$_2$O$_2$S (bulk and nanoparticles). The two first methods are the sulfidation of an oxygenated phase such as an oxide or a hydroxide (**Figure 7**, pathway A) and the oxidation of sulfides (**Figure 7**, pathway B). In the latter case, the term "oxidation" names a substitution between sulfur and oxygen and does not imply oxido-reduction processes. This process is challenging: the partial oxygenation of sulfides is hard to control because sulfates are easily formed. To the best of our knowledge, only bulk materials were synthesized this way.

The reduction of sulfates and oxysulfates is also possible (**Figure 7**, pathway C). It is generally excluded for the formation of nanoparticles as it demands high temperatures (≥800°C). Finally, another way to achieve the synthesis of metal oxysulfides is the co-insertion of oxygen and sulfur. Decompositions of organic precursors containing oxygen or sulfur are especially helpful for this method (**Figure 7**, pathway D). For syntheses in which oxygen rate has to be finely controlled, inert atmosphere assured by N$_2$ or argon is mandatory.

Since 20 years, a broad spectrum of techniques has been developed to yield Ln$_2$O$_2$S nanoparticles, which remains by far the center of the oxysulfide research. Here, we chose to classify them in three groups mainly depending on the reaction medium: water, organic solvent, and others. As we focused our study on the synthesis of nanomaterials, we excluded the works dealing with particles which were systematically sub-micronic or micronic (>700-800 nm).

### Typical oxygen and sulfur sources in Ln$_2$O$_2$S nanoparticles syntheses

*Oxygen source* The oxygen source for the formation of Ln$_2$O$_2$S nanoparticles highly depends on the synthetic route (**Figure 7**).

Commonly, in the water-based syntheses, oxygen is brought by hydroxide ions with the precipitation of an intermediate oxygenated phase in basic medium. Oxygen insertion in sulfides

**SCHEME 1** | Sulfur sources typically used for the sulfidation processes leading to oxysulfides (mp, melting point; bp, boiling point; Sol., solubility). The first neighbor of sulfur in the molecule is indicated.
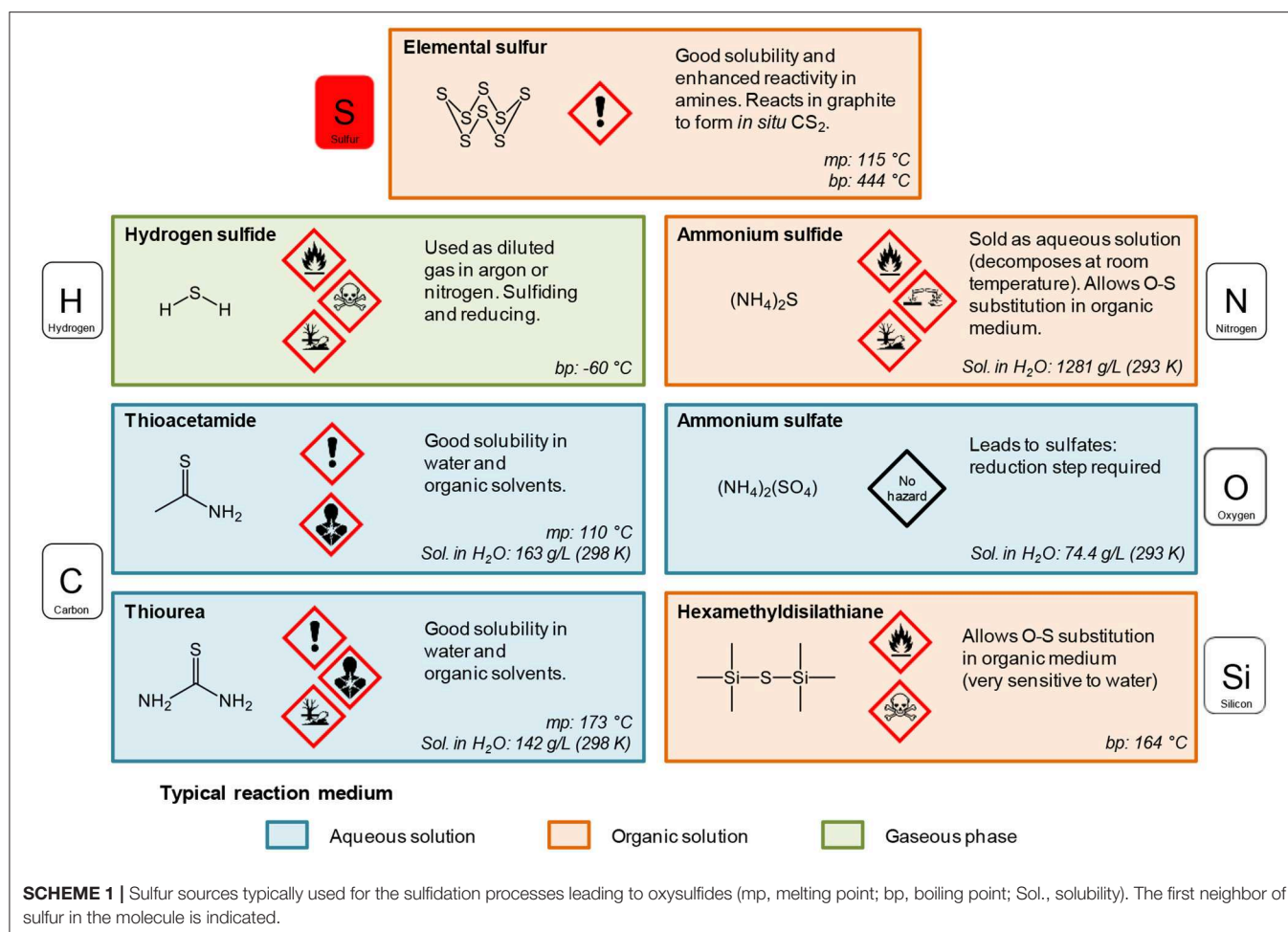
$Ln_2S_3$ has never been performed for nanoparticles, to the best of our knowledge. Molecular precursors such as lanthanide formate or lanthanide acetylacetonate contain enough oxygen for the targeted composition. In organic medium, the use of ketones as ligands enables the formation of *in situ* water when an amine is present. The thermal decomposition of single-source precursors with sulfide ligands can be performed in air or pure dioxygen to give $Ln_2O_2S$ nanoparticles. In the case of reduction of sulfates and oxysulfates, no additional source of oxygen is required.

*Sulfur sources* (**Scheme 1**). In water, sulfidation is mainly carried out by solid-gas reaction with $H_2S$ or *in situ* formed $CS_2$ using elemental sulfur heated in graphite or in presence of carbon. Nevertheless, a significant amount of syntheses also use sulfur sources soluble in water, such as thiourea or thioacetamide that initiate the sulfidation process. Elemental sulfur can also be used in organic medium especially dissolved in amines. Recently, substitution of oxygen by sulfur was carried out by ammonium sulfide and hexamethyldisilathiane (HMDTS).

## Exotic Syntheses

Classical nanoparticles syntheses consist in heating hydrophobic or water-soluble inorganic precursors in aqueous or organic media, possibly sealed and/or pressurized and often followed by a thermal treatment which helps sulfidation and/or crystallization. In marge of these techniques, unconventional synthetic methods can be found. They involve unusual solvents, like molten salts, or are performed in uncommon conditions (electrospinning, combustion, and so on). This section describes such syntheses.

### Boron-Sulfur Method

In 2008, Huang et al. adapted the boron-sulfur method, originally destined to the synthesis of sulfides, to the synthesis of $La_2O_2S$ and $Nd_2O_2S$ (Huang et al., 2008). In this synthesis, nanowires of the lanthanide hydroxide $Ln(OH)_3$ (formed by reaction between $Ln(NO_3)_3$ and $KOH$) are directly heated in presence of boron and elemental sulfur $S_8$ placed in a neighboring crucible. The driving force of the reaction is the strong affinity of boron with oxygen, which leads to the formation of $B_2O_3$ as a by-product.

When the reaction is maintained for 24 h at 400°C, $LnS_2$ nanowires are obtained. Using shorter reactions times (500°C, 10 min), sulfidation of the wire is partial and $Ln_2O_2S$ can be obtained (**Figure 8A**).

This solid-state reaction preserves the shape of the precursor. Also, it is one of the rare techniques that enable the formation of $Ln_2O_2S_2$ nanomaterials using in some conditions an excess
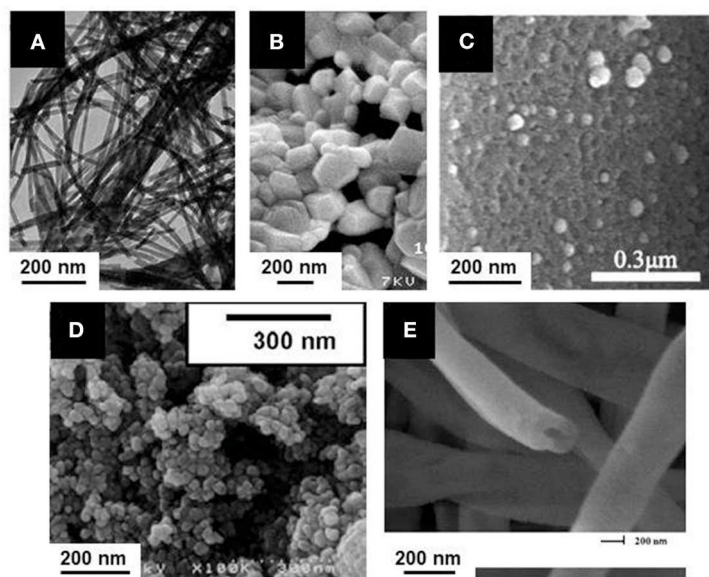
**FIGURE 8 |** $Ln_2O_2S$ nanoparticles obtained from unconventional synthetic methods: **(A)** Boron-sulfur method ($La_2O_2S$:Eu nanowires); Adapted with permission from (Huang et al., 2008), copyright (2008) American Chemical Society. **(B)** Combustion ($La_2O_2S$:Yb, Er nanoparticles); Adapted from Hakmeh et al. (2015) with permission of Elsevier. **(C)** Thermal decomposition of a gel of Pomelo skins ($Ce_2O_2S$ nanoparticles supported on carbon); Adapted with permission from Yang et al. (2017), copyright (2017) American Chemical Society. **(D)** Emulsion liquid membrane system ($Y_2O_2S$:Yb, Er nanoparticles); Adapted with permission from Hirai et al. (2002), copyright (2002) American Chemical Society. **(E)** Electrospinning ($Y_2O_2S$: Yb, Er hollow nanofiber). Adapted from Han et al. (2015a) with permission of The Royal Society of Chemistry.

amount of sulfur compared with the targeted stoichiometry to ensure complete reactions. Nevertheless, only a small quantity of reactants were loaded in the crucible, leading to <15 mg of product per reaction. Also, the remaining species ($B_2O_3$, sulfur in excess) were washed with toxic $CS_2$.

## Combustion Synthesis

In order to get a swift synthesis, Hakmeh et al. (2015) developed a combustion synthesis by mixing lanthanide nitrates [$La(NO_3)_3$, $Er(NO_3)_3$ and $Yb(NO_3)_3$] with thioacetamide in ethanol. The precursors were rapidly inserted in a furnace at 500°C. Two successive flames evidenced first the ignition of ethanol, then the exothermic decomposition of the organic compounds, leading to an increase of the temperature and eventually to the formation of particles. A post-treatment at high temperature was also necessary ($H_2S$ in $N_2$, 2 h, 1,000°C) and resulted in large particles with a typical size around 300-500 nm (**Figure 8B**).

## N,S Dual Doped Carbon Supported $Ce_2O_2S$

Recently, an original catalyst for oxygen reduction reaction (ORR) was obtained by using the thermal decomposition of a vegetal, which provides the carbon support for the inorganic catalyst (Yang et al., 2017). Cerium nitrate [$Ce(NO_3)_3$] was dissolved in water along with thiourea and then pomelo skins were added to the solution in order to form a gel. After drying, the gel was annealed at 900-950°C for 2 h to get $Ce_2O_2S$ supported on carbon doped by nitrogen and sulfur. When the reaction temperature was set to 850 or 1,000°C, the reaction led to the formation of $CeO_2$. The TEM observation of the catalyst



**SCHEME 2 |** Examples of surfactants employed by Wang et al. to synthesize $Y_2O_2S$:Eu in molten NaCl (Wang et al., 2014).
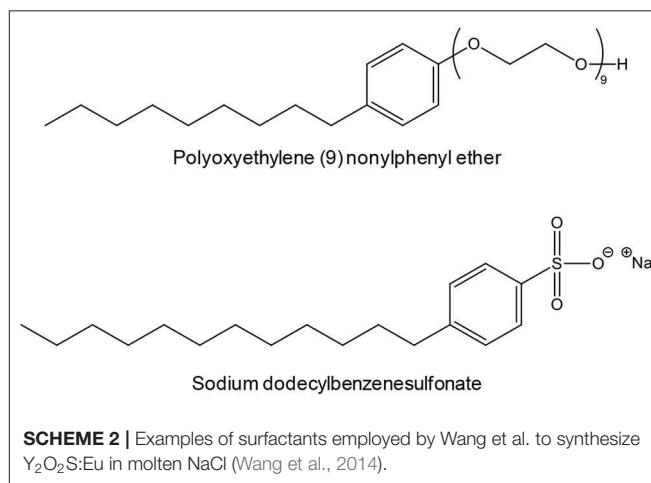
shows 50-100 nm crystals of $Ce_2O_2S$ disseminated on the surface of the samples (**Figure 8C**). The porous structure, inherited from the pomelo precursor and the oxygen vacancies evidenced by the authors make this material suitable for the ORR.

## Emulsion Liquid Membrane System (ELM)

Emulsion Liquid Membrane System (ELM) employs a water-in-oil-in-water (W/O/W) double emulsion. Originally, ELM was applied to separate metals. Here, the double emulsion is used for the formation of doped yttrium and gadolinium oxalates. These intermediates are converted to oxysulfides,

**FIGURE 9 |** Europium-doped yttrium oxysulfide nanoparticles with different morphologies obtained via the composite-hydroxide-mediated method and their precursors. **(A)** SEM image of bulk $Y_2O_2S:Eu$. **(B)** SEM image of $Y(OH)_3$ nanobelts. **(C)** SEM image of $Y(OH)_3$ nanorods. **(D)** SEM image of $Y_2O_2S:Eu$ nanobelts. **(E)** SEM image of $Y_2O_2S:Eu$ nanorods. **(F)** TEM and **(G)** HRTEM images of $Y_2O_2S:Eu$ nanobelts. **(H)** High-magnification SEM image of $Y_2O_2S:Eu$ nanobelts. **(I)** High-magnification SEM image of $Y_2O_2S:Eu$ nanorods. **(J)** TEM and **(K)** HRTEM images of $Y_2O_2S:Eu$ nanorods. Insets are corresponding SAED patterns. Adapted from Thirumalai et al. (2011a), copyright (2011) The Institution of Engineering and Technology.

$Y_2O_2S:Yb$, Er, and $Gd_2O_2S:Eu$, by a solid-state reaction with sulfur vapor (Hirai et al., 2002; Hirai and Orikoshi, 2004). Typically, a first emulsion is obtained by mechanical agitation of an organic phase containing kerosene with bis(1,1,3,3-tetramethylbutyl)phosphinic acid (DTMBPA) (or 2-methyl-2-ethylheptanoïc acid, VA-10) as extractant and sorbitan sesquioleate as surfactant and an aqueous phase containing oxalic acid. This emulsion is then added to the external water phase which contains the metal ions (chloride or nitrates) and the double emulsion is produced by mechanical stirring. The oxalate compounds are thus produced at ambient temperature, and the system is demulsified using ethylene glycol. Oxysulfides nanoparticles of 50-100 nm are then obtained by annealing the powders at 600-1,000°C in sulfur vapor generated at 200°C by elemental sulfur and carried by a $N_2$ flow (**Figure 8D**).

## Synthesis in Molten Sodium Chloride

The synthesis in molten salts is an emerging technique which consists in the use of one or several salts as solvents for an inorganic reaction. An eutectic mixture can even be used to benefit from a lower melting point. Molten salts are typically suitable for reaction temperatures between 300 and 1,000°C, which enable the formation of nanoparticles while avoiding their

sintering (Portehault et al., 2011; Gouget et al., 2017). After cooling, the particles are obtained in a matrix composed by the salts that are washed with water or alcohols.

Molten sodium chloride (melting point: 801°C) was chosen for the one-pot synthesis of $Y_2O_2S:Eu$. $Y(NO_3)_3$, $Eu(NO_3)_3$ and NaOH were mixed and stirred before the addition of NaCl, $S_8$ and a surfactant (Wang et al., 2014). After grinding, the mixture was heated to 850°C in a CO atmosphere for 4 h, and then cooled and washed.

Depending on the surfactant, the particles were either sub-micrometric or nanoscaled, but the morphology was quite irregular and the size polydisperse in all cases. For instance, polyoxyethylene (9) nonylphenyl ether (**Scheme 2**) gave 150-250 nm particles while sodium dodecylbenzenesulfonate (**Scheme 2**) gave 0.5-1.5 μm particles.

## Composite-Hydroxide-Mediated Method

The composite-hydroxide-mediated method is also a synthesis in molten salts, but with hydroxides. Thirumalai et al. (2011a) adapted this method to the synthesis of Eu-doped yttrium oxysulfide by heating concentrated yttrium acetate $Y(CH_3COO)_3$ in an eutectic mixture of NaOH and KOH in an autoclave. As the eutectic of the mixture is 165°C, the autoclave was heated

| Element | Ln$_2$O$_3$ €/100 g[a] | Ln$_2$O$_3$ 99.99%, €/100 g[b] | Ln(NO$_3$)$_3$·xH$_2$O 99.9%, €/100 g[b] | Cost[c] |
|---|---|---|---|---|
| Y | 0.26 | 230 | 140 (99.8%) | ● |
| La | 0.16 | 139 | 89 | ● |
| Ce | / | / | 359 | ● |
| Pr | 5.08 | 1,850 (99.9%) | 236 (99.99%) | ● |
| Nd | 4.04 | 722 | 113 | ● |
| Sm | 0.17 | 796 | 271 | ● |
| Eu | 3.71 | 3,140 | 2,608 | ● |
| Gd | 1.72 | 2,560 | 235 | ● |
| Tb | 38.0 | 3,900 | 1,420 | ● |
| Dy | 15.9 | 1,040 | 166 | ● |
| Ho | / | 806 (99.9%) | 776 | ● |
| Er | 2.01 | 1,064 | 233 | ● |
| Tm | / | 17,500 | 3,300 | ● |
| Yb | / | 2,120 | 430 | ● |
| Lu | / | 10,820 | 5,040 | ● |

[a] Prices on Shanghai Metal Market. Original prices units are RMB/mt or RMB/kg and were converted.
[b] Prices on Merck on October 29th 2018 for France.
[c] From more affordable to more expensive: blue-green-yellow-red.
*no stable isotope.
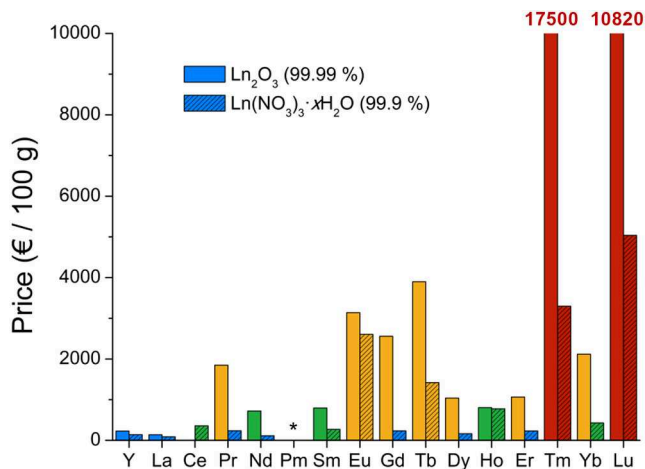


at 200°C to yield Y(OH)$_3$ nanobelts (48 h) and nanorods (24 h) (**Figure 9**).

Europium and S$_8$ were then mixed with the Y(OH)$_3$ nanomaterial at 70-80°C and underwent an undescribed sulfidation process. In any case, the product was then annealed at 600°C for 2 h in an (Ar or N$_2$)/sulfur atmosphere to form Y$_2$O$_2$S:Eu. Interestingly, the final product retained the morphology of the Y(OH)$_3$ precursor. On the other hand, the step where the product was sulfidated was particularly unclear here, as three sulfidation processes are mentioned.

## Electrospinning

Electrospinning is based on the application of a high potential difference between a polymer solution or a polymer melt and a collector. The electrical field creates charged threads that can be assembled depending on the experimental parameters such as tension, temperature, relative humidity (RH), concentration of

the precursors, viscosity, distance between capillary screen and collection screen, etc.

Lanthanide nitrates Y(NO$_3$)$_3$, Yb(NO$_3$)$_3$, and Er(NO$_3$)$_3$ and polyvinyl pyrrolidone (PVP) were dissolved in DMF and stirred 8 h (Han et al., 2015a). Fibers were produced by electrospinning. They were annealed twice: (i) at 700°C for 8 h under air to get Y$_2$O$_3$:Tb, Er fibers and (ii) at 800°C for 4 h in a CS$_2$ atmosphere (obtained by heating S$_8$ in presence of carbon) to yield Y$_2$O$_2$S:Yb, Er hollow nanofibers (**Figure 8E**). The same strategy was used to yield Y$_2$O$_2$S:Er hollow nanofibers (Han et al., 2015b). With slightly different electrospinning parameters, full nanofibers of Y$_2$O$_2$S:Yb, Er with a diameter comprised between 80 and 140 nm were obtained and studied by Lu et al. (2015).

## Anodic Aluminum Oxide Template

In 2013, Cui et al. (2013a,b) elaborated a synthesis for doped oxysulfide nanoarrays using an anodic aluminum oxide template

SCHEME 3 | Urea decomposition in water. Isocyanic acid is slowly obtained by urea thermolysis and ammoniac release. A second ammoniac molecule is released by hydrolysis which gives aqueous carbon dioxide "$H_2CO_3$."
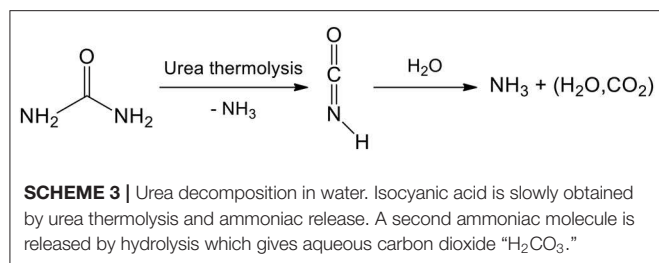
(AAO). A nitrate solution obtained by dissolution of $Y_2O_3$, $Eu_2O_3$, and $Mg(OH)_2 \cdot 4MgCO_3 \cdot 2H_2O$ in hot $HNO_3$ (65%) was diluted by ethanol. Titanium doping was then obtained by adding the reaction product of $Ti(OBu)_4$ with acetylacetone. The pH was adjusted to 1 with $HNO_3$. The sol was eventually obtained by evaporation at 80–90°C. The AAO template was dipped in the sol, dried, calcined at 600°C for 2 h and etched by NaOH (2.0 M) to give $Y_2O_3$:Eu, Mg, Ti nanoarrays. The whole process involved numerous steps and the resulting nanoarrays had to be sulfurated to $Y_2O_2S$:Eu, Mg, Ti using $S_8$ in graphite at 850°C sharp (Cui et al., 2013a). Lower and higher temperatures were indeed not adequate: they resulted, respectively, in uncomplete sulfidation or oxide formation. Besides, an optimal concentration of europium dopant for the luminescence properties was determined (6.5 mol% Eu vs. Y) (Cui et al., 2013b).

## Water-Based Syntheses

In the following syntheses, the reaction medium is water. It is an available, green, and ideal solvent for the dissolution of numerous metallic precursors, especially nitrates and chlorides.

Water also brings two main advantages: first, the availability of lanthanide precursors, and especially nitrates (that can be prepared from oxides in $HNO_3$) and water-soluble sulfur sources (thioacetamide, thiourea, ammonium sulfide, sodium sulfide, and so on; see **Scheme 1**); second, the substantial knowledge on inorganic polymerization in water. So far, in more than 90% of the articles dealing with $Ln_2O_2S$ nanoparticles, the desired feature of the material was luminescence. Luminescence is due to a controlled doping of the oxysulfide phase ($Ln^1_2O_2S$:$Ln^2$, $M^3$, $M^4$) that is achieved by co-precipitation of the main cation ($Ln^1$) with the cations that trigger the luminescence and influence its properties ($Ln^2$, and possibly $M^3$, $M^4$,...).

Water is however limiting metal oxysulfide synthesis by its relatively low boiling point. Even hydrothermal syntheses with autoclaves do not provide enough energy to obtain crystalline oxysulfide nanoparticles. In general, syntheses lead to an intermediate nanoscaled phase (which sometimes already contains sulfur) that is subsequently fully converted in oxysulfide nanoparticles with a solid-gas sulfidation (**Figure 7**). This last step remains an important drawback. It requires relatively high temperatures for nanoparticles synthesis (typically between 600 and 1,100°C) and a large excess of inert gas and sulfur which is often present under the active but toxic gaseous forms of $H_2S$ or $CS_2$. Also, it can affect the morphology of the solid by sintering or degradation of the desired phase.

The high-temperature sulfidation step remains the most challenging process here, but can be useful for other features. For luminescence purposes, the energy provided during the thermal treatment gives better-crystallized nanoparticles that present better photoluminescence properties. Moreover, doping ions can be inserted during this step.

### Gelatin-Templated Synthesis

Reported in 2008 by Liu et al., this synthesis stands out through the original use of gelatin and the way the oxysulfide phase is obtained (Liu et al., 2008).

First, the appropriate amounts of lanthanum, terbium, and europium nitrates obtained from dissolution of $La_2O_3$, $Tb_4O_7$, and $Eu_2O_3$ in nitric acid are mixed and heated with gelatin at 80°C in $H_2O$. The obtained translucent gelatin sol turns into a gel at 0°C. Small pieces of the gel are soaked into $NH_3 \cdot H_2O$ and $La(OH)_3$:Eu, Tb precipitates inside the gel. Violent stirring can then turn the gel into sol again, and $(NH_4)_2(SO_4)$ is added in stoichiometric amount. After drying and annealing at 500°C for 2 h in air, a powder of oxysulfate $La_2O_2SO_4$:Eu, Tb nanoparticles is formed. The oxysulfate nanoparticles are then converted to oxysulfide nanoparticles by solid-gas reaction using $H_2$ as reducing gas (700–800°C, 2 h).

The pathway of oxysulfate reduction is quite rare in the oxysulfide nanoparticles literature, as it often requires high temperatures and long reaction times. Here, the nanoparticles however keep a reasonable 50 nm diameter. On the other hand, this synthesis comprises a myriad of steps, generates two intermediary phases and requires two heat treatments above 500°C.

### Sol-gel Polymer Thermolysis

This strategy is based on the elaboration of an organic network in which the inorganic nanoparticles nucleate and grow in a controlled way. The network is then burnt to free the nanoparticles. It is analogous to the Pechini method used for oxide synthesis for which a tridimensional polyester network is elaborated by reaction of trisodium citrate and ethylene glycol for instance (Pechini, 1967).

Dhanaraj et al. published in 2003 a first version of a sol-gel polymer thermolysis strategy to yield $Y_2O_2S$:Eu nanoparticles (Dhanaraj et al., 2003). $Y(NO_3)_3$ and $Eu(NO_3)_3$ were obtained from the corresponding oxides. Urea, formaldehyde and elemental sulfur were then added and the network was formed at 60°C. By condensation of urea and formaldehyde along with water evaporation, a gel was obtained. After thermolysis at 500°C in sulfidating atmosphere, $Y_2O_2S$:Eu nanoparticles were formed. Based on the XRD pattern, the product was not pure (small peaks of impurities). Despite the treatment at 500°C, the nanoparticles were quite small (around 30–50 nm) but presented an unclear morphology and aggregation. The work of Dai et al. in 2008 on $La_2O_2S$:Eu which deals with the effects of $Eu^{3+}$ concentration on the photoluminescence is based on the same synthetic route (Dai et al., 2008).

One year later, Dhanaraj et al. published a second version of the protocol that led to hexagonal nanoplates with a size between 7 and 15 nm, tunable via the reactants concentrations

(Dhanaraj et al., 2004). The thermolysis process was divided in two steps: first, the sol/network solid was heated at 500°C for 2 h to get $Y_2O_3$:Eu nanoparticles, and was subsequently digested by a thiosulfate solution. After water evaporation, a second thermal treatment at 500°C (1 h) burnt the mixture to yield $Y_2O_2S$:Eu nanoparticles. The authors did not obtain a pure product yet, based on XRD analysis, but this time they identified sodium polysulfides as side-products. Later, Thirumalai and Nakkiran reused this strategy, succeeded in washing the by-products (Thirumalai et al., 2007) and deeply investigated the nanoparticles: optical (Thirumalai et al., 2007, 2008a) and electronic properties (Thirumalai et al., 2008a) were discussed as well as the photo-assisted relaxation of surface states (Nakkiran et al., 2007).

## Syntheses in Water at Atmospheric Pressure

Because of the attractiveness of luminescent water-dispersible nanoparticles, the pursuit of doped oxysulfide nanoparticles led to the publication and the refinement of synthetic strategies in water. However, the reported syntheses illustrate the complexity of obtaining oxysulfides at low temperatures in water: most often, the authors choose to precipitate an unsulfurated intermediary doped phase [$Ln(OH)_3$, $Ln(OH)(CO_3)$ for instance] that can be amorphous or not. Thus, the syntheses presented in this section are worthwhile for oxide-, hydroxide-, or hydroxycarbonate-based nanomaterials. The intermediate nanoparticles are then sulfidated, most often with a solid-gas or alternatively with a solid-solid reaction.

Interestingly, the conditions for lanthanide oxysulfide nanoparticles syntheses in water are majorly optimized on $Gd_2O_2S$ and $Y_2O_2S$ because of their well-known luminescent properties and also maybe for the relatively low price of the related precursors (**Table 2**).

### Urea-based syntheses

*Decomposition of urea in water.* Generally, the precipitation of the lanthanide salts is performed via the basification of the reaction medium. Thus, a significant amount of research has focused on the cheap, safe, highly available, and water-soluble urea. Urea is indeed known to decompose in ammonia [$pKa(NH_{4+},NH_3) = 9.25$] and aqueous carbon dioxide which can carbonate aqueous lanthanide species (**Scheme 3**).

The concomitant release of ammonia and aqueous carbon dioxide is used in particular for the precipitation of lanthanide hydroxycarbonates $Ln(OH)CO_3$ that turned out to be a suitable precursor of lanthanide oxysulfide nanoparticles. In the absence of sulfur source, further decomposition of this intermediate leads instead to lanthanide oxide. This was demonstrated in the pioneering work of Matijević and Hsu (1987) in the context of the fabrication of well-calibrated lanthanide colloids.

*Syntheses with urea in water.* The first aqueous synthesis of oxysulfide nanoparticles was reported by Kawahara et al. (2006; **Table 3**). Using yttrium and europium nitrates $Y(NO_3)_3$ and $Eu(NO_3)_3$ along with urea, an europium-doped hydroxide precursor $Y(OH)_3$:Eu was obtained by heating the mixture possibly in the presence of a glycol (ethylene glycol, propylene

glycol, or hexamethylene glycol). The isolated powder of $Y(OH)_3$:Eu was then heated between 800 and 1,200°C with $Na_2CO_3$ and sulfur to create a sulfidating vapor and yield $Y_2O_2S$:Eu nanoparticles. XRD showed that the crystalline phase was pure $Y_2O_2S$. The obtained nanoparticles were facetted crystals of 100-300 nm length. Above 1,100°C, sintering made the particles sub-micrometric ($\geq$600 nm).

Xing et al. (2009) then developed an inspiring but complex protocol to synthesize $Y_2O_2S$:Yb, Ho upconversion nanoparticles (Xing et al., 2009). A solution of lanthanide nitrates $Y(NO_3)_3$, $Yb(NO_3)_3$, and $Ho(NO_3)_3$ and a solution of urea were separately prepared. The latter solution was added to the first that had been pre-heated at 60°C and the mixture was then heated at 82°C. After cooling and aging during 48 h, a white amorphous precipitate [likely $Y(OH)CO_3$] (Tian et al., 2017) was dried and converted to $Y_2O_3$:Yb, Ho via calcination (600°C, 1 h, air). Then, the oxide was sulfidated at 800°C for 1 h with a sulfur vapor created by $S_8$ at 400°C and conveyed by an argon flow. It enabled the formation of size-monodisperse and non-aggregated nanoparticles with an average diameter of *ca* 80 nm. The diameter could also be tuned by adjusting the reaction time (aging step). Several works are based on Xing's synthesis with slight modifications. Luo et al. added a small amount of oleic acid in the urea mixture and performed the sulfidation at only 600°C to form the same $Y_2O_2S$:Yb, Ho nanoparticles (Luo et al., 2009). In the same group, Pang et al. (2010) reported additional reactions that coated the nanoparticles with functionalized silica using a derived Stöber process with polyvinylpyrrolidone (PVP), aqueous ammonia, teraethylorthosilicate (TEOS), and aminopropyltriethoxysilane (APTES) in a second step (**Figure 10**). Sulfidation of hydrated $Ln(OH)CO_3$:$Eu^{3+}$ nanoparticles (Ln = Gd, Dy, Ho) was alternatively performed under a flow of $H_2S$ at 750°C for 90 min followed by an annealing under Ar at 850°C for 4 h (Verelst et al., 2010; Osseni, 2012) This constitutes the sole reported route to $Dy_2O_2S$ and $Ho_2O_2S$ nanoparticles, to the best of our knowledge.

Also based on Xing's work, Bakhtiari et al. (2015) later studied the effect of europium concentration on $Y_2O_2S$:Eu nanoparticles size and luminescence. Very recently, Tian et al. succeeded in forming upconverting core-shell nanoparticles $Y_2O_2S$:Er@$Y_2O_2S$:Yb,Tm by applying Xing's method twice to form the oxide-oxide compound $Y_2O_3$:Er@$Y_2O_3$:Yb,Tm as an intermediate (Tian et al., 2017). Solid-gas reaction with sulfur vapor at 800°C finally provided the oxysulfide nanoparticles. After the shell formation, $Y_2O_3$:Er@$Y_2O_3$:Yb,Tm nanoparticles were well-separated (**Figure 11A**). After sulfidation, the nanoparticles were aggregated because of sintering (**Figure 11B**). Nevertheless, the shell prevented the quenching of the $Er^{III}$ luminescence and multicolor fluorescence was achieved thanks to $Er^{III}$/$Tm^{III}$ co-doping (**Figure 11C**).

$Y_2O_2S$:Eu, Mg, Ti nanoparticles were also synthesized for persistent luminescence applications by Ai et al. (2010a). $Y(OH)CO_3$:Eu was obtained by heating a mixture of $Y(NO_3)_3$, $Eu(NO_3)_3$, and urea at 90°C for 2 h. The final product is obtained by a two-step thermal treatment developed by Li et al. (2009), It involves first $S_8$ in graphite at 800°C for 4 h, which creates *in situ* reactive $CS_2$, and then solid-solid reaction with doping

**TABLE 3 |** Precipitation from aqueous solutions at atmospheric pressure.

| References Phase | Metal sources | Precipitation step(s) | Annealing step(s) | Intermediary phase(s) | Final Morphology (Final size) |
|---|---|---|---|---|---|
| Kawahara et al. (2006) $Y_2O_2S$:Eu | $Y(NO_3)_3$ $Eu(NO_3)_3$ | 1/Urea, glycol 100°C, 5 h | 2/$S_8$, $Na_2CO_3$ 800–1,200°C, 2 h | 1/$Y(OH)_3$:Eu | Nanocrystals (100–300 nm for $T \leq 1,100°C$) |
| Xing et al. (2009) $Y_2O_2S$:Yb,Ho Pang et al. (2010) $Y_2O_2S$:Yb,Ho@$SiO_2$-APTES Bakhtiari et al. (2015) $Y_2O_2S$:Eu | $Y(NO_3)_3$ $Yb(NO_3)_3$ $Ho(NO_3)_3$ | 1/Urea 82°C 2/Aging r.t., 48 h | 3/Air, 600°C, 1 h 4/S vapor ($S_8$ at 400°C) Ar, 800°C, 1 h | 2/$Y(OH)CO_3$:Yb,Ho[a] 3/$Y_2O_3$:Yb,Ho (after annealing in air) | Nanospheres (Ø ≈ 70 nm) |
| Luo et al. (2009) $Y_2O_2S$:Yb,Ho | $Y(NO_3)_3$ $Yb(NO_3)_3$ $Ho(NO_3)_3$ | 1/Urea (oleic acid) 82°C 2/Aging r.t., 48 h | 3/Air, 600°C, 1 h 4/S vapor ($S_8$ at 400°C) Ar, 550–600°C, 1 h | 2/$Y(OH)CO_3$:Yb,Ho[a] 3/$Y_2O_3$:Yb,Ho | Nanospheres (Ø ≈ 50 nm) |
| Ai et al. (2010b) $Y_2O_2S$:Eu,Mg,Ti | $Y(NO_3)_3$ $Eu(NO_3)_3$ | 1/Urea 90°C, 3 h | 2/Air, 700°C, 2 h 3/$S_8$ in graphite ($CS_2$) 800°C, 4 h 4/$TiO_2$, $Mg(OH)_2$·$4Mg(CO_3)$·$6H_2O$ 1,100°C, 4 h | 2/$Y_2O_3$:Eu | Hollow submicrospheres (Ø = 350–400 nm) |
| Ai et al. (2010a) $Y_2O_2S$:Eu,Mg,Ti | $Y(NO_3)_3$ $Eu(NO_3)_3$ | 1/Urea 90°C, 2 h | 2/$S_8$ in graphite ($CS_2$) 800°C, 4 h 3/$TiO_2$, $Mg(OH)_2$·$4Mg(CO_3)$·$6H_2O$ 1,100°C, 4 h | 1/$Y(OH)CO_3$:Eu | Nanospheres (Ø = 100–150 nm) |
| Fu et al. (2010) $Y_2O_2S$:Yb,Ho | $Y(NO_3)_3$ $Yb(NO_3)_3$ $Ho(NO_3)_3$ | 1/$Na_2CO_3$ PEG 4000 | 2/Air, 600°C, 1 h 3/S vapor ($S_8$ at 400°C) Ar, 800°C, 1 h | 1/$Y(OH)CO_3$:Yb,Ho[a] 2/$Y_2O_3$:Yb,Ho | Nanocrystals (30–100 nm) |
| Osseni (2012) $Gd_2O_2S$:Eu $Dy_2O_2S$:Eu $Ho_2O_2S$:Eu | $Gd(NO_3)_3$ $Dy(NO_3)_3$ $Ho(NO_3)_3$ $Eu(NO_3)_3$ | 1/Urea EtOH 85°C | 2/Ar/$H_2S$ (83/17 $v/v$) 750°C, 90 min 3/Ar, 850°C, 4 h | 1/$Gd(OH)CO_3$·$H_2O$:Eu $Dy(OH)CO_3$·$H_2O$:Eu $Ho(OH)CO_3$·$H_2O$:Eu | Nanospheres (Ø = 60 nm for Gd, 170 nm for Dy, 53 nm for Ho) |
| Osseni et al. (2011) $Gd_2O_2S$:Eu@$mSiO_2$ $Gd_2O_2S$:Eu@$SiO_2$-APTMS | $Gd(NO_3)_3$ $Eu(NO_3)_3$ | 1/Urea EtOH 85°C | 2/Ar/$H_2S$ (83/17 $v/v$) 750°C, 90 min 3/Ar, 850°C, 4 h | 1/$Gd(OH)CO_3$·$H_2O$:Eu | Nanospheres, tunable diameter with EtOH volume (Ø = 100–250 nm) Silica coating: 10 nm |
| Yan et al. (2013a) $Ln_2O_2S$:Tb (Ln = Gd, Y) Yan et al. (2013b) $Y_2O_2S$:Tb,Er | $Ln(NO_3)_3$ $Tb(NO_3)_3$ $(Er(NO_3)_3)$ | 1/Urea ~100°C, 1 h | 2/$Na_2CO_3$, $S_8$, $Ln_2O_3$ 900°C, 1 h | 1/$Ln(OH)CO_3$·$H_2O$:Tb or $Y(OH)CO_3$·$H_2O$:Tb,Er | Nanocrystals (50–200 nm) |
| Hernández-Adame et al. (2014) $Gd_2O_2S$:Tb | $Gd(NO_3)_3$ $Tb(NO_3)_3$ | 1/Urea | 2/Air, 800°C, 2 h 3/S vapor ($S_8$ at 900°C) $N_2$, 900°C, 3 h | 1/$Gd(OH)CO_3$·$H_2O$:Tb 2/$Gd_2O_3$:Tb | Good conditions give nanospheres (Ø = 100 nm) |
| Tian et al. (2015) $Y_2O_2S$:Yb,Er | $Y(NO_3)_3$ $Yb(NO_3)_3$ $Er(NO_3)_3$ | 1/$NH_4HCO_3$ $NH_3$·$H_2O$ r. t. | 2/S vapor ($S_8$ at 400°C) $N_2$, 900°C, 1 h | 1/$Y(OH)_x(CO_3)_y$:Yb,Er | Aggregated nanocrystals (30 nm) |
| Cichos et al. (2016) $Gd_2O_2S$:Eu | $Gd(NO_3)_3$ $Eu(NO_3)_3$ | 1/Urea ~100°C (a) 2 h, (b) 24 h | 2/$S_8$, Ar 950°C, 1 h | 1/(a) amorphous (b) $Gd(OH)CO_3$:Eu | (a) Nanospheres (Ø ≈ 130 nm) (b) Microcrystals (≈ 1 μm) |
| Bagheri et al. (2016) $Gd_2O_2S$:Pr | $Gd(NO_3)_3$ $Pr(NO_3)_3$ | 1/Urea ~100°C, 1 h | 2/Air, 600°C, 1 h 3/$S_8$, 900°C, 1 h | 1/$Gd(OH)CO_3$·$H_2O$:Pr[a] | Nanospheres (Ø = 25–80 nm) |
| Tian et al. (2017) $Y_2O_2S$:Er@$Y_2O_2S$:Yb,Tm | $Y(NO_3)_3$ $Er(NO_3)_3$ $Yb(NO_3)_3$ $Tm(NO_3)_3$ | 1/Urea 82°C 2/Aging r.t., 48 h | 3/S vapor ($S_8$ at 800°C) Ar, 800°C, 40 min | 2/$Y_2O_3$:Er 2'/$Y_2O_3$Er@$Y_2O_3$:Yb,Tm | Aggregated crystals (50–150 nm) |

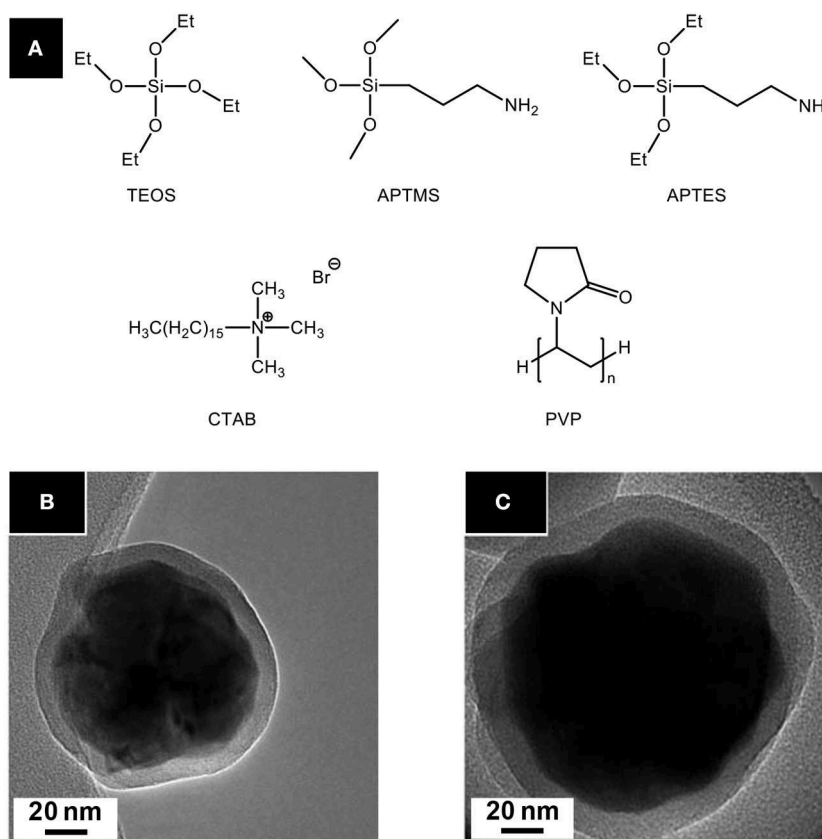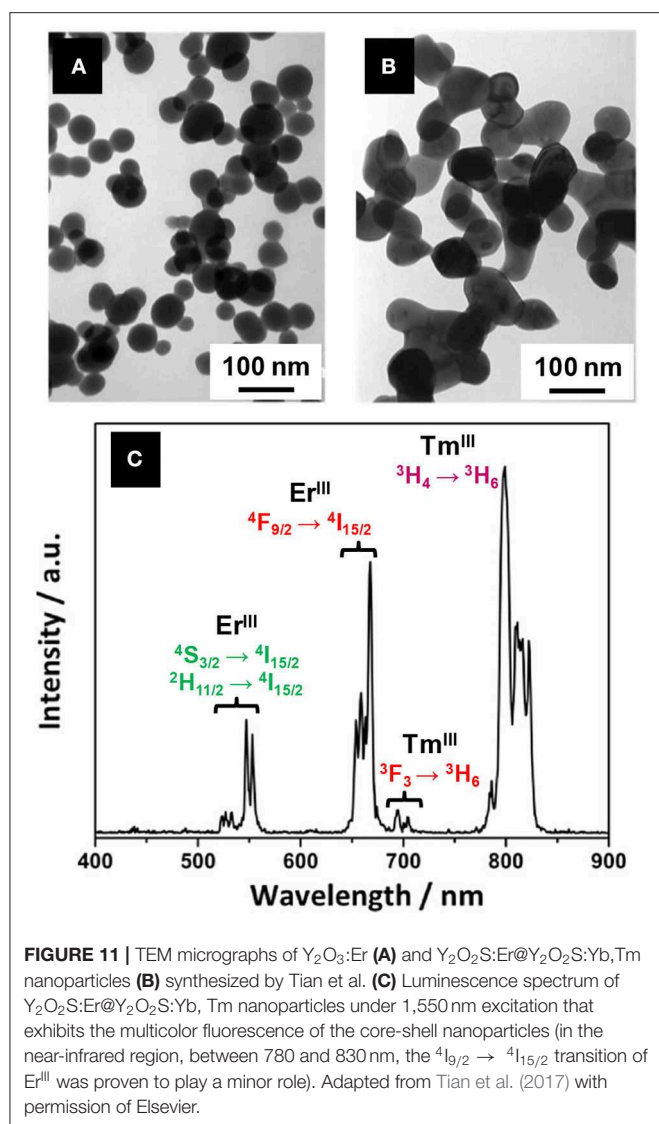[a]Intermediary phase deduced from later works.

**FIGURE 10 | (A)** Precursors and additives commonly used for nanoparticles silica coating. Tetraethylorthosilicate (TEOS) is used as silica precursor; 3-aminopropyltrimethoxysilane (APTMS), and 3-aminopropyltriethoxysilane (APTES) are rather employed for silica functionalization. TEM micrographs of $Gd_2O_2S:Eu@SiO_2$-APTMS **(B)** and $Gd_2O_2S:Eu@mSiO_2$ **(C)** nanoparticles from Osseni et al. (mSiO$_2$ stands for mesoporous silica). Adapted from Osseni et al. (2011) with permission of The Royal Society of Chemistry.

solids (here $Mg(OH)_2 \cdot 4MgCO_3 \cdot 6H_2O$ and $TiO_2$). The same year, Ai et al. (2010b) presented an original morphology for the same phase. Hollow submicrospheres were obtained using templating 350-400 nm carbon submicrospheres obtained by hydrothermal glucose decomposition (autoclave, 160°C, 9 h). Before sulfidation and Mg/Ti doping, $Y_2O_3$:Eu was obtained when removing carbon by thermal treatment at 700°C (2 h, air).

In 2011, Osseni et al. reported the first synthesis of $Gd_2O_2S$:Eu nanoparticles starting from nitrates and urea in a water/ethanol mixture ($H_2O/EtOH = 80/20$ $v/v$) (Osseni et al., 2011). After dissolution, the reactants were heated to 85°C to form a doped hydroxycarbonate precursor $Gd(OH)CO_3 \cdot H_2O$:Eu. After isolation and drying, a heat treatment in two steps was performed. First, sulfidation was performed by $Ar/H_2S$ at 750°C for 90 min and then the nanoparticles were maintained at 850°C for 4 h under argon atmosphere only. The final nanoparticles were crystalline and spherical. Diameter was tunable by varying the $H_2O/EtOH$ ratio and reaction time. Interestingly, two techniques of deposition of silica on the nanoparticles were presented. The shell was either formed of mesoporous silica using TEOS and cetyltrimethylammonium bromide (CTAB) or functionalized by a silica/APTMS shell using TEOS

and 3-aminopropyltrimethoxysilane (APTMS). In particular, mesoporous silica was found to enhance the luminescence properties of the nanoparticles. Multimodal imaging was recently applied using these $Gd_2O_2S$:Eu nanoparticles (Santelli et al., 2018).

A slightly different strategy, close to the work of Xing et al. on yttrium, was adopted in 2013 by Yan et al. (2013a) for the formation of terbium-doped oxysulfide nanoparticles of gadolinium and yttrium. $Tb(NO_3)_3$ and $Gd(NO_3)_3$ were dissolved in water around 100°C, and then urea was added. After filtration and drying, $Gd(OH)CO_3 \cdot H_2O$:Tb was obtained. The sulfidation process was quite complex: the precursor is mixed with $Na_2CO_3$ and sulfur but is also covered by a second mixture composed of $Gd_2O_3$, $Na_2CO_3$, and $S_8$. The bottom layer was washed in hot water and filtrated after being fired at 900°C for 1 h. The crystalline phases $Gd_2O_2S$ or alternatively $Y_2O_2S$ were pure (based on XRD) and the polydispersity of the diameter was significant (average diameter around 100–120 nm). Yan et al. also studied the role of the doping ions in the luminescence mechanism of $Y_2O_2S$:Tb, Er nanoparticles (Yan et al., 2013b). In 2016, Bagheri et al. fabricated a scintillator screen composed of $Gd_2O_2S$:Pr nanoparticles synthesized via a similar nitrate/urea

**FIGURE 11 |** TEM micrographs of $Y_2O_3$:Er **(A)** and $Y_2O_2$S:Er@$Y_2O_2$S:Yb,Tm nanoparticles **(B)** synthesized by Tian et al. **(C)** Luminescence spectrum of $Y_2O_2$S:Er@$Y_2O_2$S:Yb, Tm nanoparticles under 1,550 nm excitation that exhibits the multicolor fluorescence of the core-shell nanoparticles (in the near-infrared region, between 780 and 830 nm, the $^4I_{9/2} \rightarrow$ $^4I_{15/2}$ transition of Er$^{III}$ was proven to play a minor role). Adapted from Tian et al. (2017) with permission of Elsevier.

reaction (Bagheri et al., 2016). However, the sulfidation process is a solid-solid reaction with $S_8$ at 900°C for 1 h.

In 2014, Hernández-Adame et al. extensively studied the influence of the reaction conditions on the morphology of Gd(OH)CO$_3$:Tb and Gd$_2$O$_2$S:Tb, by mixing an urea aqueous solution with an aqueous solution of Tb(NO$_3$)$_3$ and Gd(NO$_3$)$_3$, and performing two thermal treatments (at 800°C under air and at 900°C under a N$_2$/S atmosphere; Hernández-Adame et al., 2014). The precursor concentrations, the temperature of the stock solutions of nitrates and urea and the time and temperature of reactions were varied (**Figure 12**). Eventually, only one set of conditions gave regular spherical nanoparticles (Ø ≈ 100 nm): a nitrate solution at 6.0 $10^{-3}$ M, pre-heated at 65°C, and a urea solution at 0.5 M, at room temperature, reacting for 90 min at 85°C (**Figure 12B**). Hernández-Adame et al. recently completed their work with a comprehensive study of the effects of the terbium concentration on the luminescence properties of their nanoparticles (Hernandez-Adame et al., 2018).

Recently, Cichos et al. studied three different syntheses of europium-doped Gd$_2$O$_2$S nanoparticles starting from nitrates and urea: (i) heating water at around 100°C for 2 h using an oil bath, (ii) heating a Teflon bottle at 100°C for 24 h, and (iii) heating an autoclave at 120°C for 12 h (see the autoclave section; Cichos et al., 2016). After reaction, the isolated solids were heated with an excess of sulfur under argon at 950°C for 1 h to yield Gd$_2$O$_2$S:Eu particles. In case (i), the intermediary solid was amorphous but the particles were spherical and quite monodisperse in diameter (**Figure 13A**). After sulfidation, crystalline Gd$_2$O$_2$S:Eu nanoparticles with a diameter close to 135 nm were obtained. The surface was rougher than the amorphous precursor's one. The Teflon bottle method [case (ii)] gave micrometric hydroxycarbonate Gd(OH)CO$_3$ particles (**Figure 13B**) that were converted to Gd$_2$O$_2$S:Eu micrometric crystals and was thus not suitable for nanoparticles synthesis.
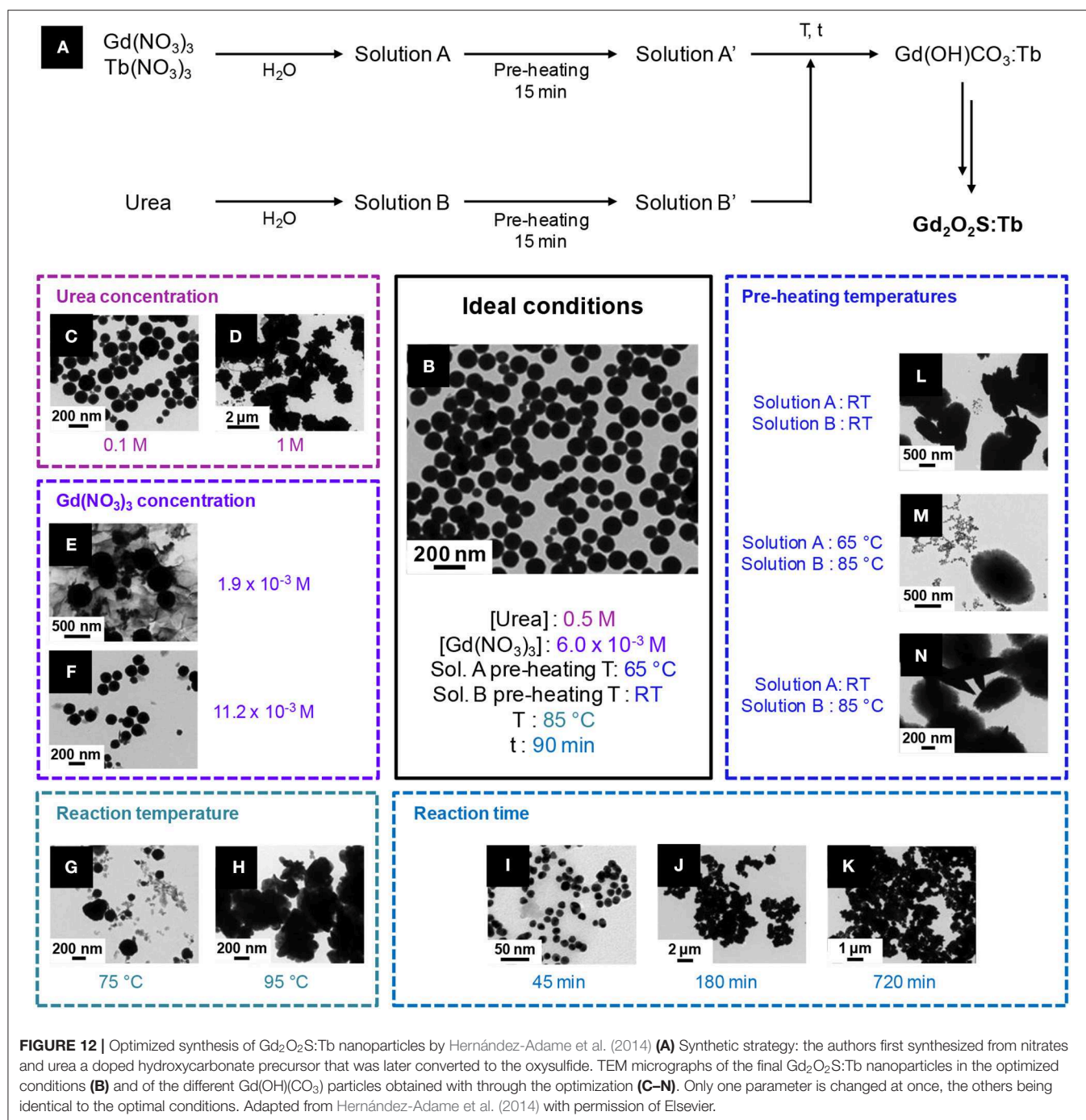
### Other precipitation routes from aqueous solutions

Closely related to urea's precipitating method, an aqueous ammonia/ammonium hydrogenocarbonate precipitation of nitrates was reported by Tian et al. (2015). A NH$_4$HCO$_3$/NH$_3$·H$_2$O solution was added dropwise to a nitrate solution including Y(NO$_3$)$_3$, Yb(NO$_3$)$_3$, and Er(NO$_3$)$_3$. A white precipitate of Y(OH)$_x$(CO$_3$)$_y$:Yb, Er was obtained and dried. The Y$_2$O$_2$S:Yb, Er nanoparticles were obtained using sulfur vapor (S$_8$ heated at 400°C) carried by N$_2$ at 900°C for 1 h. The small but aggregated crystalline nanoparticles (Ø ≈ 30 nm) were phase-pure, based on XRD. Here, the use of ammonium hydrogenocarbonate and aqueous ammonia enabled the authors to carry out the reaction without heating whereas urea needed thermolysis.

Regarding upconverting oxysulfide nanoparticles, Fu et al. (2010) chose Na$_2$CO$_3$ to form intermediate solids which were then sulfidated. After dissolution of Y(NO$_3$)$_3$, Yb(NO$_3$)$_3$, and Ho(NO$_3$)$_3$, the nitrate solution was added in a 0.1 M solution of Na$_2$CO$_3$ containing PEG 4000 as surfactant. A solid precipitated, was isolated and dried. It was heated at 600°C to yield Y$_2$O$_3$:Yb, Ho. Then, the oxide was converted to oxysulfide using Xing's thermal treatment described in the previous section. Interestingly, Na$_2$CO$_3$ enables the authors to work at ambient temperature in the first step whereas urea required thermolysis. However, two thermal treatments were necessary to reach the oxysulfide product. Moreover, an irregular faceted morphology and a significant polydispersity in size were found in the final sample.

### Aqueous Reactions Under Autogenic Pressure

This section is dedicated synthesis in aqueous solution under pressure, in autoclave. We already mentioned the low boiling point of water as a strong limitation if we consider the temperatures commonly required for crystalline nanoparticles synthesis. Synthesis under pressure might be a way to overcome this limitation. Unfortunately, like the precipitation reactions at atmospheric pressure, the reported syntheses in hydrothermal conditions mainly focus on producing an intermediate solid that requires sulfidation in a second step (**Table 4**). Nevertheless, these

**FIGURE 12 |** Optimized synthesis of $Gd_2O_2S$:Tb nanoparticles by Hernández-Adame et al. (2014) **(A)** Synthetic strategy: the authors first synthesized from nitrates and urea a doped hydroxycarbonate precursor that was later converted to the oxysulfide. TEM micrographs of the final $Gd_2O_2S$:Tb nanoparticles in the optimized conditions **(B)** and of the different $Gd(OH)(CO_3)$ particles obtained with through the optimization **(C–N)**. Only one parameter is changed at once, the others being identical to the optimal conditions. Adapted from Hernández-Adame et al. (2014) with permission of Elsevier.

syntheses expanded the range of available morphologies for the final oxysulfide nanoparticles.

In the late 2000's, Thirumalai et al. (2008b, 2009a) reported the hydrothermal synthesis of $Gd_2O_2S$:Eu (**Table 4**, entries 1, 2). Starting with an amorphous precipitate (obtained by adjusting the pH of an aqueous solution of $Gd(NO_3)_3$ with NaOH), they obtained $Gd(OH)_3$ nanoscaled materials (hexagonal nanocrystals, nanotubes, nanobelts, …) after the hydrothermal treatment. The influence of the pH of precipitation

and the temperature and duration of the hydrothermal define the morphology of the material. After impregnation of the solid with $Eu^{3+}$ ions in a aqueous solution, sulfidation was performed using a $CS_2$ atmosphere generated by reaction of sulfur and carbon. The morphology of $Gd(OH)_3$ was retained in the final $Gd_2O_2S$:Eu nanopowder, with only slight size decreases. The nanomaterials are well-crystallized and the morphology is finely adjustable varying the reaction conditions. Unfortunately, an undescribed sulfidation process is performed before the annealing step. It is

**FIGURE 13 |** Structural and morphological variations of $Gd_2O_2S$ precursors obtained by Cichos et al. (2016). Depending on the heating process, strong variations are observed: amorphous spherical nanoparticles (**A** with the size distribution in inset), hydroxycarbonate microcrystals (**B**) or carbonate microcrystals (**C**) can be obtained. Adapted from Cichos et al. (2016) with permission of Elsevier.

probably similar to the one mentioned before for the composite hydroxide method conducted by the same group (Thirumalai et al., 2011a). Moroever, an original study on the photo-induced impedance is presented. Interestingly, the morphology is retained also with other lanthanides, as similar results were obtained by Thirumalai et al. (2009b) on $Y_2O_2S$:Eu (**Table 4**, entry 3).

The oxysulfides nanoparticles obtained by hydrothermal syntheses were also extensively studied by Li, Ai, Liu et al. who obtained $Y_2O_2S$:Eu,Mg,Ti nanoparticles (**Table 4**, entries 4, 5, and 6; Li et al., 2009, 2010; Ai et al., 2010c). This combination of doping ions is typical for persistent luminescence. Aqueous ammonia $NH_3 \cdot H_2O$ was used as a base for precipitation of hydroxides. The authors then inserted the dopants by solid-solid reaction in the annealing step with $Eu_2O_3$, $Mg(OH)_2 \cdot 4Mg(CO_3) \cdot 6H_2O$, and $TiO_2$. Moreover, they noticed that using $CS_2$ formed *in situ*, rather than solid $S_8$, is crucial to keep the morphology. With $S_8$, the $Y(OH)_3$ nanotubes turned into hexagonal nanoparticles after the annealing step.

The group of Cui and Liu also put great efforts on the characterization of such nanoparticles (**Table 4**, entries 7 and 8; Cui et al., 2014b; Huang et al., 2014; Liu et al., 2014a,c). Soluble sources [$Eu(NO_3)_3$, $Mg(NO_3)_2$ and $Ti(OBu)_4$] were employed as reactants rather than solids for doping. Thus, a moderated sulfidation annealing temperature ($\leq 800^\circ$C) was employed to yield $Y_2O_2S$:Eu, Mg, Ti nanotubes. The synthesis (Cui et al., 2014b), the influence of earth-alkaline or metal

$M^{II}$ ion (Huang et al., 2014; Liu et al., 2014b), the effect of the relative concentration of $Mg^{II}$ and $Ti^{IV}$ (Liu et al., 2014a), and the $Eu^{III}$ concentration were separately studied (Cui et al., 2014a). Later, Yuan et al. (2016) also reported mild conditions to synthesize composite $Y_2O_3$:Eu/$Y_2O_2S$:Eu nanoparticles starting from soluble nitrate precursors (**Table 4**, entry 12; Yuan et al., 2016). The particles were crystalline but presented an irregular morphology. They were incorporated in dye-sensitized solar cells that were fabricated by the group. An enhancement of the cell efficiency was measured thanks to the light scattering properties of the nanocomposite.

A rare example of $Lu_2O_2S$:Eu nanocrystals was reported in 2015 by Wang et al. (**Table 4**, entry 9). PVP K30 followed by a solution of thiourea in ethanol were added to lutetium nitrate dissolved in a mixture of water and ethylene glycol. Perfectly regular nanorods were obtained after a thermal treatment with a sulfidizing atmosphere. Here again, the sulfidizing step mechanism was not studied in detail.

In 2016, Cichos et al. tested an hydrothermal synthesis (**Table 4**, entry 10) to yield doped $Gd_2(CO_3)_3$:Eu particles in comparison with reactions at atmospheric pressure (Cichos et al., 2016). The authors noticed that this method is rather not adapted to the synthesis of nanoparticles: several populations are obtained, including micrometric irregular crystals (**Figure 13C**).

The synthesis reported by Rosticher et al. (2016) is a promising exception (**Table 4**, entry 11). The crucial difference lies in the sulfidation method. An excess of water-soluble thioacetamide was incorporated before the hydrothermal heating after precipitation of amorphous $Gd(OH)_3$:Eu, Mg, Ti with NaOH. This allowed incorporation of sulfur before the annealing step, which could conveniently be performed under inert atmosphere. Its role was only to improve the cristallinity and the luminescence performances of the powder.
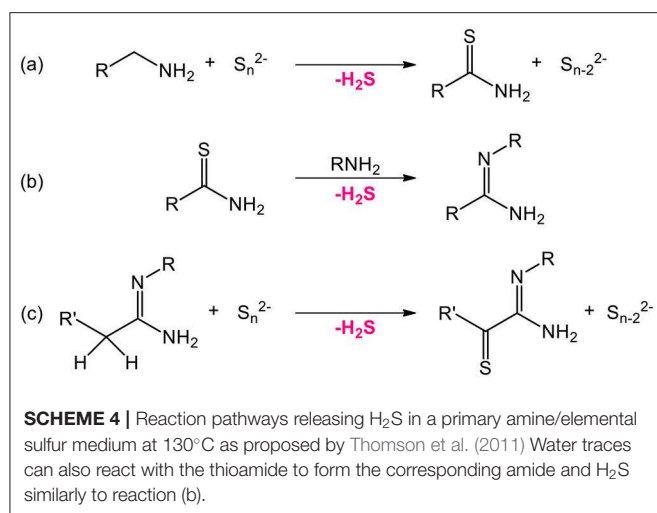
## Conclusion

The formation of oxysulfide nanoparticles in water encounters several limits. Because of the aqueous solvent, excess oxygen favors the formation of intermediary phases such as hydroxides, hydroxycarbonates, or oxides. Only an adequate sulfidation annealing step at high temperatures enables the formation of the oxysulfide nanoparticles. Nevertheless, it can affect the morphology of the nanoparticles with aggregation and sintering.

Moreover, the synthesis of the intermediary phases is also challenging. Precise reaction parameters have to be employed, with long optimization processes. In **Figures 12**, **13**, we reminded for instance the works of Hernández-Adame et al. and Cichos et al. on the synthesis of doped gadolinium oxysulfide nanoparticles with urea. Not only the reaction temperature and time had a great effect on the final morphology of the intermediates: concentrations of the reactants, pre-heating temperatures, heating techniques are also crucial to obtain the desired product.

Working in organic medium then seems to be a suitable solution to overcome the excess available oxygen.

**TABLE 4 |** Hydrothermal syntheses of $Ln_2O_2S$ nanomaterials.

| References Phase | Metal sources | Additives | Hydrothermal step | Annealing step | Morphology (size) |
|---|---|---|---|---|---|
| Thirumalai et al. (2008b) $Gd_2O_2S$:Eu | $Gd(NO_3)_3$ $Eu(NO_3)_3$ | NaOH (pH ≈ 11) | 130–150°C 24–48 h | Ar/$CS_2$/S/C, 700°C, 2–3 h | Nanotubes (50 nm × few μm) |
| (Thirumalai et al., 2009a)) $Gd_2O_2S$:Eu | $Gd(NO_3)_3$ $Eu(NO_3)_3$ | NaOH (7 ≤ pH ≤ 13) | 100–180°C 12–48 h | Ar/$CS_2$/S/C, 700°C, 2–3 h | Tunable: Spheres (Ø 15 nm) + hexagonal crystals (20–30 nm) Nanosheets (15 × 80 $nm^2$), Nanobelts (25 nm × few μm) Nanotubes (15 × 200 $nm^2$), Nanorods (15 × 100 $nm^2$) Nanowires (15 × 250 $nm^2$) |
| Thirumalai et al. (2009b) $Y_2O_2S$:Eu | $Y(NO_3)_3$ $Eu(NO_3)_3$ | NaOH (7 ≤ pH ≤ 13) | 100–180°C 12–48 h | Ar/$CS_2$/S/C, 600°C, 2 h | Tunable: Spherical (15 nm) + hexagonal crystals (20–40 nm) Nanosheets (15 × 70 $nm^2$), Nanobelts (25 nm × few μm) Nanotubes (10 × 200 $nm^2$), Nanorods (10 × 70 $nm^2$) Nanowires (15 × 250 $nm^2$) |
| Li et al. (2009) $Y_2O_2S$:Eu,Mg,Ti | $Y(NO_3)_3$ | $NH_3 \cdot H_2O$ | 260°C 5 h | 1/$S_8$ in graphite ($CS_2$), 800°C, 4 h 2/$Eu_2O_3$, $TiO_2$, $Mg(OH)_2 \cdot 4Mg(CO_3) \cdot 6H_2O$, 1100°C, 4 h | Nanorods (50 × 400 $nm^2$) |
| Li et al. (2010) $Y_2O_2S$:Eu,Mg,Ti | $Y(NO_3)_3$ | NaOH (pH ≈ 14) | 180°C 12 h | $H_2$, $S_8$, $Na_2CO_3$, $Eu_2O_3$, $TiO_2$, $Mg(OH)_2 \cdot 4Mg(CO_3) \cdot 6H_2O$ 600–800°C, 4 h | Hexagonal nanoparticles (30–50 nm) |
| Ai et al. (2010c) $Y_2O_2S$:Eu,Mg,Ti | $Y(NO_3)_3$ | NaOH (pH ≈ 13) | 180°C 12 h | 1/$S_8$ in graphite ($CS_2$), 800°C, 4 h 2/$Eu_2O_3$, $TiO_2$, $Mg(OH)_2 \cdot 4Mg(CO_3) \cdot 6H_2O$, 1100°C, 4 h | Nanotubes (100–200 nm × 1–3 μm) |
| Cui et al. (2014b), Liu et al. (2014b) Cui et al. (2014a), Liu et al. (2014a) $Y_2O_2S$:Eu,Mg,Ti | $Y(NO_3)_3$ $Eu(NO_3)_3$ $Mg(NO_3)_2$ $Ti(OBu)_4$ | NaOH (pH ≈ 13) | 180°C 12 h | $S_8$/C ($CS_2$), 600–800°C, 6 h | Nanotubes (200 nm × 3 μm) |
| Huang et al. (2014) $Y_2O_2S$:Eu,Zn,Ti | $Y(NO_3)_3$ $Eu(NO_3)_3$ $Zn(NO_3)_2$ $Ti(OBu)_4$ | NaOH (pH ≈ 13) | 180°C 12 h | $S_8$/C ($CS_2$), 600–800°C, 6 h | Nanotubes (200 nm × 3 μm) |
| Wang et al. (2015) $Lu_2O_2S$:Eu | Lu(NO3)3 Eu(NO3)3 | NaOH (pH ≈ 11) Thiourea, PVP K30 | 200°C 24 h | S/$N_2$, 600°C, 2 h | Nanorods (20 × 500 $nm^2$) |
| Cichos et al. (2016) $Gd_2O_2S$:Eu | $Gd(NO_3)_3$ $Eu(NO_3)_3$ | Urea | 120°C 12 h | $S_8$, Ar, 950°C, 1 h | Irregular microcrystals (≥ 1 μm) + submicrospheres (300–500 nm) |
| Rosticher et al. (2016) $Gd_2O_2S$:Eu,Mg,Ti | $Gd(NO_3)_3$ $Eu(NO_3)_3$ $Mg(NO_3)_2$ $TiCl_4$ | NaOH (pH ≈ 8) Thioacetamide | 200°C 2 h | Ar, 700°C, 2 h | Nanospheres (Ø = 20 nm) + facetted crystals (50–100 nm) |
| Yuan et al. (2016) $Y_2O_3$:Eu/$Y_2O_2S$:Eu | $Y(NO_3)_3$ $Eu(NO_3)_3$ | NaOH | 100°C 5 h | $S_8$, $N_2$, 600°C, 1 h | Irregular morphology (≤150 nm) |

**SCHEME 4 |** Reaction pathways releasing $H_2S$ in a primary amine/elemental sulfur medium at 130°C as proposed by Thomson et al. (2011) Water traces can also react with the thioamide to form the corresponding amide and $H_2S$ similarly to reaction (b).

## Syntheses in Organic Medium

The following section is dedicated to the reactions mainly performed in organic medium. Thanks to the availability of high boiling-point solvents, the temperature of the reaction medium can reach 200-300°C much easier than in water. Moreover, the control of the nanoparticles size and morphology in organic solvents is easily attainable using surfactants.

In the case of lanthanide oxysulfide nanoparticles, we also note several benefits of organic medium for the stoichiometry:

(i) the control of the oxygen concentration that is assured by the absence of excess reactive oxygen brought by water and reactions under inert atmosphere,

(ii) the use of molecular sulfur sources with for instance the possibility of decomposing hydrophobic single-source precursors (typically, lanthanide complexes with sulfur-containing ligands) or the dissolution and activation of elemental sulfur in primary amines, as they react to form reactive alkylammonium polysulfides which release *in situ* $H_2S$ (**Scheme 4**; Thomson et al., 2011).

In both cases, the amount of reactive anions can be set to the desired value by playing on the concentration and the nature of the reactants. In water-based reactions, an excess of water in the precipitation step was followed by an excess of sulfur during the annealing step. Thus, organic medium brings the possibility to finely control the stoichiometry of the anions and one could expect that it leads to different oxysulfide compositions apart from thermodynamics considerations.

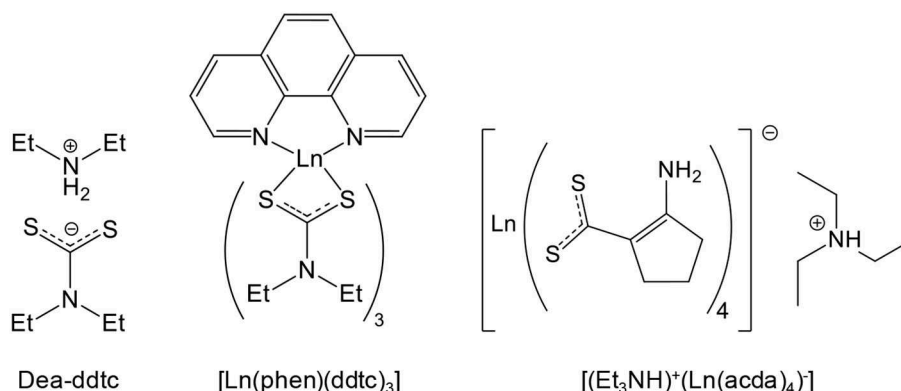### Decomposition of Sulfur-Containing Single-Source Precursors

The decomposition of lanthanide complexes bearing ligands with sulfur in the presence of dioxygen can lead to oxysulfide nanoparticles. It was shown for the first time in 2006 in a communication by Zhao et al. who developed the synthesis of thin monodisperse hexagonal nanoplates of $Eu_2O_2S$, $Sm_2O_2S$ and $Gd_2O_2S$ (Zhao et al., 2006a). In a mixture of organic solvents and surfactants typical for colloidal synthesis (1-octadecene, oleic acid and oleylamine), $[Eu(phen)(ddtc)_3]$ (phen = 1,10-phenanthroline, ddtc = diethyldithiocarbamate; **Scheme 5**) was decomposed under air at 290°C in 45 min, forming anistropic nanocrystals ($15 \times 1.7$ nm (Flahaut et al., 1958; **Figure 14**). For the first time, the observation of self-assembled oxysulfide nanoplates to nanowires is made (**Figures 14A–C**). The nanoplates are piled one above each other, because of the hydrophobic interaction between the surface surfactant chains of oleic acid (oleylamine-metal bonds are weaker than oleic acid-metal bonds; Cheon et al., 2004).

Interestingly, EuS ($Eu^{II}$) nanocrystals were obtained with the same synthesis but under inert atmosphere with oleylamine alone (which played the role of reducing agent; Zhao et al., 2006b). A more detailed study on the pyrolysis of the $[Ln(phen)(ddtc)_3]$ precursor and the nanoparticles properties was also reported. A noticeable work using the same strategy was conducted by Tan et al. (2016). In comparison with europium, the decomposition of $[La(phen)(ddtc)_3]$ and $[Pr(phen)(ddtc)_3]$ only yielded LaS and PrS. From oxidation of the sulfides, oxysulfates nanoparticles of $La_2O_2SO_4$ and $Pr_2O_2SO_4$ were obtained. The nanoparticles of $Eu_2O_2S$, $La_2O_2SO_4$, and $Pr_2O_2SO_4$ were then tested for the water-gas-shift reaction.

Lin et al. (2016) obtained europium- and terbium-doped $Gd_2O_2S$ and europium-doped $Tb_2O_2S$ by decomposition of the same precursor. Although the morphology of the nanoparticles was not perfectly regular, and the crystallinity not optimal, an extensive luminescence study was performed and biologic tests (*in vivo* imaging, cell viability) were conducted. The latter required a coating with 3-aminopropyltriethoxysilane (**Figure 10**) and grafting of methoxy-polyethyleneglycol and Alexa Fluor 660 (photostable red dye which emits photons in the wavelength range of 630-650 nm).

In 2012, He et al. (2009) described a similar decomposition of a precursor formed *in situ*. The reaction yielded europium oxysulfide nanorods. In this synthesis, europium oleate, oleylamine, 1,10-phenanthroline, and dodecanethiol were heated at 320°C under inert atmosphere before hot injection of diethylammonium diethyldithiocarbamate (dea-ddtc, **Scheme 5**) dissolved in oleylamine. Nanorods were isolated after 1 h of reaction. The oxygen source was not explicitly discussed, but it was likely the oleate ions in the europium-oleate complex. Even if dea-ddtc is the most probable sulfur source, the introduction of dodecanethiol was not discussed. Nevertheless, this report showed that forming the single-source precursor *in situ* was a viable strategy. The non-stoichiometric character of the $Eu_{2+x}O_2S$ nanoparticles was evidenced by the Eu/S ratio measured by EDS. Non-stoichiometry is attributed to $Eu^{II}$ in the solid and was already observed for the bulk phase in the 1960's by Ballestracci and Quezel who estimated that 1% of the europium atoms were divalent thanks to neutron diffraction and magnetic measurements (Ballestracci et al., 1968; Quezel et al., 1970). He et al. (2009) also described magnetic properties of europium oxysulfide nanoparticles and confirm the $Eu^{II}/Eu^{III}$ ratio, even if the average composition $Eu_{2.11}O_2S$ corresponds to about 15% of $Eu^{II}$. Moreover, an electrophoretic deposition of the nanorods was proposed.

Ghosh et al. reported another precursor to obtain Eu$_2$O$_2$S nanoparticles (Ghosh et al., 2016). According to the authors, La$_2$O$_2$S and Nd$_2$O$_2$S can also be prepared with a similar procedure. Synthesized from europium nitrate, triethylamine (Et$_3$N) and 2-aminocyclopentene-1-dithiocarboxylic acid (Hacda), [(Et$_3$NH)$^+$(Eu(acda)$_4$)$^-$] was decomposed via three different methods (**Scheme 6**).
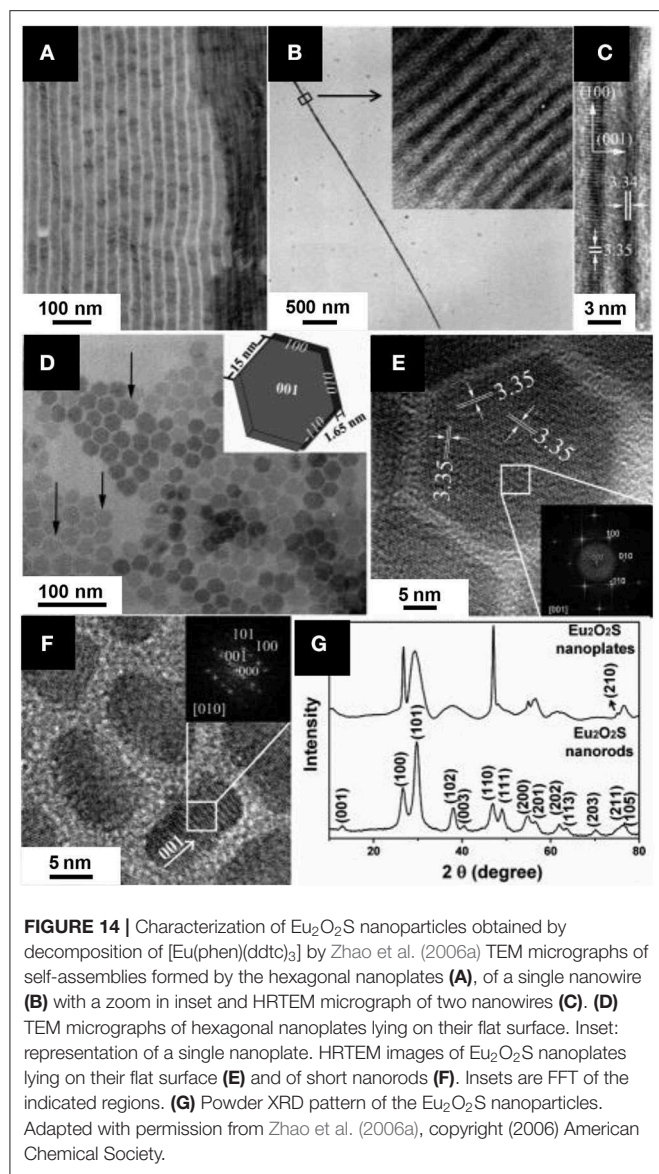
By heating the precursor in an OM/OA/ODE mixture, ultrathin nanoplates of Eu$_2$O$_2$S were obtained. However, the 0.3 nm reported thickness is quite surprising, as it would represent a single monolayer of the solid, and there is no correlated peak extinction in the corresponding XRD pattern. Using similar conditions with OM only led to rod-like nanoparticles (7 × 3 nm$^2$). Finally, hot injection of [(Et$_3$NH)$^+$(Eu(acda)$_4$)$^-$] and trioctylphosphine (TOP) led to polydisperse nanospheres with an average diameter of 13 nm. The catalytic activity of Eu$_2$O$_2$S, and especially its activity as a peroxidase mimic, was deeply investigated. Because Eu$_2$O$_2$S catalyzed the oxidation of 3,3′,5,5′-tetramethylbenzidine (TMB) in presence of H$_2$O$_2$ and neither La$_2$O$_2$S nor Nd$_2$O$_2$S succeeded in it, the authors concluded to a mechanism involving the Eu$^{III}$/Eu$^{II}$ redox couple.

## Syntheses With High Boiling-Point Organic Solvents at Atmospheric Pressure

Also colloidal synthesis in organic solvents have been used for years in the synthesis of metal and metal oxide nanoparticles, the first report for metal oxysulfides was published by Ding et al. (2011). Lanthanide acetylacetonate Ln(acac)$_3$ (1 equiv.), elemental sulfur (1 equiv.), and sodium acetylacetonate (1 equiv.) were added in an OM/OA/ODE mixture and heated for 45 min. at 310°C under inert atmosphere after degassing under vacuum at 120°C (**Figure 15**). Size-monodisperse hexagonal nanoplates of Ln$_2$O$_2$S were obtained. They were thin (a few monolayers) and 5–40 nm wide depending on the lanthanide. The composition of the powder showed a lack of sulfur (Na$_{0.4}$La$_{1.6}$O$_2$S$_{0.6}$), which was attributed to terminal [Ln$_2$O$_2$]$^{2+}$ layers. The crucial advantage of this method is its high versatility: La$_2$O$_2$S, Pr$_2$O$_2$S, Nd$_2$O$_2$S, Sm$_2$O$_2$S, Eu$_2$O$_2$S, Gd$_2$O$_2$S, Tb$_2$O$_2$S

were prepared. The sodium ions, added in stoichiometric amounts, were proposed to help the crystallization and favor the oxysulfide formation. The hypothesis of the authors is that the close ionic radii of sodium [$r$(Na$^I$(VII)) = 1.26 Å] and larger lanthanide ions [$r$(La$^{III}$(VII)) = 1.24 Å to $r$(Tb$^{III}$(VII)) = 1.12 Å] enables cation exchanges in the solid and favors the oxysulfide crystallization. Lithium ions were tested and were efficient for Y$_2$O$_2$S synthesis. In 2013, a more complete study (experimental study and calculations based on density functional theory) on the alkaline additives on the formation and morphology of the obtained nanocrystals also showed the possible use of potassium to synthesize oxysulfide nanoparticles (La$_2$O$_2$S, Eu$_2$O$_2$S, Gd$_2$O$_2$S, and Yb$_2$O$_2$S; Zhang et al., 2013). The hypothesis of alkali insertion in the crystal structure was recently disputed: the alkali would serve as a stabilizing species for the formation of a lamellar alkali-oleate phase (as observed with sodium) rather than as a doping ion in the Ln$_2$O$_2$S structure (Larquet et al., 2020). In 2017, Lei et al. investigated the roles of yttrium and sodium in the formation and growth of Gd$_2$O$_2$S, by using them separately or combined. They also demonstrated that a large excess of sulfur allows forming gadolinium oxysulfide nanoplates without adding sodium ions (Lei et al., 2017).

In 2017, Tan and Li announced the formation iron/sodium co-doped lanthanum oxysulfide nanoparticles (Na, La)$_2$O$_2$S:Fe (Tan and Li, 2017). Such doping with light transition metal is very rare due to ionic radii mismatch. Thus, according to the authors, only a limited amount of iron would have been able to substitute lanthanum, and surprisingly, no contraction of the lattice was observed despite the ionic radii difference [$r$(La$^{III}$(VII)) = 1.24 Å; $r$(Fe$^{III}$(VII)) ≈ 0.85 Å]. Even though such iron doping would be very interesting for catalytic features, it is quite unclear that iron was well-inserted in the La$_2$O$_2$S phase. In 2015, Jiang et al. employed Ding's synthesis and demonstrated the possible use of La$_2$O$_2$S:Eu nanoparticles as optical temperature sensors ("nanothermometer") (Jiang et al., 2015). Our group recently investigated the reactivity of Ln$_2$O$_2$S hexagonal nanoplates formed with a stoichiometric amount of sulfur and demonstrated different oxidation processes in

**FIGURE 14 |** Characterization of $Eu_2O_2S$ nanoparticles obtained by decomposition of $[Eu(phen)(ddtc)_3]$ by Zhao et al. (2006a) TEM micrographs of self-assemblies formed by the hexagonal nanoplates **(A)**, of a single nanowire **(B)** with a zoom in inset and HRTEM micrograph of two nanowires **(C)**. **(D)** TEM micrographs of hexagonal nanoplates lying on their flat surface. Inset: representation of a single nanoplate. HRTEM images of $Eu_2O_2S$ nanoplates lying on their flat surface **(E)** and of short nanorods **(F)**. Insets are FFT of the indicated regions. **(G)** Powder XRD pattern of the $Eu_2O_2S$ nanoparticles. Adapted with permission from Zhao et al. (2006a), copyright (2006) American Chemical Society.

bimetallic $Gd_{2(1-y)}Ce_{2y}O_2S$ nanoparticles. It enabled us to prove that highly unstable $Ce_2O_2S$ nanoparticles can also be formed with the help of sodium ions, as long as it is isolated and stored under strict inert conditions (Larquet et al., 2017). The thermal stability of the nanoparticles was investigated under inert and oxidizing atmosphere, highlighting the possibility to remove the oleate surface ligands by a mild thermal treatment (Larquet et al., 2019a). Moreover, both magnetic properties (Larquet et al., 2019b) and optical ones (bandgap) (Larquet et al., 2019c) could be tuned as a function of the Gd:Ce ratio.

Gu et al. managed to obtain yttrium, gadolinium, erbium, and ytterbium oxysulfide nanoplates using oleylamine as only solvent and $H_2S$ as sulfurating agent. $Ln(acac)_3$ and oleylamine were degassed at 120°C and then heated at 280°C for 1 h under a $H_2S/N_2$ flow (20/80 $v/v$, 60 mL/min) to yield $Ln_2O_2S$ nanoplates (Gu et al., 2013). Again, sodium ions were shown to help the crystallization of the nanoplates but were not necessary in

this case. $Y_2O_2S$, $Eu_2O_2S$, $Gd_2O_2S$, $Er_2O_2S$, and $Yb_2O_2S$ were prepared by this route.

Another method was reported in 2013 by Ma et al. (2013) to synthesize europium-doped lanthanum oxysulfide $La_2O_2S$:Eu. Lanthanide formates $La(HCOO)_3$ and $Eu(HCOO)_3$ were heated at 260°C in the presence of elemental sulfur (2 equiv. of S) in triethylenetetramine (TETA) and dodecanethiol (DT) (**Figure 16**). After 12 h, $La_2O_2S$:Eu nanocrystals were obtained with triethylenetetramine/dodecanethiol ratio being 1:2 and the nanospheres diameter was around 100 nm. Without dodecanethiol, 100 nm in width and 10 nm in thickness $La_2O_2S$:Eu nanoplates were obtained.

The amine/thiol ratio influenced the morphology. When the TETA/DT ratio was 3:1 or 1:1, micronic structures were obtained. Interestingly, other precursors $[La(NO_3)_3, LaCl_3, La_2O_3,$ and $La(OH)_3]$ were not selective enough or did not completely react [impurities of $La(OH)_3$ or $La_2O_3$ based on XRD]. Also, shorter reaction times with TETA/DT = 3:1 for the exhibited the rare $La_{10}OS_{14}$ intermediary phase with LaOOH and $La_2(SO_4)_3$. Although the crystals are large and the selectivity can be improved, it is to the best of our knowledge the only occurrence of a promising protocol for nanoscaled $Ln_{10}OS_{14}$.

## Solvothermal Syntheses in Autoclave

In 2000, Li et al. tested a direct and simple solvothermal sulfidation process for numerous lanthanide oxides. $Ln_xO_y$ powders (Ln = Y, Sc, La, Pr, Nd, Eu, Sm, Gd, Ho, Er, Yb, or Lu) and $S_8$ were suspended in ethylenediamine and heated in autoclave at 150°C for 8 h (Li et al., 2000). Aggregated and irregularly-shaped crystalline spherical nanoparticles of $Pr_2O_2S$, $Eu_2O_2S$, and $Gd_2O_2S$ were obtained with this method (<50 nm). The authors suggested an anion-exchange mechanism between the $O^{-II}$ in the $Ln_xO_y$ crystal and the $S^{-II}$ available in polyanions when $S_8$ reacts with TETA. They supposed next that oxysulfide nuclei could leave the surface of the oxide to grow apart.

For Ln = La, Nd, Sm, Ho, and Er, the conversion was incomplete ($Ln_2O_2S$ and $Ln_xO_y$ on the XRD pattern) and no change was observed with longer reaction times. Only the starting oxide was observed for Ln = Y, Sc, Yb, and Lu. In 2012, $Gd_2O_2S$:Eu and $Gd_2O_2S$:Er, Yb nanoplates were also obtained by Liu et al. in ethylenediamine using gadolinium nitrate and elemental sulfur (Liu et al., 2012). PVP (K29-32) or OM was added to a solution of the lanthanide nitrate in ethanol. The resulting solution was added dropwise into ethylenediamine and sulfur. The autoclave was heated at 220°C for at least 4 h to form crystalline hexagonal nanoplates. With OM, subsequent aggregation in flower-like structures was observed. Separated nanocrystals of irregular shape were obtained with PVP. $Y_2O_2S$:Eu and $Y_2O_2S$:Er, Yb were obtained from yttrium acetate by the same group with PVP and a thermal treatment at 250°C for 24 h (Liu et al., 2014a). Various self-assemblies of the nanoparticles were formed, depending on the presence of PVP, sulfur concentration, and so on.

Song et al. (2010) obtained $Gd_2O_2S$:Eu and $Gd_2O_2S$:Tb nanospheres from the solvothermal treatment of lanthanide nitrates in a mixture of ethanol and ethylene glycol, containing polyvinylpyrrolidone (PVP K30, M = 40,000 g/mol) and thiourea. The autoclave was heated at 200°C for 24 h and the
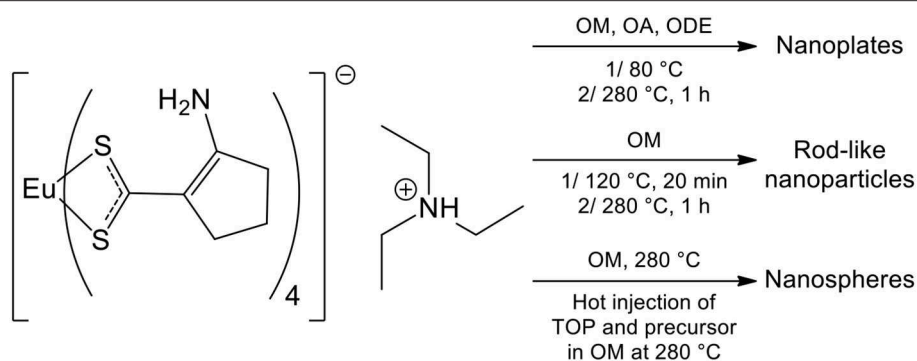
isolated solid was then sulfidized in a N$_2$/S atmosphere at 600-800°C to form doped gadolinium oxysulfide nanoparticles. PVP is believed to be responsible for the spherical morphology, and polymer residues were evidenced on the rough surface of the nanoparticles. They presented a good crystallinity and a good monodispersity in diameter. Their size was tunable between 150 nm and 1.25 μm by varying the PVP content and the ethanol/ethylene glycol ratio. A similar strategy was used by Deng et al. to yield Y$_2$O$_2$S:Sm hollow nanospheres (Ø = 140-200 nm; Deng et al., 2012a). The thermal treatment was based on Li's work (Y$_2$O$_2$S nanoparticles hydrothermal synthesis, **Table 4**, entry 4; Li et al., 2009). The authors first proposed a mechanism involving H$_2$S/CO$_2$ bubbles to explain the holes, but finally declared in a second paper on Y$_2$O$_2$S:Eu, Mg, Ti nanoparticles that NH$_3$/CO$_2$ bubbles were more likely the templating agents (Deng et al., 2012b). Similarly to Song's spheres, the surface was rough and the nanoparticles seemed to be constituted with smaller units.

Thirumalai et al. (2011b) have mainly focused their work on water-based syntheses, but also prepared various morphologies of Gd$_2$O$_2$S:Eu nanoparticles in oleylamine. GdCl$_3$·6H$_2$O and EuCl$_3$·6H$_2$O were introduced in hot oleylamine and various amounts of thioacetamide were added. The resulting solution was heated in an autoclave at 120-240°C for 12-24 h. Flower-like nanocrystals (≈10 nm), nanospheres (Ø = 5-10 nm) and nanorods of various lengths (Ø = 6 nm) were obtained depending on the reaction conditions and the thioacetamide amount. An excess of sulfur was proposed to be mandatory to ensure a high chemical potential, which promoted the formation of nanorods. Despite the good morphology control, the XRD patterns of the nanoparticles showed a poor crystallinity of the materials: only broad peaks were observed. It is intriguing because nanorods presented big crystal domains, and HRTEM images showed large and regular lattices.

## TRANSITION METAL OXYSULFIDES NANOPARTICLES

Transition metal bulk oxysulfides are quite rare. Zinc, titanium, molybdenum, and tungsten oxysulfide were nevertheless obtained. Most of the time, they were obtained under the form of amorphous thin films or particles.

Because of the electronegativity and atomic number differences between the two anions, transition metals will preferentially bind to one of them (in the hard and soft acids and bases theory, oxygen is a hard base and sulfur a soft base). Also, keeping reduced sulfur *id est* avoiding sulfates or other oxidized sulfur species is highly difficult because of their good thermodynamic stability.
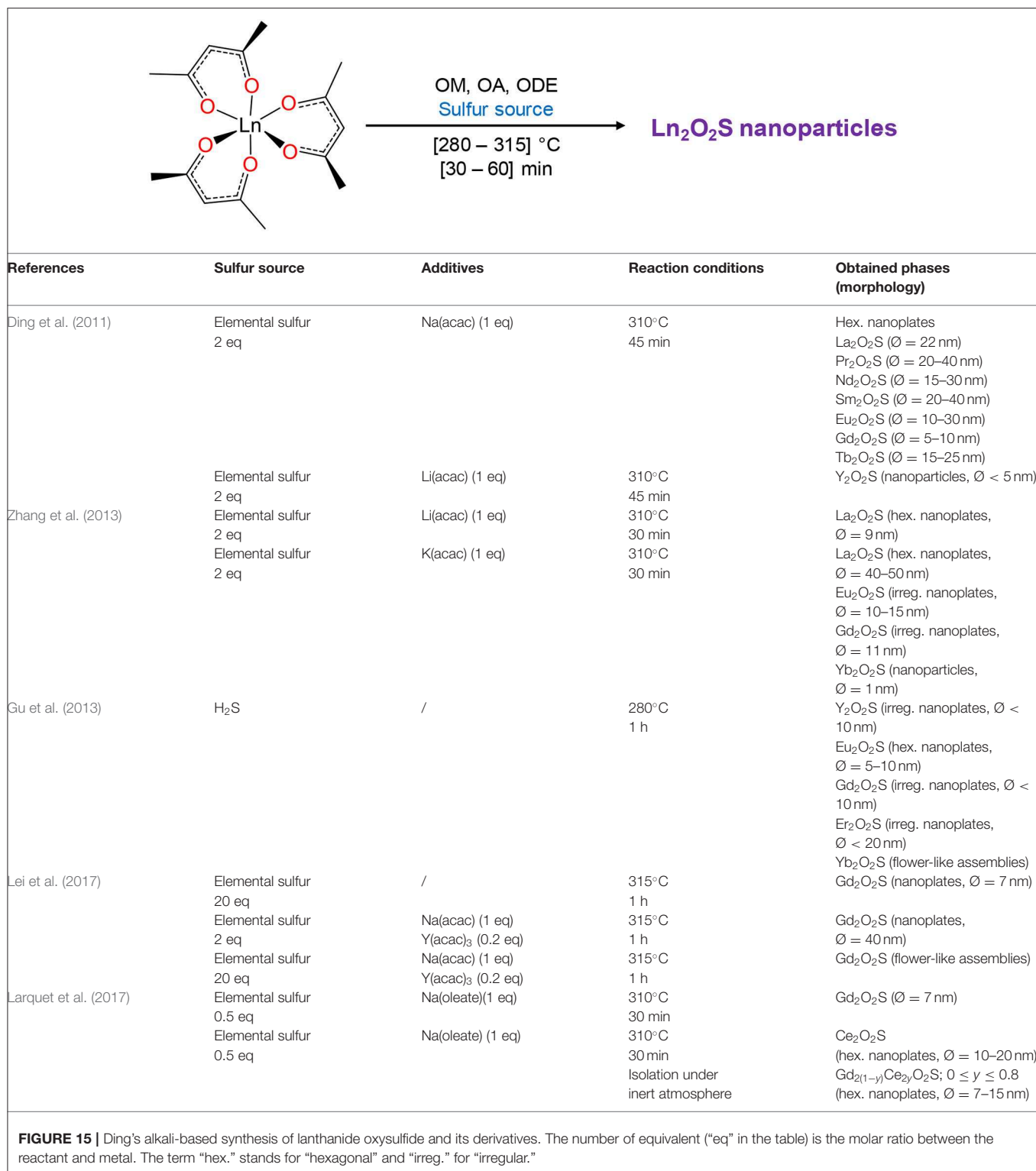
## Challenging Synthesis, Tricky Characterization

In the previous section, we detailed numerous syntheses of Ln$_2$O$_2$S nanoparticles. It is an exception in the oxysulfide family, as it remains to the best of our knowledge the only structure for which monophasic crystalline nanoparticles could be formed. Today, a vast and promising land of metal oxysulfide nanoparticles, especially involving transition metals, must be explored. With such nanoparticles with transitions metals and chalcogens, new applications could emerge, such as heterogeneous catalysis, photocatalysis, battery materials, superconduction, and so on.

Several advantages are intrinsically brought by soft reaction conditions (compared with typical synthesis of bulk crystals) and the nanoscale. Mild temperatures and small grain size can unlock metastable structures. Also, diffusion processes are much faster over nanometric distances and lead to efficient substitution reactions with nanoscaled materials. It opens new synthetic strategies to transform preformed oxide, sulfide, or metal nanoparticles in oxysulfide nanoparticles.

However, synthesizing transition metal ternary oxysulfides is particularly challenging. The ionic radius difference between O$^{-II}$ (1.26 Å) and S$^{-II}$ (1.70 Å) associated with the variable affinities with the metal make the substitution reactions highly difficult. Energy input by heating is especially not recommended for nanoparticles synthesis because of excessive growth and sintering.

Despite these difficulties, transition metal oxysulfide nanoparticles were already prepared. A few examples will be detailed in the next section. The main issue consists of identifying

| References | Sulfur source | Additives | Reaction conditions | Obtained phases (morphology) |
| --- | --- | --- | --- | --- |
| Ding et al. (2011) | Elemental sulfur 2 eq | Na(acac) (1 eq) | 310°C 45 min | Hex. nanoplates La$_2$O$_2$S (Ø = 22 nm) Pr$_2$O$_2$S (Ø = 20–40 nm) Nd$_2$O$_2$S (Ø = 15–30 nm) Sm$_2$O$_2$S (Ø = 20–40 nm) Eu$_2$O$_2$S (Ø = 10–30 nm) Gd$_2$O$_2$S (Ø = 5–10 nm) Tb$_2$O$_2$S (Ø = 15–25 nm) |
| | Elemental sulfur 2 eq | Li(acac) (1 eq) | 310°C 45 min | Y$_2$O$_2$S (nanoparticles, Ø < 5 nm) |
| Zhang et al. (2013) | Elemental sulfur 2 eq | Li(acac) (1 eq) | 310°C 30 min | La$_2$O$_2$S (hex. nanoplates, Ø = 9 nm) |
| | Elemental sulfur 2 eq | K(acac) (1 eq) | 310°C 30 min | La$_2$O$_2$S (hex. nanoplates, Ø = 40–50 nm) Eu$_2$O$_2$S (irreg. nanoplates, Ø = 10–15 nm) Gd$_2$O$_2$S (irreg. nanoplates, Ø = 11 nm) Yb$_2$O$_2$S (nanoparticles, Ø = 1 nm) |
| Gu et al. (2013) | H$_2$S | / | 280°C 1 h | Y$_2$O$_2$S (irreg. nanoplates, Ø < 10 nm) Eu$_2$O$_2$S (hex. nanoplates, Ø = 5–10 nm) Gd$_2$O$_2$S (irreg. nanoplates, Ø < 10 nm) Er$_2$O$_2$S (irreg. nanoplates, Ø < 20 nm) Yb$_2$O$_2$S (flower-like assemblies) |
| Lei et al. (2017) | Elemental sulfur 20 eq | / | 315°C 1 h | Gd$_2$O$_2$S (nanoplates, Ø = 7 nm) |
| | Elemental sulfur 2 eq | Na(acac) (1 eq) Y(acac)$_3$ (0.2 eq) | 315°C 1 h | Gd$_2$O$_2$S (nanoplates, Ø = 40 nm) |
| | Elemental sulfur 20 eq | Na(acac) (1 eq) Y(acac)$_3$ (0.2 eq) | 315°C 1 h | Gd$_2$O$_2$S (flower-like assemblies) |
| Larquet et al. (2017) | Elemental sulfur 0.5 eq | Na(oleate) (1 eq) | 310°C 30 min | Gd$_2$O$_2$S (Ø = 7 nm) |
| | Elemental sulfur 0.5 eq | Na(oleate) (1 eq) | 310°C 30 min Isolation under inert atmosphere | Ce$_2$O$_2$S (hex. nanoplates, Ø = 10–20 nm) Gd$_{2(1−y)}$Ce$_{2y}$O$_2$S; 0 ≤ y ≤ 0.8 (hex. nanoplates, Ø = 7–15 nm) |

**FIGURE 15 |** Ding's alkali-based synthesis of lanthanide oxysulfide and its derivatives. The number of equivalent ("eq" in the table) is the molar ratio between the reactant and metal. The term "hex." stands for "hexagonal" and "irreg." for "irregular."

and evidencing the oxysulfide nature of the compound. Because excessive heating tends to stabilize sulfate or separate oxides and sulfides rather than crystallize an oxysulfide structure, the reported structures are mainly amorphous.

Identification and characterization of such phases is much harder than crystalline nanoparticles. In particular, inductively coupled plasma atomic emission spectroscopy (ICP-AES), X-ray fluorescence (XRF), and energy dispersive X-ray spectroscopy

FIGURE 16 | Reaction of Ma et al. (2013) to yield $La_2O_2S$ nanoparticles.



FIGURE 17 | Adapted from Nelson et al. (2016) **(A)** Synthetic strategy of $CoO_xS_y$ hollow nanoparticles. TEM micrographs of $CoO_xS_y$ nanoparticles with $y = 0$ **(B)**; 0.18 **(C)**; 1.03 **(D)**; 1.27 **(E)**. **(F)** Rotationally averaged SAED patterns of the various $CoO_xS_y$ nanoparticles. Reference lines in green indicate CoO Bragg peaks (JCPDS 00-048-1719). Adapted from Nelson et al. (2016) with permission of the Royal Chemical Society.

(EDS) are suitable techniques to evidence the presence of sulfur, but the determination of the nanoparticles' precise oxygen content remains a challenge. High resolution transmission electron microscopy and energy filtered transmission electron microscopy (EFTEM) constitute an elegant solution, but requires well-dispersed nanoparticles and will not provide accurate quantitative data. Moreover, it is hard to conclude about the precise localization of the atoms: are they in the whole particle or only at the surface (because of ligands for instance)?

The identification of the nature of the chemical bonds and oxidation states inside the material is a supplementary issue, yet this is required to differentiate oxysulfides from sulfates. It becomes highly problematic when the composition of a solid is unclear. Infrared and Raman spectroscopies are particularly appropriate for amorphous oxysulfide identification because M-O and M-S bonds generally present very distinguishable signatures. However, only qualitative analysis is possible. X-Ray photoemission spectroscopy (XPS) brings some clues but investigates only the very surface. X-ray absorption spectroscopy, such as XANES or EXAFS (at O K-edge, S K-edge, M K, L, or M-edge) is able to characterize the whole sample and gives precious information on the oxidation states and chemical bonds. However, surface and core cannot be distinguished and only average information is obtained, so that one should be very careful about hypothesis and interpretations. Furthermore, it must be noticed that the required energies for the different edges involves the use of different X-ray ranges (soft for oxygen, tender for sulfur, hard for the metal K-edge) and consequently the use of distinct beamlines. The analysis of the pair distribution function of the diffuse background of X-ray diffraction patterns (PDF) is expected to bring solutions as it can be applied to the analysis of amorphous compounds. Still, it remains a poorly studied technique in the field of nanoparticles analysis.
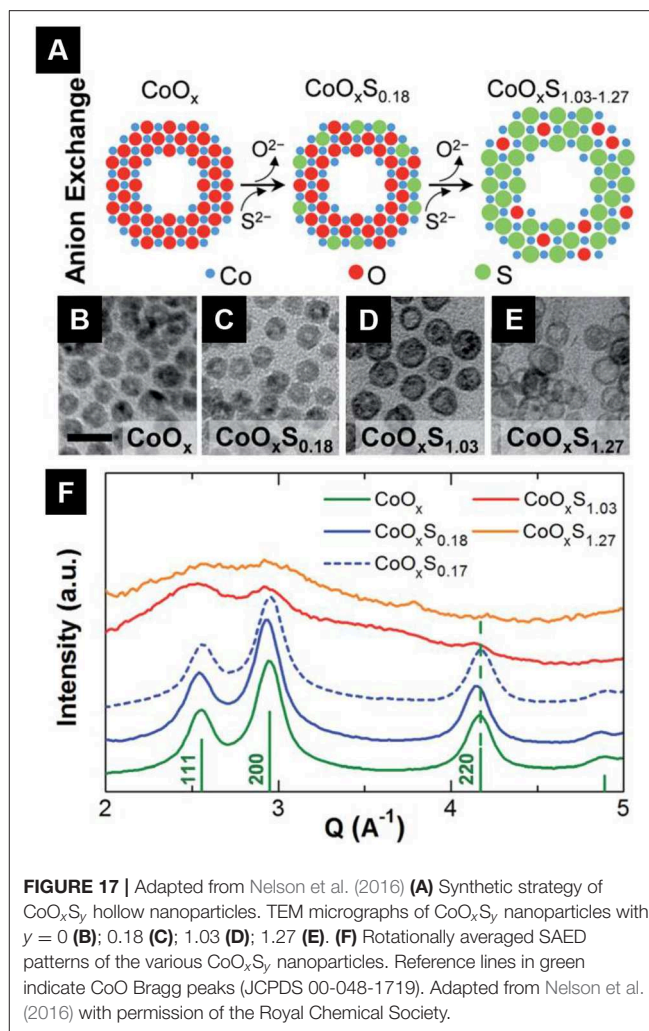
Finally, we emphasized the fact that oxysulfide nanoparticles can be metastable or unstable phases. It reinforces the difficulty to store, transfer, manipulate, and characterize them (for instance in air-filled room atmosphere and devices or when heating upon irradiation by electron or X-ray beams).

## Amorphous and Crystalline Cobalt Oxysulfide

In 2016, Nelson et al. reported the formation of cobalt oxysulfide $CoO_xS_y$ hollow nanoparticles (Nelson et al., 2016). The strategy consisted in the substitution of oxygen anions by sulfur anions in cobalt oxide hollow nanoparticles, using ammonium sulfide dissolved in oleylamine at $100°C$ (**Figure 17A**). The sulfur content was adjustable via the nominal $(NH_4)_2S$ amount, with a saturation of the sulfur content at $y \approx 1.3$. With low sulfur contents ($y < 0.2$), the particles keep the crystalline structure of CoO but with higher sulfur contents, the nanoparticles became amorphous (**Figure 17F**). The hollow nanosphere morphology was preserved during the whole experiment (**Figures 17B–E**).

No direct proof of the oxidation state of sulfur is brought by the authors. Nevertheless, annealing the sulfur-rich nanoparticles

led to the formation of cobalt sulfides (possibly in a mixture with CoO). It supported the presence of reduced sulfur in the nanoparticles.

## Crystalline $ZnO_{1-x}S_x$ Nanoparticles

Crystalline zinc oxysulfide was obtained at the nanoscale. In 2009, Park et al. carried out the substitution of oxygen atoms in ZnO by sulfur using hexamethyldisilathiane (**Scheme 1**) and obtained ZnS crystalline hollow nanoparticles (**Figure 18**; Park et al., 2009). The driving force of the reaction with ZnO is the formation of very stable Si–O bonds.

During the substitution process, the authors were able to isolate ZnO@ZnS core-shell crystalline nanoparticles, which are composed by a core of ZnO and a shell of isostructural ZnS wurtzite structure.

The process was accompanied by the so-called "nanoscale Kirkendall effect," which refers to the hollowing of the nanoparticles as a consequence of unbalanced diffusion rates (Wang et al., 2013). Because $Zn^{II}$ diffuse outwards faster than $S^{-II}$ inwards, the reaction finally led to a hollow ZnS structure. HRTEM and EFTEM also showed that the final ZnS nanoparticles were obtained through the formation of heteroepitaxial ZnO@ZnS intermediates that release the high interface energy by the diffusion of the core into the shell (**Figure 19**). The composition analyses of core-shell intermediates indeed showed that oxygen is not only localized in the core of the nanoparticle, but also in the shell. It suggested that the substitution process with hexamethyldisilathiane took place in the shell region where oxygen had migrated.

The reaction resulted in the formation of crystalline $ZnO_{1-x}S_x$ located in the shell. Furthermore, the authors were able to obtain pure hollow $ZnO_{1-x}S_x$ nanoparticles by thermally annealed the core-shell intermediates. Interestingly, the diffusion processes spontaneously occurred without sulfurating reagents and led to hollow $ZnO_{1-x}S_x$ alloys.

The research on zinc oxysulfide nanoparticles has grown in the last years. Pandey et al. (2013, 2014) managed to obtain the whole composition range ($0 \leq x \leq 1$) of nanoparticles. They obtained $ZnO_{1-x}S_x$ crystalline nanoparticles by a solution combustion method. $Zn(acetate)_2$ and thiourea were incorporated in a mixture of ethanol and ethylene glycol (4:1) and then placed in a hot furnace (350°C) for 2 h. They showed that the bandgap varied with the sulfur content and that $ZnO_{1-x}S_x$ nanoparticles can photocatalyze the degradation of methyl orange. In 2017, Zhang et al. underlined the importance of doped zinc oxide to understand the intriguing ferromagnetic properties of certain $d^0$ components and used the same combustion method than Pandey (Zhang et al., 2017). As a consequence of oxidation by air, they measured a significant amount of sulfate groups at the surface of their nanoparticles using XPS. Abdullah et al. (2017) synthesized $ZnO_{1-x}S_x$ nanoparticles using zinc(II) acetate and thioacetamide for the photocatalysis of the hydrogen evolution reaction. Gultom et al. (2017) in the same group also showed that nickel-doped $ZnO_{1-x}S_x$ nanoparticles were suitable for hydrogen production.



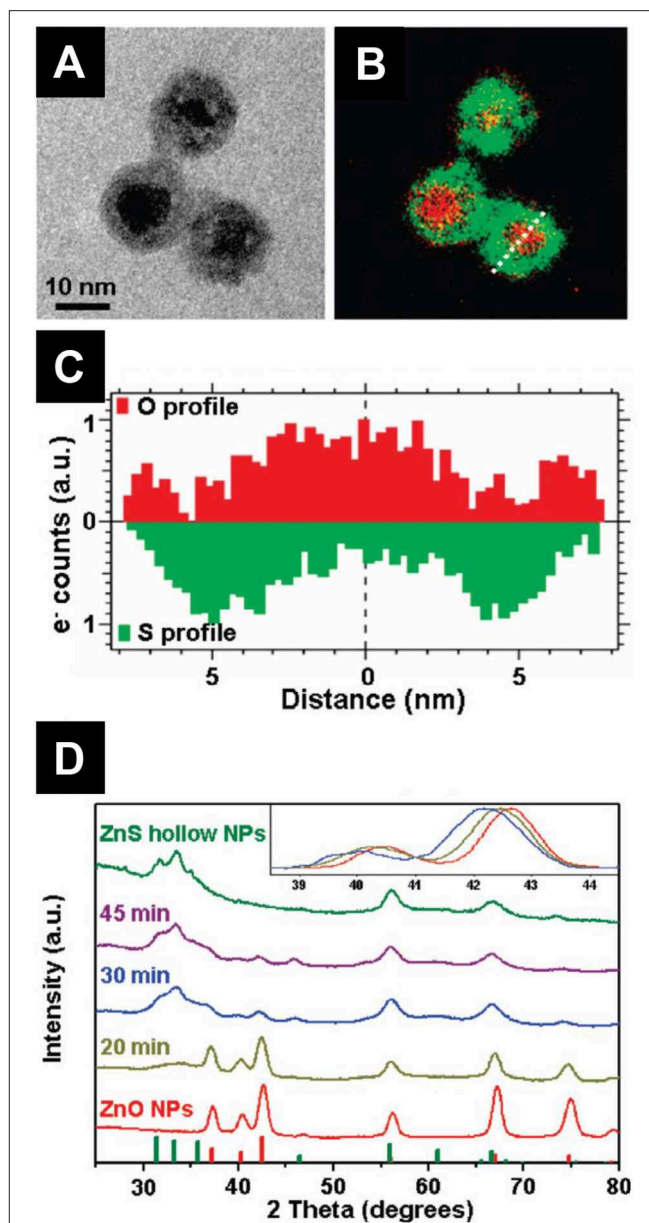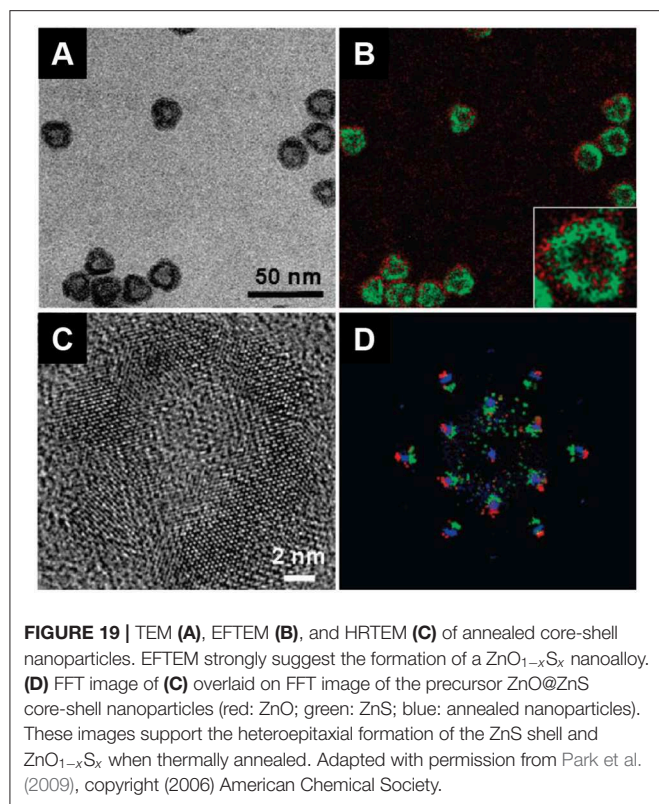FIGURE 18 | TEM **(A)** and EFTEM **(B)** images of ZnO@ZnS nanoparticles. **(C)** Oxygen and sulfur composition along the cross-section in **(B)**. **(D)** XRD patterns of the nanoparticles from ZnO to ZnS through ZnO@ZnS core-shell nanoparticles. Inset: Normalized pattern in the [38.5°; 44.5°] 2θ region. The small shifts of the diffraction peaks toward low 2θ values indicate a lattice dilatation caused by sulfur insertion. Adapted with permission from Park et al. (2009), copyright (2006) American Chemical Society.

## Other Proposed Transition Metal Oxysulfides

Crystalline nano-aggregates of cobalt nickel oxysulfides $(CoNi)O_yS_z$ were claimed by Liu (2013). However, the author noticed that sulfur only existed in oxidized species ($S^{IV}$, $S^{VI}$) in the material using XPS. By definition, it cannot be called "oxysulfide" but should rather be named "oxysulfate."

**FIGURE 19 |** TEM **(A)**, EFTEM **(B)**, and HRTEM **(C)** of annealed core-shell nanoparticles. EFTEM strongly suggest the formation of a $ZnO_{1-x}S_x$ nanoalloy. **(D)** FFT image of **(C)** overlaid on FFT image of the precursor ZnO@ZnS core-shell nanoparticles (red: ZnO; green: ZnS; blue: annealed nanoparticles). These images support the heteroepitaxial formation of the ZnS shell and $ZnO_{1-x}S_x$ when thermally annealed. Adapted with permission from Park et al. (2009), copyright (2006) American Chemical Society.

In 2017, Liu et al. reported "fullerene-like oxysulfide hollow nanospheres" (Liu et al., 2017). The name is also abusively employed in this case, as the authors demonstrated that their nanoparticles are composed of crystalline nickel sulfide mixed with amorphous nickel oxide.

## GENERAL CONCLUSION

The oxysulfide family is full of surprises. Most of its members are strictly synthetic because of size and electronegativity differences of oxygen and sulfur. It explains why these compounds were obtained as pure materials and identified relatively late in the history of Chemistry. However, since the 1950's, many compositions have been synthesized, from the simplest ternary compounds to oxysulfide materials containing five or more different atoms.

Among this family, $Ln_2O_2S$ must be pointed out. It was the first discovered phase, and represents one of the simplest oxysulfide compositions. It is nearly the only one for which the

scientific community proposed various applications especially in the domain of imaging. Consequently, it led to the development of numerous synthetic approaches for $Ln_2O_2S$ nanoparticles. Size, morphology, composition, and reactivity of $Ln_2O_2S$ nanoparticles are more and more controlled and understood. However, there is still an open door for the study of novel $Ln_2O_2S$ nanoparticles. Surprisingly, nanoscaled $Ln_2O_2S$ with heavy lanthanides remain hard to obtain. To the best of our knowledge, $Tm_2O_2S$ nanoparticles were never prepared. Also, most of the articles focus on the luminescence applications. Yet, in the domain of catalysis for instance, europium, cerium, or ytterbium redox properties have only been poorly explored in such compounds. Lastly, at this point there is no general method to control the size and shape of these nanoparticles on a broad range: only slight adjustments are proposed so far. Such control would enable understanding the influence of the nanoscale on the electric, magnetic, and optical properties. In particular, controlling the nanoparticles thickness could allow to identify the transition between a regime of indirect bandgap (as in the bulk) to the direct one.

Regarding transition metals, their integration in quaternary oxysulfides at bulk scale is successful. Recently, lanthanide-free compositions were obtained. Still, crystalline ternary oxysulfides are very rare, and the characterization of the amorphous products is still incomplete, even if molybdenum or titanium oxysulfide thin films for instance were explored in many studies. One of the challenges is to identify preparation route that lead to crystalline compounds that are easier analyzed by structural techniques. The synthesis of nanoscaled materials with accelerated diffusion processes and possible metastable phases, the developments of characterization techniques and the promising field of applications of transition metals oxysulfides should start an unprecedented area of novel oxysulfide syntheses, identifications and applications.

## AUTHOR CONTRIBUTIONS

All authors listed have made a substantial, direct and intellectual contribution to the work, and approved it for publication.

## FUNDING

## REFERENCES

Abdullah, H., Kuo, D. H., and Chen, X. (2017). High efficient noble metal free Zn(O,S) nanoparticles for hydrogen evolution. *Int. J. Hydrogen Energy* 42, 5638–5648. doi: 10.1016/j.ijhydene.2016.11.137

Abraham, K. M., and Pasquariello, D. M. (1993). Synthesis, characterization, and lithium battery applications of molybdenum oxysulfides. *Chem. Mater.* 5, 1233–1241. doi: 10.1021/cm00033a009

Abraham, K. M., Pasquariello, D. M., and Willstaedt, E. B. (1989). Lithium/molybdenum oxysulfide secondary batteries. *J. Electrochem. Soc.* 136:576. doi: 10.1149/1.2096686

Afanasiev, P., and Bezverkhy, I. (2003). Genesis of vesicle-like and tubular morphologies in inorganic precipitates: amorphous Mo

oxysulfides. *J. Phys. Chem. B* 107, 2678–2683. doi: 10.1021/jp02 1655k

Ai, P. F., Li, W. Y., Xiao, L. Y., Li, Y. D., Wang, H. J., and Liu, Y. L. (2010a). Monodisperse nanospheres of yttrium oxysulfide: synthesis, characterization, and luminescent properties. *Ceram. Int.* 36, 2169–2174. doi: 10.1016/j.ceramint.2010.05.025

Ai, P. F., Liu, Y. L., Li, W. Y., and Xiao, L. Y. (2010c). Synthesis and luminescent characterization of $Y_2O_2S$: $Eu^{3+}$, $Mg^{2+}$, $Ti^{4+}$ nanotubes. *Phys. B Condens. Matter* 405, 3360–3364. doi: 10.1016/j.physb.2010.05.005

Ai, P. F., Liu, Y. L., Xiao, L. Y., Wang, H. J., and Meng, J. X. (2010b). Synthesis of $Y_2O_2S$:$Eu^{3+}$, $Mg^{2+}$, $Ti^{4+}$ hollow microspheres via homogeneous precipitation route. *Sci. Technol. Adv. Mater.* 11:035002. doi: 10.1088/1468-6996/11/3/035002

Ajithkumar, G., Yoo, B., Goral, D. E., Hornsby, P. J., Lin, A.-L., Ladiwala, U., et al. (2013). Multimodal bioimaging using a rare earth doped $Gd_2O_2S$:Yb/Er phosphor with upconversion luminescence and magnetic resonance properties. *J. Mater. Chem. B* 1, 1561–1572. doi: 10.1039/c3tb00551h

Aliev, O. M., and Tanryverdiev, V. S. (1997). The synthesis and some physical properties of rare-earth oxysulfostibnites. *Zhurnal Neorg. Khimii* 42, 1918–1921.

Altmannshofer, S., and Johrendt, D. (2008). Synthesis, crystal structure and magnetism of the new oxysulfide $Ce_3NbO_4S_3$. *Zeitschrift für Anorg. Allg. Chem.* 634, 1361–1364. doi: 10.1002/zaac.200800078

Alves, R. V., Buchanan, R. A., Wickersheim, K. A., and Yates, E. A. C. (1971). Neodymium-activated lanthanum oxysulfide: a new high-gain laser material. *J. Appl. Phys.* 42, 3043–3048. doi: 10.1063/1.1660681

Auzel, F. (2004). Upconversion and anti-stokes processes with f and d ions in solids. *Chem. Rev.* 104, 139–174. doi: 10.1021/cr020357g

Bagheri, A., Rezaee Ebrahim Saraee, K., Shakur, H. R., and Zamani Zeinali, H. (2016). Synthesis and characterization of physical properties of $Gd_2O_2S$:$Pr^{3+}$ semi-nanoflower phosphor. *Appl. Phys. A Mater. Sci. Process.* 122:553. doi: 10.1007/s00339-016-0058-z

Bakhtiari, H., Ghasemi, M. R., Hashemizadeh Aghda, A., Noorkojouri, H., Sarabadani, P., and Zeeb, M. (2015). Effect of europium dopant concentration on particle size and luminescence of yttrium oxysulfide nanoparticles prepared by urea homogenous precipitation. *J. Clust. Sci.* 26, 1671–1681. doi: 10.1007/s10876-015-0866-x

Bakke, J. R., Tanskanen, J. T., Hägglund, C., Pakkanen, T. A., and Bent, S. F. (2012). Growth characteristics, material properties, and optical properties of zinc oxysulfide films deposited by atomic layer deposition. *J. Vac. Sci. Technol.* 30:01A135. doi: 10.1116/1.3664758

Ballestracci, R. (1967). Structure cristalline des oxydisulfures de terres rares $Ln_2O_2S_2$. *Mater. Res. Bull.* 2, 473–479. doi: 10.1016/0025-5408(67)90068-2

Ballestracci, R., Bertaut, E. F., and Quezel, G. (1968). Etude par diffraction neutronique et mesures magnetiques des oxysulfures de terres rares $T_2O_2S$. *J. Phys. Chem. Solids* 29, 1001–1014. doi: 10.1016/0022-3697(68)90236-9

BaQais, A., Curutchet, A., Ziani, A., Ait Ahsaine, H., Sautet, P., Takanabe, K., et al. (2017). Bismuth silver oxysulfide for photoconversion applications: structural and optoelectronic properties. *Chem. Mater.* 29, 8679–8689. doi: 10.1021/acs.chemmater.7b02664

Baybarz, R. D., Fahey, J. A., and Haire, R. G. (1974). The preparation, crystal structures and some properties of californium oxysulfate and oxysulfide. *J. Inorg. Nucl. Chem.* 36, 2023–2027. doi: 10.1016/0022-1902(74)80716-5

Besançon, P. (1973). teneur en oxygene et formule exacte d'une famille de composes habituellement appeles "Variété β" Ou "Phase Complexe" des sulfures de terres rares. *J. Solid State Chem.* 7, 232–240. doi: 10.1016/0022-4596(73)90159-X

Besançon, P., Carré, D., Guittard, M., and Flahaut, J. (1970). Sur une famille de composes usuellement appeles "Variété Beta Des Sulfures de Terres Rares." *Comptes Rendus Hebd. l'Acad. Sci.* 271, 679–682.

Besançon, P., Carré, D., and Laruelle, P. (1973). Mécanisme de la solution solide des oxysulfures de terres rares l10s15–xox. *Acta Crystallogr. Sect. B Struct. Crystallogr. Cryst. Chem.* 29, 1064–1066. doi: 10.1107/S0567740873 003869

Biltz, W. (1908). Über die sulfide der seltenen erden. 1. mitteilung: über cersulfide und ihre existenzgebiete. *Berichte der Dtsch. Chem. Gesellschaft* 41, 3341–3350. doi: 10.1002/cber.19080410310

Biondo, V., Sarvezuk, P. W. C., Ivashita, F. F., Silva, K. L., Paesano, A., and Isnard, O. (2014). Geometric magnetic frustration in $RE_2O_2S$ oxysulfides (RE=Sm, Eu and Gd). *Mater. Res. Bull.* 54, 41–47. doi: 10.1016/j.materresbull.2014. 03.008

Blandy, J. N., Abakumov, A. M., Christensen, K. E., Hadermann, J., Adamson, P., Cassidy, S. J., et al. (2015). Soft chemical control of the crystal and magnetic structure of a layered mixed valent manganite oxide sulfide. *APL Mater.* 3:041520. doi: 10.1063/1.4918973

Boller, H. (1973). Die Kristallstruktur von $Bi_2O_2Se$. *Monatshefte Chem.* 104, 916–919. doi: 10.1007/BF00903904

Boyer, C., Deudon, C., and Meerschaut, A. (1999). Synthesis and structure determination of the new $Sm_2Ti_2O_5S_0$ compound. *Comptes Rendus l'Académie des Sci. IIC* 2, 93–99. doi: 10.1016/S1387-1609(99)80007-3

Boyer-Candalen, C., Deudon, C., and Meerschaut, A. (2000a). Synthesis and structure determination of $Nd_{16}Ti_5S_{17}O_{17}$. *J. Solid State Chem.* 152, 554–559. doi: 10.1006/jssc.2000.8730

Boyer-Candalen, C., and Meerschaut, A. (2000). Synthesis and structure determination of the new compound La∼$_{10.8}Nb_5O_2OS_{10}$. *J. Solid State Chem.* 152, 348–352. doi: 10.1006/jssc.2000.8662

Boyer-Candalen, C., Meerschaut, A., and Palvadeau, P. (2000b). Crystal structure determination of the new compound $Sm_3NbO_4S_3$. *Mater. Res. Bull.* 35, 1593–1601. doi: 10.1016/S0025-5408(00)00371-8

Brennan, T. D., and Ibers, J. A. (1992). Metal-metal bonding and mixed-valent tantalum in $La_2Ta_3S_2O_8$. *J. Solid State Chem.* 98, 82–89. doi: 10.1016/0022-4596(92)90072-4

Brixner, L. H. (1987). New X-ray phosphors. *Mater. Chem. Phys.* 16, 253–281. doi: 10.1016/0254-0584(87)90102-7

Broadley, S., Gál, Z. A., Corà, F., Smura, C. F., and Clarke, S. J. (2005). Vertex-linked $ZnO_2S_2$ tetrahedra in the oxysulfide BaZnOS: a new coordination environment for zinc in a condensed solid. *Inorg. Chem.* 44, 9092–9096. doi: 10.1021/ic051240o

Buck, V. (1991). Lattice parameters of sputtered MoS2 films. *Thin Solid Films* 198, 157–167. doi: 10.1016/0040-6090(91)90334-T

Bulte, J. W. M., and Kraitchman, D. L. (2004). Iron oxide MR contrast agents for molecular and cellular imaging. *NMR Biomed.* 17, 484–499. doi: 10.1002/nbm.924

Carcaly, C., Flahaut, J., Guittard, M., and Palazzi, M. (1981). Un Composé à Structure Feuilletée $(LaO)_4Ag1,5Ga1,5S5$. *Mater. Res. Bull.* 16, 1367–1374. doi: 10.1016/0025-5408(81)90055-6

Cario, L., Deudon, C., Meerschaut, A., and Rouxel, J. (1998). Synthesis and structure determination of $La_8Ti_{10}S_{24}O_4$. *J. Solid State Chem.* 136, 46–50. doi: 10.1006/jssc.1997.7649

Cario, L., Kabbour, H., Guillot-Deudon, C., and Meerschaut, A. (2003). A mixed-valent niobium oxysulfide, $La_2Nb_3S_2O_8$. *Acta Crystallogr. Sect. C Cryst. Struct. Commun.* 59, i55–i56. doi: 10.1107/S01082701030 09570

Cario, L., Popa, A. F., Lafond, A., Guillot-Deudon, C., Kabbour, H., Meerschaut, A., et al. (2007). Cation deficient layered ruddlesden–popper-related oxysulfides $La_2LnMS_2O_5$ (Ln = La, Y; M = Nb, Ta). *Inorg. Chem.* 46, 9584–9590. doi: 10.1021/ic700422r

Carré, D., Laruelle, P., and Besançon, P. (1970). Structure cristalline de la pretendue variete β des sulfures de terres rares de composition $Pr_{10}S_{14}O$. *Comptes Rendus Hebd. l'Académie des Sci.* 270:537.

Céolin, R., and Rodier, N. (1976). Structure cristalline de l'oxysulfure de cerium et de bismuth $CeBiOS_2$. *Acta Crystallogr. Sect. B Struct. Crystallogr. Cryst. Chem.* 32, 1476–1479. doi: 10.1107/S05677408760 05591

Chan, G. H., Deng, B., Bertoni, M., Ireland, J. R., Hersam, M. C., Mason, T. O., et al. (2006). Syntheses, structures, physical properties, and theoretical studies of $CeM_xOS$ (M = Cu, Ag; x ≈ 0.8) and CeAgOS. *Inorg. Chem.* 45, 8264–8272. doi: 10.1021/ic061041k

Charkin, D. O., Plotnikov, V. A., Sadakov, A. V., Omel'yanovskii, O. E., and Kazakov, S. M. (2011). Synthesis of novel rare earth—iron oxide chalcogenides with the $La_2Fe_2O_3Se_2$ structure. *J. Alloys Compd.* 509, 7344–7348. doi: 10.1016/j.jallcom.2011.04.127

Chen, H., Moore, T., Qi, B., Colvin, D. C., Jelen, E. K., Hitchcock, D. A., et al. (2013). Monitoring PH-triggered drug release from radioluminescent

nanocapsules with X-Ray excited optical luminescence. *ACS Nano* 7, 1178–1187. doi: 10.1021/nn304369m

Cheon, J., Kang, N. J., Lee, S. M., Lee, J. H., Yoon, J. H., and Oh, S. J. (2004). Shape evolution of single-crystalline iron oxide nanocrystals. *J. Am. Chem. Soc.* 126, 1950–1951. doi: 10.1021/ja038722o

Cherry, S. R. (2006). Multimodality *in vivo* imaging systems: twice the power or double the trouble? *Annu. Rev. Biomed. Eng.* 8, 35–62. doi: 10.1146/annurev.bioeng.8.061505.095728

Cichos, J., Karbowiak, M., Hreniak, D., and Strek, W. (2016). Synthesis and characterization of monodisperse $Eu^{3+}$ doped gadolinium oxysulfide nanocrystals. *J. Rare Earths* 34, 850–856. doi: 10.1016/S1002-0721(16)60105-9

Cody, J. A., Deudon, C., Cario, L., and Meerschaut, A. (1997). Synthesis and structure determination of a new cerium titanium oxysulfide $[Ce_{20}Ti_{11}S_{44}O_6]$. *Mater. Res. Bull.* 32, 1181–1192. doi: 10.1016/S0025-5408(97)00094-9

Cody, J. A., and Ibers, J. A. (1995). Synthesis and characterization of the new rare-earth/transition-metal oxysulfides $La_6Ti_2S_8O_5$ and $La_4Ti_3S_4O_8$. *J. Solid State Chem.* 114, 406–412. doi: 10.1006/jssc.1995.1062

Cui, C., Jiang, G., Huang, P., Wang, L., and Liu, D. (2014a). Effect of $Eu^{3+}$ concentration on the luminescence properties of $Y_2O_2S:Eu^{3+}$, $Mg^{2+}$, $Ti^{4+}$ nanotubes. *Ceram. Int.* 40, 4725–4730. doi: 10.1016/j.ceramint.2013.09.015

Cui, C., Jiang, G., Huang, P., Wang, L., and Liu, D. (2014b). Synthesis and characterization of $Y_2O_2S:Eu^{3+}$, $Mg^{2+}$, $Ti^{4+}$ nanotubes via hydrothermal method. *J. Lumin.* 145, 665–668. doi: 10.1016/j.jlumin.2013.08.055

Cui, C. E., Lei, X., Huang, P., Wang, L., and Yang, F. (2013a). Influence of sulfuretted temperature on the luminescent properties of $Y_2O_2S:Eu^{3+}$, $Mg^{2+}$, $Ti^{4+}$ nanoarrays. *J. Lumin.* 138, 138–142. doi: 10.1016/j.jlumin.2013.02.013

Cui, C. E., Liu, H., Huang, P., and Wang, L. (2013b). Influence of $Eu^{3+}$ doping concentration on the luminescence properties of $Y_2O_2S:$ $Eu^{3+}$, $Mg^{2+}$, $Ti^{4+}$ nanoarrays via sol–gel template method. *Opt. Mater.* 36, 495–499. doi: 10.1016/j.optmat.2013.10.016

Dai, Q., Song, H., Wang, M., Bai, X., Dong, B., Qin, R., et al. (2008). Size and concentration effects on the photoluminescence of $La_2O_2S:Eu^{3+}$ nanocrystals. *J. Phys. Chem. C* 112, 19399–19404. doi: 10.1021/jp808343f

Delacotte, C., Pérez, O., Pautrat, A., Berthebaud, D., Hébert, S., Suard, E., et al. (2015). Magnetodielectric effect in crystals of the noncentrosymmetric CaOFeS at low temperature. *Inorg. Chem.* 54, 6560–6565. doi: 10.1021/acs.inorgchem.5b00879

Deng, S., Xue, Z., Liu, Y., Lei, B., Xiao, Y., and Zheng, M. (2012b). Synthesis and characterization of $Y_2O_2S:Eu^{3+}$, $Mg^{2+}$, $Ti^{4+}$ hollow nanospheres via a template-free route. *J. Alloys Compd.* 542, 207–212. doi: 10.1016/j.jallcom.2012.07.060

Deng, S. Q., Xue, Z. P., Yang, Y. H., Yang, Q., and Liu, Y. L. (2012a). Template-free fabrication and luminescent characterization of highly uniform and monodisperse $Y_2O_2S:Sm^{3+}$ hollow submicrospheres. *J. Mater. Sci. Technol.* 28, 666–672. doi: 10.1016/S1005-0302(12)60114-5

Deudon, C., Meerschaut, A., Cario, L., and Rouxel, J. (1995). Preparation and crystal structure determination of $La_{20}Ti_{11}S_{44}O_6$. *J. Solid State Chem.* 120, 164–169. doi: 10.1006/jssc.1995.1392

Deulkar, S. H., Huang, J. L., and Neumann-Spallart, M. (2010). Zinc oxysulfide thin films grown by pulsed laser deposition. *J. Electron. Mater.* 39, 589–594. doi: 10.1007/s11664-009-1069-8

Dhanaraj, J., Geethalakshmi, M., Jagannathan, R., and Kutty, T. R. (2004). $Eu^{3+}$ doped yttrium oxysulfide nanocrystals – crystallite size and luminescence transition(S). *Chem. Phys. Lett.* 387, 23–28. doi: 10.1016/j.cplett.2004.01.079

Dhanaraj, J., Jagannathan, R., and Trivedi, D. C. (2003). $Y_2O_2S:$ $Eu^{3+}$ nanocrystals—synthesis and luminescent properties. *J. Mater. Chem.* 13, 1778–1782. doi: 10.1039/B302073H

Ding, Y., Gu, J., Ke, J., Zhang, Y. W. W., and Yan, C. H. H. (2011). Sodium doping controlled synthesis of monodisperse lanthanide oxysulfide ultrathin nanoplates guided by density functional calculations. *Angew. Chem. Int. Ed. Engl.* 50, 12330–12334. doi: 10.1002/anie.201105025

Doussier-Brochard, C., Chavillon, B., Cario, L., and Jobic, S. (2010). Synthesis of P-Type transparent LaOCuS nanoparticles via soft chemistry. *Inorg. Chem.* 49, 3074–3076. doi: 10.1021/ic902521r

Dubois, V., Pecquenard, B., Soulé, S., Martinez, H., and Le Cras, F. (2017). Dual cation- and anion-based redox process in lithium titanium oxysulfide thin film cathodes for all-solid-state lithium-ion batteries. *ACS Appl. Mater. Interfaces* 9, 2275–2284. doi: 10.1021/acsami.6b11987

Dugué, J., Carré, D., and Guittard, M. (1978). Etude structurale des oxysulfures de cerium(III) et cerium(IV). I. structure cristalline de l'oxysulfure de cerium $Ce_4O_4S_3$. *Acta Crystallogr. B* 34, 3564–3568. doi: 10.1107/S0567740878011607

Dugué, J., Carré, D., and Guittard, M. (1979). Etude structurale des oxysulfures de cerium(III) et cerium(IV). II. structure cristalline de l'oxysulfure de cerium $Ce_6O_6S_4$. *Acta Crystallogr. B* 35, 1550–1554. doi: 10.1107/S056774087900710X

Dugué, J., Tien, V., and Laruelle, P. (1985). Structure de l'oxysulfure de Lanthane et de Vanadium, $La_5V_3O_7S_6$. *Acta Crystallogr. Sect. C Cryst. Struct. Commun.* 41, 1146–1148. doi: 10.1107/S0108270185006928

Dugué, J., Vovan, T., and Villers, J. (1980a). Etude structurale des oxysulfures de chrome(Ill) et de terres rares. I. Structure de l'oxysulfure $LaCrOS_2$. *Acta Crystallogr. B* 36, 1291–1294. doi: 10.1107/S0567740880005948

Dugué, J., Vovan, T., and Villers, J. (1980b). Etude structurale des oxysulfures de chrome(III) et de terres rares. II. Structure de l'oxysulfure $CeCrOS_2$. *Acta Crystallogr. B* 36, 1294–1297. doi: 10.1107/S056774088000595X

Dupin, J., Gonbeau, D., Martin-Litas, I., Vinatier, P., and Levasseur, A. (2001). Amorphous oxysulfide thin films MOySz (M=W, Mo, Ti) XPS characterization: structural and electronic pecularities. *Appl. Surf. Sci.* 173, 140–150. doi: 10.1016/S0169-4332(00)00893-X

Eastman, E. D., Brewer, L., Bromley, L. A., Gilles, P. W., and Lofgren, N. L. (1951). Preparation and properties of the oxide-sulfides of cerium, zirconium, thorium and uranium 2. *J. Am. Chem. Soc.* 73, 3896–3898. doi: 10.1021/ja01152a100

Eisman, G. A., and Steinfink, H. (1982). The synthesis of HfOS. *J. Solid State Chem.* 43, 225–226. doi: 10.1016/0022-4596(82)90233-X

Endo, T., Doi, Y., Wakeshima, M., Suzuki, K., Matsuo, Y., Tezuka, K., et al. (2017). Magnetic properties of the melilite-type oxysulfide $Sr_2MnGe_2S_6O$: magnetic interactions enhanced by anion substitution. *Inorg. Chem.* 56, 2459–2466. doi: 10.1021/acs.inorgchem.6b02505

Engström, M., Klasson, A., Pedersen, H., Vahlberg, C., Käll, P.-O., and Uvdal, K. (2006). High proton relaxivity for gadolinium oxide nanoparticles. *Magn. Reson. Mater. Physics, Biol. Med.* 19, 180–186. doi: 10.1007/s10334-006-0039-x

Flahaut, J., Guittard, M., and Patrie, M. (1958). Les oxysulfures $Me_2O_2S$ des éléments du groupe des terres rares. *Bull. Soc. Chim. Fr.* 7, 990–994.

Fu, Y., Cao, W., Peng, Y., Luo, X., and Xing, M. (2010). The upconversion luminescence properties of the $Yb^{3+}$-$Ho^{3+}$ system in nanocrystalline $Y_2O_2S$. *J. Mater. Sci.* 45, 6556–6561. doi: 10.1007/s10853-010-4744-5

Gastaldi, L., Carré, D., and Pardo, M. P. (1982). Structure de l'oxysulfure d'indium et de lanthane $In_6La_{10}O_6S_{17}$. *Acta Crystallogr. Sect. B Struct. Crystallogr. Cryst. Chem.* 38, 2365–2367. doi: 10.1107/S0567740882008802

Genuit, D., Bezverkhyy, I., and Afanasiev, P. (2005). Solution preparation of the amorphous molybdenum oxysulfide $MoOS_2$ and its use for catalysis. *J. Solid State Chem.* 178, 2759–2765. doi: 10.1016/j.jssc.2005.06.016

Ghosh, A. B., Saha, N., Sarkar, A., Dutta, A. K., Biswas, P., Nag, K., et al. (2016). Morphological tuning of $Eu_2O_2S$ nanoparticles, manifestation of peroxidase-like activity and glucose assay use. *New J. Chem.* 40, 1595–1604. doi: 10.1039/C5NJ02705E

Goga, M., Seshadri, R., Ksenofontov, V., Gütlich, P., and Tremel, W. (1999). $Ln_2Ti_2S_2O_5$ (Ln = Nd, Pr, Sm): a novel series of defective ruddlesden–popper phases. *Chem. Commun.* 7, 979–980. doi: 10.1039/a809737b

Golodnitsky, D., Nathan, M., Yufit, V., Strauss, E., Freedman, K., Burstein, L., et al. (2006b). Progress in three-dimensional (3D) Li-Ion microbatteries. *Solid State Ionics* 177, 2811–2819. doi: 10.1016/j.ssi.2006.02.048

Golodnitsky, D., Yufit, V., Nathan, M., Shechtman, I., Ripenbein, T., Strauss, E., et al. (2006a). Advanced materials for the 3D microbattery. *J. Power Sources* 153, 281–287. doi: 10.1016/j.jpowsour.2005.05.029

Gonbeau, D., Guimon, C., Pfister-Guillouzo, G., Levasseur, A., Meunier, G., and Dormoy, R. (1991). XPS study of thin films of titanium oxysulfides. *Surf. Sci.* 254, 81–89. doi: 10.1016/0039-6028(91)90640-E

Gouget, G., Debecker, D. P., Kim, A., Olivieri, G., Gallet, J.-J., Bournel, F., et al. (2017). *In situ* solid–gas reactivity of nanoscaled metal borides from molten salt synthesis. *Inorg. Chem.* 56, 9225–9234. doi: 10.1021/acs.inorgchem.7b01279

Gu, J., Ding, Y., Ke, J., Zhang, Y., and Yan, C. (2013). Controllable synthesis of monodispersed middle and heavy rare earth oxysulfide nanoplates based on the principles of HSAB theory. *Acta Chim. Sin.* 71:360. doi: 10.6023/A12121014

Guittard, M., Benazeth, S., Dugué, J., Jaulmes, S., Palazzi, M., Laruelle, P., et al. (1984). Oxysulfides and oxyselenides in sheets, formed by a rare earth element and a second metal. *J. Solid State Chem.* 51, 227–238. doi: 10.1016/0022-4596(84)90338-4

Guittard, M., Jaulmes, S., Loireau-Lozac'h, A. M., Mazurier, A., Berguer, F., and Flahaut, J. (1985). Étude du systeme La$_2$S$_3$-La$_2$O$_3$-Ga$_2$O$_3$-Ga$_2$S$_3$: description structurale des phases quaternaires et approche du diagramme de phase. *J. Solid State Chem.* 58, 276–289. doi: 10.1016/0022-4596(85)90210-5

Guittard, M., Vovan, T., Julien-Pouzol, M., Jaulmes, S., Laruelle, P., and Flahaut, J. (1986). Mise en evidence et etude structurale d'une famille de composes en feuillet de formule generale (UO)2RS3 (R = Gd à Lu et Y). *Zeitschrift Anorg. Allg. Chem.* 540, 59–66. doi: 10.1002/zaac.19865400909

Gultom, N. S., Abdullah, H., and Kuo, D.-H. (2017). Enhanced photocatalytic hydrogen production of noble-metal free Ni-Doped Zn(O,S) in ethanol solution. *Int. J. Hydrogen Energy* 42, 25891–25902. doi: 10.1016/j.ijhydene.2017.08.198

Guo, G., Wang, Y., Chen, J., Zhuang, H., Huang, J., and Zhang, Q. (1995). Samarium tantalum oxysulfide, Sm$_2$Ta$_3$S$_2$O$_8$. *Acta Crystallogr. Sect. C Cryst. Struct. Commun.* 51, 1964–1966. doi: 10.1107/S0108270195005026

Haire, R. G., and Fahey, J. A. (1977). The oxysulfates and oxysulfides of americium, curium and berkelium. *J. Inorg. Nucl. Chem.* 39, 837–841. doi: 10.1016/0022-1902(77)80165-6

Hakmeh, N., Chlique, C., Merdrignac-Conanec, O., Fan, B., Cheviré, F., Zhang, X., et al. (2015). Combustion synthesis and up-conversion luminescence of La$_2$O$_2$S:Er$^{3+}$,Yb$^{3+}$ nanophosphors. *J. Solid State Chem.* 226, 255–261. doi: 10.1016/j.jssc.2015.02.015

Han, L., Hu, Y., Pan, M., Xie, Y., Liu, Y., Li, D., et al. (2015a). A new tactic to achieve Y$_2$O$_2$S:Yb$^{3+}$/Er$^{3+}$ up-conversion luminescent hollow nanofibers. *CrystEngComm* 17, 2529–2535. doi: 10.1039/C4CE02527J

Han, L., Pan, M., Hu, Y., Xie, Y., Liu, Y., Li, D., et al. (2015b). A novel scheme to obtain Y$_2$O$_2$S:Er$^{3+}$ upconversion luminescent hollow nanofibers via precursor templating. *J. Am. Ceram. Soc.* 98, 2817–2822. doi: 10.1111/jace.13696

Hauser, O. (1907). Notiz über die darstellung der oxysulfide des zirkoniums und thoriums. *Zeitschrift für Anorg. Chemie* 53, 74–77. doi: 10.1002/zaac.19070530107

He, W., Zhang, J., Wang, L., and Zhang, Q. (2009). Preparation and properties of nanocrystal SmBO$_3$ by nitrate-citrate sol-gel combustion method. *J. Rare Earths* 27, 231–233. doi: 10.1016/S1002-0721(08)60225-2

Hernández-Adame, L., Méndez-Blas, A., Ruiz-García, J., Vega-Acosta, J. R., Medellín-Rodríguez, F. J., and Palestino, G. (2014). Synthesis, characterization, and photoluminescence properties of Gd:Tb oxysulfide colloidal particles. *Chem. Eng. J.* 258, 136–145. doi: 10.1016/j.cej.2014.07.067

Hernandez-Adame, L., Palestino, G., Meza, O., Hernandez-Adame, P. L., Vega-Carrillo, H. R., and Sarhid, I. (2018). Effect of Tb$^{3+}$ concentration in the visible emission of terbium-doped gadolinium oxysulfide microspheres. *Solid State Sci.* 84, 8–14. doi: 10.1016/j.solidstatesciences.2018.07.021

Hirai, T., and Orikoshi, T. (2004). Preparation of yttrium oxysulfide phosphor nanoparticles with infrared-to-green and -blue upconversion emission using an emulsion liquid membrane system. *J. Colloid Interface Sci.* 273, 470–477. doi: 10.1016/j.jcis.2003.12.013

Hirai, T., Orikoshi, T., and Komasawa, I. (2002). Preparation of Y$_2$O$_3$:Yb,Er infrared-to-visible conversion phosphor fine particles using an emulsion liquid membrane system. *Chem. Mater.* 14, 3576–3583. doi: 10.1021/cm0202207

Huang, F. Q., Brazis, P., Kannewurf, C. R., and Ibers, J. A. (2000). Synthesis, structure, electrical conductivity, and band structure of the rare-earth copper oxychalcogenide La$_5$Cu$_6$O$_4$S$_7$. *J. Solid State Chem.* 155, 366–371. doi: 10.1006/jssc.2000.8926

Huang, P., Liu, D., Cui, C. E., Wang, L., and Jiang, G. (2014). Synthesis and luminescence properties of red long-lasting phosphor Y$_2$O$_2$S:Eu$^{3+}$, Zn$^{2+}$, Ti$^{4+}$ nanotubes via hydrothermal method. *Appl. Phys. A* 116, 759–765. doi: 10.1007/s00339-013-8145-x

Huang, Y. Z., Chen, L., and Wu, L. M. (2008). Crystalline nanowires of Ln$_2$O$_2$S, Ln$_2$O$_2$S$_2$, LnS$_2$ (Ln = La, (Nd), and La$_2$O$_2$S:Eu$^{3+}$. conversions via the boron-sulfur method that preserve shape. *Cryst. Growth Des.* 8, 739–743. doi: 10.1021/cg700751j

Ijjaali, I., Deng, B., and Ibers, J. A. (2005). Seven new rare-earth transition-metal oxychalcogenides: syntheses and characterization of Ln$_4$MnOSe$_6$ (Ln=La, Ce, Nd), Ln$_4$FeOSe$_6$ (Ln=La, Ce, Sm), and La$_4$MnOS$_6$. *J. Solid State Chem.* 178, 1503–1507. doi: 10.1016/j.jssc.2005.02.022

Inoue, M., Ueda, Y., Negishi, H., Sasaki, M., Ohba, T., Kitano, Y., et al. (1986). Effect of sulphur doping on the electrical properties of γ-Mo$_4$O$_{11}$

crystals. *J. Less Common Met.* 115, 261–268. doi: 10.1016/0022-5088(86)90148-7

Iparraguirre, I., Azkargorta, J., Merdrignac-Conanec, O., Al-Saleh, M., Chlique, C., Zhang, X., et al. (2012). Laser action in Nd$^{3+}$-doped lanthanum oxysulfide powders. *Opt. Express* 20:23690. doi: 10.1364/OE.20.023690

Ishikawa, A., Takata, T., Kondo, J. N., Hara, M., Kobayashi, H., and Domen, K. (2002). Oxysulfide Sm$_2$Ti$_2$S$_2$O$_5$ as a stable photocatalyst for water oxidation and reduction under visible light irradiation (λ ≤ 650 Nm). *J. Am. Chem. Soc.* 124, 13547–13553. doi: 10.1021/ja0269643

Ishikawa, A., Takata, T., Matsumura, T., Kondo, J. N., Hara, M., Kobayashi, H., et al. (2004). Oxysulfides Ln$_2$Ti$_2$S$_2$O$_5$ as stable photocatalysts for water oxidation and reduction under visible-light irradiation. *J. Phys. Chem. B* 108, 2637–2642. doi: 10.1021/jp036890x

Jain, A., Kumar, A., Dhoble, S. J., and Peshwe, D. R. (2016). Persistent luminescence: an insight. *Renew. Sustain. Energy Rev.* 65, 135–153. doi: 10.1016/j.rser.2016.06.081

Jaulmes, S. (1978). Oxysulfure de gallium et de lanthane LaGaOS$_2$. *Acta Crystallogr. Sect. B Struct. Crystallogr. Cryst. Chem.* 34, 2610–2612. doi: 10.1107/S0567740878008705

Jaulmes, S., Godlewski, E., Palazzi, M., and Etienne, J. (1982). Deux structures isotypes a sites anioniques et cationiques lacunaires: (CeO)$_4$Ga$_2$S$_5$ et (LaO)$_4$As$_2$S$_5$. *Acta Crystallogr. Sect. B Struct. Crystallogr. Cryst. Chem.* 38, 1707–1710. doi: 10.1107/S0567740882007006

Jaulmes, S., Julien-Pouzol, M., Dugué, J., Laruelle, P., Vovan, T., and Guittard, M. (1990). Structure de l'oxysulfure d'uranium et de lutécium, (UOS)$_4$LuS. *Acta Crystallogr. Sect. C Cryst. Struct. Commun.* 46, 1205–1207. doi: 10.1107/S0108270189011418

Jaulmes, S., Mazurier, A., and Guittard, M. (1983). Structure de l'oxypentasulfure de gallium et de trilanthane, GaLa$_3$OS$_5$. *Acta Crystallogr. Sect. C Cryst. Struct. Commun.* 39, 1594–1597. doi: 10.1107/S0108270183009397

Jellinek, F. (1962). A tetragonal form of zirconium oxide sulfide, ZrOS. *Acta Chem. Scand.* 16, 791–792. doi: 10.3891/acta.chem.scand.16-0791

Jiang, G., Wei, X., Chen, Y., Duan, C., Yin, M., Yang, B., et al. (2015). Luminescent La$_2$O$_2$S:Eu$^{3+}$ nanoparticles as non-contact optical temperature sensor in physiological temperature range. *Mater. Lett.* 143, 98–100. doi: 10.1016/j.matlet.2014.12.057

Julien-Pouzol, M., Jaulmes, S., Guittard, M., and Laruelle, P. (1978). Oxysulfure de scandium Sc$_2$O$_2$S. *J. Solid State Chem.* 26, 185–188. doi: 10.1016/0022-4596(78)90150-0

Jüstel, T., Nikol, H., and Ronda, C. (1998). New developments in the field of luminescent materials for lighting and displays. *Angew. Chemie Int. Ed.* 37, 3084–3103. doi: 10.1002/(SICI)1521-3773(19981204)37:22<3084::AID-ANIE3084>3.0.CO;2-W

Kabbour, H., Cario, L., Deudon, C., and Meerschaut, A. (2003). A gadolinium and niobium oxide sulfide, Gd$_3$NbS$_3$O$_4$. *Acta Crystallogr. Sect. E Struct.* 59, i101–i102. doi: 10.1107/S1600536803013035

Kabbour, H., Cario, L., Moëlo, Y., and Meerschaut, A. (2004). Synthesis, X-Ray and optical characterizations of two new oxysulfides: LaInS$_2$O and La$_5$In$_3$S$_9$O$_3$. *J. Solid State Chem.* 177, 1053–1059. doi: 10.1016/j.jssc.2003.10.012

Kawahara, Y., Petrykin, V., Ichihara, T., Kijima, N., and Kakihana, M. (2006). Synthesis of high-brightness sub-micrometer Y$_2$O$_2$S red phosphor powders by complex homogeneous precipitation method. *Chem. Mater.* 18, 6303–6307. doi: 10.1021/cm060609k

Khodadad, P., Tek, T., Flahaut, J., and Domange, L. (1965). Sur une nouvelle famille de combinaisons chimiques des terres rares les oxydisulfures de formule generale L$_2$O$_2$S$_2$. *Comptes Rendus Hebd. l'Acad. Sci.* 260, 2235–2238.

Klemm, W., Meisel, K., and Vogel, H. U. (1930). Über die sulfide der seltenen erden. *Zeitschrift Anorg. Allg. Chem.* 190, 123–144. doi: 10.1002/zaac.19301900113

Koyama, E., Nakai, I., and Nagashima, K. (1984). Crystal chemistry of oxide–chalcogenides. II. Synthesis and crystal structure of the first bismuth oxide–sulfide, Bi$_2$O$_2$S. *Acta Crystallogr. Sect. B Struct. Sci.* 40, 105–109. doi: 10.1107/S010876818400183X

Kryza, D., Taleb, J., Janier, M., Marmuse, L., Miladi, I., Bonazza, P., et al. (2011). Biodistribution study of nanometric hybrid gadolinium oxide particles as a multimodal SPECT/MR/optical imaging and theragnostic agent. *Bioconjug. Chem.* 22, 1145–1152. doi: 10.1021/bc1005976

Kupčík, V. (1967). Die kristallstruktur des kermesits, $Sb_2S_2O$. *Naturwissenschaften* 54, 114. doi: 10.1007/BF00640574

Kusainova, A. M., Berdonosov, P. S., Akselrud, L. G., Kholodkovskaya, L. N., Dolgikh, V. A., and Popovkin, B. A. (1994). New layered compounds with the general composition (MO) (CuSe), where M = Bi, Nd, Gd, Dy, and BiOCuS: syntheses and crystal structure. *J. Solid State Chem.* 112, 189–191. doi: 10.1006/jssc.1994.1285

Larquet, C., Carriere, D., Nguyen, A. M., Le, T. K. C., Frogneux-Plé, X., Génois, I., et al. (2020). Unraveling the role of alkali cations in the growth mechanism of $Gd_2O_2S$ nanoparticles. *Chem. Mater.* 32, 1131–1139. doi: 10.1021/acs.chemmater.9b04059

Larquet, C., Hourlier, D., Nguyen, A.-M., Torres-Pardo, A., Gauzzi, A., Sanchez, C., et al. (2019a). Thermal stability of oleate-stabilized $Gd_2O_2S$ nanoplates in inert and oxidizing atmospheres. *ChemNanoMat.* 5, 539–546. doi: 10.1002/cnma.201800578

Larquet, C., Klein, Y., Hrabovsky, D., Gauzzi, A., Sanchez, C., and Carenco, S. (2019b). Tunable magnetic properties of $(Gd,Ce)_2O_2S$ oxysulfide nanoparticles. *Eur. J. Inorg. Chem.* 2019, 762–765. doi: 10.1002/ejic.201801466

Larquet, C., Nguyen, A.-M., Glais, E., Paulatto, L., Sassoye, C., Selmane, M., et al. (2019c). Band gap engineering from cation balance: the case of lanthanide oxysulfide nanoparticles. *Chem. Mater.* 31, 5014–5023. doi: 10.1021/acs.chemmater.9b00450

Larquet, C., Nguyen, A. M., Ávila-Gutiérrez, M., Tinat, L., Lassalle-Kaiser, B., Gallet, J. J., et al. (2017). Synthesis of $Ce_2O_2S$ and $Gd_{2(1--y)}Ce_2yO_2S$ nanoparticles and reactivity from *in situ* X-Ray absorption spectroscopy and X-Ray photoelectron spectroscopy. *Inorg. Chem.* 56, 14227–14236. doi: 10.1021/acs.inorgchem.7b02336

Lauxmann, P., and Schleid, T. (2000). CuPrOS: kein einprägsames akronym, vielmehr ein echtes quaternäres chalkogenid mit aufgefülltem pbfcl-struktur. *Zeitschrift Anorg. Allg. Chem.* 626, 2253–2255. doi: 10.1002/1521-3749(200011)626:11<2253::AID-ZAAC2253>3.0.CO;2-N

Lee, D. S., and Jeong, H. D. (2014). Distinct band gap tunability of zinc oxysulfide (ZnOS) thin films synthesized from thioacetate-capped ZnO nanocrystals. *Appl. Sci. Converg. Technol.* 23, 376–386. doi: 10.5757/ASCT.2014.23.6.376

Lei, L., Zhang, S., Xia, H., Tian, Y., Zhang, J., and Xu, S. (2017). Controlled synthesis of lanthanide-doped $Gd_2O_2S$ nanocrystals with novel excitation-dependent multicolor emissions. *Nanoscale* 9, 5718–5724. doi: 10.1039/C7NR00454K

Levasseur, A., Schmidt, E., Meunier, G., Gonbeau, D., Benoist, L., and Pfister-Guillouzo, G. (1995). New amorphous molybdenum oxysulfide thin films their characterization and their electrochemical properties. *J. Power Sources* 54, 352–355. doi: 10.1016/0378-7753(94)02100-H

Levasseur, A., Vinatier, P., and Gonbeau, D. (1999). X-Ray photoelectron spectroscopy: a powerful tool for a better characterization of thin film materials. *Bull. Mater. Sci.* 22, 607–614. doi: 10.1007/BF02749975

Leverenz, H. W. (1949). Luminescent solids (phosphors). *Science* 109, 183–195. doi: 10.1126/science.109.2826.183

Li, W., Liu, Y., and Ai, P. (2010). Synthesis and luminescence properties of red long-lasting phosphor $Y_2O_2S:Eu^{3+}$, $Mg^{2+}$, $Ti^{4+}$ nanoparticles. *Mater. Chem. Phys.* 119, 52–56. doi: 10.1016/j.matchemphys.2009.07.037

Li, W., Liu, Y., Ai, P., and Chen, X. (2009). Synthesis and characterization of $Y_2O_2S:Eu^{3+}$, $Mg^{2+}$, $Ti^{4+}$ nanorods via a solvothermal routine. *J. Rare Earths* 27, 895–899. doi: 10.1016/S1002-0721(08)60358-0

Li, Y., Huang, Y., Bai, T., and Li, L. (2000). Straightforward conversion route to nanocrystalline monothiooxides of rare earths through a high-temperature colloid technique. *Inorg. Chem.* 39, 3418–3420. doi: 10.1021/ic9912169

Lin, S. L., Liu, T. Y., Lo, C. L., Wang, B. S., Lee, Y. J., Lin, K. Y., et al. (2016). Synthesis, surface modification, and photophysical studies of $Ln_2O_2S:Ln'^{3+}$ (Ln = Gd, Tb, Eu; Ln' = Tb and/or Eu) nanoparticles for luminescence bioimaging. *J. Lumin.* 175, 165–175. doi: 10.1016/j.jlumin.2016.01.037

Lindic, M. H., Martinez, H., Benayad, A., Pecquenard, B., Vinatier, P., Levasseur, A., et al. (2005a). XPS investigations of TiOySz amorphous thin films used as positive electrode in lithium microbatteries. *Solid State Ionics* 176, 1529–1537. doi: 10.1016/j.ssi.2005.04.007

Lindic, M. H., Pecquenard, B., Vinatier, P., Levasseur, A., Martinez, H., Gonbeau, D., et al. (2005b). Characterization of Rf sputtered TiOySz thin films. *Thin Solid Films* 484, 113–123. doi: 10.1016/j.tsf.2005.02.014

Lissner, F., and Schleid, T. (1992). Über sulfide und oxidsulfide des samariums/on sulfides and oxysulfides of samarium. *Zeitschrift für Naturforsch. B* 47, 1614–1620. doi: 10.1515/znb-1992-1116

Liu, D., Cui, C., Huang, P., Wang, L., and Jiang, G. (2014b). Luminescent properties of red long-lasting phosphor $Y_2O_2S:Eu^{3+}$, $M^{2+}$ (M=Mg, Ca, Sr, Ba), $Ti^{4+}$ nanotubes via hydrothermal method. *J. Alloys Compd.* 583, 530–534. doi: 10.1016/j.jallcom.2013.08.196

Liu, D., Huang, P., Cui, C., Wang, L., and Jiang, G. (2014a). Effects of simultaneous change of $Mg^{2+}$ and $Ti^{4+}$ contents on the luminescence properties of $Y_2O_2S:Eu^{3+}$, $Mg^{2+}$, $Ti^{4+}$ nanotubes. *Ceram. Int.* 40, 117–122. doi: 10.1016/j.ceramint.2013.05.111

Liu, H., Liu, P., Su, X., Liu, J., Li, X., Luo, H., et al. (2014c). One-pot solvothermal synthesis of singly doped $Eu^{3+}$ and Codoped $Er^{3+}$, $Yb^{3+}$ heavy rare earth oxysulfide $Y_2O_2S$ nano-aggregates and their luminescence study. *RSC Adv.* 4, 57048–57053. doi: 10.1039/C4RA10276B

Liu, J., Luo, H., Liu, P., Han, L., Zheng, X., Xu, B., et al. (2012). One-pot solvothermal synthesis of uniform layer-by-layer self-assembled ultrathin hexagonal $Gd_2O_2S$ nanoplates and luminescent properties from single doped $Eu^{3+}$ and Codoped $Er^{3+}$, $Yb^{3+}$. *Dalt. Trans.* 41, 13984–13988. doi: 10.1039/c2dt31610b

Liu, J., Yang, Y., Ni, B., Li, H., and Wang, X. (2017). Fullerene-like nickel oxysulfide hollow nanospheres as bifunctional electrocatalysts for water splitting. *Small* 13:1602637. doi: 10.1002/smll.201602637

Liu, L. (2013). Nano-aggregates of cobalt nickel oxysulfide as a high-performance electrode material for supercapacitors. *Nanoscale* 5, 11615–11619. doi: 10.1039/c3nr03533f

Liu, Z., Sun, X., Xu, S., Lian, J., Li, X., Xiu, Z., et al. (2008). $Tb^{3+}$- and $Eu^{3+}$-doped lanthanum oxysulfide nanocrystals. gelatin-templated synthesis and luminescence properties? *J. Phys. Chem. C* 112, 2353–2358. doi: 10.1021/jp0764687

Lu, X., Yang, M., Yang, L., Ma, Q., Dong, X., and Tian, J. (2015). $Y_2O_2S:Yb^{3+}$, $Er^{3+}$ nanofibers: novel fabrication technique, structure and up-conversion luminescent characteristics. *J. Mater. Sci. Mater. Electron.* 26, 4078–4084. doi: 10.1007/s10854-015-2947-x

Luo, X., Cao, W., and Xing, M. (2009). Upconversion luminescence properties of monodisperse spherical $Y_2O_2S:Yb,Ho$ nanocrystals. *J. Mater. Res.* 24, 1756–1760. doi: 10.1557/jmr.2009.0208

Ma, D., Liu, S., Zhang, Y., Zhang, C., and Huang, S. (2013). Controlled synthesis of $Eu^{3+}$-doped $La_2O_2S$ nanophosphors by refluxing method. *J. Exp. Nanosci.* 8, 434–441. doi: 10.1080/17458080.2011.591002

Mao, S., Liu, Q., Gu, M., Mao, D., and Chang, C. (2008). Long lasting phosphorescence of $Gd_2O_2S:Eu,Ti,Mg$ nanorods via a hydrothermal routine. *J. Alloys Compd.* 465, 367–374. doi: 10.1016/j.jallcom.2007.10.119

Marcon, J. P. (1967a). Sulfures de neptunium. *Comptes Rendus Hebd. l'Académie des Sci.* 265:235.

Marcon, J. P. (1967b). Oxysulfures de plutonium. *Comptes Rendus Hebd. l'Acad. Sci.* 264, 1475–1476.

Markushev, V. M., Ter-Gabriélyan, N. É., Briskina, C. M., Belan, V. R., and Zolin, V. F. (1990). Stimulated emission kinetics of neodymium powder lasers. *Sov. J. Quantum Electron.* 20, 773–777. doi: 10.1070/QE1990v020n07ABEH006817

Martin, I., Vinatier, P., Levasseur, A., Dupin, J., and Gonbeau, D. (1999). XPS analysis of the lithium intercalation in amorphous tungsten oxysulfide thin films. *J. Power Sources* 81–82, 306–311. doi: 10.1016/S0378-7753(99)00129-9

Martinez, H., Benayad, A., Gonbeau, D., Vinatier, P., Pecquenard, B., and Levasseur, A. (2004). Influence of the cation nature of high sulfur content oxysulfide thin films MOySz (M=W, Ti) studied by XPS. *Appl. Surf. Sci.* 236, 377–386. doi: 10.1016/j.apsusc.2004.05.010

Martin-Litas, I., Vinatier, P., Levasseur, A., Dupin, J., Gonbeau, D., and Weill, F. (2002). Characterisation of r.f. sputtered tungsten disulfide and oxysulfide thin films. *Thin Solid Films* 416, 1–9. doi: 10.1016/S0040-6090(02)00717-4

Martin-Litas, I., Vinatier, P., Levasseur, A., Dupin, J. C., and Gonbeau, D. (2001). Promising thin films ($WO_{1.0}S_2$ and $WO_{1.35}S_{2.2}$) as positive electrode materials in microbatteries. *J. Power Sources* 97–98, 545–547. doi: 10.1016/S0378-7753(01)00730-3

Martin-Litas, I., Vinatier, P., Levasseur, A., Dupin, J. C., and Gonbeau, D. (2003). Electrochemical properties of tungsten oxysulphide thin films as

positive electrodes for lithium microbatteries. *Bull. Mater. Sci.* 26, 673–681. doi: 10.1007/BF02706762

Matijević, E., and Hsu, W. P. (1987). Preparation and properties of monodispersed colloidal particles of lanthanide compounds. *J. Colloid Interface Sci.* 118, 506–523. doi: 10.1016/0021-9797(87)90486-3

Mayer, J. M., Schneemeyer, L. F., Siegrist, T., Waszczak, J. V., and Van Dover, B. (1992). New layered iron-lanthanum-oxide-sulfide and -selenide phases: $Fe_2La_2O_3E_2$ (E=S,Se). *Angew. Chemie Int. Ed. English* 31, 1645–1647. doi: 10.1002/anie.199216451

Mazurier, A., Guittard, M., and Jaulmes, S. (1982). Structure cristalline d'un oxysulfure isotype de La Mélilite, $La_{3,33}Ga_6O_2S_{12}$. *Acta Crystallogr. Sect. B Struct. Crystallogr. Cryst. Chem.* 38, 379–382. doi: 10.1107/S0567740882003021

McCullough, J. D., Brewer, L., and Bromley, L. A. (1948). The crystal structure of zirconium oxysulfide, ZrOS. *Acta Crystallogr.* 1, 287–289. doi: 10.1107/S0365110X4800079X

Meignen, V., Cario, L., Lafond, A., Moëlo, Y., Guillot-Deudon, C., and Meerschaut, A. (2004b). Crystal structures of two new oxysulfides $La_5Ti_2MS_5O_7$ (M=Cu, Ag): evidence of anionic segregation. *J. Solid State Chem.* 177, 2810–2817. doi: 10.1016/j.jssc.2004.04.023

Meignen, V., Lafond, A., Cario, L., Deudon, C., and Meerschaut, A. (2003). A new lanthanum titanium oxysulfide, $La_{16}Ti_5S_{17+x}O_{17}$, with x = 0.75 (9). *Acta Crystallogr. Sect. C Cryst. Struct. Commun.* 59, i63–i64. doi: 10.1002/chin.200341009

Meignen, V., Meerschaut, A., Cario, L., and Lafond, A. (2004a). Synthesis and crystal structure of a new oxysulfide $Gd_{6+x}Ti_4-XS_{10}-YO_{6+y}$ (Where x ∼ 0.04 and y ∼ 0.27). *Zeitschrift fur Naturforsch.* 59, 4–9. doi: 10.1515/znb-2004-0903

Meignen, V., Meerschaut, A., Cario, L., and Lafond, A. (2005). Synthesis and crystal structure of a new oxychalcogenide $La_5Ti$∼$_{3.25}Zr$∼$_{0.25}S_5O_{9.25}$. *J. Solid State Chem.* 178, 1637–1643. doi: 10.1016/j.jssc.2005.03.003

Meng, S., Zhang, X., Zhang, G., Wang, Y., Zhang, H., and Huang, F. (2015). Synthesis, crystal structure, and photoelectric properties of a new layered bismuth oxysulfide. *Inorg. Chem.* 54, 5768–5773. doi: 10.1021/acs.inorgchem.5b00436

Meunier, G., Dormoy, R., and Levasseur, A. (1989). New positive-electrode materials for lithium thin film secondary batteries. *Mater. Sci. Eng. B* 3, 19–23. doi: 10.1016/0921-5107(89)90173-6

Meunier, G., Dormoy, R., and Levasseur, A. (1991). New amorphous titanium oxysulfides obtained in the form of thin films. *Thin Solid Films* 205, 213–217. doi: 10.1016/0040-6090(91)90302-E

Meyer, B. K., Merita, S., and Polity, A. (2013). On the synthesis and properties of ternary copper oxide sulfides ($Cu_2O_{1-X}S_x$). *Phys. status solidi* 7, 360–363. doi: 10.1002/pssr.201206538

Michail, C. M., Fountos, G. P., Liaparinos, P. F., Kalyvas, N. E., Valais, I., Kandarakis, I. S., et al. (2010). Light emission efficiency and imaging performance of $Gd_2O_2S$:Eu powder scintillator under x-Ray radiography conditions. *Med. Phys.* 37, 3694–3703. doi: 10.1118/1.3451113

Muijsers, J. C., Weber, T., Vanhardeveld, R. M., Zandbergen, H. W., and Niemantsverdriet, J. W. (1995). Sulfidation study of molybdenum oxide using $MoO_3/SiO_2/Si_{(100)}$ model catalysts and Mo-IV3-sulfur cluster compounds. *J. Catal.* 157, 698–705. doi: 10.1006/jcat.1995.1335

Nakai, I., Nagashima, K., Koto, K., and Morimoto, N. (1978). Crystal chemistry of oxide–chalcogenide. I. The crystal structure of sarabauite $CaSb_{10}O_{10}S_6$. *Acta Crystallogr. Sect. B Struct. Crystallogr. Cryst. Chem.* 34, 3569–3572. doi: 10.1107/S0567740878011619

Nakkiran, A., Thirumalai, J., and Jagannathan, R. (2007). Luminescence blinking in $Eu^{3+}$ doped yttrium oxysulfide ($Y_2O_2S$:$Eu^{3+}$) quantum-dot ensembles: photo-assisted relaxation of surface state(S). *Chem. Phys. Lett.* 436, 155–161. doi: 10.1016/j.cplett.2007.01.009

Nelson, A., Fritz, K. E., Honrao, S., Hennig, R. G., Robinson, R. D., and Suntivich, J. (2016). Increased activity in hydrogen evolution electrocatalysis for partial anionic substitution in cobalt oxysulfide nanoparticles. *J. Mater. Chem. A* 4, 2842–2848. doi: 10.1039/C5TA08706F

Ogino, H., Shimoyama, J., Kishio, K., Katsura, Y., Tsuboi, M., Yamanoi, K., et al. (2012). Excitonic luminescence in two-dimensionally confined layered sulfide oxides. *Appl. Phys. Lett.* 101:191901. doi: 10.1063/1.4764941

Okabe, T., Van Tendeloo, G., Van Landuyt, J., Amelinckx, S., and Guittard, M. (1988). Long-period stacking variants in the homologous series $U_2La_{2n-2}O_2nS_{n+1}$. *J. Solid State Chem.* 72, 376–389. doi: 10.1016/0022-4596(88)90041-2

Olofinjana, B., Egharevba, G. O., Eleruja, M. A., Jeynes, C., Adedeji, A. V., Akinwunmi, O. O., et al. (2010). Synthesis and some properties of metal organic chemical vapour deposited molybdenum oxysulphide thin films. *J. Mater. Sci. Technol.* 26, 552–557. doi: 10.1016/S1005-0302(10)60084-9

Orlandi, P., Moëlo, Y., Meerschaut, A., and Palvadeau, P. (1999). Lead-antimony sulfosalts from Tuscany (Italy). I. Scainiite, $Pb_{14}Sb_{30}S_{54}O_5$, the First Pb-Sb oxy-sulfosalt, from buca della vena mine. *Eur. J. Mineral.* 11, 949–954. doi: 10.1127/ejm/11/6/0949

Osseni, S. A. (2012). *Nanoplateformes Hybrides Multimodales Pour l'imagerie Médicale*. Toulouse: Université de Toulouse.

Osseni, S. A., Lechevallier, S., Verelst, M., Dujardin, C., Dexpert-Ghys, J., Neumeyer, D., et al. (2011). New nanoplatform based on $Gd_2O_2S$:$Eu^{3+}$ core: synthesis, characterization and use for *in vitro* bio-labelling. *J. Mater. Chem.* 21, 18365–18372. doi: 10.1039/c1jm13542b

Otzschi, K., Ogino, H., Shimoyama, J., and Kishio, K. (1999). New candidates for superconductors; a series of layered oxysulfides ($Cu_2S_2$)($Sr_{n+1}MnO_{3n-1}$). *J. Low Temp. Phys.* 117, 729–733. doi: 10.1023/A:1022545228168

Ouvrard, G., Tchangbédji, G., Deniard, P., and Prouzet, E. (1995). Structural, physical and electrochemical characteristics of a vanadium oxysulfide, a cathode material for lithium batteries. *J. Power Sources* 54, 246–249. doi: 10.1016/0378-7753(94)02077-G

Palazzi, M. (1981). Préparation et affinement de la structure de (LaO) CuS. *Comptes Rendus Hebd. l'Acad. Sci.* 292, 789–791.

Palazzi, M., Carcaly, C., and Flahaut, J. (1980). Un nouveau conducteur ionique (LaO)AgS. *J. Solid State Chem.* 35, 150–155. doi: 10.1016/0022-4596(80)90487-9

Palazzi, M., and Jaulmes, S. (1981). Structure du conducteur ionique (LaO)AgS. *Acta Crystallogr. Sect. B Struct. Crystallogr. Cryst. Chem.* 37, 1337–1339. doi: 10.1107/S0567740881005876

Pandey, S. K., Pandey, S., Pandey, A. C., and Mehrotra, G. K. (2013). Zinc oxysulfide ternary alloy nanocrystals: a bandgap modulated photocatalyst. *Appl. Phys. Lett.* 102:233110. doi: 10.1063/1.4810910

Pandey, S. K., Pandey, S., Parashar, V., Yadav, R. S., Mehrotra, G. K., and Pandey, A. C. (2014). Bandgap engineering of colloidal zinc oxysulfide via lattice substitution with sulfur. *Nanoscale* 6, 1602–1606. doi: 10.1039/C3NR04457B

Pang, T., Cao, W., Xing, M., Feng, W., Xu, S., and Luo, X. (2010). Preparation and upconversion luminescence of monodisperse $Y_2O_2S$:Yb/Ho-Silica/Aminosilane core-shell nanoparticles. *J. Rare Earths* 28, 509–512. doi: 10.1016/S1002-0721(09)60142-3

Pardo, M.-P., Céolin, R., and Guittard, M. (1976). Sur les oxysulfures a deux éléments metalliques, terre rare et bismuth, ou terre rare et antimoine. *Comptes rendus Hebd. l'Acad. Sci.* 283, 735–738.

Park, J., Zheng, H., Jun, Y., and Alivisatos, A. P. (2009). Hetero-epitaxial anion exchange yields single-crystalline hollow nanoparticles. *J. Am. Chem. Soc.* 131, 13943–13945. doi: 10.1021/ja905732q

Pasquariello, D. M., Dunn, W. J., and Abraham, K. M. (1990). "Rechargeable Lithium-Molybdenum Oxysulfide Batteries," in *Proceedings of the 34th International Power Sources Symposium* (Cherry Hill, NJ: IEEE), 94–97. doi: 10.1109/IPSS.1990.145800

Pechini, M. P. (1967). *Method of Preparing Lead and Alkaline Earth Titanates and Niobates and Coating Method Using the Same to Form a Capacitor*. US Patent No. 3330697.

Petoral, R. M., Söderlind, F., Klasson, A., Suska, A., Fortin, M. A., Abrikossova, N., et al. (2009). Synthesis and characterization of $Tb^{3+}$-doped $Gd_2O_3$ nanocrystals: a bifunctional material with combined fluorescent labeling and MRI contrast agent properties. *J. Phys. Chem. C* 113, 6913–6920. doi: 10.1021/jp808708m

Petrova, S. A., Mar'evich, V. P., Zakharov, R. G., Selivanov, E. N., Chumarev, V. M., and Udoeva, L. Y. (2003). Crystal structure of zinc calcium oxysulfide. *Dokl. Chem.* 393, 255–258. doi: 10.1023/B:DOCH.0000003458.35866.40

Pitha, J. J., Smith, A. L., and Ward, R. (1947). The preparation of lanthanum oxysulfide and its properties as a base material for phosphors stimulated by infrared 1. *J. Am. Chem. Soc.* 69, 1870–1871. doi: 10.1021/ja01200a009

Platzer-Björkman, C., Törndahl, T., Abou-Ras, D., Malmström, J., Kessler, J., and Stolt, L. (2006). Zn(O,S) buffer layers by atomic layer deposition in Cu(In,Ga)Se$_2$ based thin film solar cells: band alignment and sulfur gradient. *J. Appl. Phys.* 100:044506. doi: 10.1063/1.2222067

Polat, I., Aksu, S., Altunbaş, M., and Bacaksiz, E. (2011b). Microstructural, optical and magnetic properties of cobalt-doped zinc oxysulfide thin films. *Mater. Chem. Phys.* 130, 800–805. doi: 10.1016/j.matchemphys.2011.07.069

Polat, I., Aksu, S., Altunbaş, M., and Bacaksiz, E. (2012). The influence of diffusion temperature on the structural, optical, and magnetic properties of nickel-doped zinc oxysulfide thin films. *Phys. Status Solidi* 209, 160–166. doi: 10.1002/pssa.201127248

Polat, I., Aksu, S., Altunbaş, M., Yilmaz, S., and Bacaksiz, E. (2011a). The influence of diffusion temperature on the structural, optical and magnetic properties of manganese-doped zinc oxysulfide thin films. *J. Solid State Chem.* 184, 2683–2689. doi: 10.1016/j.jssc.2011.07.017

Popovkin, B. A., Kusainova, A. M., Dolgikh, V. A., and Akselrud, L. G. (1998). New layered phases of the MOCuX (M = Ln, Bi; X = S, Se, TE) family: a geometric approach to the explanation of phase stability. *Russ. J. Inorg. Chem.* 43, 1471–1475.

Portehault, D., Devi, S., Beaunier, P., Gervais, C., Giordano, C., Sanchez, C., et al. (2011). A general solution route toward metal boride nanocrystals. *Angew. Chemie Int. Ed.* 50, 3262–3265. doi: 10.1002/anie.201006810

Pratx, G., Carpenter, C. M., Sun, C., Rao, R. P., and Xing, L. (2010b). Tomographic molecular imaging of X-Ray-excitable nanoparticles. *Opt. Lett.* 35, 3345–3347. doi: 10.1364/OL.35.003345

Pratx, G., Carpenter, C. M., Sun, C., and Xing, L. (2010a). X-Ray luminescence computed tomography via selective excitation: a feasibility study. *IEEE Trans. Med. Imaging* 29, 1992–1999. doi: 10.1109/TMI.2010.2055883

Qiao, Y., Hu, X., Liu, Y., Liang, G., Croft, M. C., and Huang, Y. (2013). Surface modification of MoOxSy on Porous TiO$_2$ nanospheres as an anode material with highly reversible and ultra-fast lithium storage properties. *J. Mater. Chem. A* 1:15128. doi: 10.1039/c3ta13582a

Quezel, G., Ballestracci, R., and Rossat-Mignod, J. (1970). Proprietes magnetiques des oxysulfures de terres rares. *J. Phys. Chem. Solids* 31, 669–684. doi: 10.1016/0022-3697(70)90201-5

Ramacharyulu, P. V. R. K., Praveen Kumar, J., Prasad, G. K., and Sreedhar, B. (2014). Sulphur doped nano TiO$_2$: synthesis, characterization and photocatalytic degradation of a toxic chemical in presence of sunlight. *Mater. Chem. Phys.* 148, 692–698. doi: 10.1016/j.matchemphys.2014.08.036

Range, K.-J., Lange, K. G., and Gietl, A. (1990). Rare earth sulphide oxides Ln$_2$S$_2$O (Ln = Er, Tm, Yb): high pressure synthesis and crystal structure. *J. Less Common Met.* 158, 137–145. doi: 10.1016/0022-5088(90)90440-U

Resende, L. V., and Morais, C. A. (2015). Process development for the recovery of europium and yttrium from computer monitor screens. *Miner. Eng.* 70, 217–221. doi: 10.1016/j.mineng.2014.09.016

Ronda, C., Jüstel, T., and Nikol, H. (1998). Rare earth phosphors: fundamentals and applications. *J. Alloys Compd.* 275–277, 669–676. doi: 10.1016/S0925-8388(98)00416-2

Rossner, W., and Grabmaier, B. C. (1991). Phosphors for X-Ray detectors in computed tomography. *J. Lumin.* 48–49, 29–36. doi: 10.1016/0022-2313(91)90072-4

Rosticher, C., Viana, B., Fortin, M. A., Lagueux, J., Faucher, L., and Chanéac, C. (2016). Gadolinium oxysulfide nanoprobes with both persistent luminescent and magnetic properties for multimodal imaging. *RSC Adv.* 6, 55472–55478. doi: 10.1039/C6RA05030A

Royce, M. R. (1968). *Rare Earth Activated Yttrium and Gadolinium Oxy-Chalcogenide Phosphors.* U.S. Patent N°3418246.

Rutt, O. J., Hill, T. L., Gál, Z. A., Hayward, M. A., and Clarke, S. J. (2003). The cation-deficient ruddlesden–popper oxysulfide Y$_2$Ti$_2$O$_5$S$_2$ as a layered sulfide: topotactic potassium intercalation to form KY$_2$Ti$_2$O$_5$S$_2$. *Inorg. Chem.* 42, 7906–7911. doi: 10.1021/ic0301730

Salter, E. J. T., Blandy, J. N., and Clarke, S. J. (2016). Crystal and magnetic structures of the oxide sulfides CaCoSO and BaCoSO. *Inorg. Chem.* 55, 1697–1701. doi: 10.1021/acs.inorgchem.5b02615

Sambrook, T., Smura, C. F., Clarke, S. J., Ok, K. M., and Halasyamani, P. S. (2007). Structure and physical properties of the polar oxysulfide CaZnOS. *Inorg. Chem.* 46, 2571–2574. doi: 10.1021/ic062120z

Santelli, J., Lechevallier, S., Baaziz, H., Vincent, M., Martinez, C., Mauricot, R., et al. (2018). Multimodal gadolinium oxysulfide nanoparticles: a versatile contrast agent for mesenchymal stem cell labeling. *Nanoscale* 10, 16775–16786. doi: 10.1039/C8NR03263G

Schleid, T. (1991a). A new oxysulfide of terbium - Tb$_2$OS$_2$. *Eur. J. Solid State Inorg. Chem.* 28, 557–562.

Schleid, T. (1991b). Zwei formen von Dy$_2$OS$_2$. *Zeitschrift für Anorg. und Allg. Chemie* 602, 39–47. doi: 10.1002/zaac.19916020105

Schleid, T. (1992). Crystal structures of D-Y$_2$S$_3$ and Y$_2$OS$_2$. *Eur. J. Solid State Inorg. Chem.* 29, 1015–1028.

Schleid, T., and Weber, F. A. (1998). Crystal structure of dekagadoliiiium(III) oxide tetradekasulfide, Gd$_{10}$OS$_{14}$. *Zeitschrift für Krist* 213:32. doi: 10.1524/ncrs.1998.213.14.32

Schmidt, E., Meunier, G., and Levasseur, A. (1995a). Electrochemical properties of new amorphous molybdenum oxysulfide thin films. *Solid State Ionics* 76, 243–247. doi: 10.1016/0167-2738(94)00284-Y

Schmidt, E., Sourisseau, C., Meunier, G., and Levasseur, A. (1995b). Amorphous molybdenum oxysulfide thin films and their physical characterization. *Thin Solid Films* 260, 21–25. doi: 10.1016/0040-6090(94)06463-6

Schmidt, E., Weill, F., Meunier, G., and Levasseur, A. (1994). New amorphous molybdenum oxysulfides obtained in the form of thin films and their characterization by TEM. *Thin Solid Films* 245, 34–39. doi: 10.1016/0040-6090(94)90873-7

Selivanov, E. N., Chumarev, V. M., Gulyaeva, R. I., Mar'evich, V. P., Vershinin, A. D., Pankratov, A. A., et al. (2004). Composition, structure, and thermal expansion of Ca$_3$Fe$_4$S$_3$O$_6$ and CaFeSO. *Inorg. Mater.* 40, 845–850. doi: 10.1023/B:INMA.0000037931.30753.56

Selwyn, L., McKinnon, W., and Dahn, J. (1987). Lack of oxygen substitution in the chevrel compound Mo$_6$S$_8$. *Solid State Commun.* 64, 1025–1028. doi: 10.1016/0038-1098(87)91023-4

Sheets, W. C., Stampler, E. S., Kabbour, H., Bertoni, M. I., Cario, L., Mason, T. O., et al. (2007). Facile synthesis of BiCuOS by hydrothermal methods. *Inorg. Chem.* 46, 10741–10748. doi: 10.1021/ic7014622

Shi, L., Sordillo, L. A., Rodríguez-Contreras, A., and Alfano, R. (2016). Transmission in near-infrared optical windows for deep brain imaging. *J. Biophotonics* 9, 38–43. doi: 10.1002/jbio.201500192

Sinsermsuksakul, P., Hartman, K., Bok Kim, S., Heo, J., Sun, L., Hejin Park, H., et al. (2013). Enhancing the efficiency of SnS solar cells via band-offset engineering with a zinc oxysulfide buffer layer. *Appl. Phys. Lett.* 102:053901. doi: 10.1063/1.4789855

Smith, L. A. C., Trudeau, M. L., Provencher, M., Smith, M. E., and Antonelli, D. M. (2016). Low-temperature synthesis and electrochemical properties of mesoporous titanium oxysulfides. *ChemElectroChem* 3, 256–265. doi: 10.1002/celc.201500463

Smura, C. F., Parker, D. R., Zbiri, M., Johnson, M. R., Gál, Z. A., and Clarke, S. J. (2011). High-spin cobalt(II) ions in square planar coordination: structures and magnetism of the oxysulfides Sr$_2$CoO$_2$Cu$_2$S$_2$ and Ba$_2$CoO$_2$Cu$_2$S$_2$ and their solid solution. *J. Am. Chem. Soc.* 133, 2691–2705. doi: 10.1021/ja109553u

So, W. W., LaCour, A., Aliev, V. O., and Dorhout, P. K. (2004). Synthesis and characterization of a new quaternary lanthanum oxythioantimonite: La$_6$Sb$_4$O$_{12}$S$_3$. *J. Alloys Compd.* 374, 234–239. doi: 10.1016/j.jallcom.2003.11.108

Song, Y., You, H., Huang, Y., Yang, M., Zheng, Y., Zhang, L., et al. (2010). Highly uniform and monodisperse Gd$_2$O$_2$S:Ln$^{3+}$ (Ln = Eu, Tb) submicrospheres: solvothermal synthesis and luminescence properties. *Inorg. Chem.* 49, 11499–11504. doi: 10.1021/ic101608b

Sterba, J. (1904). Contribution to the study of several combinations of cerium. *Ann. Chim. Phys.* 2, 193–232.

Stocks, K., Eulenberger, G., and Hahn, H. (1980). Darstellung und kristallstruktur von HfOS. *Zeitschrift Anorg. Allg. Chem.* 463, 105–109. doi: 10.1002/zaac.19804630114

Sun, W., Zhu, K., Xu, H., Yang, X., Yu, M., Li, X., et al. (2017). Enhanced absorbing property of Sm$_2$O$_2$S laser absorbant by doping Er$^{3+}$/Tm$^{3+}$. *J. Mater. Sci. Mater. Electron.* 28, 697–701. doi: 10.1007/s10854-016-5578-y

Sutorik, A. C., and Kanatzidis, M. G. (1994). Ba$_6$Ti$_5$S$_{15}$O: a new metal/oxysulfide resulting from the inclusion of BaO into the BaTiS$_3$ structure type. *Chem. Mater.* 6, 1700–1704. doi: 10.1021/cm00046a023

Suzuki, T., Hisatomi, T., Teramura, K., Shimodaira, Y., Kobayashi, H., and Domen, K. (2012). A titanium-based oxysulfide photocatalyst: La$_5$Ti$_2$MS$_5$O$_7$ (M = Ag, Cu) for water reduction and oxidation. *Phys. Chem. Chem. Phys.* 14, 15475–15481. doi: 10.1039/c2cp43132g

Tan, S., and Li, D. (2017). Enhancing oxygen storage capability and catalytic activity of lanthanum oxysulfide (La$_2$O$_2$S) nanocatalysts by sodium and iron/sodium doping. *ChemCatChem* 10, 550–558. doi: 10.1002/cctc.201701117

Tan, S., Paglieri, S. N., and Li, D. (2016). Nano-scale sulfur-tolerant lanthanide oxysulfide/oxysulfate catalysts for water–gas-shift reaction in a novel reactor configuration. *Catal. Commun.* 73, 16–21. doi: 10.1016/j.catcom.2015.10.007

Tanryverdiev, V. S., Aliev, O. M., and Aliev, I. I. (1995). Synthesis and physicochemical properties of LnBiOS$_2$. *Inorg. Mater.* 31, 1361–1363.

Tchangbedji, G., Odink, D. A., and Ouvrard, G. (1993). V$_2$O$_4$S — a new transition metal oxysulfide as positive for lithium batteries. *J. Power Sources* 44, 577–581. doi: 10.1016/0378-7753(93)80205-4

Tchangbédji, G., Prouzet, E. P., and Ouvrard, G. (1994). A new soft chemistry synthesized vanadium oxysulfide. *Mater. Sci. Forum* 152–153, 319–322. doi: 10.4028/www.scientific.net/MSF.152-153.319

Teske, C. L. (1985). Über oxidsulfide mit akermanitstruktur CaLaGa$_3$S$_6$O, SrLaGa$_3$S$_6$O, La$_2$ZnGa$_2$S$_6$O und Sr$_2$ZnGe$_2$S$_6$O. *Zeitschrift Anorg. Allg. Chem.* 531, 52–60. doi: 10.1002/zaac.19855311208

Thankalekshmi, R. R., and Rastogi, A. C. (2012). Structure and optical band gap of ZnO$_{1-x}$S$_x$ thin films synthesized by chemical spray pyrolysis for application in solar cells. *J. Appl. Phys.* 112:063708. doi: 10.1063/1.4754014

Thirumalai, J., Chandramohan, R., Auluck, S., Mahalingam, T., and Srikumar, S. R. (2009b). Controlled synthesis, optical and electronic properties of Eu$^{3+}$ doped yttrium oxysulfide (Y$_2$O$_2$S) nanostructures. *J. Colloid Interface Sci.* 336, 889–897. doi: 10.1016/j.jcis.2009.04.042

Thirumalai, J., Chandramohan, R., Divakar, R., Mohandas, E., Sekar, M., and Parameswaran, P. (2008b). Eu$^{3+}$ doped gadolinium oxysulfide (Gd$_2$O$_2$S) nanostructures—synthesis and optical and electronic properties. *Nanotechnology* 19:395703. doi: 10.1088/0957-4484/19/39/395703

Thirumalai, J., Chandramohan, R., Sekar, M., and Rajachandrasekar, R. (2008a). Eu$^{3+}$ doped yttrium oxysulfide quantum structures—structural, optical and electronic properties. *J. Nanoparticle Res.* 10, 455–463. doi: 10.1007/s11051-007-9276-9

Thirumalai, J., Chandramohan, R., Valanarasu, S., Vijayan, T., a., Somasundaram, R. M., et al. (2009a). Shape-selective synthesis and opto-electronic properties of Eu$^{3+}$-doped gadolinium oxysulfide nanostructures. *J. Mater. Sci.* 44, 3889–3899. doi: 10.1007/s10853-009-3531-7

Thirumalai, J., Chandramohan, R., Valanarasu, S., Vijayan, T. A., and Ezhilvizhian, S. (2011a). Synthesis and chemical properties of Y$_2$O$_2$S:Eu$^{3+}$ nanostructures using composite-hydroxide-mediated method. *Micro Nano Lett.* 6, 614–618. doi: 10.1049/mnl.2011.0252

Thirumalai, J., Chandramohan, R., and Vijayan, T. A. (2011b). Synthesis, characterization and formation mechanism of monodispersed Gd$_2$O$_2$S:Eu$^{3+}$ nanocrystals. *J. Mater. Sci. Mater. Electron.* 22, 936–943. doi: 10.1007/s10854-010-0240-6

Thirumalai, J., Jagannathan, R., and Trivedi, D. C. (2007). Y$_2$O$_2$S:Eu$^{3+}$ nanocrystals, a strong quantum-confined luminescent system. *J. Lumin.* 126, 353–358. doi: 10.1016/j.jlumin.2006.08.064

Thomson, J. W., Nagashima, K., Macdonald, P. M., and Ozin, G. A. (2011). From sulfur–amine solutions to metal sulfide nanocrystals: peering into the oleylamine–sulfur black box. *J. Am. Chem. Soc.* 133, 5036–5041. doi: 10.1021/ja1109997

Tian, Y., Fu, Y., Xing, M., and Luo, X. (2015). Upconversion luminescence properties of Y$_2$O$_3$:Yb, Er and Y$_2$O$_2$S:Yb, Er nanoparticles prepared by complex precipitation. *J. Nanomater.* 2015:573253. doi: 10.1155/2015/573253

Tian, Y., Lu, F., Xing, M., Ran, J., Fu, Y., Peng, Y., et al. (2017). Upconversion luminescence properties of Y$_2$O$_2$S:Er$^{3+}$@Y$_2$O$_2$S:Yb$^{3+}$,Tm$^{3+}$ core-shell nanoparticles prepared via homogeneous co-precipitation. *Opt. Mater.* 64, 58–63. doi: 10.1016/j.optmat.2016.11.031

Tien, V., Guittard, M., Dugué, J., and Flahaut, J. (1988). Les combinaisons U$_2$R$_{2n-2}$O$_{2n}$S$_{n+1}$ Formées Par Les Lanthanides Légers (R = Ce à Tb) avec n = 2 et 3 et dans le cas du lanthane avec N= 2 à 6. *J. Solid State Chem.* 73, 11–18. doi: 10.1016/0022-4596(88)90047-3

Tillinski, R., Näther, C., Winkler, B., and Bensch, W. (2001). Synthesis and crystal structure of K$_6$Ti$_6$S$_{18}$O: a new coordination compound containing discrete Ti$_6$O units in a chalcogenide environment. *Zeitschrift Anorg. Allg. Chem.* 627, 2576–2580. doi: 10.1002/1521-3749(200112)627:12<2576::AID-ZAAC2576>3.0.CO;2-A

Tóth, É., Helm, L., and Merbach, A. E. (2002). "Relaxivity of MRI contrast agents," in *Topics in Current Chemistry*, ed W. Krause (Berlin; Heidelberg: Springer), 221. doi: 10.1007/3-540-45733-X_3

Tranchitella, L. J., Fettinger, J. C., and Eichhorn, B. W. (1996). Synthesis and structural analysis of Sr$_{5.8}$La$_{4.4}$Ti$_{7.8}$S$_{24}$O$_4$ and La$_{14}$Ti$_8$S$_{33}$O$_4$ : two new oxysulfides containing a common [(Ti$_4$S$_2$O$_4$)(TiS$_6$)$_{4/2}$]$^{12-}$ layer. *Chem. Mater.* 8, 2265–2271. doi: 10.1021/cm960001j

Tranchitella, L. J., Fettinger, J. C., Heller-Zeisler, S. F., and Eichhorn, B. W. (1998). La$_{8+x}$ Ti$_{8+y}$ S$_{24}$O$_4$ compounds where x + y ≤ 2: a series of phases with mixed-valent titanium. *Chem. Mater.* 10, 2078–2085. doi: 10.1021/cm970663o

Tsujimoto, Y., Juillerat, C. A., Zhang, W., Fujii, K., Yashima, M., Halasyamani, P. S., et al. (2018). Function of tetrahedral ZnS$_3$O building blocks in the formation of SrZn$_2$S$_2$O: a phase matchable polar oxysulfide with a large second harmonic generation response. *Chem. Mater.* 30, 6486–6493. doi: 10.1021/acs.chemmater.8b02967

Ueda, K., Takafuji, K., and Hosono, H. (2003). Preparation and crystal structure analysis of CeCuOS. *J. Solid State Chem.* 170, 182–187. doi: 10.1016/S0022-4596(02)00061-0

Umarji, A. M., Rao, G. V. S., Sankaranarayana, V., Rangarajan, G., and Srinivasan, R. (1980). Synthesis and properties of O-containing chevrel phases, A$_x$Mo$_6$S$_6$O$_2$ (A = Co, Ni, Cu and Pb). *Mater. Res. Bull.* 15, 1025–1031. doi: 10.1016/0025-5408(80)90229-9

Valldor, M., Rößler, U. K., Prots, Y., Kuo, C.-Y., Chiang, J. C., Hu, Z., et al. (2015). Synthesis and characterization of Ba[CoSO]: magnetic complexity in the presence of chalcogen ordering. *Chem. A Eur. J.* 21, 10821–10828. doi: 10.1002/chem.201501024

Verelst, M. Dexpert-Ghys, J., Marchin, L., Mauricot, R., Osseni, S. A., and Lechevallier, S. (2010). *Nanoparticules Luminescentes Utilisables En Tant que Marqueurs Et Procede Pour Leur Preparation*. French patent: FR1057296/14-09-2010.

Vovan, T., Dugué, J., and Guittard, M. (1978). Oxysulfures mixtes de chrome III et de terres rares. *Mater. Res. Bull.* 13, 1163–1166. doi: 10.1016/0025-5408(78)90204-0

Vovan, T., Dugué, J., and Guittard, M. (1981). Oxysulfures mixtes de vanadium et de terre rare de formule generale R$_5$V$_3$S$_6$O$_7$ (R = lanthane a neodyme). *Comptes Rendus l'Acad. Sci.* 292, 957–959.

Wang, G., Zou, H., Zhang, B., Sun, Y., Huo, Q., Xu, X., et al. (2015). Preparation and luminescent properties of 1D Lu2O2S:Eu3+ Nanorods. *Opt. Mater. (Amst).* 45, 131–135. doi: 10.1016/j.optmat.2015.03.020

Wang, W., Dahl, M., and Yin, Y. (2013). Hollow nanocrystals through the nanoscale kirkendall effect. *Chem. Mater.* 25, 1179–1189. doi: 10.1021/cm3030928

Wang, Z., Cheng, P., He, P., Hu, F., Luo, L., and Zhou, Q. (2014). Controlled Y$_2$O$_2$S: Eu$^{3+}$ nanocrystals prepared by the molten salt synthesis for solid state lighting. *Nanosci. Nanotechnol. Lett.* 6, 1053–1057. doi: 10.1166/nnl.2014.1878

Weber, T., Muijsers, J. C., van Wolput, J. H. M. C., Verhagen, C. P. J., and Niemantsverdriet, J. W. (1996). Basic reaction steps in the sulfidation of crystalline MoO$_3$ to MoS$_2$ as studied by X-Ray photoelectron and infrared emission spectroscopy. *J. Phys. Chem.* 100, 14144–14150. doi: 10.1021/jp961204y

Wichelhaus, W. (1978a). The rare-earth oxide disulfides La$_2$O$_2$S$_2$, Pr$_2$O$_2$S$_2$, and Nd$_2$O$_2$S$_2$. *Naturwissenschaften* 65, 593–594. doi: 10.1007/BF00364913

Wichelhaus, W. (1978b). Ce$_4$O$_4$S$_3$: a mixed-valence cerium oxide sulfide. *Angew. Chemie Int. Ed.* 17, 451–452. doi: 10.1002/anie.197804511

Wontcheu, J., and Schleid, T. (2003). Crystal structure of digadolinium(III) oxide disulfide, Gd$_2$OS$_2$. *Zeitschrift für Krist.* 218, 285–286. doi: 10.1524/ncrs.2003.218.jg.307

Xing, M., Cao, W., Pang, T., and Ling, X. (2009). Synthesis of monodisperse spherical Y$_2$O$_2$S:Yb,Ho upconversion nanoparticles. *Solid State Commun.* 149, 911–914. doi: 10.1016/j.ssc.2009.03.031

Yan, X., Fern, G. R., Withnall, R., and Silver, J. (2013a). Effects of the host lattice and doping concentration on the colour of Tb$^{3+}$ cation emission in Y$_2$O$_2$S:Tb$^{3+}$ and Gd$_2$O$_2$S:Tb$^{3+}$ nanometer sized phosphor particles. *Nanoscale* 5, 8640–8646. doi: 10.1039/c3nr01034a

Yan, X., Fern, G. R., Withnall, R., and Silver, J. (2013b). Contrasting behaviour of the co-activators in the luminescence spectra of $Y_2O_2S:Tb^{3+}$, $Er^{3+}$ nanometre sized particles under UV and red light excitation. *Nanoscale* 5, 1091–1096. doi: 10.1039/C2NR33391K

Yang, G., Yan, Z., and Xiao, T. (2012). Low-temperature solvothermal synthesis of visible-light-responsive S-doped $TiO_2$ nanocrystal. *Appl. Surf. Sci.* 258, 4016–4022. doi: 10.1016/j.apsusc.2011.12.092

Yang, L., Cai, Z., Hao, L., Xing, Z., Dai, Y., Xu, X., et al. (2017). Nano $Ce_2O_2S$ with highly enriched oxygen-deficient $Ce^{3+}$ sites supported by N and S dual-doped carbon as an active oxygen-supply catalyst for the oxygen reduction reaction. *ACS Appl. Mater. Interfaces* 9, 22518–22529. doi: 10.1021/acsami.7b04997

Yee, C.-H., Birol, T., and Kotliar, G. (2015). Guided design of copper oxysulfide superconductors. *Europhys. Lett.* 111:17002. doi: 10.1209/0295-5075/111/17002

Yu, R., An, Y., Wang, C., Wang, H., Wu, Y., Chen, J., et al. (2012). Tunable yellowish-green to green $(Ca_{1-x}Sr_x)LaGa_3S_6O:Eu^{2+}$ phosphors for potential LED application. *Electrochem. Solid-State Lett.* 15:J1. doi: 10.1149/2.017201esl

Yu, R., Deng, B., Zhang, G., An, Y., Zhang, J., and Wang, J. (2011). Luminescence properties of $Ce^{3+}$-activated $SrLaGa_3S_6O$ and application in white LEDs. *J. Electrochem. Soc.* 158, J255–J259. doi: 10.1149/1.3601850

Yu, R., Wang, J., Zhang, M., Zhang, J., Yuan, H., and Su, Q. (2008). A new blue-emitting phosphor of $Ce^{3+}$-activated $CaLaGa_3S_6O$ for white-light-emitting diodes. *Chem. Phys. Lett.* 453, 197–201. doi: 10.1016/j.cplett.2008.01.039

Yuan, G., Li, M., Yu, M., Tian, C., Wang, G., and Fu, H. (2016). *In Situ* synthesis, enhanced luminescence and application in dye sensitized solar cells of $Y_2O_3/Y_2O_2S:Eu^{3+}$ nanocomposites by reduction of $Y_2O_3:Eu^{3+}$. *Sci. Rep.* 6:37133. doi: 10.1038/srep37133

Yufit, V., Nathan, M., Golodnitsky, D., and Peled, E. (2003). Thin-film lithium and lithium-ion batteries with electrochemically deposited molybdenum oxysulfide cathodes. *J. Power Sources* 122, 169–173. doi: 10.1016/S0378-7753(03)00401-4

Zachariasen, W. H. (1949a). Crystal chemical studies of the 5f-series of elements. VII. The crystal structure of $Ce_2O_2S$, $La_2O_2S$ and $Pu_2O_2S$. *Acta Crystallogr.* 2, 60–62. doi: 10.1107/S0365110X49000138

Zachariasen, W. H. (1949b). Crystal chemical studies of the 5 f -series of elements. X. sulfides and oxysulfides. *Acta Crystallogr.* 2, 291–296. doi: 10.1107/S0365110X49000758

Zhang, G., Cui, Q., and Liu, G. (2016). Efficient near-infrared quantum cutting and downshift in $Ce^{3+}$-$Pr^{3+}$ Codoped $SrLaGa_3S_6O$ suitable for solar spectral converter. *Opt. Mater.* 53, 214–217. doi: 10.1016/j.optmat.2016.01.042

Zhang, G., Liu, C., Wang, J., Kuang, X., and Su, Q. (2011). An intense charge transfer broadband sensitized near-infrared emitting $CaLaGa_3S_6O:Yb^{3+}$ phosphor suitable for solar spectral convertor. *Opt. Express* 19, 24314–24319. doi: 10.1364/OE.19.024314

Zhang, G., Liu, C., Wang, J., Kuang, X., and Su, Q. (2012). A dual-mode solar spectral converter $CaLaGa_3S_6O:Ce^{3+},Pr^{3+}$: UV-Vis-NIR luminescence properties and solar spectral converting mechanism. *J. Mater. Chem.* 22, 2226–2232. doi: 10.1039/C1JM14942C

Zhang, G., Wang, J., Chen, Y., and Su, Q. (2010). Two-Color Emitting of $Ce^{3+}$ and $Tb^{3+}$ co-doped $CaLaGa_3S_6O$ for UV LEDs. *Opt. Lett.* 35, 2382–2384. doi: 10.1364/OL.35.002382

Zhang, H., Liu, G., Cao, Y., Chen, J., Shen, K., Kumar, A., et al. (2017). The magnetic and adsorption properties of $ZnO_{1-x}S_x$ nanoparticles. *Phys. Chem. Chem. Phys.* 19, 26918–26925. doi: 10.1039/C7CP03470A

Zhang, P., Hong, Z., Wang, M., Fang, X., Qian, G., and Wang, Z. (2005b). Luminescence characterization of a new long afterglow phosphor of single Ti-Doped $Y_2O_2S$. *J. Lumin.* 113, 89–93. doi: 10.1016/j.jlumin.2004.08.056

Zhang, T., Gu, J., Ding, Y., Zhang, Y. W., and Yan, C. H. (2013). Experimental and theoretical studies on the controlled synthesis of alkali-metal-doped rare-earth oxysulfide nanocrystals. *Chempluschem* 78, 515–521. doi: 10.1002/cplu.201300092

Zhang, X., Liu, Y., Zhang, G., Wang, Y., Zhang, H., and Huang, F. (2015). Thermal decomposition of bismuth oxysulfide from photoelectric $Bi_2O_2S$ to superconducting $Bi_4O_4S_3$. *ACS Appl. Mater. Interfaces* 7, 4442–4448. doi: 10.1021/am5092159

Zhang, X., Zhang, J., Xu, J., and Su, Q. (2005a). Luminescent properties of $Eu^{2+}$-activated $SrLaGa_3S_6O$ phosphor. *J. Alloys Compd.* 389, 247–251. doi: 10.1016/j.jallcom.2004.06.092

Zhao, F., Sun, H. L., Su, G., and Gao, S. (2006b). Synthesis and size-dependent magnetic properties of monodisperse EuS nanocrystals. *Small* 2, 244–248. doi: 10.1002/smll.200500294

Zhao, F., Yuan, M., Zhang, W., and Gao, S. (2006a). Monodisperse lanthanide oxysulfide nanocrystals. *J. Am. Chem. Soc.* 128, 11758–11759. doi: 10.1021/ja0638410

Zhu, K., Ding, W., Sun, W., Han, P., Wang, L., and Zhang, Q. (2016). 1.06 Mm laser absorption properties of $Sm_2O_2S$ prepared by flux method. *J. Mater. Sci. Mater. Electron.* 27, 2379–2384. doi: 10.1007/s10854-015-4035-7

Zhu, W. J., and Hor, P. H. (1997a). Unusual layered transition-metal oxysulfides: $Sr_2Cu_2MO_2S_2$(M=Mn, Zn). *J. Solid State Chem.* 130, 319–321. doi: 10.1006/jssc.1997.7299

Zhu, W. J., and Hor, P. H. (1997b). Crystal structure of new layered oxysulfides: $Sr_3Cu_2Fe_2O_5S_2$ and $Sr_2CuMO_3S$ (M=Cr, Fe, In). *J. Solid State Chem.* 134, 128–131. doi: 10.1006/jssc.1997.7556

Zhu, W. J., and Hor, P. H. (1997c). $Sr_2CuGaO_3S$, a rare example of square pyramidal gallium. *Inorg. Chem.* 36, 3576–3577. doi: 10.1021/ic970322c

Zhu, W. J., Hor, P. H., Jacobson, A. J., Crisci, G., Albright, T. A., Wang, S. H., et al. (1997). $A_2Cu_2CoO_2S_2$ (A = Sr, Ba), a novel example of a square-planar $CoO_2$ layer. *J. Am. Chem. Soc.* 119, 12398–12399. doi: 10.1021/ja972542v

**Conflict of Interest:** The authors declare that the research was conducted in the absence of any commercial or financial relationships that could be construed as a potential conflict of interest.

frontiers
in Chemistry

Check for
updates

# Review of the Biomolecular Modification of the Metal-Organ-Framework

Qiqi Xing, Yixiao Pan, Yihe Hu and Long Wang*

*Department of Orthopedics, Xiangya Hospital, Central South University, Changsha, China*

Metal-organ frameworks (MOFs), as a kind of novel artificial material, have been widely studied in the field of chemistry. MOFs are capable of high loading capacities, controlled release, plasticity, and biosafety because of their porous structure and have been gradually functionalized as a drug carrier. Recently, a completely new strategy of combining biomolecules, such as oligonucleotides, polypeptides, and nucleic acids, with MOF nanoparticles was proposed. The synthetic bio-MOFs conferred strong protection and endowed the MOFs with particular biological functions. Biomolecular modification of MOFs to form bridges for communication between different subjects has received increased attention. This review will focus on bio-MOFs modification methods and discuss the advantages, applications, prospects, and challenges of using MOFs in the field of biomolecule delivery.

Keywords: MOF, biomolecular, modification, delivery, nano material

## BACKGROUND

The metal-organ framework (MOF), which is also known as a porous coordination polymer (PCP), is a kind of novel nanomaterial composed of metals or metal clusters, chains or layers formed by non-toxic metals (Fe, Zn, Ca, Mg, etc.) and organic compounds, such as carboxylic acid and phosphonic acid (Férey, 2008). PCPs have been widely used in the fields of chemistry and material science in applications such as gas separation and storage (Eddaoudi et al., 2002), sensing (Xu et al., 2011), catalysis (Zhuang et al., 2015), and chromatography (Li et al., 2009; Xiao et al., 2009). MOFs have a porous structure with pore sizes between 0.4 and 6 nm (Zhou et al., 2012). The inherent pore size and structure can be modulated according to the organic-metal compound category and the spatial arrangement. These characteristics enable MOFs to possess open architectures that allow them to combine with, penetrate, and encapsulate a variety of molecules. Therefore, MOFs are ideal materials for storage, protection (Liang et al., 2016b) and carrier functions (Morris and Wheatley, 2008). Recently, non-toxic and biocompatible MOFs, as newly developed materials, have been recommended for use in biological field applications, such as bio-imaging, drug delivery, and electrocatalysis (Huxford et al., 2010; Cai et al., 2015), and these functions were primarily achieved by incorporation of drugs or biological molecules with MOFs (Wang et al., 2015). Increasing numbers of drugs have been combined with different kinds of MOFs, including isoniazid (INH), which is a traditional antitubercular agent that has been loaded onto Fe-MIL-101-NH$_2$ nanoparticles to control the release of the drug and improve absorption by macrophages (Wyszogrodzka-Gaweł et al., 2019). An antibiotic (vancomycin) and targeting ligand (folic acid) could also be combined with zeolitic imidazolate framework (ZIF-8) nano MOFs to be delivered to *Staphylococcus aureus* to control infection (Chowdhuri et al., 2017). Furthermore,

loading with antitumoral and retroviral drugs to fight cancer and AIDS has greatly inspired MOF research (Horcajada et al., 2009). These successes have promoted the development of MOFs for use in the field of biology.

Biomolecules are special organic molecules produced by living systems, including nucleic acids, proteins, polysaccharides, and lipids, which cannot easily pass through a cell membrane due to their large weight and volume. Biomolecules can also be present on the cell membrane alone, but this occurs with difficulty (Whitehead et al., 2009) owing to the effect of serum nuclease (Keles et al., 2016). Delivery systems have emerged to offer superior thermal and chemical protection for biomacromolecular cargo, which is mainly divided into virus and non-viral vectors (Yoo et al., 2011; Kotterman et al., 2015). Compared with non-viral vectors, the low selectivity, potentially unsafe nature, and insertion mutations (Thomas et al., 2003; Waehler et al., 2007; Mintzer and Simanek, 2009) of viruses have limited their application in living bodies. Non-viral vectors, including organic carriers (liposomes, polymers, peptides, etc.) and inorganic carriers (silica, carbon tubes, calcium phosphate, etc.) (Sokolova and Epple, 2008; Nam et al., 2009), are also considered to be defective (Yin et al., 2014; Chira et al., 2015). Among them, poly-L-lysine, which is a cationic polymer, is one of the most common polymers used for DNA delivery (Khalil et al., 2006; Cheng and Lee, 2016). However, its biotoxicity, as well as its ATPase reduction, autophagy (Lv et al., 2006) and immunogenic responses, cannot be ignored (Tseng et al., 2009; Wan et al., 2013). Additionally, as the only non-viral delivery systems currently in clinical trials, lipid microsystems (Ginn et al., 2018) have been suggested to form large aggregates that hinder the further transportation of nanoparticles in blood (Dash et al., 1999; Das et al., 2015). It is necessary to develop a new biomacromolecule carrier with good biocompatibility and biodegradability.

As porous nanomaterials, MOFs are capable of high loading capacities, controlled release, plasticity, and biosafety, which facilitate the selective transportation of nanomaterials through the porous network (An et al., 2012). MOFs have been proposed as an attractive alternative to mitigate drawbacks that other drug delivery systems (DDSs) face (Abanades Lazaro et al., 2020). Thus, MOFs have already served as a successful drug delivery platform (Zhao et al., 2011). However, there are many differences between drug and biomolecule delivery systems (Zhuang et al., 2017). First, the electrostatic interactions and covalent bonds used to incorporate drugs might not be suitable for the incorporation of biomolecules and MOFs. Second, MOF stability should be a consideration because the addition of biomolecules might change the crystal structure. Third, targeting will be expected. Last, but not the least, a controlled-release effect is another characteristic to be encouraged. Among these requirements, the most important is the effective protection of biomolecules from external factors. In addition, the simplicity and reproducibility of material manufacturing should also be taken into account (Morris and Wheatley, 2008; Imaz et al., 2011). At present, there are two ways to combine MOFs with biomolecules. One method involves growing or depositing metal ions and organics onto a two-dimensional plane to form MOFs films, which are used to physically wrap the target molecule

(Horcajada et al., 2011; Shekhah et al., 2011). The other method involves chemical bonding, including surface modification and internal encapsulation (Doonan et al., 2017), which is particularly useful due to its high stability, capacity, and affinity.

This review will focus on the reported methods of bio-MOFs functional synthesis, including surface modification and internal encapsulation, and further discuss the advantages, applications, prospects, and challenges of MOFs in the field of biomolecule delivery.

## MOF BIOFUNCTIONALIZATION BY SURFACE MODIFICATION

In pioneering research, the biochemical surface modification of nanomaterials has been applied to biological probes and cell imaging (Wang D. et al., 2019). To date, MOFs have been modified on their surface to meet specific requirements and achieve biological functionalization, such as targeted delivery and localized release (Meng et al., 2018). These characteristics greatly improve the performance and bioutilization of MOFs (Cai et al., 2017; Huang et al., 2018). Consequently, there are two generalizable methods that postsynthetically functionalize the bulk MOF structure with biomolecules (Wang et al., 2015). The first method is the covalent combination of the modifier with an anchor on the surface of prepared MOFs before MOF synthesis. Unlike the modification of a pre-synthesized organic linker, the second method involves the coordination of the modifier directly on the surface of the post-synthesized MOF. The chelation of metal ions with target molecules is responsible for the connection (Deria et al., 2015). The unsaturated coordination metal sites on MOFs allow for the incorporation of biomolecules, and UiO-66 will be used to discern the two methods (**Figure 1**).

Via the first method, the conjugation of nucleic acid and azide-functionalized UiO-66-N$_3$ (Zr$_6$O$_4$OH$_4$(C$_8$H$_3$O$_4$-N$_3$)), which is transferred from UiO-66, was produced (Morris et al., 2014). Alkane terminal ligands could react with the azide group in UiO-66-N$_3$ via click reactions, which have been utilized to interface MOFs in bulk with a variety of organic functionalities. By the click reaction, UiO-66-N$_3$ was able to interact with dibenzyl-cyclooctyne (DBCO)-functionalized DNA and further realize cellular entry. Furthermore, the functionalized MOFs gained the ability to hybridize with diverse complementary nucleic acids in a sequence-specific fashion, which provided the possibility of the widespread bioapplication of this kind of MOF. However, the degree of DNA surface combination obtained by the first approach was approximately two times lower than that achieved by the other method, in which the surface modification of oligonucleotides resulted from metal–phosphate coordination through modified DNA and unsaturated metal sites on the MOF surface (Wang S. et al., 2017). In that process, chemically modified phosphonamidites at either the 3′ or 5′ end of the oligonucleotide were added into the colloidal suspension of synthesized UiO-66, and then the terminal phosphate moiety was adsorbed onto the MOF nanoparticles by coordination with the solvent-bound Zr sites (Deria et al., 2015). The affinity of the terminal

**FIGURE 1 |** Two methods for surface modification to MOF by DNA.
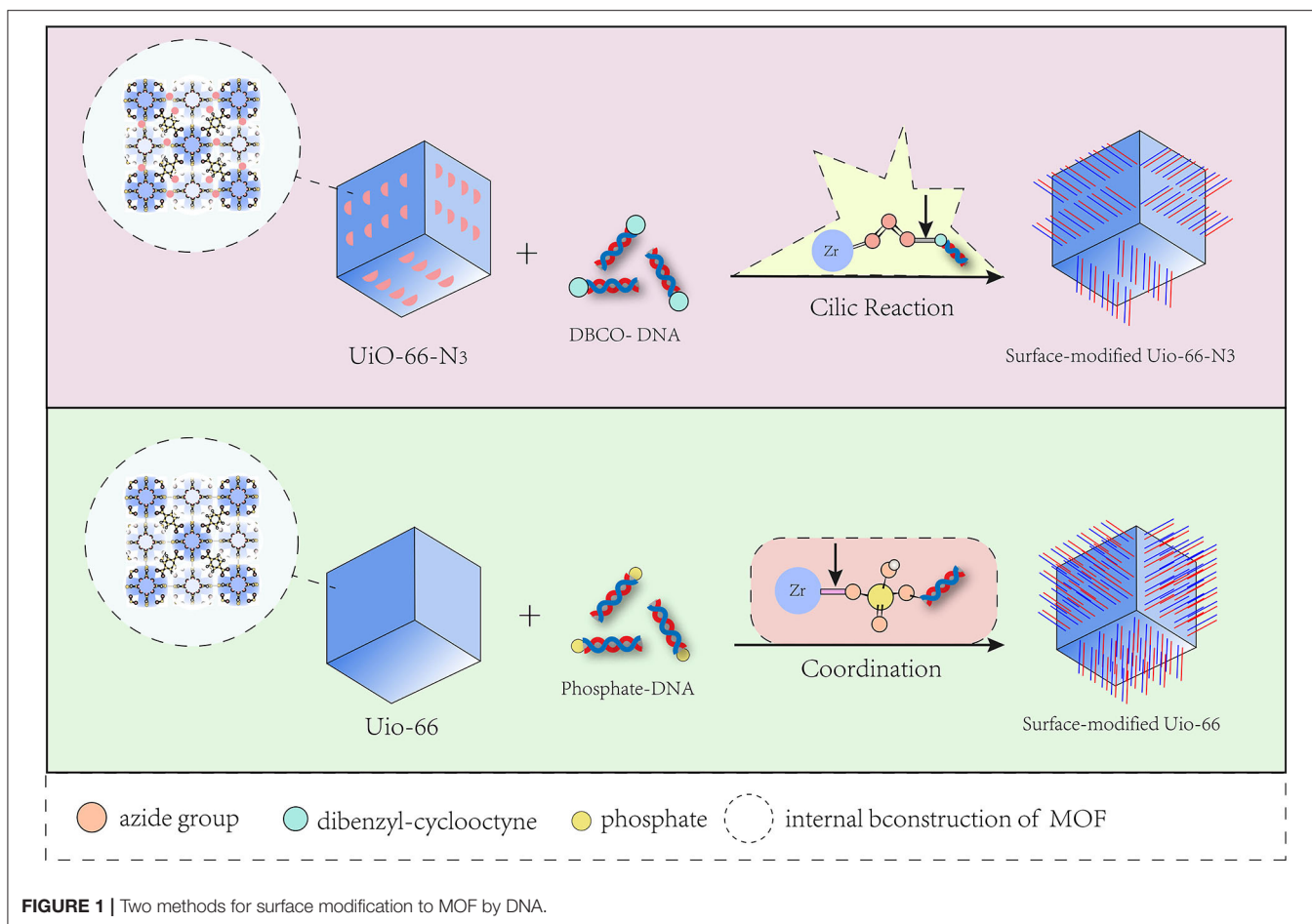
phosphate for the Zr centers was better than that of the internal phosphodiester bonds of oligonucleotides because of the increased steric hindrance encountered by the internal phosphodiester. In addition, the DNA surface coverage directly correlated with the surface second building unit (SBU) density, metal–phosphate coordination number, and bond strength of the MOF. Therefore, increased SBU coordination numbers yield higher DNA functionalization densities. Additionally, it should be mentioned that this approach to DNA-modified MOFs was independent of the category of organic linkers and was broadly applicable to a variety of metal clusters. This means that it is a general way to synthesize the regular structure of surface-modified DNA-MOFs. Based on this method, a research team then designed a nucleic acid-MOF nanoparticle using NU-1000 and PCN-222/MOF-545, which acted as a host to easily and effectively deliver a variety of proteins into cells (Wang S. et al., 2019).

Through in-depth research, many kinds of biomolecules have been developed for the surface modification with different MOFs, such as oligopeptides that form metal-peptide frameworks with copper and calcium due to carboxylic acid chelation (Mantion et al., 2008). Surface combination has become an important and general way to obtain biofunctionalized MOFs.

## MOF BIOFUNCTIONALIZATION BY INTERNAL MODIFICATION

Unlike surface modification, internal modification involves a higher-level combination, which involves the encapsulation of molecules by MOFs. The molecules can be better protected and bound more tightly by internal modification than by surface modification. Through encapsulation, MOFs could act as carriers to deliver large drugs and biomolecules, as well as to achieve the condition-triggered release of drugs from a vehicle (Roth et al., 2018). Compared with drugs, proteins, and nucleotides have more complicated multistructures, which means that conformational changes are always unavoidable and might disrupt their function (Wickner, 2005) when they are transported through nano channels to enter the cell. Therefore, a carrier would be necessary and important. Among nano delivery systems, MOFs are novel and outstanding. Taking enzymes as an example, MOF (Hudson et al., 2008) crystals have an increased encapsulation efficiency, recyclability, and an excellent enzyme-catalytic performance (Rapoport, 2007) compared to mesoporous silica (Lykourinou et al., 2011). However, biomacromolecules similar in size to MOF pores were hardly able to be loaded into the framework via postsynthetic infiltration (Chen et al., 2012). Recently, two methods for

encapsulating target molecules into MOFs at the beginning of synthesis were proposed. Here, we utilize zeolitic imidazolate frameworks (ZIFs) as an example because of their growth characteristics under mild biocompatible conditions (Zhuang et al., 2014) to describe two internally modified methods (**Figure 2**), which are coprecipitation (Lu et al., 2012; Shieh et al., 2015) and biomimetic mineralization (Liang et al., 2015).

The coprecipitation method was proposed by Lyu et al. (2014), who added a solution containing cytochrome c (cyt c) and polyvinylpyrrolidone (PVP) to a methanol solution of 2-methylimidazole and zinc nitrate hexahydrate to achieve cyt-ZIF nanoparticles. A transmission electron microscope (TEM) showed that $Zn^{2+}$ and 2-methylimidazole were first assembled into rod-shaped crystals. Then, rhombohedral dodecahedral crystals formed 24 h later, indicating that ZIF-8 was formed first, before the protein was embedded. In addition, Liu demonstrated the generality of coprecipitation by loading horseradish peroxidase and lipase onto ZIF-8 and ZIF-10. The biomimetic mineralization method was inspired by a natural process according to the specific ability of amino acids, peptides, and enzymes to concentrate inorganic cations in biominerals (Trzaskowski et al., 2007; Hwang et al., 2013). This is a new and simple method to rapidly encapsulate proteins, enzymes, and DNA into MOFs, as suggested by Liang et al. (2015). Bio-ZIF could be prepared by mixing an aqueous solution containing 2-methylimidazole and bovine serum albumin (BSA) with an aqueous solution of zinc acetate at room temperature, depending on the nucleation of the ZIF-8 precursor. Coordination between the Zn cations and the carbonyl group of the proteins is formed naturally. Different from the crystals separated from the mixture of ZIF-8 and BSA, the BSA-ZIF synthesized by mineralization was shown to encapsulate BSA and perfectly retain the structure of the enzyme. When the biomimetically mineralized ZIF-8 layer was removed via pH modulation, the released biomacromolecule retained its native activity. Additionally, the category of encapsulated biomacromolecules was enlarged by biomimetic mineralization, and the crystal morphology of bio-MOF had a unique dependence on the biomacromolecule.

Coprecipitation and biomimetic mineralization are generally known as "one-pot" methods because in both methods, biomolecules are initially mixed with MOF precursors and surrounded by grown MOF materials instead of occupying cavities. The difference is that PVP is utilized to functionalize the precursor and optimize the crystallization of ZIF-8 in coprecipitation. PVP is an amphiphilic, non-ionic polymer used as an efficient MOF nucleating agent to support size and shape control and stabilize nanoparticles during synthesis (Li and Zhang, 2006). In the mineralization method, the nucleation of precursors in an aqueous solution allows ZIF-8 to form a protective layer without PVP. According to a comparative study of the two methods, the loading rate of protein was equivalent. Compared with that of free enzymes, biomimetic mineralization expanded the temperature range of enzymatic biological activity, that is, within a certain temperature range, biomimetic mineralization would have a better protective effect on the enzyme than coprecipitation (Liang et al., 2016a).



**FIGURE 2 |** Two methods for internal modification to MOF by biomolecule.
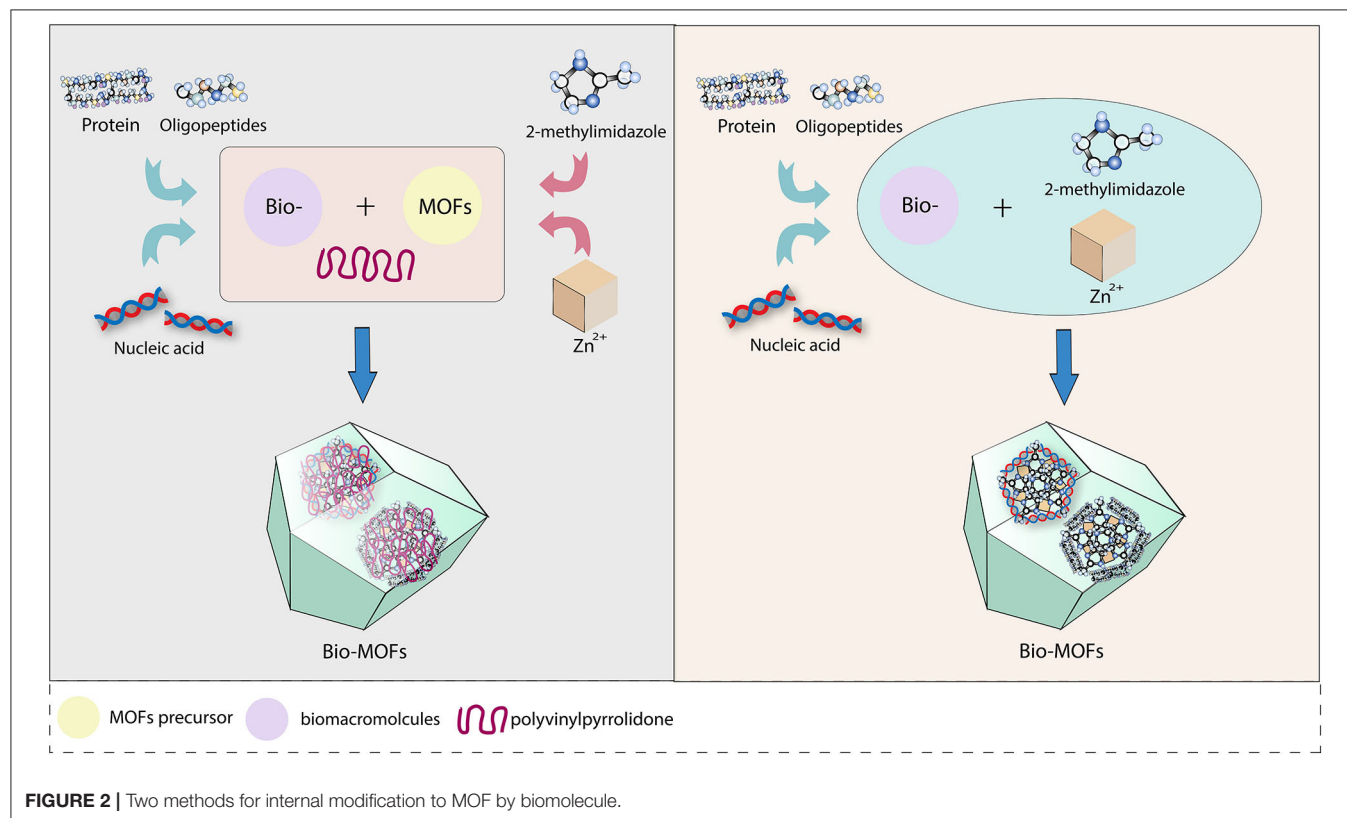
In addition, the stability of the enzymes encapsulated via biomimetic mineralization was enhanced, probably due to the rigid ZIF-8 structure restricting the structural rearrangement at elevated temperatures (Hartmann and Kostrov, 2013). Moreover, the distribution of cavities throughout the crystals was analyzed by thermal enzymatic decomposition, which indicated that this was more likely to expose the enzyme to the external environment in coprecipitation. In summary, mineralization was the preferred choice for biomolecule encapsulation (He et al., 2016).

In addition, the colloidal stability of the synthetic material should be considered seriously in terms of physiological factors, for example, protein-containing solution. The surface coating is proposed to stabilize the structure of nanoparticles, such as silica, (Della Rocca et al., 2011) hydrophobic polydimethysiloxane (PDMS) (Zhang et al., 2014), and hydrogel. Hydrogels are structurally various and functional materials composed of cross-linked hydrophilic polymers. The network endows a hydrogel with stability, which is a prominent advantage in embedding and protecting other materials. Additionally, the local release of cargo from a hydrogel can be achieved by degradation under specific environmental conditions. For instance, Cu-MOF has been embedded in poly-(polyethyleneglycol citrate-co-N-isopropylacrylamide) (PPCN), which is an intrinsically antioxidant thermoresponsive citrate-based hydrogel, and MOF NPs didn't degrade in a protein solution as a result of protection by the hydrogel coating (Xiao et al., 2016). The pH-sensitive carboxymethylcellulose (CMC) biopolymer was used to protect and carry the 5-FU encapsulated MOF-5 nanohybrid (5-FU@MOF-5) through the digestive system (Javanbakht et al., 2019). It should be mentioned that high biocompatibility and biodegradability are crucial properties of hydrogels, which bring numerous possibilities for use in the biomedical field (Fu et al., 2018). However, electronic interactions between positively charged metal ions in MOFs and negatively charged ions in hydrogels may limit gelation. The type of metal atoms in the MOF must be considered. In a word, the hydrogel coating method can be applied to entrap MOF NPs as a mechanism to slow degradation and thus prevent aggregation.

# ADVANTAGES, PROSPECTS, AND CHALLENGES

## Bio-MOF Advantages
### MOFs Remarkably Protect the Activity of Biomolecules

As nanoparticles synthesized from organic and inorganic components, MOFs are able to combine with a variety of molecules and offer superior thermal and chemical protection for their cargo (Liang et al., 2015). MOFs have been successfully developed not only in the field of drug release (Zhuang et al., 2014) but also in the study of biomacromolecules. The "micro enzyme" catalase (MP-11) and high-molecular weight molecules such as cytochrome c (104 amino acids), organophosphorus acid anhydrolase (440 amino acids) (Li et al., 2016), and bacillus subtilis lipase (BSL2) could be encapsulated by MOFs (He et al.,

2015). The framework could effectively maintain the skeletal integrity, biological activity, and reusability of proteins (Cao et al., 2016). It was reported that two enzymes, α-glucosidase (GAA) and glucose oxidase (GOx), could be assembled on one Cu-MOF molecule to generate a bifunctional hybrid enzyme-catalytic framework reactor, which could be utilized for the highly sensitive and stable screening of GAA inhibitors (Zhong et al., 2019). In terms of nucleic acids, low-molecular weight (MW) molecules such as oligonucleotide CpG ODNs (Zhang et al., 2017) and ssDNA (11, 22, 33, and 53 nucleotides) (Peng et al., 2018) have been wrapped and combined with MOFs. However, to the best of our knowledge, it is challenging to safely deliver nucleic acids with a high MW. The latest research showed that even macromolecular plasmid DNA could be successfully embedded into a ZIF-8 carrier by the biomimetic mineralization method (Li Y. et al., 2019), so that the pDNA could be protected when it passed through the cell membrane into the lysosome and to then be released around the cell nucleus (**Figure 3**). Additionally, a 25-kD polyethyleneimine (PEI) capping agent was added to improve the ZIF-8 crystal structure strength, loading capacity, pH-responsive release, and binding affinity to pDNA. The synthetic nanoparticle pDNA@ZIF-8-PEI 25 kD performed better than pDNA@ZIF-8, with improved gene expression and high transfection efficacy in various types of cells, possibly because of the enhanced positive charge that facilitated binding and internalization of the nucleic acid molecule. In summary, MOFs can be used as carriers of various biomolecules and play an effective protective role during delivery.

## New Characteristics of MOFs Endowed by Molecules
### Stability

MOF nanoparticles can be structurally affected by biomolecular modification. For example, the insertion of an enzyme was beneficial to the construction process of MOFs (Liang et al., 2016a). The binding of oligopeptides could lead to adaptive changes in metal-peptide frameworks (MPFs), which showed differences in porosity and organometallic framework strength according to the different types of amino acids used, such as glycine, threonine, and alanine (Carlos et al., 2012). In addition, lipid-functionalized MOFs have shown better stability in aqueous solution than unmodified MOFs (Wuttke et al., 2015; Zhuang et al., 2015). Liu et al. (2018) proved that Zr MOF nanoparticles bound to single-stranded DNA (ssDNA) showed better stability than did unbound particles over 24 h. In addition, the interaction strength and pore geometry influence the absorption and release kinetics, as well as the way the matrix diffuses inside and outside the pores (Carlos et al., 2012).

### Targeting Movement and Local Release

Modification not only changes the MOF structure but also endows new characteristics. Cell-targeting capabilities should be mentioned first. The mechanism of targeting is always related to the bio-MOF's bioactive group. The most common targeting method is the coupling of the ligand-receptor through distinguishing the specific recipient from the other cells. A manganese MOF modified by small cyclic arginine-glycine-aspartate (RGD) peptides has been verified to target angiogenic

**FIGURE 3 |** Process of pDNA growing with ZIF-8 precursors and transportion into cell.
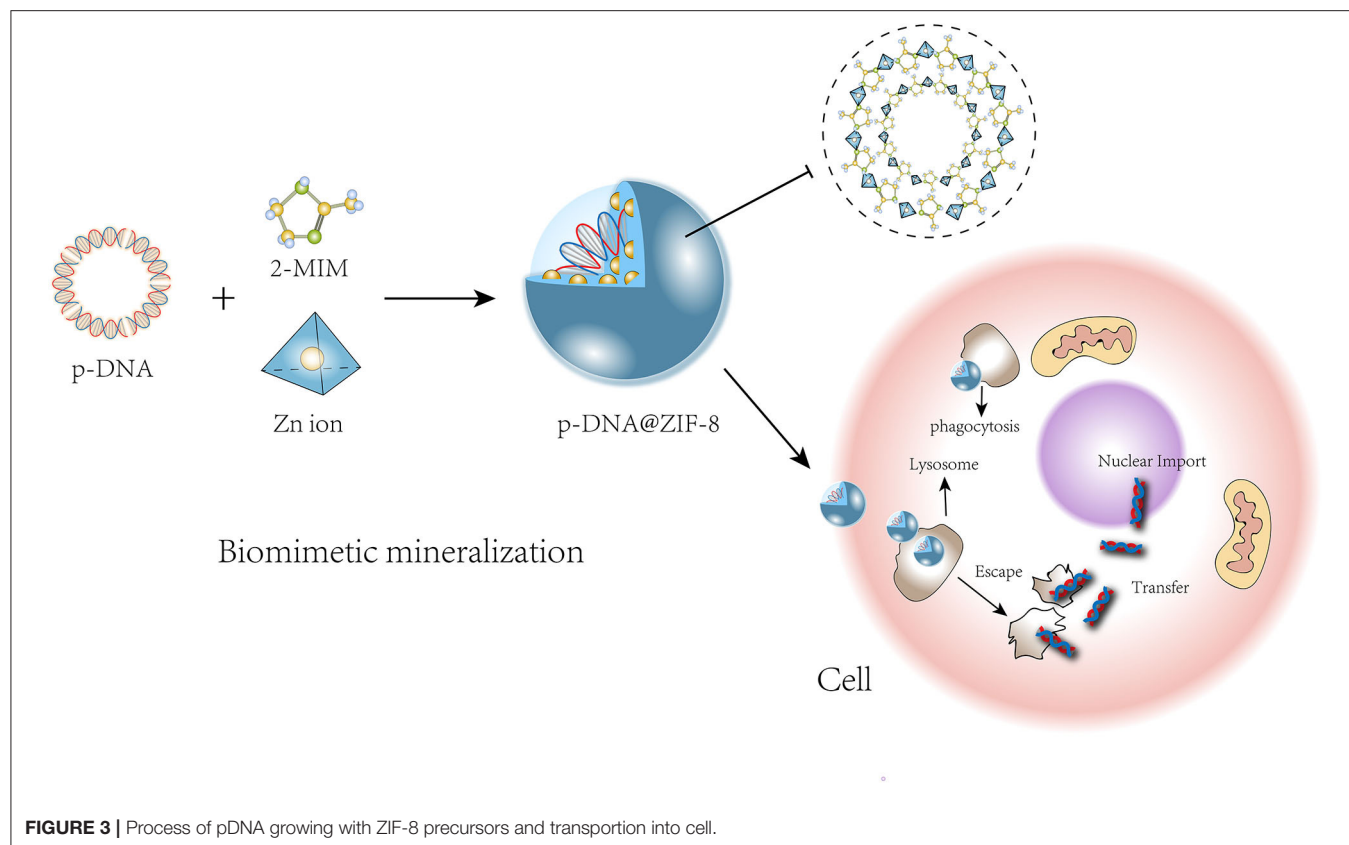
cancer cells well by binding to the upregulated αvβ3 integrin (Taylor et al., 2008). A terminal cyclic RGD-SH peptide was modified onto a hybrid MOF, and the nanoparticle was proven to have a targeting ability for HeLa cells (Wang D. et al., 2018). Folic acid-bovine serum albumin (FA-BSA) was a significant targeting connector for cancer cells, which resulted from efficient internalization via FA-receptors-mediated endocytosis (Jiang et al., 2018). Polysaccharide hyaluronic acid (HA) acts as a cancer-targeting ligand when connected with MOF, too, because it recognizes the overexpressed CD44 that occurs in many cancer cells (Liu et al., 2016; Kim et al., 2019). Another important mechanism of bio-MOFs' targeting movement is the sensing of chemical gradients in environments, which has previously been discovered in bacteria. We can achieve directional motion by endowing MOFs with pH-sensitive biomolecules. Ikezoe et al. (2015) encapsulated the diphenylalanine (DPA) peptide, which could facilitate Cu-MOF movement based on an asymmetric surface tension distribution through the dissolution and self-assembling character of DPA. The solubility of PDA is sensitive to pH gradients. With a higher pH, the solubility of the DPA peptide increased, leading the MOF to lose the surface gradient, thus terminating the motion. In this way, the directional movement of MOF NPs was achieved.

In addition, controllable release is another exciting characteristic (McKinlay et al., 2010), which benefits from the fact that some kinds of MOFs can be degraded in certain environments (Park et al., 2006; Lin and Anseth, 2008). ZIF-8

has good biodegradability under acidic conditions (Della Rocca et al., 2011; Zheng et al., 2016). The ZIF-8/CpG-ODN complex showed good stability in a physiological environment, but the complex effectively released CpG ODNs under acidic conditions corresponding to the endolysosome identified by Toll-like receptor 9 (TLR 9). Moreover, ZIF-8 could significantly improve the uptake of CpG ODNs by RAW264.7 cells and further promote the secretion of immune cytokines *in vitro* and *in vivo* (Li Y. et al., 2019).

## Applications, Prospects, and Challenges

As a novel platform for bioapplications, MOFs have made rapid progress and have constantly provided new methods for biomolecular delivery systems. MOF formation occurs because of the coordination between metal atoms and the organism, and different numbers and categories of metals or organic compounds will produce a variety of constructs, such as those resulting from bimetallic organism synthesis. Recently, a new multivariate modulation of Zr-MOF UiO-66 (Abanades Lazaro et al., 2020) was reported. Multivariate modulation allows the incorporation of up to three drugs containing either carboxylates or phosphates as metal-binding units to coordinate with the defect sites of metal clusters in UiO-66. The one-pot synthesis of solvothermal compounds retained Uio-66 crystallinity and porosity so that other drugs could be further loaded. This research revealed the broader prospects and bioapplications of MOFs. MOFs are also used in the field of bioprobes.

The Cu-MOF was combined with a ssDNA probe labeled with carboxyfluorescein through electrostatic interactions and/or hydrogen bonding, which was used to detect Hg via the coordination motif between Hg and ssDNA (Huang et al., 2019). Another new application involved encapsulating viral nanoparticles to produce a vaccine carrier, so that the integrity of the virus and the biosafety and immunogenicity of the overall composite was enhanced due to the non-toxicity and good biocompatibility of the MOF (Luzuriaga et al., 2019).

However, the use of MOFs as potential carriers for the intracellular transmission of proteins (Liang et al., 2015) and nucleic acids (Wang S. et al., 2017; Wang Z. et al., 2017; Peng et al., 2018) is still in the preliminary stage (Alsaiari et al., 2017; Chen et al., 2018). There are some barriers that need to be resolved in the process of the bioapplication of MOFs. For example, in the future, the induction and growth-affecting factors of proteins or nucleic acids in morphological structures need further study, which will allow large double-stranded DNA molecules to be wrapped in MOFs. The biological stability of bio-MOFs is another constraint. Coating may be a good choice to escape from immune system, such as poly-lactide-co-glycolide (PLGA) and cell membrane (Wang L. et al., 2018; Li J.-Y. et al., 2019). We team has invented a cell membrane-coated nanodrug deliver system to improve biocompatibility, and it has been proved the embedded drug can cleverly escape identification and clearance from the immune system, effectively prolong the blood circulation time and accurately accumulate in the target tumor tissues (Wang et al., 2020). In addition, some researchers have cautioned that most enzyme-MOF research has been focused on enzyme encapsulation in particle form, which means that solid support is essential, but this may limit the material flexibility for further practical applications (Izzah Binti Mohammad et al., 2018). Therefore, the use of versatile modalities, such as flexible ZIF-8 thin films, for the synthesis of bio-MOFs is required.

Currently, bio-MOF cascade reactions in cells have been put forward as a novel strategy. How to utilize the synergy of modified molecules in nanoparticles during working processes in organisms is still an unanswered question. For instance, in multimodal cancer therapies, the synergistic cancer starvation/ROS-mediated/chemotherapy strategy has been designed to cleverly work together in cancer cells. Glucose oxidase (GOX) modified onto the surface of MOF(Fe) catalyzes glucose into hydrogen peroxide ($H_2O_2$) and gluconic acid ($H^+$) in cancer cells, and then $H^+$ can degrade the organic framework to release camptothecin (CPT) for chemotherapy (Liu et al., 2019). In my opinion, to date, the research of bio-MOFs has always been focused on single molecules or on multiple molecules acting independently in unrelated processes. This kind of therapeutic effect is slight, but the effects will be different when we make use of all linked and correlated nodes in entire reaction chains, such as the chain of ROS-induced oxidation. In the latest research, MOF(Fe) is used to promote ROS-induced oxidative damage in cancer cells, and chloroquine modification will inhibit lysosome autophagy, so that this nanodrug can cut off the self-protection node under the oxidative stress chain and improve the anti-cancer effect (Yang et al., 2020). As we can see, the regulation of multiple reactive nodes in a biological chain can be achieved by setting the reaction times of substances loaded onto MOFs. I believe that achieving synergistic effects to maximize the efficiency of bio-MOFs will be a point that attracts the focus of scientists.

Finally, the development direction of bio-MOFs must be toward clinical applications, and transformations are in development, such as targeted protein or DNA biosensors (Osman et al., 2019) and delivery (Wang S. et al., 2019). There is a wider range of utilization of bio-MOFs. Through interdisciplinary research, bio-MOFs will have a significant impact on various fields including chemistry, genetics, biology, and materials science (Wu et al., 2018). We hope that genetic diagnosis, biological-targeted therapy, and therapeutic drug encapsulation can be improved through the use of MOFs in the future.

## AUTHOR CONTRIBUTIONS

QX, YH, and LW contributed conception and design of the study. QX wrote the first draft of the manuscript. LW revised the manuscript. YP wrote sections of the manuscript. All authors contributed to manuscript revision, read, and approved the submitted version.

## FUNDING

## REFERENCES

Abanades Lazaro, I., Wells, C. J. R., and Forgan, R. S. (2020). Multivariate modulation of the Zr MOF UiO-66 for defect-controlled multimodal anticancer drug delivery. *Angew. Chem. Int. Ed. Engl.* 132, 5249–5255. doi: 10.1002/ange.201915848

Alsaiari, S.-K., Patil, S., Alyami, M., Alamoudi, K.-O., Aleisa, F.-A., Merzaban, J.-S., et al. (2017). Endosomal escape and delivery of CRISPR/Cas9 genome editing machinery enabled by nanoscale zeolitic imidazolate framework. *J. Am. Chem. Soc.* 140, 143–146. doi: 10.1021/jacs.7b11754

An, J., Farha, O.-K., Hupp, J.-T., Pohl, E., Yeh, J.-I., and Rosi, N.-L. (2012). Metal-adeninate vertices for the construction of an exceptionally porous metal-organic framework. *Nat. Commun.* 3:604. doi: 10.1038/ncomms1618

Cai, W., Chu, C.-C., Liu, G., and Wáng, Y.-X. (2015). Metal-organic framework-based nanomedicine platforms for drug delivery and molecular imaging. *Small* 11, 4806–4822. doi: 10.1002/smll.201500802

Cai, W., Gao, H., Chu, C., Wang, X., Wang, J., Zhang, P., et al. (2017). Engineering phototheranostic nanoscale metal–organic frameworks for multimodal imaging-guided cancer therapy. *ACS Appl. Mater. Interfaces* 9, 2040–2051. doi: 10.1021/acsami.6b11579

Cao, Y., Wu, Z., Wang, T., Xiao, Y., Huo, Q., and Liu, Y. (2016). Immobilization of *Bacillus subtilis* lipase on a Cu-BTC based hierarchically porous metal–organic framework material: a biocatalyst for esterification. *Dalton Trans.* 45, 6998–7003. doi: 10.1039/C6DT00677A

Carlos, M.-G., Warren, J.-E., Stylianou, K.-C., Flack, N.-L., and Rosseinsky M.-J. (2012). Enhanced stability in rigid peptide-based porous materials. *Angew. Chem. Int. Ed. Engl.* 51, 11044–11048. doi: 10.1002/anie.201203929

Chen, T.-T., Yi, J.-T., Zhao, Y.-Y., and Chu, X. (2018). Biomineralized metal–organic framework nanoparticles enable intracellular delivery and endo-lysosomal release of native active proteins. *J. Am. Chem. Soc.* 140, 9912–9920. doi: 10.1021/jacs.8b04457

Chen, Y., Lykourinou, V., Vetromile, C., Hoang, T., Ming, L.-J., and Larsen, R. W. (2012). How can proteins enter the interior of a MOF? Investigation of cytochrome *c* translocation into a MOF consisting of mesoporous cages with microporous windows. *J. Am. Chem. Soc.* 134, 13188–13191. doi: 10.1021/ja305144x

Cheng, X., and Lee, R.-J. (2016). The role of helper lipids in lipid nanoparticles (LNPs) designed for oligonucleotide delivery. *Adv. Drug Delivery Rev.* 99, 129–137. doi: 10.1016/j.addr.2016.01.022

Chira, S., Jackson, C.-S., Oprea, I., Ozturk, F., Pepper, M.-S., Diaconu, I., et al. (2015). Progresses towards safe and efficient gene therapy vectors. *Oncotarget* 6:30675. doi: 10.18632/oncotarget.5169

Chowdhuri, A.-R., Das, B., Kumar, A., Tripathy, S., Roy, S., and Sahu, S.-K. (2017). One-pot synthesis of multifunctional nanoscale metal-organic frameworks as an effective antibacterial agent against multidrug-resistant *Staphylococcus aureus*. *Nanotechnology* 28:095102. doi: 10.1088/1361-6528/aa57af

Das, S. K., Menezes, M. E., Bhatia, S., Wang, X. Y., Emdad, L., and Sarkar, D. (2015). Gene therapies for cancer: strategies, challenges and successes. *J. Cell. Physiol.* 230, 259–271. doi: 10.1002/jcp.24791

Dash, P.-R., Read, M.-L., Barrett, L.-B., Wolfert, M.-A., and Seymour, L.-W. (1999). Factors affecting blood clearance and *in vivo* distribution of polyelectrolyte complexes for gene delivery. *Gene Ther.* 6, 643–650. doi: 10.1038/sj.gt.3300843

Della Rocca, J., Liu, D., and Lin, W. (2011). Nanoscale metal-organic frameworks for biomedical imaging and drug delivery. *Acc. Chem. Res.* 44, 957–968. doi: 10.1021/ar200028a

Deria, P., Bury, W., Hod, I., Kung, C.-W., Karagiaridi, O., Hupp, J. T., et al. (2015). MOF functionalization via solvent-assisted ligand incorporation: phosphonates vs carboxylates. *Inorg. Chem.* 54, 2185–2192. doi: 10.1021/ic502639v

Doonan, C., Riccò, R., Liang, K., Bradshaw, D., and Falcaro, P. (2017). Metal–organic frameworks at the biointerface: synthetic strategies and applications. *Acc. Chem. Res.* 50, 1423–1432. doi: 10.1021/acs.accounts.7b00090

Eddaoudi, M., Kim, J., Rosi, N., Vodak, D., Wachter, J., O'Keeffe, M., et al. (2002). Systematic design of pore size and functionality in isoreticular MOFs and their application in methane storage. *Science* 295, 469–472. doi: 10.1126/science.1067208

Férey, G. (2008). Hybrid porous solids: past, present, future. *Chem. Soc. Rev.* 37, 191–214. doi: 10.1039/B618320B

Fu, L.-H., Qi, C., Ma, M.-G., and Wan, P. (2018). Multifunctional cellulose-based hydrogels for biomedical applications. *J. Mater. Chem. B* 7, 1541–1562. doi: 10.1039/c8tb02331j

Ginn, S.-L., Amaya, A. K., Alexander, I. E., Edelstein, M., and Abedi, M. R. (2018). Gene therapy clinical trials worldwide to 2017: an update. *J. Gene Med.* 20:e3015. doi: 10.1002/jgm.3015

Hartmann, M., and Kostrov, X. (2013). Immobilization of enzymes on porous silicas—benefits and challenges. *Chem. Soc. Rev.* 42:6277. doi: 10.1039/c3cs60021a

He, C., Liu, D., and Lin, W. (2015). Nanomedicine applications of hybrid nanomaterials built from metal–ligand coordination bonds: nanoscale metal–organic frameworks and nanoscale coordination polymers. *Chem. Rev.* 115, 11079–11108. doi: 10.1021/acs.chemrev.5b00125

He, H., Han, H., Shi, H., Tian, Y., Sun, F., and Song, Y. (2016). Construction of thermophilic lipase-embedded metal–organic frameworks via biomimetic mineralization: a biocatalyst for ester hydrolysis and kinetic resolution. *ACS Appl. Mater. Interfaces* 8, 24517–24524. doi: 10.1021/acsami.6b05538

Horcajada, P., Chalati, T., Serre, C., Gillet, B., Sebrie, C., Baati, T., et al. (2009). Porous metal–organic-framework nanoscale carriers as a potential platform for drug delivery and imaging. *Nat. Mater.* 9, 172–178. doi: 10.1038/nmat2608

Horcajada, P., Gref, R., Baati, T., Allan, P.-K., Maurin, G., Couvreur, P., et al. (2011). Metal–organic frameworks in biomedicine. *Chem. Rev.* 112, 1232–1268. doi: 10.1021/cr200256v

Huang, N.-H., Li, R.-T., Fan, C., Wu, K.-Y., Zhang, Z., and Chen, J.-X. (2019). Rapid sequential detection of $Hg^{2+}$ and biothiols by a probe DNA—MOF hybrid sensory system. *J. Inorg. Biochem.* 197:110690. doi: 10.1016/j.jinorgbio.2019.04.004

Huang, X., He, Z., Guo, D., Liu, Y., Song, J., Yung, B. C., et al. (2018). "Three-in-one" nanohybrids as synergistic nanoquenchers to enhance no-wash fluorescence biosensors for ratiometric detection of cancer biomarkers. *Theranostics* 8, 3461–3473. doi: 10.7150/thno.25179

Hudson, S., Cooney, J., and Magner, E. (2008). Proteins in mesoporous silicates. *Angew. Chem. Int. Ed. Engl.* 47, 8582–8594. doi: 10.1002/anie.200705238

Huxford, R. C., Della Rocca, J., and Lin, W. (2010). Metal–organic frameworks as potential drug carriers. *Curr. Opin. Chem. Biol.* 14, 262–268. doi: 10.1016/j.cbpa.2009.12.012

Hwang, E.-T., Tatavarty, R., Chung, J., and Gu, M.-B. (2013). New functional amorphous calcium phosphate nanocomposites by enzyme-assisted biomineralization. *ACS Appl. Mater. Interfaces* 5, 532–537. doi: 10.1021/am302580p

Ikezoe, Y., Fang, J., Wasik, T.-L., Shi, M., Uemura, T., Kitagawa, S., et al. (2015). Peptide–metal organic framework swimmers that direct the motion toward chemical targets. *Nano Lett.* 15, 4019–4023. doi: 10.1021/acs.nanolett.5b00969

Imaz, I., Rubio-Martínez, M., An, J., Solé-Font, I., Rosi, N. L., and Maspoch, D. (2011). Metal–biomolecule frameworks (MBioFs). *Chem. Commun.* 47, 7287–7302. doi: 10.1039/c1cc11202c

Izzah Binti Mohammad, M., Razmjou, A., Liang, K., Asadnia, M., and Chen, V. (2018). MOF-based enzymatic microfluidic biosensor via surface patterning and biomineralization. *ACS Appl. Mater. Interfaces* 11, 1807–1820. doi: 10.1021/acsami.8b16837

Javanbakht, S., Hemmati, A., Namazi, H., and Heydari, A. (2019). Carboxymethylcellulose-coated 5-fluorouracil@MOF-5 nano-hybrid as a bio-nanocomposite carrier for the anticancer oral delivery. *Int. J. Biol. Macromol.* 155, 876–882. doi: 10.1016/j.ijbiomac.2019.12.007

Jiang, W., Zhang, H., Wu, J., Zhai, G., Li, Z., and Luan, Y. (2018). CuS@MOF-based well-designed quercetin delivery system for chemo-photothermal therapy. *ACS Appl. Mater. Interfaces* 10, 34513–34523. doi: 10.1021/acsami.8b13487

Keles, E., Song, Y., Du, D., Dong, W.-J., and Lin, Y. (2016). Recent progress in nanomaterials for gene delivery applications. *Biomater. Sci.* 4, 1291–1309. doi: 10.1039/C6BM00441E

Khalil, I. A., Kogure, K., Akita, H., and Harashima, H. (2006). Uptake pathways and subsequent intracellular trafficking in nonviral gene delivery. *Pharmacol. Rev.* 58, 32–45. doi: 10.1124/pr.58.1.8

Kim, E., Lee, S., Jin, E., Palanikumar, L., Lee, J.-H., Kim, J.-C., et al. (2019). MOF X biopolymer: collaborative combination of metal-organic framework and biopolymer for advanced anticancer therapy. *ACS Appl. Mater. Interfaces* 11, 27512–27520. doi: 10.1021/acsami.9b05736

Kotterman, M.-A., Chalberg, T.-W., and Schaffer, D.-V. (2015). Viral vectors for gene therapy: translational and clinical outlook. *Annu. Rev. Biomed. Eng.* 17, 63–89. doi: 10.1146/annurev-bioeng-071813-104938

Li, J.-Y., Hu, H.-Y., Jiang, Z.-C., Chen, S.-J., Pan, Y.-X., Guo, Q., et al. (2019). Near-infrared-induced IR780-loaded PLGA nanoparticles for photothermal therapy to treat breast cancer metastasis in bones. *RSC Adv.* 9, 35976–35983. doi: 10.1039/C9RA05813C

Li, J. R., Kuppler, R. J., and Zhou, H. C. (2009). Selective gas adsorption and separation in metal-organic frameworks. *Chem. Soc. Rev.* 38, 1477–1504. doi: 10.1039/b802426j

Li, P., Moon, S.-Y., Guelta, M.-A., Harvey, S.-P., Hupp, J.-T., and Farha, O.-K. (2016). Encapsulation of a nerve agent detoxifying enzyme by a mesoporous zirconium metal–organic framework engenders thermal and long-term stability. *J. Am. Chem. Soc.* 138, 8052–8055. doi: 10.1021/jacs.6b03673

Li, Y., Zhang, K., Liu, P., Chen, M., Zhong, Y., Ye, Q., et al. (2019). Encapsulation of plasmid dna by nanoscale metal–organic frameworks for efficient gene transportation and expression. *Adv. Mater.* 31:1901570. doi: 10.1002/adma.201901570

Li, Z., and Zhang, Y. (2006). Monodisperse silica-coated polyvinylpyrrolidone/NaYF4 nanocrystals with multicolor upconversion

fluorescence emission. *Angew. Chem. Int. Ed. Engl.* 45, 7732–7735. doi: 10.1002/anie.200602975

Liang, K., Coghlan, C.-J., Bell, S.-G., Doonan, C., and Falcaro, P. (2016a). Enzyme encapsulation in zeolitic imidazolate frameworks: a comparison between controlled co-precipitation and biomimetic mineralisation. *Chem. Commun.* 52, 473–476. doi: 10.1039/C5CC07577G

Liang, K., Ricco, R., Doherty, C.-M., Styles, M.-J., Bell, S., Kirby, N., et al. (2015). Biomimetic mineralization of metal-organic frameworks as protective coatings for biomacromolecules. *Nat. Commun.* 6:7240. doi: 10.1038/ncomms8240

Liang, K., Richardson, J.-J., Cui, J., Caruso, F., Doonan, C.-J., and Falcaro, P. (2016b). Metal-organic framework coatings as cytoprotective exoskeletons for living cells. *Adv. Mater.* 28, 7910–7914. doi: 10.1002/adma.201602335

Lin, C.-C., and Anseth, K.-S. (2008). PEG hydrogels for the controlled release of biomolecules in regenerative medicine. *Pharm. Res.* 26, 631–643. doi: 10.1007/s11095-008-9801-2

Liu, C., Chen, Z., Wang, Z., Li, W., Ju, E., Yan, Z., et al. (2016). A graphitic hollow carbon nitride nanosphere as a novel photochemical internalization agent for targeted and stimuli-responsive cancer therapy. *Nanoscale* 8, 12570–12578. doi: 10.1039/C5NR07719B

Liu, Y., Hou, W., Xia, L., Cui, C., Wan, S., Jiang, Y., et al. (2018). ZrMOF nanoparticles as quenchers to conjugate DNA aptamers for target-induced bioimaging and photodynamic therapy. *Chem. Sci.* 9, 7505–7509. doi: 10.1039/C8SC02210K

Liu, Z., Li, T., Han, F., Gan, Y., Wang, Y., Shi, J., et al. (2019). A cascade-reaction enabled synergistic cancer starvation/ROS-mediated/chemotherapy with enzyme modified Fe-based MOF. *Biomater. Sci.* 7, 3683–3692. doi: 10.1039/C9BM00641A

Lu, G., Li, S., Guo, Z., Farha, O.-K., Hauser, B.-G., Qi, X., et al. (2012). Imparting functionality to a metal–organic framework material by controlled nanoparticle encapsulation. *Nat. Chem.* 4, 310–316. doi: 10.1038/nchem.1272

Luzuriaga, M.-A., Welch, R.-P., Dharmarwardana, M., Benjamin, C.-E., Li, S., Shahrivarkevishahi, A., et al. (2019). Enhanced stability and controlled delivery of MOF encapsulated vaccines and their immunogenic response *in vivo*. *ACS Appl. Mater. Interfaces* 11, 9740–9746. doi: 10.1021/acsami.8b20504

Lv, H., Zhang, S., Wang, B., Cui, S., and Yan, J. (2006). Toxicity of cationic lipids and cationic polymers in gene delivery. *J. Control. Release* 114, 100–109. doi: 10.1016/j.jconrel.2006.04.014

Lykourinou, V., Chen, Y., Wang, X.-S., Meng, L., Hoang, T., Ming, L.-J., et al. (2011). Immobilization of MP-11 into a mesoporous metal–organic framework, MP-11@mesoMOF: a new platform for enzymatic catalysis. *J. Am. Chem. Soc.* 133, 10382–10385. doi: 10.1021/ja2038003

Lyu, F., Zhang, Y., Zare, R.-N., Ge, J., and Liu, Z. (2014). One-pot synthesis of protein-embedded metal–organic frameworks with enhanced biological activities. *Nano Lett.* 14, 5761–5765. doi: 10.1021/nl5026419

Mantion, A., Massüger, L., Rabu, P., Palivan, C., McCusker, L. B., and Taubert, A. (2008). Metal-peptide frameworks (MPFs): "bioinspired" metal organic frameworks. *J. Am. Chem. Soc.* 130, 2517–2526. doi: 10.1021/ja0762588

McKinlay, A. C., Morris, R. E., Horcajada, P., Férey, G., Gref, R., Couvreur, P., et al. (2010). BioMOFs: metal-organic frameworks for biological and medical applications. *Angew. Chem. Int. Ed. Engl.* 49, 6260–6266. doi: 10.1002/anie.201000048

Meng, H.-M., Hu, X.-X., Kong, G.-Z., Yang, C., Fu, T., Li, Z.-H., et al. (2018). Aptamer-functionalized nanoscale metal–organic frameworks for targeted photodynamic therapy. *Theranostics* 8, 4332–4344. doi: 10.7150/thno.26768

Mintzer, M.-A., and Simanek, E.-E. (2009). Nonviral vectors for gene delivery. *Chem. Rev.* 109, 259–302. doi: 10.1021/cr800409e

Morris, R. E., and Wheatley, P. S. (2008). Gas storage in nanoporous materials. *Angew. Chem. Int. Ed. Engl.* 47, 4966–4981. doi: 10.1002/anie.200703934

Morris, W., Briley, W.-E., Auyeung, E., Cabezas, M. D., and Mirkin, C.-A. (2014). Nucleic acid–metal organic framework (MOF) nanoparticle conjugates. *J. Am. Chem. Soc.* 136, 7261–7264. doi: 10.1021/ja503215w

Nam, H.-Y., Park, J.-H., Kim, K., Kwon, I.-C., and Jeong, S.-Y. (2009). Lipid-based emulsion system as non-viral gene carriers. *Arch. Pharm. Res.* 32, 639–646. doi: 10.1007/s12272-009-1500-y

Osman, D. I., El-Sheikh, S. M., Sheta, S. M., Ali, O. I., Salem, A. M., Shousha, W. G., et al. (2019). Nucleic acids biosensors based on metal-organic framework (MOF): paving the way to clinical laboratory diagnosis. *Biosens. Bioelectron.* 141:111451. doi: 10.1016/j.bios.2019.111451

Park, K.-S., Ni, Z., Cote, A.-P., Choi, J.-Y., Huang, R., and Uribe-Romo, F.-J. (2006). Exceptional chemical and thermal stability of zeolitic imidazolate frameworks. *Proc. Natl. Acad. Sci. U.S.A.* 103, 10186–10191. doi: 10.1073/pnas.0602439103

Peng, S., Bie, B., Sun, Y., Liu, M., Cong, H., Zhou, W., et al. (2018). Metal-organic frameworks for precise inclusion of single-stranded DNA and transfection in immune cells. *Nat. Commun.* 9:1293. doi: 10.1038/s41467-018-03650-w

Rapoport, T.-A. (2007). Protein translocation across the eukaryotic endoplasmic reticulum and bacterial plasma membranes. *Nature* 450, 663–669. doi: 10.1038/nature06384

Roth, S.-K., Epley, C.-C., Novak, J.-J., McAndrew, M.-L., Cornell, H.-D., Zhu J., et al. (2018). Photo-triggered release of 5-fluorouracil from a MOF drug delivery vehicle. *Chem. Commun.* 54, 7617–7620. doi: 10.1039/C8CC01601A

Shekhah, O., Liu, J., Fischer, R.-A., and Wöll, C. (2011). MOF thin films: existing and future applications. *Chem. Soc. Rev.* 40:1081. doi: 10.1039/c0cs00147c

Shieh, F.-K., Wang, S.-C., Yen, C.-I., Wu, C.-C., Dutta, S., Chou, L.-Y., et al. (2015). Imparting functionality to biocatalysts via embedding enzymes into nanoporous materials by a *de novo* approach: size-selective sheltering of catalase in metal–organic framework microcrystals. *J. Am. Chem. Soc.* 137, 4276–4279. doi: 10.1021/ja513058h

Sokolova, V., and Epple, M. (2008). Inorganic nanoparticles as carriers of nucleic acids into cells. *Angew. Chem. Int. Ed. Engl.* 47, 1382–1395. doi: 10.1002/anie.200703039

Taylor, K.-M., Rieter, W.-J., and Lin, W. (2008). Manganese-based nanoscale metal–organic frameworks for magnetic resonance imaging. *J. Am. Chem. Soc.* 130, 14358–14359. doi: 10.1021/ja803777x

Thomas, C.-E., Ehrhardt, A., and Kay, M.-A. (2003). Progress and problems with the use of viral vectors for gene therapy. *Nat. Rev. Genet.* 4, 346–358. doi: 10.1038/nrg1066

Trzaskowski, B., Adamowicz, L., and Deymier, P.-A. (2007). A theoretical study of zinc(II) interactions with amino acid models and peptide fragments. *J. Biol. Inorg. Chem.* 13, 133–137. doi: 10.1007/s00775-007-0306-y

Tseng, Y. C., Mozumdar, S., and Huang, L. (2009). Lipid-based systemic delivery of siRNA. *Adv. Drug Deliv. Rev.* 61, 721–731. doi: 10.1016/j.addr.2009.03.003

Waehler, R., Russell, S.-J., and Curiel, D.-T. (2007). Engineering targeted viral vectors for gene therapy. *Nat. Rev. Genet.* 8, 573–587. doi: 10.1038/nrg2141

Wan, C., Allen, T.-M., and Cullis, P.-R. (2013). Lipid nanoparticle delivery systems for siRNA-based therapeutics. *Drug Deliv. Transl. Res.* 4, 74–83. doi: 10.1007/s13346-013-0161-z

Wang, D., Wu, H., Zhou, J., Xu, P., Wang, C., Shi, R., et al. (2018). *In situ* one-pot synthesis of MOF-polydopamine hybrid nanogels with enhanced photothermal effect for targeted cancer therapy. *Adv. Sci.* 5:1800287. doi: 10.1002/advs.201800287

Wang, D., Zhao, C., Gao, G., Xu, L., Wang, G., and Zhu, P. (2019). Multifunctional NaLnF$_4$@MOF-Ln nanocomposites with dual-mode luminescence for drug delivery and cell imaging. *Nanomaterials* 9:1274. doi: 10.3390/nano9091274

Wang, L., Chen, S., Pei, W., Huang, B., and Niu, C. (2020). Magnetically targeted erythrocyte membrane coated nanosystem for synergistic photothermal/chemotherapy of cancer. *J. Mater. Chem. B* 8, 4132–4142. doi: 10.1039/D0TB00364F

Wang, L., Chen, S., Zhu, Y., Zhang, M., Tang, S., Li, J., et al. (2018). Triple-modal imaging-guided chemo-photothermal synergistic therapy for breast cancer with magnetically targeted phase-shifted nanoparticles. *ACS Appl. Mater. Interfaces* 10, 42102–42114. doi: 10.1021/acsami.8b16323

Wang, S., Chen, Y., Wang, S., Li, P., Mirkin, C. A., and Farha, O. K. (2019). DNA-functionalized metal-organic framework nanoparticles for intracellular delivery of proteins. *J. Am. Chem. Soc.* 141, 2215–2219. doi: 10.1021/jacs.8b12705

Wang, S., McGuirk, C.-M., Ross, M.-B., Wang, S., Chen, P., Xing, H., et al. (2017). General and direct method for preparing oligonucleotide-functionalized metal–organic framework nanoparticles. *J. Am. Chem. Soc.* 139, 9827–9830. doi: 10.1021/jacs.7b05633

Wang, S., Morris, W., Liu, Y., McGuirk, C.-M., Zhou, Y., Hupp, J.-T., et al. (2015). Surface-specific functionalization of nanoscale metal-organic frameworks. *Angew. Chem. Int. Ed. Engl.* 54, 14738–14742. doi: 10.1002/anie.201506888

Wang, Z., Fu, Y., Kang, Z., Liu, X., Chen, N., Wang, Q., et al. (2017). Organelle-specific triggered release of immunostimulatory oligonucleotides from intrinsically coordinated DNA–metal–organic frameworks with soluble exoskeleton. *J. Am. Chem. Soc.* 139, 15784–15791. doi: 10.1021/jacs.7b07895

Whitehead, K.-A., Langer, R., and Anderson, D.-G. (2009). Knocking down barriers: advances in siRNA delivery. *Nat. Rev. Drug Discovery* 8, 129–138. doi: 10.1038/nrd2742

Wickner, W. (2005). Protein translocation across biological membranes. *Science* 310, 1452–1456. doi: 10.1126/science.1113752

Wu, Q., Niu, M., Chen, X., Tan, L., Fu, C., Ren, X., et al. (2018). Biocompatible and biodegradable zeolitic imidazolate framework/polydopamine nanocarriers for dual stimulus triggered tumor thermo-chemotherapy. *Biomaterials* 162, 132–143. doi: 10.1016/j.biomaterials.2018.02.022

Wuttke, S., Braig, S., Preiß, T., Zimpel, A., Sicklinger, J., Bellomo, C., et al. (2015). MOF nanoparticles coated by lipid bilayers and their uptake by cancer cells. *Chem. Commun.* 51, 15752–15755. doi: 10.1039/C5CC06767G

Wyszogrodzka-Gaweł, G., Dorozynski, P., Giovagnoli, S., Strzempek, W., Pesta, E., Weglarz, W. P., et al. (2019). An inhalable theranostic system for local tuberculosis treatment containing an isoniazid loaded metal organic framework Fe-MIL-101-NH2—from raw MOF to drug delivery system. *Pharmaceutics* 11:687. doi: 10.3390/pharmaceutics11120687

Xiao, B., Byrne, P.-J., Wheatley, P.-S., Wragg, D.-S., Zhao, X., and Fletcher, A.-J. (2009). Chemically blockable transformation and ultraselective low-pressure gas adsorption in a non-porous metal organic framework. *Nat. Chem.* 1, 289–294. doi: 10.1038/nchem.254

Xiao, J., Chen, S., Yi, J., Zhang, H.-F., and Ameer, G. A. (2016). A cooperative copper metal-organic framework-hydrogel system improves wound healing in diabetes. *Adv. Funct. Mater.* 27:1604872. doi: 10.1002/adfm.201604872

Xu, H., Liu, F., Cui, Y., Chen, B., and Qian, G. (2011). A luminescent nanoscale metal-organic framework for sensing of nitroaromatic explosives. *Chem. Commun.* 47:3153. doi: 10.1039/c0cc05166g

Yang, B., Ding, L., Yao, H., Chen, Y., and Shi, J. (2020). A metal-organic framework (MOF) Fenton nanoagent-enabled nanocatalytic cancer therapy in synergy with autophagy inhibition. *Adv. Mater.* 32:1907152. doi: 10.1002/adma.201907152

Yin, H., Kanasty, R. L., Eltoukhy, A. A., Vegas, A. J., Dorkin, J. R., and Anderson, D. G. (2014). Non-viral vectors for gene-based therapy. *Nat. Rev. Genet.* 15, 541–555 doi: 10.1038/nrg3763

Yoo, J. W., Irvine, D. J., Discher, D. E., and Mitragotri, S. (2011). Bio-inspired, bioengineered and biomimetic drug delivery carriers. *Nat. Rev. Drug. Discovery* 10, 521–535. doi: 10.1038/nrd3499

Zhang, H., Chen, W., Gong, K., and Chen, J. (2017). Nanoscale zeolitic imidazolate framework-8 as efficient vehicles for enhanced delivery of CpG oligodeoxynucleotides. *ACS Appl. Mater. Interfaces* 9, 31519–31525. doi: 10.1021/acsami.7b09583

Zhang, W., Hu, Y., Ge, J., Jiang, H.-L., and Yu, S.-H. (2014). A facile and general coating approach to moisture/water-resistant metal–organic frameworks with intact porosity. *J. Am. Chem. Soc.* 136, 16978–16981. doi: 10.1021/ja509960n

Zhao, D., Tan, S., Yuan, D., Lu, W., Rezenom, Y.-H., et al. (2011). Surface functionalization of porous coordination nanocages via click chemistry and their application in drug delivery. *Adv. Mater.* 23, 90–93. doi: 10.1002/adma.201003012

Zheng, H., Zhang, Y., Liu, L., Wan, W., Guo, P., Nyström, A. M., et al. (2016). One-pot synthesis of metal-organic frameworks with encapsulated target molecules and their applications for controlled drug delivery. *J. Am. Chem. Soc.* 138, 962–968. doi: 10.1021/jacs.5b11720

Zhong, Y., Yu, L., He, Q., Zhu, Q., Zhang, C., Cui, X., et al. (2019). Bifunctional hybrid enzyme-catalytic metal organic framework reactor for α-glucosidase inhibitor screening. *ACS Appl. Mater. Interfaces* 11:32769. doi: 10.1021/acsami.9b11754

Zhou, H.-C., Long, J.-R., and Yaghi, O.-M. (2012). Introduction to metal organic frameworks. *Chem. Rev.* 112, 673–674. doi: 10.1021/cr300014x

Zhuang, J., Chou, L.-Y., Sneed, B.-T., Cao, Y., Hu, P., and Feng, L., et al. (2015). Surfactant-mediated conformal overgrowth of core-shell metal-organic framework materials with mismatched topologies. *Small* 11, 5551–5555. doi: 10.1002/smll.201501710

Zhuang, J., Kuo, C.-H., Chou, L.-Y., Liu, D.-Y., Weerapana, E., and Tsung, C.-K. (2014). Optimized metal-organic-framework nanospheres for drug delivery: evaluation of small-molecule encapsulation. *ACS Nano* 8:2812–2819. doi: 10.1021/nn406590q

Zhuang, J., Young, A.-P., and Tsung, C.-K. (2017). Integration of biomolecules with metal-organic frameworks. *Small* 13:1700880. doi: 10.1002/smll.201700880

# Rational Design and *in-situ* Synthesis of Ultra-Thin β-Ni(OH)$_2$ Nanoplates for High Performance All-Solid-State Flexible Supercapacitors

Shensong Wang[1], Changqin Tan[1], Linfeng Fei[2], Haitao Huang[2]*, Shujun Zhang[3], Hao Huang[1], Xinyi Zhang[1], Qiu-an Huang[4], Yongming Hu[1]* and Haoshuang Gu[1]

[1] Hubei Key Laboratory of Ferro- and Piezoelectric Materials and Devices, Faculty of Physics and Electronic Science, Hubei University, Wuhan, China, [2] Department of Applied Physics, The Hong Kong Polytechnic University, Hong Kong, China, [3] Institute for Superconducting & Electronic Materials, Australian Institute of Innovative Materials, University of Wollongong, Wollongong, NSW, Australia, [4] College of Science/Institute for Sustainable Energy, Shanghai University, Shanghai, China

The all-solid-state flexible supercapacitor (AFSC), one of the most flourishing energy storage devices for portable and wearable electronics, attracts substantial attentions due to their high flexibility, compact size, improved safety, and environmental friendliness. Nevertheless, the current AFSCs usually show low energy density, which extremely hinders their practical applications. Herein, ultra-thin β-Ni(OH)$_2$ nanoplates with thickness of 2.4 ± 0.2 nm are *in-situ* grown uniformly on Ni foam by one step hydrothermal treatment. Thanks to the ultra-thin nanostructure, β-Ni(OH)$_2$ nanoplates shows a specific capacitance of 1,452 F g$^{-1}$ at the scan rate of 3 mV s$^{-1}$. In addition, the assembled asymmetric AFSC [Ni(OH)$_2$//Activated carbon] shows a specific capacitance of 198 F g$^{-1}$. It is worth noting that the energy density of the AFSC can reach 62 Wh kg$^{-1}$ while keeping a high power density of 1.5 kW kg$^{-1}$. Furthermore, the fabricated AFSCs exhibit satisfied fatigue behavior and excellent flexibility, and about 82 and 86% of the capacities were retained after 5,000 cycles and folding over 1,500 times, respectively. Two AFSC in series connection can drive the electronic watch and to run stably for 10 min under the bending conditions, showing a great potential for powering portable and wearable electronic devices.

Keywords: β-Ni(OH)$_2$, ultra-thin nanoplates, energy density, flexibility, all-solid-state supercapacitors

## HIGHLIGHTS

- Ultra-thin β-Ni(OH)$_2$ nanoplates with thickness of 2.4 nm are designed and *in-situ* synthesized.
- The all-solid-state flexible supercapacitors show a high energy density of 62 Wh kg$^{-1}$.
- The supercapacitors exhibit excellent flexibility and stability and show great promise for practical applications.

## INTRODUCTION

With the rapid development of portable and wearable electronic devices, the demand for high-performance, flexible, and safe energy storage devices has increased dramatically energy

(Huang et al., 2016). As a kind of emerging power sources, supercapacitors (SCs), whose power and densities are between the gap of batteries and dielectric capacitors, have drawn widespread attention owing to their ultrahigh power density, long lifetime, fast charging–discharging rate, etc. (Zhao et al., 2018). Compared to traditional liquid-electrolyte-based SCs, SCs based on solid-state electrolytes show their great potential for portable devices (Meng et al., 2010; Yang, 2020). However, up to now, the commercial application of AFSCs is still challenged because the energy density is much lower than that of rechargeable batteries. To date, a variety of materials have been explored as the electrode materials for fabricating high energy density SCs, which can be categorized into carbon materials and pseudocapacitive materials roughly (Peng et al., 2014). It has been demonstrated that pseudocapacitive materials are of great significance in achieving both high energy density and power density SCs such as transition metal oxides, hydroxides, dichalcogenides or nitrides, and conducting polymers (Wu et al., 2017). Among them, $Ni(OH)_2$ has been extensively studied because of the fascinating features of excellent redox behavior, high theoretical capacity, and natural abundance. Especially, the unique two-dimensional (2D) laminar structure with sufficient interlayer space causing by intercalated water molecules and ions can provide transport channels for electrolyte and improve the charge storage ability (Zha et al., 2017). Generally, $Ni(OH)_2$ has two types of crystal structures, i.e., α and β phase. In comparison to α-$Ni(OH)_2$, β-$Ni(OH)_2$ has better stability and longer lifetime in an alkaline electrolyte (Cai et al., 2004). Nevertheless, analogous to other pseudocapacitive materials, β-$Ni(OH)_2$ often shows an inferior capacity in practical application, which may be caused by the small specific surface area. It has been reported that special designed nanostructures, such as nanoflowers (Zhao et al., 2016), nanospheres (Qin et al., 2018), nanoplates (Wang et al., 2010), and nanowires (Dong et al., 2014), are effective approaches to improve the energy storage capacity of β-$Ni(OH)_2$, which exhibit large capacitance because of their abundant active sites benefiting from large surface. However, as a kind of typical 2D nanomaterial, the layers aggregation and stacking of β-$Ni(OH)_2$ caused by hydrogen bond and electrostatic interactions may impede the ion transport and decrease the active sites, resulting in unsatisfactory capacitance and rate capability (Zha et al., 2017). Consequently, to avoid aggregation and stacking, *in-situ* growing ultra-thin β-$Ni(OH)_2$ with few layers is significant to improve the electrochemical performance.

In this work, β-$Ni(OH)_2$ nanoplates with ultra-thin thickness are *in-situ* grown on Ni foam by a facile hydrothermal process at low temperature. An asymmetric AFSC based on ultra-thin β-$Ni(OH)_2$ nanoplates was fabricated, in which the β-$Ni(OH)_2$, PAAK/KOH, activated carbon (AC), and Ni foam served as the positive electrode material, electrolyte, negative electrode material, and current collector, respectively. The power density, energy density, reliability with cycling, and folding are systematically investigated. Finally, the practical applications of the asymmetric AFSC are also presented.

## MATERIALS AND METHODS

### Preparation and Characterizations of Ultra-Thin β-Ni(OH)₂ Nanoplates

All of the materials are of analytical grade and used without further purification. The preparation procedure is illustrated in **Figure 1**. Briefly, 1.1215 g of $Ni(NO_3)_2·6H_2O$ and 1.1632 g of $C_6H_{12}N_4$ were added into a beaker containing 40 ml deionized water, and the mixture was magnetically stirred until it became clear to obtain the precursor solution. Then, a piece of Ni foam with size of $1 \times 2$ cm was cleaned by ultrasonication in acetone, 2 M HCl solution, and deionized water, respectively. After drying, the mass of Ni foam is marked $m_0$. Subsequently, the clean Ni foam was added into a Teflon liner together with the precursor solution. After that, the Teflon liner was sealed by a reaction kettle and heated in an oven. After reaction at 80°C for 20 h, taking the Ni foam out and wash it with ethanol and deionized water, and then drying it at 60°C in vacuum. Finally, the color of Ni foam changed from the initial silvery white to light green after drying, and the mass was marked $m_1$. The mass loading of β-$Ni(OH)_2$ nanoplates (m) is about 1.6 mg cm$^{-2}$, which can be calculated by equation: $m = m_1 - m_0$.

The structure, morphology, and composition of the samples were studied by using an X-ray diffractometer (XRD, D8 Advance, Bruker), a field-emission scanning electron microscope (FESEM; JEOL JSM7100F), and an atomic force microscope (AFM, Dimension FastScan, Bruker). X-ray photoelectron spectroscopy (XPS) measurement was performed on an ESCALAB 250xi XPS spectrometer, using monochromatic Al Ka X-rays.
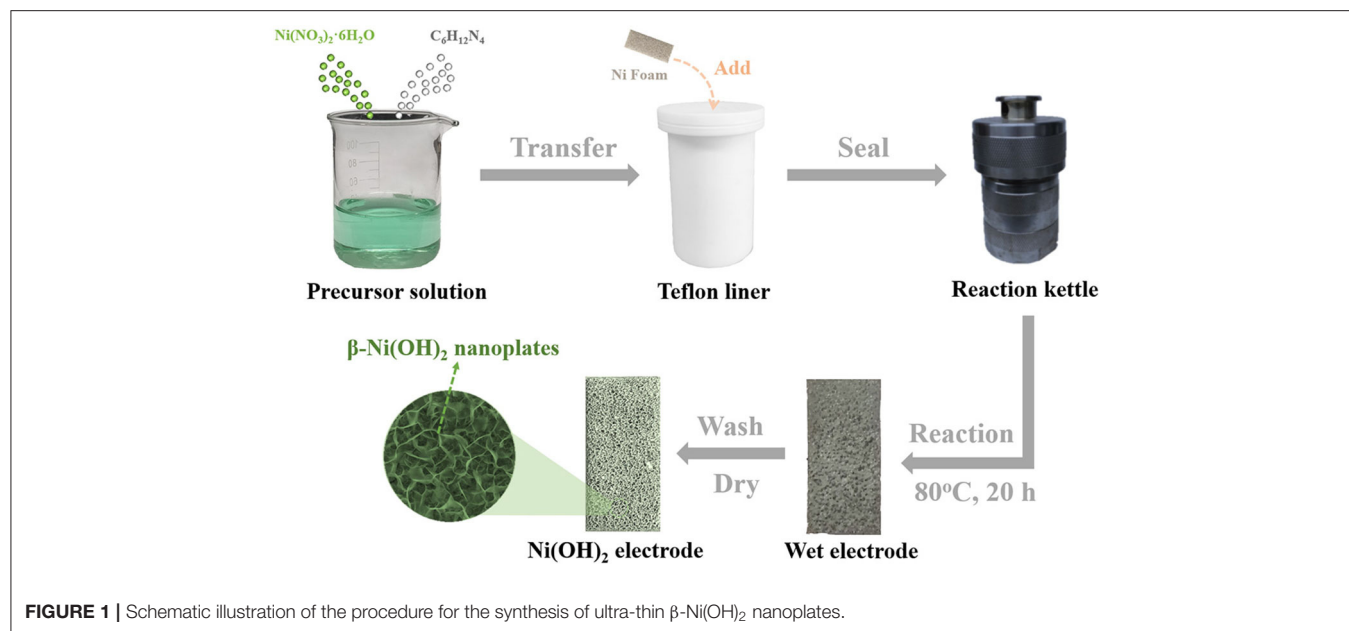
### Assembly of Asymmetric AFSC and Electrochemical Measurement

The slurry of asymmetric AFSCs was prepared by mixing acetylene black, poly(vinylidene fluoride), and AC with N-methyl-2-pyrrolidone in a mass ratio of 1:1:8. Then, the slurry was dip-coated on the Ni foam ($1 \times 2$ cm) and dried at 120°C for 10 h. The mass loading of negative material (AC) was calculated by Equation 1 based on the charge balance between positive and negative electrode (Guo et al., 2019).

$$\frac{m_+}{m_-} = \frac{C_- V_-}{C_+ V_+} - \tag{1}$$

Where $m_+$ (g) and $m_-$ (g) are the active material mass of positive and negative electrode, respectively. $C_+$ (F g$^{-1}$) and $C_-$ (F g$^{-1}$) stand for the specific capacitance of positive and negative electrode, respectively. $V_+$ (V) and $V_-$ (V) are the potential window of positive and negative electrode, respectively. The mass of the AC is about 1.6 mg cm$^{-2}$, respectively.

By mixing 2 g of KOH, 2 g of PAAK, and 20 ml of deionized water under stirring at room temperature, the PAAK/KOH gel electrolyte is ready to use when it became clear and transparent. A filter paper was served as the separator. Finally, the three

**FIGURE 1** | Schematic illustration of the procedure for the synthesis of ultra-thin β-Ni(OH)$_2$ nanoplates.

components [positive electrode β-Ni(OH)$_2$, negative electrode AC, and separator] dip-coated with the prepared electrolyte were assembled into an asymmetric AFSC.

The electrochemical performance of the β-Ni(OH)$_2$ electrode was studied using a three-electrode system. β-Ni(OH)$_2$, Hg/HgO, platinum foil (2 m × 2 cm), and 1 M of KOH aqueous solution were used as the work electrode, reference electrode, counter electrode, and electrolyte, respectively. The electrochemical tests such as alternating current electrochemical impedance spectroscopy (EIS), galvanostatic charge/discharge (GCD), and cyclic voltammetry (CV) were performed by means of the Zahner electrochemical workstation (CIMPS-2). The cycling stability was studied by using the LANHE battery testing system (CT2001A). The electrochemical performance of the asymmetric AFSCs was also studied by the same testing devices.

## RESULTS AND DISCUSSIONS

**Figure 2A** shows the XRD pattern of the as *in-situ* grown sample. In order to display the sample diffraction peaks more intuitively, the diffraction intensity has been processed by logarithm. One can see that the diffraction peaks at 20.2, 33.6, 38.8, and 59.8° correspond to (001), (100), (101), and (110) of Ni(OH)$_2$, respectively, which is consistent with β-Ni(OH)$_2$ (JCPDS 14-0117) (Ji et al., 2013). Meanwhile, there are other three dark yellow peaks locating at 44.5, 51.8, and 76.4°, which belong to the diffractions of the Ni foam (JCPDS 04-0850) (Kim et al., 2017). **Figures 2B,C** show the SEM images of β-Ni(OH)$_2$ with different magnifications. It is obvious that the β-Ni(OH)$_2$ nanoplates are *in-situ* grown uniformly on the surface of Ni foam, forming three-dimensional porous network structure. From the inset of **Figure 2C**, it can be seen that the nanoplates

are extremely thin. In order to further determine the thickness of β-Ni(OH)$_2$ nanoplates, AFM image is shown in **Figure 2D** and **Supplementary Figure 1**. It can be seen that the morphology is irregular after ultrasonic treatment. Using the Step Model in NanoScope Analysis Software, we can obtain the step height of selected area in nanoplate. Considering that there is a little error in the AFM test, the thickness distribution is shown in **Supplementary Figure 1**. It can be seen that the thickness of β-Ni(OH)$_2$ nanoplate is about 2.4 ± 0.2 nm, which is much thinner than those of β-Ni(OH)$_2$ in previous reports (Lu et al., 2011; Li et al., 2020). **Figures 2E,F** shows the XPS curves of Ni and O elements in Ni(OH)$_2$ nanoplate. The peak of Ni 2p$_{3/2}$ is located at 855.6 eV with a shake-up satellite (denoted as "Sat.") peak at about 861.5 eV; meanwhile, Ni 2p$_{1/2}$ characteristic peak is located at 873.2 eV with a shake-up satellite peak at about 879.9 eV. The spin-orbit splitting energy of Ni 2p1/2 and Ni 2p3/2 is at 17.6 eV, corresponding to the chemical state of Ni$^{2+}$ (Chang et al., 2014). In addition, two oxygen bonds peaks can be observed from the O1s spectrum in **Figure 2F**. The peak at 531.2 eV is attributed to the nickel–oxygen bonds and the peak at 533.9 eV may be attributed to the physic/chemisorbed water on the surface of β-Ni(OH)$_2$ nanoplates (Chang et al., 2014).

**Figure 3** shows the electrochemical performance of as-prepared electrode based on ultra-thin β-Ni(OH)$_2$ nanoplates [Ni(OH)$_2$@Ni Foam] using the three-electrode system (vs. Hg/HgO). **Figure 3A** is the comparison of CV curves of bare Ni foam and Ni(OH)$_2$@Ni Foam electrodes at a scan rate of 3 mV s$^{-1}$. It can be seen that the curve of Ni Foam electrode has a quite small area, indicating that the Ni foam has a slight capacitance. In addition, after hydrothermal reaction, the Ni(OH)$_2$ nanoplates grows on the surface of Ni foam, which may hinder the electrolyte from contacting the nickel foam extremely, resulting in a smaller capacitance contribution in energy storage.
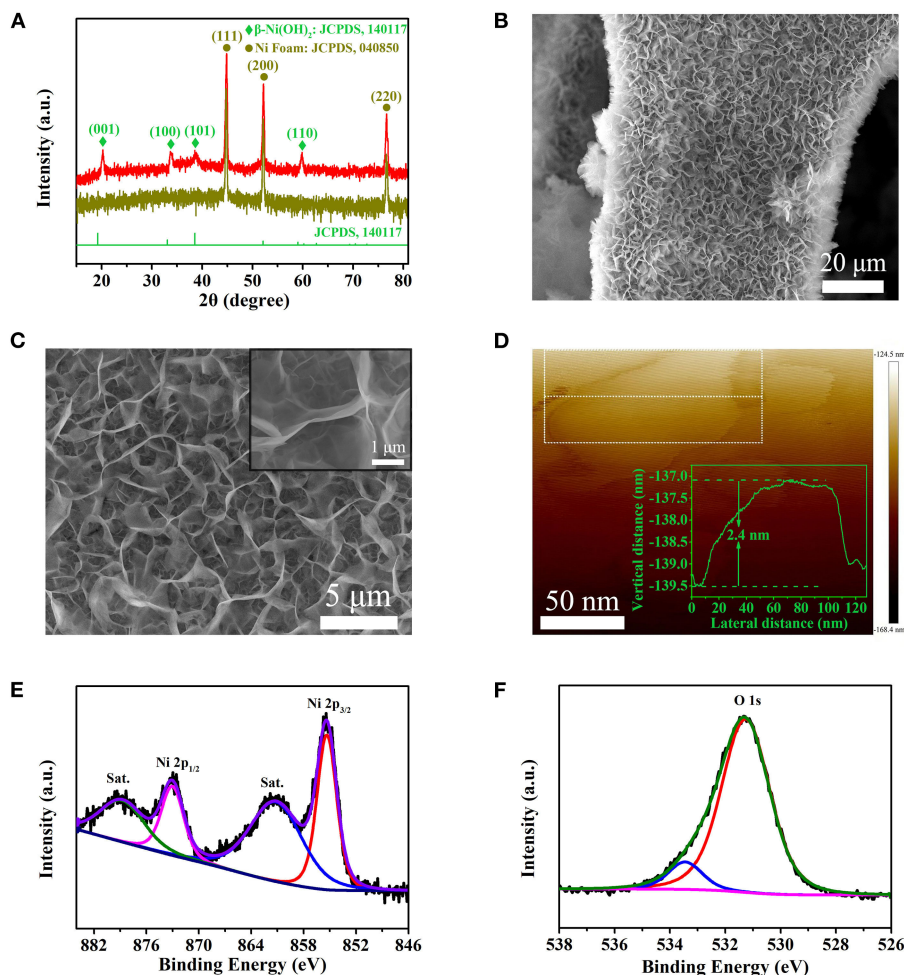
**FIGURE 2 |** Phase, microstructural, and chemical state analysis of Ni(OH)$_2$ nanoplates. **(A)** XRD patterns. **(B,C)** The SEM images at different magnifications. Inset of C is a high-magnification SEM image. **(D)** AFM image of ultra-thin Ni(OH)$_2$ nanoplates, inset is the thickness curve. **(E)** XPS peaks of Ni 2p. **(F)** XPS peaks of O1s.

**Supplementary Figure 2** shows the comparison of GCD curves, which also demonstrates that the Ni foam has a tiny capacitance. Therefore, we can approximately ignore the contribution of Ni foam in the capacitance calculation process. The CV curves of Ni(OH)$_2$ nanoplates are obtained at different scan rates ranging in potential window from 0 to 0.7 V (**Figure 3B**). The typical irregular shapes with clear redox peaks can be observed, revealing that Faradaic redox reactions dominate the energy storage. The redox reaction during charging-discharging process might be described as follows:

$$\text{Ni(OH)}_2 + \text{OH}^- \rightleftharpoons \text{NiOOH} + \text{H}_2\text{O} + e^- \tag{2}$$

It's obvious that two redox peaks are almost symmetrical, indicating that the electrode based on β-Ni(OH)$_2$ nanoplates has excellent reversibility. In addition, all the CV curves can still keep similar shape at different scan rates, revealing a good stability.

According to the CV curves, the specific capacitance (F g$^{-1}$) of the β-Ni(OH)$_2$ electrode can be calculated through following

equation (Wu et al., 2017):

$$C = \frac{\oint I \text{d}V}{2mv\Delta V} \tag{3}$$

Where $I$ (A) is the instantaneous current in CV curve, $m$ (g) is the mass of the active material, $v$ (mV s$^{-1}$) is the scan rate which represents the speed of the potential change during the positive and negative sweeps in the CV measurement, and $\Delta V$ (V) is the applied potential window which presents the range of potential change.

The specific capacitance and rate capability at different scan rates are shown in **Supplementary Figure 3**. Especially, the gravimetric capacitance achieves as high as 1,452 F g$^{-1}$ at the scan rate of 3 mV s$^{-1}$. Of particular importance is that β-Ni(OH)$_2$ electrode also possesses excellent rate capability, remaining a superior capacitance value of 60% (869 F g$^{-1}$) at a scan rate of 20 mV s$^{-1}$, which attributes to the unique ultra-thin structure. **Figure 3C** shows the GCD curves obtained at different charging and discharging current densities. The obvious
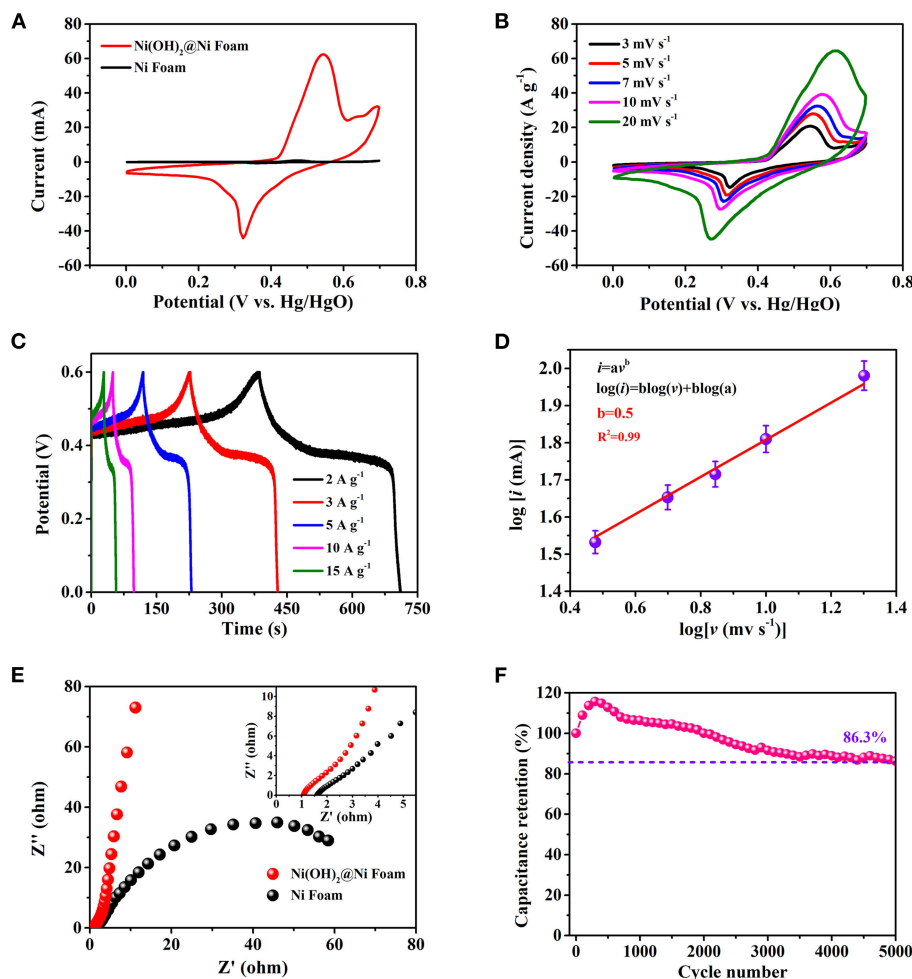
**FIGURE 3 |** Three-electrodes electrochemical measurements of β-Ni(OH)$_2$ electrodes in 1 M of KOH aqueous solution. **(A)** CV curves of the electrodes with scan rates from 3 to 20 mV s$^{-1}$. **(B)** Specific capacitance and capacitance retention at different current densities. **(C)** GCD curves at various current densities. **(D)** Dependence of peak current and sweep speed after taking the logarithm. **(E)** Impedance Nyquist plots of the three-electrodes. **(F)** The cyclability of the electrode, the capacitance retention remains 86.3% after 5,000 cycles.

potential plateaus correspond to the pseudocapacitive behavior during the energy conversion and storage. Superior reversible redox capacity can also be demonstrated from the symmetric curves. To further understand the charge storage mechanism of as-prepared ultra-thin β-Ni(OH)$_2$ nanoplates, the capacity contribution category is discussed in detail. According to the CV curves, the peak current (*i*, mA) and scan rate (*v*, mV s$^{-1}$) obey the following functional relationship (Ju et al., 2020; Wang et al., 2020):

$$i = av^b \tag{4}$$

$$\log(i) = b\log(v) + b\log(a) \tag{5}$$

Where a and b are adjustable parameters. After linear fitting log(*i*) and log(*v*), the curve shows in **Figure 3D** and the Adj. R-Square is about 0.99. According to the curve, it can be obtained that the *b*-value is 0.5, which means that the ultra-thin β-Ni(OH)$_2$ nanoplates belongs to battery type material and the capacity

comes from the Faraday intercalation reaction controlled by diffusion (Wang et al., 2007). This result corresponds to the GCD curve mentioned above, which has obvious potential plateaus as same as battery type material (Fleischmann et al., 2020). In this regard, designing ultra-thin nanostructure to avoid the layers from aggregation and stacking is of great significance. The *b*-values also indicate that the as-prepared β-Ni(OH)$_2$ nanoplates have excellent channels for ions intercalation. As for the electrical and ionic conductivities of β-Ni(OH)$_2$ electrode, the Nyquist plot with the frequency from 100 kHz to 10 mHz is obtained *via* the EIS-test (**Figure 3E**). In the low frequency region, the Nyquist plot is almost a vertical line, while the shape of bare Ni foam is like an semi-circle, suggesting the β-Ni(OH)$_2$ nanoplates have good capacitive behavior. In the range of high frequency region, it can be concluded that the equivalent series resistance is about 1.1 Ω (R$_{ESR}$, including the solution resistance, the contact resistance among active material and substrate, and the internal resistance of the active material) (Zhao et al., 2018), indicating
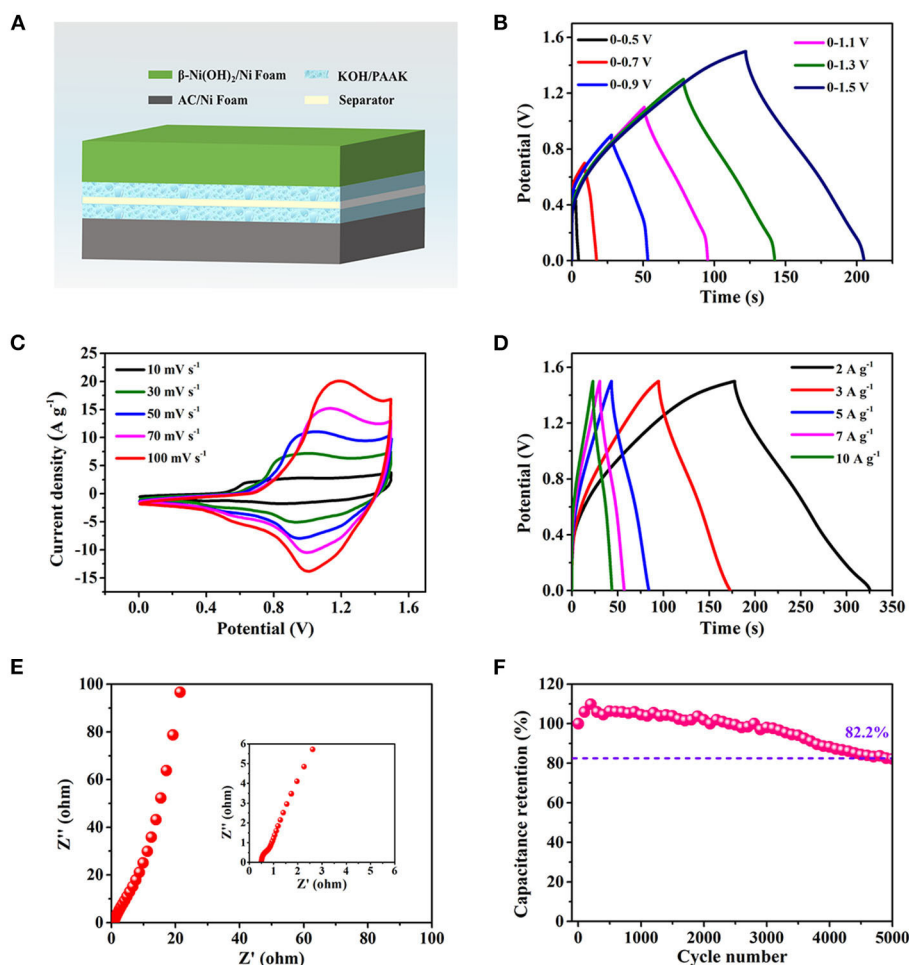
**FIGURE 4** | The electrochemical performance of the asymmetric AFSC device. **(A)** Schematic of the assembled AFSC device. **(B)** GCD curves at various potential windows. **(C)** CV curves at different scan rates. **(D)** GCD curves at different current densities. **(E)** EIS result of the AFSC. **(F)** Capacitance retention after 5,000 cycling times.

a small electrode resistance as well as fast charge-transfer rate between the β-Ni(OH)₂ nanoplates and electrolyte. Meanwhile, the bare Ni foam shows a larger $R_{ESR}$ of 1.6 Ω, which may be due to that the nickel oxide formed on the surface of the Ni foam during charging and discharging hinders the charge transfer. The smaller $R_{ESR}$ of Ni(OH)₂ electrode also indicates that the Ni(OH)₂ nanoplates growth on the surface of Ni foam can prevent electrolyte from contacting the nickel foam. **Figure 3F** shows the cycling stability of β-Ni(OH)₂ electrode after charging-discharging 5,000 times at 3 A g⁻¹. The capacitance increases about 15% during the first 300 cycles, which may be caused by the activation effect (Zhang et al., 2015). After 5,000 cycles, the specific capacitance stills retain 86.3% of the original value, demonstrating a good cycling stability.

To further evaluate the application potential of β-Ni(OH)₂ electrode for energy storage, a rechargeable asymmetric AFSC configuration is built based on AC negative electrode and β-Ni(OH)₂ positive electrode, as schematically illustrated in **Figure 4A**. **Fi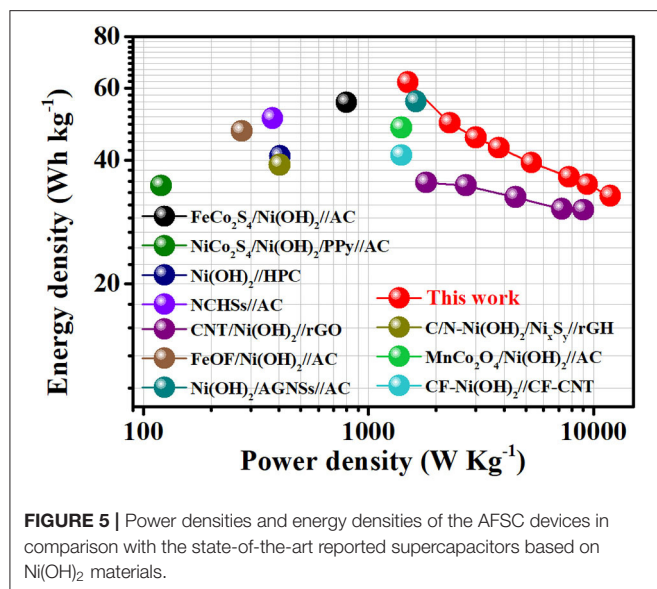gure 4B** shows that the asymmetric AFSC has a high and stable potential window of 1.5 V, which is important to enhance the energy density. **Figure 4C** is the result of CV measurement for the assembled AFSC at different scan rates. There are obvious redox reactions during the charging and discharging process, and the similar shapes indicate the assembled AFSC has excellent stability. **Figure 4D** is the GCD curves at different current densities and the detail discharging curves are shown in **Supplementary Figure 4**.

According to the GCD curves, the specific capacitance (F g⁻¹) of the AFSC can be calculated by Equation 6 (Wu et al., 2017):

$$C = \frac{I\Delta t}{m\Delta V} \qquad (6)$$

Where $I$ (A) is the discharge current, $m$ (g) is the mass of the active material, $\Delta t$ (s) is the discharge time, and $\Delta V$ (V) is the potential window.

The specific capacitances at different current densities are shown in **Supplementary Figure 5**. It can be seen that the capacitance is 198 F g⁻¹, gradually decreasing to 104.6 F g⁻¹ as

**FIGURE 5** | Power densities and energy densities of the AFSC devices in comparison with the state-of-the-art reported supercapacitors based on Ni(OH)$_2$ materials.

the current density increasing from 2 to 15 A g$^{-1}$, where a good capacity retention value of 53% is exhibited at 15 A g$^{-1}$. This phenomenon maybe due to the diffusion movement of electrolyte ions is limited during high charging-discharging process. Thus, only the outer surface of β-Ni(OH)$_2$ nanoplates can be used to storage charge, resulting in a low electrochemical utilization of the electrode materials.

To further study the capacitive behavior, the Nyquist plot is presented in **Figure 4E**. A straight line can be observed in the range of low frequency, the slope of which represents the Warburg resistance (Rw), which is caused by the diffusing resistance of electrolyte ions transferring into the interior of ultra-thin β-Ni(OH)$_2$ nanoplates (Zhao et al., 2018). The straight line almost parallels to the imaginary axis, revealing the β-Ni(OH)$_2$ electrode has low Rw and fast ions diffusion. From the magnified area of the high frequency portion, it can be determined that the R$_{ESR}$ of the asymmetric AFSC is 0.5 Ω (Inset of **Figure 4E**). Moreover, the β-Ni(OH)$_2$-based AFSC also shows good cycling stability (**Figure 4F**). After 5,000 cycles at 3 A g$^{-1}$, the capacitance still retains 82.2%.

In addition, the energy density (E, Wh kg$^{-1}$) and power density (P, W kg$^{-1}$) of the AFSC can be calculated by the following equations (Wu et al., 2017):

$$E = \frac{C\Delta V^2 \times 1000}{2 \times 3600} \tag{7}$$

$$P = \frac{E \times 3600}{\Delta t} \tag{8}$$

Where C (F g$^{-1}$) is the specific capacitance, $\Delta V$ (V) is the potential window and $\Delta t$ (s) is the discharge time.

**Figure 5** shows the Ragone plot of performance comparison between our AFSC and the state-of-the-art reported supercapacitors based on Ni(OH)$_2$. Impressively, at a

power density of 1.5 kW kg$^{-1}$, the AFSC can keep a high energy density of 62 Wh kg$^{-1}$. Even under a high power density of 12 kW kg$^{-1}$, the specific energy density can still achieve 32.7 Wh kg$^{-1}$. Moreover, it is worth noting that the value reported here has exceeded those reported work recently such as FeCo$_2$S$_4$/Ni(OH)$_2$//AC (55.3 Wh kg$^{-1}$), NiCo$_2$S$_4$/Ni(OH)$_2$/PPy//AC (34.7 Wh kg$^{-1}$), Ni(OH)$_2$//HPC (40.9 Wh kg$^{-1}$) etc. (**Supplementary Table 1**; Ghosh et al., 2015; Salunkhe et al., 2015; Zhao et al., 2016; Wang et al., 2017; Liang et al., 2018; Liu et al., 2018; Qin et al., 2018; Yang et al., 2018; Zhang et al., 2018; Zhou et al., 2020). The excellent electrochemical performance of the asymmetric AFSC is attributed to the unique nanostructure of β-Ni(OH)$_2$. The nanoplates *in-situ* growing on Ni Foam form a porous network structure, which can not only prevent aggregation but also improve ion transport in the whole electrode and the electrolyte accessibility of β-Ni(OH)$_2$. Meanwhile, the ultra-thin thickness of the nanoplates can effectively avoid the influence caused by layers stacking. (All detailed electrochemical performance of the AFSC is listed in **Supplementary Table 2**.)

Considering that different applications have special requirements for capacity and potential, two AFSCs are assembled in both parallel (**Figure 6A**) and series connections (**Figure 6B**). Obviously, compared with the individual AFSC, the discharge time of two AFSC in parallel connection is much longer at the same current density, indicating that the capacity is increased by parallel connection. In the meantime, the potential window of two ASFCs connected in series is enlarged to 3 V. These results indicate that fabricated asymmetric AFSC can satisfy different demands in term of potential window and capacity. The background of **Figure 6B** is two blue LEDs in parallel, which can run for 5 min powered by two ASFCs connected in series charged to 3 V. Similarly, an electronic watch also can be driven by two AFSCs (**Supplementary Figure 6**). Flexibility is also an importance index for practical application. As shown in **Figure 6C**, at different bending angles, the changes in size and shape of the CV curves are almost unchanged, indicating that the AFSC still maintains good chemical stability under bending. Moreover, after folding for 1,500 times at 180 degrees, the capacity still maintains 86% of the original value, which further confirms the good flexibility of the AFSC (**Figure 6D**). Besides, attaching two AFSCs in series to the PET board and wrapping them around the hand, an electronic watch still can be powered stably for 10 min. These results give evidence that the fabricated AFSC possesses a high potential for applying in flexible and wearable electronic device.

## CONCLUSIONS

Ultra-thin β-Ni(OH)$_2$ nanoplates grown on Ni foam are successfully prepared by a facile method. The β-Ni(OH)$_2$ electrode exhibits a large specific capacitance and high rate capability. The asymmetric AFSC shows superior performance
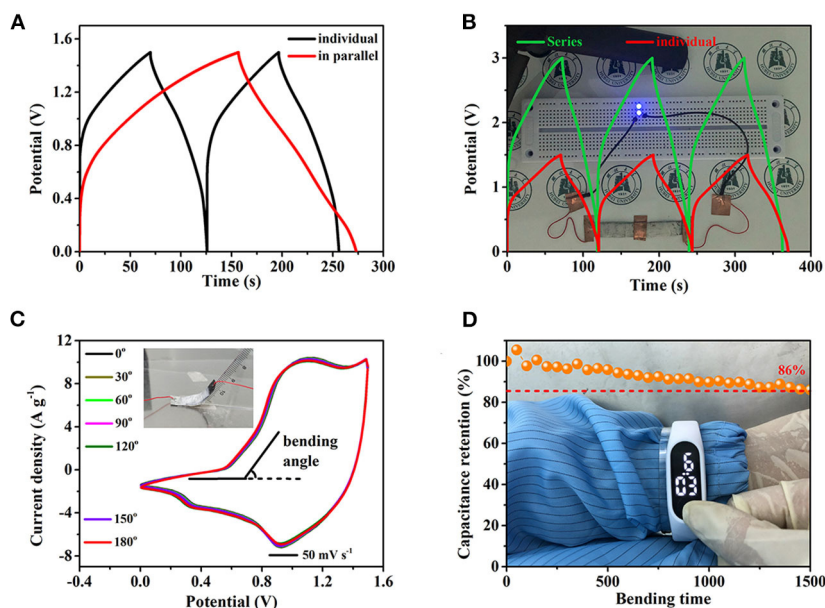
**FIGURE 6 |** The practical application of AFSC devices. **(A)** GCD curves of two AFSC devices connected in parallel. **(B)** GCD curves of two AFSC devices connected in series, the background is the two working blue LEDs. **(C)** Bending angle-tests of the AFSC, inset is the digital photograph. **(D)** Capacitance retention of the AFSC after 1,500 times (bending angle: 180°), the background shows a digital watch driven by two AFSCs connected in series.

such as potential window (1.5 V), energy density (62 Wh kg$^{-1}$ at the power density of 1.5 kW kg$^{-1}$), cycling stability (about 82% capacitance remained over 5,000 cycles), and flexibility (about 86% capacitance remained over 1,500 folding times). The demonstrated performance for AFSCs suggests a great potential to convert and store energy for portable and wearable electronic devices. This work demonstrates that the rational design of ultra-thin nanostructure is an effective strategy to improve the electrochemical performance of 2D materials.

## DATA AVAILABILITY STATEMENT

The raw data supporting the conclusions of this article will be made available by the authors, without undue reservation.

## AUTHOR CONTRIBUTIONS

All authors listed have made a substantial, direct and intellectual contribution to the work, and approved it for publication.

## SUPPLEMENTARY MATERIAL

The Supplementary Material for this article can be found online at: https://www.frontiersin.org/articles/10.3389/fchem. 2020.602322/full#supplementary-material

## REFERENCES

Cai, F.-S., Zhang, G.-Y., Chen, J., Guo, X.-L., Liu, H.-K., and Dou, S.-X. (2004). Ni(OH)₂ tubes with mesoscale dimensions as positive-electrode materials of alkaline rechargeable batteries. *Angew. Chem. Int. Ed.* 43, 4212–4216. doi: 10.1002/anie.200460053

Chang, I.-C., Chen, T.-T., Yang, M.-H., Chiu, H.-T., and Lee, C.-Y. (2014). Self-powered electrochemical deposition of Cu@Ni(OH)₂ nanobelts for high performance pseudocapacitors. *J. Mater. Chem. A* 2:10370. doi: 10.1039/C4TA01152J

Dong, X.-L., Guo, Z.-Y., Song, Y.-F., Hou, M.-Y., Wang, J.-Q., Wang, Y.-G., et al. (2014). Flexible and wire-shaped micro-supercapacitor based on Ni(OH)₂-nanowire and ordered mesoporous carbon electrodes. *Adv. Funct. Mater.* 24, 3405–3412. doi: 10.1002/adfm.201304001

Fleischmann, S., Mitchell, J.-B., Wang, R., Zhan, C., Jiang, D., Presser, V., et al. (2020). Pseudocapacitance: from fundamental understanding to high power energy storage materials. *Chem. Rev.* 120, 6738–67382. doi: 10.1021/acs.chemrev.0c00170

Ghosh, D., Mandal, M., and Das, C.-K. (2015). Solid state flexible asymmetric supercapacitor based on carbon fiber supported hierarchical Co(OH)ₓCO₃

and Ni(OH)$_2$. *Langmuir* 31, 7835–7843. doi: 10.1021/acs.langmuir.5b 00649

Guo, Y.-Q., Hong, X.-F., Wang, Y., Li, Q., Meng, J.-S., Dai, R.-T., et al. (2019). Multicomponent hierarchical Cu-doped NiCo-LDH/CuO double arrays for ultralong-life hybrid fiber supercapacitor. *Adv. Funct. Mater.* 29:1809004. doi: 10.1002/adfm.201809004

Huang, P., Lethien, C., Pinaud, S., Brousse, K., Laloo, R., Turq, V., et al. (2016). On-chip and freestanding elastic carbon films for micro-supercapacitors. *Science* 351, 691–695. doi: 10.1126/science.aad3345

Ji, J.-Y., Zhang, L.-L., Ji, H.-X., Li, Y., Zhao, X., Bai, X., et al. (2013). Nanoporous Ni(OH)$_2$ thin film on 3D ultrathin-graphite foam for asymmetric supercapacitor. *ACS Nano* 7, 6237–6243. doi: 10.1021/nn4021955

Ju, L.-C., Wang, G.-Z., Liang, K., Wang, M.-Y., Sterbinsky, G.-E., Feng, Z.-F., et al. (2020). Significantly improved cyclability of conversion-type transition metal oxyfluoride cathodes by homologous passivation layer reconstruction. *Adv. Energy Mater.* 10:1903333. doi: 10.1002/aenm.201903333

Kim, S.-I., Kang, J.-H., Kim, S.-W., and Jan J.-H. (2017). A new approach to high-performance flexible supercapacitors: mesoporous three-dimensional Ni-electrodes. *Nano Energy* 39, 639–646. doi: 10.1016/j.nanoen.2017.07.050

Li, J.-B., Liu, Y., Cao, W., and Chen, N. (2020). Rapid *in situ* growth of β-Ni(OH)$_2$ nanosheet arrays on nickel foam as an integrated electrode for supercapacitors exhibiting high energy density. *Dalton Trans.* 49, 4956–4966. doi: 10.1039/D0DT00687D

Liang, M.-M., Zhao, M.-S., Wang, H.-Y., Shen, J.-F., and Song, X.-P. (2018). Enhanced cycling stability of hierarchical NiCo$_2$S$_4$@Ni(OH)$_2$@Ppy core-cell nanotube arrays for aqueous asymmetric supercapacitors. *J. Mater. Chem. A* 6, 2482–2493. doi: 10.1039/C7TA10413H

Liu, F.-Y., Chu, X., Zhang, H.-T., Zhang, B.-B., Long, H.-S., Wang, Z.-X., et al. (2018). *Facilely synthesis of self-assembly 3D porous Ni(OH)2 with high capacitance for hybrid supercapacitors. Electrochim Acta* 269, 102–110. doi: 10.1016/j.electacta.2018.02.130

Lu, Z.-Y., Chang, Z., Zhu, W., and Sun X.-M. (2011). Beta-phased Ni(OH)$_2$ nanowall film with reversible capacitance higher than theoretical faradic capacitance. *Chem. Commun.* 47, 9651–9653. doi: 10.1039/c1cc13796d

Meng, C.-Z., Liu, C.-H., Chen, L.-Z., Hu, C.-H., and Fan, S.-S. (2010). Highly flexible and all-solid-state paperlike polymer supercapacitors. *Nano Lett.* 10, 4025–4031. doi: 10.1021/nl1019672

Peng, X., Peng, L.-L., Wu, C.-Z., and Xie, Y. (2014). Two dimensional nanomaterials for flexible supercapacitors. *Chem. Soc. Rev.* 43, 3303–3323. doi: 10.1039/c3cs60407a

Qin, Q.-Q., Liu, J.-Q., Mao, W.-P., Xu, C.-X., Lan, B.-B., Wang, Y., et al. (2018). Ni(OH)$_2$/CNTs hierarchical spheres for foldable all-solidstate supercapacitor with high specific energy. *Nanoscale* 10, 7377–7381. doi: 10.1039/C8NR00895G

Salunkhe, R.-R., Lin, J.-J., Malgras, V., Dou, S.-X., Kim, J.-H., and Yamauchi, Y. (2015). Large-scale synthesis of coaxial carbon nanotube/Ni(OH)$_2$ composites for asymmetric supercapacitor application. *Nano Energy* 11, 211–218. doi: 10.1016/j.nanoen.2014.09.030

Wang, G.-Z., Aubin, M., Mehta, A., Tian, H.-J., Chang, J.-F., and Kushima, A. (2020). Stabilization of Sn anode through structural reconstruction of a Cu–Sn intermetallic coating layer. *Adv. Mater.* 32:2003684. doi: 10.1002/adma.202003684

Wang, H.-L., Casalongue, H.-S., Liang, Y.-Y., and Dai, H.-J. (2010). Ni(OH)$_2$ nanoplates grown on graphene as advanced electrochemical pseudocapacitor materials. *J. Am. Chem. Soc.* 132, 7472–7477. doi: 10.1021/ja102267j

Wang, J., Polleux, J., Lim, J., and Dunn, B. (2007). Pseudocapacitive contributions to electrochemical energy storage in TiO$_2$ (Anatase) nanoparticles. *J. Phys. Chem. C* 111, 14925–14931. doi: 10.1021/jp074464w

Wang, M.-Q., Li, Z.-Q., Wang, C.-X., Zhao, R.-Z., Li, C. X., Guo, D. X., et al. (2017). Novel core–shell FeOF/Ni(OH)$_2$ hierarchical nanostructure for all-solid-state flexible supercapacitors with enhanced performance. *Adv. Funct. Mater.* 27:1701014. doi: 10.1002/adfm.201701014

Wu, Z., Li, L., Yan, J.-M., and Zhang, X.-B. (2017). Materials design and system construction for conventional and new-concept supercapacitors. *Adv. Sci.* 4:1600382. doi: 10.1002/advs.201600382

Yang, H.-X., Zhao, D.-L., Lin, H., Tian, X.-M., Han, X.-Y., Duan, Y.-J., et al. (2018). Activated graphene nanosheets/spinule-like Ni(OH)$_2$ composite as cathode materials or high performance supercapacitors. *Electrochim Acta* 292, 468–476. doi: 10.1016/j.electacta.2018.09.185

Yang, Y. (2020). A mini-review: emerging all-solid-state energy storage electrode materials for flexible devices. *Nanoscale* 12, 3560–3573. doi: 10.1039/C9NR08722B

Zha, D.-S., Sun, H.-H., Fu, Y.-S., Ouyang, X.-P., and Wang, X. (2017). Acetate anion-intercalated nickel-cobalt layered double hydroxide nanosheets supported on Ni foam for high-performance supercapacitors with excellent long-term cycling stability. *Electrochim Acta* 236, 18–27. doi: 10.1016/j.electacta.2017.03.108

Zhang, L.-S., Ding, Q.-W., Huang, Y.-P., Gu, H.-H., Miao, Y.-E., and Liu, T.-X. (2015). Flexible hybrid membranes with Ni(OH)$_2$ nanoplatelets vertically grown on electrospun carbon nanofibers for high-performancesupercapacitors. *ACS Appl. Mater. Interfaces* 7, 22669–22677. doi: 10.1021/acsami.5b07528

Zhang, Y., Yu, L., Hu, R., Zhang, J.-L., Niu, R.-C., Qian, X.-Y., et al. (2018). Biomass-derived C/N co-doped Ni(OH)$_2$/Ni$_x$S$_y$ with sandwich structure for supercapacitors. *J. Mater. Chem. A* 6, 17417–17425. doi: 10.1039/C8TA06072J

Zhao, J., Li, Z., Yuan, X., Yang, Z., Zhang, M., Meng, A., et al. (2018). A high-energy density asymmetric supercapacitor based on Fe$_2$O$_3$ nanoneedle arrays and NiCo$_2$O$_4$/Ni(OH)$_2$ hybrid nanosheet arrays grown on SiC nanowire networks as free-standing advanced electrodes. *Adv. Energy Mater.* 8:1702787. doi: 10.1002/aenm.201702787

Zhao, Y., Hu, L.-F., Zhao, S.-Y., and Wu, L.-M. (2016). Preparation of MnCo$_2$O$_4$@Ni(OH)$_2$ core–shell flowers for asymmetric supercapacitor materials with ultrahigh specific capacitance. *Adv. Funct. Mater.* 26, 4085–4093. doi: 10.1002/adfm.201600494

Zhou, S.-Y., Liu, Y., Yan, M., Sun, L., Luo, B.-F., Yang, Q.-J., et al. (2020). Design of FeCo$_2$S$_4$@Ni(OH)$_2$ core-shell hollow nanotube arrays on carbon paper for ultra-high capacitance in supercapacitors. *Electrochim Acta* 2020:136337. doi: 10.1016/j.electacta.2020.136337

# Different Benzendicarboxylate-Directed Structural Variations and Properties of Four New Porous Cd(II)-Pyridyl-Triazole Coordination Polymers

Ying Zhao[1†], Jin Jing[2†], Ning Yan[2], Min-Le Han[1], Guo-Ping Yang[2*] and Lu-Fang Ma[1*]

[1] College of Chemistry and Chemical Engineering, Luoyang Normal University, Luoyang, China, [2] Key Laboratory of Synthetic and Natural Functional Molecule of Ministry of Education, Shaanxi Key Laboratory of Physico-Inorganic Chemistry, College of Chemistry & Materials Science, Northwest University, Xi'an, China

Four new different porous crystalline Cd(II)-based coordination polymers (CPs), i. e., $[Cd(mdpt)_2]\cdot 2H_2O$ (**1**), $[Cd_2(mdpt)_2(m\text{-}bdc)(H_2O)_2]$ (**2**), $[Cd(Hmdpt)(p\text{-}bdc)]\cdot 2H_2O$ (**3**), and $[Cd_3(mdpt)_2(bpdc)_2]\cdot 2.5NMP$ (**4**), were obtained successfully by the assembly of Cd(II) ions and bitopic 3-(3-methyl-2-pyridyl)-5-(4-pyridyl)-1,2,4-triazole (Hmdpt) in the presence of various benzendicarboxylate ligands, i.e., 1,3/1,4-benzenedicarboxylic acid ($m\text{-}H_2bdc$, $p\text{-}H_2bdc$) and biphenyl-4,4′-bicarboxylate ($H_2bpdc$). Herein, complex **1** is a porous 2-fold interpenetrated four-connected 3D **NbO** topological framework based on the mdpt⁻ ligand; **2** reveals a two-dimensional (2D) **hcb** network. Interestingly, **3** presents a three-dimensional (3D) rare interpenetrated double-insertion supramolecular net *via* 2D ···ABAB··· layers and can be viewed as an **fsh** topological net, while complex **4** displays a 3D **sqc117** framework. Then, the different gas sorption performances were carried out carefully for complexes **1** and **4**, the results of which showed **4** has preferable sorption than that of **1** and can be the potential $CO_2$ storage and separation material. Furthermore, the stability and luminescence of four complexes were performed carefully in the solid state.

Keywords: coordination polymers, structural variations, topologies, gas adsorption, luminescent properties

## INTRODUCTION

The coordination polymers (CPs) have gained considerable research interest by the self-assembly of various organic linkers (including different functional groups) with metal ions/clusters due to their special topological nets and broad applications (Wang et al., 2014, 2015; Smith et al., 2015; Wang and Wang, 2015; Dey et al., 2017; Hong et al., 2017; Islamoglu et al., 2017; Kariem et al., 2017; Lin et al., 2017; Li et al., 2018; Xing and Janiak, 2020; Zhang et al., 2020). Generally, the coordination preference of the nature of ligands and geometries of ions are the primary considerations in the preparation process of CPs. However, other factors, such as the choice of auxiliary ligands, pH,

template effect, as well as reaction temperature, etc., are considered to be the great roles in the fabrications of the desired structures (Chen et al., 2015; Song et al., 2015; Waller et al., 2015; Blandez et al., 2016; Lannoeye et al., 2016; Manna et al., 2016; Rosa et al., 2016; Lu et al., 2017). Besides, the typical non-covalent supramolecular interlocks, including H-bonding, $\pi \cdots \pi$ stacking, etc., may also help to fine-tune the structural assemblies (Wheeler, 2013; Yadav and Gorbitz, 2013; Bhattacharya et al., 2014, 2016; DeFuria et al., 2016; Ju et al., 2016; Li et al., 2016, 2017; Song et al., 2016; Yao et al., 2016; Park et al., 2017). Thus, it is essential to explore these factors to further help study the relationship of structures and properties.

The current research findings have presented that N-containing heterocyclic ligands possess excellent binding abilities with different center metal ions to construct various CPs. Further, most of them may be acted as the neutral building units and also as the anionic units by releasing the acidic N-H groups of the ligands, showing more versatile coordination fashions (Lin et al., 2010, 2011; Chen et al., 2013; Li et al., 2019). Recently, there are some studies mainly focused on the N-heterocycles and their derivatives with five-membered rings (including the imidazole, triazole, or tetrazole groups, etc.) and multicarboxylate as mixed ligands to build different porous CPs (Pachfule and Banerjee, 2011; Chen et al., 2013; Liu et al., 2014; Qin et al., 2014; Wang et al., 2014; Du et al., 2015; Li et al., 2016, 2017; Yan et al., 2017), which often show exceptional gas sorption and luminescent performances. Similarly, the phenlycarboxylate tectons have also been proven to be the great candidates to yield functional CPs because of their abundant coordination modes with ions (Chen et al., 2013; Li et al., 2015; Jin et al., 2016; Wu et al., 2017).

As a combination of the above stated facts and our previous works, a rigid N-heterocyclic 3-(3-methyl-2-pyridyl)-5-(4-pyridyl)-1,2,4-triazole (Hmdpt) ligand was deliberately chosen with three kinds of phenyldicarboxylate linkers, i.e., 1,3/1,4-benzenedicarboxylate (m-H$_2$bdc, p-H$_2$bdc) and biphenyl-4,4′-dicarboxylate (H$_2$bpdc) to prepare porous CPs in this study. The Hmdpt tecton has lots of coordination sites and also can be the excellent hydrogen bonding donor/acceptor in the assembly of new CPs. Herein, four new Cd(II)-CPs, [Cd(mdpt)$_2$]·2H$_2$O (1), [Cd$_2$(mdpt)$_2$(m-bdc)(H$_2$O)$_2$] (2), [Cd(Hmdpt)(p-bdc)]·2H$_2$O (3), as well as [Cd$_3$(mdpt)$_2$(bpdc)$_2$]·2.5NMP (4), were synthesized successfully. Complex 1 displays a 2-fold interlocked four-connected *NbO* framework; 2 reveals a two-dimensional (2D) *hcb* network. More interestingly, complex 3 presents a three-dimensional (3D) rare interlocked double-insertion *fsh* supramolecular net *via* 2D ···ABAB··· layers, while 4 is a 3D *sqc117* network. Their structural diversity indicates that the different secondary benzendicarboxylate linkers have great influence on the assembly process of new CPs. The stability and luminescence were investigated carefully for four complexes in the solid state. Especially, the different gas sorption performances have been carried out for 1 and 4 in detail, indicating 4 has preferable adsorption than that of 1 and can be the potential CO$_2$ capture/separation material.

## EXPERIMENTAL SECTION

### Materials and General Methods

All the reagents/solvents were brought to use in the experiments with no further purification. The characterization methods of the four complexes are given in section Materials and General Methods. Because the synthesis processes of four CPs are very similar, thus the synthesis of CP 1 is only presented herein briefly, and others can be found in the supporting information.

Synthesis of [Cd(mdpt)$_2$]·2H$_2$O (1). A mixture of 3CdSO$_4$·8H$_2$O (0.05 mmol, 38.5 mg), Hmdpt (0.05 mmol, 11.8 mg), DMA (4 ml), and H$_2$O (6 ml) was mixed in a 25-ml Teflon-lined stainless steel vessel, which was heated at 120°C for 72 h and then cooled to room temperature at the rate of 10°C/h to form colorless block crystals. Yield is 63% (based on Hmdpt). Elemental analysis of 1, calculated (%): C 51.75, N 23.22, H 3.98; found: C 51.68, N 23.38, H 3.73. Fourier Transform Infrared spectra (FT-IR) (cm$^{-1}$): 3,525 (m), 3,436 (m), 3,244 (m), 1,612 (m), 1,424 (m), 1,110 (s), 839 (w), 716 (w), 608 (s).

### X-Ray Crystal Structure Determinations

The instruments used for X-ray crystallographic measurements and the refinement methods and details by SHELXL-97 (Sheldrick, 1997) are displayed in section X-Ray Crystal Structure Determinations. The crystallographic data of four CPs are listed in **Table 1**. The Cambridge Crystallographic Data Centre (CCDC) numbers of the four CPs are 1543594–1543597, respectively.

## RESULTS AND DISCUSSION

### Structure Description of [Cd(mdpt)$_2$]·2H$_2$O (1)

Based on the X-ray single-crystal diffraction of complex 1, it crystallizes in the *R*-3 trigonal system. Each Cd(II) ion is coordinated octahedrally with 2-pyridyl/triazolate N atoms from two mdpt⁻ linkers as the *trans* fashion as well as 4-pyridyl N atoms from the adjacent units (**Figure 1A**), and the similar complex of which has been reported before (Lin et al., 2010). The Cd–N lengths are the 2.215–2.408 Å, and the angles *via* Cd(II) center are 71.27° (8)−180.0°.

The mdpt⁻ linker holds two coordination fashions, i.e., bridged/chelated bidentate fashions ($\eta^1\mu_1\chi^1$ and $\eta^2\mu_1\chi^2$) in 1, to coordinate with Cd(II) ions (**Figure 1B** and **Supplementary Figure 4**) to form a porous 3D framework (**Figure 1C**), and the void volume ratio of which is about 23.2% after exclusion of the guest water molecules by the calculation of PLATON program. Topologically, each ligand links two Cd(II) centers and each Cd(II) center joins four different bridged linkers, respectively. Thus, complex 1 displays a 2-fold four-connected interpenetrating *NbO* topological type with the $(6^4.8^2)$ point symbol (**Figure 1D**).
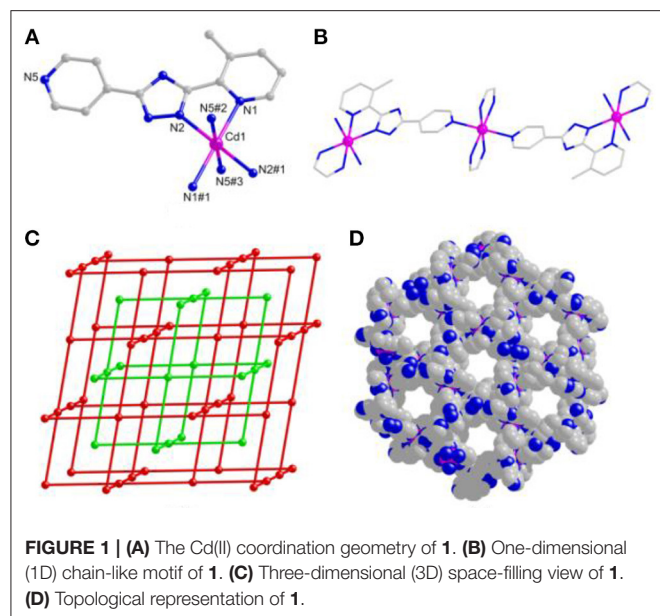
### Structure Description of [Cd$_2$(mdpt)$_2$(m-bdc)(H$_2$O)$_2$] (2)

When the different carboxylate ligands are introduced in the reaction systems, Cd(II) centers are more prone to coordinate

| Complexes | 1 | 2 | 3 | 4 |
|---|---|---|---|---|
| Formula | $C_{26}H_{24}CdN_{10}O_2$ | $C_{34}H_{28}Cd_2N_{10}O_6$ | $C_{21}H_{19}CdN_5O_6$ | $C_{66.5}H_{58.5}Cd_3N_{12.5}O_{10.5}$ |
| Mass | 602.93 | 897.48 | 549.81 | 1,537.66 |
| Crystal system | Trigonal | Monoclinic | Monoclinic | Monoclinic |
| Space group | $R\text{-}3$ | $P2_1/c$ | $P2_1/n$ | $C2/c$ |
| $a$ [Å] | 27.122 (4) | 21.920 (2) | 9.9364 (12) | 30.332 (4) |
| $b$ [Å] | 27.122 (4) | 7.1964 (8) | 14.6653 (18) | 11.0553 (13) |
| $c$ [Å] | 10.7626 (17) | 30.860 (2) | 15.4981 (19) | 21.499 (3) |
| $\alpha$ [°] | 90 | 90 | 90 | 90 |
| $\beta$ [°] | 90 | 134.521(4) | 103.739 (2) | 114.604 (2) |
| $\gamma$ [°] | 120 | 90 | 90 | 90 |
| $V$ [Å³] | 6856 (3) | 3470.9 (5) | 2193.8 (5) | 6554.7 (14) |
| $Z$ | 9 | 1 | 4 | 4 |
| $D_{calcd.}$ [g·cm⁻³] | 1.275 | 1.710 | 1.665 | 1.307 |
| $\mu$ [mm⁻¹] | 0.747 | 1.286 | 1.044 | 1.015 |
| $F$ [000] | 2646 | 1768 | 1104 | 2552 |
| GOOF | 1.069 | 1.182 | 1.014 | 1.019 |
| $R_1{}^a$ [I>2σ(I)] | 0.0292 | 0.0418 | 0.0235 | 0.0488 |
| $wR_2{}^b$ (all data) | 0.0699 | 0.1603 | 0.0840 | 0.1661 |

$^aR_1 = \sum||F_o|\text{-}|F_c||/\sum|F_o|$, $^bwR_2 = [\sum w(F_o^2\text{-} F_c^2)^2/ \sum w(F_o^2)^2]^{1/2}$.



**FIGURE 1 | (A)** The Cd(II) coordination geometry of **1**. **(B)** One-dimensional (1D) chain-like motif of **1**. **(C)** Three-dimensional (3D) space-filling view of **1**. **(D)** Topological representation of **1**.

with O atoms than N atoms *via* the soft–hard acid–base (SHAB) principle, thus making various dimensionalities and structures of complexes (Zhang S. et al., 2013; Zhang X. et al., 2013). Herein, complex **2** has the $P2_1/c$ monoclinic system. The asymmetric unit holds two independent Cd(II) centers, two mdpt⁻, one *m*-bdc²⁻ linker, as well as two coordinated waters. All the Cd(II) ions have the hexa-coordinated geometries and possess the similar modes to link different ligands. Each Cd(II) center makes coordination with two O atoms of one *m*-bdc²⁻, one O atom of water

molecule, and three N atoms of two different mdpt⁻ tectons (**Figure 2A**). The Cd–O/Cd–N distances are 2.272–2.434/2.267–2.371 Å, respectively; and the angles *via* Cd(II) ion are 55.49°-175.63° (**Supplementary Table 1**).

In **2**, Cd(II) ions are connected through mdpt⁻ ligand to give rise to a 1D wave-like motif (**Figure 2B**). These adjacent 1D chains are further extended by *m*-bdc²⁻ tectons to yield a waved 2D layered structure along the *a* axis (**Figure 2C**). Topologically, each mdpt⁻ and *m*-bdc²⁻ linker two Cd(II) centers, which can be regarded as three-connected nodes, thus, the 2D structure can be viewed as a three-connected $(6^3)$ ***hcb*** net (**Figure 2D**). In addition, there exist the different hydrogen H-bonding interlocks $(N_2\cdots O_5, N_7\cdots O_6)$ in the adjacent parallel 2D networks, which help to combine these 2D motifs as a final 3D supramolecular structure (**Figure 3**).

## Structure Description of [Cd(Hmdpt)(*p*-bdc)]·2H₂O (3)

Compared with the *m*-H₂bdc ligand, the distance of the carboxylate groups of *p*-H₂bdc is much farther to each other, which thus results in the various mode with Cd(II) centers and structure of **3**. Compound **3** has the $P2_1/n$ monoclinic system. The building block consists of a Cd(II) center, an Hmdpt, a *p*-bdc²⁻ tecton, and two guest waters. Each Cd(II) center adopts a seven-coordinated environment in which four O atoms are from the same *p*-bpc²⁻ and three N atoms are derived from two Hmdpt linkers (**Figure 4A**). The Cd–N/Cd–O lengths are 2.363∼2.374/2.329∼2.5175Å, and the angles *via* Cd(II) ion are 53.56–162.80° (**Supplementary Table 1**).

In **3**, the N atoms of Hmdpt ligand adopt 2-pyridyl and triazolate 1-nitrogens chelating and 4-pyridyl bridging modes
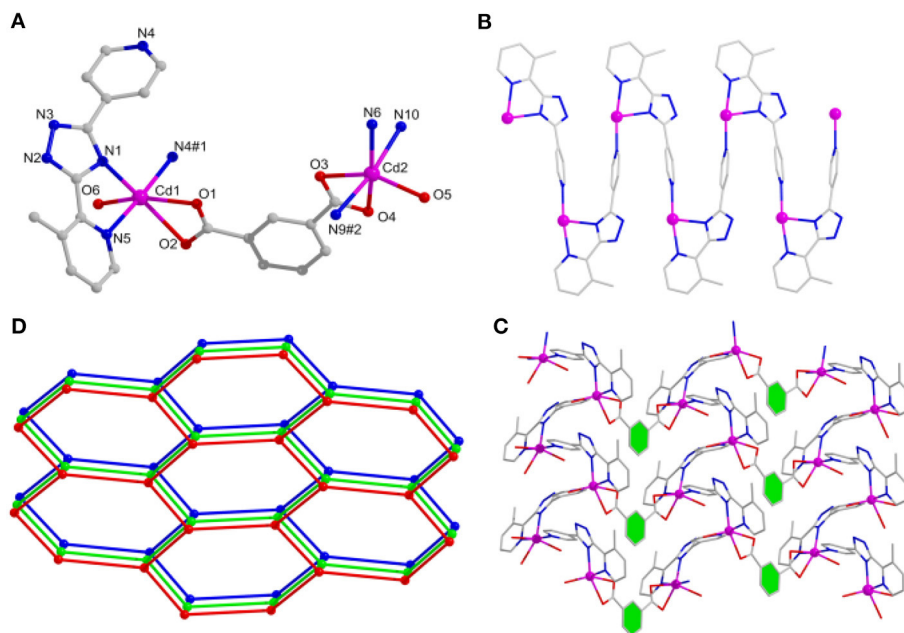
FIGURE 2 | (A) The Cd(II) coordination environments of 2. (B) One-dimensional (1D) chain motif of 2 along *a* axis. (C) Two-dimensional (2D) layered structure of 2. (D) Topological net of 2.
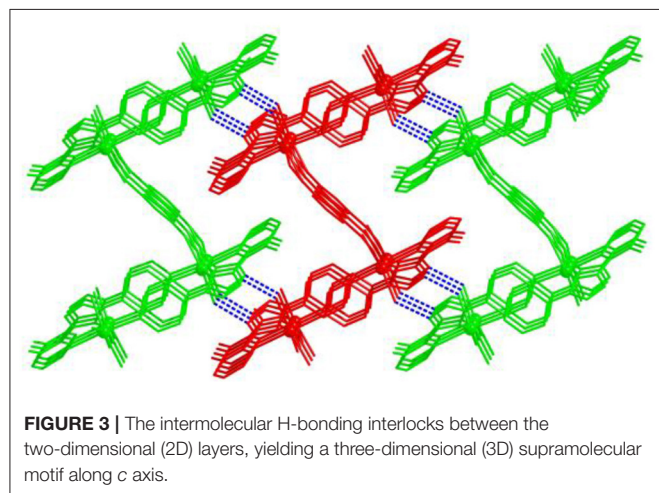


FIGURE 3 | The intermolecular H-bonding interlocks between the two-dimensional (2D) layers, yielding a three-dimensional (3D) supramolecular motif along *c* axis.



FIGURE 4 | (A) The Cd(II) coordination geometry of 3. (B) The binuclear unit of 3. (C) The two-dimensional (2D) layered motif of 3 *via* the *a* axis. (D) The 2-fold interlocked topology of 3.

with two Cd(II) ions, forming a secondary building unit $[Cd_2(mdpt)_2]$ (**Figure 4B**), which produced an infinite 1D chain motif through $p\text{-bdc}^{2-}$ ligand (**Supplementary Figure 1**). The neighboring 1D chains were successfully bridged by $p\text{-bdc}^{2-}$ linkers to produce a new 2D layer via the *a* axis (**Figure 4C**). Like that of complex **2**, although **3** is also a 2D layered motif, however, the 2D layers are characterized by the accumulation of ···ABAB··· fashion. Further, the hydrogen bonds between the AA layers and water molecule $O_6$ form a 3D supramolecular network and then interpenetrate with the 3D net held by the BB layers (**Supplementary Figure 2**). When the topological method is employed for analyzing the structure, complex **3** can
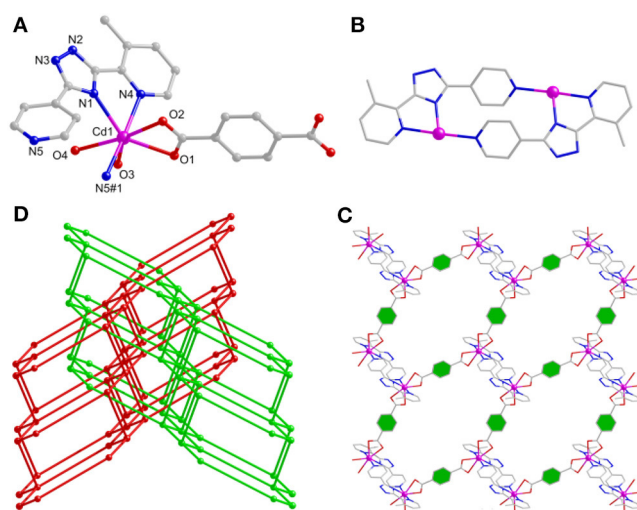
be simplified as (4,6)-connected *fsh* framework, and the point symbol of which is $(4^3.6^3)_2(4^6.6^6.8^3)$ (**Figure 4D**).

## Structure Description of $[Cd_3(mdpt)_2(bpdc)_2]\cdot2.5NMP$ (4)

Due to the distance of two carboxylate groups of $H_2$bpdc longer than those of **3**, thereby, a 3D dense framework of **4** is

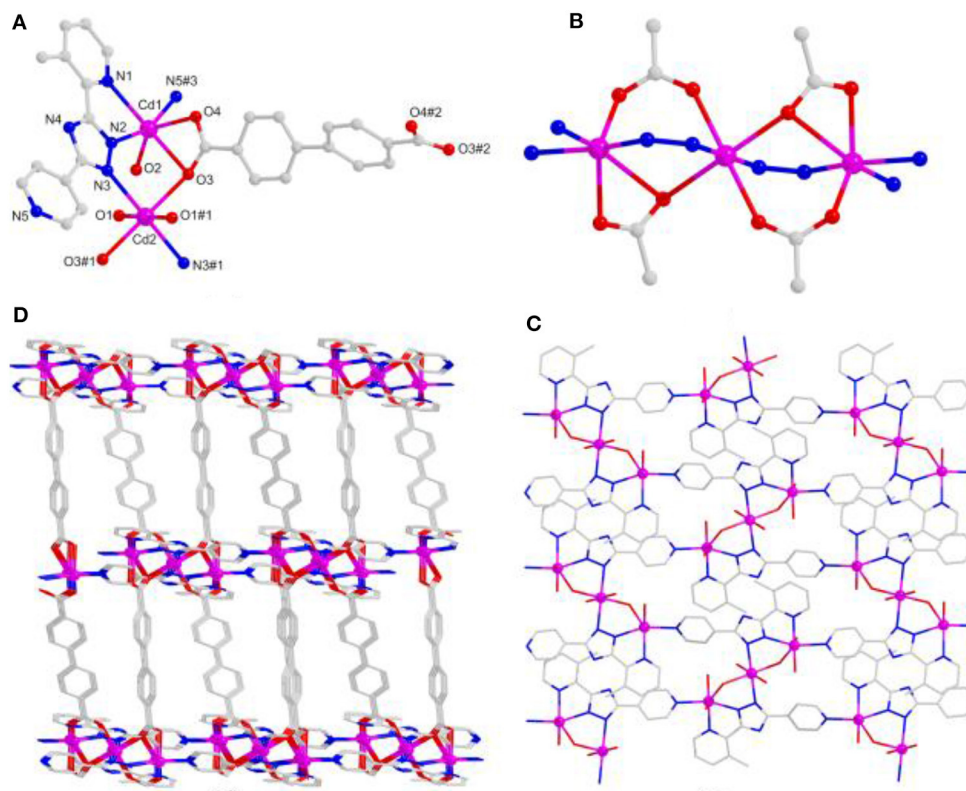**FIGURE 5 | (A)** The Cd(II) coordination geometries of **4**. **(B)** The [Cd$_3$($\mu_2$-COO)$_4$N$_4$] SBU of **4**. **(C)** The two-dimensional (2D) layered motif based on mdpt$^-$ tectons of **4** via the *a* axis. **(D)** The three-dimensional (3D) porous structure of **4** via the *b* axis.

formed. Complex **4** crystallizes in the monoclinic *C2/c* crystal system. There contain three kinds of Cd(II) centers, two mdpt$^-$ tectons, as well as two bpdc$^{2-}$ linkers to form the asymmetric unit. The Cd–O/Cd–N distances are 2.185–2.613/2.229–2.395 Å, respectively.

Due to the twist of the two benzene rings, which makes the Cd1 and Cd2 centers adopt the same hexa-coordinated geometries but different coordination environments, where the Cd1 center takes coordination with three O atoms of bridging bpdc$^{2-}$ tectons and three N atoms of mdpt$^-$ linkers, the Cd2 center is bonded with four O atoms of bridging bpdc$^{2-}$ tectons as well as two N atoms of mdpt$^-$ linkers (**Figure 5A**). The deprotonated carboxylates exhibit $\eta^2\mu_2\chi^3$ and $\eta^2\mu_2\chi^2$ (**Supplementary Figure 5**) coordination modes and the N2, N3 of the mdpt$^-$ ligands are coordinated with three Cd(II) ions to result in a new [Cd$_3$($\mu_2$-COO)$_4$N$_4$] secondary building unit (SBU) (**Figure 5B**). Such SBUs are further bridged by mdpt$^-$ tectons to afford a 2D [Cd$_3$(mdpt)$_2$] layered motif along the *a* axis (**Figure 5C**). Moreover, these 2D adjacent motifs are further supported by introducing the flexible bpdc$^{2-}$ linkers as the pillars to produce a 3D porous pillar-layered framework along the *b* axis (**Figure 5D**). As shown in **Supplementary Figure 4**, a pore space-filling structure is presented, and the void ratio is about 32.9% based on the PLATON program calculation. From a topological viewpoint, each Cd SBU may be simplified as the eight-connected
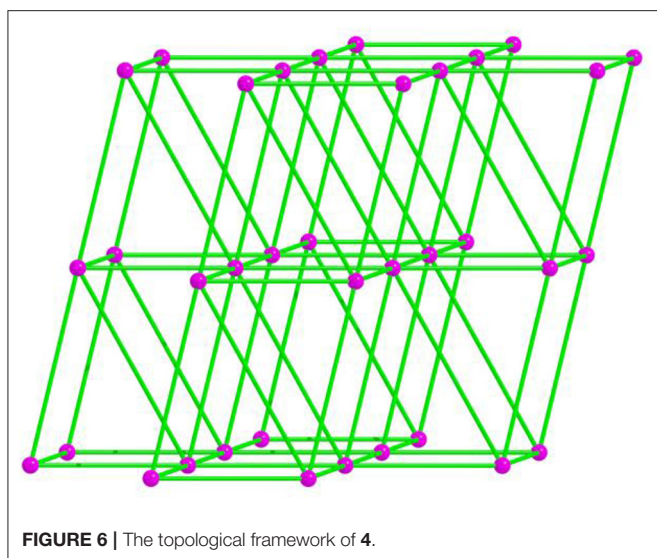
nodes, and the overall net thus forms a $(3^6.4^{12}.5^8.6^2)$ *sqc117* net (**Figure 6**).

From the above structural features of four CPs, it can be found that the different auxiliary tectons may give rise to the new structural variations and then further help to fine-tune the properties of CPs. In the same reaction systems, the minor differences of the ligands will make great changes in the assembly processes of CPs, the benefit of which should be explored carefully to control the fabrications of new CPs with desired structures and performances.

## Powder X-Ray Diffraction Measurement and Thermal Stabilities

The mass identities and phase purity of the four complexes were tested by comparisons of the experimental and the simulated powder X-ray diffraction (PXRD) patterns from the X-ray single-crystal data (**Supplementary Figure 6**), indicating the high-quality crystalline products.

The Thermogravimetric analysis (TGA) data were also tested carefully for studying the stability of the four complexes (**Supplementary Figure 7**). It is found that complex **1** firstly loses its guest waters in ~30–113°C [observed (obsd.) ~5.9%, calculated (calcd.) ~4.7%] and then collapse the linkers gradually. For complex **2**, a plateau is observed from the beginning to 30°C and then a ~3.3% loss in ~30–201°C, which

**FIGURE 6** | The topological framework of **4**.



**FIGURE 7** | The $CO_2/CH_4$ sorption isotherms of **1a** at 195K.

matches well with the removal of two coordinated waters (calcd. ~4.0%); the second ~22% loss appears in ~315–366°C, which is attributed to a collapsed $m$-$H_2$bdc ligand, and then the rest of the ligand starts to decompose gradually. Complex **3** loses guest waters in ~30–100°C (obsd. ~6.3%, calcd. ~6.6%), then follows a plateau of stability to ~306°C, and then an abrupt 29% loss in ~306–349°C, matching with the $p$-bdc loss (calcd. ~30%). Complex **4** incurs a ~15.4% loss in ~30–267°C for reduction in all NMP molecules (calcd. ~16.1%), then holds the stability to ~357°C.

## Gas Sorption of Complexes 1 and 4

The gas capture isotherms were tested carefully to prove the void properties of **1** for $CO_2$ and $CH_4$. The crystalline product of **1** was soaked in $CH_2Cl_2$ for 24 h and then dried under vacuum at 80°C to afford the desolvated **1a**. The gas captures of **1a** were performed carefully at 195 and 273K, respectively. At 1 atm, the uptake amount is 55.1 cm$^3$ g$^{-1}$ (1.08 wt.%) for $CO_2$ (**Figure 7**), which is greatly higher than the $CH_4$ uptake (16.4 cm$^3$ g$^{-1}$, 0.12 wt.%) at 195K. The gas sorption of $CO_2/CH_4$ was also performed at 273K (**Supplementary Figure 9**), and the $CO_2/CH_4$ uptake is 29.6/11.0 cm$^3$ g$^{-1}$ (0.58/0.08 wt.%) at 1 atm, respectively. Interestingly, the hysteresis effect is found for the $CO_2$ sorption of **1a**, the reason of which might be the interactions of framework with $CO_2$ to hinder the $CO_2$ from the host framework in the sorption/desorption procedure (Biswas et al., 2013; Boldog et al., 2013; Liang et al., 2013; Han et al., 2017). Further, the PXRD patterns still closely matched well with the stimulated patterns of **1** (**Supplementary Figure 6**), indicating that the sample after heating retained the intact host framework.

Compared with complex **1**, **4** has preferable adsorption property, which may arise from introducing auxiliary $H_2$bpdc ligand to give rise to more active sites and the flexibility of two benzene rings. Thus, the sorption isotherms were measured for $N_2/CO_2/CH_4$ to verify the porosity of **4**. Herein, **4** is soaked in $CH_2Cl_2$ for 24 h and dried at 150°C under vacuum to
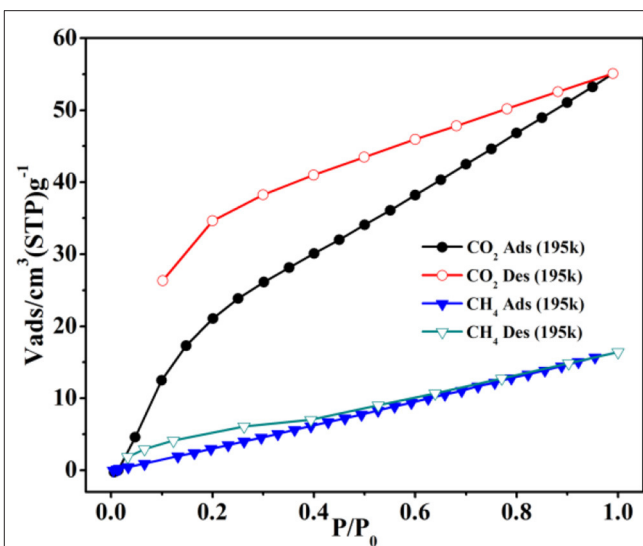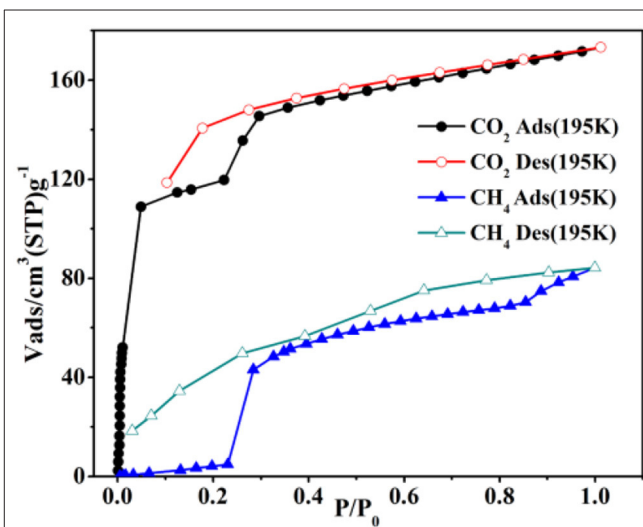


**FIGURE 8** | The $CO_2/CH_4$ sorption isotherms of **4a** at 195K.

yield the desolvated crystalline product (**4a**) successfully, which is proved by the combination of the TGA and FT-IR tests (**Supplementary Figure 8**). At 77K and 1 atm, the $N_2$ uptake is 8.74 cm$^3$ g$^{-1}$ and the capture isotherm has an obvious hysteresis in the sorption/desorption process (**Supplementary Figure 10**).

At 195K and 1 atm, the $CO_2$ sorption has a higher capture amount (34.04 wt.%, 173.28 cm$^3$ g$^{-1}$) to further prove the pore performances of **4a**. The Brunner-Emmet-Teller (BET) and Langmuir surface areas are 273.65/382.56 m$^2$ g$^{-1}$. Interestingly, the $CO_2$ sorption exhibits a double abrupt increase at 0.04, 0.22 atm as a significant hysteretic desorption curve (**Figure 8**). In the initial step, the $CO_2$ sorption amount is adsorbed as 109 cm$^3$ g$^{-1}$ (21.41 wt.%) for **4a**, and then the isotherm has a sudden increase in the second step ($P/P_0 = 0.2$) and finally keeps the saturation.
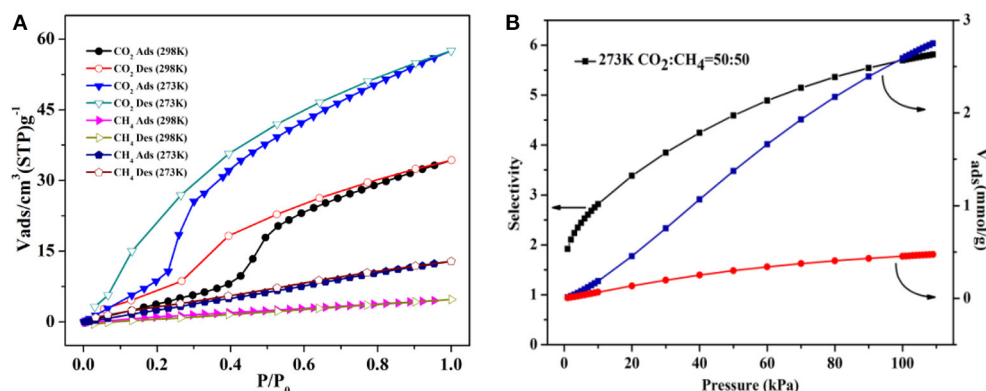
**FIGURE 9 | (A)** The $CO_2/CH_4$ isotherms of **4a** at 273/298K. **(B)** The ideal adsorbed solution theory (IAST) selectivity for equimolar $CO_2/CH_4$ mixture at 273K.

The desorption process does not retrace the capture process, which shows the different hysteresis, and the amount is 119 $cm^3$ $g^{-1}$ ($P/P_0 = 0.1$) at the end of desorption. The incomplete desorption suggests there exist the interactions of $CO_2$ and pore surface. Generally, this phenomenon in rigid metal-organic framework (MOFs) may be ascribed to the sorbate/sorbent interlocks as the gases capture by surfaces of the structure, obtaining the various pores as it breathes (Bezuidenhout et al., 2015; Ichikawa et al., 2016; Esfandiari et al., 2017). When at relatively lower pressures, the two distorted benzene groups of bpdc$^{2-}$ ligand make the pore open, thus, leading to a rather large hysteresis.

The sorption isotherm of $CH_4$ shows a lower amount (6.02 wt.%, 84.19 $cm^3$ $g^{-1}$) at 195K and 1 atm (**Figure 8**). However, it has a more obvious abrupt step with two sudden increases at 0.22/0.85 atm, which is similar to the $CO_2$ isotherm. The $CO_2$ is captured as 3.08 wt.% (43.23 $cm^3$ $g^{-1}$) for **4a** in the initial step, and then the isotherm holds a sharp increase ($P/P_0 > 0.85$) and finally keeps the saturation. And the desorption process also displays the several steps at the corresponding points. As a result, the large hysteresis loops happen, leading that the $CH_4$ is packed in the structure at the lower pressures and not released right now on decreasing the external pressure (Liu et al., 2013; Handke et al., 2014; Ju et al., 2015; Hiraide et al., 2017; Sun et al., 2017).

The $CO_2/CH_4$ sorption properties of **4a** were also explored at 273/298K. The $CO_2$ uptake amounts are 57.53 $cm^3$ $g^{-1}$ (11.3 wt.%) and 34.28 $cm^3$ $g^{-1}$ (6.7 wt.%) at 273/298 K, 1 atm (**Figure 9A**), and the $CH_4$ amounts are 12.83 $cm^3$ $g^{-1}$ (0.9 wt.%) and 4.75 $cm^3$ $g^{-1}$ (0.3 wt.%) at 273/298K. These results indicate that **4a** has the selectivity for $CO_2$ molecules, which is more evident at the higher temperature. Thus, the $CO_2/CH_4$ selectivity of **4a** is calculated by ideal adsorbed solution theory (IAST) at 273K (Chen et al., 2015) (**Supplementary Figure 11**). Here, the $CO_2/CH_4$ molar fraction is set as 50/50 to simulate the content of biogas mixture (**Figure 9B**). The results present that $CO_2$ selectivity rapidly ascends with increasing load for both mixed contents over $CH_4$, and the selectivity $CO_2/CH_4$ is calculated as 5.7 from the equimolar gas phase mixture at 1 atm.

The capture enthalpy ($Q_{st}$) was estimated to explore the $CO_2$ affinity via the Virial equation of sorption isotherms at
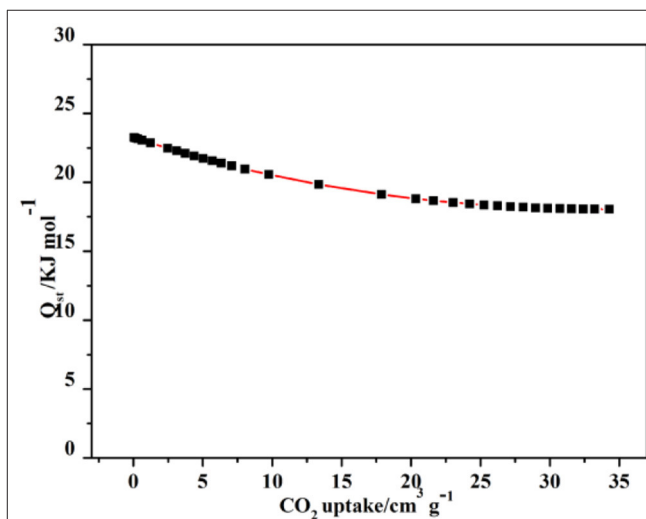


**FIGURE 10 |** The $CO_2$ $Q_{st}$ of **4a** at 273K.

273K (**Supplementary Figure 12**), revealing **4a** has a higher $CO_2$ affinity at high loading amount. The $Q_{st}$ has a slow decrease by the $CO_2$ increasing capture; however, it is 23.2 kJ mol$^{-1}$ at the final (**Figure 10**). This value is comparable to those of the hydrated HKUST-1, MAF-2, JUC-132, JLU-Liu, and NOTT-140 (30, 27, 30, 30, and 25 kJ/mol), but higher than those of most "benchmark CPs," such as CuBTTri, MOF-5, and UMCM-1 (21, 17, 12 kJ/mol) (Wang et al., 2015) Thereby, complex **4** may be explored as a great gas adsorbent in many fields.

## Luminescent Properties

Due to the great luminescent performances of the Hmdpt linker and d$^{10}$ complexes (Chou et al., 2014; Kumar et al., 2014; Hu et al., 2015; Ye et al., 2015; Wang et al., 2016; Hong et al., 2017; Lim et al., 2017), the solid-state photoluminescence properties have been studied for the four complexes and Hmdpt as well as the various auxiliary benzendicarboxylates at room temperature (**Figure 11** and **Supplementary Figure 13**), the emissions of
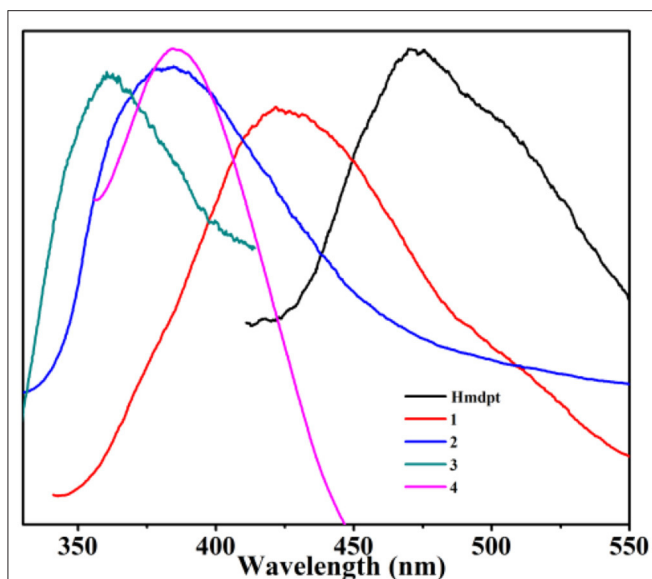
**FIGURE 11 |** The solid-state luminescent emission spectra of the four coordination polymers (CPs) and Hmdpt linker.

## CONCLUSION

In summary, four new CPs with rigid Hmdpt and different benzendicarboxylate linkers have been successfully obtained. The different auxiliary carboxylates resulted in a series of new various structural CPs. Complex **1** has a 2-fold interlocked **NbO** net; **2** presents the 2D three-connected **hcb** net; **3** shows the double-insertion 3D **fsh** supramolecular network; and **4** displays a 3D eight-connected **sqc117** net. The $CH_4/CO_2$ sorption behaviors of **1** and **4** have been carefully carried out at different temperatures. Remarkably, complex **4** has preferable sorption and high $CO_2$ selectivity, making it as a useful gas storage/separation functional material.

## DATA AVAILABILITY STATEMENT

The datasets presented in this study can be found in online repositories. The names of the repository/repositories and accession number(s) can be found in the article/**Supplementary Material**.

## AUTHOR CONTRIBUTIONS

All authors listed have made a substantial, direct and intellectual contribution to the work, and approved it for publication.

## SUPPLEMENTARY MATERIAL

The Supplementary Material for this article can be found online at: https://www.frontiersin.org/articles/10.3389/fchem.2020.616468/full#supplementary-material

which are given in **Supplementary Table 2**. The free Hmdpt shows the band at 472 nm when excited at 307 nm, attributing to the $\pi^* \to \pi$ transition of the intra-ligand (Lin et al., 2017). The four complexes have their specific emissions, the bands of which were presented at 425 nm ($\lambda_{ex} = 321$ nm) for **1**, 380 nm ($\lambda_{ex} = 305$ nm) for **2**, 360 nm ($\lambda_{ex} = 289$ nm) for **3**, as well as 386 nm ($\lambda_{ex} = 336$ nm) for **4**, respectively. These emission bands are greatly similar to the free Hmdpt emission for the $\pi-\pi^*$ or $n-\pi^*$ intra-ligand transition (Sun et al., 2013; Wenger, 2013; Zou et al., 2013; Chen et al., 2017). In contrast to the Hmdpt, the emissions of four CPs have the similar blue shifts, which are considered to be the energy transfer from the Hmdpt ligand to the Cd(II) centers for the ligand-to-metal charge transfer (LMCT) (Cao et al., 2017).

## REFERENCES

Bezuidenhout, C., Smith, V., Bhatt, P., Esterhuysen, C., and Barbour, L. (2015). Extreme carbon dioxide sorption hysteresis in open-channel rigid metal-organic frameworks. *Angew. Chem. Int. Ed.* 54, 2079–2083. doi: 10.1002/anie.201408933

Bhattacharya, B., Layek, A., Alam, M., Maity, D. K., Chakrabarti, S., Ray, P. P., et al. (2014). Cd(II) based metal-organic framework behaving as a Schottky barrier diode. *Chem. Commun.* 50, 7858–7861. doi: 10.1039/c4cc00827h

Bhattacharya, B., Maity, D. K., Layek, A., Jahiruddin, S., Halder, A., Dey, A., et al. (2016). Multifunctional mixed ligand metal organic frameworks: X-ray structure, adsorption, luminescence and electrical conductivity with theoretical correlation. *CrystEngComm.* 18, 5754–5763. doi: 10.1039/C6CE01173J

Biswas, S., Couck, S., Denysenko, D., Bhunia, A., Grzywa, M., Denayer, J., et al. (2013). Sorption and breathing properties of difluorinated MIL-47 and Al-MIL-53 frameworks. *Micropor. Mesopor. Mat.* 181, 175–181. doi: 10.1016/j.micromeso.2013.07.030

Blandez, J. F., Portillo, A. S., Navalón, S., Álvaro, M., Horcajada P, and García, H. (2016). Influence of functionalization of terephthalate linker on the catalytic activity of UiO-66 for epoxide ring opening. *J. Mol. Cat. A Chem.* 425, 332–339. doi: 10.1016/j.molcata.2016.10.022

Boldog, I., Domasevitch, K., Baburin, I., Ott, H., Gil-Hernandez, B., Sanchiz, J., et al. (2013). A rare alb-4,8-Cmce metal-coordination network based on tetrazolate and phosphonate functionalized 1,3,5,7-tetraphenyladamantane. *CrystEngComm.* 15, 1235–1243. doi: 10.1039/C2CE26819A

Cao, L., Li, H., Xu, H., Wei, Y., and Zang, S. (2017). Diverse dissolution-recrystallization structural transformations and sequential Förster resonance energy transfer behavior of a luminescent porous Cd-MOF. *Dalton Trans.* 46, 11656–11663. doi: 10.1039/C7DT02697H

Chen, D., Ma, X., Shi, W., and Cheng, P. (2015). Solvent-induced topological diversity of two Zn(II) metal-organic frameworks and high sensitivity in recyclable detection of nitrobenzene. *Cryst. Growth Des.* 15, 3999–4004. doi: 10.1021/acs.cgd.5b00614

Chen, S. S., Qiao, R., Sheng, L. Q., Zhao, Y., Yang, S., Chen, M. M., et al. (2013). Cadmium(II) and zinc(II) complexes with rigid 1-(1H-imidazol-4-yl)-3-(4H-tetrazol-5-yl)benzene and varied carboxylate ligands. *CrystEngComm.* 15, 5713–5725. doi: 10.1039/C3CE40150B

Chen, W., Lin, Y., Zhang, X., Xu, N., and Cheng, P. (2017). A new cadmium-organic framework fluorescent sensor for Al3+ and Ca2+ ions in aqueous medium. *Inorg. Chem. Commun.* 79, 29–32. doi: 10.1016/j.inoche.2017.03.010

Chou, C., Hu, F., Wu, K., Duan, T., Chi, Y., Liu, S., et al. (2014). 4,4′,5,5′-Tetracarboxy-2,2′-bipyridine Ru(II) sensitizers for dye-sensitized solar cells. *Inorg. Chem.* 53, 8593–8599. doi: 10.1021/ic501178f

DeFuria, M. D., Zeller, M., and Genna, D. T. (2016). Removal of pharmaceuticals from water via π-π stacking interactions in perfluorinated metal–organic frameworks. *Cryst. Growth Des.* 16, 3530–3534. doi: 10.1021/acs.cgd.6b00488

Dey, A., Bairagi, D., and Biradha, K. (2017). MOFs with PCU topology for the inclusion of one-dimensional water cages: selective sorption of water vapor, CO₂, and dyes and luminescence properties. *Cryst. Growth Des.* 17, 3885–3892. doi: 10.1021/acs.cgd.7b00502

Du, L., Wang, H., Liu, G., Xie, D., Guo, F., Hou, L., et al. (2015). Structural diversity of five new bitriazole-based complexes: luminescence, sorption, and magnetic properties. *Dalton Trans.* 44, 1110–1119. doi: 10.1039/C4DT03129F

Esfandiari, K., Ghoreyshi, A., and Jahanshahi, M. (2017). Using artificial neural network and ideal adsorbed solution theory for predicting the CO₂/ch4 selectivities of metal-organic frameworks: a comparative study. *Ind. Eng. Chem. Res.* 56, 14610–14622. doi: 10.1021/acs.iecr.7b03008

Han, G., Wang, K., Peng, Y., Zhang, Y., Huang, H., and Zhong, C. (2017). Enhancing higher hydrocarbons capture for natural gas upgrading by tuning van der waals interactions in fcu-type Zr-MOFs. *Ind. Eng. Chem. Res.* 56, 14633–14641. doi: 10.1021/acs.iecr.7b03341

Handke, M., Weber, H., Lange, M., Mollmer, J., Lincke, J., Glaser, R., et al. (2014). Network flexibility: control of gate opening in an isostructural series of Ag-MOFs by linker substitution. *Inorg. Chem.* 53, 7599–7607. doi: 10.1021/ic500908r

Hiraide, S., Tanaka, H., Ishikawa, N., and Miyahara, M. (2017). Intrinsic thermal management capabilities of flexible metal-organic frameworks for carbon dioxide separation and capture. *ACS Appl. Mater. Interfaces* 9, 41066–41077. doi: 10.1021/acsami.7b13771

Hong, X. J., Wei, Q., Cai, Y. P., Zheng, S. R., Yu, Y., Fan, Y. Z., et al. (2017). 2-fold interpenetrating bifunctional Cd-metal-organic frameworks:highly selective adsorption for CO2 and sensitive luminescent sensing of nitro aromatic 2,4,6-trinitrophenol. *ACS Appl. Mater. Interfaces* 9, 4701–4708. doi: 10.1021/acsami.6b14051

Hu, F., Shi, Y., Chen, H., and Lang, J. (2015). A Zn(II) coordination polymer and its photocycloaddition product: syntheses, structures, selective luminescence sensing of iron(III) ions and selective absorption of dyes. *Dalton Trans.* 44, 18795–18803. doi: 10.1039/C5DT03094C

Ichikawa, M., Kondo A; Noguchi, H., Kojima, N., Ohba, T., H., Kajiro H, Hattori, Y., et al. (2016). Double-step gate phenomenon in CO2 sorption of an elastic layer-structured MOF. *Langmuir* 32, 9722–9726. doi: 10.1021/acs.langmuir.6b02551

Islamoglu, T., Goswami, S., Li, Z. Y., Howarth, A. J., Farha, O. K., and Hupp, J. T. (2017). Postsynthetic tuning of metal-organic frameworks for targeted applications. *Acc. Chem. Res.* 50, 805–813. doi: 10.1021/acs.accounts.6b00577

Jin, J., Wu, J., Yang, G., Wu, Y., and Wang, Y. (2016). A microporous anionic metal-organic framework for a highly selective and sensitive electrochemical sensor of Cu2+ ions. *Chem. Commun.* 52, 8475–8478. doi: 10.1039/C6CC03063G

Ju, P., Jiang, L., and Lu, T. (2015). A three-dimensional dynamic metal-organic framework with fourfold interpenetrating diamondoid networks and selective adsorption properties. *Inorg. Chem.* 54, 6291–6295. doi: 10.1021/acs.inorgchem.5b00592

Ju, Z. F., Yan, S. C., and Yuan, D. Q. (2016). *De novo* tailoring pore morphologies and sizes for different substrates in a urea-containing MOFs catalytic platform. *Chem. Mater.* 28, 2000–2010. doi: 10.1021/acs.chemmater.5b03999

Kariem, M., Kumar, M., Yawer, M., and Sheikh, H. N. (2017). Solvothermal synthesis and structure of coordination polymers of Nd(III) and Dy(III) with rigid isophthalic acid derivatives and flexible adipic acid. *J. Mol. Struct.* 1150, 438–446. doi: 10.1016/j.molstruc.2017.08.111

Kumar, P., Paul, A., and Deep, A. (2014). A luminescent nanocrystal metal organic framework for chemosensing of nitro group containing organophosphate pesticides. *Anal. Methods.* 6, 4095–4101. doi: 10.1039/C3AY42189A

Lannoye, J., Voorde, B. V., Bozbiyik, B., Reinsch, H., Denayer, J., and Vos, D. D. (2016). An aliphatic copper metal-organic framework as versatile shape selective adsorbent in liquid phase separations. *Microp. Mesop. Mater.* 226, 292–298. doi: 10.1016/j.micromeso.2016.01.044

Li, J., Yang, G., Wei, S., Gao, R., Bai, N., and Wang, Y. (2015). Two microporous metal-organic frameworks with suitable pore size displaying the high CO2/CH4 selectivity. *Cryst. Growth Des.* 15, 5382–5387. doi: 10.1021/acs.cgd.5b00997

Li, J. X., Li, Y. F., Liu, L. W., and Cui, G. H. (2018). Luminescence, electrochemical and photocatalytic properties of sub-micron nickel(II) and cobalt(II) coordination polymers synthesized by sonochemical process. *Ultrason. Sonochem.* 41, 196–205. doi: 10.1016/j.ultsonch.2017.09.039

Li, N., Chang, Z., Huang, H., Feng, R., He, W. W., Zhong, M., et al. (2019). Specific K+ binding sites as CO2 traps in a porous MOF for enhanced CO₂ selective sorption. *Small* 15:1900426. doi: 10.1002/smll.201900426

Li, P. Z., Wang, X. J., Liu, J., Lim, J. S., Zou, R. Q., and Zhao, Y. L. (2016). A triazole-containing metal-organic framework as a highly effective and substrate size-dependent catalyst for CO2 conversion. *J. Am. Chem. Soc.* 138, 2142–2145. doi: 10.1021/jacs.5b13335

Li, X. Y., Shi, W. J., Wang, X. Q., Ma, L. N., Hou, L., and Wang, Y. Y. (2017). Luminescence modulation, white light emission, and energy transfer in a family of lanthanide metal-organic frameworks based on a planar π-conjugated ligand. *Cryst. Growth Des.* 17, 4217–4224. doi: 10.1021/acs.cgd.7b00530]

Liang, L., Yang, C., Ma, Y., and Deng, H. (2013). In situ hydrothermal syntheses of five new cadmium(II) coordination polymers based on 3-(1H-tetrazol-5-yl)benzoate ligand. *CrystEngComm.* 15, 365–375. doi: 10.1039/C2CE26720A

Lim, S., Jeong, S., Kang, D., Song, J., Jo, H., Lee, W., et al. (2017). Luminescent metal-organic framework sensor: exceptional Cd2+ turn-on detection and first *in situ* visualization of Cd2+ ion diffusion into a crystal. *Chem. Eur. J.* 23, 4803–4809. doi: 10.1002/chem.201604252

Lin, J. B., Lin, R. B., Cheng, X. N., Zhang, J. P., and Chen, X. M. (2011). Solvent/additive-free synthesis of porous/zeolitic metal azolate frameworks from metal oxide/hydroxidew. *Chem. Commun.* 47, 9185–9187. doi: 10.1039/C1CC12763B

Lin, J. B., Zhang, J. P., and Chen, X. M. (2010). Nonclassical active site for enhanced gas sorption in porous coordination polymer. *J. Am. Chem. Soc.* 132, 6654–6656. doi: 10.1021/ja1009635

Lin, Y., Zhang, X., Chen, W., Shi, W., and Cheng, P. (2017). Three cadmium coordination polymers with carboxylate and pyridine mixed ligands: luminescent sensors for Fe(III) and Cr(VI) ions in an aqueous medium. *Inorg. Chem.* 56, 11768–11778. doi: 10.1021/acs.inorgchem.7b01790

Liu, B., Li, Y., Hou, L., Yang, G., Wang, Y., and Shi, Q. (2013). Dynamic Zn-based metal-organic framework: stepwise adsorption, hysteretic desorption and selective carbon dioxide uptake. *J. Mater. Chem. A.* 1, 6535–6538. doi: 10.1039/C3TA10918F

Liu, J. Y., Wang, Q., Zhang, L. J., Y. B., Xu, Y. Y., Zhang X, Zhao, C. Y., et al. (2014). Anion-exchange and anthracene-encapsulation within copper(II) and manganese(II)-triazole metal-organic confined space in a single crystal-to-single crystal transformation fashion. *Inorg. Chem.* 53, 5972–5985. doi: 10.1021/ic500183b

Lu, N. Y., Zhou, F., Jia, H. H., Wang, H. Y., Fan, B. B., and Li, R. F. (2017). Dry-gel conversion synthesis of Zr-based metal-organic frameworks. *Ind. Eng. Chem. Res.* 56, 14155–14163. doi: 10.1021/acs.iecr.7b04010

Manna, B., Desai, A. V., and Ghosh, S. K. (2016). Neutral N-donor ligand based flexible metal-organic frameworks. *Dalton Trans.* 45, 4060–4072. doi: 10.1039/C5DT03443D

Pachfule, P., and Banerjee, R. (2011). Porous nitrogen rich cadmium-tetrazolate based Metal Organic Framework (MOF) for H2 and CO2 uptake. *Cryst. Growth Des.* 11, 5176–5181. doi: 10.1021/cg201054f

Park, S. S., Hendon, C. H., Fielding, A. J., Walsh, A., Keeffe, M., and Dinca, M. (2017). The organic secondary building unit: strong intermolecular π interactions define topology in MIT-25, a mesoporous MOF with proton-replete channels. *J. Am. Chem. Soc.* 139, 3619–3622. doi: 10.1021/jacs.6b13176

Qin, L., Ju, Z., Wang, Z., Meng, F., Zheng, H., and Chen, J. (2014). Interpenetrated metal-organic framework with selective gas adsorption and luminescent properties. *Cryst. Growth Des.* 14, 2742–2746. doi: 10.1021/cg500269h

Rosa, I. M. L., Costa, M. C. S., Vitto, B. S., Amorim, L., Correa, C. C., Pinheiro, C. B., et al. (2016). Influence of synthetic methods in the structure and dimensionality of coordination polymers. *Cryst. Growth Des.* 16, 1606–1616. doi: 10.1021/acs.cgd.5b01716

Sheldrick, G. M. (1997). *SHELXL-97. Program for Refinement of Crystal Structures.* Gottingen: University of Göttingen.

Smith, M. K., Angle, S. R., and Northrop, B. H. (2015). Preparation and analysis of cyclodextrin-based metal-organic frameworks: laboratory experiments adaptable for high school through advanced undergraduate students. *J. Chem. Educ.* 92, 368–372. doi: 10.1021/ed500540t

Song, J. Y., Ahmed, I., Seo, P. W., and Jhung, S. H. (2016). UiO-66-type metal-organic framework with free carboxylic acid:versatile adsorbents via h-bond for both aqueous and nonaqueous phases. *ACS. Appl. Mater. Interfaces* 8, 27394–27402. doi: 10.1021/acsami.6b10098

Song, Y., Feng, M. L., Wu, Z. F., and Huang, X. Y. (2015). Solvent-assisted construction of diverse Mg-TDC coordination polymers. *CrystEngComm.* 17, 1348–1357. doi: 10.1039/C4CE02288B

Sun, D., Han, L., Yuan, S., Deng, Y., Xu, M., and Sun, D. (2013). Four new Cd(II) coordination polymers with mixed multidentate N-donors and biphenyl-based polycarboxylate ligands: syntheses, structures, and photoluminescent properties. *Cryst. Growth Des.* 13, 377–385. doi: 10.1021/cg301573c

Sun, Y., Hu, Z., Zhao, D., and Zeng, K. (2017). Probing nanoscale functionalities of metal-organic framework nanocrystals. *Nanoscale* 9, 12163–12169. doi: 10.1039/C7NR04245K

Waller, P. J., Gandara, F., and Yaghi, O. M. (2015). Chemistry of covalent organic frameworks. *Acc. Chem. Res.* 48, 3053–3063. doi: 10.1021/acs.accounts.5b00369

Wang, D., Liu, B., Yao, S., Wang, T., Li, G., Huo, Q., et al. (2015). A polyhedral metal-organic framework based on the supermolecular building block strategy exhibiting high performance for carbon dioxide capture and separation of light hydrocarbons. *Chem. Commun.* 51, 15287–15289. doi: 10.1039/C5CC06162H

Wang, H., Yi, F. Y., Dang, S., Tian, W. G., and Sun, Z. M. (2014). Rational assembly of Co/Cd-MOFs featuring topological variation. *Cryst. Growth Des.* 14, 147–156. doi: 10.1021/cg4013334

Wang, S., and Wang, X. C. (2015). Multifunctional metal-organic frameworks for photocatalysis. *Small* 11, 3097–3112. doi: 10.1002/smll.201500084

Wang, Z., Qin, L., Chen, J., and Zheng, H. (2016). H-bonding interactions induced two isostructural Cd(II) metal-organic frameworks showing different selective detection of nitroaromatic explosives. *Inorg. Chem.* 55, 10999–11005. doi: 10.1021/acs.inorgchem.6b01521

Wenger, O. (2013). Vapochromism in organometallic and coordination complexes: chemical sensors for volatile organic compounds. *Chem. Rev.* 113, 3686–3733 doi: 10.1021/cr300396p

Wheeler, S. E. (2013). Understanding substituent effects in noncovalent interactions involving aromatic rings. *Chem. Res.* 46, 1029–1038. doi: 10.1021/ar300109n

Wu, Y., Qian, J., Yang, G., Yang, F., Liang, Y., Zhang, W., et al. (2017). High $CO_2$ uptake capacity and selectivity in a fascinating nanotube-based metal-organic framework. *Inorg. Chem.* 56, 908–913. doi: 10.1021/acs.inorgchem.6b02491

Xing, S., and Janiak, C. (2020). Design and properties of multiple-emitter luminescent metal–organic frameworks. *Chem. Commun.* 56, 12290–12306. doi: 10.1039/D0CC04733C

Yadav, V. N., and Gorbitz, C. H. (2013). A supramolecular 2:1 guanidinium-carboxylate based building block for generation of water channels and clusters in organic materials. *CrystEngComm.* 15, 439–442. doi: 10.1039/C2CE26572A

Yan, Y. T., Zhang, S. S., Yang, G. P., Zhang, W. Y., Zhang, F., Cao, F., et al. (2017). The influence of coordination modes and active sites of a 5-(triazol-1-yl) nicotinic ligand on the assembly of diverse MOFs. *Dalton Trans.* 46, 9784–9793. doi: 10.1039/C7DT01523B

Yao, R. X., Cui, X., Jia, X. X., Zhang, F. Q., and Zhang, X. M. (2016). A luminescent zinc(II) Metal-Organic Framework (MOF) with conjugated π-electron ligand for high iodine capture and nitroexplosive detection. *Inorg. Chem.* 55, 9270–9275. doi: 10.1021/acs.inorgchem.6b01312

Ye, R., Zhang, X., Zhai, J., Qin, Y., Zhang, L., Yao, Y., et al. (2015). N-donor ligands enhancing luminescence properties of seven Zn/Cd(II) MOFs based on a large rigid π-conjugated carboxylate ligand. *CrystEngComm.* 17, 9155–9166. doi: 10.1039/C5CE01884F

Zhang, S., Jiang, F., Wu, M., Chen, L., Luo, J., and Hong, M. (2013). pH modulated assembly in the mixed-ligand system Cd(II)-dpstc-phen: structural diversity and luminescent properties. *CrystEngComm.* 15, 3992–4002. doi: 10.1039/C3CE27108K

Zhang, X., Chen, Z., Liu, X., Hanna, S. L., Wang, X., Taheri-Ledari, R., et al. (2020). A historical overview of the activation and porosity of metal–organic frameworks. *Chem. Soc. Rev.* 49, 7406–7427. doi: 10.1039/D0CS00997K

Zhang, X., Zhou, J., Shi, W., Zhang, Z., and Cheng, P. (2013). Two cadmium(II) coordination polymers constructed by carboxylate and pyridine mixed ligands: synthesis, structure and luminescent properties. *CrystEngComm.* 15, 9738–9744. doi: 10.1039/C3CE41073K

Zou, J. Y., Gao, H. L., Shi, W., Cui, J. Z., and Cheng, P. (2013). Auxiliary ligand-assisted structural diversities of three metal-organic frameworks with potassium 1H-1,2,3-triazole-4,5 -dicarboxylic acid: syntheses, crystal structures and luminescence properties. *CrystEngComm.* 15, 2682–2687. doi: 10.1039/C3CE26854C

# Advantages of publishing in Frontiers

**OPEN ACCESS**
Articles are free to read for greatest visibility and readership

**FAST PUBLICATION**
Around 90 days from submission to decision

**HIGH QUALITY PEER-REVIEW**
Rigorous, collaborative, and constructive peer-review

**TRANSPARENT PEER-REVIEW**
Editors and reviewers acknowledged by name on published articles

**Frontiers**
Avenue du Tribunal-Fédéral 34
1005 Lausanne | Switzerland

**Visit us:** www.frontiersin.org
**Contact us:** frontiersin.org/about/contact

**REPRODUCIBILITY OF RESEARCH**
Support open data and methods to enhance research reproducibility

**DIGITAL PUBLISHING**
Articles designed for optimal readership across devices

**FOLLOW US**
@frontiersin

**IMPACT METRICS**
Advanced article metrics track visibility across digital media

**EXTENSIVE PROMOTION**
Marketing and promotion of impactful research

**LOOP RESEARCH NETWORK**
Our network increases your article's readership